4. Thin film mechanics

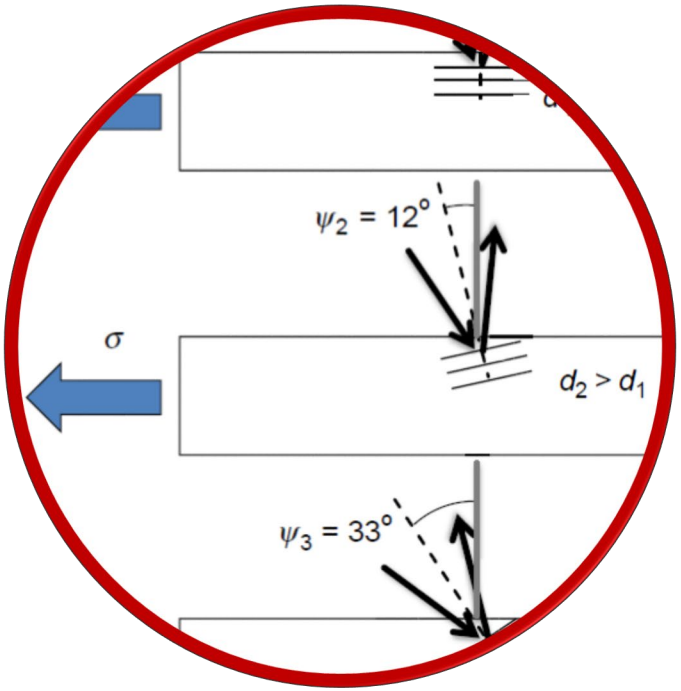

Mechanics of thin films and coated components

Further reading:

- J. Mencik: Mechanics of components with treated or coated surfaces, Springer, New York, 1995
- L.B. Freund & S. Suresh, Thin Film Materials, Cambridge University Press, 2006

Mechanics of thin films and coated components

- Coated components are ubiquitous in many industrial applications
- Stresses can appear in the system due to
  - Deposition process
  - Thermal loading
  - Mechanical loading
- Analytical solutions can help to assess the situation
  - For simple geometries
  - Far away from edges
  - Steady state heat-flow
- Analytical solutions give a fast insight in potential mechanisms and allow predicting potential trends
- For more complex cases, finite element simulations offer higher precision, but offer only single solution per simulation

Elastic stresses in bimaterial plates

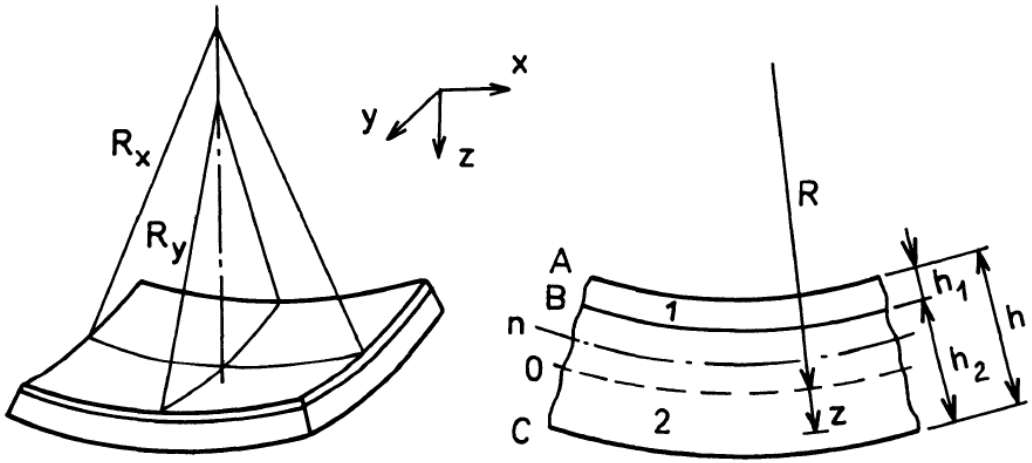

Fig. 13 Bi-layer plate - general layout and coordinate system.

- Analytical modeling of coated components can offer fast insights into the possible failure mechanisms and the factors influencing system performance
- First, we will define the stress and strain distribution inside the layered system as well as their relationships with the external forces and moments
- Then, we will discuss different loading scenarios in more detail

J. Mencik, Springer, 1995

Elastic stresses in bimaterial plates

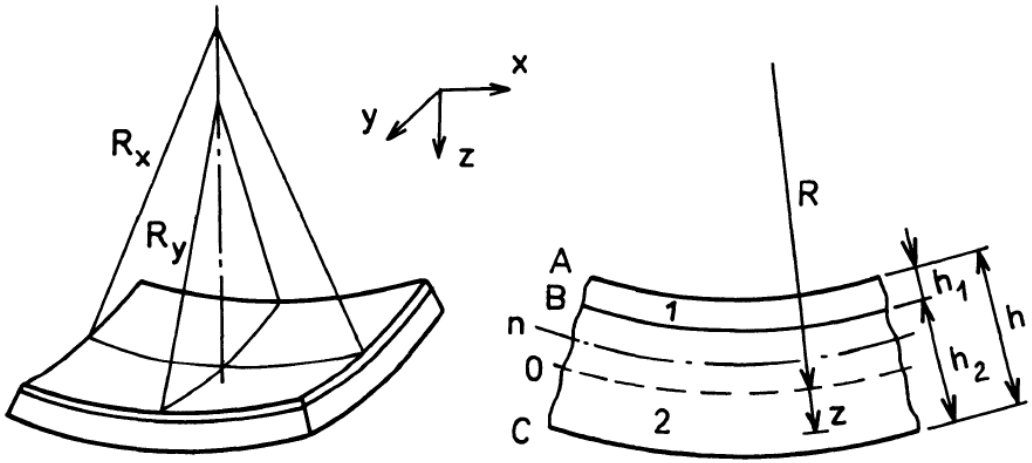

Fig. 13 Bi-layer plate - general layout and coordinate system.

Assumptions:

- System deforms according to Kirchhoff theory of thin plates:
  - normal stress component $\sigma_{zz} = 0$
  - material lines that are straight and perpendicular to the midplane of the coated substrate initially remain so after deformation
  - all components of displacement gradient are very small compared to unity so that linear theory of elasticity is applicable

J. Mencik, Springer, 1995

Stresses caused by differences in thermal expansion

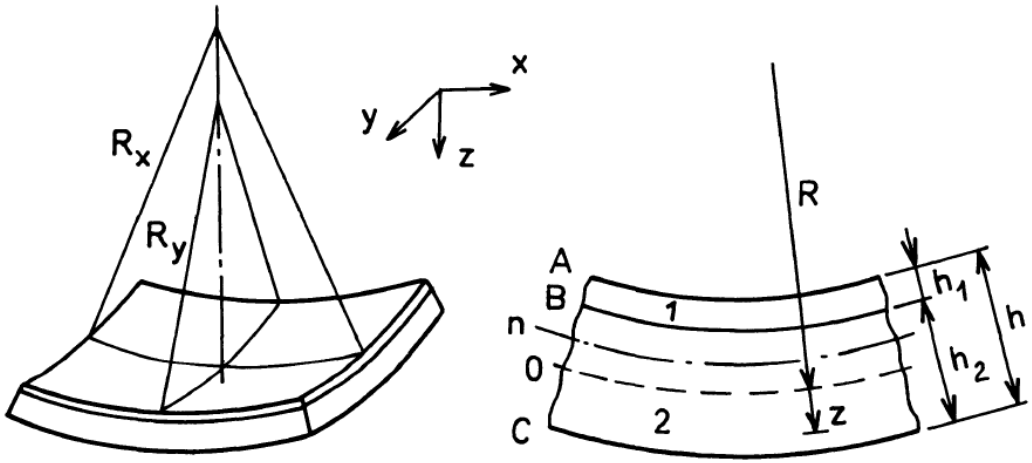

Fig. 13 **Bi-layer plate - general layout and coordinate system.**

- Differences in thermal expansion coefficients of film and substrate will lead to stresses and can cause different effects depending on the boundary conditions and properties, e.g.
  - Substrate bending
  - Interface failure leading to delamination
  - Cracking in the film
- Analytical modeling of the situation can give a quick overview of the relevant factors.

J. Mencik, Springer, 1995

Stresses caused by differences in thermal expansion

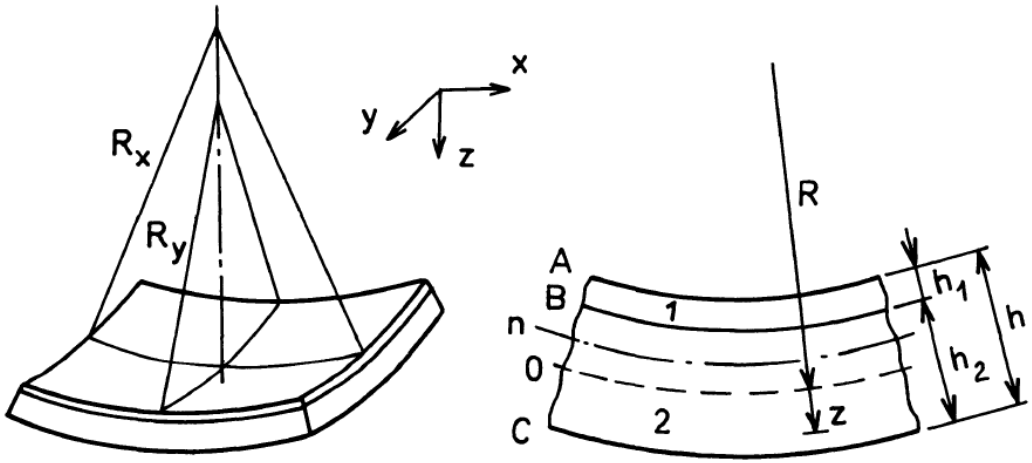

Fig. 13 Bi-layer plate - general layout and coordinate system.

- Stresses distribution in layer (1) and substrate (2)

$$\sigma_1(z) = E_1'[\epsilon(z) + \alpha_1[T_0 - T(z)]]$$

$$\sigma_2(z) = E_2'[\epsilon(z) + \alpha_2[T_0 - T(z)]]$$

- Biaxial moduli of elasticity of layer (1) and substrate (2)

$$E_1' = E_1/(1 - \nu_1)$$

$$E_2' = E_2/(1 - \nu_2)$$

Stresses caused by differences in thermal expansion

- **Case 1: No deformation of coated plate**
  - Plate remains flat, strains are constant within layer and substrate

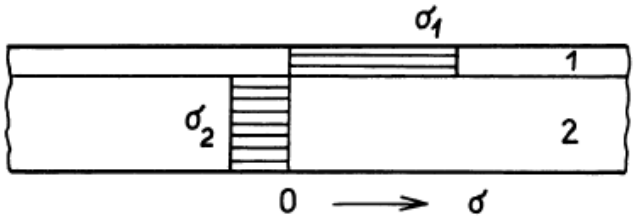

- Constant strain: $$\epsilon_0 = - \frac{\alpha_1 E_1' h_1 + \alpha_2 E_2' h_2}{E_1' h_1 + E_2' h_2} (T_0 - T)$$

- Stress in the thin film (1): $$\sigma_1 = \frac{(\alpha_1 - \alpha_2)(T_0 - T)}{\frac{1 - \nu_1}{E_1} - \frac{1 - \nu_2}{E_2} \frac{h_1}{h_2}}$$

- Stress in the substrate (2): $$\sigma_2 = - \sigma_1 \frac{h_1}{h_2}$$

Stresses caused by differences in thermal expansion

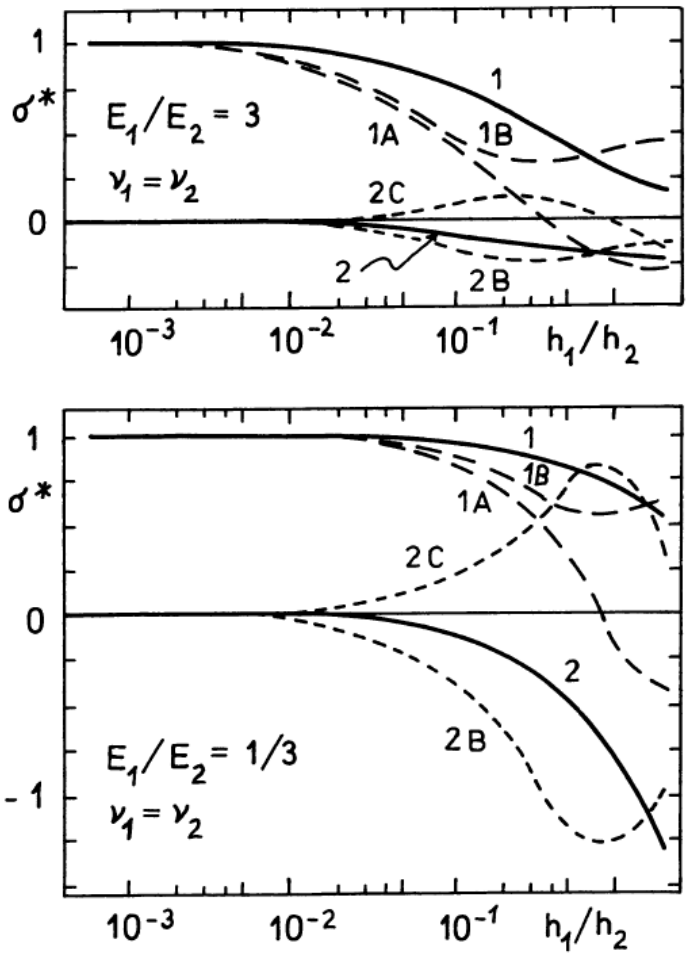

Fig. 15 Stresses due to a difference in thermal expansion versus the ratio of the thickness of the coating (h_1) and the substrate (h_2). ——— plate without deflection; – – – – – and · · · · · · plates with free deflection; $\sigma = \sigma^* (\alpha_1 - \alpha_2)(T_0 - T) E_1 /(1 - \nu_1)$

- All stresses increase for
  - Larger difference in a
  - Larger temperature interval
  - Higher E_i and v_i
- Stresses also depend on
  - Ratio of thicknesses h_1/h_2
  - Ratio E_1/E_2
  - Boundary conditions of the plate (free, fixed)

J. Mencik, Springer, 1995

Stresses caused by differences in thermal expansion

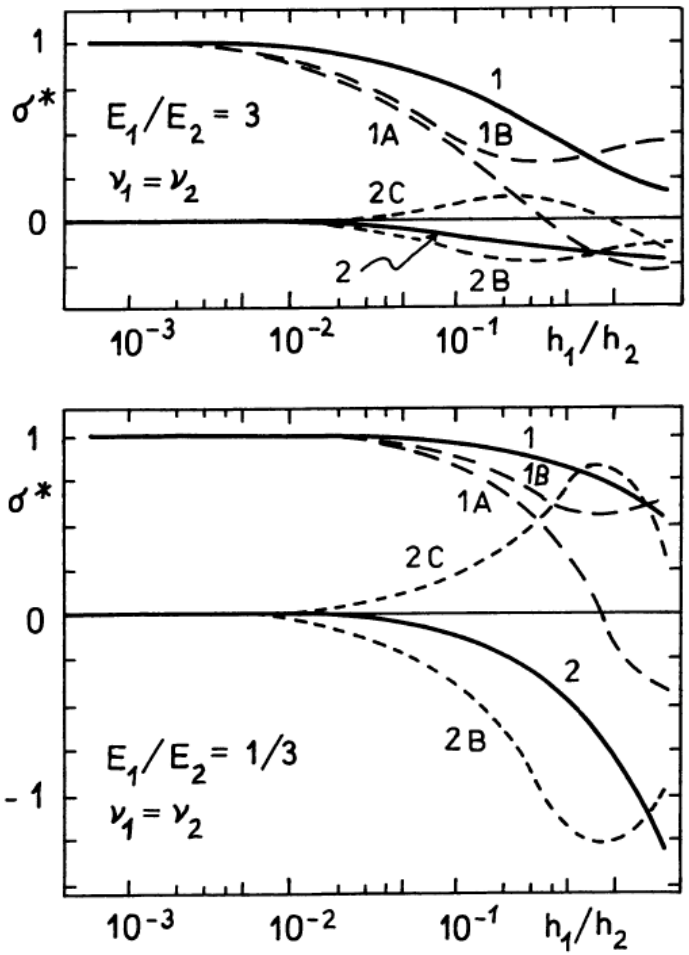

Fig. 15 Stresses due to a difference in thermal expansion versus the ratio of the thickness of the coating (h_1) and the substrate (h_2). ——— plate without deflection; – – – – – and · · · · · · plates with free deflection; $\sigma = \sigma^* (\alpha_1 - \alpha_2)(T_0 - T) E_1 /(1 - \nu_1)$

- For increasing h_1/h_2
  - Layer stress decreases
  - Substrate stress increases
- These changes start at lower h_1/h_2 and are larger for
  - Higher stiffness ratio E_1/E_2

J. Mencik, Springer, 1995

Stresses caused by differences in thermal expansion

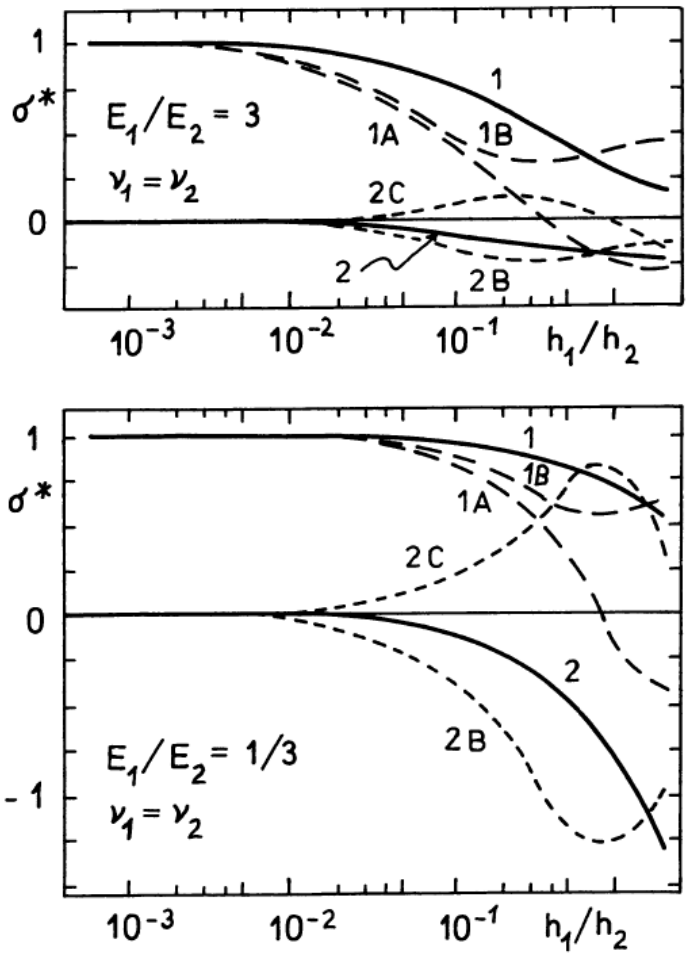

Fig. 15 Stresses due to a difference in thermal expansion versus the ratio of the thickness of the coating (h_1) and the substrate (h_2). ——— plate without deflection; – – – – – and · · · · · · plates with free deflection; $\sigma = \sigma^* (\alpha_1 - \alpha_2)(T_0 - T) E_1 /(1 - \nu_1)$

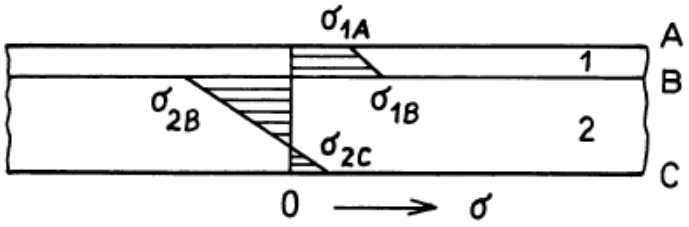

- Due to superposition of tension and bending stresses:
  - σ2B has opposite sign as σ1B
  - σ2C has the same sign as σ1A
  - σ1B is always larger than σ1A

J. Mencik, Springer, 1995

Application example: wafer curvature measurement

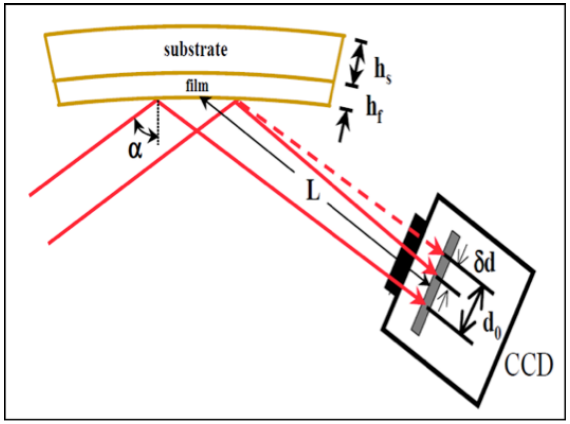

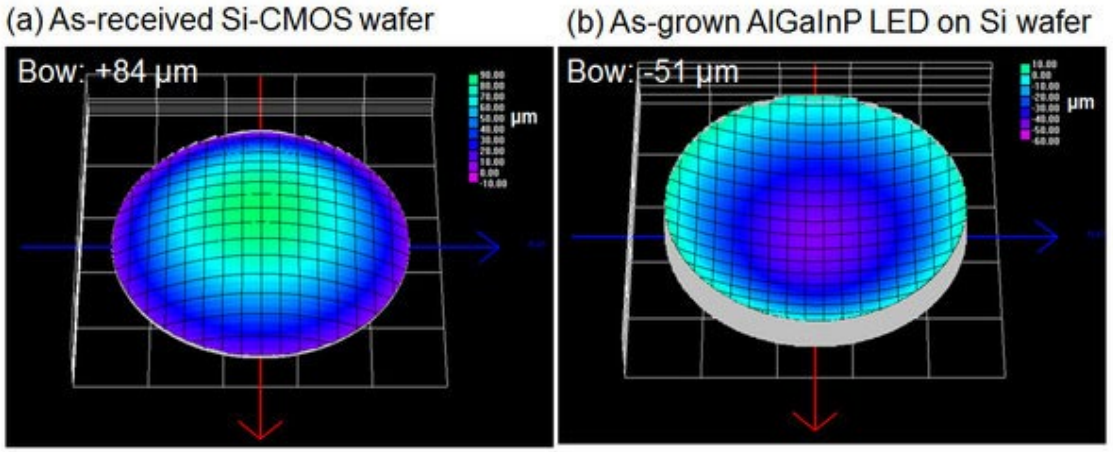

- Differential beam spacing $\delta d/d_0$ caused by a bending of the film/substrate stack is measured
- This can be related to to differences in film stress and thermal expansion coefficient.
- The high resolution of the differential beam spacing ensures high measurement sensitivity of about $6 \cdot 10^{-5}$ GPa·µm stress-thickness product

Thermal barrier coatings

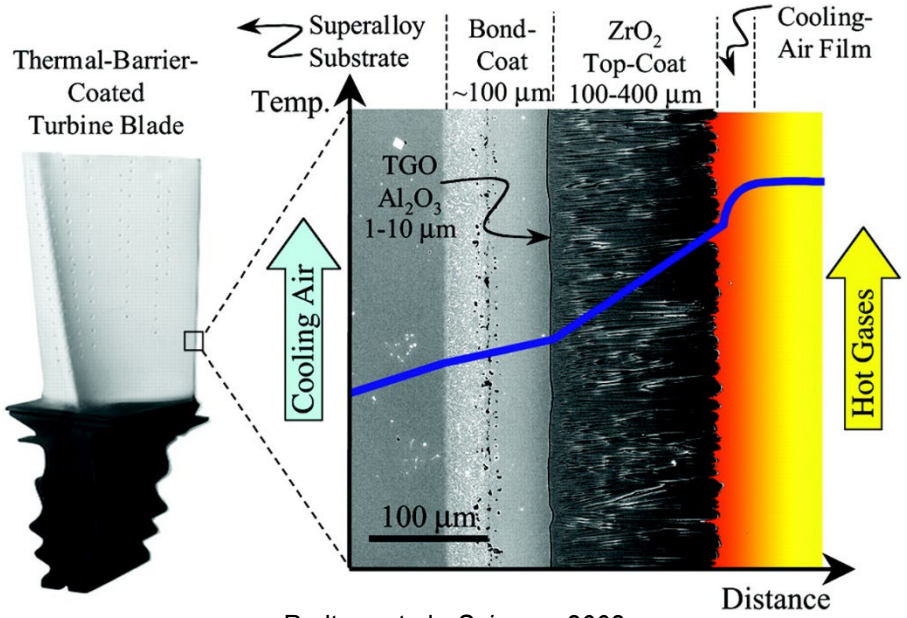

Padture et al., *Science, 2002*

- Thermal barrier coatings are used today to provide thermal insulation for metallic components in gas turbines
- Low thermal conductivity leads to significant temperature gradient in the coated system
- Differences in temperature and thermal expansion coefficients between TBC, BC, and substrate lead to stresses that can cause cracking and delamination

Stresses caused by inhomogeneous temperature distribution

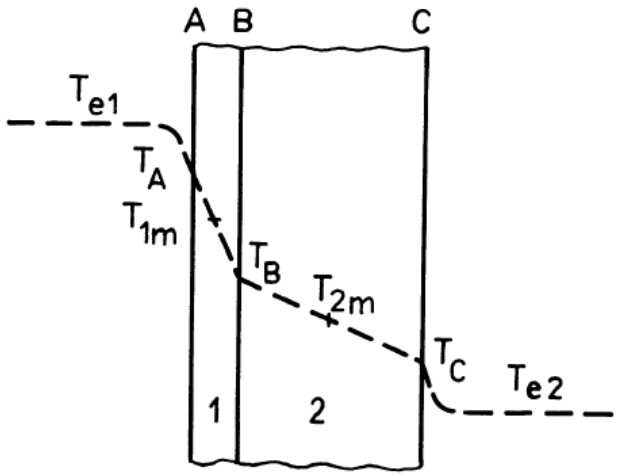

Fig. 16 Temperature distribution in a bi-layer plate, steady heat flow.

- Inhomogeneous temperature distribution inside a coated component leads to thermal stresses
- To determine stresses, the temperature profile must be known

J. Mencik, Springer, 1995

Stresses caused by inhomogeneous temperature distribution

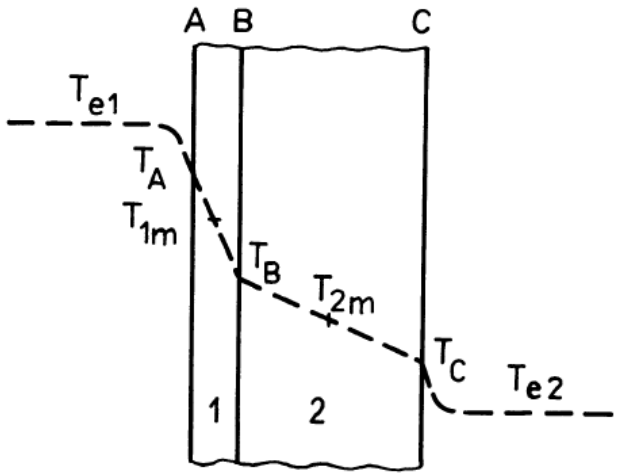

Fig. 16 Temperature distribution in a bi-layer plate, steady heat flow.

- Simple case: steady state heat flow through coated plane wall
  - Linear temperature distribution: Only temperatures at surfaces and at the interface must be determined
  - Stresses are biaxially isotropic and also linearly distributed.

Stresses caused by inhomogeneous temperature distribution

- If plate cannot deflect: 1/R = 0, $\varepsilon(z)=\varepsilon_0$, P=0
- Stresses at surface and interface in layer and substrate:

$$\sigma_{1A,B} = E_1' \left(\frac{\alpha_2 \Delta T_2 - \alpha_1 \Delta T_1}{1 + \eta' \kappa} + \alpha_1 (T_{1m} - T_{A,B}) \right)$$

$$T_{1m} = (T_A + T_B)/2$$

$$T_1 = T_{1m} - T_0$$

$$\sigma_{2B,C} = E_2' \left(\frac{\alpha_1 \Delta T_1 - \alpha_2 \Delta T_2}{1 + 1/(\eta' \kappa)} + \alpha_2 (T_{2m} - T_{B,C}) \right)$$

$$T_{2m} = (T_B + T_C)/2$$

$$T_2 = T_{2m} - T_0$$

J. Mencik, Springer, 1995

Stresses caused by inhomogeneous temperature distribution

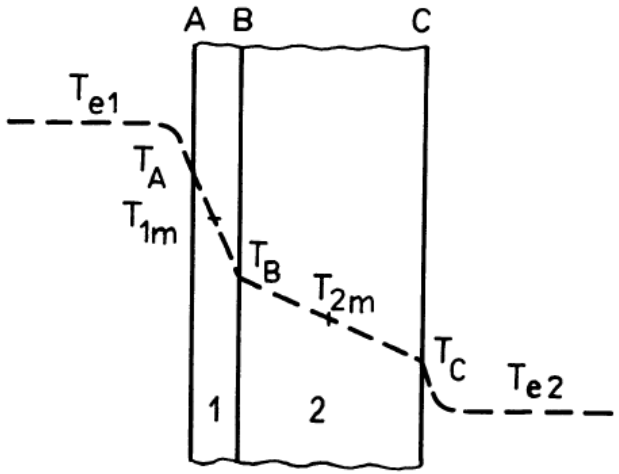

Fig. 16 Temperature distribution in a bi-layer plate, steady heat flow.

- Constrained plate:
  - Relatively simple analytical solution
  - Maximum stress always at the surface
- Free plate:
  - More complex analytical solution
  - Maximum stress can also appear at the interface

J. Mencik, Springer, 1995

Stretchable electronics

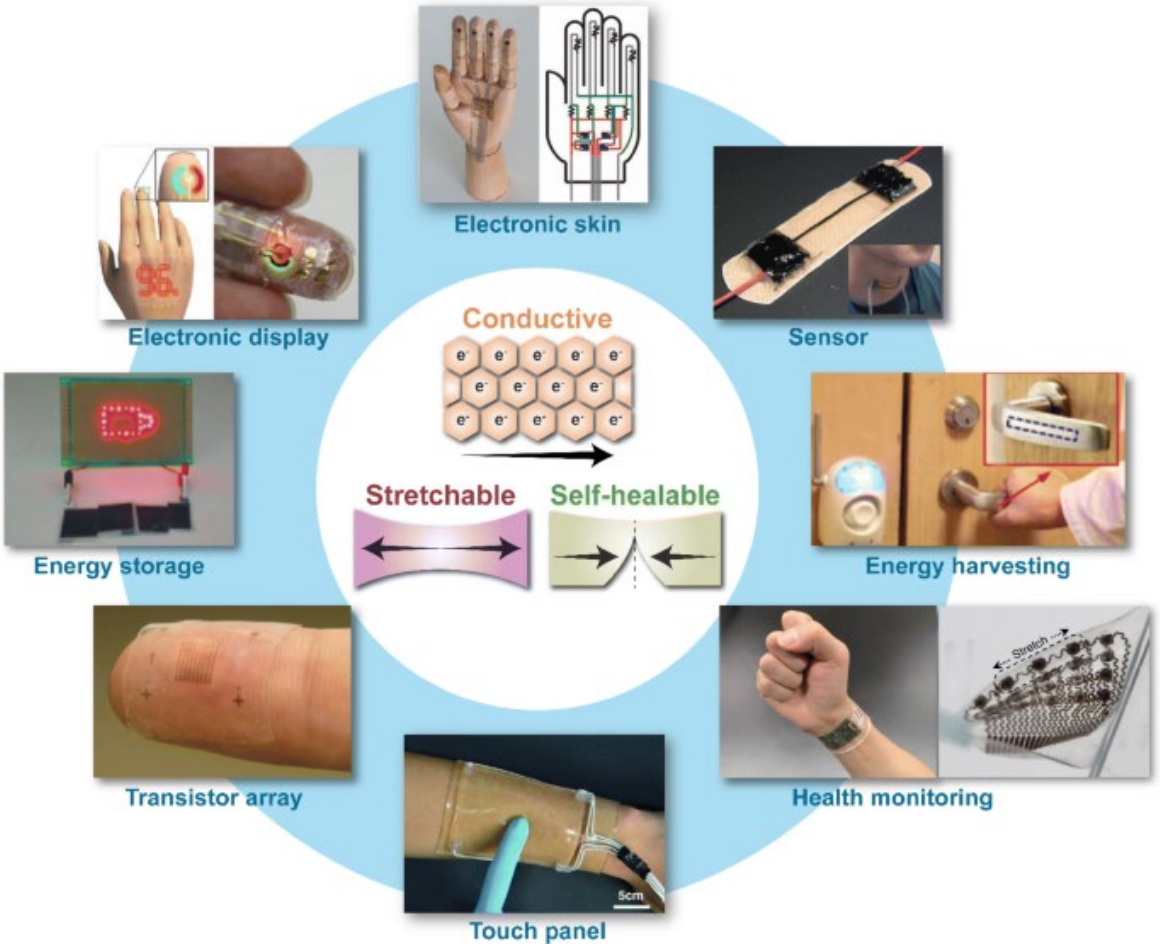

Zhao et al., *Nano Convergence, 2019*

Stresses caused by membrane forces

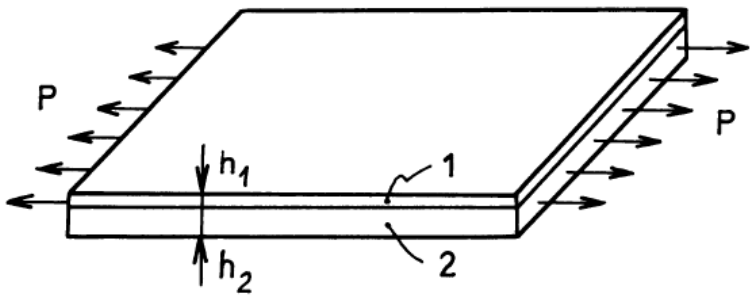

Fig. 17 Bi-layer plate loaded by membrane force.

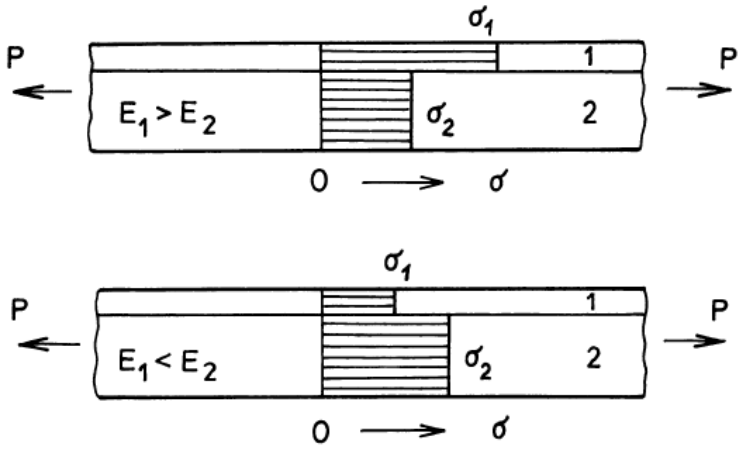

Fig. 18 Stress distribution in a bi-layer plate loaded by membrane force.

- Example: Membrane force P, homogeneous properties in layer (1) and substrate (2), plate cannot bend freely
- Stresses in x direction if $v_1 = v_2$:

$$\sigma_{1x} = P_x \frac{E_1}{E_1 h_1 + E_2 h_2}$$

$$\sigma_{2x} = P_x \frac{E_2}{E_1 h_1 + E_2 h_2} = \sigma_{1x} \frac{E_2}{E_1}$$

Stresses caused by membrane forces

$$\sigma_{1x} = \frac{P_x}{h}\,\frac{\eta\,(1+\kappa)}{1+\eta\,\kappa} = \sigma_{x,h}\,\sigma_1^*$$

$$\sigma_{2x} = \frac{P_x}{h}\,\frac{1+\kappa}{1+\eta\,\kappa} = \sigma_{x,h}\,\sigma_2^*$$

$$\sigma_{x,h} = P_x / h$$

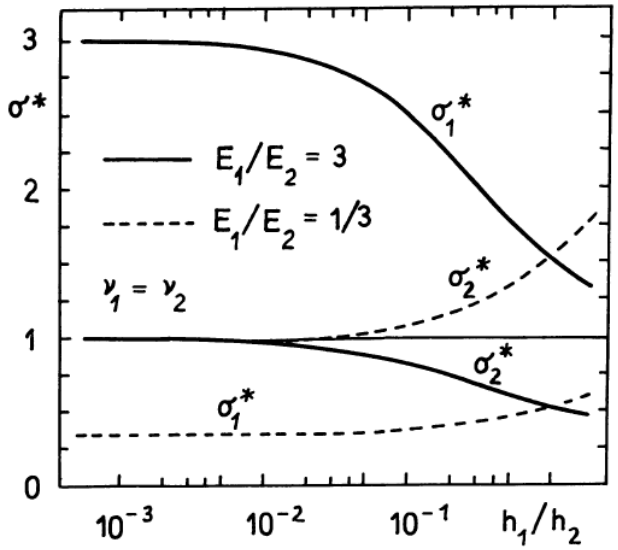

Fig.19 Stresses due to membrane force P versus the relative thickness of the coating and substrate, h_1/h_2; $\sigma = \sigma^* P/(h_1 + h_2)$.

- $E_1 > E_2$: ratio of membrane stress in coating to average stress decreases with increasing coating thickness
- $E_1 < E_2$: ratio of membrane stresses in both domains increase for larger coating thickness

J. Mencik, Springer, 1995

Stresses caused by membrane forces

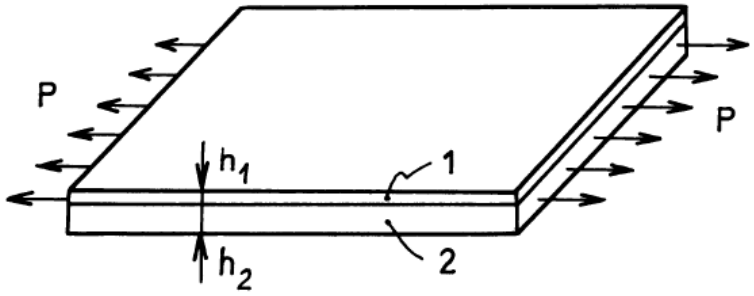

Fig. 17 Bi-layer plate loaded by membrane force.

- Example: Membrane force P, homogeneous properties in layer (1) and substrate (2), plate cannot bend freely
- Stresses in x direction if $v_1 = v_2$:

$$\sigma_{1x} = P_x \frac{E_1}{E_1 h_1 + E_2 h_2}$$

$$\sigma_{2x} = P_x \frac{E_2}{E_1 h_1 + E_2 h_2} = \sigma_{1x} \frac{E_2}{E_1}$$

J. Mencik, Springer, 1995

Stresses caused by membrane forces

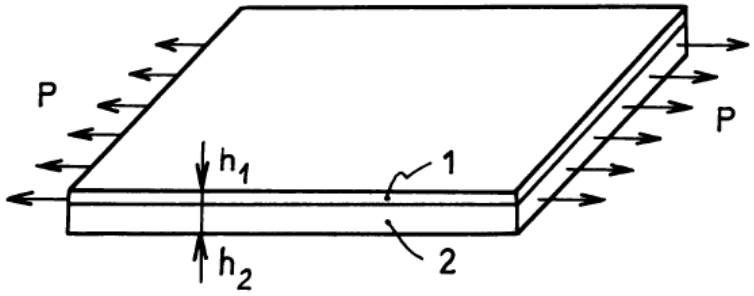

Fig. 17 Bi-layer plate loaded by membrane force.

- What if $\nu_1 \neq \nu_2$?

$$\sigma_{1x} = P_x \frac{E_1}{E_1 h_1 + \frac{1-\nu_2\nu}{1-\nu_1\nu}\frac{1-\nu_1^2}{1-\nu_2^2} E_2 h_2}$$

$$\sigma_{1y} = \sigma_{1x} \frac{\nu_1 - \nu}{1 - \nu_1\nu}$$

$$\nu = \frac{\frac{\nu_1}{1-\nu_1^2} E_1 h_1 + \frac{\nu_2}{1-\nu_2^2} E_2 h_2}{\frac{1}{1-\nu_1^2} E_1 h_1 + \frac{1}{1-\nu_2^2} E_2 h_2}$$

J. Mencik, Springer, 1995

Stresses caused by membrane forces

- Longitudinal stresses in loading direction:
  - Have equal sign in layer (1) and substrate (2)
  - Magnitudes have the same ratio as the elastic moduli E_1,E_2
- Lateral stresses normal to loading direction:
  - Have opposite signs in layer (1) and substrate (2)
  - Are in reciprocal ratio to the layer thickness
  - Are higher for larger differences $\nu_1 - \nu$ or $\nu_2 - \nu$
- Poisson ratio of layered plate lies between ν_1 ($E_1h_1 \gg E_2h_2$) and ν_2 ($E_1h_1 \ll E_2h_2$)
- Lateral stresses are highest for very thin coatings ($h_1 \ll h_2$):

$$\sigma_{1y} \approx \frac{\nu_1 - \nu_2}{1 - \nu_1\nu_2}\,\sigma_{1x} = \frac{0.2 - 0.3}{1 - 0.2\times 0.3}\,\sigma_{1x} = -0.106\,\sigma_{1x}$$

- Lateral stresses are lower, but note the opposite sign!

J. Mencik, Springer, 1995

Stresses caused by membrane forces

- Lateral stresses caused by differences in ν have opposite signs in layer (1) and substrate (2)
  - Causes a bending moment!
- If the plate can deform freely, it will deflect in lateral direction
  - Membrane and bending stresses appear together
  - Analytical treatment is very difficult!
- Special case of very thin coatings ($h_1 \ll h_2$):

$$\sigma_{1x} = \frac{E_1}{E_2} \frac{1}{1-\nu_1^2} \left[\sigma_{2x}(1 - \nu_1\nu_2) + \sigma_{2y}(\nu_1 - \nu_2) \right]$$

$$\sigma_{1y} = \frac{E_1}{E_2} \frac{1}{1-\nu_1^2} \left[\sigma_{2y}(1 - \nu_1\nu_2) + \sigma_{2x}(\nu_1 - \nu_2) \right]$$

- Substrate stresses in this case ($h_1 \ll h_2$) can be determined as if no coating was present.

J. Mencik, Springer, 1995

Appication: delamination and buckling of pn-junctions

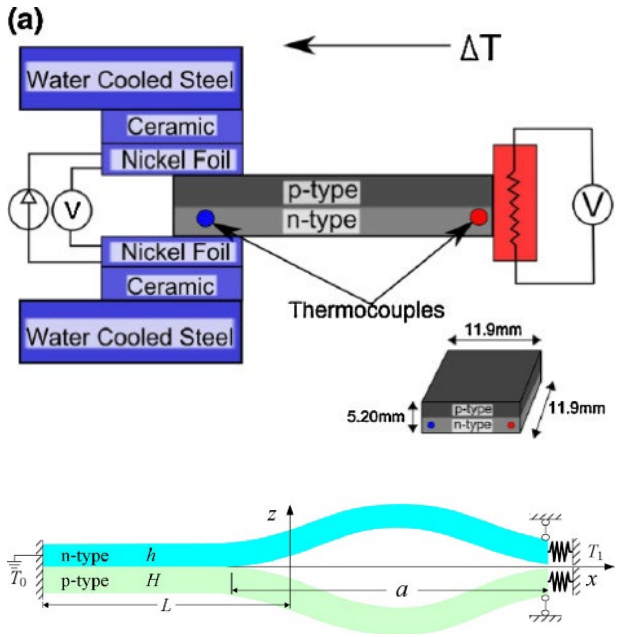

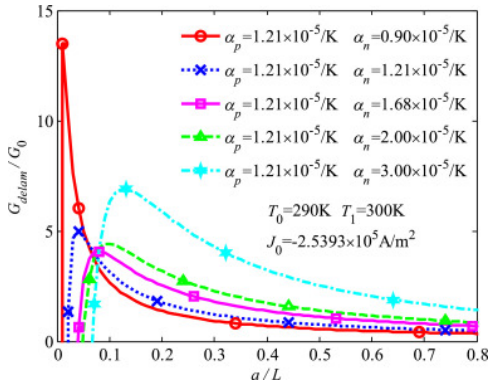

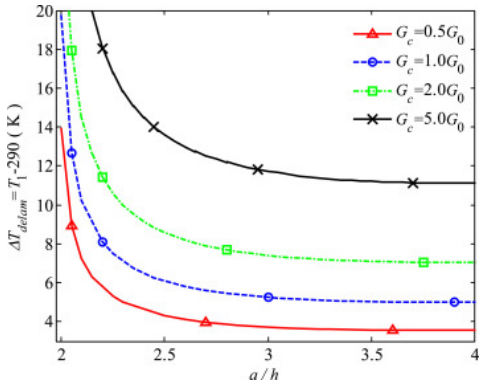

- Delamination and buckling of a thin film thermoelectric generator composed of pn-junction
- Delamination energy release rate for different temperature loads and thermal expansion coefficients is studied
- Critical temperature difference of delamination and buckling initiations is a function of the fracture toughness of the interface

Cui et al., Int J of Mech Sci, 2018

Stresses caused by bending

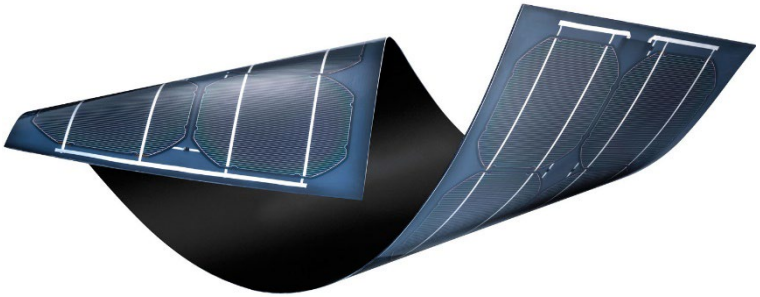

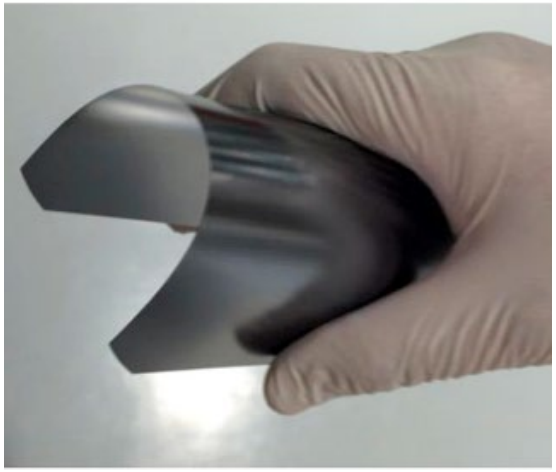

- Thin films on flexible substrates can be subjected to significant bending deformation, both for polymeric (left) and thin semiconductor substrates (right)
- In this case, the stress at the interface between substrate and thin film as well as the stress in the thin film need to be studied
- Bending stresses are especially likely to lead to crack nucleation, as the highest tensile stresses act directly at the free surfaces.

Stresses caused by bending

- Coating and substrate homogeneous, $v_1 = v_2$, plate loaded by M_x

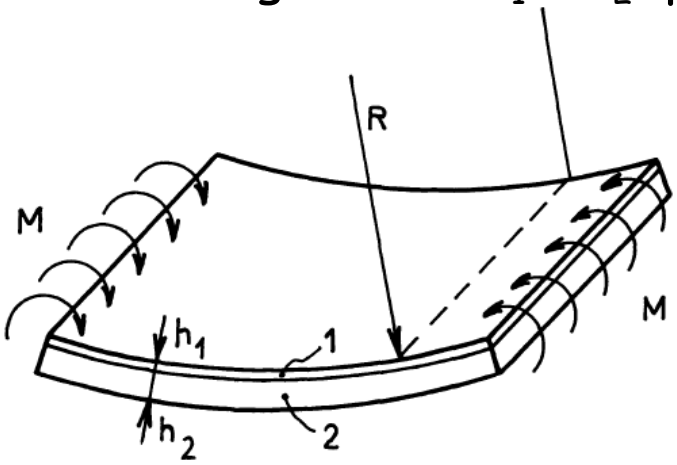

Fig. 20 Bi-layer plate loaded by bending moment.

- Strain distribution: $\epsilon_x(z) = \epsilon_{x,0} + z/R_x \quad , \quad \epsilon_y(z) = 0$
- Here, the coordinate system is placed such that its origin is at the interface between film and substrate
- The strain is composed of the strain at the interface and a linear variation in strain as a function of z proportional to the bending radius R_x.
- The strain in y direction is negligible, as the average strain in x-direction is 0.

Stresses caused by bending

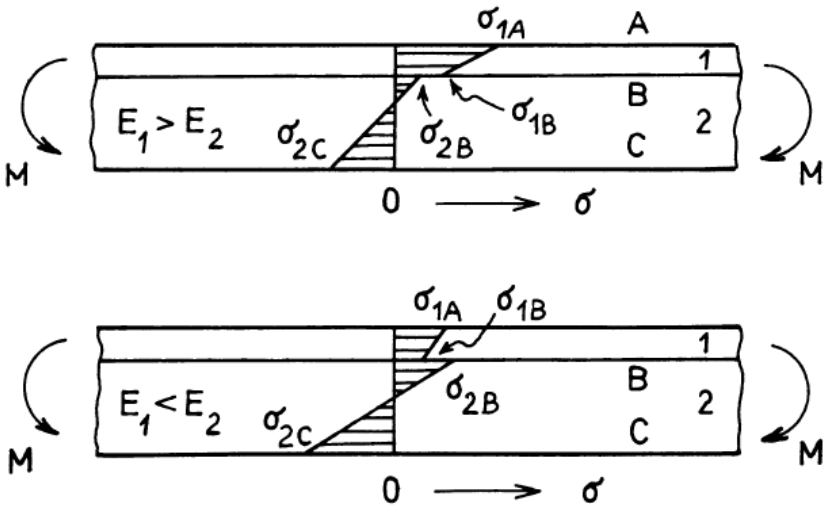

Fig. 21 Stress distribution in a bi-layer plate loaded by bending moment.

$$\sigma_{1A} = \sigma_{max}(1+\kappa)^2(\eta''\kappa^2 + 2\kappa + 1)\eta''/\Phi$$

$$\sigma_{1B} = \sigma_{max}(1+\kappa)^2(1-\eta''\kappa^2)\eta''/\Phi$$

$$\sigma_{2B} = \sigma_{max}(1+\kappa)^2(1-\eta''\kappa^2)/\Phi$$

$$\sigma_{2C} = -\sigma_{max}(1+\kappa)^2(\eta''\kappa^2 + 2\eta''\kappa + 1)/\Phi$$

$$\sigma_{max} = 6M_x/h^2$$

- Stress distribution within layer (1) and substrate (2) is linear
- Only stresses at surfaces and interface must be known
- Expressions can be simplified for small coating thickness ($\kappa \approx 0$)
- Plate deforms into a part of a cylindrical surface, $\varepsilon_y = 0$

- Lateral stress: $\sigma_y(y) = \nu\,\sigma_x(z)$

Stresses in coatings on curved surfaces

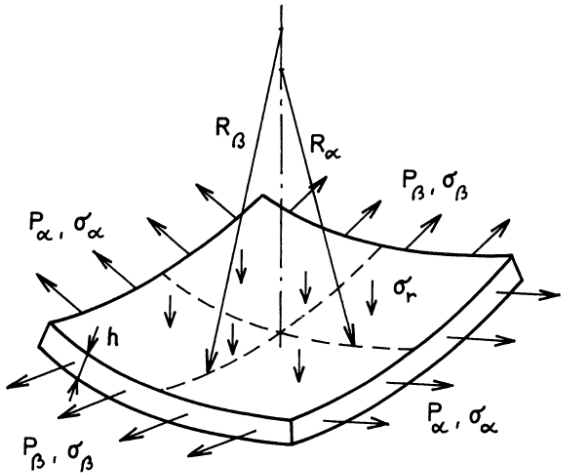

Fig. 22 Stresses and forces in a thin coating on a curved surface.

- Radial stresses perpendicular to the layer-substrate interface:

$$\sigma_r = -\left(\frac{P_\alpha}{R_\alpha} + \frac{P_\beta}{R_\beta} \right)$$

- R_i radii of curvature in direction i, P_i forces acting in direction i
- Relationship between forces P_i and stresses σ_i in direction i:

$$P_\alpha = \int_0^h \sigma_\alpha(z)\,dz \quad , \quad P_\beta = \int_0^h \sigma_\beta(z)\,dz$$

J. Mencik, Springer, 1995

Stresses in coatings on curved surfaces

- If coating is thin compared to substrate and curvature:
  - Influence of coating can be neglected

$$\sigma_r = -h\left(\frac{\sigma_\alpha}{R_\alpha} + \frac{\sigma_\beta}{R_\beta}\right)$$

- Radial stresses are higher for larger h and smaller R_i
- Coating:
  - Stress decreases linearly with distance from interface to 0 at surface
- Substrate:
  - Stress can decrease or stay constant depending on shape of body

J. Mencik, Springer, 1995

Stresses in coatings on curved surfaces

- Procedure to calculate thermal stresses in thin coating:
  - Calculate σ_i regardless of curvature using formula for flat plates

$$\sigma_{1\varphi} = \sigma_{1z} \approx \frac{E_1}{1 - \nu_1}(\alpha_1 - \alpha_2)(T_0 - T)$$

  - σ_r is given in general by

$$\sigma_r = -\sigma_{1\varphi}\frac{h}{R}$$

  - σ_r follows to be in this case:

$$\sigma_r = -\frac{E_1}{1 - \nu_1}(\alpha_1 - \alpha_2)(T_0 - T)\frac{h}{R}$$

J. Mencik, Springer, 1995

Example: Stresses on longitudinally loaded coated rod

- Axial stress in the rod:

$$\sigma_{2z} = \frac{P}{\pi R^2}$$

- Axial coating stress:

$$\sigma_{1z} = \frac{1 - \nu_1 \nu_2}{1 - \nu_1^2} \frac{E_1}{E_2} \sigma_{2z}$$

- Circumferential coating stress:

$$\sigma_{1\varphi} = \frac{\nu_1 - \nu_2}{1 - \nu_1^2} \frac{E_1}{E_2} \sigma_{2z}$$

- Radial stress at the interface:

$$\sigma_r = \frac{\nu_2 - \nu_1}{1 - \nu_1^2} \frac{E_1}{E_2} \frac{h}{R} \sigma_{2z}$$

J. Mencik, Springer, 1995

Stresses on longitudinally loaded coated rod

- Problem: Bilayer cylinder stressed due to different thermal expansion coefficients

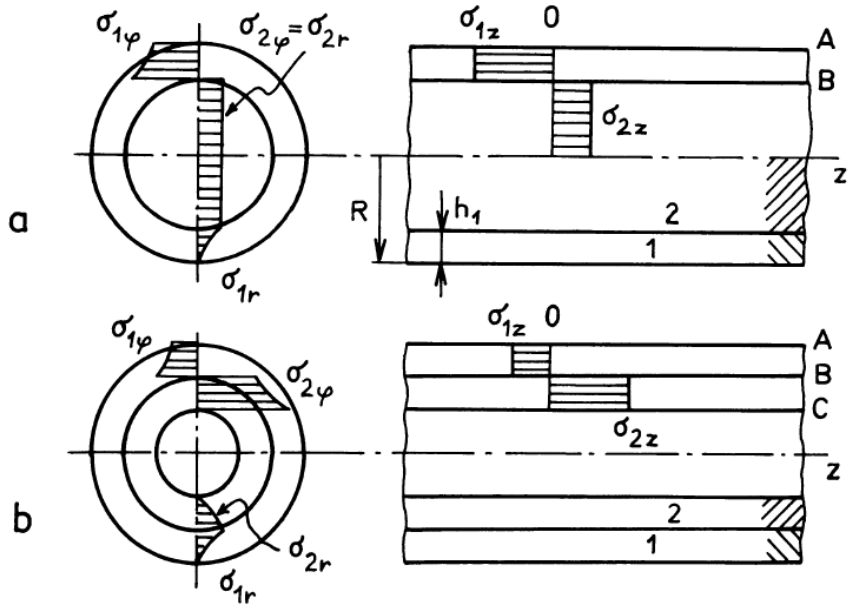

Fig. 23 Stress distribution in a bi-layer cylinder due to a difference in thermal expansion of the inner and outer layers. a - inner cylinder is solid, b - inner cylinder is hollow

- For thick coatings (h≈R):
  - Radial stresses are higher
  - Circumferential and axial stress distribution also changes

Stresses on longitudinally loaded coated rod

- Analytical solution for $E_1=E_2$:

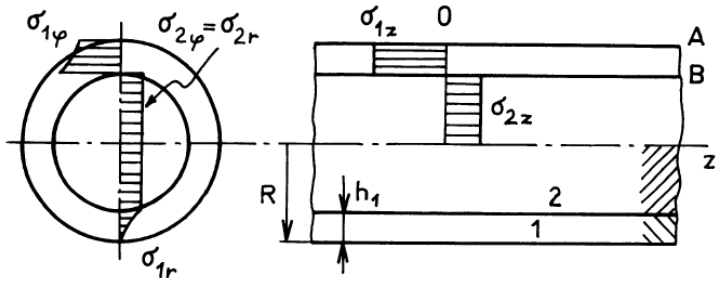

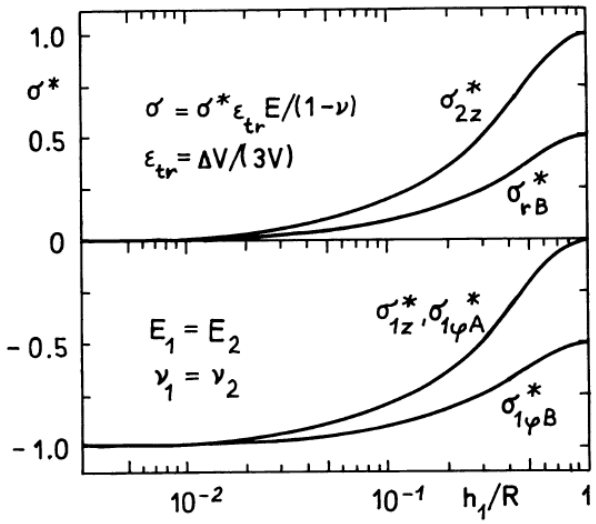

Fig. 24 Residual stress in a surface-treated cylindrical rod as a function of the relative thickness of the layer, h_1, to the rod radius, R. $\sigma = \sigma^* \epsilon_{tr} E/(1 - \nu)$, $\epsilon_{tr} = \Delta V/(3V)$ - free relative elongation of the layer due to phase transformation or a similar change

Circumferential stress in layer at A:

$$\sigma_{1\varphi A} = -\epsilon_{tr} E'(1-\kappa)^2$$

Circumferential stress in layer at B:

$$\sigma_{1\varphi B} = -\epsilon_{tr} E'[1+(1-\kappa)^2]/2$$

Radial stress at the interface at B:

$$\sigma_{rB} = \epsilon_{tr} E'[1-(1-\kappa)^2]/2$$

Circumferential stress in substrate at B:

$$\sigma_{2\varphi} = \sigma_{2r} = \sigma_{rB}$$

Axial stress in substrate:

$$\sigma_{2z} = 2\,\sigma_{rB}$$

Axial stress in layer:

$$\sigma_{1z} = \sigma_{1\varphi A}$$

$\kappa = h_1/R$, $E' = E/(1-\nu)$ and ϵ_{tr} $(= \Delta V/3V)$

J. Mencik, Springer, 1995

Elastic-plastic deformation of thin films

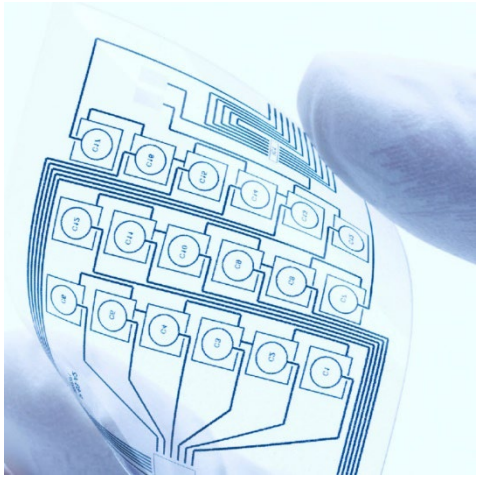

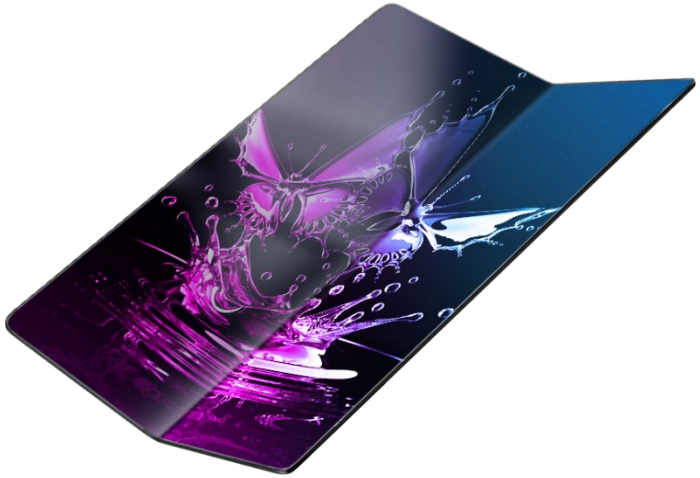

- Thin films on flexible substrates undergo substantial deformations
- This can lead to an overstraining of the thin film and, depending on the strength and toughness of the film, to crack formation or plastic deformation
- Analytical models may be used to obtain a better understanding of the elastoplastic behaviour of thin films on elastic substrates and is a fast way to design suitable systems that can withstand the envisioned laoding scenario

Elastic-plastic deformation

- Bi-layer plate, no out-of-plane bending, ideal elastic-plastic materials
- Loading: biaxial isotropic tension

- Linear elastic regime:

$$\sigma_1 = E_1' \epsilon \quad , \quad \sigma_2 = E_2' \epsilon$$

- Total load per unit length of the plate:

$$P = \sigma_1 h_1 + \sigma_2 h_2 = \epsilon \left(E_1' h_1 + E_2' h_2 \right)$$

- Stresses in layer (1) and substrate (2):

$$\sigma_1 = P E_1' / \left(E_1' h_1 + E_2' h_2 \right)$$

$$\sigma_2 = P E_2' / \left(E_1' h_1 + E_2' h_2 \right)$$

J. Mencik, Springer, 1995

Elastic-plastic deformation

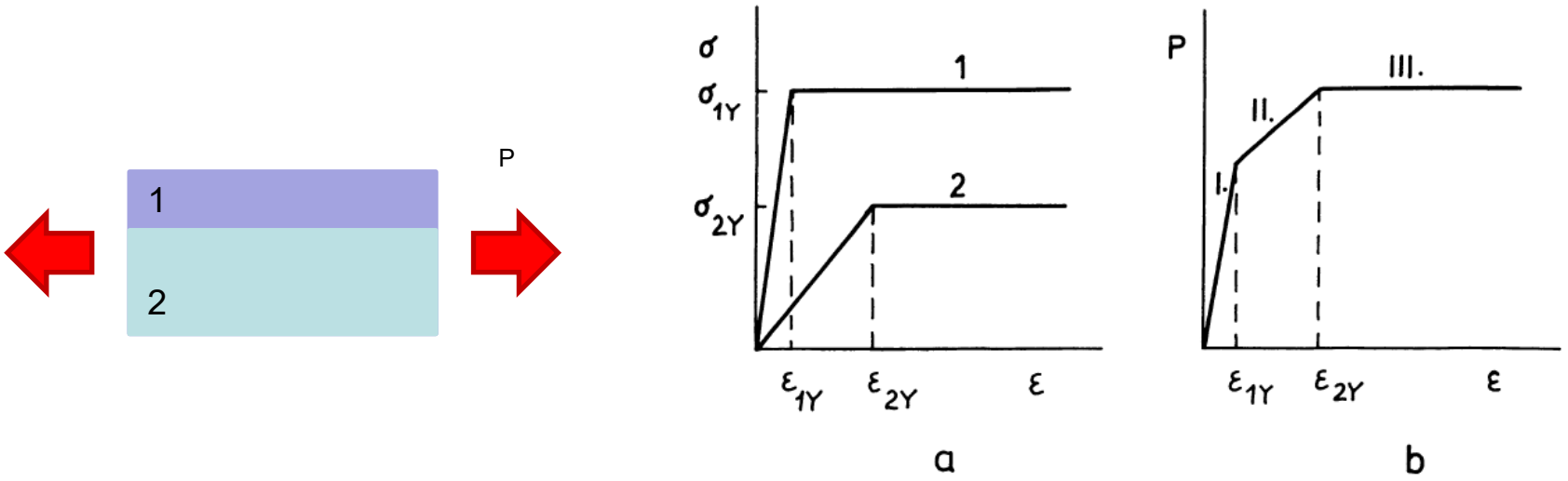

Fig.25 Bi-layer plate loaded in isotropic tension: a - stress-strain diagrams of layer 1 and 2, b - load-strain diagram for the plate.

Yield point is reached in layer (1) with lower yield strain at:

$$\epsilon' = \epsilon_{1Y} = \sigma_{1Y} / E_1'$$

This corresponds to a critical load P':

$$P' = \sigma_{1Y} h_1 \left(1 + \frac{E_2' h_2}{E_1' h_1} \right)$$

J. Mencik, Springer, 1995

Elastic-plastic deformation

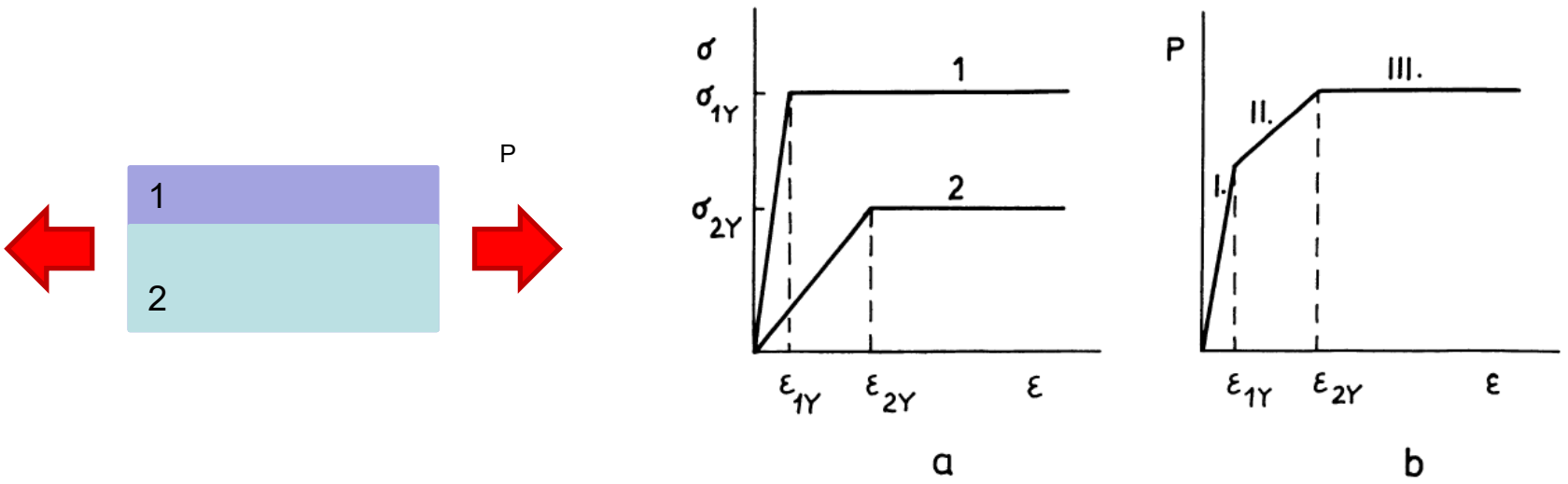

Fig.25 Bi-layer plate loaded in isotropic tension: a - stress-strain diagrams of layer 1 and 2, b - load-strain diagram for the plate.

If load increases further past P', stress in (1) remains constant:

$$P = \sigma_{1Y} h_1 + \sigma_2 h_2 = E_1' h_1 \epsilon_{1Y} + E_2' h_2 \epsilon$$

The plate deforms like this until also the substrate (2) yields at:

$$P'' = \sigma_{1Y} h_1 + \sigma_{2Y} h_2$$

Elastic-plastic deformation

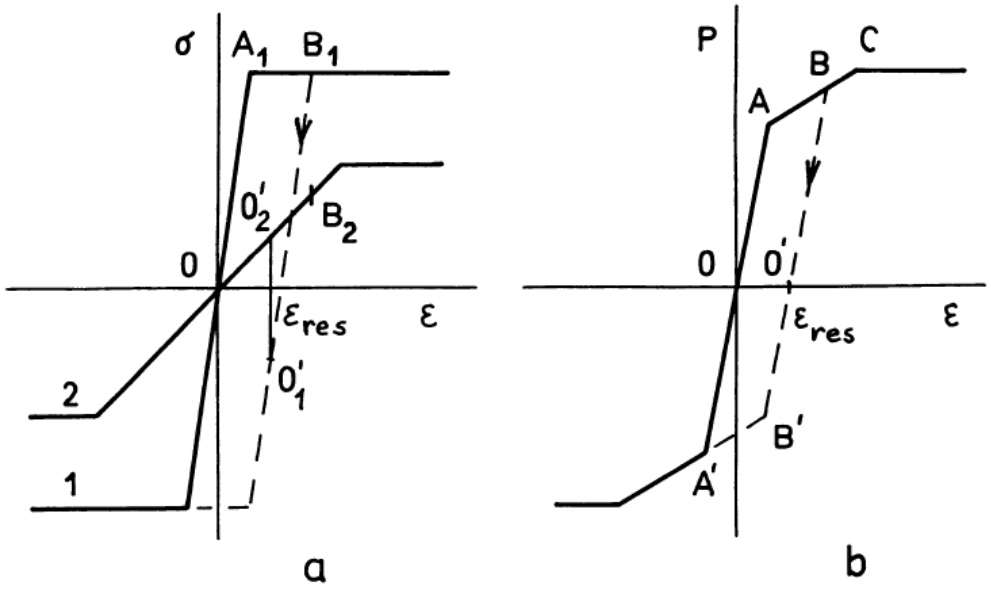

Fig. 26 Stresses in an elastoplastic bi-layer plate after unloading and reloading; P - total load, σ - stress, ϵ - strain

- If P<P': Elastic unloading, no residual deformation
- If P'<P<P'': Plastic deformation of layer (1)
- If P=P'': Plastic deformation of both layer (1) and substrate (2)

- Loading-unloading path: 0-A_i-B_i-$0_i'$ and 0-A-B-0'

Elastic-plastic deformation

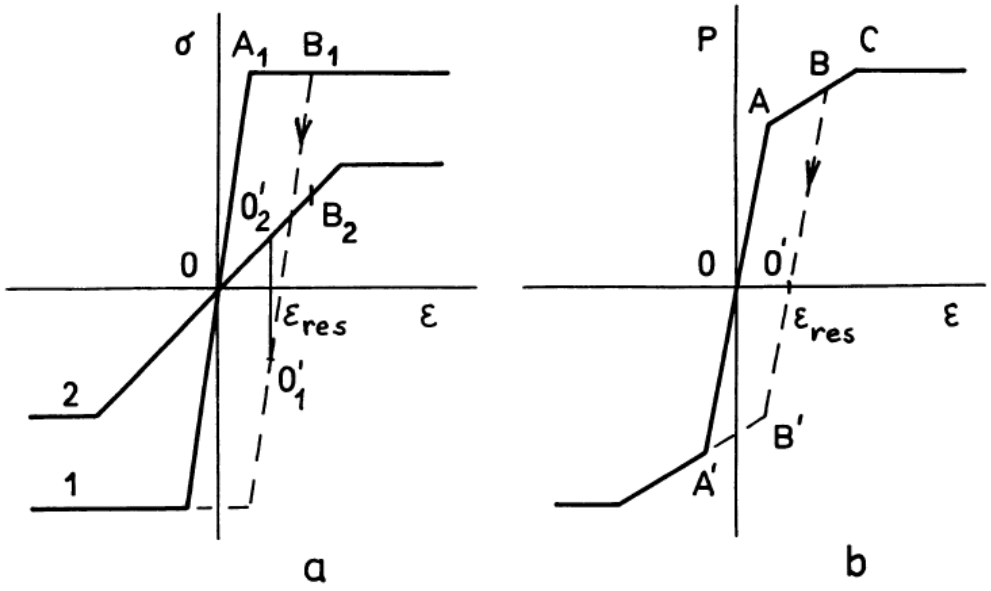

Fig. 26 Stresses in an elastoplastic bi-layer plate after unloading and reloading; P - total load, σ - stress, ϵ - strain

- Residual stresses in layer (1) and substrate (2):

$$\sigma_{1\,res} = \sigma_{1\,Y} - \frac{P}{h_1} \Big/ \left(1 + \frac{E_2'}{E_1'}\frac{h_2}{h_1}\right)$$

$$\sigma_{2\,res} = -\sigma_{1\,res}\frac{h_1}{h_2}$$

J. Mencik, Springer, 1995

Elastic-plastic bending

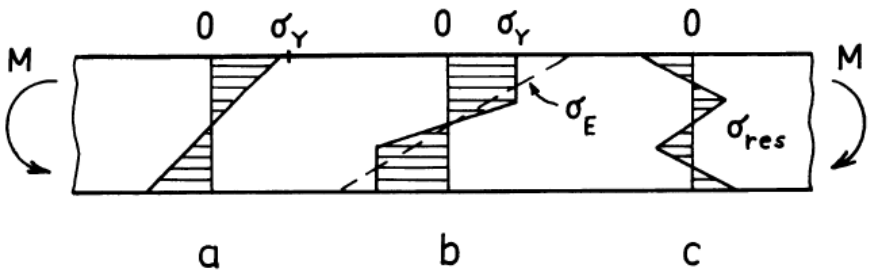

Fig. 28 Distribution of stresses in a bent beam: a - situation under load, elastic deformations, b - situation under load, elastoplastic deformations, c - situation after unloading; σ_E - stress determined according to Hooke's law, σ_Y - yield strength, σ_{res} - residual stress

- If $h_1 < 0.05\ h_2$: Strain in layer (1) is constant and equal to substrate (2) interface strain
- For biaxial isotropic bending, yielding occurs at

$$\epsilon_1 = \epsilon_{1Y} = \sigma_{1Y} / E_1'$$

- Bending continues until ε_{1fin} causing permanent deformation of the layer:

$$\epsilon_{1p} = \epsilon_{1fin} - \epsilon_{1y}$$

- Residual stress in the coating:

$$\sigma_{1res} = E_1' \epsilon_{1p}$$

J. Mencik, Springer, 1995

Example: Electro-Mechanical Testing

50 nm Au
10 nm Cr

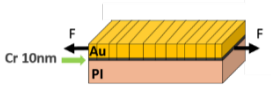

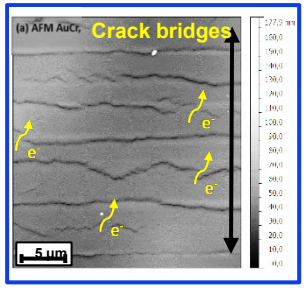

ε=15%

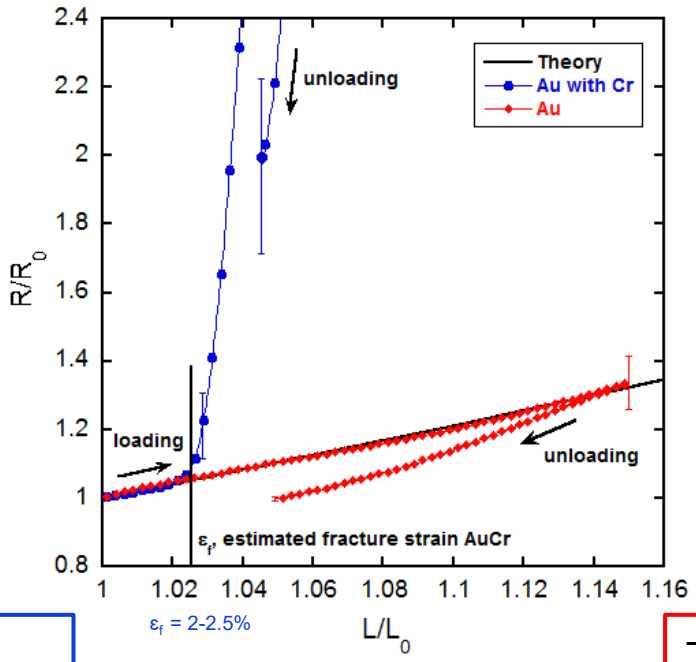

50 nm Au

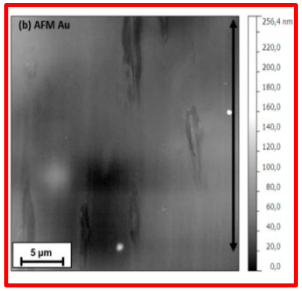

ε=15%

→ **brittle**
→ Deviation ~ cracking onset
→ $R_{end} > R_0$

→ **very ductile**
→ No sign of cracks in R
→ $R_{end} \sim R_0$

Theory:

$$\frac{R}{R_0} = \left(\frac{L}{L_0}\right)^2 = (1+\varepsilon)^2$$

B. Putz et al. Scripta Mat. 2015

Film Strain + resistance – Insitu[2]

Theory:

$$\frac{R}{R_0} = \left(\frac{L}{L_0}\right)^2 = (1+\varepsilon)^2$$

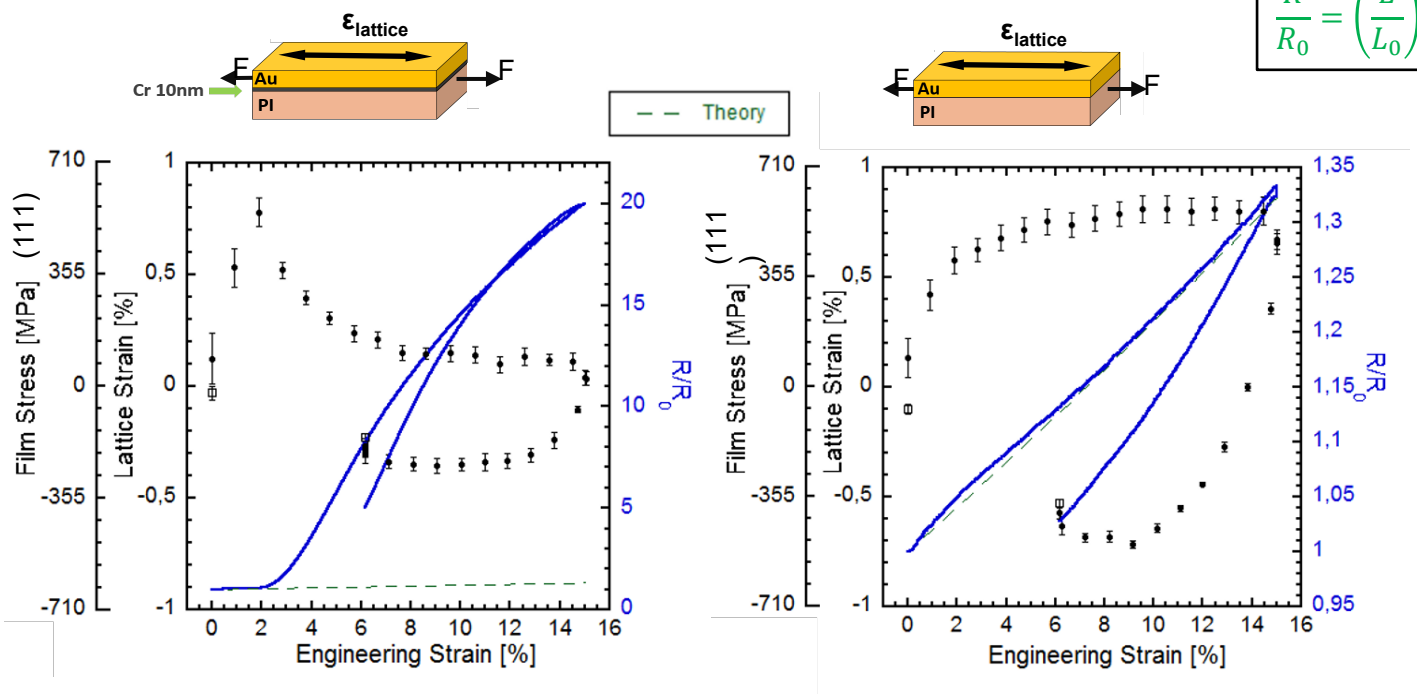

- Peak in lattice strain corresponds to increase in film resistance
- Crack formation!

- lattice strain reaches a plateau around 2% eng. strain
- R-curve gives no sign of cracks in the metal layer

B. Putz et al. Mrs Advances, 2016

Stresses near edges and interfaces

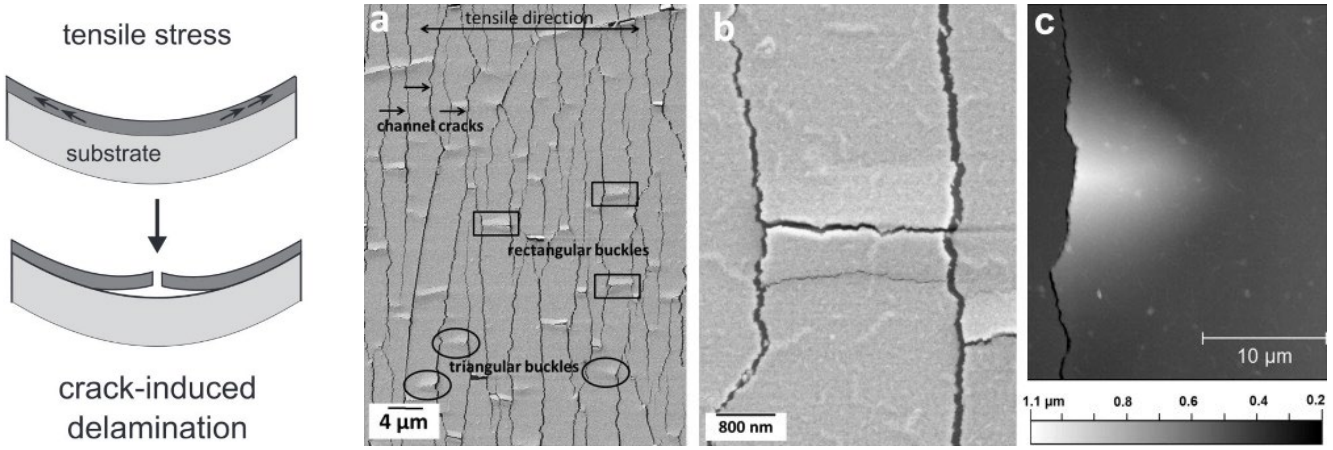

F. Toth et al., Acta Materialia, 2013

- In case of structured or cracked films, the stress distribution at the film-substrate interface as well as in the film in proximity to the free edges is altered
- An analytical treatment allows estimating the spatial variation of film and interfacial stresses near the free edge
- Examples of issues where this is relevant include periodic crack spacing in failed thin films, crack-induced delamination of thin films, or crack free regions of thin films near free edges

Stresses near edges and interfaces

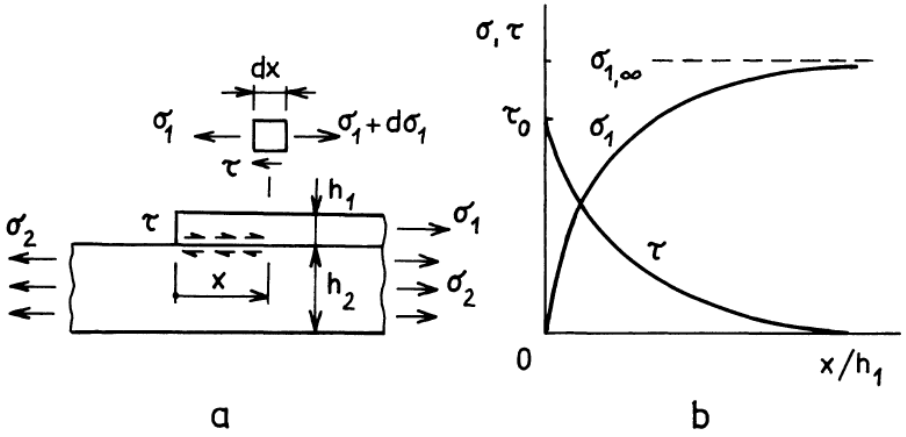

Fig. 30 Approximate distribution of the membrane stress (σ_1) in a coating and shear stress (τ) at the free edge.

- Loading of layer is transferred from substrate by shear stress

$$\frac{d\sigma_1(x)}{dx} = \frac{\tau(x)}{h_1} \quad , \quad \frac{d\sigma_2(x)}{dx} = -\frac{\tau(x)}{h_2}$$

- Neutral plane displacement u_1, u_2. Mean strains of (1) and (2) are:

$$\epsilon_1(x) = \frac{du_1}{dx} \quad , \quad \epsilon_2(x) = \frac{du_2}{dx}$$

Stresses near edges and interfaces

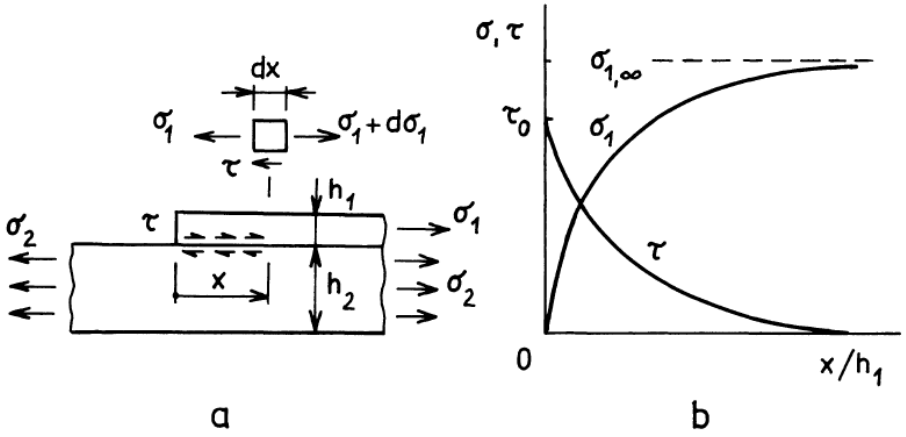

Fig. 30 Approximate distribution of the membrane stress (σ_1) in a coating and shear stress (τ) at the free edge.

- Average elastic stresses if $v_1 = v_2$:

$$\sigma_1(x) = E_1 \epsilon_1(x) = E_1 \frac{du_1}{dx} \quad , \quad \sigma_2(x) = E_2 \frac{du_2}{dx}$$

- Assumption: shear stress proportional to relative shift of layer (1) and substrate (2)

$$\tau = k_\tau (u_1 - u_2) \qquad \text{with} \qquad k_\tau \approx G_i / h_i$$

J. Mencik, Springer, 1995

Stresses near edges and interfaces

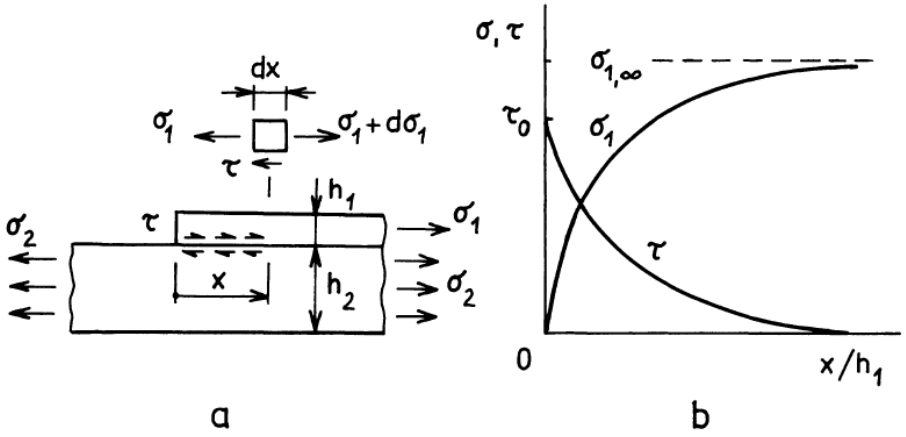

Fig. 30 Approximate distribution of the membrane stress (σ_1) in a coating and shear stress (τ) at the free edge.

- System of differential equations can be solved for σ1, τ:

$$\sigma_1(x) = \sigma_{1,\infty}(1 - e^{-\lambda x})$$

$$\tau(x) = \sigma_{1,\infty} h_1 \lambda e^{-\lambda x} = \tau_0 e^{-\lambda x}$$

with $$\lambda = \sqrt{k_\tau \left[(E_1 h_1)^{-1} + (E_2 h_2)^{-1} \right]}$$

- Approximate relation for negligible interlayer thickness:

$$\lambda \approx 1 / \left[h_1 \sqrt{1 + (E_1 / E_2)} \right]$$

J. Mencik, Springer, 1995

Stresses near edges and interfaces

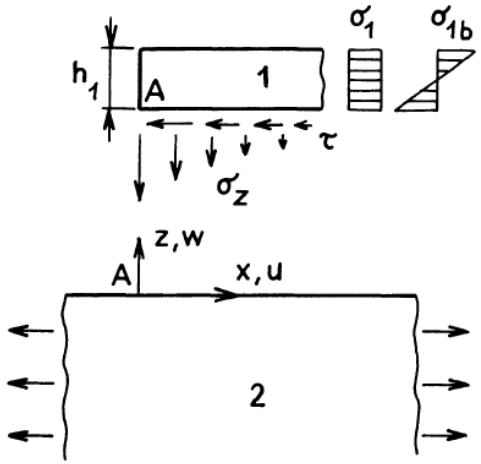

- Interfacial shear stress and membrane stress in layer (1) lead to generation of a moment trying to lift up the free edge of the layer.

$$M(x) = \sigma_1(x)\frac{h_1}{2} = \int_0^{h_1} \sigma(x,z)\,z\,dz = \int_0^x \left[\tau(\xi)\frac{h_1}{2}\right] d\xi$$

- As a result, a stress σ_z perpendicular to the interface and a bending stress in the coating σ_b are generated

Stresses near edges and interfaces

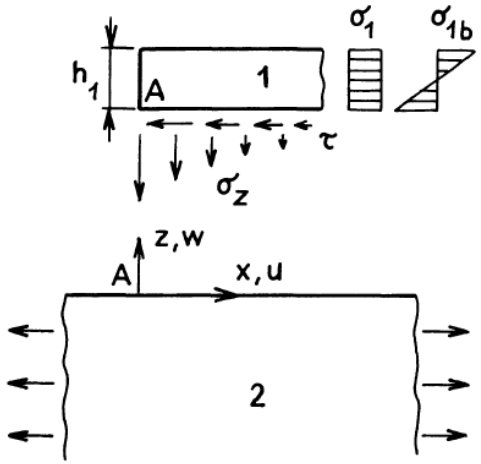

- Stress σ_z perpendicular to the interface:

$$\sigma_z = k_\sigma w$$

w…increase in distance between the neutal planes of (1) and (2)
K_σ…normal stiffness of the interlayer

J. Mencik, Springer, 1995

Stresses near edges and interfaces

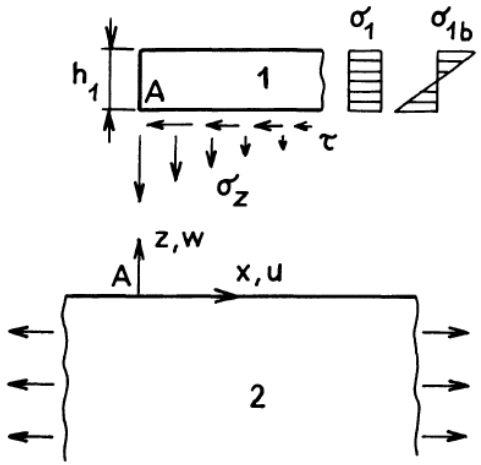

- Bending differential equation of a beam on elastic foundation loaded by a distributed moment:

$$\frac{d^4 w}{dx^4} + \frac{12\, k_\sigma}{E_1'' h_1^3} w = \frac{6}{E_1'' h_1^2} \frac{d\tau}{dx}$$

with

$$E_1'' = E_1/(1 - \nu^2)$$

J. Mencik, Springer, 1995

Stresses near edges and interfaces

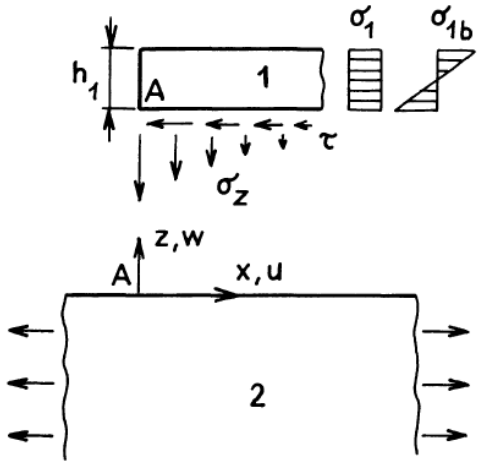

- Solution considering coating length >> thickness

$$w(x) = e^{-\beta x}\left(C_1 \cos \beta x + C_2 \sin \beta x\right) - C_3 e^{-\lambda x}$$

with

$$\beta = \sqrt[4]{3\,k_\sigma / (E_1'' h_1^3)} \quad , \quad \lambda = \sqrt{k_\tau / (E_1 h_1)}$$

J. Mencik, Springer, 1995

Stresses near edges and interfaces

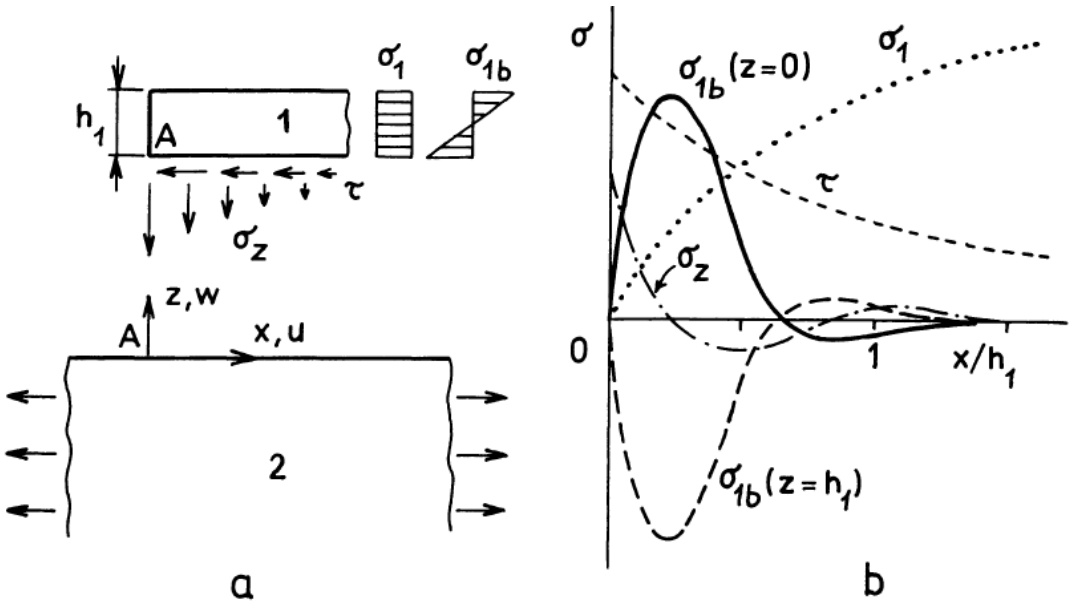

Fig. 31 Approximate distribution of the bending stress (σ_{1b}) in a coating and stress perpendicular to the interface (σ_z) at the free edge.

- Solution for w(x) allows to compute σ_z and σ_b:

$$\sigma_z = k_\sigma w$$

$$\sigma_{1,b}(x) = - E_1'' \frac{h_1}{2} \frac{d^2 w}{dx^2}$$

Stresses near edges and interfaces

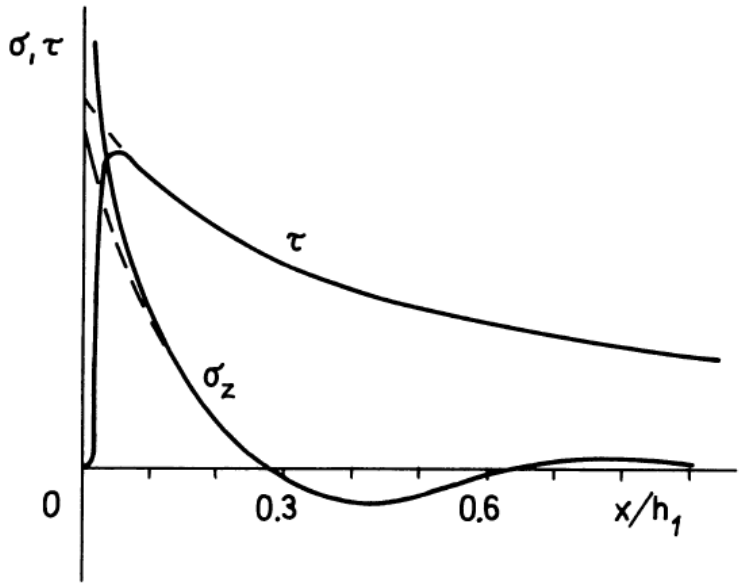

Fig. 32 Distribution of the normal stress (σ_z) and shear stress (τ) in the vicinity of the free edge of a coating. Dashed curves - a simplified (thin beam) theory.

- Treatment using beam theory good approximation for x/h>0.1
- More elaborate treatment: Shear stress drops to 0 near edge
- Normal stress increases even more than predicted by beam theory near the edge

J. Mencik, Springer, 1995

Stresses near edges and interfaces

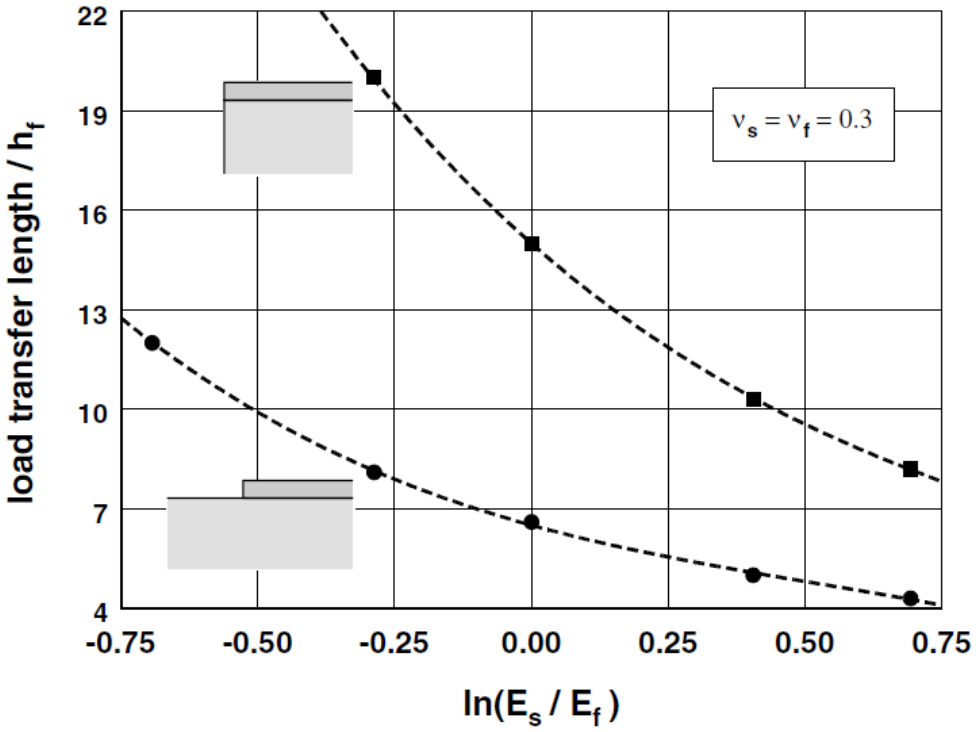

Fig. 4.8. The dependence of load transfer length near the free edge of a film with a remote biaxial mismatch stress σ_m on the modulus ratio of the two materials. The load transfer length is defined as the distance from the free edge of the film at which the internal force resultant has increased to a value equal to 90% of its remote asymptotic value of $\sigma_m h_f$, and this length was determined by means of the numerical finite element method. Results are shown for the case when the substrate extends indefinitely far beyond the free film edge and when the substrate edge coincides with the film edge.

Example: Crack-free regions in structured thin films

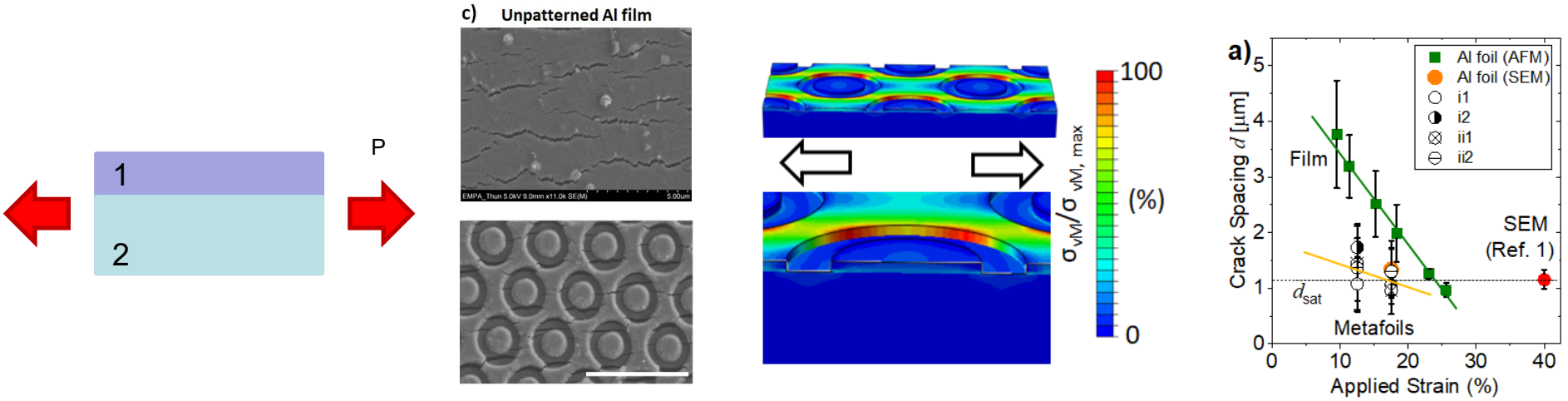

- 100nm Al film (1) on 30 µm polyimide tape (2)
- Stretching the film past the yield point leads eventually to crack formation at elevated strains (>10%)
- crack spacing saturates at approximately 10x film thickness
- Nanostructuring the film allows controlling crack spacing and generating crack-free domains
- Numerical simulations show that stress in central domains is significantly lower (compare to analytical solution)

Delamination of thin films

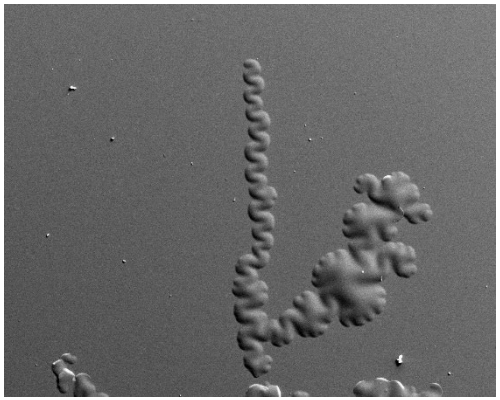

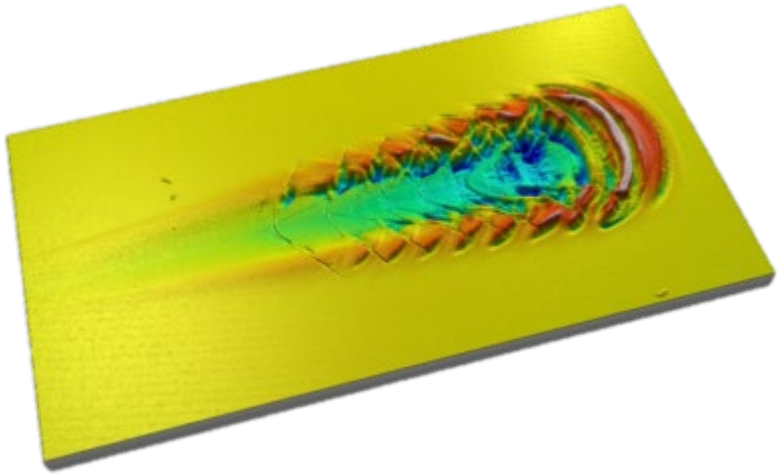

- Delamination is a common failure mode of thin films and coatings. The probability of delamination depends on the adhesion of the two materials, the thickness of the film, internal or mismatch stresses in the system, and other factors like mismatch of thermal expansion coefficients
- An analytical treatment allows understanding the basic relationships between the relevant factors and designing the system from the beginning in such a way that delamination is unlikely

Fracture mechanics in a homogeneous material

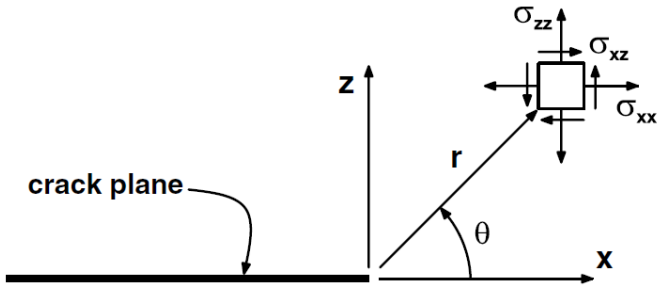

- Stress intensity factors for mode 1 and mode 2 loading are the scalar amplitudes of the asymptotic expansions of the stress field around the crack tip:

$$\sigma_{zz} = \frac{K_{\mathrm{I}}}{\sqrt{2\pi r}} \Sigma_{zz}^{\mathrm{I}} + o(1), \qquad \sigma_{xz} = \frac{K_{\mathrm{II}}}{\sqrt{2\pi r}} \Sigma_{xz}^{\mathrm{II}}$$

$$K_{\mathrm{I}} = \lim_{r \to 0} \sqrt{2\pi r}\, \sigma_{zz}(r, 0). \qquad K_{\mathrm{II}} = \lim_{r \to 0} \sqrt{2\pi r}\, \sigma_{xz}(r, 0).$$

- Energy release rate for planar crack growth is related to stress intensity factors for homogeneous materials by:

$$\mathcal{G} = \frac{1 - \nu^2}{E} \left(K_{\mathrm{I}}^2 + K_{\mathrm{II}}^2 \right) = \frac{1}{\bar{E}} \left(K_{\mathrm{I}}^2 + K_{\mathrm{II}}^2 \right).$$

Fracture mechanics in elastically dissimilar materials

Substrate	Film	E_s (GPa)	ν_s	E_f (GPa)	ν_f	D_1	D_2
Si (100)	Al	130	0.28	70	0.35	–0.28	–0.04
Si (100)	Cu	130	0.28	130	0.34	0.02	0.03
Si (100)	W	130	0.28	85	0.30	–0.20	–0.04
Al_2O_3	Al	372	0.25	70	0.35	–0.67	–0.14
Al_2O_3	Au	372	0.25	78	0.44	–0.61	–0.03
Al_2O_3	Mo	372	0.25	324	0.31	–0.05	0.01
Al_2O_3	Ni	372	0.25	200	0.31	–0.28	–0.05
SiO_2	Cu	71	0.16	130	0.34	0.34	0.14
Steel	DLC	210	0.30	80.8	0.13	–0.47	–0.15
PMMA	Al	3.4	0.30	70	0.35	0.91	0.23

- For thin films on substrates with dissimilar elastic constants, the fracture mechanical problem is governed bythe Dundurs parameters:

$$D_1 = \frac{\bar{E}_f - \bar{E}_s}{\bar{E}_f + \bar{E}_s} \qquad D_2 = \frac{1}{4}\left[\frac{\bar{E}_f(1-\nu_f)(1-2\nu_s) - \bar{E}_s(1-\nu_s)(1-2\nu_f)}{\bar{E}_f(1-\nu_f)(1-2\nu_s) + \bar{E}_s(1-\nu_s)(1-2\nu_f)}\right]$$

- For certain material combinations, we can assume that $D_2 = 0$. In this case, the energy release rate can be expressed as:

$$\mathcal{G} = \frac{\bar{E}_f + \bar{E}_s}{2\bar{E}_f\bar{E}_s}\left(K_I^2 + K_{II}^2\right) = \frac{1}{\bar{E}_s(1+D_1)}\left(K_I^2 + K_{II}^2\right)$$

Delamination of a thin film due to internal stress

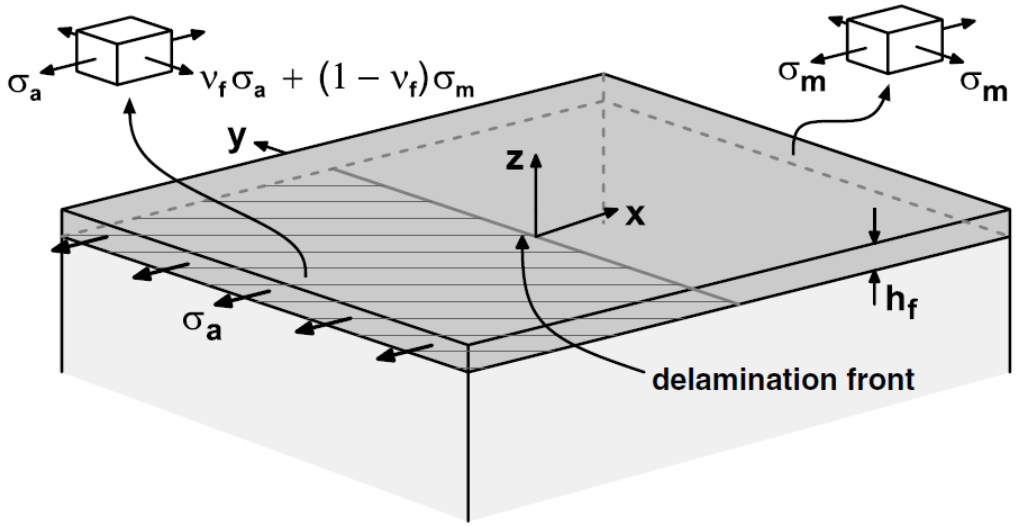

- Problem of spontaneous delamination of a thin film on a thick substrate due to internal stresses in the coating
- Linear elastic behaviour is assumed for both materials
- It is further assumed that the energy necessary to drive a crack is constant for both materials and not a function of internal stress
- A homogeneous biaxial tensile stress acts on the thin film

Delamination of a thin film due to internal stress

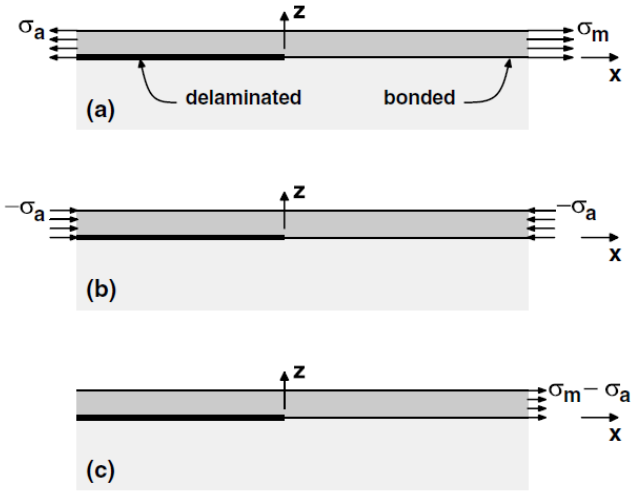

- Configuration with a thin film on a thick substrate with a delamination crack present for $x < 0$
  - a) If $\sigma_a \neq \sigma_m$, then some traction has to be transmitted across the interface for $x > 0$
  - b) A uniform biaxial stress acts on the thin film and no traction is transmitted across the interface
  - c) Superposition of the two stress fields in a) and b) results in stress $\sigma_x=\sigma_a-\sigma_m$ far ahead of the delamination front and $\sigma_x=0$ far behind it.
- The stress field around the crack tip therefore scales with $\sigma_a - \sigma_m$

Delamination of a thin film due to internal stress

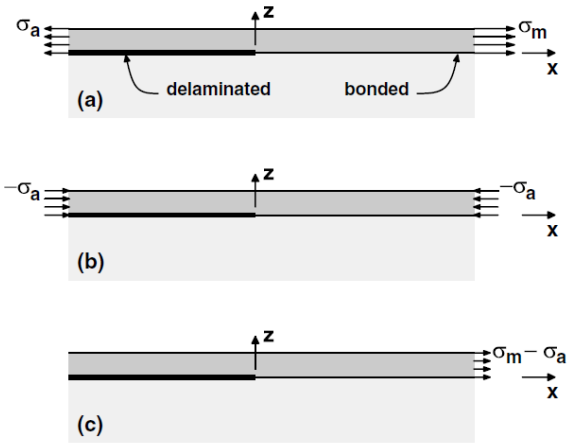

- Energy release rate for delamination of a thin film:

$$\mathcal{G} = \frac{1-\nu_f^2}{2E_f}(\sigma_m - \sigma_a)^2 h_f$$

- For a straight delamination front and a free film edge:

$$\frac{(1+\nu_f)E_f}{2(1-\nu_f)}\epsilon_m^2 h_f = \Gamma$$

- This allows calculating the critical film thickness for which spontaneous delamination will occur for a given strain mismatch.

$$(h_f)_{cr} = 2\frac{(1-\nu_f)\Gamma}{(1+\nu_f)E_f\epsilon_m^2} = 2\frac{\bar{E}_f\Gamma}{\sigma_m^2}$$

Delamination of a thin film due to internal stress

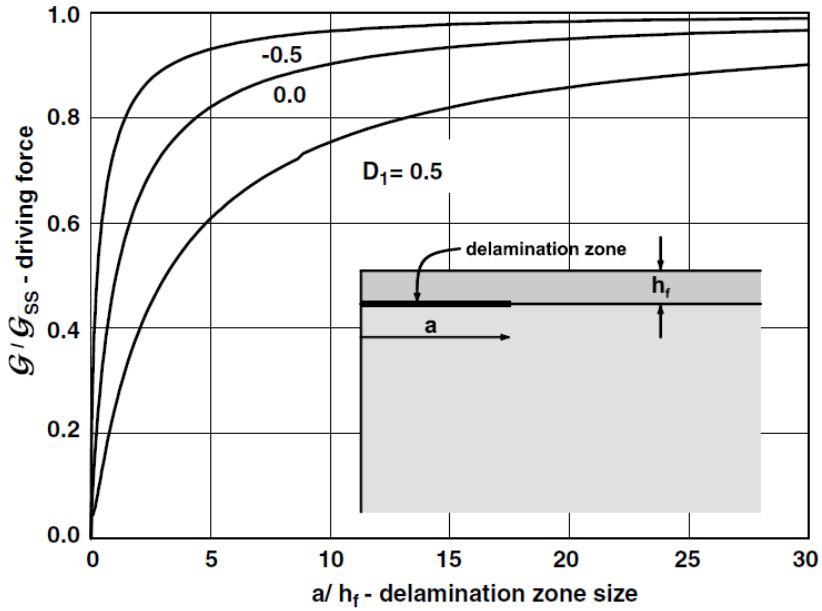

- Energy release rate near a film edge is lower than a steady state propagating delamination leading to an initiation barrier at free edges
- No analytical solution exists, but numerical simulations can assess this issue (Yu et al., 2001)
- Effect is small: Energy release rate is already 90% of the steady state value if the delamination front has advanced by only 5% of the film thickness from the free edge.

Exercise: Delamination due to thermal mismatch

Consider a thin film of Aluminum (thickness 1 μm), deposited at 220°C on a (100) Si substrate, (thickness 300 μm, diameter 200 mm). The thermoelastic properties are E_f = 70 GPa, ν_f = 0.35, α_f = 23 × 10^{-6} K^{-1}, E_s = 130 GPa, ν_s = 0.28, and α_s = 3 × 10^{-6} K^{-1}. The film-substrate system is stress-free at the deposition temperature.

- Determine the fracture energy of the interface if the energy release rate due to the mismatch strain of the film with respect to the substrate at a temperature of 20 °C is just enough to propagate a straight delamination front along the interface.
- In an attempt to facilitate the deposition of thicker aluminum films, the processing conditions were modified in such a way that the interface separation energy was guaranteed to be at least 5 J m−2. Find the thickness of the aluminum film for which spontaneous delamination of a straight front would occur at the minimum guaranteed interface separation energy.

Exercise: Delamination due to thermal mismatch

Solution:

epitaxy

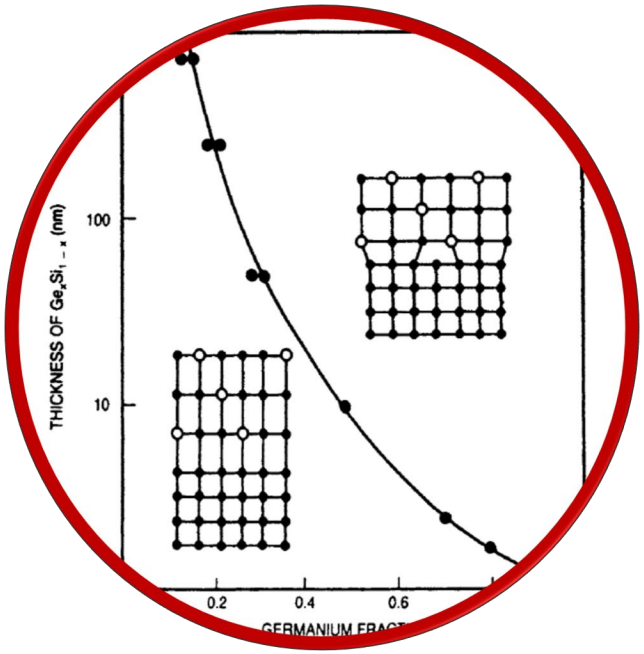

epitaxy application examples

- Wafer scale LEDs

- Laser mouse

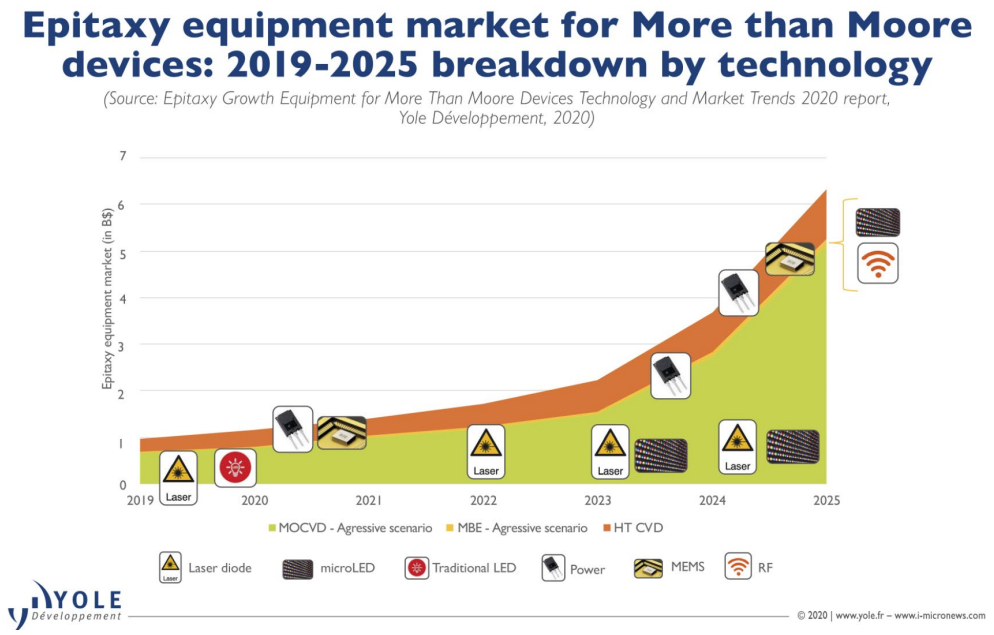

https://www.ledinside.com/news/2019/5/epitaxy_wafer_the_fundamental_phase_microled_display
http://www.yole.fr/iso_album/illus_epitaxy_equipment_materials_equipmentmarket_mtmdevices_yole_jan2020.jpg

content

- Homeepitaxy vs heteroepitaxy
- Crystallography "reloaded"
- Heteroepitaxy notation
- Epitaxial misfit: Strain energy, critical thickness, plastic relaxation
- Elastic relaxation
- Defects in epitaxial films
- Formation of misfit dislocations
- Epitaxy of compound semiconductors
- Design of epitaxial Film substrate combinations
- Liquid phase epitaxy
- ELO – epitaxial overgrowth
- MOCVD
- MBE
- Silicon heteroepitaxy
- Wafer bonding
- Devices and applications

introduction

Two types of epitaxy can be distinguished and each has important scientific and technological implications.

Homoepitaxy refers to the case where the **film and substrate are the same material**. Epitaxial (epi) Si deposited on Si wafers is the most significant example of homoepitaxy. In fact, one of the first steps in the fabrication of integrated circuit transistors in the past was CVD vapor-phase epitaxy of Si on Si. The reader may well ask why the underlying Si wafer is insufficient; why must single-crystal Si be extended by means of the epi-film layer? The reason is that the **epilayer is generally freer of defects**, is **purer** than the wafer substrate, and **can be doped independently** of it.

The second type of epitaxy is known as **heteroepitaxy** and refers to the case where **films and substrates are composed of different materials**, e.g., AlAs deposited on GaAs. Heteroepitaxy is the more common phenomenon. Optoelectronic devices such as light-emitting diodes (LEDs) and lasers utilizing compound semiconductors, are based on heteroepitaxial film structures.

Ohring 2002

Basic crystal structures and important planes

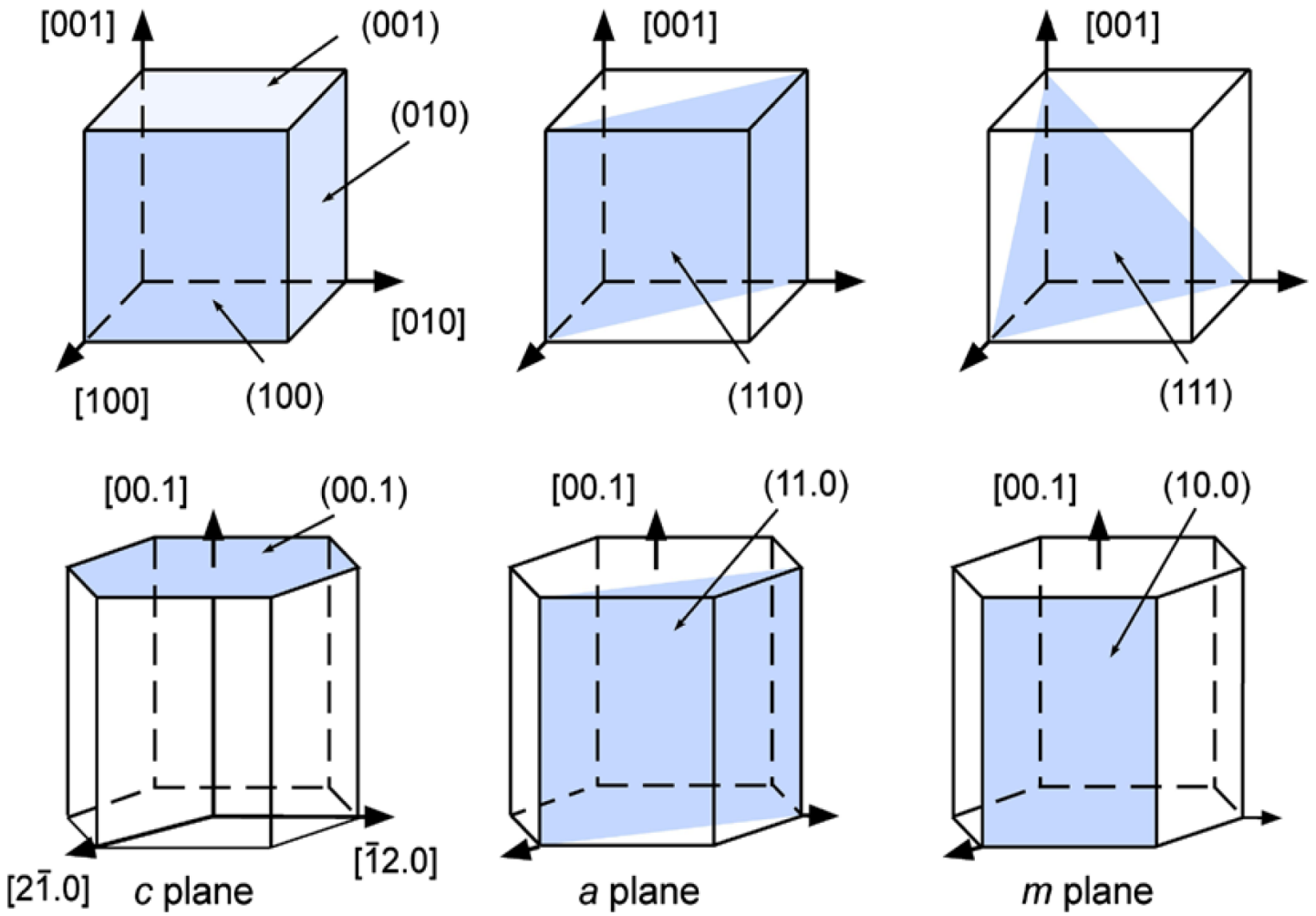

Fig. 2.1 Position of important planes and their Miller indices for cubic and hexagonal lattices

Pohl 2013

Wafer flats (up to 4 inch)

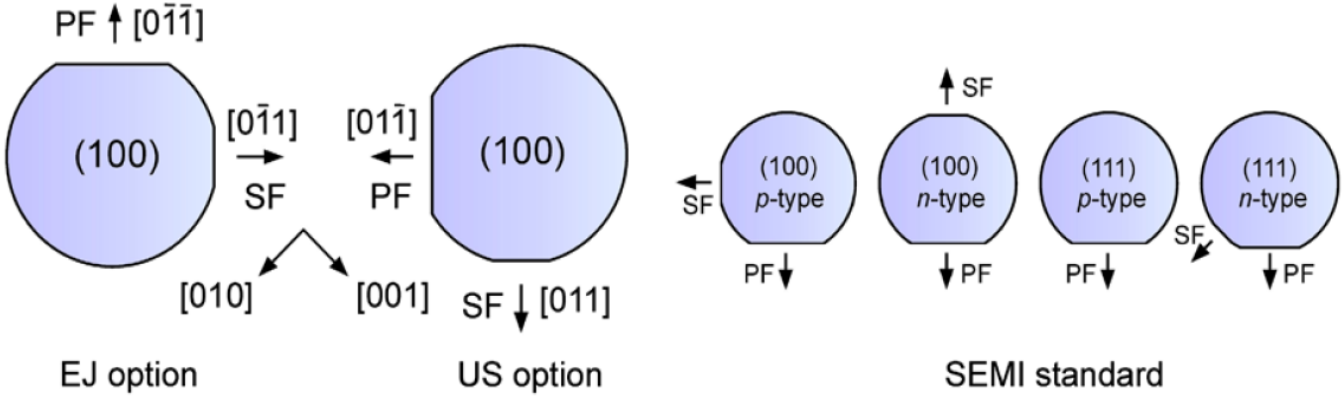

Fig. 2.2 Semiconductor wafers with standard flat orientations according various options. *PF* and *SF* denote primary and secondary flats, respectively. The *arrows* along [010] and [001] refer to the coordinate system of the two wafers on the *left hand side*

Semiconductor wafers with standard flat orientations. PF and SF denote primary and secondary flats, respectively. The arrows along [010] and [001] refer to the coordinate system of the two wafers on the left hand side.

Pohl 2013

Homoepitaxy vers heteroeepitaxy

1) If the **lattice mismatch** is **zero or very small**, then the heterojunction interfacial structure is essentially like that for homoepitaxy.

2) the two **lattices strain** to accommodate their crystallographic differences

3) **dislocation defects form at the interface** (relaxed epitaxy).

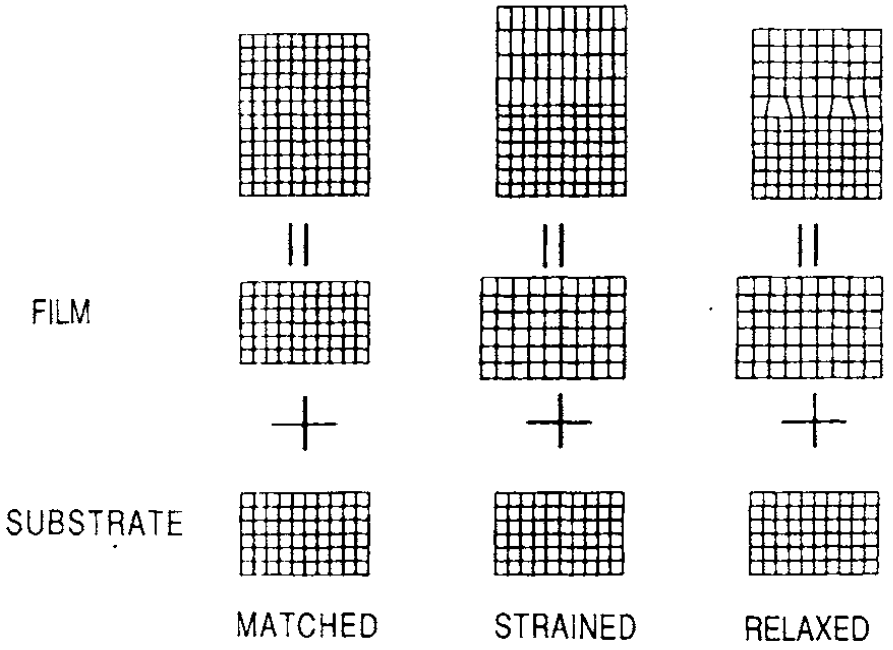

Ohring 2002

Heteroeepitaxy - notation

The indices of the **overgrowth plane are written as (HKL)** while those of the **parallel substrate plane** at the common interface are taken as **(hkl)**. The corresponding parallel directions in the overgrowth and substrate planes, denoted by [UVW] and [uvw], respectively, must also be specified.

This tetrad of indices, written by convention serves to define the epitaxial geometry.

As an example, **for parallel epitaxy of Ni on Cu**, the notation would read

(001)Ni//(001)Cu;
[100]Ni//[100]Cu.

In this case **both planes and directions coincide**.

For the example

(lll)PbTe//(lll)$MgAl_2O_4$;[211]PbTe//[101]$MgAl_2O_4$

The **interfacial plane is common but the directions are not**.

Ohring 2002

Metal/semiconductor heteroeepitaxy

A sharp, defect-free interface between cobalt silicide ($CoSi_2$) and Si can be obtained. Similar epitaxial relationships hold between $NiSi_2$ and Si.

Both silicides have cubic CaF_2 structures with respective lattice parameters of 5.365 Å and 5.406 Å. These are close to the a_o value for Si, i.e., 5.431 A, and therefore, the resulting lattice misfit for $CoSi_2$is simply

f = (5.431 - 5.365)/5.365 = 0.0123.

Other metal silicide films do not exhibit the same epitaxial quality.

Ohring 2002

Epitaxial misfit I

As described by **van der Merwe** any **epitaxial layer having a lattice-parameter mismatch with the substrate of less than ~9% would grow initially pseudomorphically**. Initially, very thin films strain elastically to have the same interatomic spacing as the substrate, making the **interface coherent** with atoms on either side lining up.

With **increasing film thickness** the rising total elastic strain energy will eventually **exceed the energy associated with a relaxed structure** consisting of an **array of misfit dislocations**. separated by wide regions of relatively good fit.

At this point the **initially strained film ideally decomposes to this relaxed structure** where a **portion of the misfit is relieved by dislocations**.

As the **film continues to grow, more misfit is relieved** until at infinite thickness the elastic strain is totally eliminated.

Ohring 2002

Epitaxial misfit II

Throughout it is assumed that film and substrate have **the same Young's (Y) modulus and same shear μ modulus**.

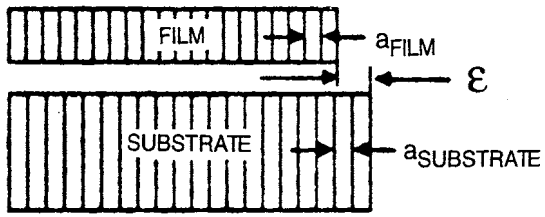

d < d_c. In the early stages of film growth, elastic strain energy E_e (per unit area) increases with d as

$$E_e = Y\, d\varepsilon^2/(1-\nu)$$

where ε **is the biaxial elastic strain** and ν is Poisson's ratio. No dislocations are present in the film.

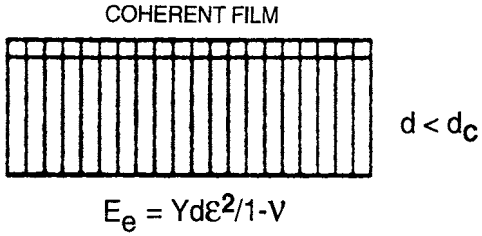

d > d_c. Now consider the **formation of (misfit) dislocations** at the film-substrate interface as a means of relieving the elastic strain that develops during further film growth. If the **dislocations are assumed to be arrayed in a square grid** of side S, the elastic strain in the film is reduced from its initial misfit value to ε = f - b / S

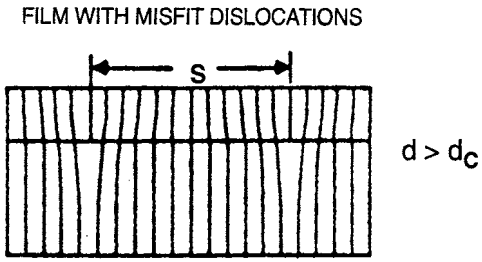

Ohring 2002

Epitaxial misfit III

b/S is proportional to the number of misfit dislocations at the interface and when **b/S=f the film strain vanishes**.

each dislocation **threads the entire film thickness** and extends the lateral film length by the Burgersvector magnitude, b.

The **total strain energy E_T** (per unit area) is a sum of the **elastic and dislocation energy E_d** (per unit area) or

$$E_T = \frac{Yd(f - b/S)^2}{(1-\nu)} + \frac{\mu b^2 2\ln(\beta d/b)}{4\pi(1-\nu)S}.$$

(elastic) (dislocation)

The second term has been derived from the energy per unit length of a dislocation is

$$[\mu b^2/4\pi(1-\nu)]\ln(R_0/b) + E_c,$$

where R_o is a radius about the dislocation where the strain field terminates, and E_c is the dislocation core energy.

Physically the equation indicates that strain energy is a volume energy that increases linearly with film thickness. In contrast, dislocation energy is nearly constant with only a weak logarithmic dependence on d arising from R_o.

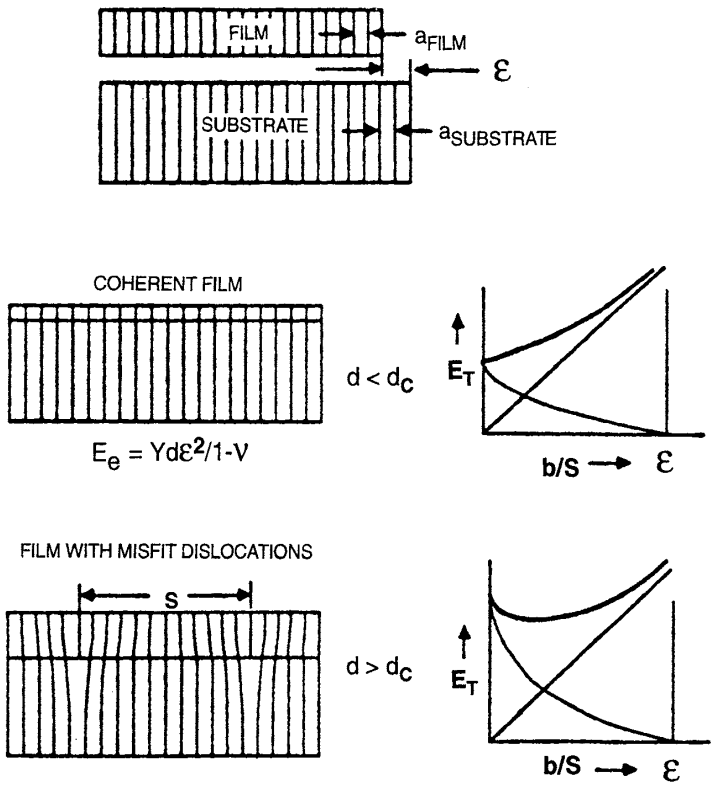

Figure 8-7 Illustration of the Matthews–Blakeslee equilibrium theory of misfit-dislocation formation. (Top) Coherent film is produced when $d < d_c$. (Bottom) Film with misfit dislocations result when $d > d_c$. (From Ref. 18. Reprinted with permission of W. D. Nix.)

Ohring 2002

Epitaxial misfit IV

The fact that there is a **minimum in E_T at a nonzero b/S value** reveals that the structure is in mechanical equilibrium only if dislocations are present.

By minimizing the total energy with respect to dislocation number, i.e.,
$dE_T/d(b/S) = 0$, and evaluating the resulting expression **at b/S = 0**, the critical film thickness (d_c) is

$$d_c = \frac{b}{8\pi(1+\nu)f}\ln(\beta d_c/b),$$

For **films thicker than d_c, misfit dislocations appear.** In the region where d_c is approximately a few thousand angstroms, d_c is roughly b/2f.

This means that the film will be pseudomorphic until the accumulated misfit fd_c exceeds about half the unit cell dimension or b/2.

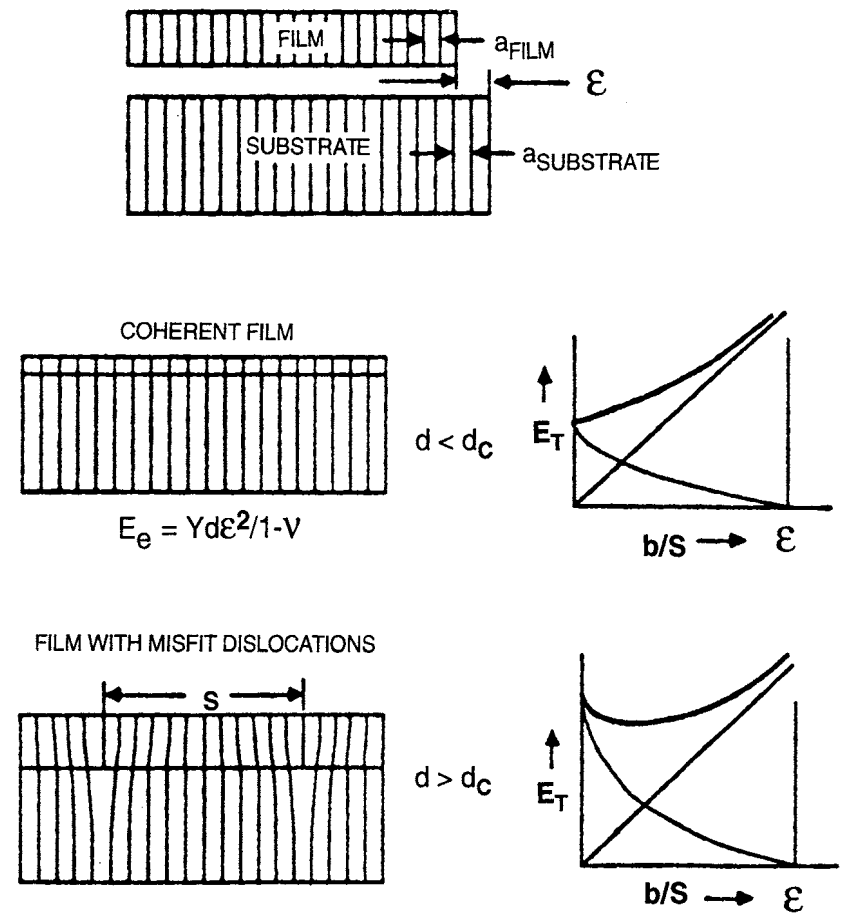

Figure 8-7 Illustration of the Matthews–Blakeslee equilibrium theory of misfit-dislocation formation. (Top) Coherent film is produced when $d < d_c$. (Bottom) Film with misfit dislocations result when $d > d_c$. (From Ref. 18. Reprinted with permission of W. D. Nix.)

Ohring 2002

Defects in Ge_xSi_{1-x}/Si films

Nature is kinder to us than the Matthews theory would suggest, and considerably thicker films than predicted d_c can be deposited in practice.

The reason is that Ge_xSi_{1-x} strained-layer films are not in equilibrium. Extended dislocation arrays do not form instantaneously with well-defined spacings; rather, dislocations nucleate individually over an area determined by a width w and unit depth, over which atoms above and below the slip plane are displaced by at least b/2.

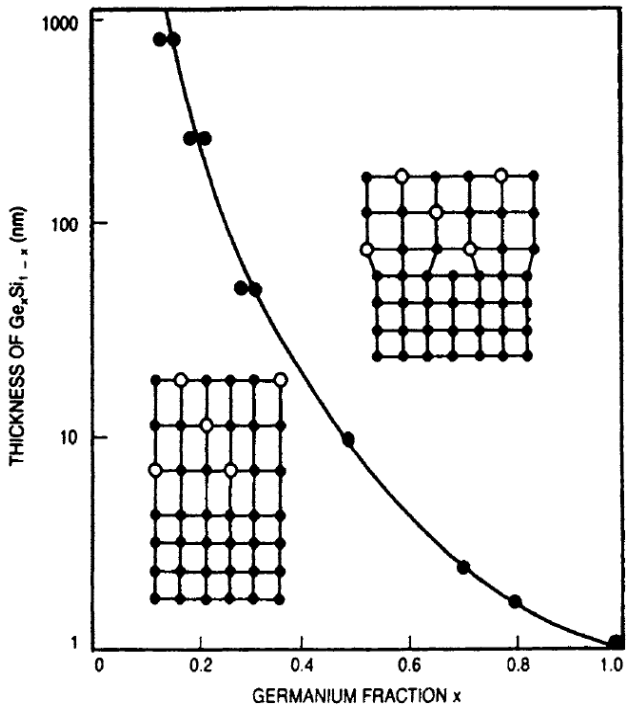

Figure 8-8 Experimentally determined limits for defect-free strained-layer epitaxy of Ge_xSi_{1-x} on Si. Note that f is proportional to Ge fraction. (From Ref. 22.)

Ohring 2002

Defects in Ge_xSi_{1-x}/Si films II

These films exhibit interesting strain-induced **modulations in surface morphology** that are shown in the TEM cross-sectional image.

The **surface ripples** arise because the film is under compressive stress, a consequence of the fact that lattice parameters of Ge-Si solid-solution alloys necessarily exceed those for Si.

As a result the lattice-plane spacing of the film shrinks near the cusplike troughs and expands at the rounded peaks as schematically depicted.

A **flat surface might be expected** to represent the minimum energy configuration. However, when **relieval of film strain-energy outweighs the tendency of surface energy** to smooth steps arising from the relaxation distortion, roughening of the surface occurs.

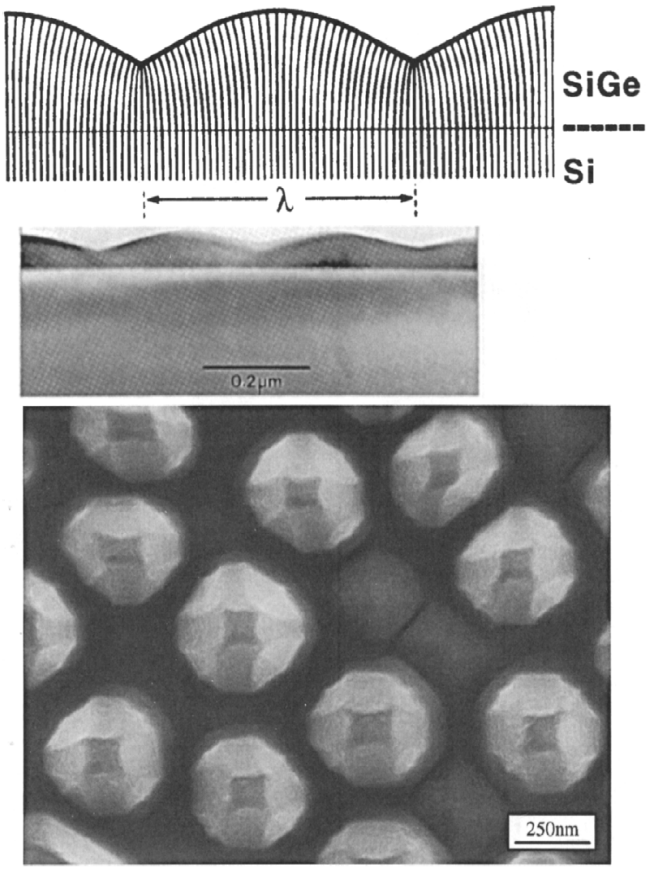

Figure 8-9 (Top) Cross-sectional [100] TEM image of strain-induced surface ripples on an uncapped $Ge_{0.81}Si_{0.19}$ film and accompanying schematic depiction of the distortion of vertical lattice planes. (After Ref. 23. Reprinted with the permission of the author.) (Bottom) Scanning electron micrograph top-view of faceted pyramid and dome-shaped islands formed during growth of a 40 nm thick $Si_{0.7}Ge_{0.3}$ alloy film on (001) Si. Film growth was by UHVCVD (Section 8.6.3.2) at 690°C. The largest islands are 70 nm high. (Courtesy of F. M. Ross, IBM, T. J. Watson Research Center.)

Ohring 2002

Defects in epitaxial films I

Semiconductor wafers are now largely "dislocation free";

in **silicon** there are fewer than **10 dislocations/cm^2**

for **GaAs** the dislocation density is typically less than **1000/cm^2**.

It is well known that **dislocations, twins, and stacking faults degrade many device properties** by **lowering carrier concentrations and mobilities**.

They create states in the energy gap and serve to reduce the minority carrier lifetime and quantum efficiency of photonic devices.

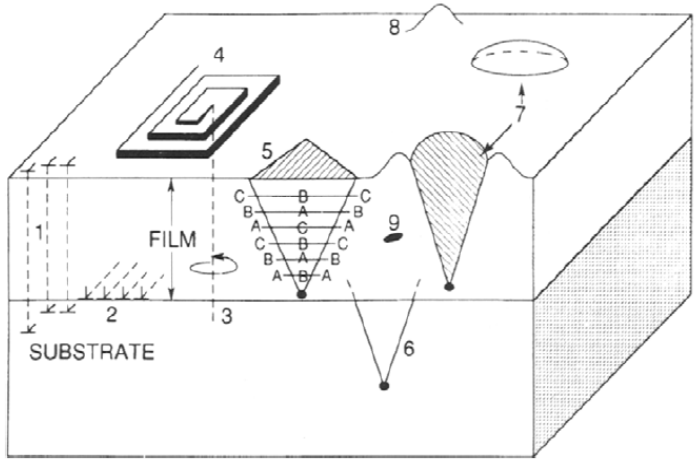

Figure 8-10 Schematic composite of crystal defects in epitaxial films. 1, Threading edge dislocations; 2, interfacial misfit dislocations; 3, threading screw dislocation; 4, growth spiral; 5, stacking fault in film; 6, stacking fault in substrate; 7, oval defect; 8, hillock; 9, precipitate or void.

Ohring 2002

Defects in epitaxial films II

Defects from the substrate:

(4) propagation of an **emergent screw dislocation spiral** from the substrate surface into the growing film.

(5) Stacking faults: **faceted growth hillocks** which nucleate at the film-substrate interface and nest within the epitaxial layer

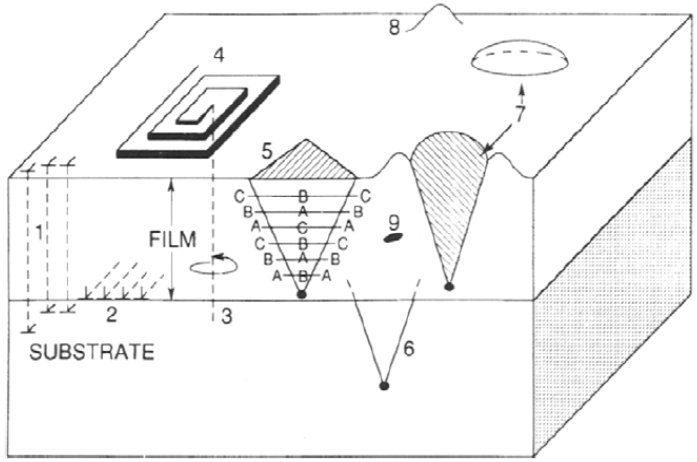

Figure 8-10 Schematic composite of crystal defects in epitaxial films. 1, Threading edge dislocations; 2, interfacial misfit dislocations; 3, threading screw dislocation; 4, growth spiral; 5, stacking fault in film; 6, stacking fault in substrate; 7, oval defect; 8, hillock; 9, precipitate or void.

Ohring 2002

Formation of misfit dislocations

Although misfit **dislocations lie in planes parallel to the substrate-film interface**, they generally **originate from threading dislocations**.

These **pierce through the film, the substrate, or both and** lie in crystallographic planes that intersect the interface plane.

As it extends into the stressed film **the threading component glides or bends** in the slip plane. This dislocation segment bends more and more as the film thickens and becomes increasingly stressed.

Correspondingly, the threading dislocation portion in the oppositely stressed substrate moves slightly in the opposite direction. Finally, at the critical thickness d>dc, **the film dislocation is able to glide infinitely, leaving behind a stable misfit dislocation at the interface**.

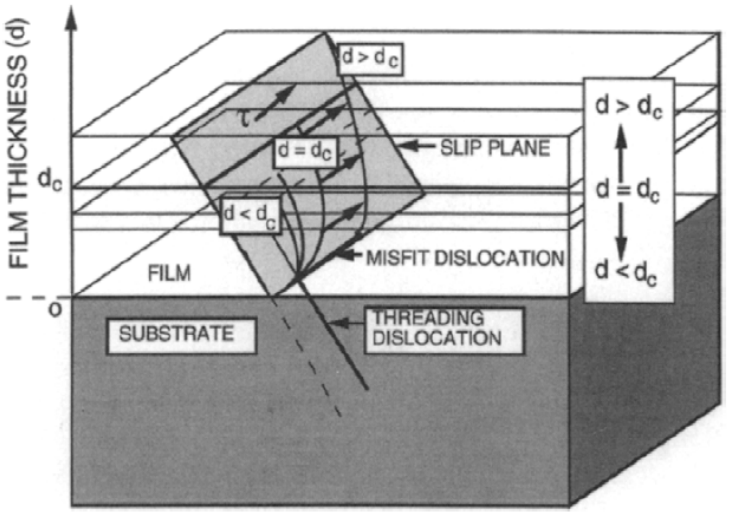

Figure 8-11 A depiction of how stress on thin film plane causes threading dislocation from substrate to form a misfit dislocation when $d > d_c$. (After Refs. 18 and 28.)

Ohring 2002

Formation of misfit dislocations

Misfit dislocations have been often observed by transmission electron microscopy. For example, a misfit dislocation array, generated during relaxation of a SiGe alloy film on (100) Si.

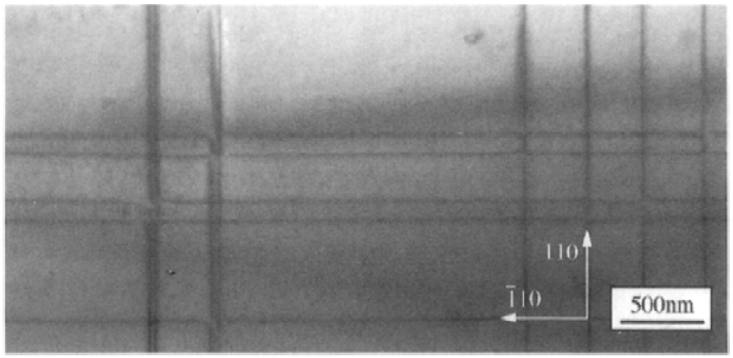

Figure 8-12 Misfit dislocation array generated during relaxation of a 200 nm thick $Si_{0.85}Ge_{0.15}$ alloy film on (001) Si. Bright field 220 transmission electron micrograph taken after MBE growth and 700°C annealing. (Courtesy of F. M. Ross, IBM, T. J. Watson Research Center.)

Ohring 2002

Epitaxy of compound semiconductors

When light is emitted from or absorbed in a semiconductor, **energy as well as momentum must be conserved**.

In a **direct bandgap semiconductor** the carrier transitions between the valence and conduction bands occur without change in momentum of the two states involved.

In the energy momentum or equivalent energy-wave vector, parabola-like (E vs k) representation of semiconductor bands emission of light occurs by a **vertical electron descent** from the **minimum conduction band energy level** to the **maximum vacant level in the valence band** (GaAs and InP).

However, in **indirect-bandgap semiconductors** (Ge and Si) the transition occurs **with a change in momentum** that is essentially **accommodated by excitation of lattice vibrations and heating of the lattice**. This makes **direct hole-electron recombination with photon emission unlikely**.

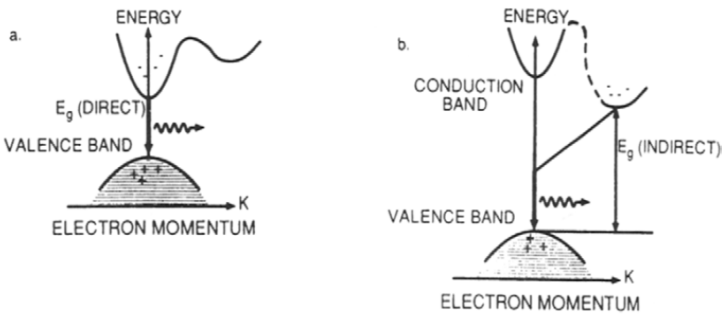

Figure 8-13 Depiction of electron transitions between conduction and valence bands in (a) direct- and (b) indirect-gap semiconductor materials.

Ohring 2002

Epitaxy of compound semiconductors – bandgap energy

If **light of intensity I_o** is incident on a semiconductor surface, the photon intensity at a depth x below the surface is **attenuated to I(x)**,

$$I(x) = I_0 \exp - \alpha x.$$

In all semiconductors α **becomes negligible** once the **wavelength exceeds the cutoff value λ_c**. This critical wavelength, is related to the bandgap energy Eg by a variant of the well-known relation E = hv or more simple

$$\lambda_c(\mu m) = 1.24/E_g(eV).$$

For **direct-bandgap semiconductors** the value **of α becomes large on the short-wavelength side of λ_c**, signifying that light is absorbed very close to the surface. For this reason even thin-film layers of GaAs are adequate, for example, in solar cell applications.

To ensure **defect-free interfaces in semiconductor film/substrate heterostructures**, it is essential that also the **lattice parameters (a_o) of both be closely matched (typically less than 0.1%)**

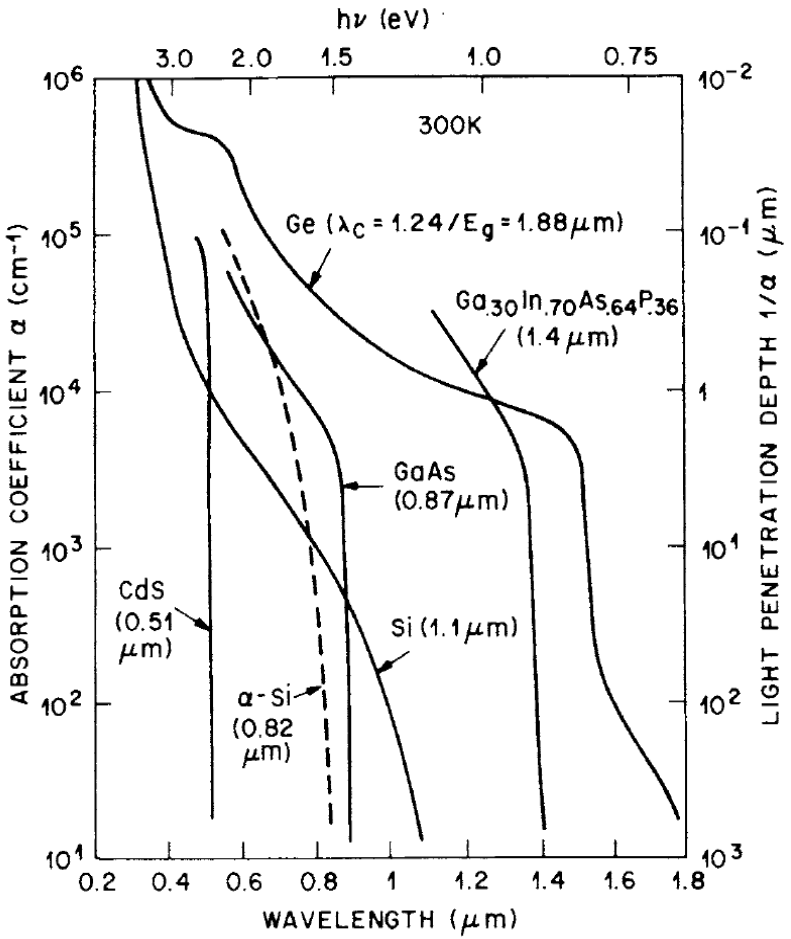

Figure 8-14 Optical absorption coefficients for various semiconductor materials. (Reprinted with permission from J. Wiley & Sons, S. M. Sze, *Semiconductor Devices—Physics and Technology*. McGraw-Hill, New York, 1985.)

Ohring 2002

Design of Epitaxial Film Substrate combinations

Elements and **binary compounds** are represented simply as **points**. **Ternary alloys** are denoted by **lines** between constituent binary compounds. *Blue* and *red* drawing denotes direct and indirect bandgap, respectively.

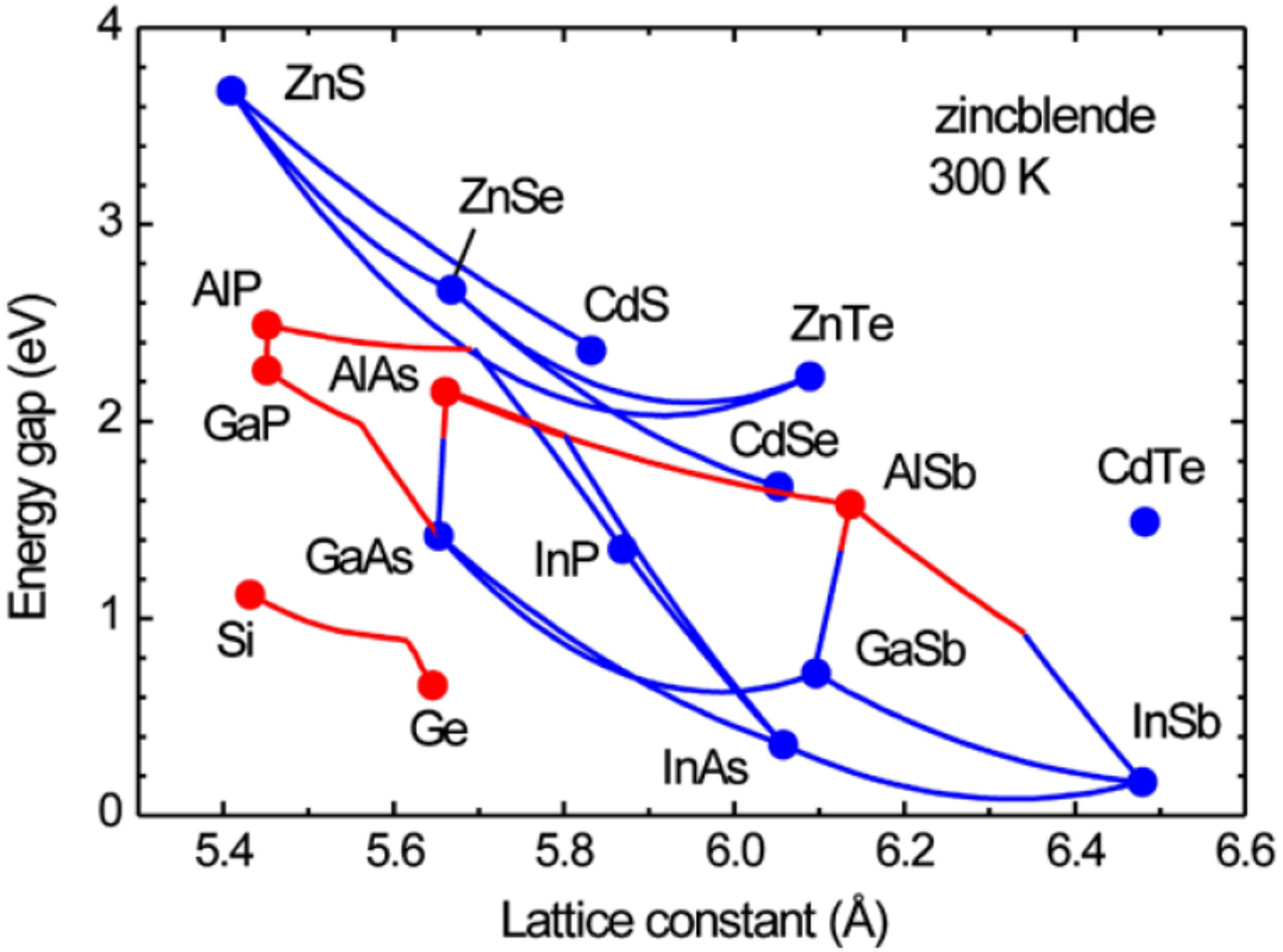

Pohl 2018

Design of Epitaxial Film Substrate combinations

Elements and **binary compounds** are represented simply as **points**. **Ternary alloys** are denoted by **lines** between constituent binary compounds. Thus the line between InP and InAs represents the collection of InP_xAs_{1-x} ternary solution alloys. Within the **areas outlined by four binary compounds are quaternary alloys**.

Solid lines represent direct-bandgap ternary compounds while the **dashed lines refer to materials with an indirect bandgap**.

Material for optoelectronic device with energy gap of 1.0 eV?

->Extend horizontal line at Eg = 1.0 eV we see that the alloys of the following pairs are crossed: GaAs-InAs; GaAs-GaSb; InP-InAs; AlAs-InAs; AlSb-GaSb; and AlSb-InSb.

Although these all appear to be potentially useful, AlSb-GaSb has an indirect bandgap and is disqualified.

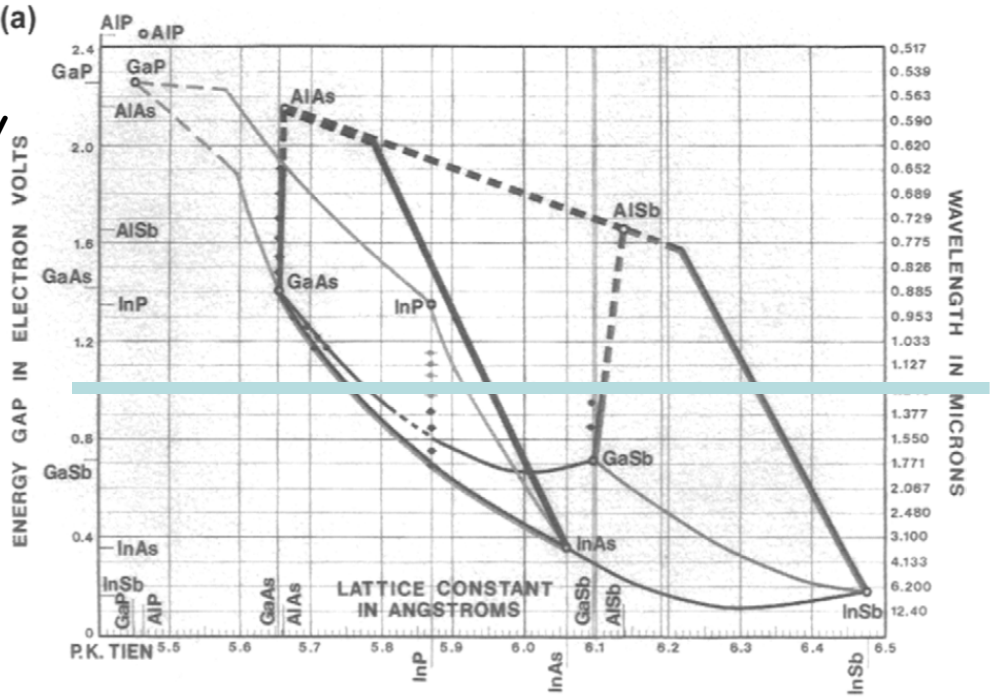

Ohring 2002

Design of Epitaxial Film Substrate combinations

Upon alloying these binary compounds we may assume, in the simplest approximation, that the resultant lattice constants and energy gaps of the ternaries are **weighted averages of the binary values**.

As an example, let us determine the composition of the desired InGaAs alloy for which a_o must equal 5.76 Angström the value at 1.0eV. For a linear law of lattice-constant mixtures, i.e., **Vegard's law,**

$a_o(In_x\ Ga_{1-x}As) = (x)\ a_o(InAs) + (1 - x)a_o(GaAs)$.

Since 5.76 - 6.07x + 5.65(1 - x), x = 0.26,

and the predicted alloy has the composition $In_{0.26}Ga_{0.74}As$

Next, consider the practical problem **of fabricating lasers emitting coherent light at 1.0eV**. In these devices, semiconductor films must be deposited on a readily available substrate, e.g., GaAs or InP, and, importantly, be lattice matched to it, which adds another round of alloy design.

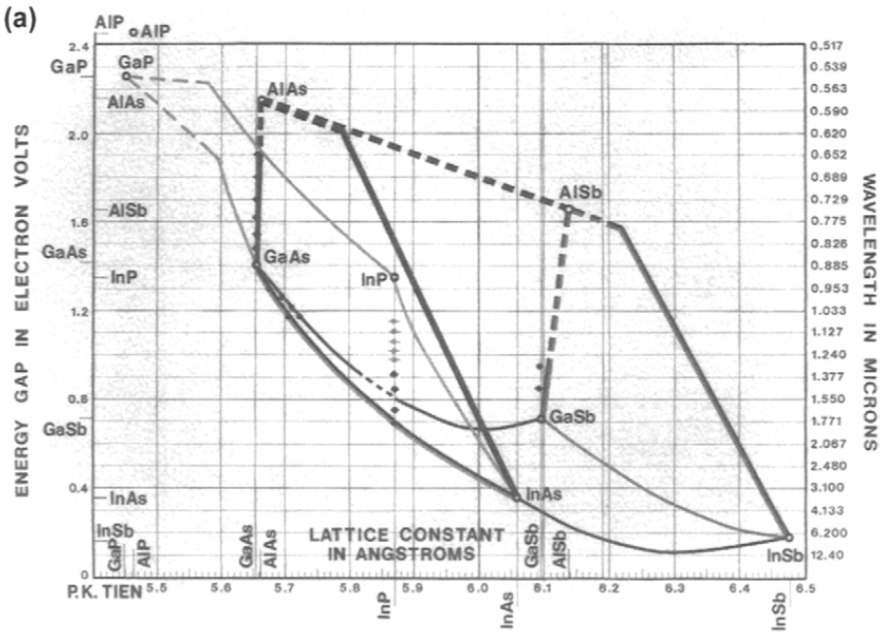

Ohring 2002

Epitaxial films from melts – liquid phase epitaxy

LPE involves the **precipitation of a crystalline film from a supersaturated melt** onto a substrate.

Consider a Ga-rich melt containing 10 at.% As. When heated above ~ 920°C all of the As dissolves. If the **melt is cooled below the liquidus temperature** into the two-phase field, it **becomes supersaturated with respect to As**.

Only a melt of lower than the original As content can now be in equilibrium with GaAs. The excess As is, therefore, rejected from solution in the form of GaAs which grows epitaxially on a suitably placed substrate.

To grow multiple **GaAs/AlGaAs heterostructures**, the seed substrate is sequentially translated past **a series of crucibles holding melts** containing various amounts of Ga and As together with such dopants as Zn, Ge, Sn, and Se.

Since growth conditions of LPE processes **are close to thermodynamic equilibrium**, atoms can efficiently migrate to the growth interface **and find energetically optimum positions**, which results in a **very low density of defects**.

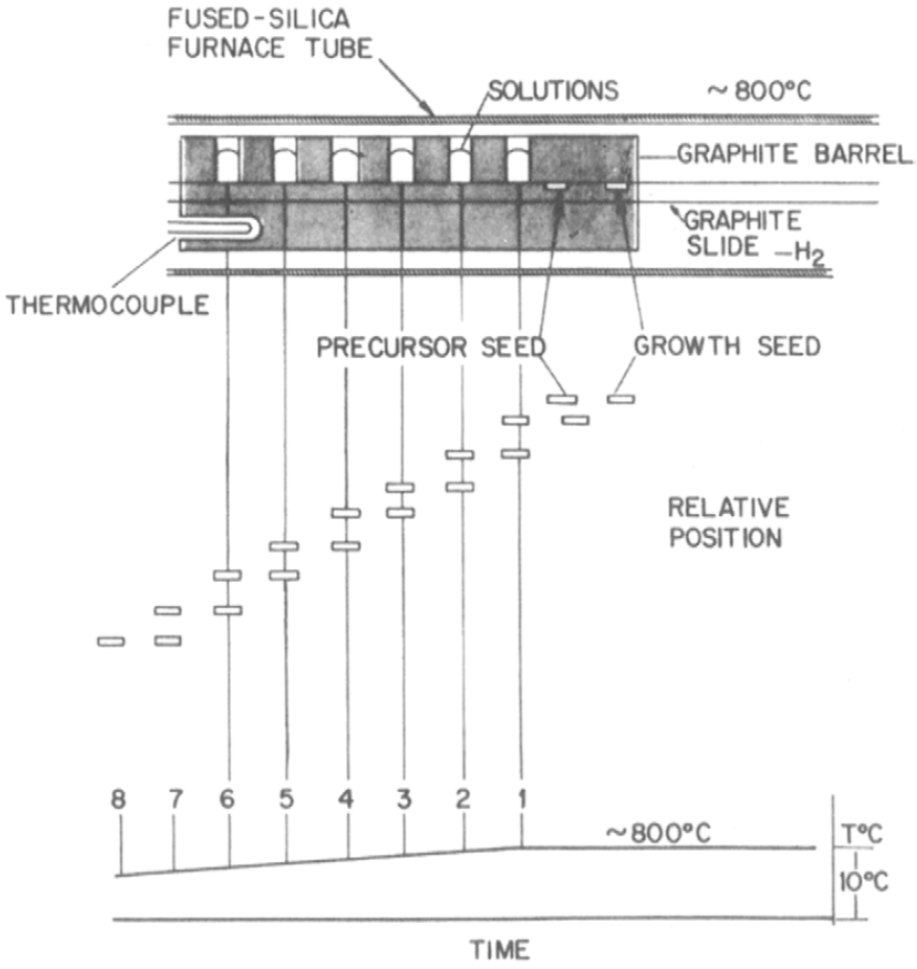

Ohring 2002

Epitaxial films from melts – lateral overgrowth

Epitaxial lateral overgrowth (ELO) is a method of selective epitaxial growth on partially masked substrates.

Prior to growth the substrate is covered by a thin SiO_2 or Si_3N_4 film which is next patterned by the standard photolithography.

The growth of the ELO layers for instance by **LPE starts selectively in mask-free seeding areas** and **proceeds laterally over the dielectric film.**

The key advantage of the ELO technique is that substrate **defects can propagate to the layer only through a narrow seed**, and therefore, a defect density in the layer should be considerably reduced.

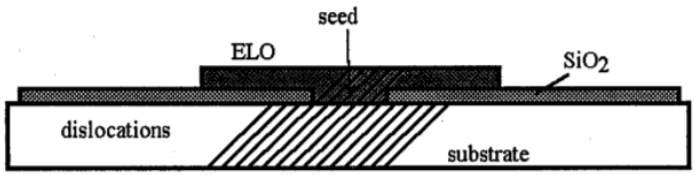

Ohring 2002

Metalorganic Vapor-Phase Epitaxy

MOCVD was invented to deposit III-V and II-VI compound semiconductor films where it is always the intent to grow **high-quality single-crystal or epitaxial films**. For this reason the acronyms **MOVPE** (metalorganic) or **OMVPE** (organometal) vapor-phase epitaxy or MOCVD are equivalently used when speaking of processes to deposit epitaxial films.

Chemically, precursors largely consist of **metal alkyl compounds** with methyl (M) and ethyl (E) groups present in twofold (di, D) or threefold (tri, T) coordination. A typical net reaction is

$$Ga(CH_3)_3 + AsH_3 \rightarrow GaAs + 3CH_4\uparrow.$$

Most metalorganic sources are liquids which are stored in bubblers. For transport to the reactor a carrier gas (usually hydrogen) with a flow Q_{MO} is introduced by a dip tube ending near the bottom. Hydrogen is used here as carrier gas and introduced into the metalorganic sources MO_1 and MO_2. MFC and PC denote mass-flow and pressure controllers, respectively

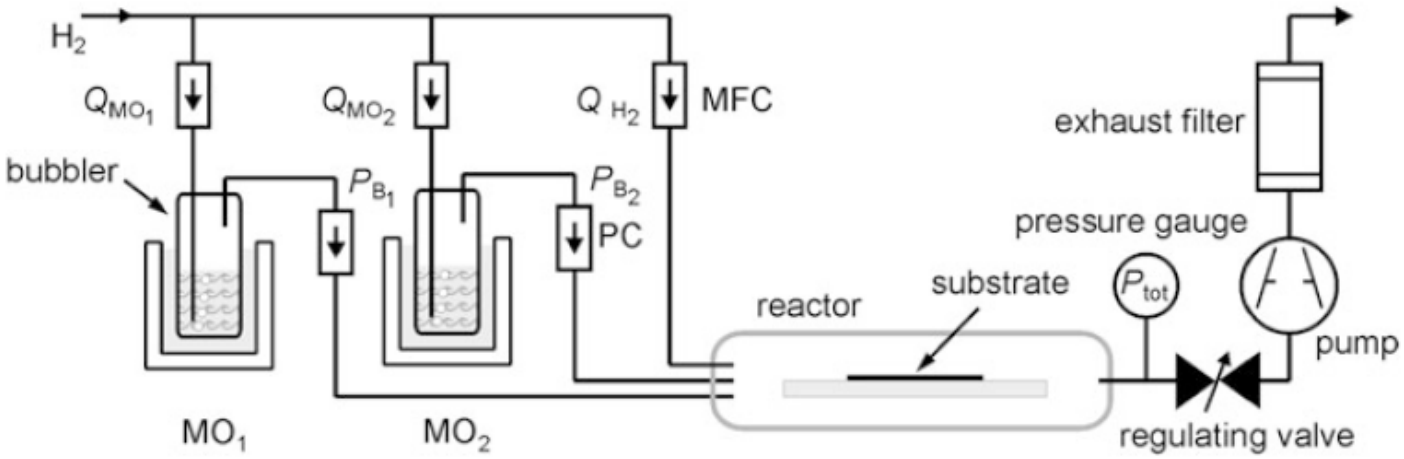

Pohl 2018

Metalorganic Vapor-Phase Epitaxy

Like **all CVD processes** the **complete treatment of the MOVPE growth process involves numerous gas phase and surface reactions, in addition to hydrodynamic aspects**. Such complex studies require a numerical approach.

In a simple CVD picture the reactants in the carrier gas represent the source.

Near the solid surface a vertical diffusive transport component originates from reactions of source molecules and incorporation into the growing layer.

All processes from adsorption at the surface to the incorporation are summarized to interface reactions.

Finally excess reaction products desorb from the interface by diffusion.

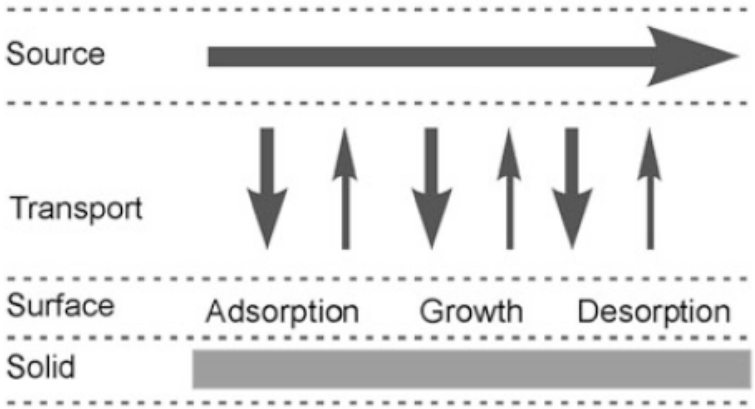

Pohl 2018

Metalorganic Vapor-Phase Epitaxy

The logarithmic scale of the GaAs growth rate: At low temperature experiment (solid) and simulation (open) show an exponential relation, indicating Precursor decomposition and interface growth reactions lead to a pronounced temperature dependence and is referred to as **kinetically limited growth**.

As the temperature is increased, the growth rate becomes nearly independent on temperature. In this range precursor decomposition and surface reactions are much faster than mass transport from the source to the interface of the growing solid. Since diffusion in the gas phase depends only weakly on temperature, this **process is called transport-limited growth**.

In the high-temperature range growth rates **decrease due to enhanced desorption** and parasitic deposition at the reactor walls, inducing a depletion of the gas phase.

Operation pressures range from 1mbar to atmospheric.

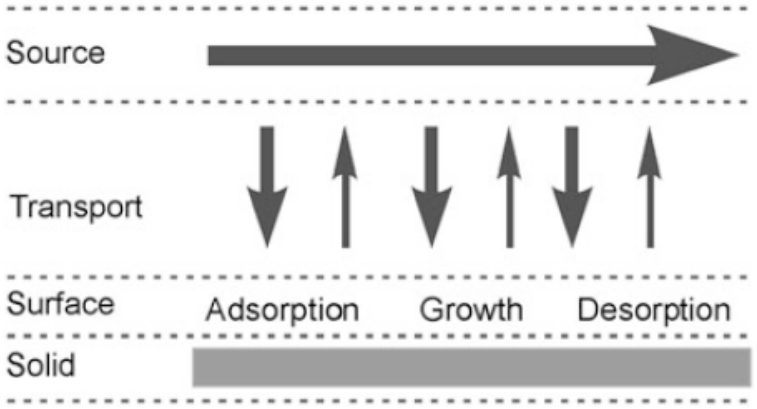

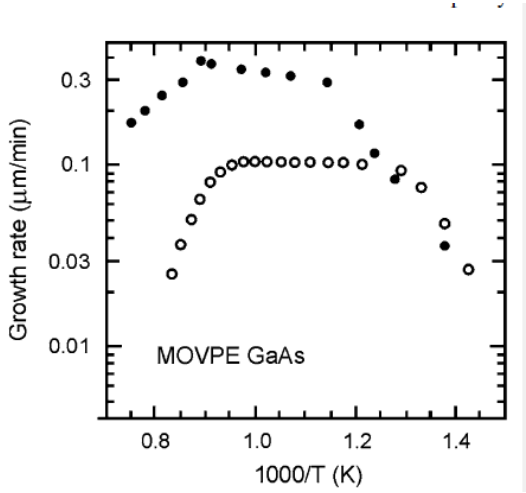

Pohl 2018

Molecular beam epitaxy

Molecular beam epitaxy essentially involves **highly controlled evaporation** in an **ultrahigh vacuum (~ 10^{-10}mbar)** system. The reaction of one or more **evaporated beams of atoms or molecules** with the single-crystal substrate yields the desired epitaxial film.

High-quality film-growth only ensues if **the surface-diffusion-incorporation time (τ_{di}) is less than for the deposition of a monolayer**. If these two times are reversed, unincorporated atoms will be physically buried by the incoming monolayer and give rise to defective layers.

Since τ_{di} is thermally activated, **a low growth temperature limit** is implied for good epitaxy. For example, at typical MBE growth rates in the range of 1 μm/h, excellent quality AlGaAs can be grown at temperatures as low as **~680°C GaAs as low as 475°C and InAs as low as 350°C**. In these results it appears that the Group III species governs the growth temperature.

Ohring 2002

Molecular beam epitaxy

An **MBE system features** independent control of beam sources and film deposition, cleanliness, and real-time structural and chemical characterization capability. In such systems precise fabrication of semiconductor heterostructures from a fraction of a micron thick down to a single monolayer is possible.

Arrayed around the substrate are semiconductor and dopant atom heating sources consisting of **either effusion cells or electron-beam guns**. The latter are employed for the high-melting Si and Ge materials. On the other hand, effusion cells are used to evaporate compound-semiconductor elements and their dopants.

An **effusion cell** is essentially an **isothermal cavity** containing a **hole through which the evaporant exits**;

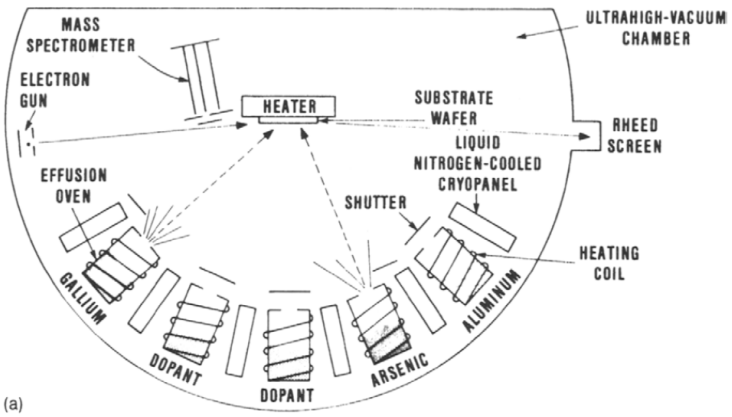

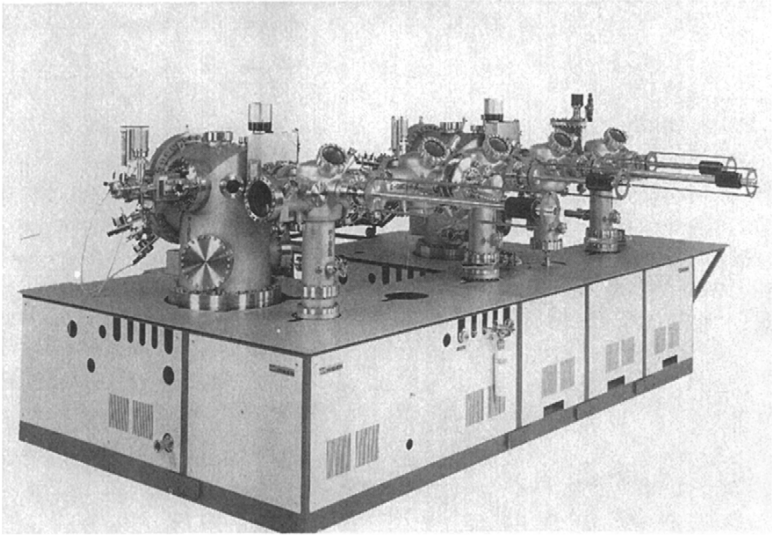

Ohring 2002

Molecular beam epitaxy

The vacuum is generated in a chamber by pumps and cryoshrouds. Usually effusion cells mounted opposite to the substrate produce beams of different species by evaporation.

The duration of the exposure on the substrate is individually controlled by shutters for a rapid change of material composition or doping.

The substrate is mounted on a heated holder and can be loaded and unloaded under vacuum conditions by a manipulating mechanism. A gauge can be placed at the position of the substrate to measure and calibrate the beam-equivalent pressure (BEP) produced by the individual sources. T

Virtually any MBE system is equipped with an electron-diffraction setup.

Molecular beam epitaxy is performed in ultra high vacuum (UHV), i.e., at a residual-gas pressure below 10^{-9} mbar. The need for such low pressure originates from the required purity of epitaxial semiconductors.

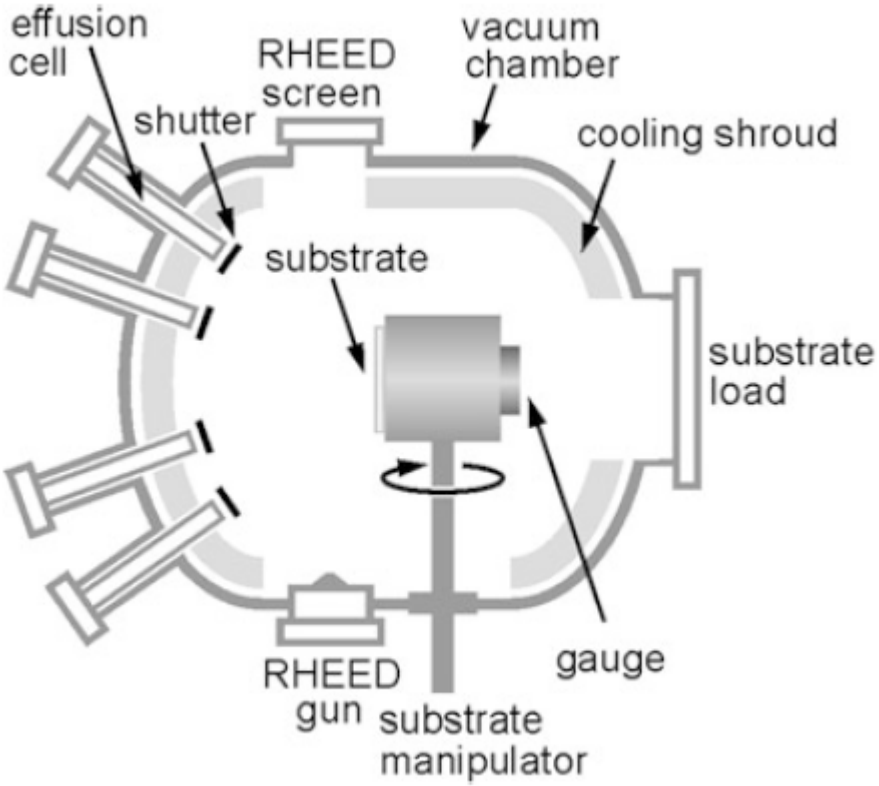

Pohl 2018

Molecular beam epitaxy – beam sources

For the production of beams from solid or liquid materials usually **Knudsen cells (K-cells)** are employed. They are based on radiative heating and are limited to a maximum temperature of ~1300 °C for **thermal evaporation**. Sources for higher temperatures mostly use **electron-beam evaporation**.

The ideal Knudsen cell is an **isothermal enclosure** which **contains the solid or liquid source** material in thermodynamic equilibrium with its vapor. Effusion occurs through **a small orifice** with an area much smaller than that of the evaporation surface of the source material, and the flux passing this aperture equals the flux of material which leaves the condensed phase to **maintain the equilibrium pressure**.

The ideal Knudsen cell with very thin orifice wall effuses particles with a **cosine angular dependence like in classical evaporation**.

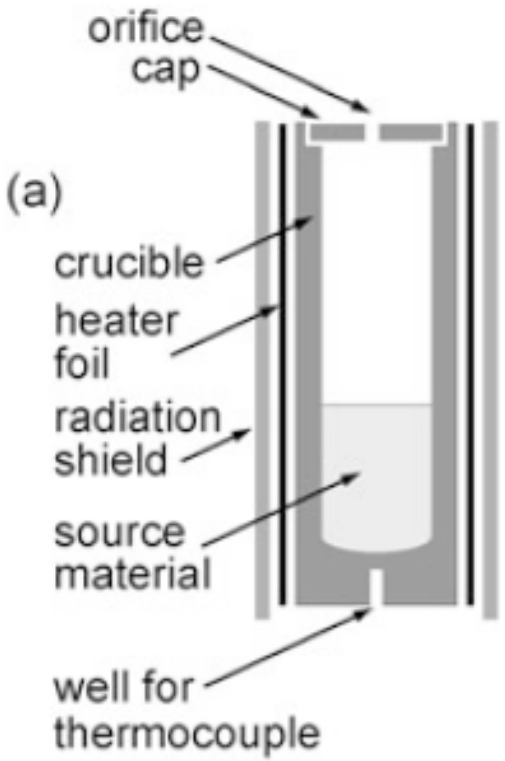

Pohl 2018

Silicon heteroepitaxy

Since the early 1960s Si has been the semiconductor of choice. Its dominance cannot, however, be attributed solely to its electronic properties, for it has mediocre carrier mobilities and only average breakdown voltage and carrier saturation velocities.

The absence of a direct bandgap rules out light emission and severely limits its efficiency as a photodetector. Silicon does, however, possess excellent mechanical and chemical properties. A high modulus of elasticity and high hardness enable Si wafers to withstand the rigors of handling.

Its great natural abundance, ability to be readily purified, possession of a highly inert and passivating oxide, and ease of device processing have all helped to secure a dominant role for Si in solid-state technology.

The idea of combining semiconductors which can be epitaxially grown on low-cost Si wafers is very attractive. Monolithic integration of III-V devices with Si integrated circuits offers the advantages of combined photonic-electronic functionality and higher speed signal processing distributed over larger substrate areas.

Ohring 2002

application example

Vertical-cavity surface-emitting lasers (VCSELs) are used in fiber communication and are also widely used in computer mice.

A VCSEL is a semiconductor laser, which emits the radiation vertically via its surface—in contrast to the more common edge-emitting lasers.

Like any laser it consists of an active zone where the light is generated, overlapping with a region where the optical wave is guided.

Light is generated by recombination of electrons and holes which are confined in quantum wells (MQW, multiple quantum well).

The generated photons contribute to the light wave which travels back and forth between two mirrors and a small fraction representing the laser radiation is allowed to emerge from the top mirror. Distributed Bragg reflectors (DBR) are used consisting typically of an GaAs based epitaxial multilayer stack.

VCSEL devices are also fabricated using quantum dots in the active region, formed in the self-organized Stranski-Krastanow growth mode.

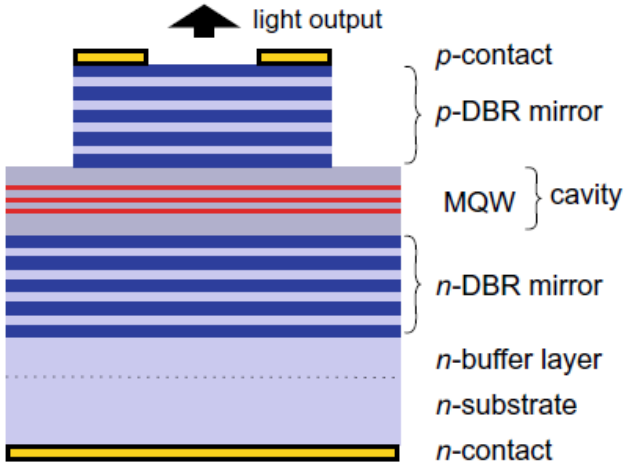

Pohl 2020

Industrial excursion: II-VI lasers in Zürich

https://ii-vi.com/

summary epitaxy

- But, by nature, heteroepitaxial thin films have proven a greater challenge to grow and exploit than bulk crystals.
- Notation: The indices of the overgrowth plane are written as (HKL) while those of the parallel substrate plane at the common interface are taken as (hkl). Note: (HKL)//(hkl); [UVW]//[uvw],
- Pseudomorphic growth with f<9%.
- Elastic strain energy scales with Elastic modulus * film thickness * strain^2
- Strain is reliefed by b/S with S dislocation distance and b Burgervector
- For film thickness larger than the critical thickness dislocations appear
- Surface ripples may relax strain energy elastically
- Defects in epitaxial films are dislocations, stacking faults, twin, growth hillocks, etc.
- Misfit dislocations propagate through threading segments through the crystal during the relaxation process
- Epitaxy of compound semiconductors: bandgap engineering through alloying and epitaxial growth on lattice mismatched substrate for defect free growth.
- Liquid phase epitaxy allows to choice of composition along the liquidus line of the phase diagram
- Epitaxial overgrowth limits dislocations to epitaxial window through SiO2 mask
- MOCVD and MBE: A collection of epitaxial vapor-phase deposition processes based on chemical (CVD, MOCVD) and physical (MBE) methods as well as hybrid combinations (MOMBE, high-vacuum CVD) have been developed.
- An MBE system features semiconductor and dopant atom heating sources consisting of either effusion cells or electron-beam guns. An effusion cell is essentially an isothermal cavity containing a hole through which the evaporant exits. These have enabled extraordinary compositional, structural, and film-thickness control of layered heteroepitaxial structures, resulting in an impressive array of GaAs and InP-based LEDs and lasers for display, recording, and optical communications applications. Ge_xSi_{1-x} materials have also been exploited in high-speed transistors used for assorted computer and communications purposes.

Ohring 2002

thin film materials mechanics

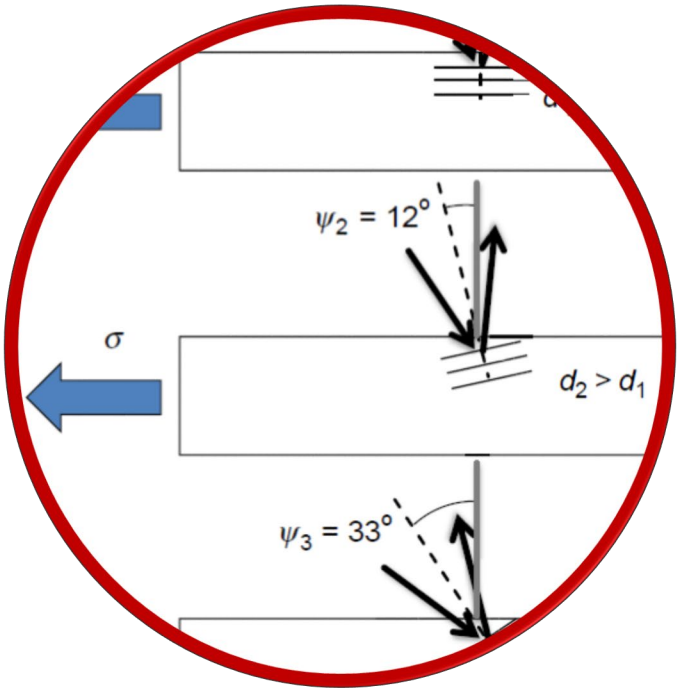

Table of contents I

Table of contents II

Importance of stresses

Strain energy release drives

- interfacial cracks and film fracture
- morphology evolution during film growth
- all type of microstructure changes

Strain engineering of physical properties

Nix 2014

Importance of stresses

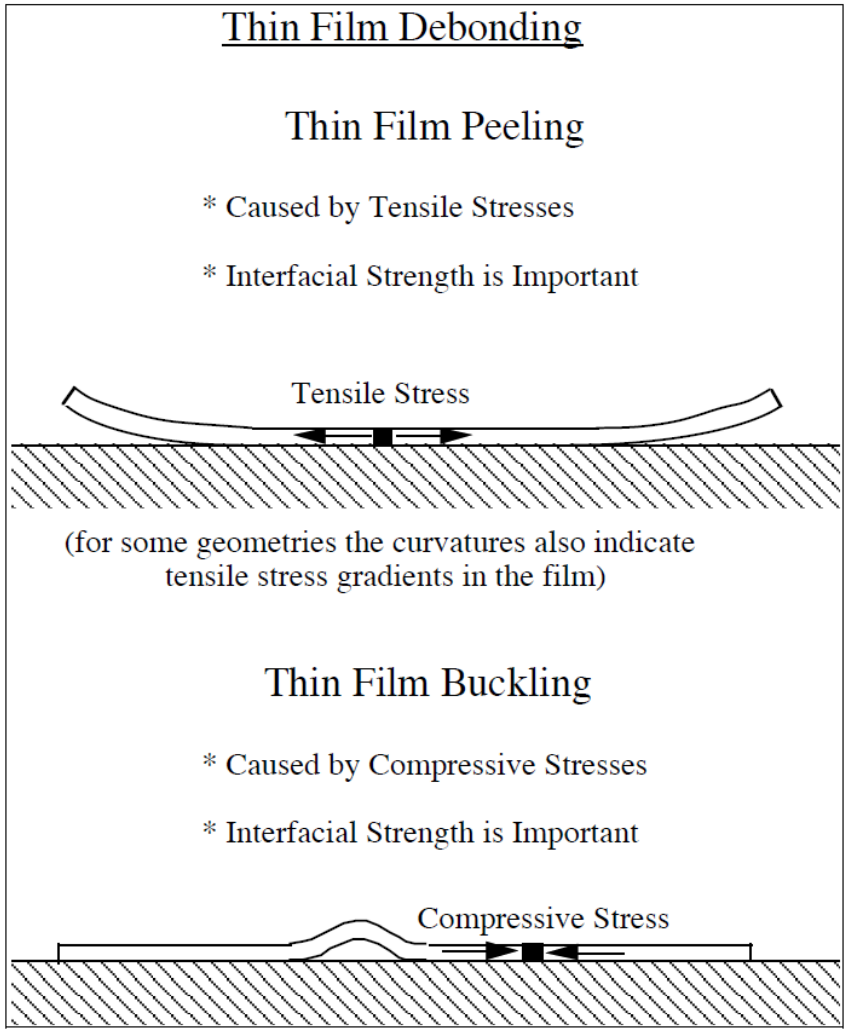

Nix 2014

Substrate curvature

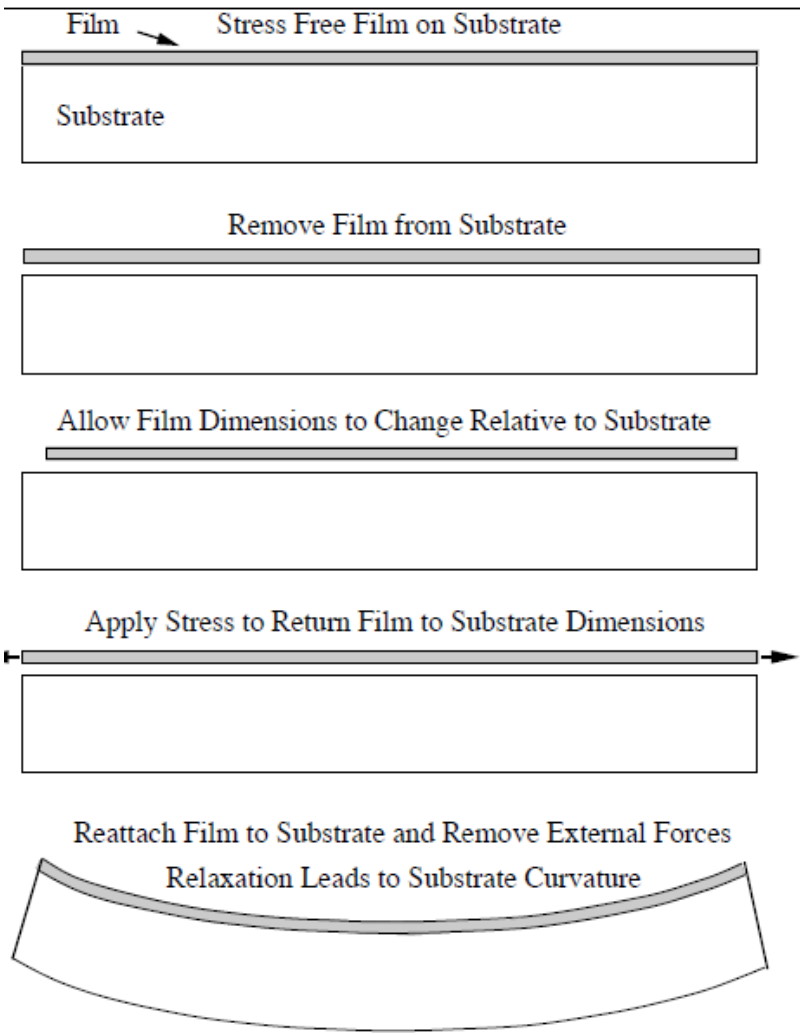

Nix 2014

Bending of a plate (without film)

M = moment per unit length applied along edges of plate.

Biaxial Bending of a Thin Plate

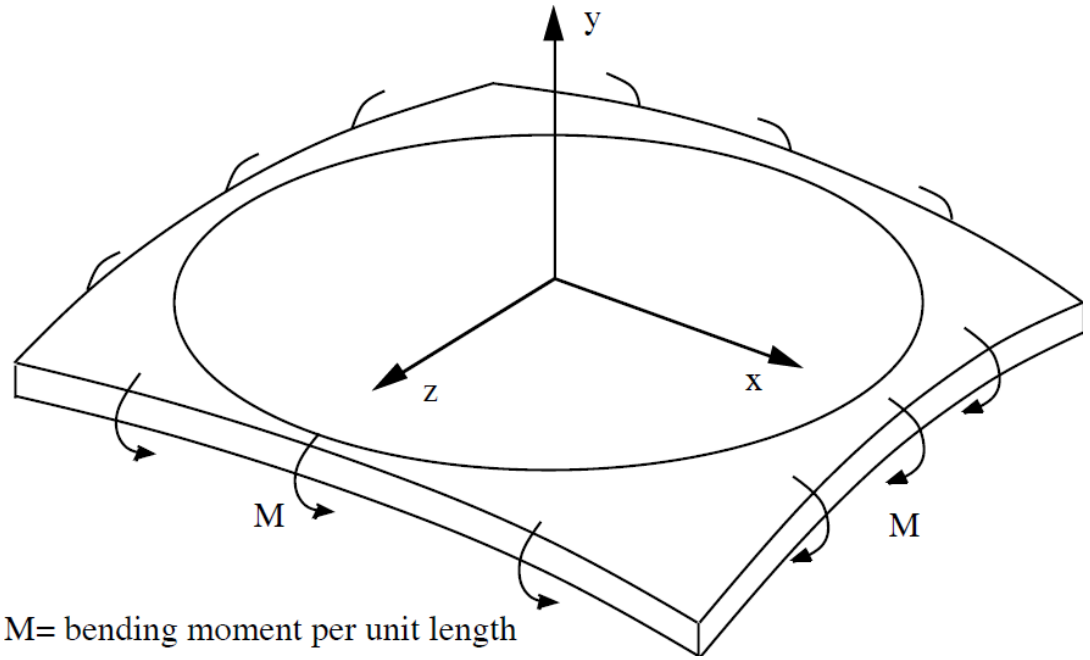

M= bending moment per unit length

Nix 2014

Bending of a plate (without film)

We now develop a relationship **between the curvature** and involved **strains**.

the stresses vary linearly through the thickness of the plate, such that the in-plane stresses are expressed as $\sigma_{xx} = \sigma_{yy} = \mathbf{c_1 z}$, and where c_1 is a constant determined by the bending moment (per unit length along the edge)

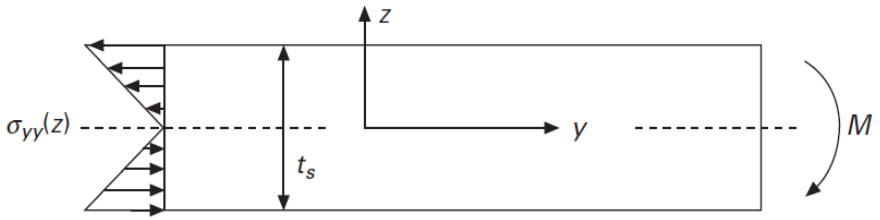

$$M = \int_{-t_s/2}^{t_s/2} \sigma_{yy} z dz = \int_{-t_s/2}^{t_s/2} c_1 z^2 dz = \frac{c_1 t_s^3}{12}$$

Solving for c_1

$$\sigma_{xx} = \sigma_{yy} = \frac{12M}{t_s^3} z,$$

The biaxial bending stress in the substrate. The bending causes the substrate to curve and from geometry

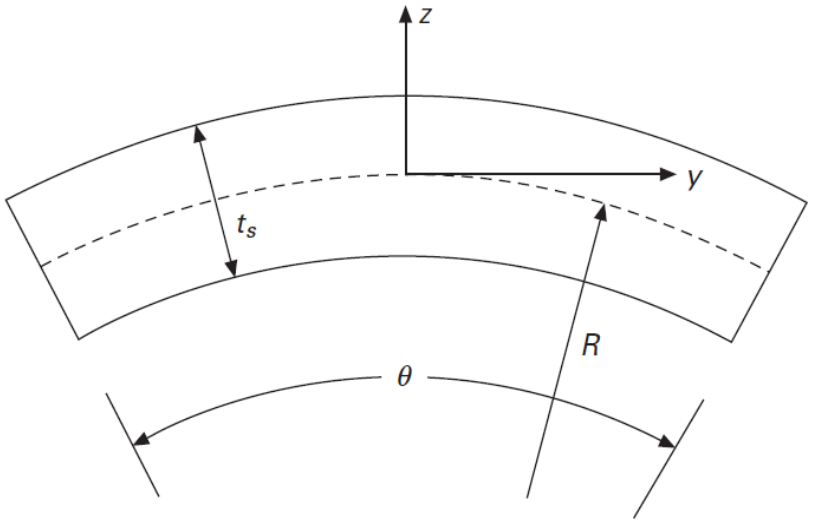

$$\varepsilon_{yy}(z) = \frac{(R+z)\,\theta - R\theta}{R\theta} = \frac{z}{R} = -\kappa z$$

where κ is the resulting curvature of the substrate. We note that the negative curvature shown in the figure results from the positive bending strain for $z > 0$.

Nix 2014

Bending of a plate (without film)

We now develop a relationship between the **curvature** and the imposed **bending moment**.

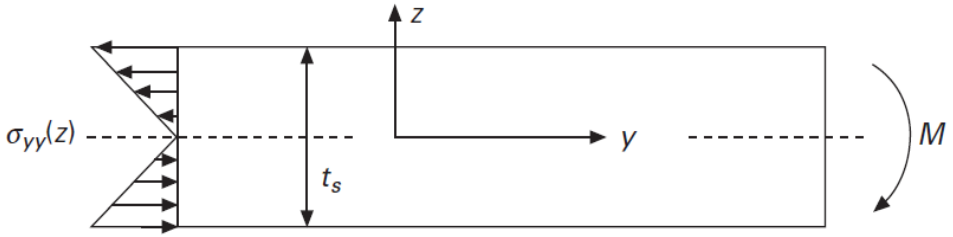

We have seen that the inplane, biaxial elastic strains in the plate can be used to find the curvature:

$\kappa = -\varepsilon_{yy}(z)/z = -\varepsilon_{xx}(z)/z.$

Using Hooke's law for an elastically isotropic solid we can express the strain as

$$\varepsilon_{yy} = \frac{1}{E_s}\left(\sigma_{yy} - \nu_s(\sigma_{xx} + \sigma_{zz})\right)$$

where E_s is Young's modulus, ν_s is Poisson's ratio, both of the plate (or substrate), $\sigma_{yy} = \sigma_{xx}$, are the in-plane biaxial stresses in the plate and $\sigma_{zz} = 0$. Using this

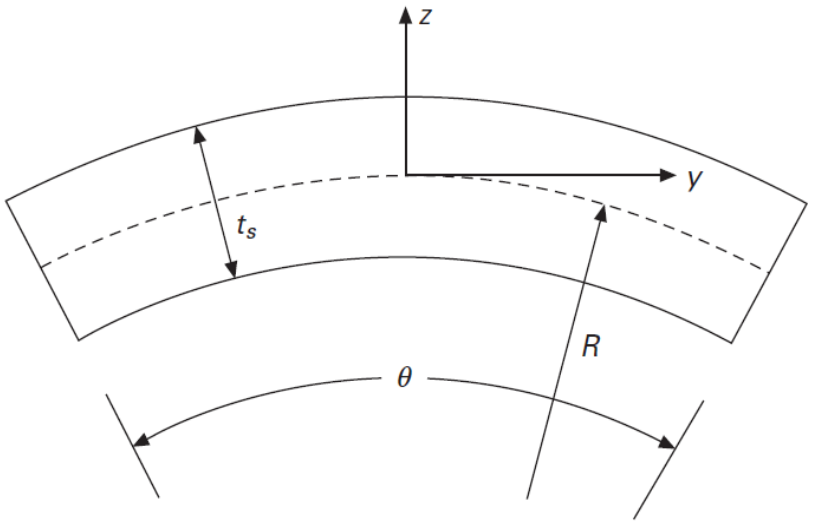

$$\kappa = -\frac{(1-\nu_s)}{E_s}\sigma_{yy}/z \qquad \text{or} \qquad \kappa = -\frac{(1-\nu_s)}{E_s}\frac{12M}{t_s^3}$$

Nix 2014

Stoney equation

We consider now a **thin film** on a **much thicker substrate** initially in a stress free state.

The forces exerted onto the substrate by the film cause it to bend.

If the biaxial stress in the film is σ_f,

then an edge force (per unit length), $\sigma_f\, t_f$,
where t_f is the thickness of the film,
must be exerted onto the film, as shown on the right.

That edge force, in turn, exerts an equal and opposite edge force (per unit length) on the substrate at the top corner of the substrate.

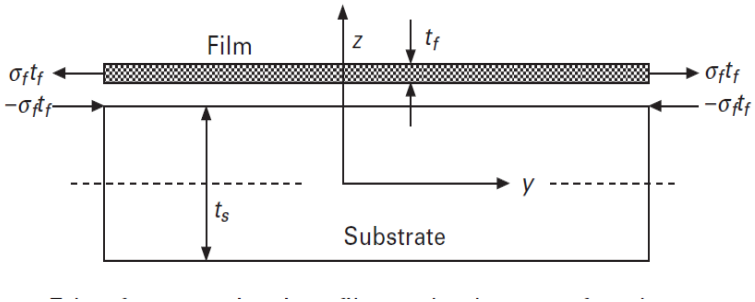

Nix 2014

Stoney equation

The result is that a bending moment,

$M = -\sigma_f t_f (t_s/2)$,

is imposed onto the substrate by the film and that causes the substrate to bend.

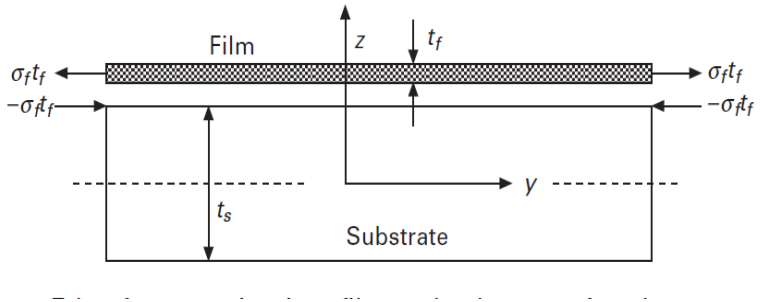

We neglect the film thickness and calculate the plate curvature

$$\kappa = -\frac{(1-\nu_s)}{E_s}\frac{12M}{t_s^3} \quad \text{or} \quad \kappa = \left(\frac{1-\nu_s}{E_s}\right)\frac{6\sigma_f t_f}{t_s^2}$$

With this relation we see that the **biaxial stress in the film** can be found by **measuring the curvature**. To be more precise we take into account the curvature the substrate might had before film deposition:

$$\sigma_f = \left(\frac{E_s}{1-\nu_s}\right)\frac{t_s^2}{6t_f}(\kappa - \kappa_o) = \left(\frac{E}{1-\nu}\right)_s \frac{t_s^2}{6t_f}\Delta\kappa$$

The famous **Stoney equation**. The term $E_s/(1-\nu_s)$ is called the biaxial elastic modulus of the substrate. We see that the stress in the film can be determined from the substrate curvature.

Nix 2014

The result is independent of the film properties

Stresses in multilayer film and substrate

The substrate stresses are about **100 times smaller than the film stresses** for typical ratios of film/substrate thickness

For **multiple thin films** that are all very thin compared to the substrate, the biaxial stress in each film causes the substrate to curve according to the Stoney equation, as if the other films were not present.

Under these conditions one might determine **the stresses in all of the films** by starting with the measured curvature of the **bare substrate** and then determining the curvature **after each of the films is deposited**.

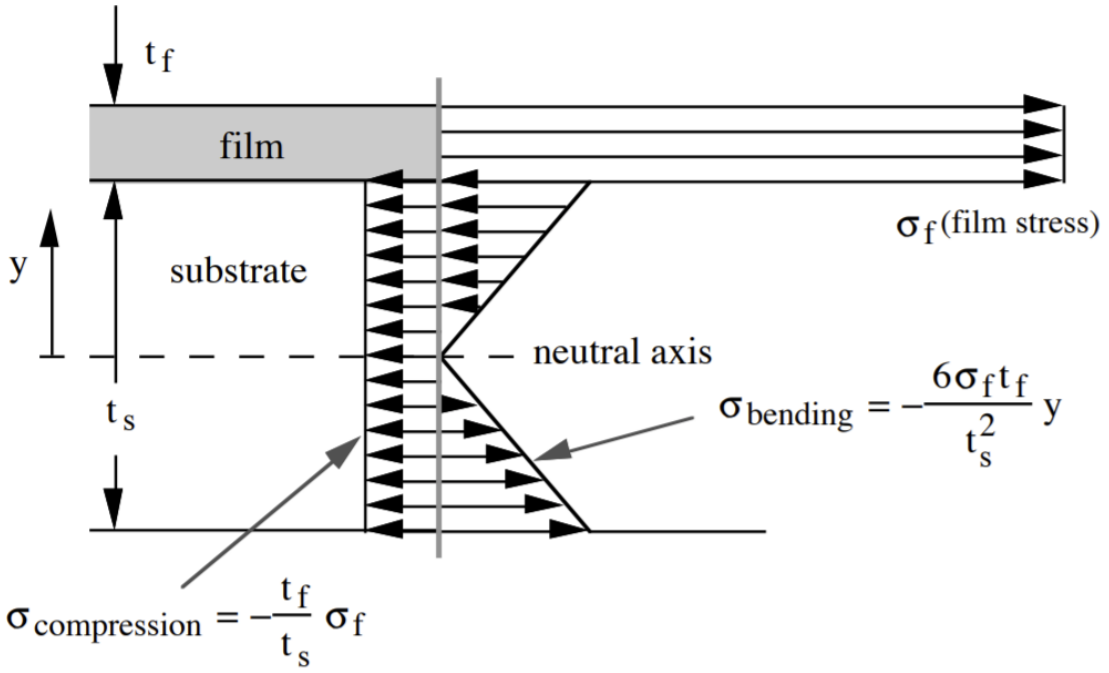

Nix 2014

Young's Modulus

If you try to measure the Young's moduls of a thin film one has to take into account grain size, porosity, anisotropy, creep, anelasticity, measurement uncertainties and load case to understand the results.

grain size

Consider a material consisting of continuum cubic grains with side d having boundaries of width δ.
The ratio of grain boundary to grain interior volume is

$3\delta/d$.

If the grain interiors have modulus E_{grain}, and the boundaries have a modulus of zero (an extreme change in bonding), then using an isostrain model (i.e., the same strain in grains and boundaries), the composite modulus of the material is:

$E = (1-3\delta/d)E_{grain}$.

For δ=0.2 nm (big!), we would need a grain size of d 6 nm (small!) to achieve a modulus reduction of only 10%.

grain size

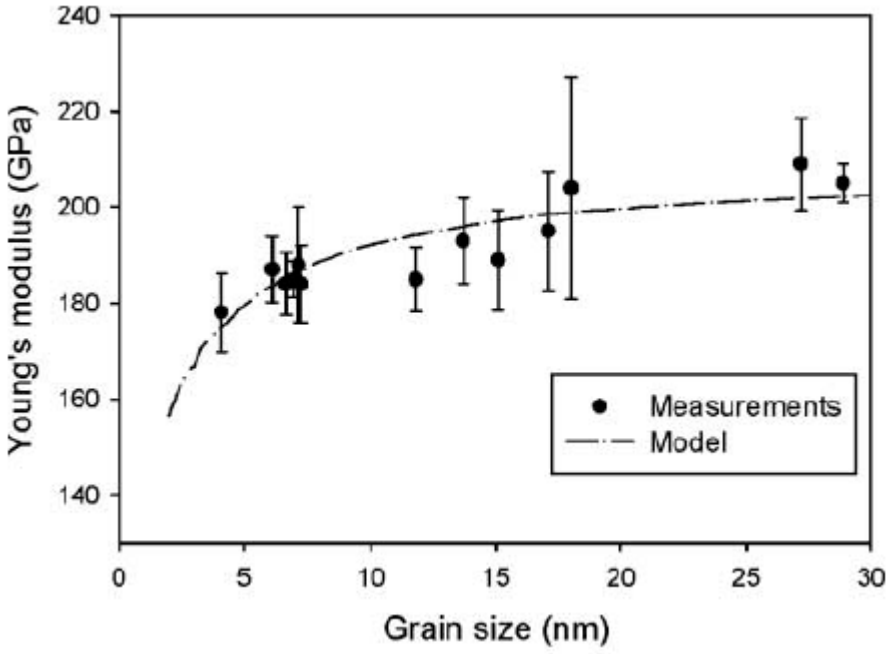

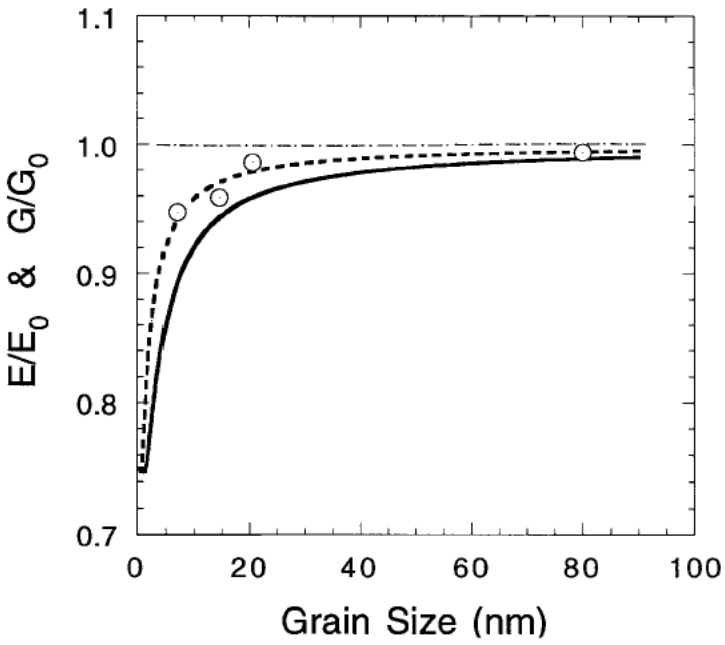

Figure 1-4 (a) Young's Modulus of electrodeposited nanocrystalline Ni and NiP alloys as a function of grain size [79]; (b) Young's and shear moduli of nanocrystalline Fe produced by mechanical attrition expressed as ratios of the conventionally accepted, coarse-grained bulk values. The dashed and solid curves correspond to a grain boundary thickness of 0.5 and 1nm, respectively. The open circles show the E/Eo values of nanocrystalline Fe versus grain size [76].

[76] T.D. Shen, C.C. Koch, T.Y. Tsui, G.M. Pharr, J. Mater. Res., 10 (1995) 2892.
[79] Y. Zhou, U. Erb, K.T. Aust, G. Palumbo, Z. Metallkd., 94, 10 (2003) 1.

Textured films

The isotropic elastic expressions are **valid** for many thin film/substrate systems, even though the materials involved are **elastically anisotropic**.

The reason is that only the **biaxial elastic moduli enter these relations** and these key elastic properties are isotropic for many epitaxial or strongly textured films.

The elastic properties of cubic metal crystals are expressed in terms of the stiffnesses, (c11, c12, c44) (or compliances (s11, s12, s44)) which describe the elastic properties in the crystal coordinate system.

For the common **<001> and <111> cubic textures we can use a modified biaxial modulus**:

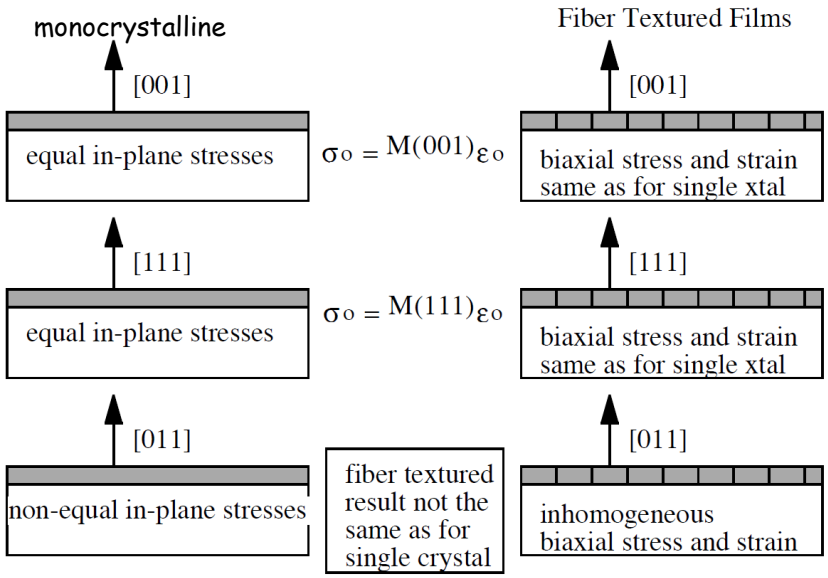

$$B_{\{111\}} = \frac{6c_{44}(c_{11} + 2c_{12})}{c_{11} + 2c_{12} + 4c_{44}} \qquad B_{\{001\}} = c_{11} + c_{12} - \frac{2c_{12}^2}{c_{11}}$$

The {011} plane for cubic solids is not elastically isotropic and the inplane stresses are different in different directions, which makes the analysis more complicated.

Nix 2014

Textured films

	c_{11} (GPa)	c_{12} (GPa)	c_{44} (GPa)	a_o (nm)	α $10^{-6}K^{-1}$	$B_{\{001\}}$ (GPa)	$B_{\{111\}}$ (GPa)
Ag	120	91	46	0.4090	18	73	172
Al	113	67	28	0.4050	23	101	116
Au	186	157	42	0.4078	14	78	189
Cu	168	121	75	0.3620	16.5	115	260
Ni	246	147	124	0.3520	13.4	217	388
Pd	227	176	72	0.3890	11.8	130	288
Pt	347	251	77	0.3924	9	235	339
Cr	352	73	101	0.2885	6	395	335
Fe	237	141	116	0.2870	11	210	367
Mo	460	179	109	0.3147	4.8	500	427
Nb	246	134	29	0.3330	7.3	234	142
Ta	265	159	83	0.3303	6.3	233	317
V	228	119	43	0.3028	8.4	223	188
W	500	198	151	0.3160	4.5	541	541
GaAs	118	53	59	0.5653	5.4	123	172
Ge	129	48	67	0.5640	5.6	141	183
Si	166	64	80	0.5431	2.6	181	230
MgO	296	95	154	0.4212	8	330	407

Nix 2014

porosity

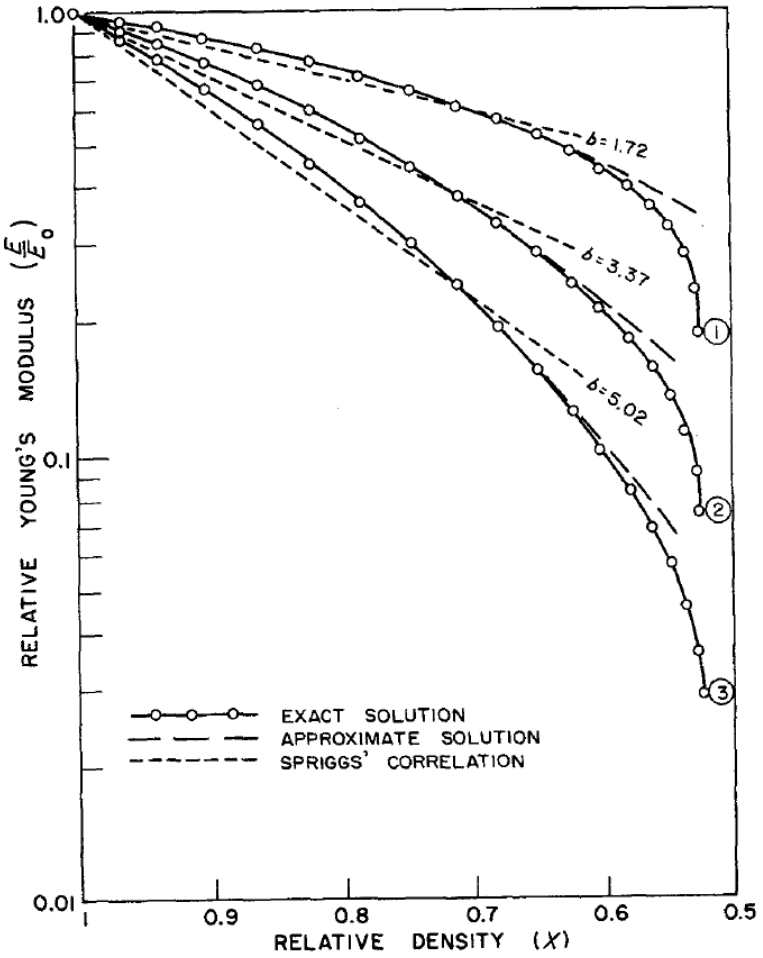

Three various porosity ranges can be usually identified, e.g., Danninger *et al*. [8] observed for sintered iron the following porosity ranges:

1. porosity·3%: fully isolated pores of nearly spherical or elliptical shape
2. porosity ¸20%: fully interconnected pores of complex shape
3. porosity between 3% and 20%: both isolated and interconnected pores are present in various amounts.

H. DANNINGER, G. JANGG, B. WEISS and R. STICKLER, *pmi* **25** (1993) 170 and 219.

Figure 3 Young's modulus of porous materials. Solid curves are the theoretical curves, broken curves are the approximate solutions and the dotted lines are the Spriggs' correlation lines.

JOURNAL OF MATERIALS SCIENCE 19 (1984) 801–808

Young's modulus of porous materials

Part 1 *Theoretical derivation of modulus–porosity correlation*

JAMES C. WANG*
State University of New York, Stony Brook, New York 11794, USA

residual stress

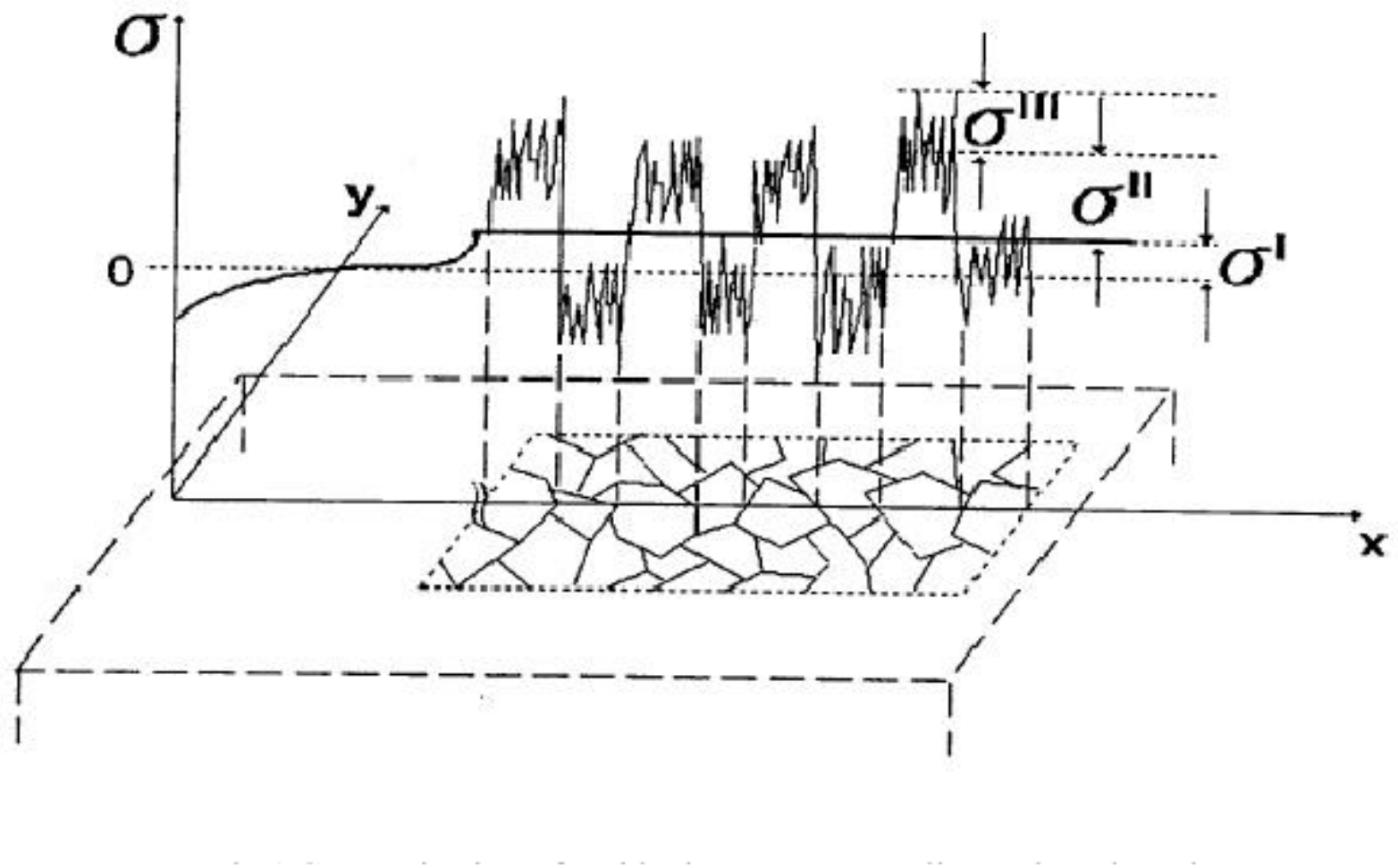

Origins of residual stress

stresses in thin films are associated with the elastic accommodation of misfit strains that can arise from various sources:
- thermal,
- epitaxial
- transformational/intrinsic/growth stress.

Nix 2014

Capillary stresses

Capillary stresses are well known in small particles that show an internal pressure according to the **Laplace-Young equation $p=2\gamma_s/r$.**

Capillarity stresses in thin films arise because there **are biaxial stresses acting in the plane of the surfaces and interfaces** in these structures.
During nucleation of a thin film for atoms taking the form of a hemispherical cap the Young's equation holds:

$$\cos\theta = \left(\frac{\gamma_s - \gamma_i}{\gamma_f}\right)$$

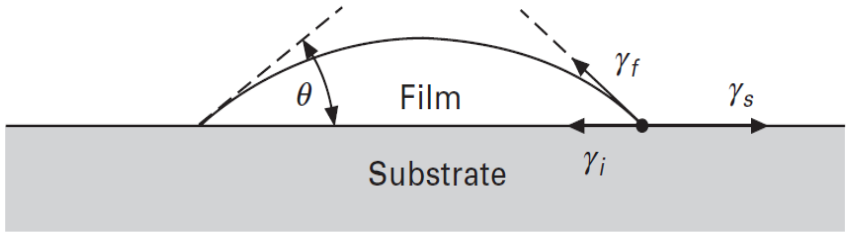

Three interfaces are present in this structure:

- the top surface of the film, with surface stress, f_f,
- the interface between the film and substrate, with interface stress, f_i,
- and the bottom surface of the substrate, with the surface stress, f_s.

Nix 2014

Capillary stresses

The **interface stresses act to elastically bend the substrate**, much like a stressed thin film would do. According to the Stoney relation, these interface stresses would cause the curvature of the substrate to change as

$$\Delta\kappa = \left(\frac{1-\nu_s}{E_s}\right)\frac{6}{t_s^2}\left(f_f + f_i - f_s\right)$$

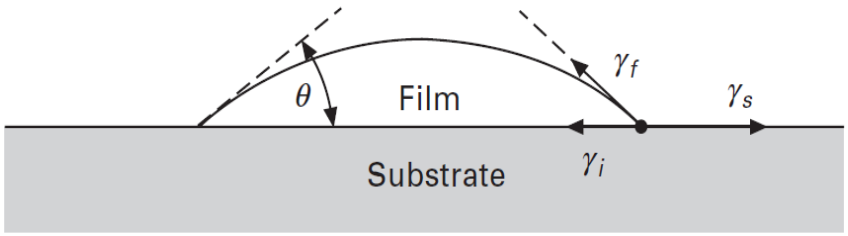

With this relation we see that the **biaxial stress in the film can be found by measuring the curvature**. To be more precise we take into account the curvature the substrate might had before film deposition:

Unless a large number of interfaces are present, such as in the case of **a metal multilayer with a very small bilayer period**, these effects are **usually much smaller than those that arise from thermal or epitaxial stresses**

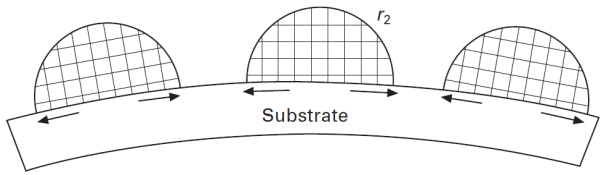

Nix 2014

Capillary stresses in multilayers

Consider a free-standing multilayer with interfaces having an interfacial stress f.

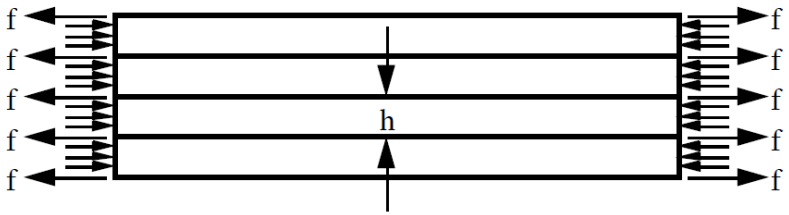

The biaxial stress induced in the multilayer is

$$\sigma = \frac{f}{h}$$

Example:
Using **h = 100Å** = 10^{-2} μm =10^{-8}m and f=1 J/m^2 we have σ=**100MPa**, which is a significant stress!

Using **h=1μm**, we have **1MPa**, which is small!

Now consider a multilayered film deposited onto a solid substrate. Each of the interfaces in the sample will have an interfacial stress and each will exert forces on the entire composite with a resulting curvature.

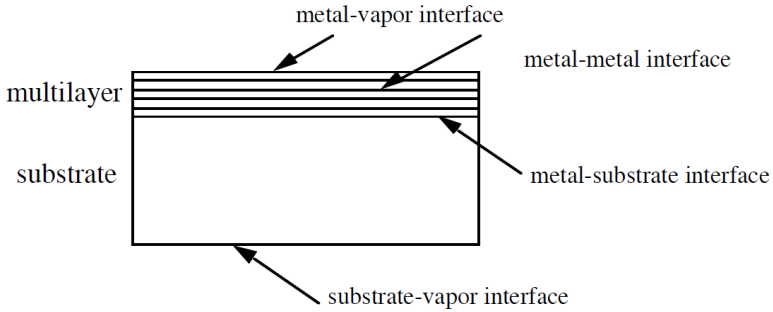

capillarity effects on a substrate

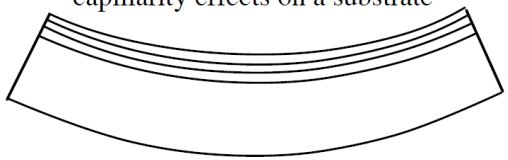

Nix 2014

thermal stresses

For any continuous film with a **thermal expansion coefficient** that **differs from that of the substrate**, a thermal stress will be generated whenever the temperature is changed.

If α_f is the linear thermal expansion coefficient of the film and as that of the substrate, then the thermal misfi t strain for a temperature change ΔT would be:

$$\varepsilon_{misfit}^{\Delta T} = (\alpha_f - \alpha_s)\,\Delta T$$

and the resulting biaxial stress would be

$$\sigma = \left(\frac{E}{1-\nu}\right)_f \varepsilon = -\left(\frac{E}{1-\nu}\right)_f (\alpha_f - \alpha_s)\,\Delta T$$

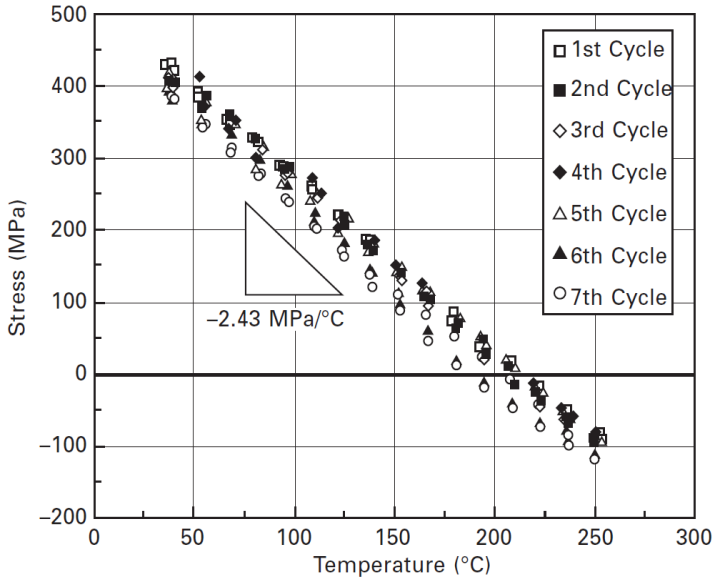

The Figure shows the measured stress in a 0.4 μm thick thin film of Al-1%Si-0.5%Cu on a silicon substrate during several thermal cycles from room temperature to 250°C.

Using the properties of pure Al and Si the slope of the stress–temperature plot might be expected to be –2.37 MPa/°C. As shown in the figure, the actual slope is about –2.43 MPa/°C, probably because the alloyed film is a little stiffer than pure Al would be.

Nix 2014

Anisotropic epitaxial stresses

We assume an <001> oriented substrate. For the in-plane elastic strain:

$\varepsilon_1 = \varepsilon_2 = - \varepsilon_{misfit} = - (a_f - a_s)/a_s \cong (a_f - a_s)/a_f$

and the resulting biaxial stress is

$$\sigma_1 = \sigma_2 = \left(c_{11} + c_{12} - \frac{2c_{12}^2}{c_{11}}\right)\varepsilon_1 = \left(c_{11} + c_{12} - \frac{2c_{12}^2}{c_{11}}\right)\left(\frac{a_s - a_f}{a_s}\right)$$

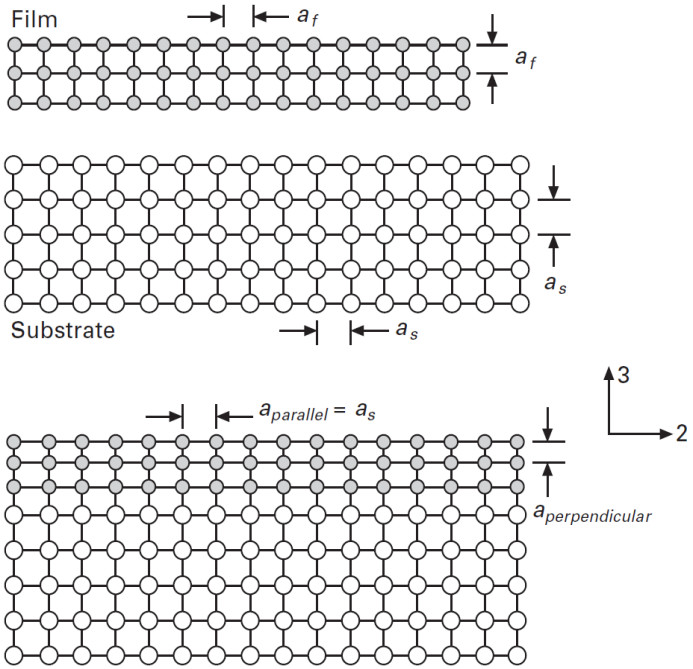

Nix 2014

Intrinsic stresses in vapor deposited polycrystalline films

For **polycrystalline metal films** that grow in the **Volmer–Weber mode**, there are a **variety of microstructural and kinetic processes that cause residual stresses** to be created during the course of growth.

These are **called intrinsic or "growth" stresses** because they **cannot be attributed to stresses associated with thermal or epitaxial misfit**.

By measuring the **curvature of a substrate during the film deposition** process, the bending force (per unit length) F/W, can be directly monitored.

Here, using the Stoney equation,

$F/W = \sigma_f t_f = B_s t_s^2 \Delta\kappa/6$,

where σ_f is the average biaxial stress in the film and t_f is the film thickness.

Force-thickness curve for constant stress

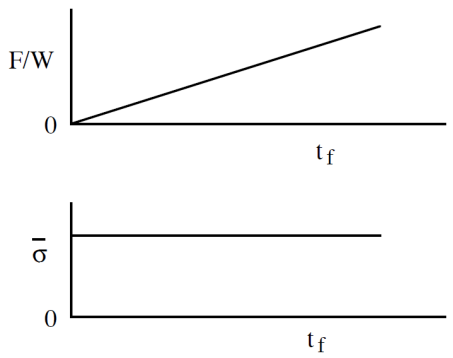

Force-thickness curve for position dependent stress

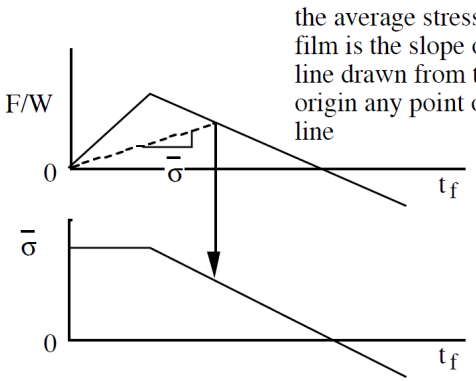

the average stress in the film is the slope of the line drawn from the origin any point on the line

Nix 2014

Intrinsic stresses in vapor deposited polycrystalline films

If the **stress in the film is uniform and independent of the thickness**, then the **bending force (per unit width) would vary linearly with film thickness.**

Force-thickness curve for constant stress

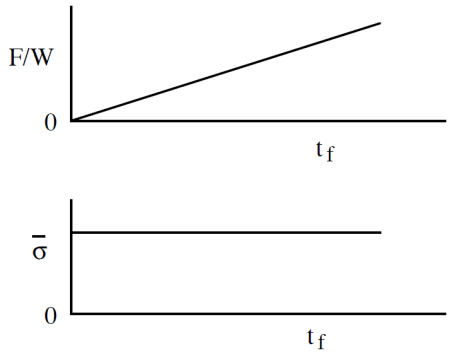

More commonly, the **stress in the film is not uniform and varies through the thickness of the deposited film.**

Force-thickness curve for position dependent stress

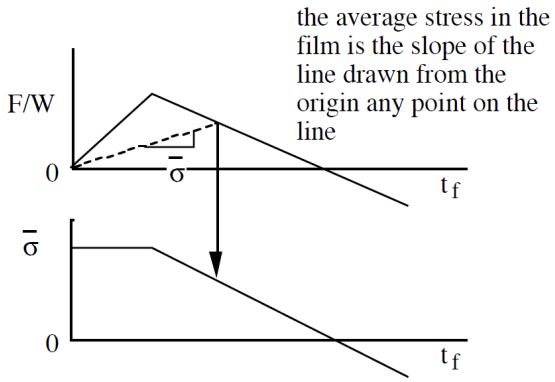

The **slope of line drawn from origin to the curve gives the average stress in the film at that thickness.**

Nix 2014

Intrinsic stresses in vapor deposited polycrystalline films

As a third example consider a film in which the **stress changes sign during growth**.
In that case the measured force (per unit width) can be expressed as

$$\frac{F}{W} = \int_0^{t_f} \sigma_f dz = B_s \frac{t_s^2}{6} \Delta\kappa$$

It follows that if the stresses in the film are frozen in and do not change as the film thickens, then the biaxial stress in the last layer of film to be deposited is.

$$\sigma_f(t_f) = \frac{d(F/W)}{dt_f} = B_s \frac{t_s^2}{6} \frac{d\Delta\kappa}{dt_f}$$

Thus the **local stress in the film is simply the slope of F/W vs. t_f.**

At **any point in the growth process** both the
- average stress in the film to that point and
- the local stress at that point

can be determined from the slopes shown in the figure.

Force-thickness curve for position dependent stress

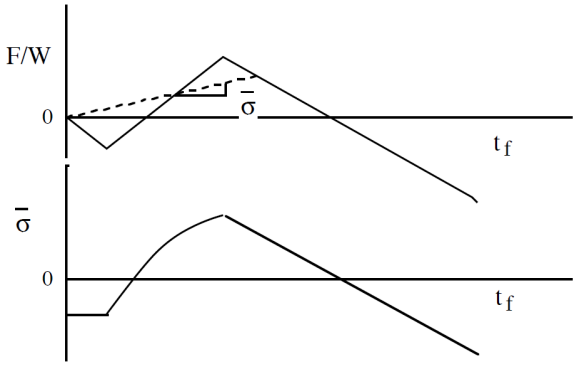

Nix 2014

typical results from in-situ curvature measurements

Abermann and Koch found that the force (per unit width) varies **about linearly for (refractory) materials with low adatom mobility**,

suggesting that the **stress developed in these materials is essentially constant** and independent of position through the thickness.

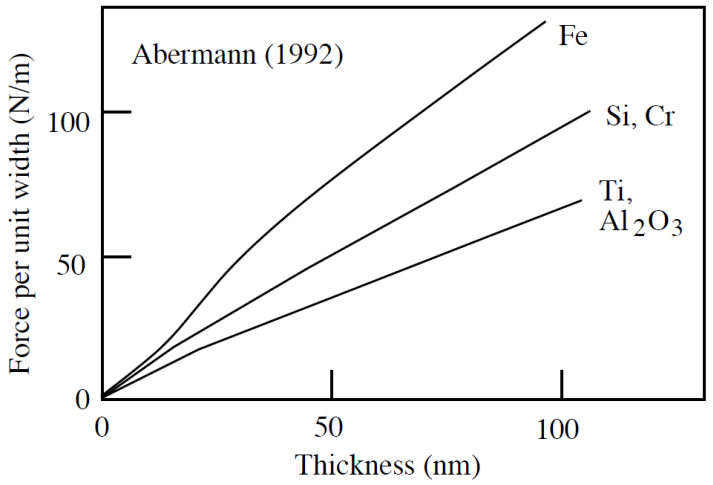

Abermann has shown that the **stress generation in metal films is very much less if the temperature is raised**.

This is shown for the evaporation of Cr as a function of temperature.

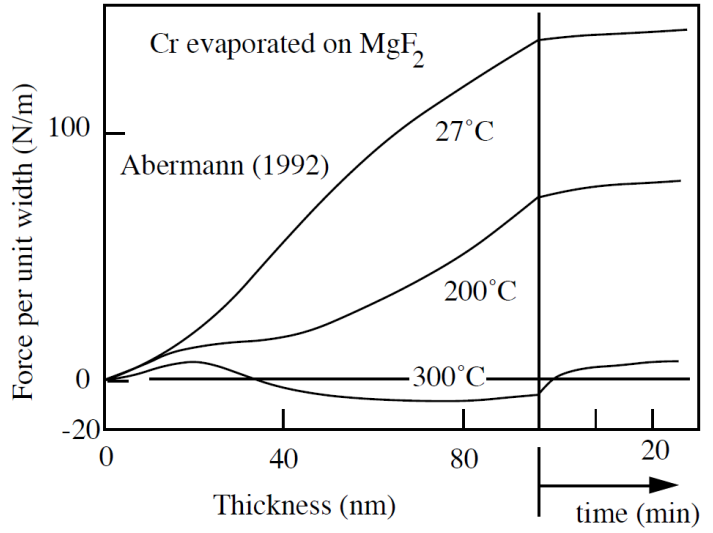

Nix 2014

typical results from in-situ curvature measurements

The data show that the measured F/W oscillates during the course of growth,

- **being negative at the start of growth** and
- **then becoming positive**
- Before again being **negative in the later stage of growth**.

The slopes at different points in the curve indicate that the stress in the film is

- **initially compressive**
- **then becomes tensile**
- and is **compressive again** in the later stages of growth.

This oscillatory behavior is widely observed for many metallic films.

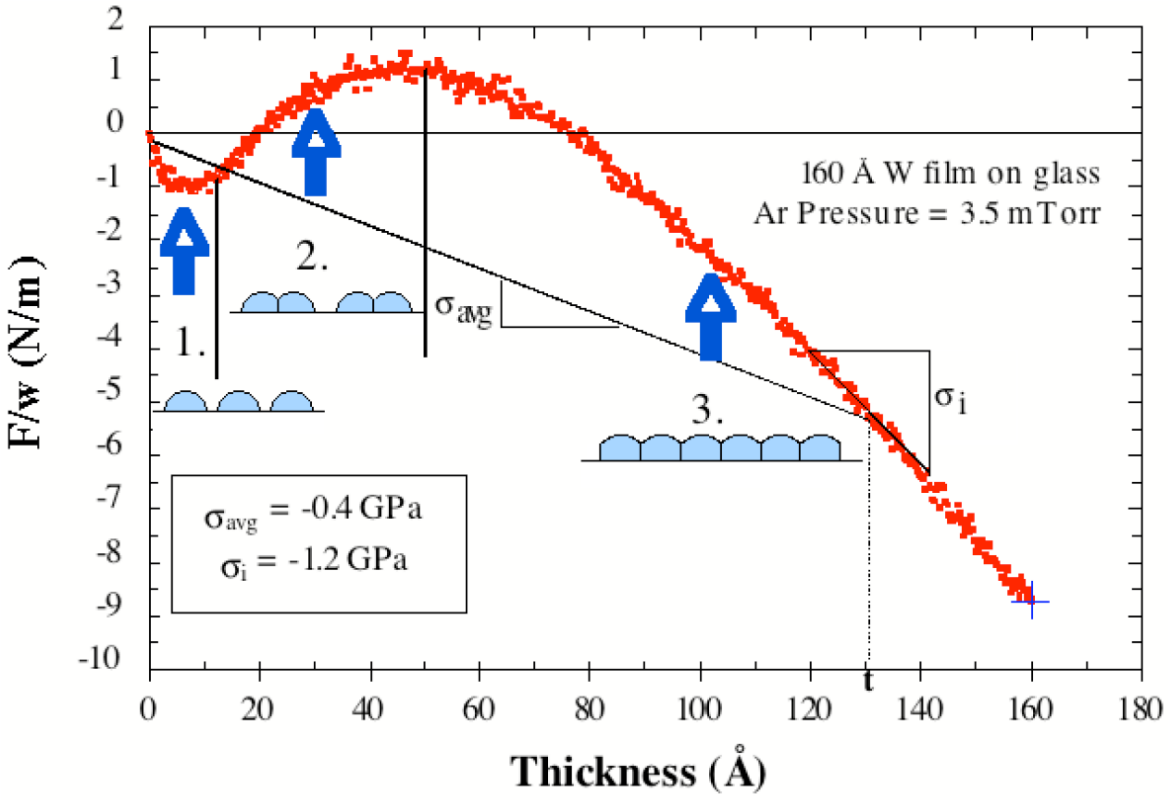

Nix 2014

Stage I: isolated crystals

For **very small crystallites the surface stress would be expected to compress the crystal lattice**, much like it would if the crystallites were isolated spherical particles.

For an isolated spherical particle of radius R the **Laplace pressure** in the particle due to the surface stress is

p = 2fs/R,

where fs is the surface stress.

The pressure would compress the crystal lattice and cause the lattice parameter, a, to be smaller than the lattice constant of the stressfree crystal, a_o:

$$\frac{a}{a_o} = 1 - \frac{p}{K} = 1 - \frac{2f_s}{KR}$$

where K is the bulk elastic modulus of the crystal.

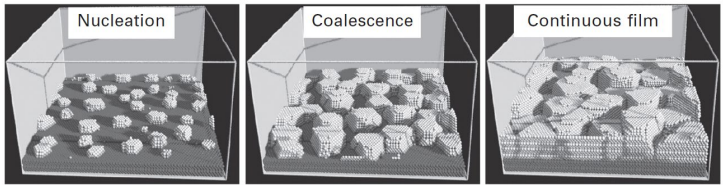

Atomistic modeling of Volmer–Weber film growth showing crystallite growth and coalescence leading to a continuous film

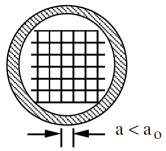

Compression of a small particle by surface stress

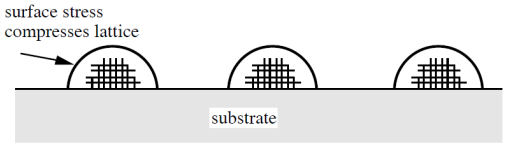

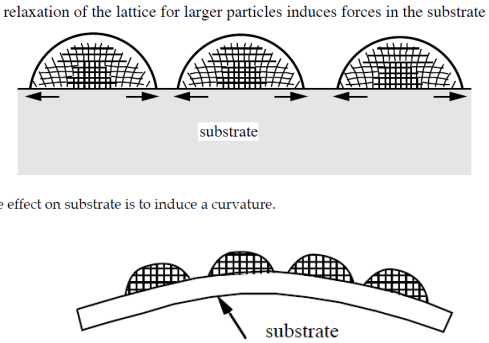

Attachment to the substrate restrains lattice expansion and this leads to compressive stresses in the film.

Stage II: crystallite coalescence

It has been shown that t**ension stresses develop in a growing film when the crystallites begin to grow together**.

As soon as crystals come into **touching contact**, we can predict that the **two free surfaces will snap together**.

The reason for this is that when they snap together they form a **single grain boundary in place of two surfaces**, and since the energy of that one boundary is much less than the energy of the two surfaces, this is a spontaneous process.

Eventually, the **zipping process** stops because the stress in the film causing the crack-like feature to grow is just balanced by the interfacial energy differences causing the crack to heal. The stress can be estimated to

$$\sigma \approx \left[2E \frac{(2\gamma_s - \gamma_{gb})}{a} \right]^{1/2}$$

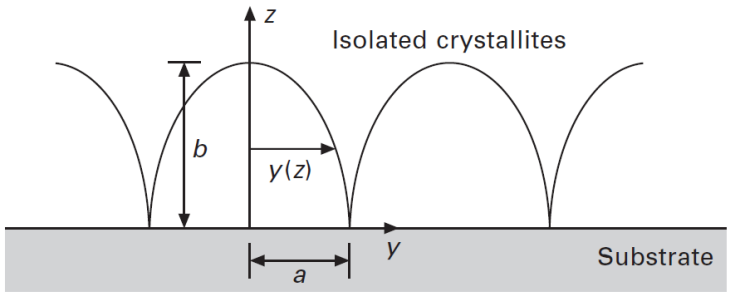

(a) Before coalescence

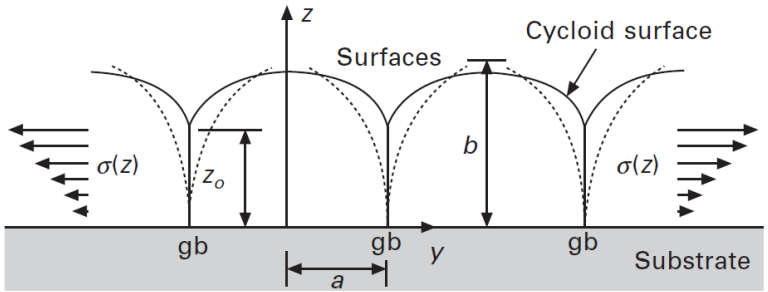

(b) After coalescence

Taking $2\gamma_s - \gamma_{gb} \cong 1.5$ **J/m²**, **E = 100 GPa and** ν **= 1/3**, we find stresses of **several GPa for crystalline sizes** in the **range of a few nanometers**.

Nix 2014

Stage III: stress evolution following coalescence

How the stresses in the film evolve after the crystallites have grown together to form a continuous film **depends on the driving forces and mobilities of the arriving atoms**.

1) the **tensile stresses** generated by crystallite coalescence are propagated into the growing film as the **arriving atoms simply grow epitaxially onto the already strained film**.

2) For metals with high adatom mobilities, such as many fcc metals grown at relatively high homologous temperatures, the **tensile excursions** associated with crystallite coalescence are soon **relaxed** because the arriving **atoms have sufficient mobility to diffuse into the grain boundaries** and gradually relax the tensile stresses as the film grows thicker.

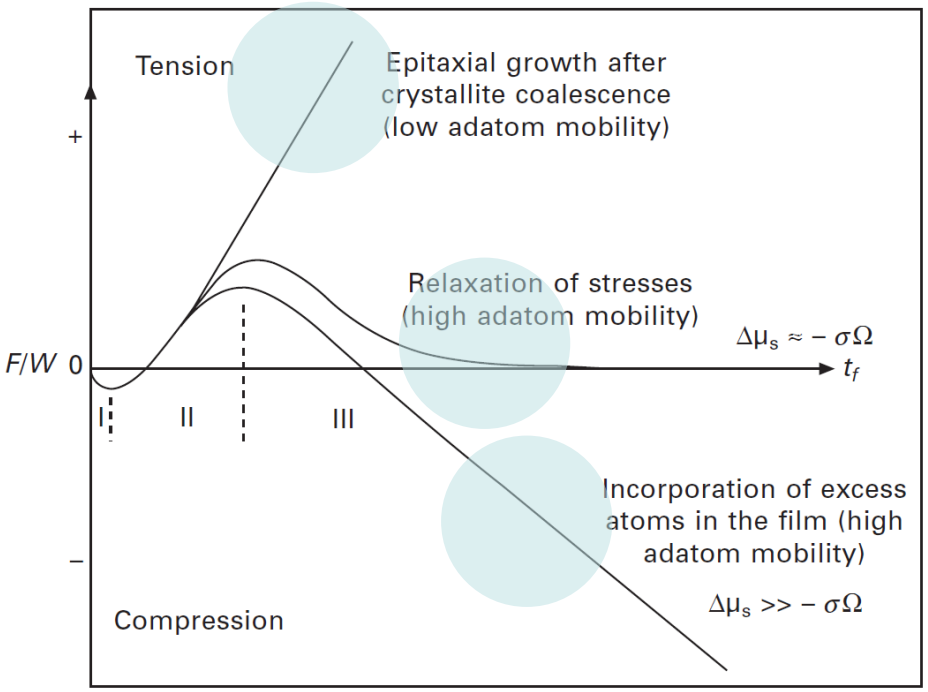

Nix 2014

Stage III: stress evolution following coalescence

We consider now a more general description of the kinetic processes leading to biaxial tensile stresses in deposited films.

The basic idea is that the film is deposited in a non-equilibrium, non-dense state. Densification after the film material is attached to the substrate leads to tension stress in the film.

Consider atoms arriving from the vapor and depositing on a growing film. Two rates are of importance and will be compared:

- Rate of arrival of depositing atoms (growth rate)
- Rate of atomic rearrangement on the surface of the growing film by surface diffusion (R surface rearrangement).

If the rate of surface rearrangement is much greater than rate of arrival, then an equilibrium structure is produced and there is no potential for film stress (discounting epitaxy and thermal stresses in this discussion).

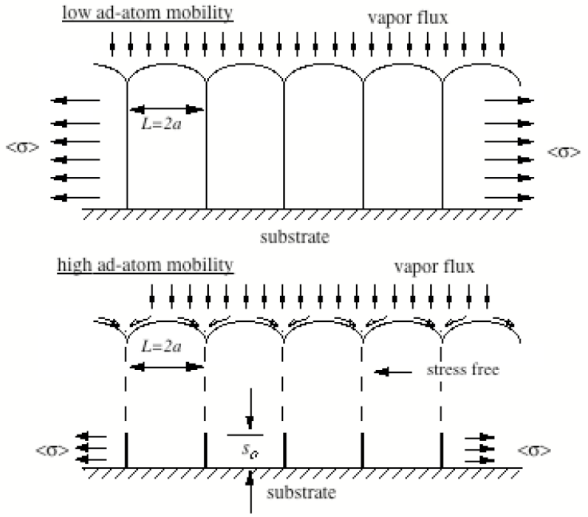

Nix 2014

Stage III: stress evolution in sputtered thin films

Another explanaton is related to the **incorporation of neutral gas species such as Ar** during deposition.

Therefore, the conclusions are:

1. Low argon pressure – The neutral argon atoms reflected from the target suffer few collisions with other gas atoms on their way to the growing film, with the consequence that many energetic argon atoms arrive at the growing film and produce high compressive stresses by "atomic peening".
2. High argon pressure – Many collisions in the gas prevent energetic argon atoms from arriving at growing film - so natural processes leading to tension prevail.

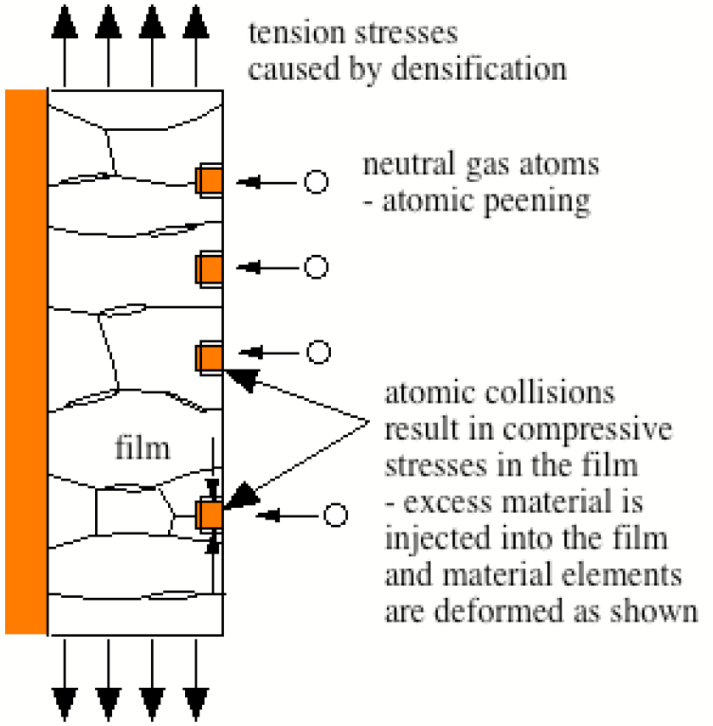

Nix 2014

vacancy annihilation

3) When crystalline films are formed by deposition onto cold substrates, the conditions are far from equilibrium and it is reasonable to expect a nonequilibrium, excess vacancy concentration to be established in the film. As these vacancies annihilate, the associated volume changes cause a stress to develop within the film.

These vacancies annihilate at the surface, interface, internal voids or dislocation core which leads to tensile stresses.

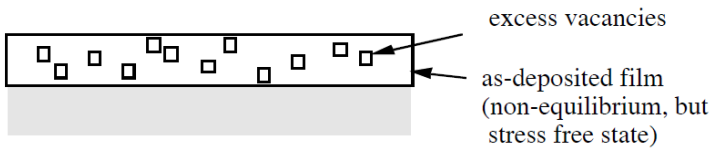

Vacancy annihilation at a free surface

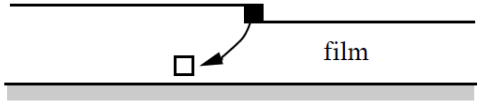

Annihilation at grain boundaries perpendicular to the film

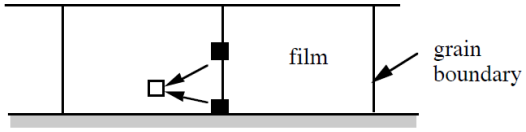

Nix 2014

stresses in films during processing – plastic deformation

the thermal misfit changes with temperature due to **difference in thermal expansion**, but there are additional mechanisms such as **plastic deformation, grain growth** and **phase changes**.

1) **Plastic deformation**:
At room temperature the stress in Al-Cu/Si is about 90 MPa (tension).

On **heating** the **tensile stress declines** as the film expands thermally more than the substrate, but the stress deviates from linear expansion relationship at a temperature of about 80°C, as the film begins to deform plastically in compression.

With **continued heating past 150°C**, the stress hardly changes at all.

On **cooling the film shrinks thermally relative to the substrate**, causing the film to be subjected to a **tensile stress**. Again, below about 350°C, the stress does not change much because of plastic extension of the film.

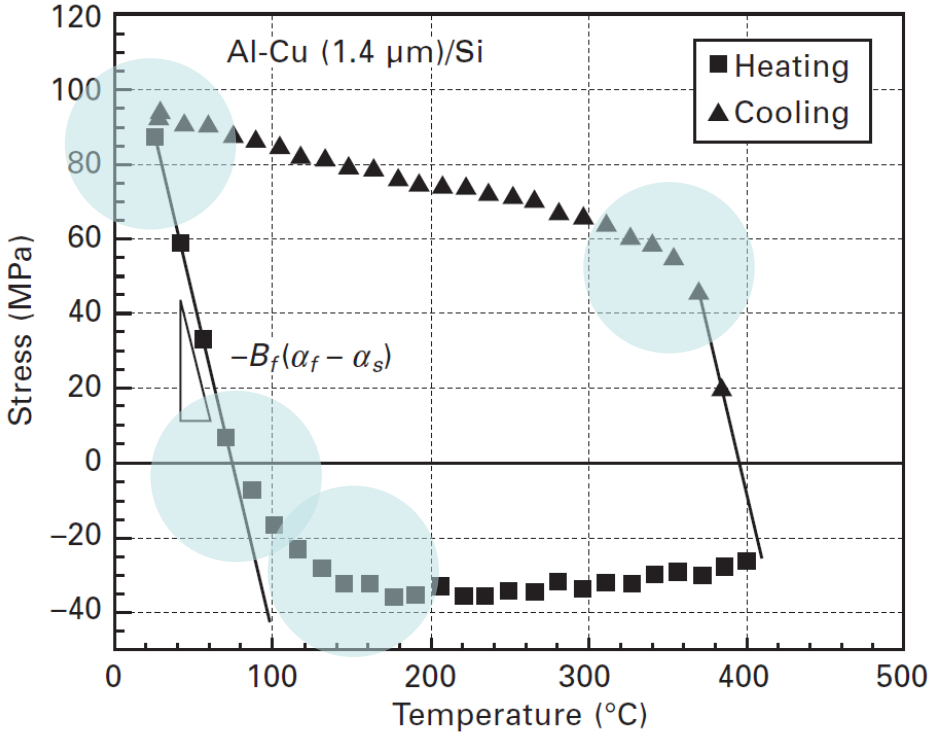

Nix 2014

stresses in films during processing – grain growth

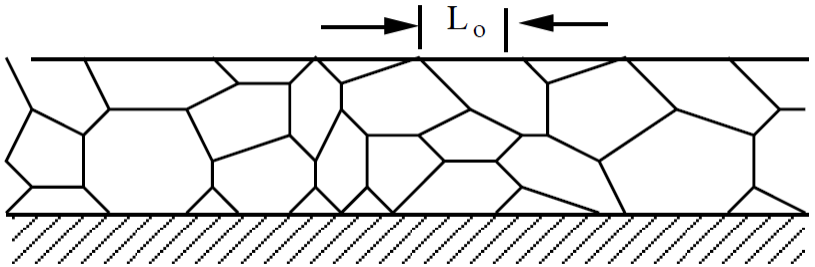

2) **Grain growth**
The **excess volume per unit area, Δa** is expected to be of order of the atomic dimension and the **grain boundary is equivalent to a gap Δa between the adjacent crystals**.

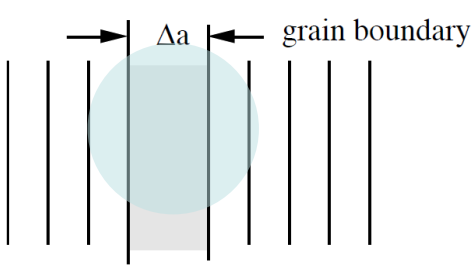

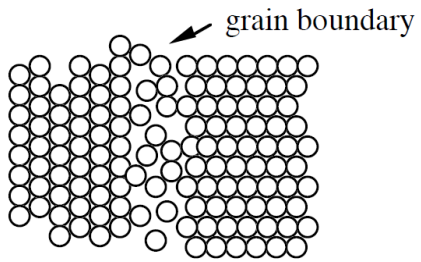

Nix 2014

stresses in films during processing – grain growth

Consider a **reference crystal volume Vref of the film** (Here, Vref is the crystal volume not including excess volume associated with the grain boundaries) with grain diameter L.

Using the model of spherical grains, the **grain boundary area per unit volume** is

$$\frac{A}{V} = \frac{1}{2}\frac{4\pi R^2}{\frac{4}{3}\pi R^3} = \frac{3}{2R} = \frac{3}{L},$$

Excess volume in the reference volume Vref is

$$V_{gb}^{xs} = V_{ref}\frac{3}{L}\Delta a\,.$$

The total volume of the polycrystalline aggregate is then

$$V_T = V_{ref} + V_{gb}^{xs} = V_{ref}\left(1 + \frac{3\Delta a}{L}\right).$$

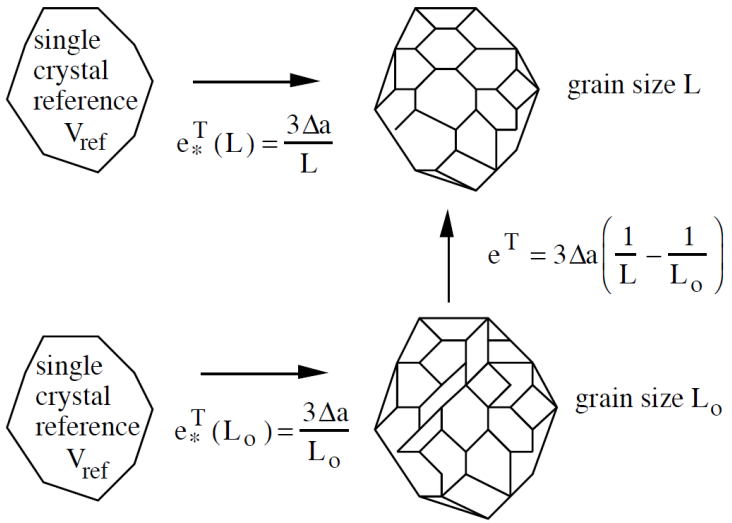

Nix 2014

stresses in films during processing – grain growth

Thus the polycrystalline solid **is dilated relative to single crystal reference by**

$$e_*^T = \frac{V_T - V_{ref}}{V_{ref}} = \frac{V_T}{V_{ref}} - 1 = \frac{3\Delta a}{L}$$

Suppose the film is deposited in stress free state with grain size L_0. Then after grain growth to grain size L, the transformation strain relative to the as deposited state is

$$e^T = 3\Delta a\left(\frac{1}{L} - \frac{1}{L_o}\right)$$

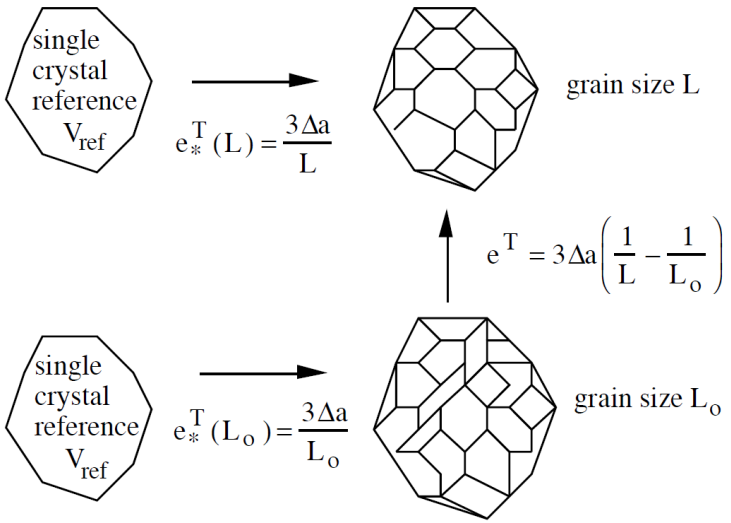

For

1/L -> 0 (infinite grain growth),
Lo = 100Å = 10 nm,
Δa= 1Å = 0.1 nm,
$(E/1\text{-}v)_{film}$ = 100GPa,

We find

σ=1GPa

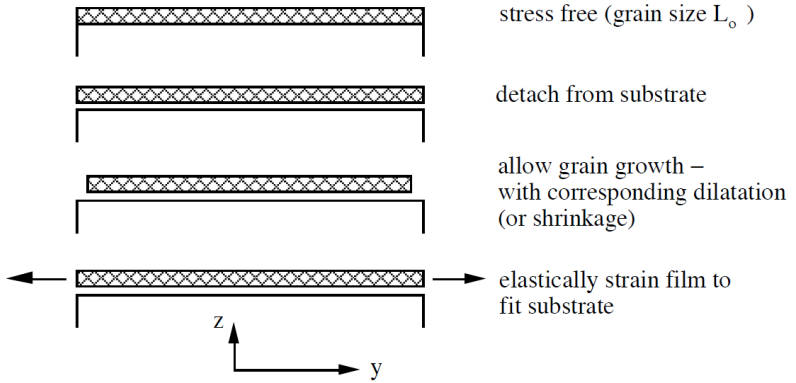

Nix 2014

stresses in films during processing – grain growth

During grain growth, **the elastic strain energy increases** as the stresses and strains in the film develop.

$$W_{el} = \frac{1}{2}\sigma_{xx}\varepsilon_{xx}^{el} + \frac{1}{2}\sigma_{yy}\varepsilon_{yy}^{el},$$

which, with the equations above becomes

$$W_{el} = \left(\frac{E}{1-\nu}\right)_{film} (\Delta a)^2 \left(\frac{1}{L_o} - \frac{1}{L}\right)^2$$

So **W_{el} increases with grain growth** - This can **stop grain growth**!

We can calculate the total energy

$$E = \frac{3\gamma_{gb}}{L} + \left(\frac{E}{1-\nu}\right)_{film} (\Delta a)^2 \left(\frac{1}{L_o} - \frac{1}{L}\right)^2,$$

If **the initial grain size is greater than the critical value, $L_o > L_{critical}$**, then **the grains will grow** in an unbounded manner **until a single crystal state** is reached.

In this case the strain energy that develops in the film is not great enough to stop the grain growth.

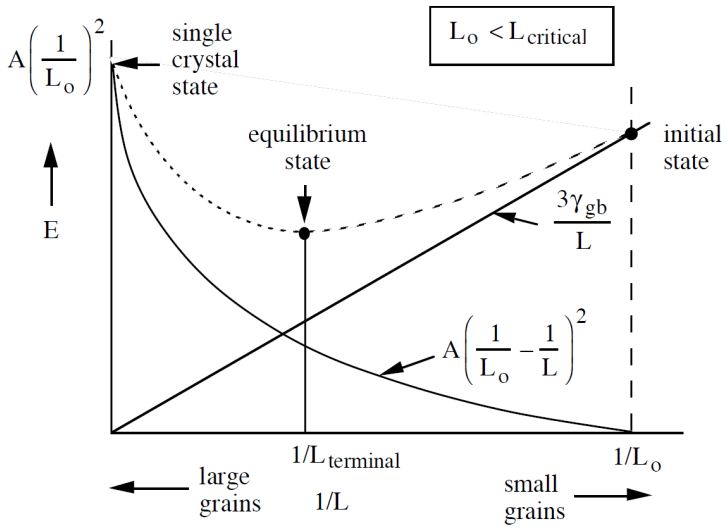

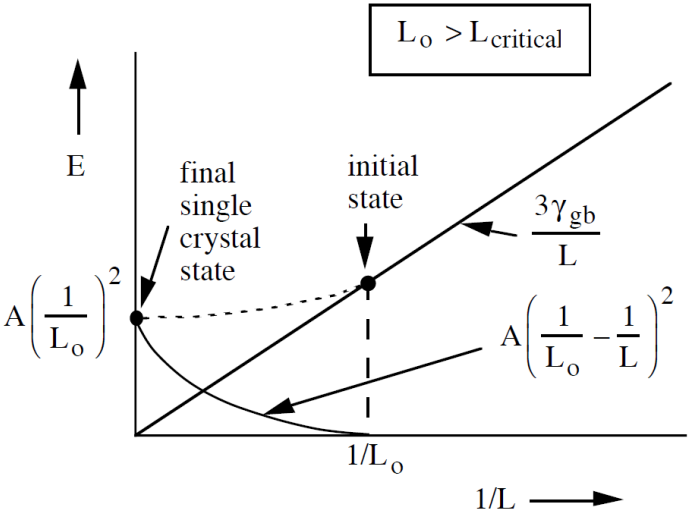

Nix 2014

stress. in films during processing – crystallizat. & phase change

A **major source of stress in alloy thin films involves volume changes** that may occur when **phase changes** occur after the films are deposited.

Alloy films are often **deposited in an amorphous state**. On **heating, the film can crystallize** to form stable crystalline phases.

A **stress develops** if the more stable phases that are created **have a different volume or density** (compared to the initial amorphous state).

Example: Ta-Si films deposited at room temperature by CVD.

The amorphous-to-crystalline transition at 450°C creates a negative misfit strain that leads to a tensile stress in the film.

On **cooling below 600°C**, the crystalline $TaSi_2$ film deforms elastically down to room temperature, leaving the film with a tensile stress of over 800 MPa.

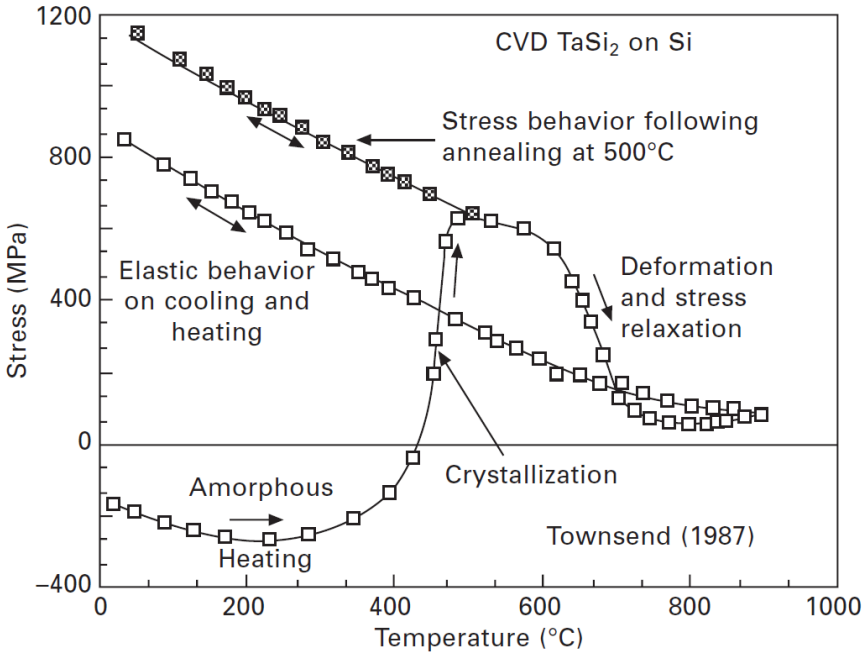

Nix 2014

stress. in films during processing – deposition techniques

In evaporated metal films the stress is invariably tensile with a typical magnitude of ~ 1 GPa.

The stress in sputtered metal films appears to be 2 - 3 times higher than for evaporated metals. Such stress values considerably exceed those for the yield stress in bulk metals.

There is no apparent strong dependence of stress on the nature of the substrate.

The magnitude of the stress in nonmetallic films is typically 100- 300 MPa.

Both compressive and tensile stresses arise in dielectric films.

Film	Process	Conditions	Stress (GPa)
SiO_2	Thermal	900–1200°C	−0.2 to −0.3
SiO_2	CVD 400°C	40 nm/min	+0.13
SiO_2	$SiH_4 + O_2$	400 nm/min	+0.38
SiO_2	CVD	450°C	+0.15
	TEOS	725°C	+0.02
SiO_2	TEOS	685°C	+0.38
	TEOS + 25% B, P		−0.02
SiO_2	Sputtered		−0.15
Si_3N_4	CVD	450–900°C	+0.7 to +1.2
Si_3N_4	Plasma	400°C	−0.7
		700°C	+0.6
Si_3N_4	Plasma 13.56 MHz	150°C	−0.3
		300°C	+0.02
Si_3N_4	Plasma 50 kHz	350°C	−1.1
Poly Si	LPCVD	560–670°C	−0.1 to −0.3
$TiSi_2$	PECVD	As-deposited	+0.4
		Annealed	+1.2
$TiSi_2$	Sputtered		+2.3
$CoSi_2$	Sputtered		+1.3
$TaSi_2$	Sputtered	800°C anneal	+3.0
$TaSi_2$	Sputtered		+1.2
W	Sputtered	200 to 400 W power	+2 to −2
W	Sputtered	5 to 15 mtorr Ar pressure	−3 to +3
Al			+0.5 to ~+1

Ohring 2003

The stress dilemma

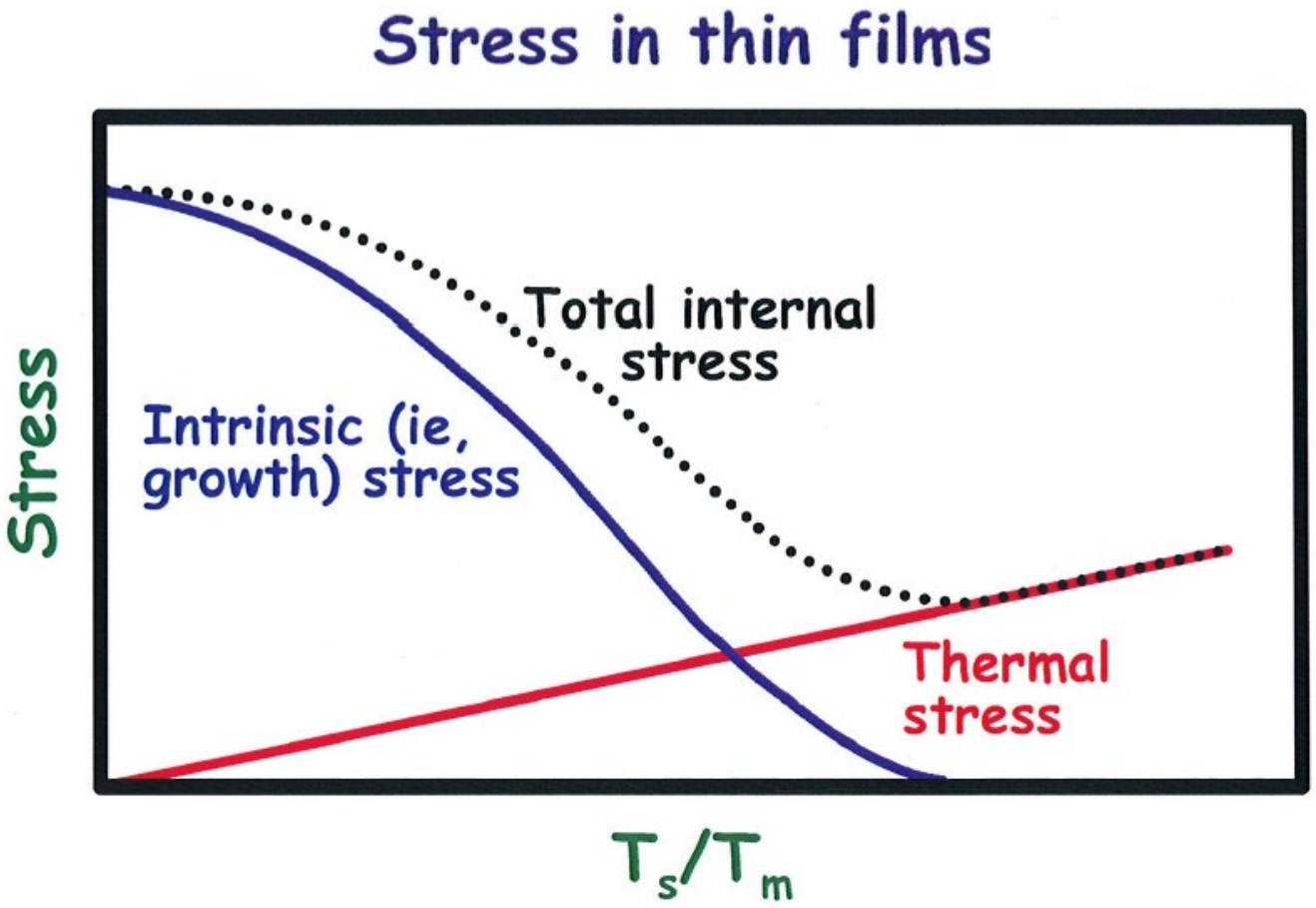

Courtousy, Joe Greene. Univ. Illinois

Summary

Stress in thin films

- Film exerts bending moment on substrate plate which leads to curvature=1/R
- Stoney equation is independent of film properties: $\sigma_f = \left(\frac{E_s}{1-\nu_s}\right)\frac{t_s^2}{6t_f}(\kappa - \kappa_o)$
- In textured films biaxial film modulus for <111> and <001> textures used, <110> more complicated
- In plane Young's modulus depends on grain size (10%less for <10nm), texture (up to 2x), porosity (~ porevolume^2)
- Stress of 1st, 2nd, 3rd order
- methods for residual stress
  - Mechanical methods: Substrate curvature via laser deflection, bending of FIB bi-metal beam
  - (Fib-)Hole drilling & edge relaxation,
  - XRD (sin2 Ψ - method measures out of plane strain and converted to in-plane stress, epi-layers and reciprocal space map,
  - Raman spectroscopy stress dependence of opt phonon frequency,
  - EBSD cross.correlation method
  - Cantilver beam methods
  - Method comparison: spatial (lateral & depth), and spectral resolution
- Types of stresses (thermal, instrinsic, epitaxial) $\sigma = \left(\frac{E}{1-\nu}\right)_f \varepsilon = -\left(\frac{E}{1-\nu}\right)_f (\alpha_f - \alpha_s)\Delta T$ $\sigma_1 = \sigma_2 = \left(c_{11} + c_{12} - \frac{2c_{12}^2}{c_{11}}\right)\varepsilon_1 = \left(c_{11} + c_{12} - \frac{2c_{12}^2}{c_{11}}\right)\left(\frac{a_s - a_f}{a_s}\right)$
- Intrinsic: Capillary, Laplace pressure of islands, Zip stress during coalescence
- Stress evolution after coalescence, Impurities, vacancies, ion bombardment
- Evolution during growth: Capillary stress: Laplace-Young equation p=2γ_s/r. ; Zip stress like healing crack, following coalescence either compressive due to epitaxy, relaxed due to adatom mobility or compressive due to incorporation of excess atoms (at GB, or bigger Ar atoms)
- Evolution during or after: vacancy annihilation, densification, crystallization, grain growth
- The stress dilemma: intrinsic stress relaxes at high deposition T, thermal increases

Techniques for residual stress measurement

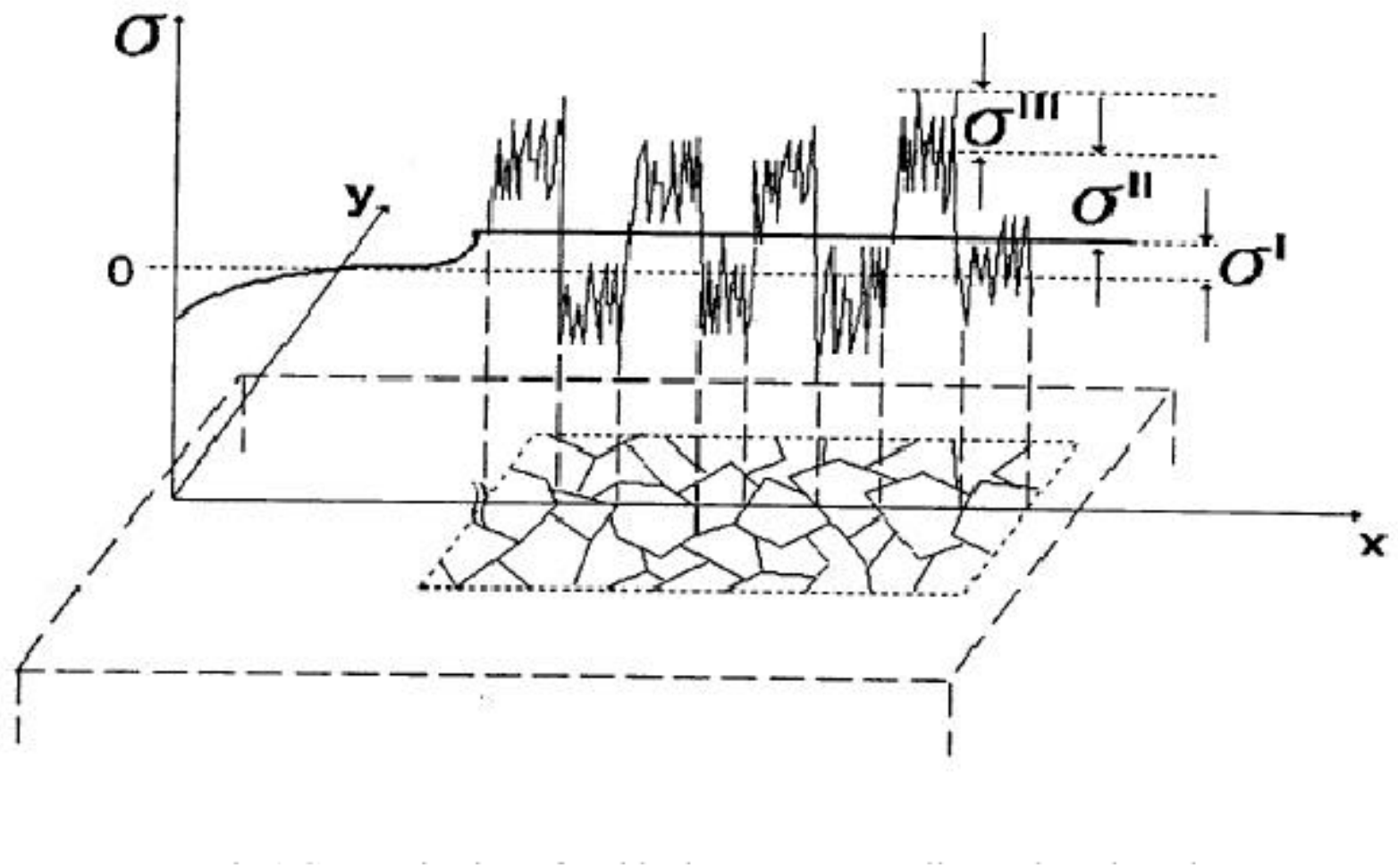

Wafer bending methods

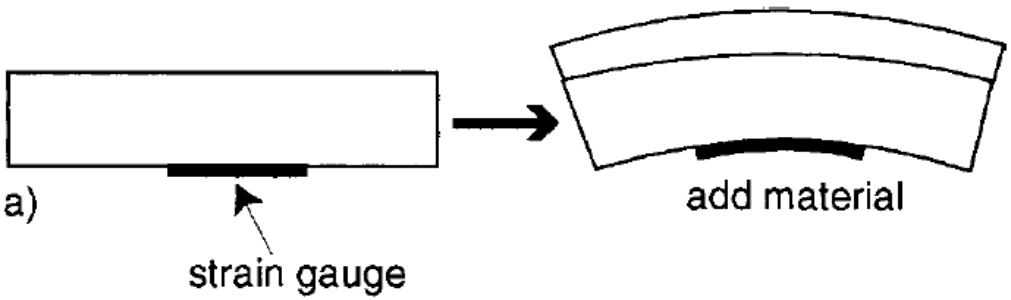

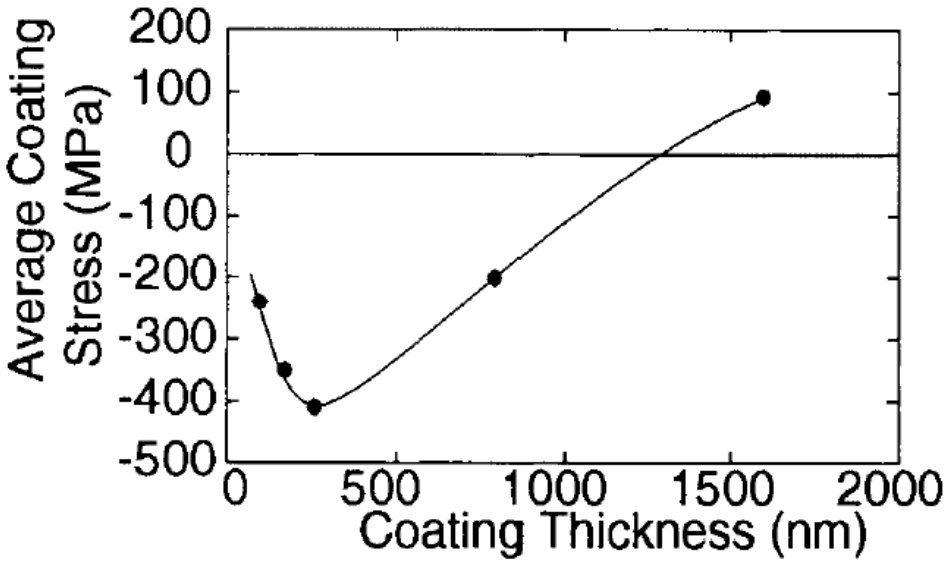

Mo on Si

Thin film approximation: Stoney equation and curvature radius R

$$\sigma_{Stoney} = \frac{E_{sub}}{1-\upsilon_{sub}} \frac{h_{sub}^2}{6 h_{lay} R}$$

hole drilling method

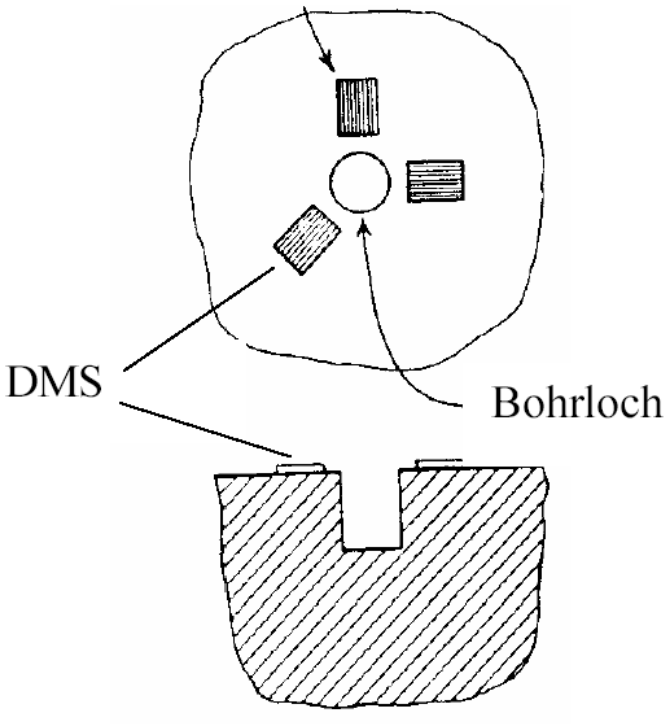

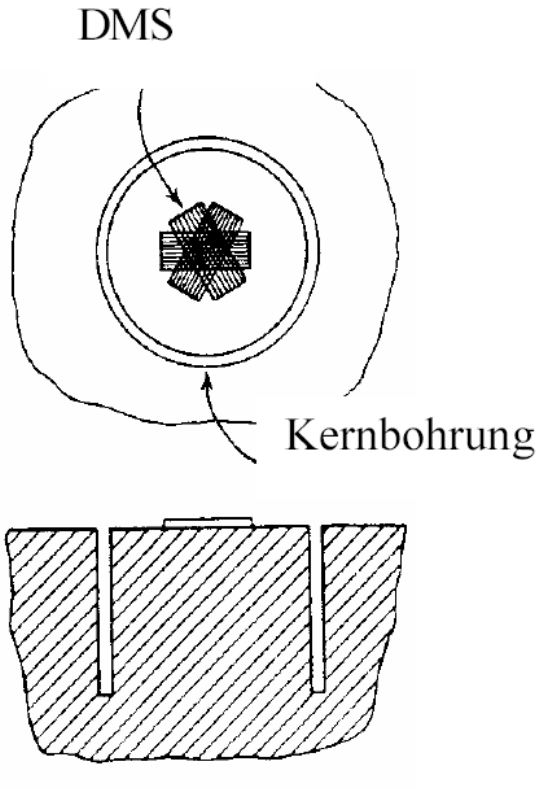

Hybrid AFM-FIB for residual stress measurement

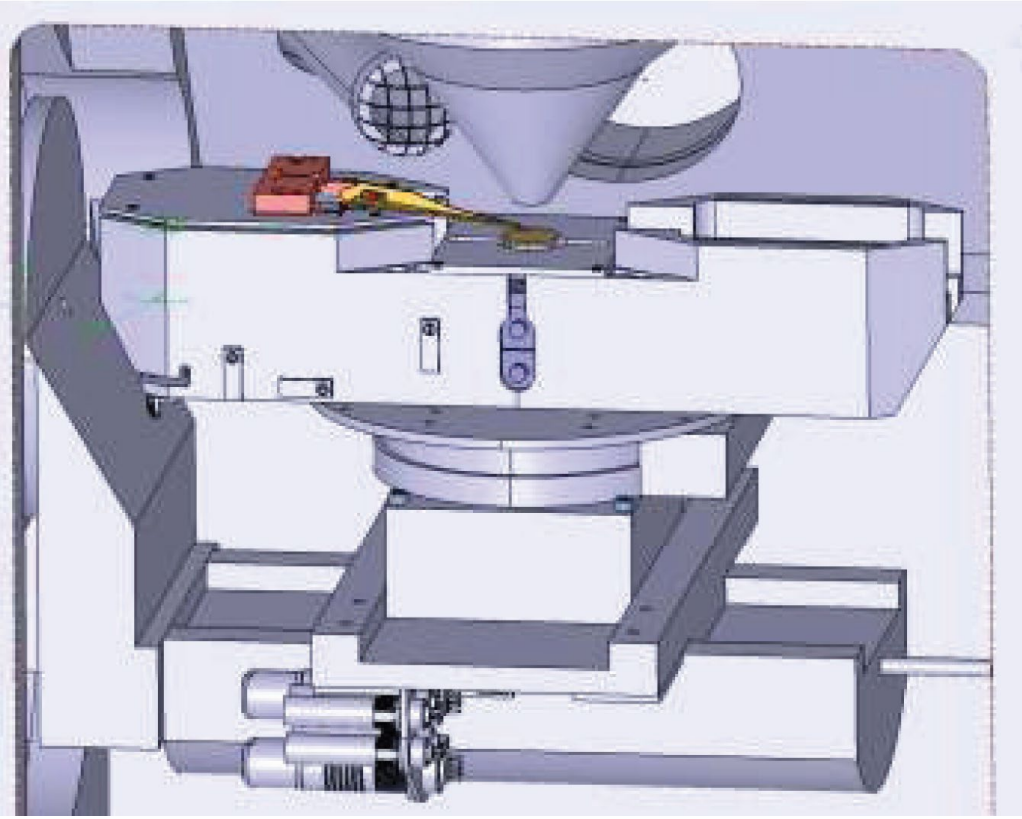

AFM inside the Tescan Lyra dual-beam FIB

Uses electrically biased, oscillating cantilever rather than laser/piezo-photodetector system

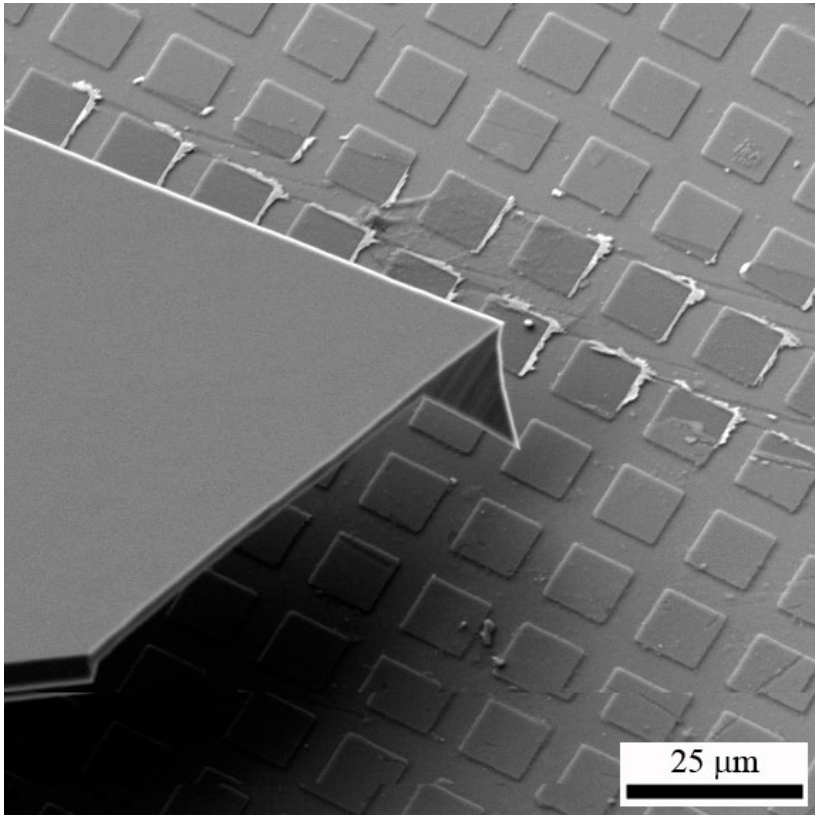

Self-sensing Akiyama probe

Resonance frequency ~45kHz

Q-factor in vacuum: 1000-3000

Residual Stress: Milling Geometries

- Incremental slot, hole or annular milling
- Monitor surface relaxation with depth
- Fiducial markers used as reference points during imaging and analysis
- Uniaxial and Biaxial stress distributions of site-specific features measurable

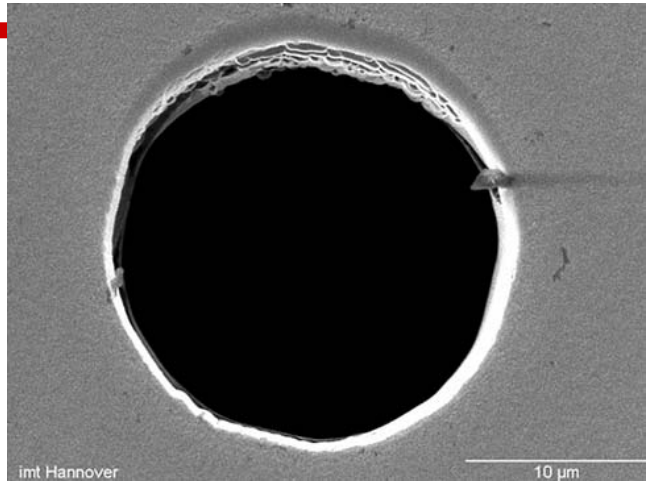

Gerdes & Gatzen, Microsyst. Technol., **15** (2009)

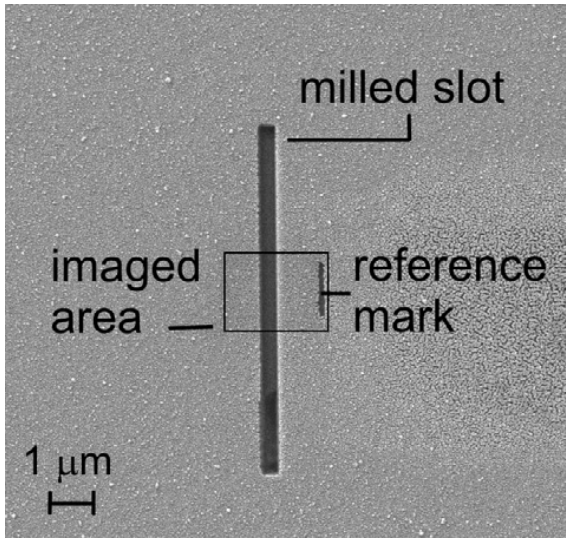

Sabaté, *et al*, Nanotechnology., **17** (2006)

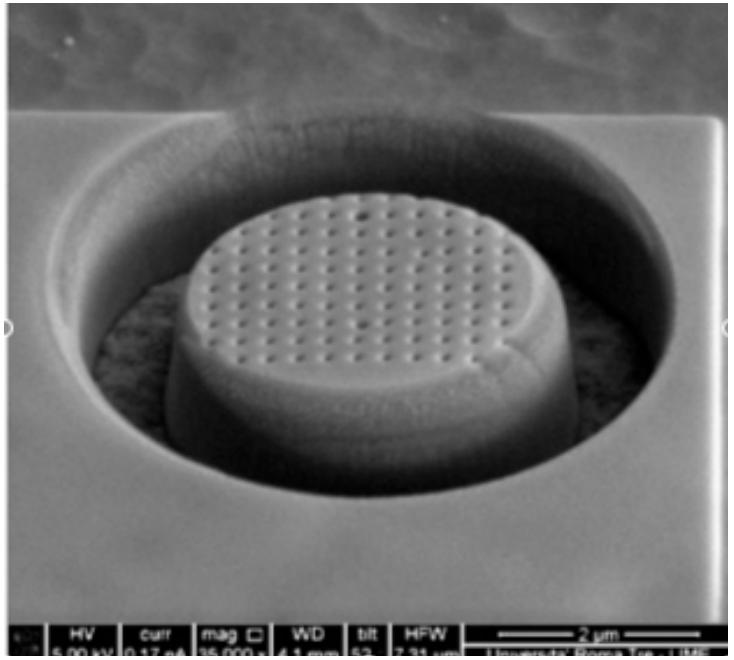

Korsunsky, *et al*, Mater. Lett., **63** (2009)

- Scan with AFM before & after milling with FIB
- Digital Image Correlation (DIC) used on both AFM and SEM images to measure stress relaxation wrt marked pattern

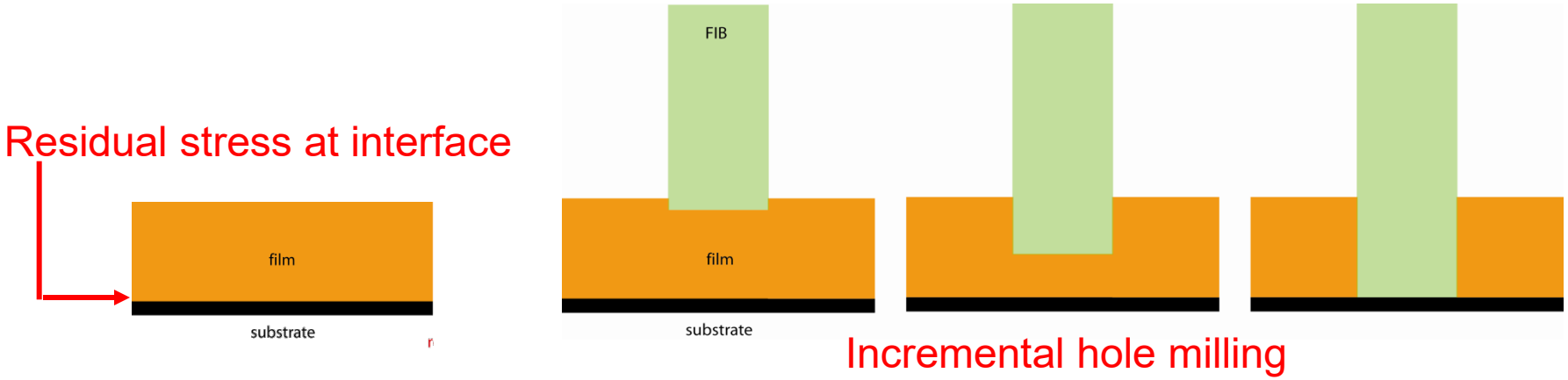

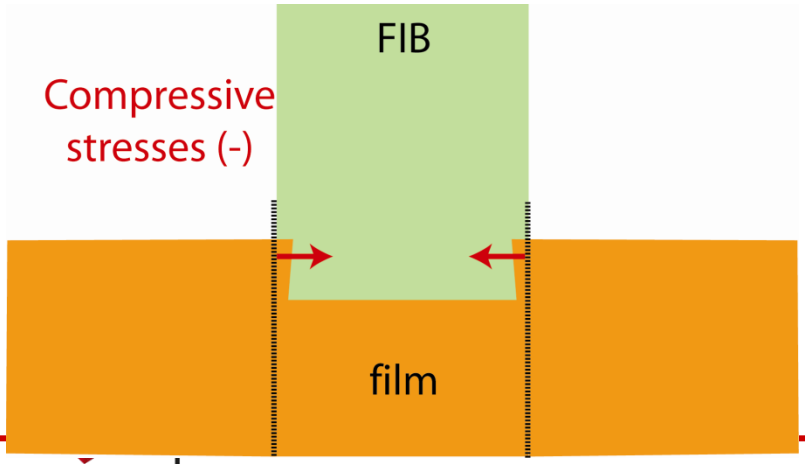

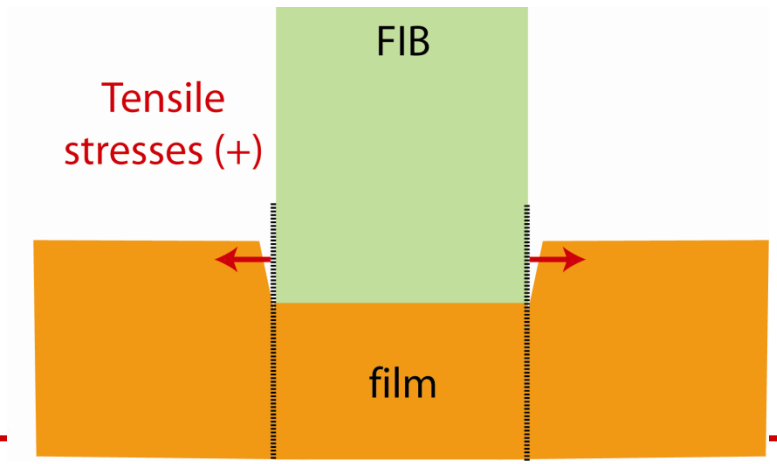

Surface will relax depending on sign of stress

X-ray diffraction

Bragg equation

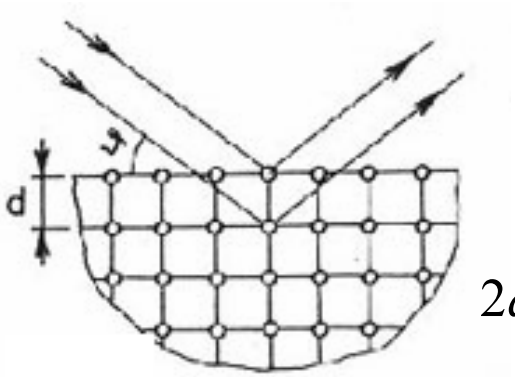

$$2d \sin \vartheta = n\lambda$$

$$\varepsilon_{\Phi\Psi} = \frac{\Delta d}{d}$$

Definition of angles

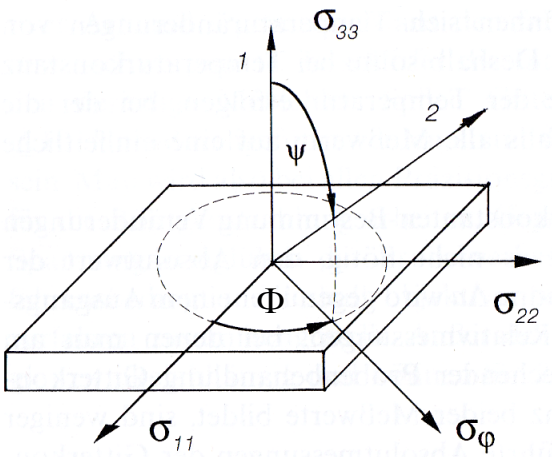

1: Probennormale
2: Messrichtung (Netzebenennormale)

X-ray diffraction

Effect of stress on plane spacing

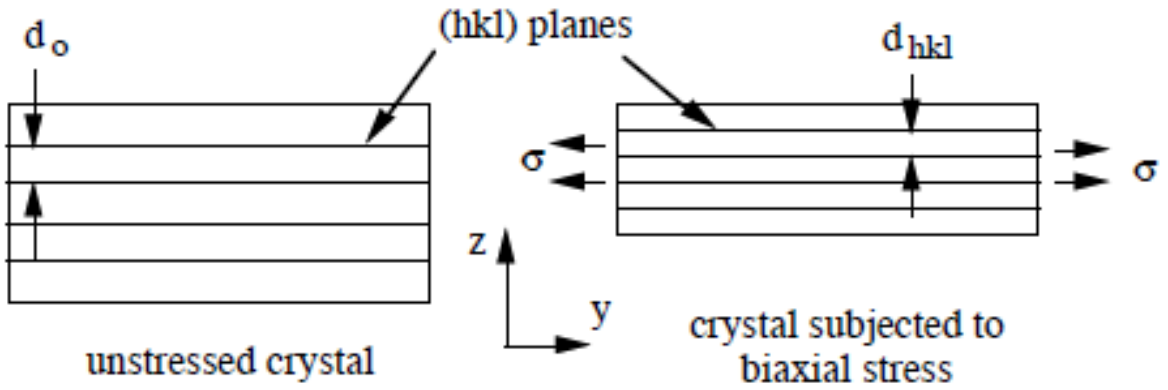

X-ray diffraction

Determination of Stresses in Thin Films by Symmetric X-Ray Diffraction

Isotropic Elasticity

Biaxial stress acting on a thin film

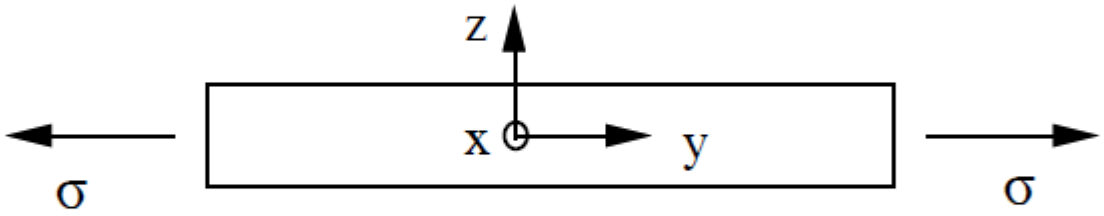

We first consider symmetric x-ray diffraction in which the scattering vector is perpendicular to the plane of the film. This permits a measurement of the spacing of those atomic planes that lie parallel to the plane of the film. This is called the symmetric reflecting geometry.

X-ray diffraction

Symmetric Reflecting Geometry

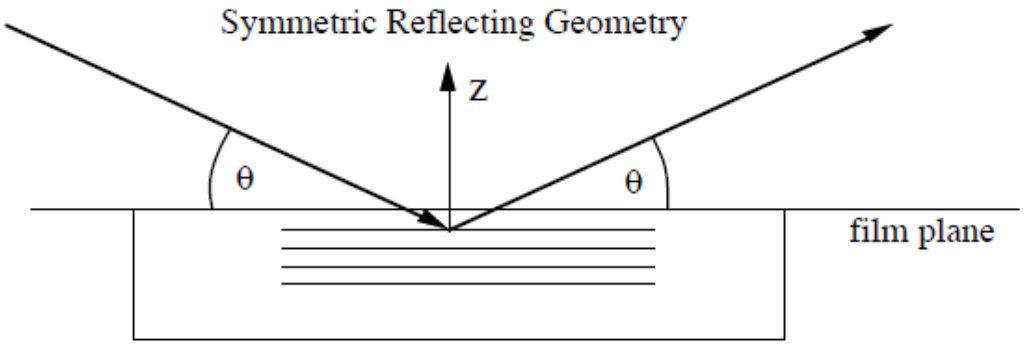

measurement of ε_{zz}

We may find the relation between the measured strain ε_{zz} and the stresses in the film using the isotropic form of Hooke's Law:

$$\varepsilon_{xx} = \varepsilon_{yy} = \frac{1}{E}\left[\sigma_{xx} - \nu\left(\sigma_{yy} + \sigma_{zz}\right)\right]$$

but, $\sigma_{zz} = 0$ for a thin film and $\sigma_{xx} = \sigma_{yy} = \sigma$ for the usual case of an equal biaxial stress, so

$$\varepsilon_{xx} = \frac{1-\nu}{E}\sigma$$

X-ray diffraction

The corresponding normal strain is

$$\varepsilon_{zz} = \frac{1}{E}\left[\sigma_{zz} - \nu\left(\sigma_{yy} + \sigma_{xx}\right)\right] = -\frac{2\nu}{E}\sigma$$

$$\varepsilon_{zz} = -\frac{2\nu}{E}\sigma .$$

So for isotropic elasticity the biaxial stress and the other strains can be found using

$$\sigma = -\frac{E}{2\nu}\varepsilon_{zz}$$

$$\varepsilon_{xx} = \varepsilon_{yy} = -\frac{1-\nu}{2\nu}\varepsilon_{zz}$$

Thus, measurement of ε_{zz} by X-ray diffraction gives the biaxial stress, σ, and biaxial strains $\varepsilon_{xx} = \varepsilon_{yy}$ if the film is elastically isotropic.

But, most crystalline solids are not elastically isotropic. So an anisotropic elastic analysis is required. Next we give some results for cubic crystals.

X-ray diffraction

$$\vec{\varepsilon} = \vec{S} \cdot \vec{\sigma}\,; \quad \vec{S} = \begin{pmatrix} 1/E & \nu/E & \nu/E & 0 & 0 & 0 \\ \nu/E & 1/E & \nu/E & 0 & 0 & 0 \\ \nu/E & \nu/E & 1/E & 0 & 0 & 0 \\ 0 & 0 & 0 & \frac{2(1-\nu)}{E} & 0 & 0 \\ 0 & 0 & 0 & 0 & \frac{2(1-\nu)}{E} & 0 \\ 0 & 0 & 0 & 0 & 0 & \frac{2(1-\nu)}{E} \end{pmatrix}$$

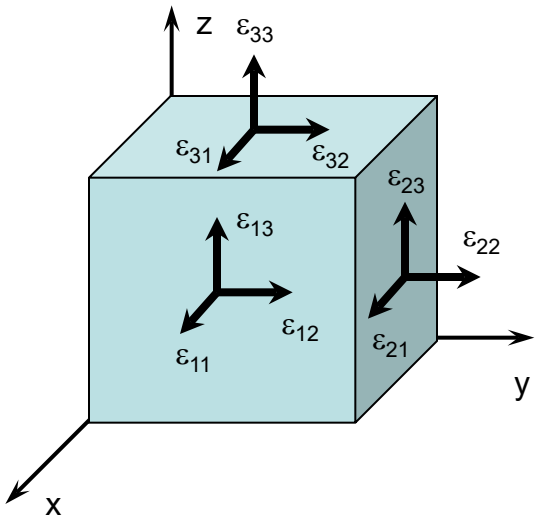

$$\varepsilon_{\Phi\Psi} = \frac{d_{\phi\psi} - d_0}{d_0} = \frac{1+\nu}{E}\left(\sigma_{11}\cos^2\phi + \sigma_{12}\sin 2\phi + \sigma_{22}\sin^2\phi - \sigma_{33}\right)\sin^2\psi +$$
$$+ \frac{1+\nu}{E}\sigma_{33} - \frac{\nu}{E}\left(\sigma_{11} + \sigma_{22} + \sigma_{33}\right) + \frac{1+\nu}{E}\left(\sigma_{13}\cos\phi + \sigma_{23}\sin\phi\right)\sin 2\psi$$

X-ray diffraction

Bi-axial stress state ($\sin^2\Phi$ Method)

$$\sigma_{13} = \sigma_{23} = \sigma_{33} = 0$$

Steigung — Achsenabschnitt

$$\frac{d_{\phi\psi} - d_0}{d_0} = \frac{1+\nu}{E}\sigma_\phi \sin^2\psi - \frac{\nu}{E}(\sigma_{11} + \sigma_{22})$$

$$\sigma_\phi = \sigma_{11}\cos^2\phi + \sigma_{12}\sin 2\phi + \sigma_{22}\sin^2\phi$$

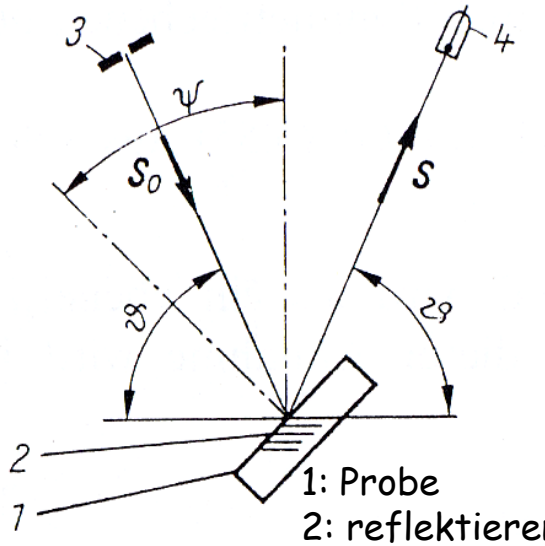

1: Probe
2: reflektierende Netzebenen
3: Eintrittsblende
4: Zählrohr

Raman spectroscopy

optical phonons

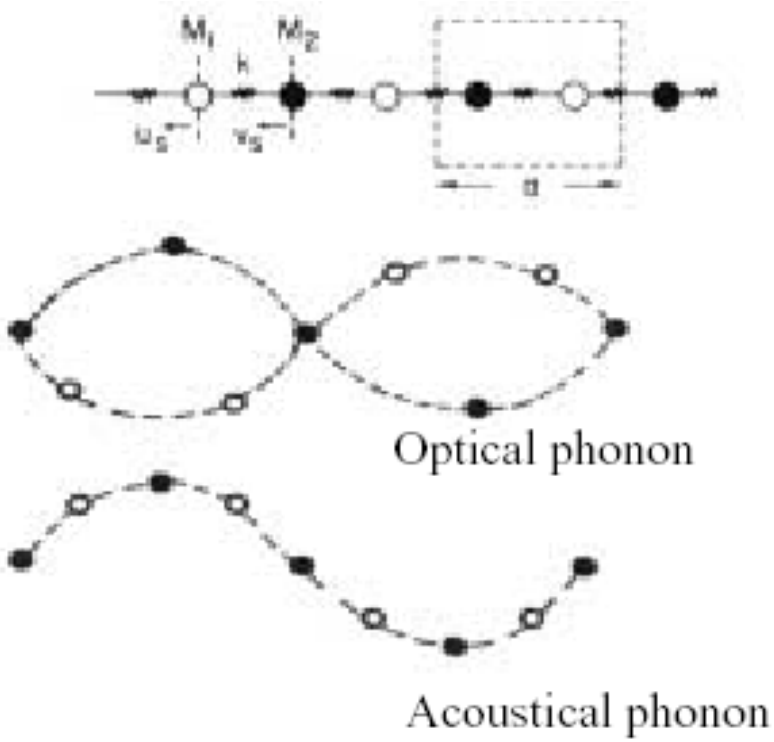

Phonon dispersion curves

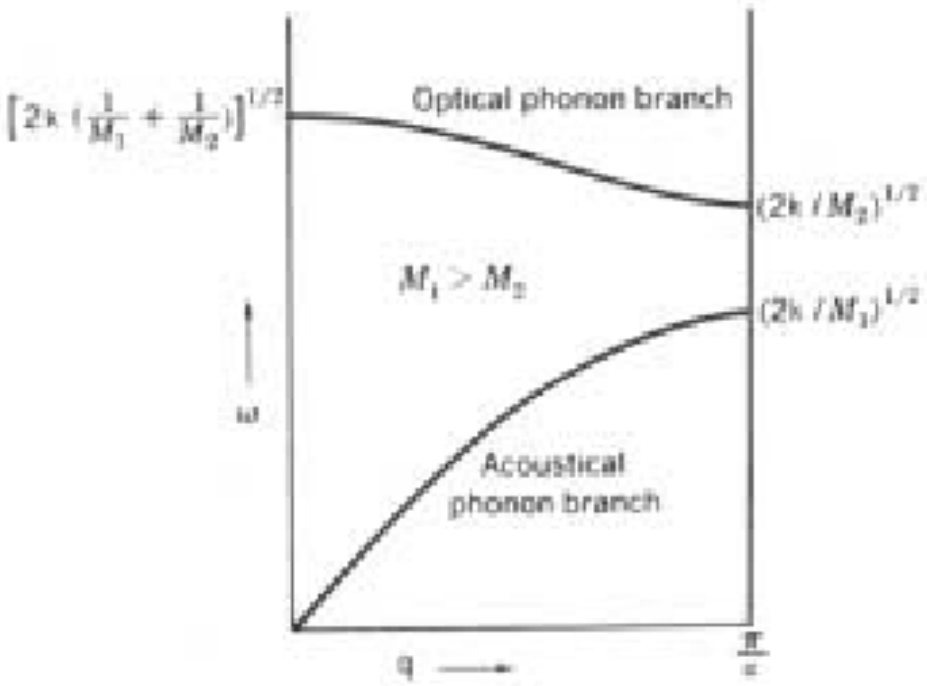

Micro-Raman sprectroscopy

instrument

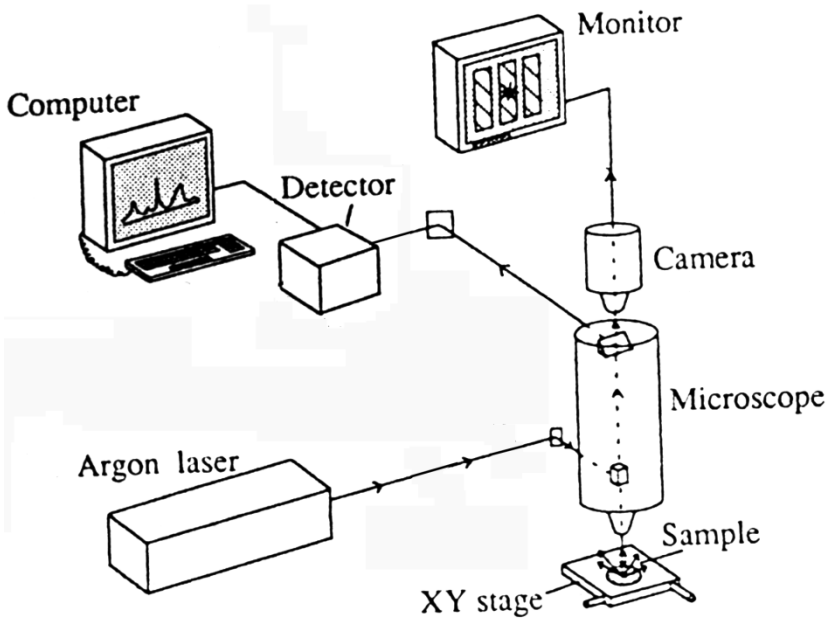

example

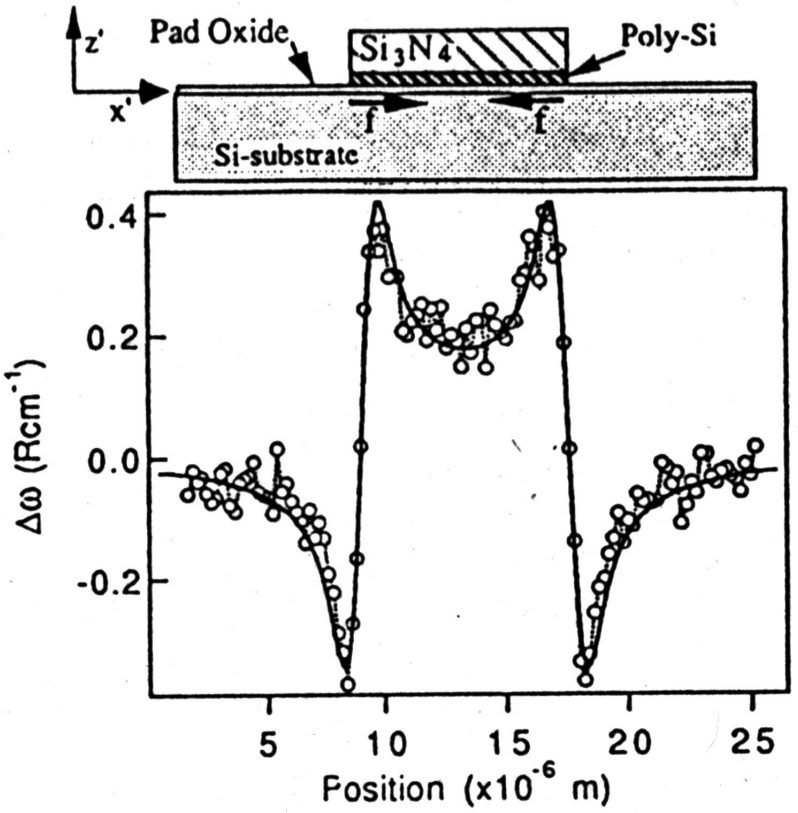

De Wolf 1996, Semicond. Sci Technol. **11**, 139

Morphology of highly oriented diamond films at different growth states

h = 300nm

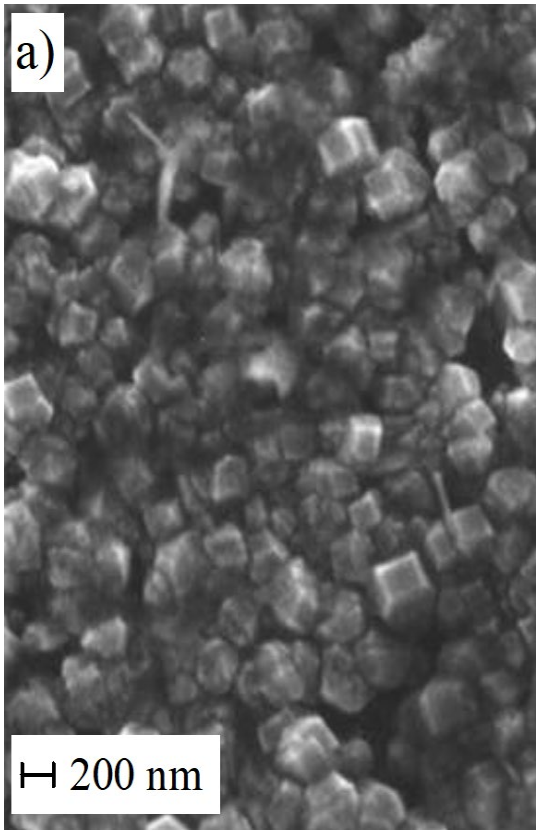

h = 4μm

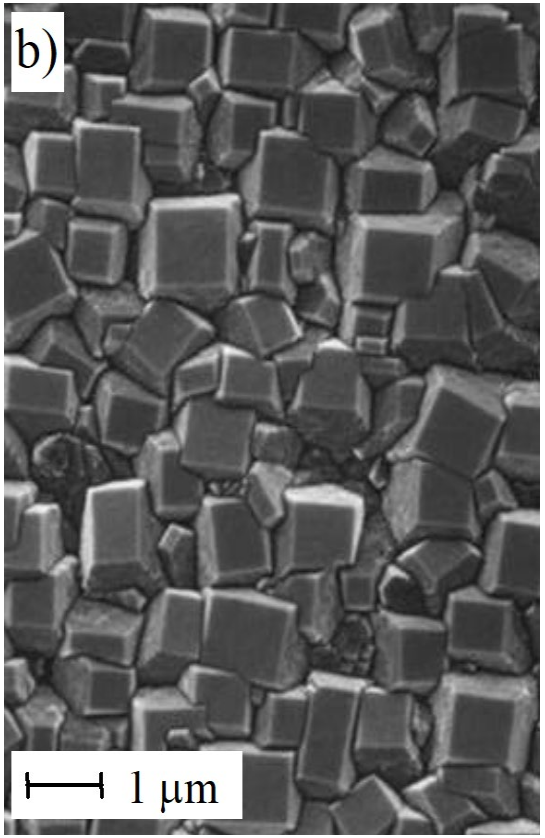

h = 47μm

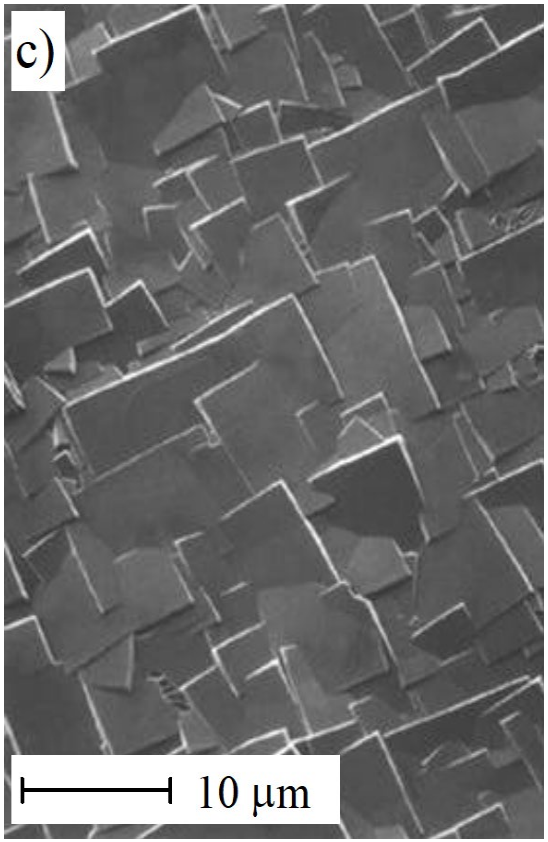

Application of Micro-Raman spectroscopy to diamond films

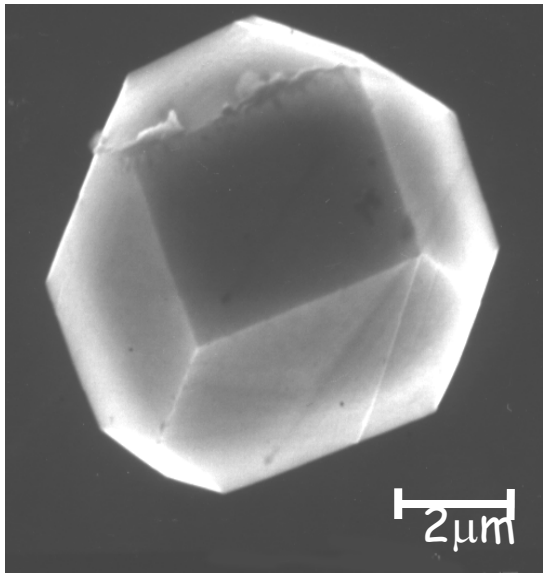

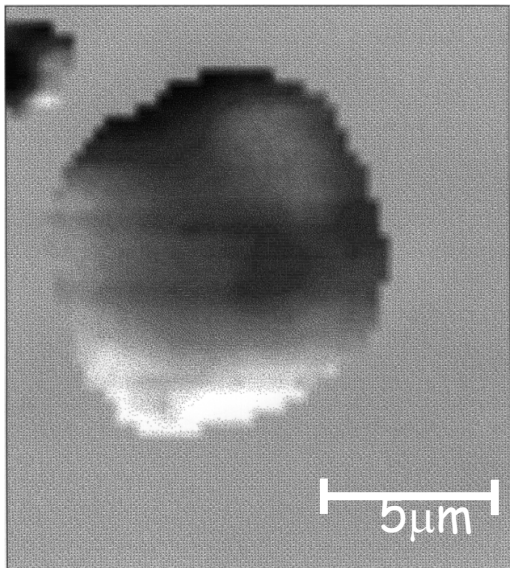

diamond peak frequency, cm^{-1}

1333.5

1333

1332.5

Reduction of stress by structuring of surfaces
Example: roughness of diamond layers

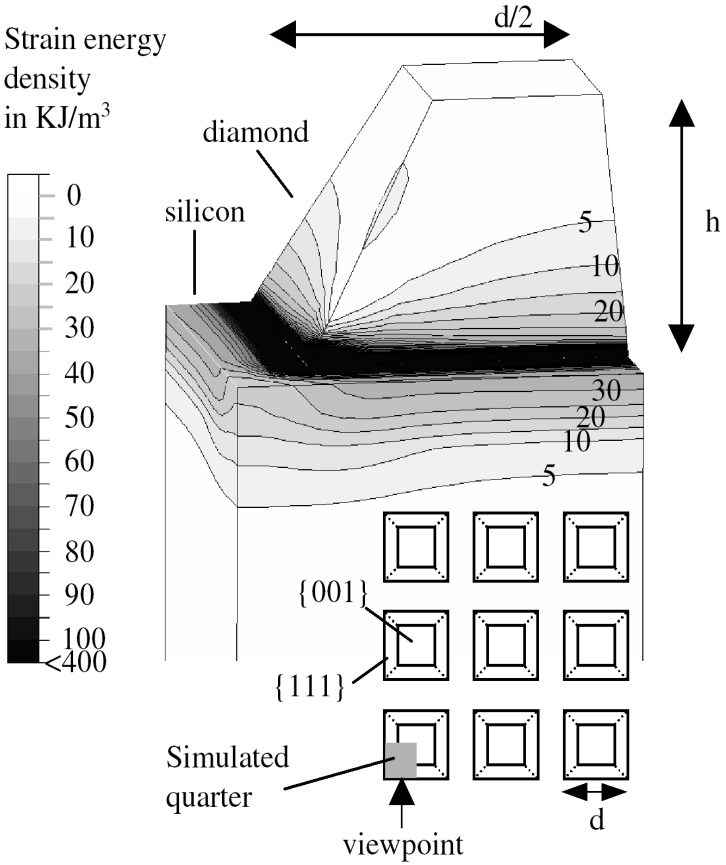

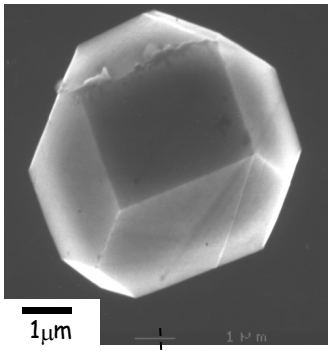

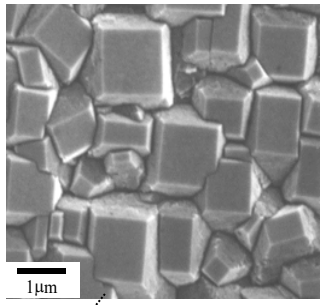

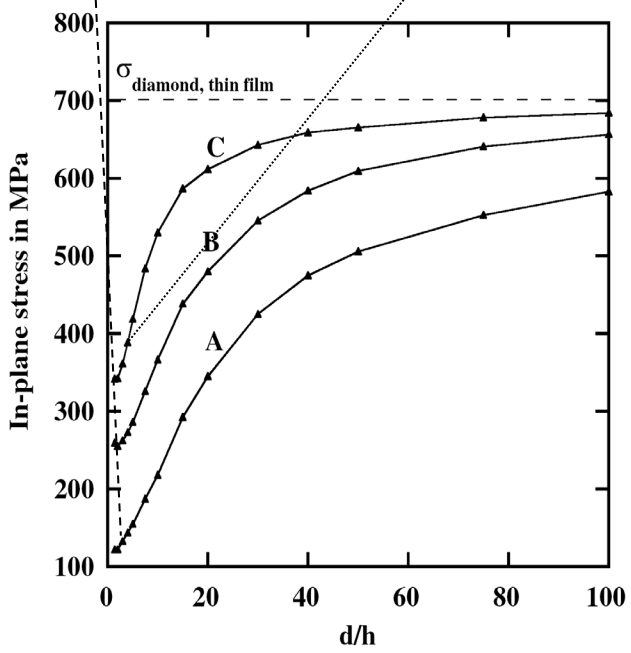

Michler 1999, Thin Solid Films **352**, 1-13

Application of Micro-Raman spectroscopy to diamond films

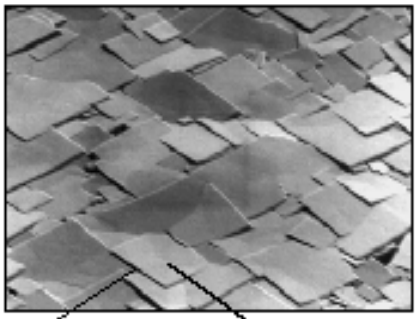

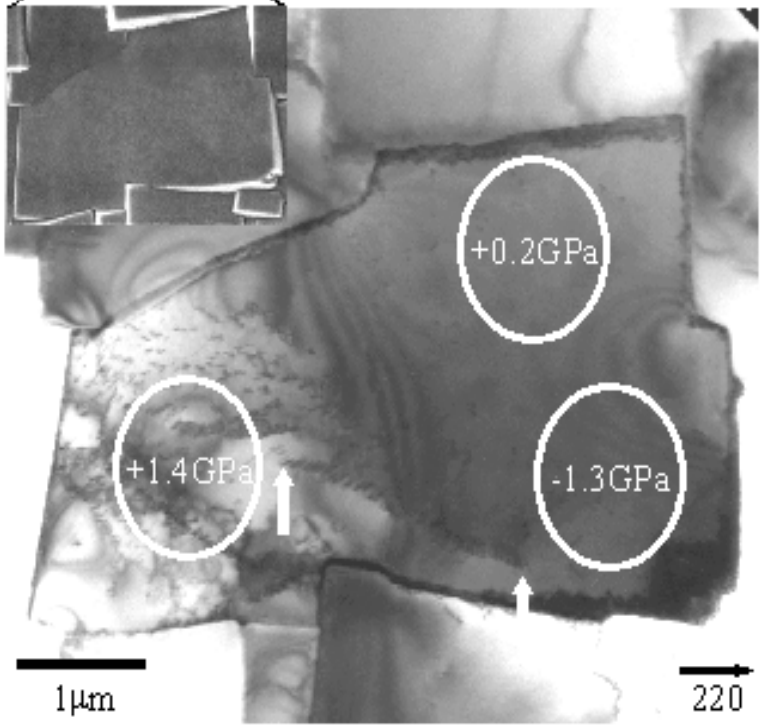

Partial wedge disclinations
are sources of internal stress

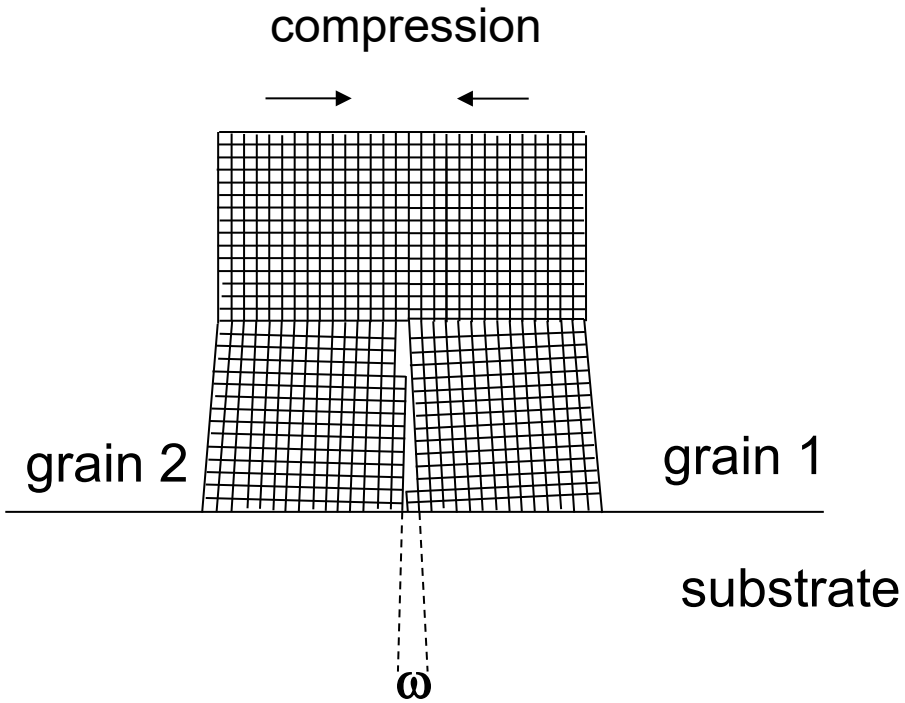

EBSD: Electron Backscatter Diffraction

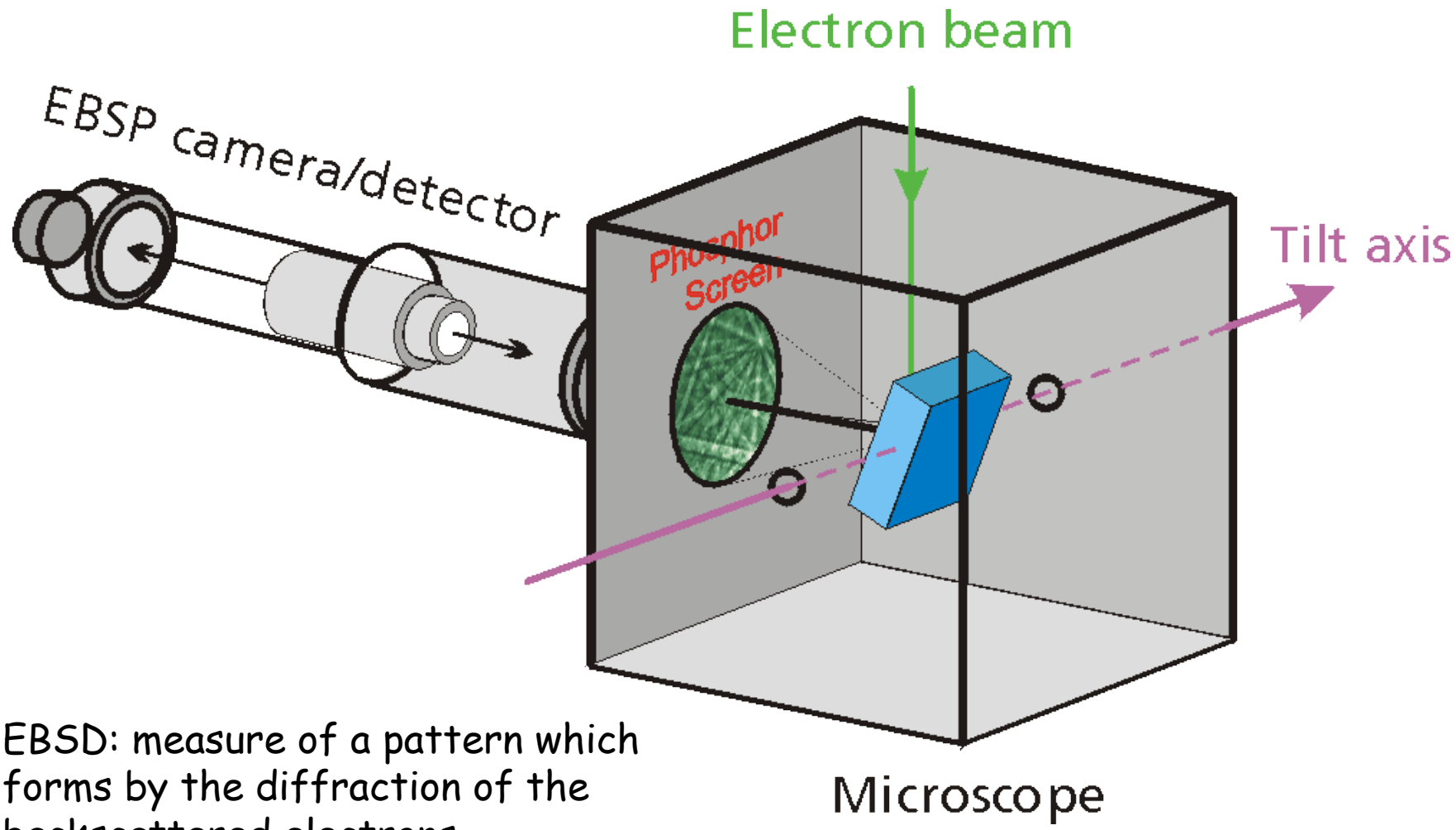

EBSD: measure of a pattern which forms by the diffraction of the backscattered electrons

EBSD Pattern Formation

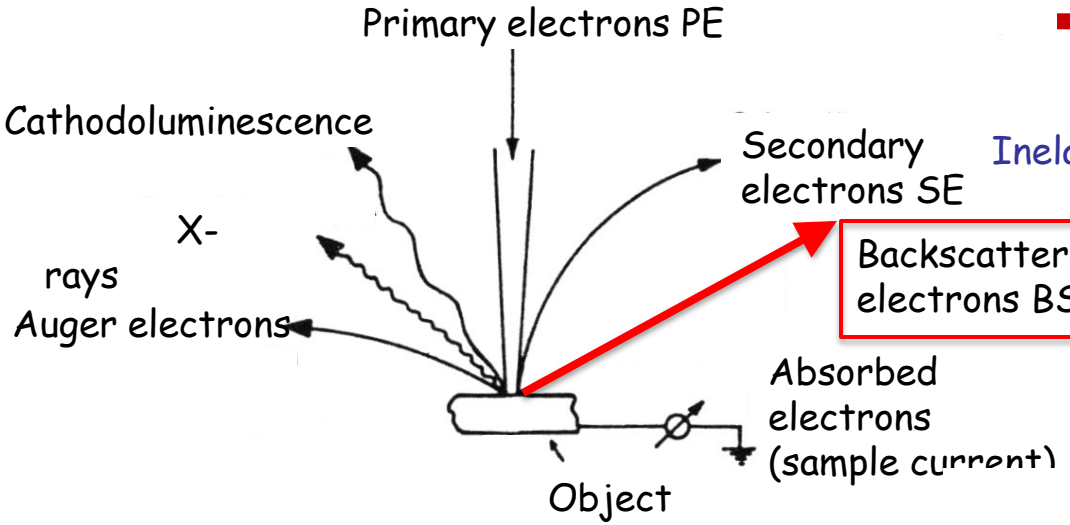

Diffraction on the lattice plane according to the Bragg law

$$\text{Bragg}: 2\, d_{hkl} \sin\theta = n\,\lambda$$

$$20\ \text{keV} \rightarrow \lambda \approx 7\ 10^{-3}\ \text{nm} \rightarrow \theta \approx 0.5°$$

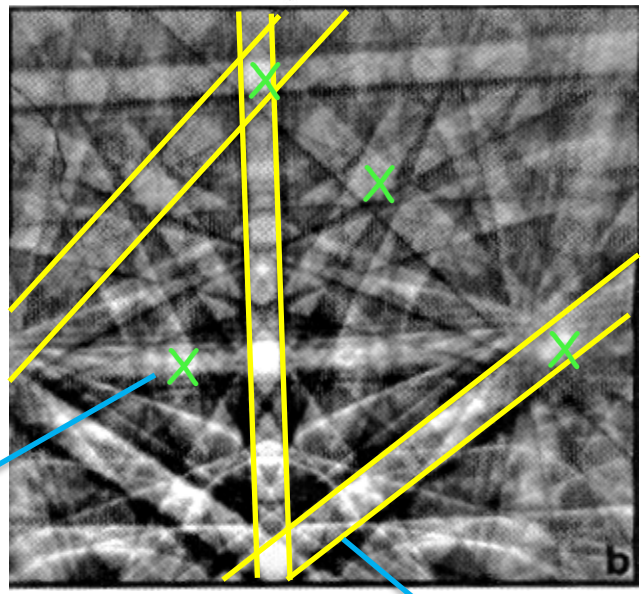

Pole

Lattice plane

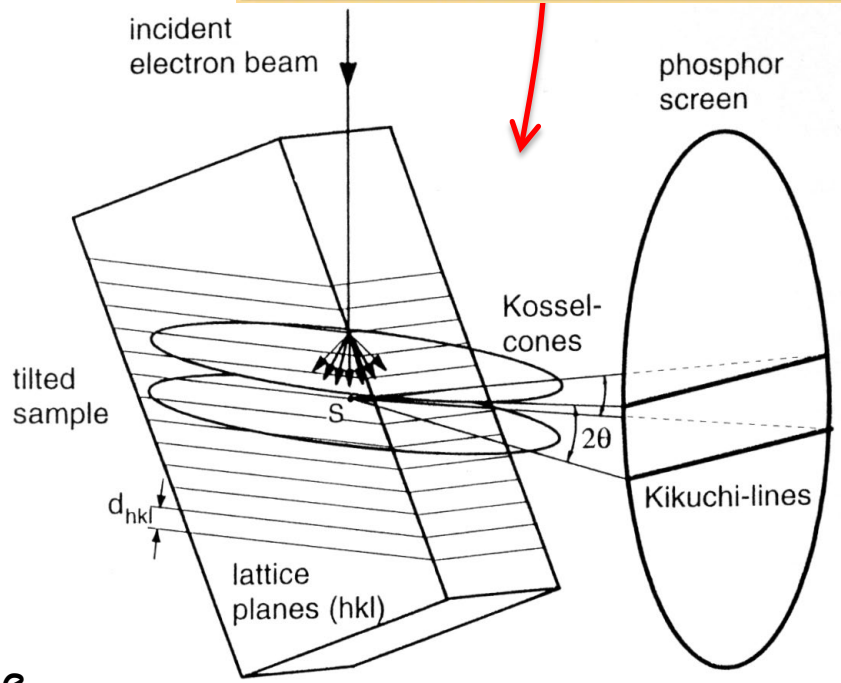

Pattern indexing

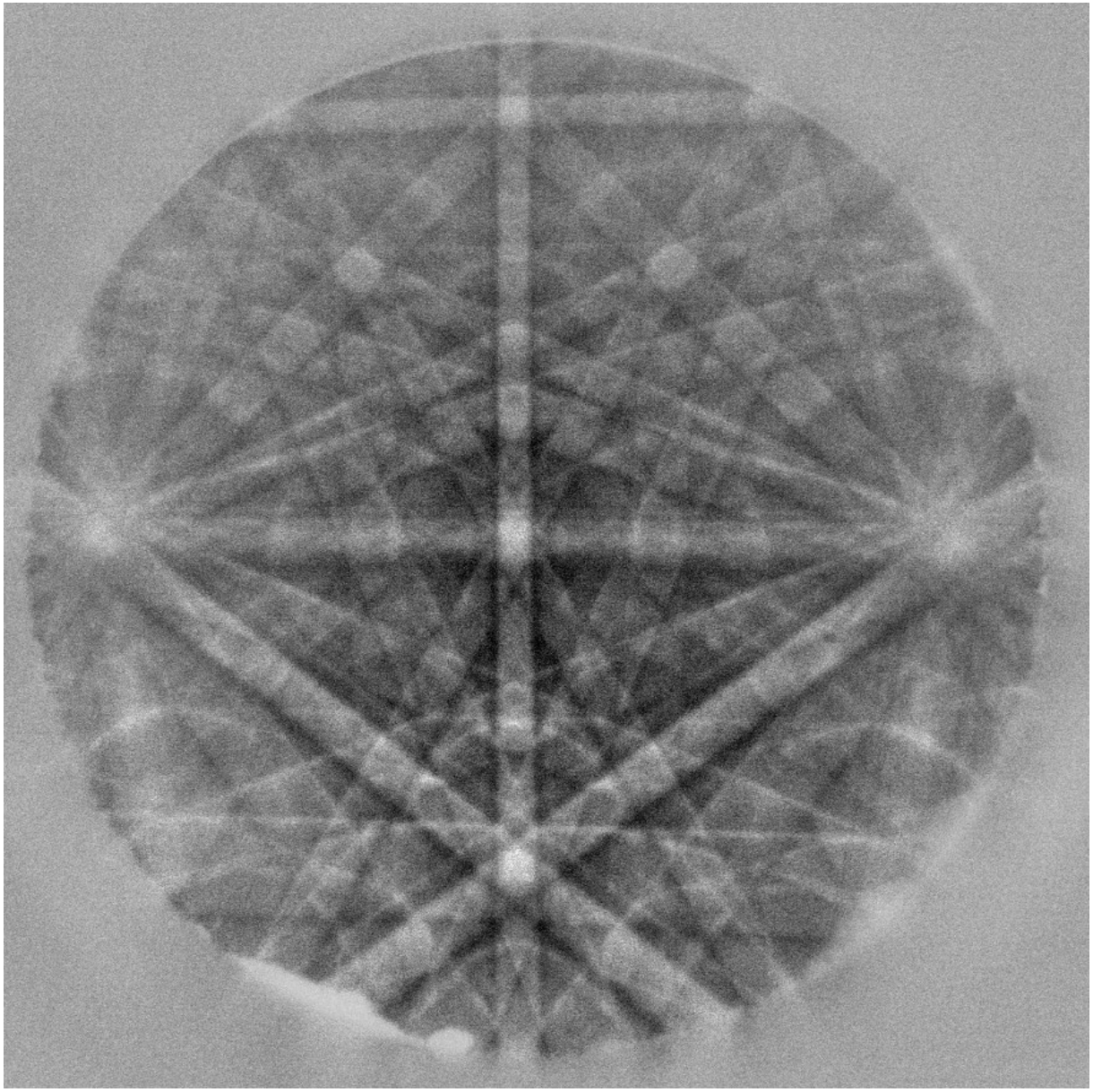

Pattern indexing Band detection

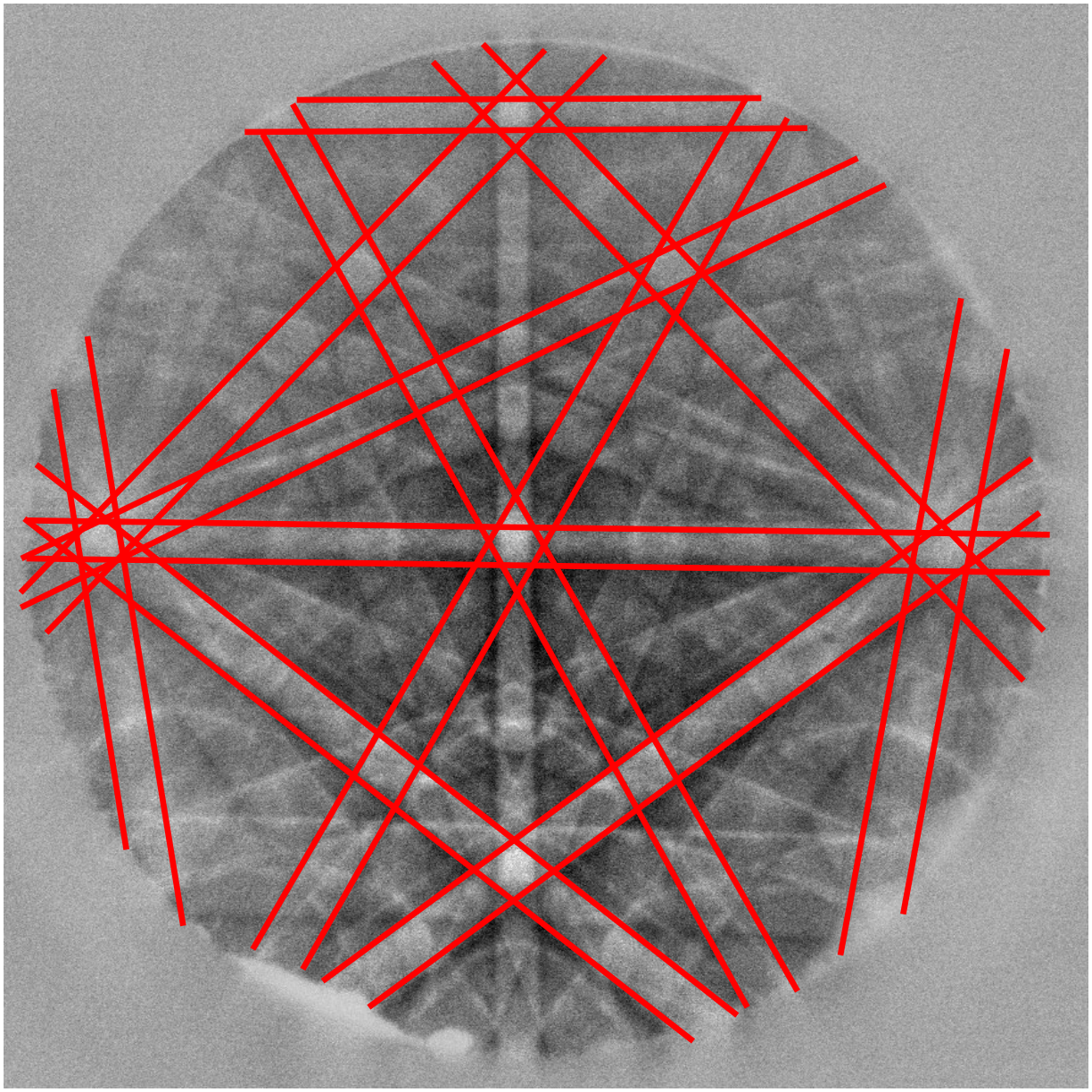

Pattern indexing ⟶ Lattice Orientation

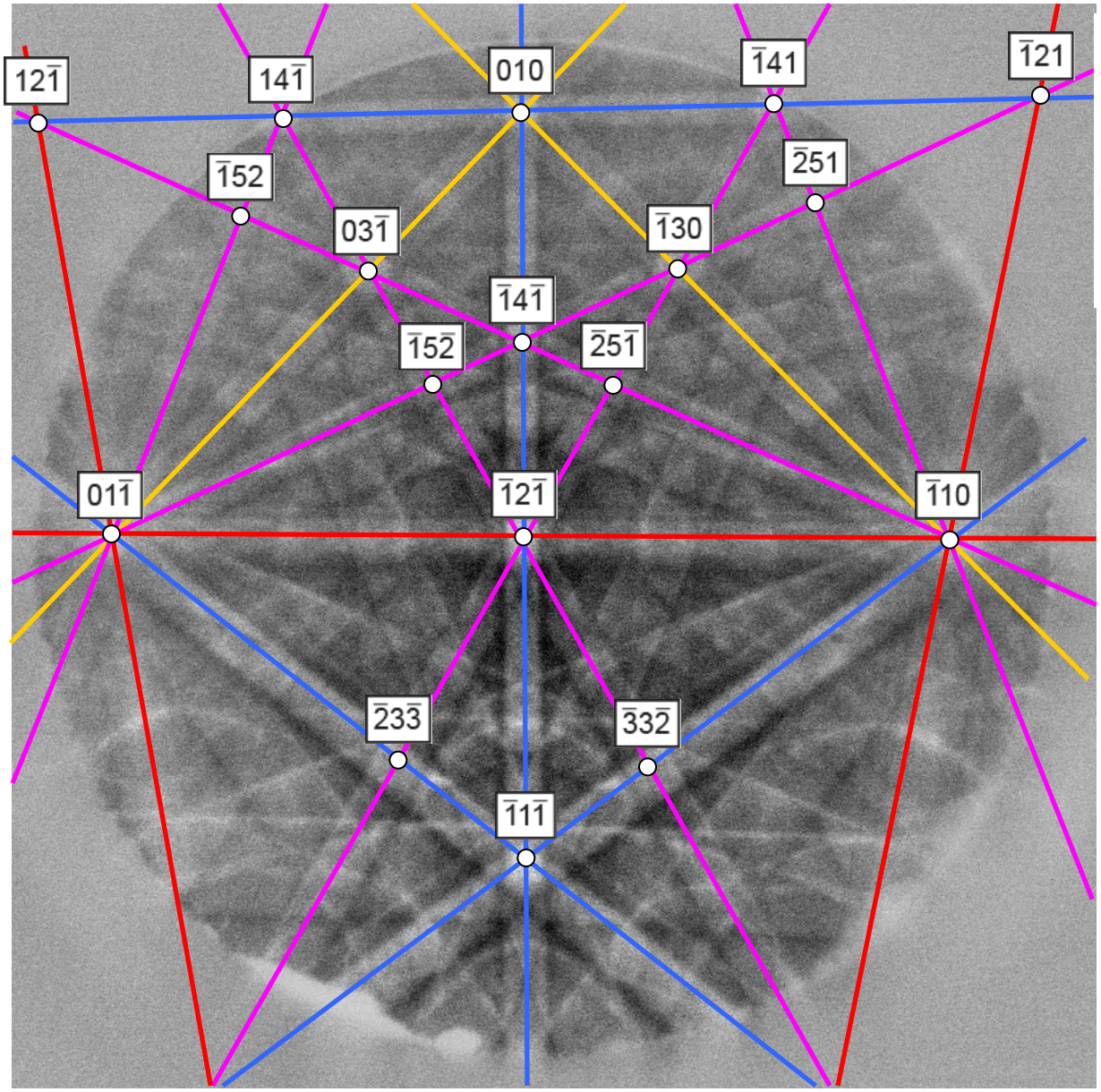

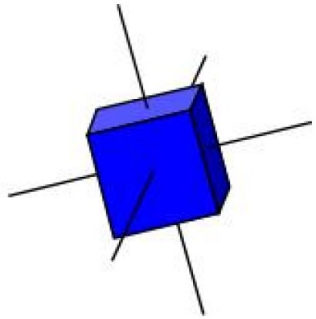

Relative precision: ~ 0.5°

OIM reference frame

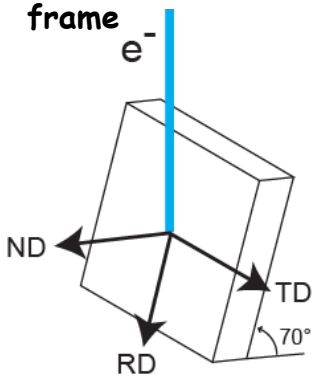

EBSD orientation mapping: Main applications:

Program OIM from EDAX

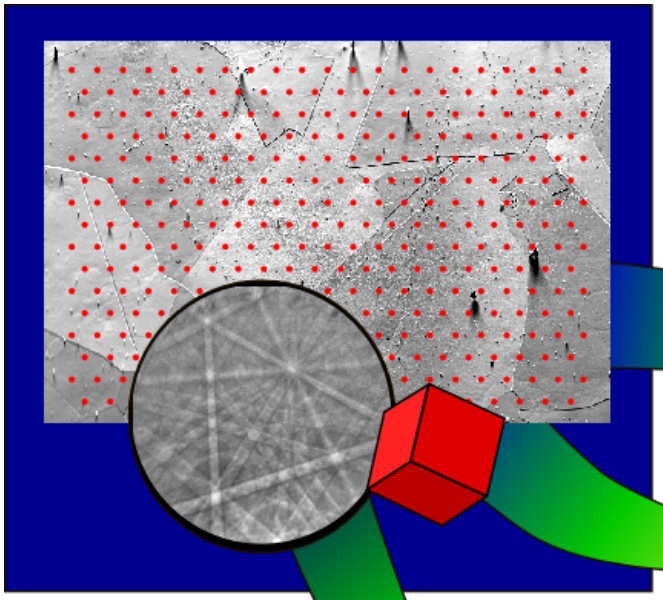

MAPS

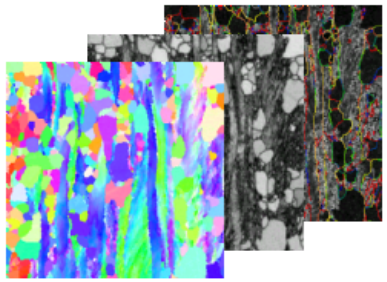

- Crystal orientation maps
- Boundaries type maps
- Pattern quality maps

CHARTS

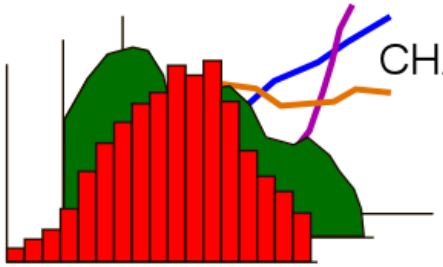

- Grain size
- Grain shape
- Grain boundaries statistics

DISCRETE ORIENTATION PLOTS

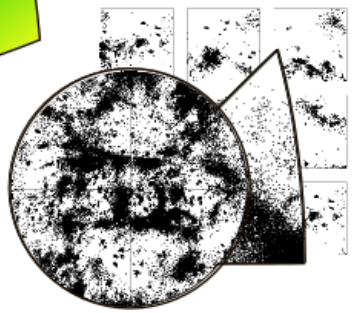

TEXTURE PLOTS

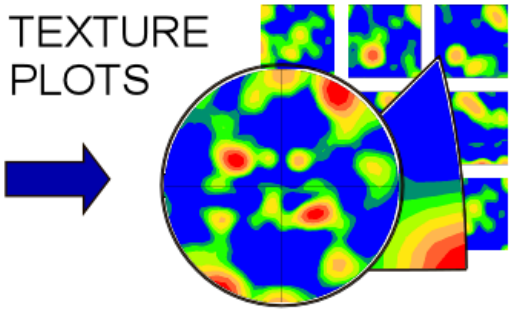

- Lattice preferred orientation, texture

Strain – stress analysis with EBSD: Cross Court

Cross-correlation between a strain free reference pattern and the pattern at the point of interest

- Rotation precision: 0.01°
- Strain resolution: 10^{-4}

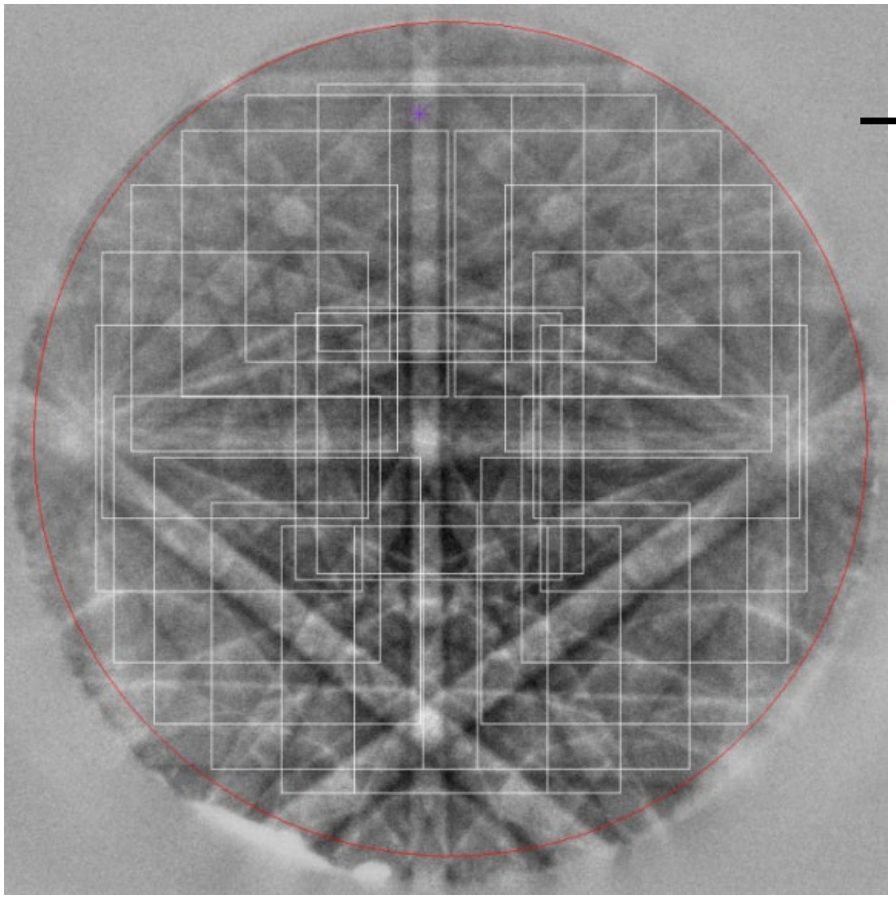

→ Shift vector for each squares

→ Displacement gradient tensor

$$\mathbf{a} = \begin{pmatrix} \frac{\partial u_1}{\partial x_1} & \frac{\partial u_1}{\partial x_2} & \frac{\partial u_1}{\partial x_3} \\ \frac{\partial u_2}{\partial x_1} & \frac{\partial u_2}{\partial x_2} & \frac{\partial u_2}{\partial x_3} \\ \frac{\partial u_3}{\partial x_1} & \frac{\partial u_3}{\partial x_2} & \frac{\partial u_3}{\partial x_3} \end{pmatrix}$$

Strain tensor

Rotation tensor

+ Crystal elastic constants and Euler angles

→ Stress tensor

A.J. Wilkinson, G. Meaden and D.J. Dingley, Ultramicr. 106 (2006); Mater. Sci. & Tech. 22 (2006)

Large scale, multicrystalline thin film silicon

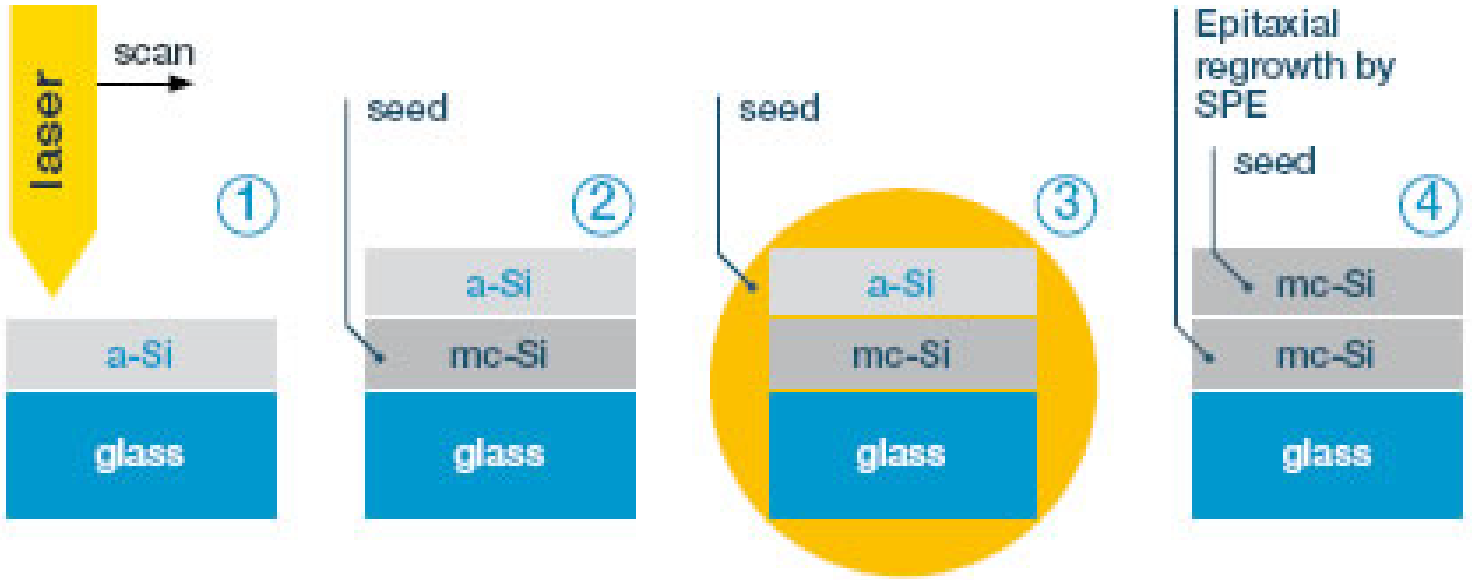

Figure 1:
Schematic of the laser-SPE process which will be established to realize large grained, low defective silicon layers on glass that have the potential for >10% efficiencies.

dislocation distribution: EBIC and OIM

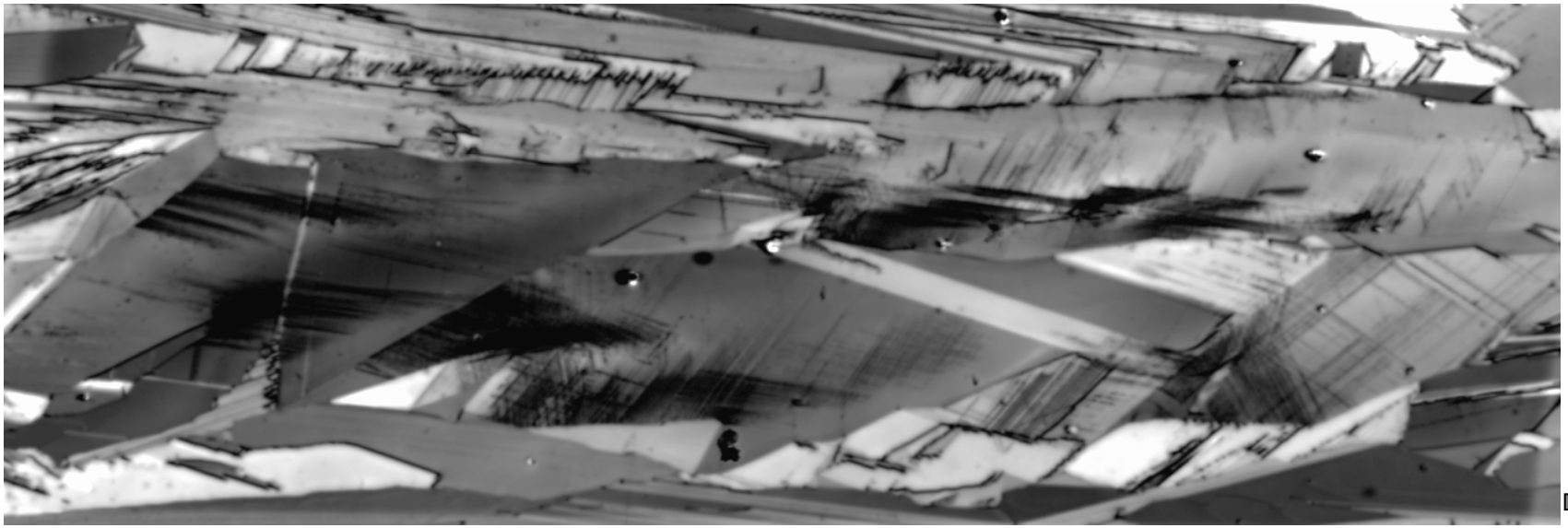

EBIC

100 μm

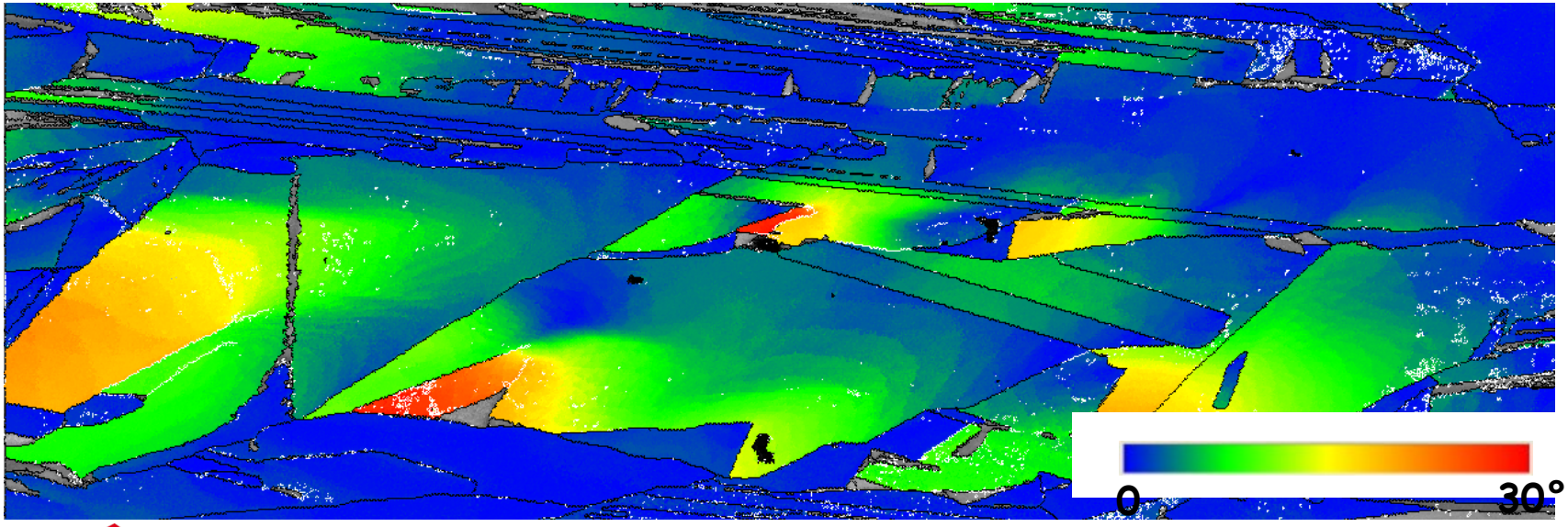

EBSD

stress concentrations: EBSD

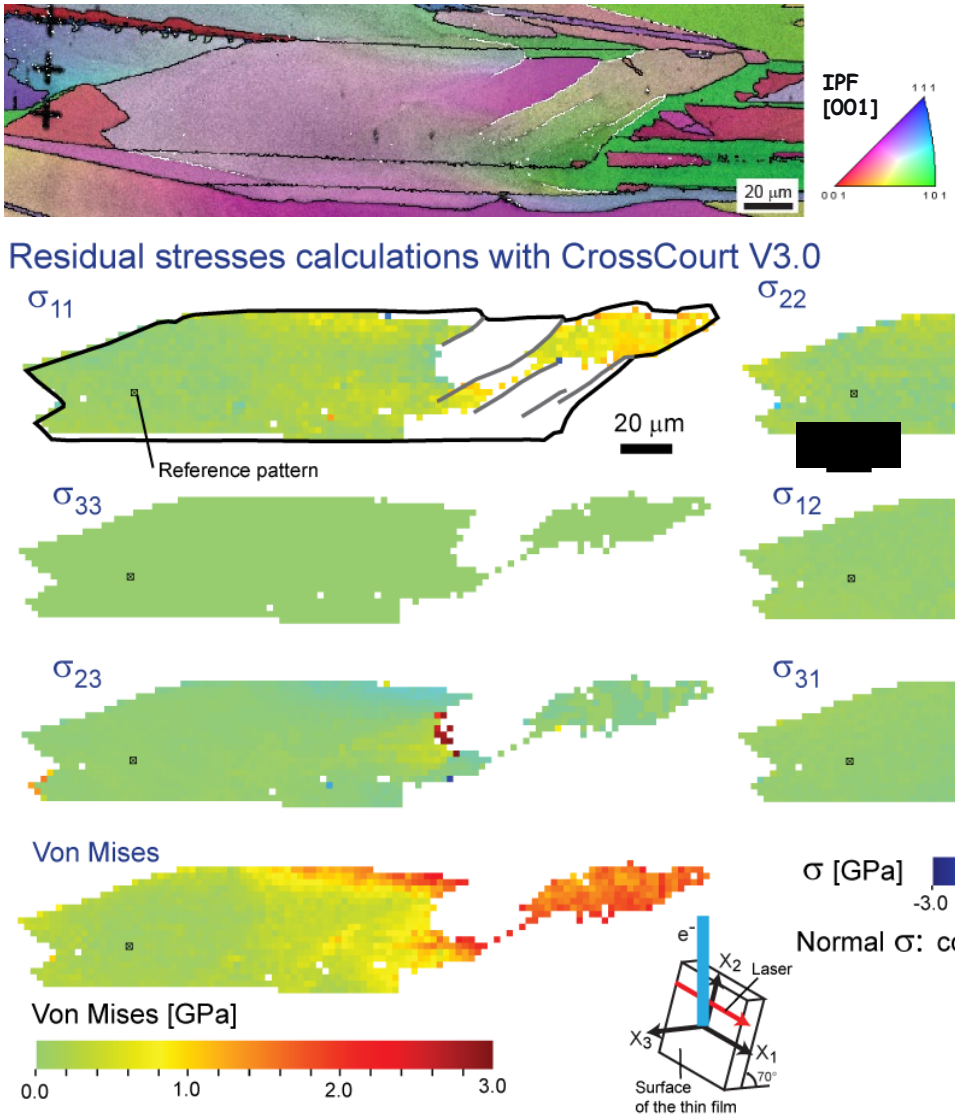

Cantilever beam methods

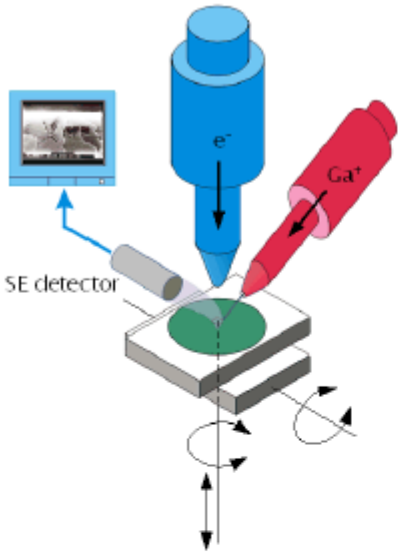

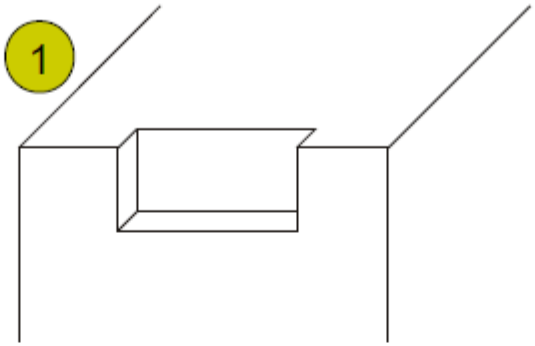

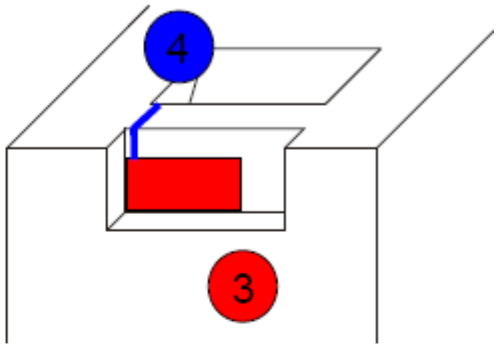

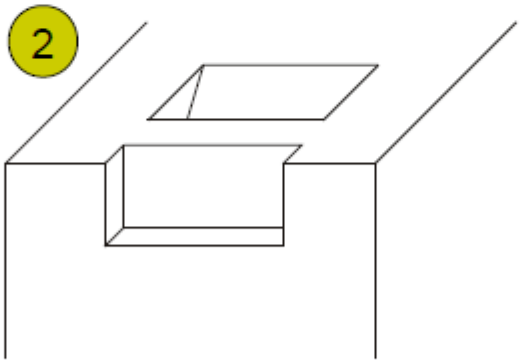

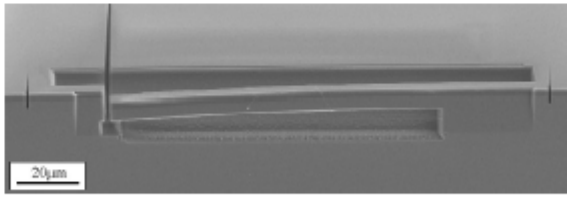

Cantilever beam methods

- fabrication of a micro cantilever by means of a FIB workstation

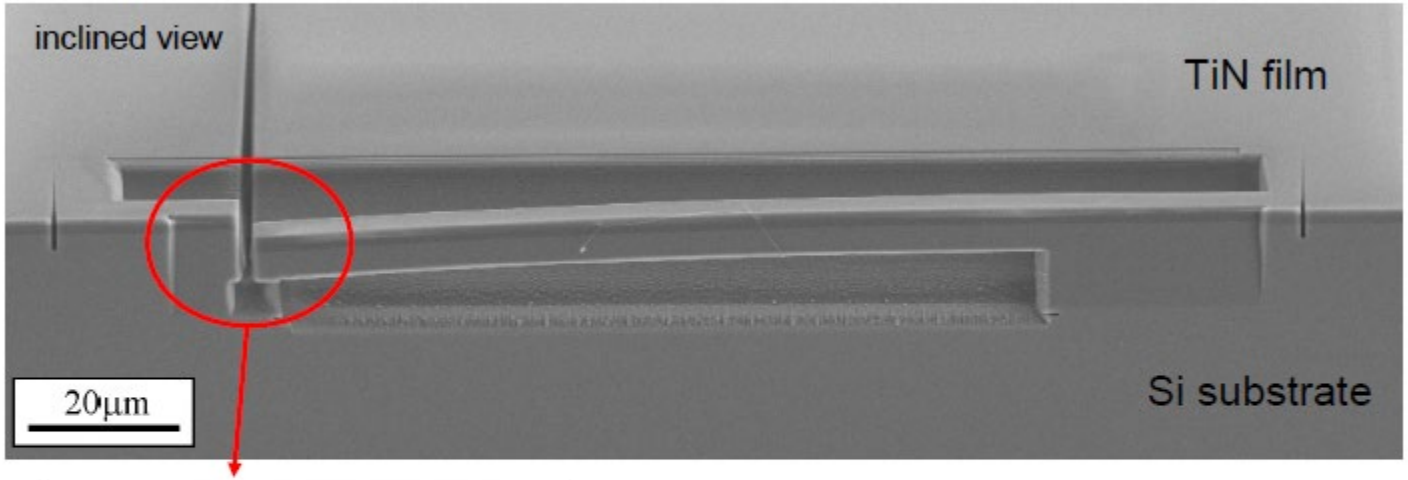

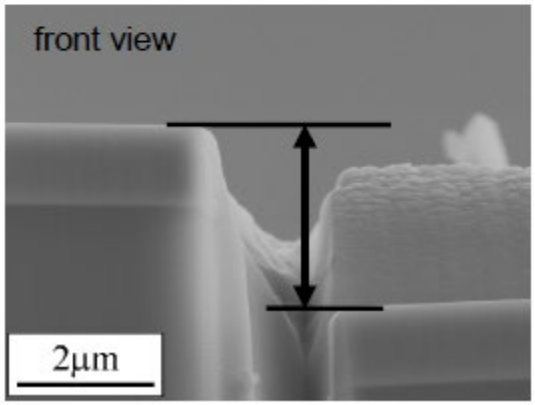

- deflection depends on the residual stresses

others

- Neutron diffraction
- CBED
- Ultrasonic measurements
- Magnetic methods

comparison

Method	Penetration	Spatial resolution	Accuracy
Hole drilling (distortion caused by stress relaxation)	$\sim 1{\cdot}2 \times$ hole diameter	50 μm depth	± 50 MPa, limited by reduced sensitivity with increasing depth
Curvature (distortion as stresses arise or relax)	0·1–0·5 of thickness	0·05 of thickness; no lateral resolution	Limited by minimum measurable curvature
X-ray diffraction (atomic strain gauge)	<50 μm (Al); <5 μm (Ti); <1 mm (with layer removal)	1 mm laterally; 20 μm depth	± 20 MPa, limited by non-linearities in $\sin^2 \psi$ or surface condition
Hard X-rays (atomic strain gauge)	150–50 mm (Al)	20 μm lateral to incident beam; 1 mm parallel to beam	$\pm 10 \times 10^{-6}$ strain, limited by grain sampling statistics
Neutrons (atomic strain gauge)	200 mm (Al); 25 mm (Fe); 4 mm (Ti)	500 μm	$\pm 50 \times 10^{-6}$ strain, limited by counting statistics and reliability of stress free references
Ultrasonics (stress related changes in elastic wave velocity)	>10 cm	5 mm	10%
Magnetic (variations in magnetic domains with stress)	10 mm	1 mm	10%
Raman	<1 μm	<1 μm approx.	$\Delta\lambda \approx 0{\cdot}1$ cm$^{-1} \equiv 50$ MPa

Table of contents I

Table of contents II

plastic deformation, size effects and hardness

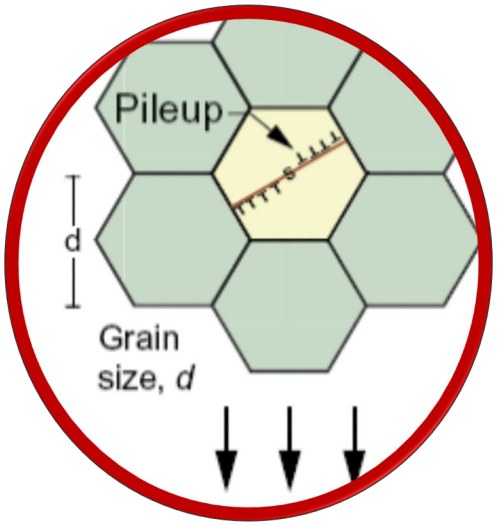

mechanical properties of nanocrystalline solids

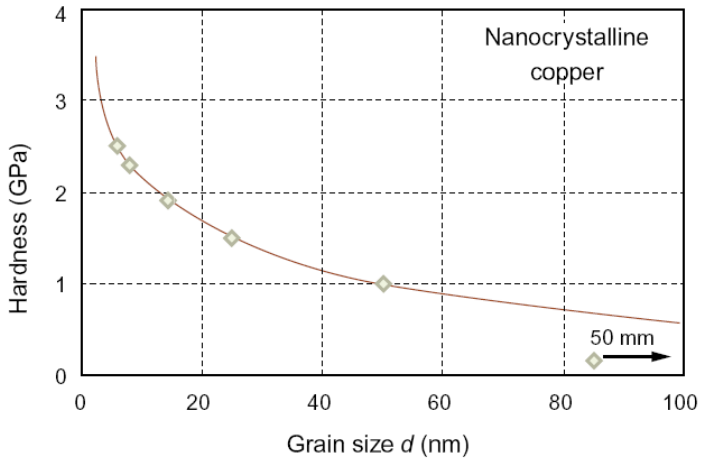

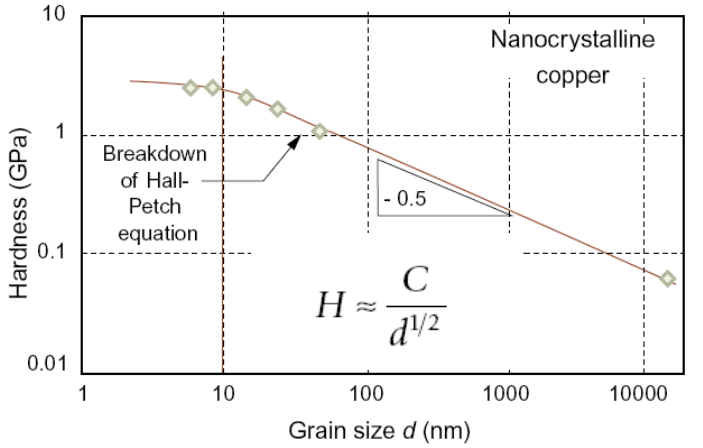

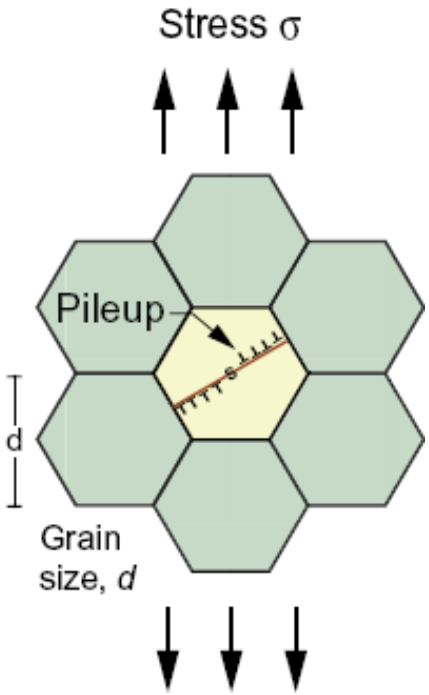

plasticity of multilayers - mechanisms

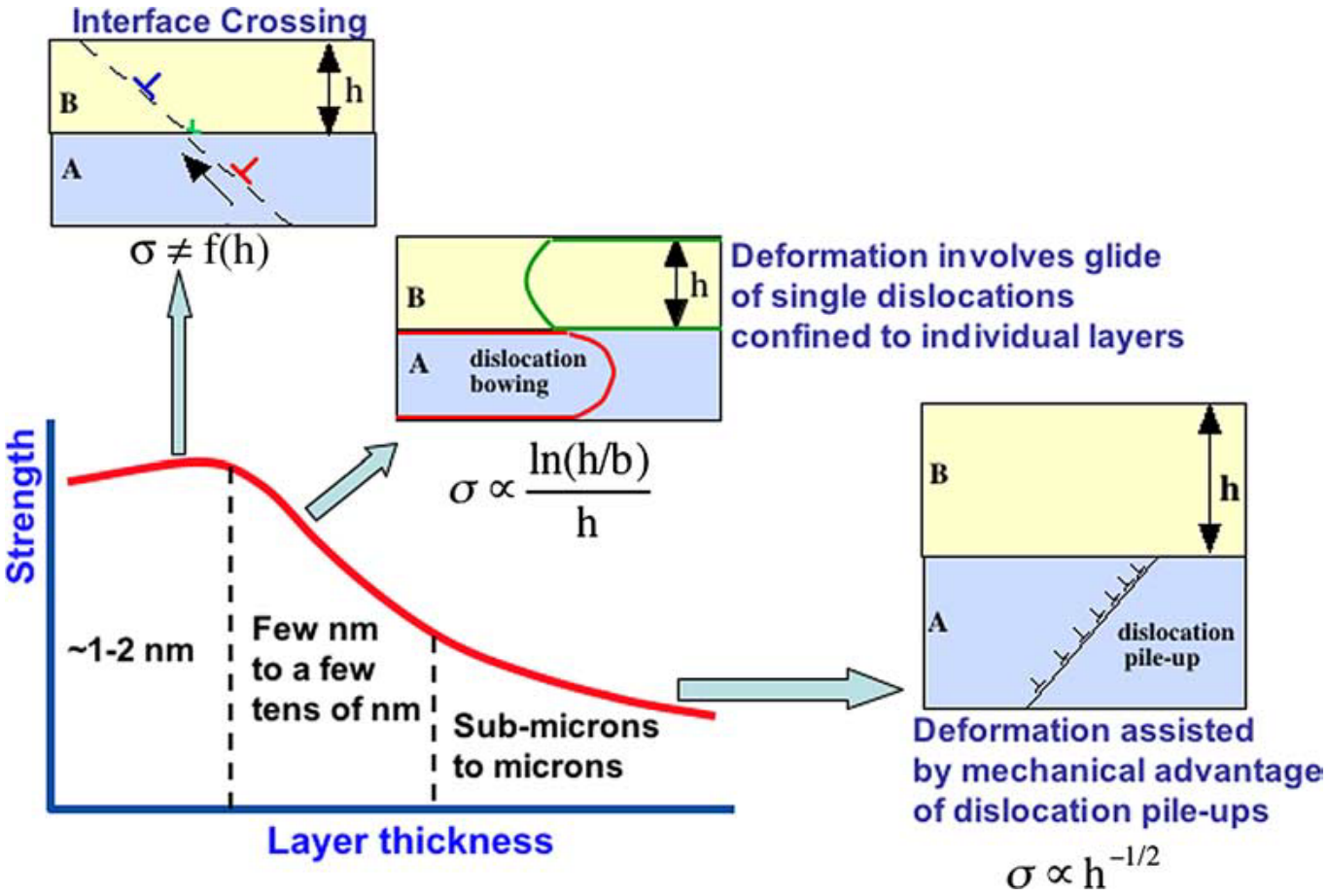

(A. Misra, R.G. Hoagland, J.P. Hirth, Acta Mater., (2005)

external size effects

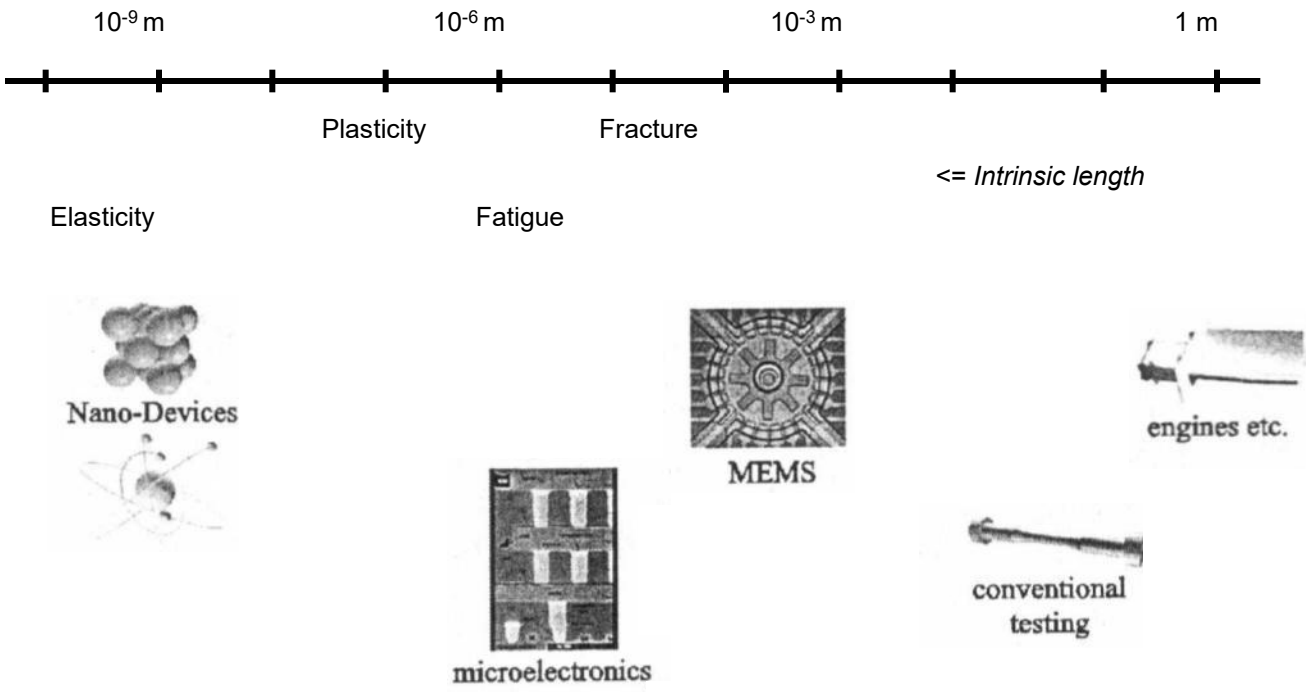

Object dimensions < intrinsic length scale => mechanical properties differ from the macroscale

O. Kraft, C. Volkert (2001) Adv. Eng. Mater. 3, 99

external size effects

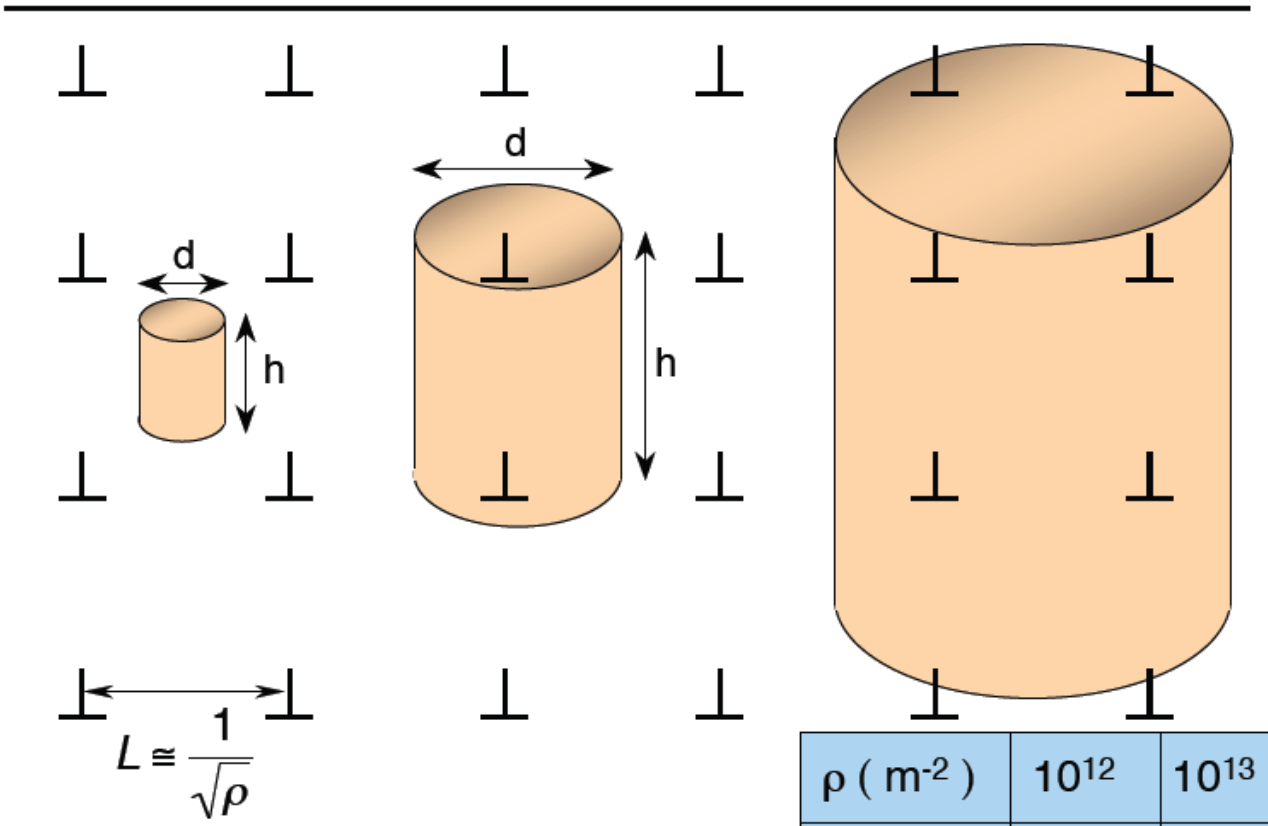

ρ (m^{-2})	10^{12}	10^{13}	10^{14}
L (μm)	1.0	0.3	0.1

internal & external size effects

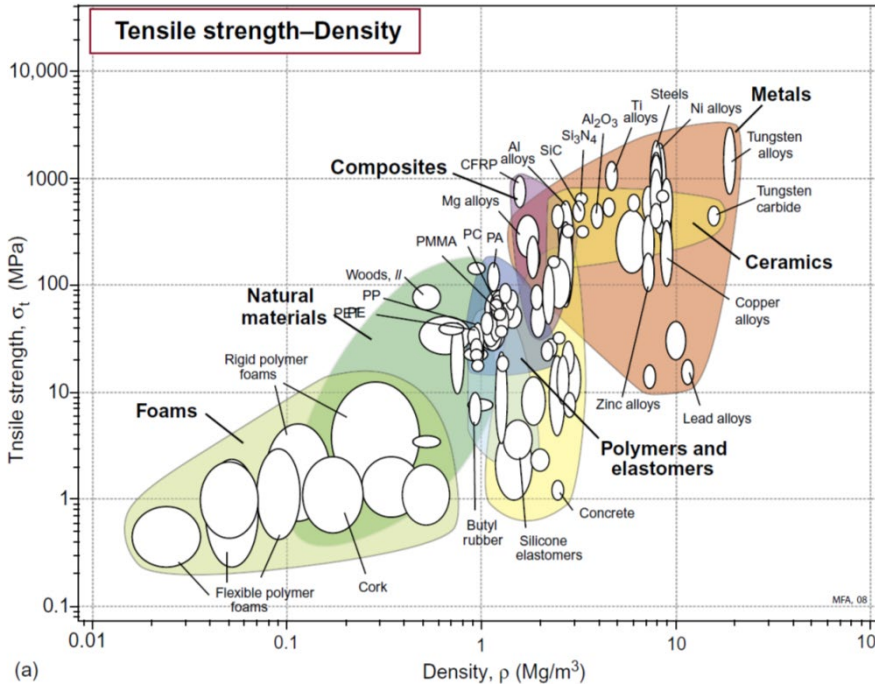

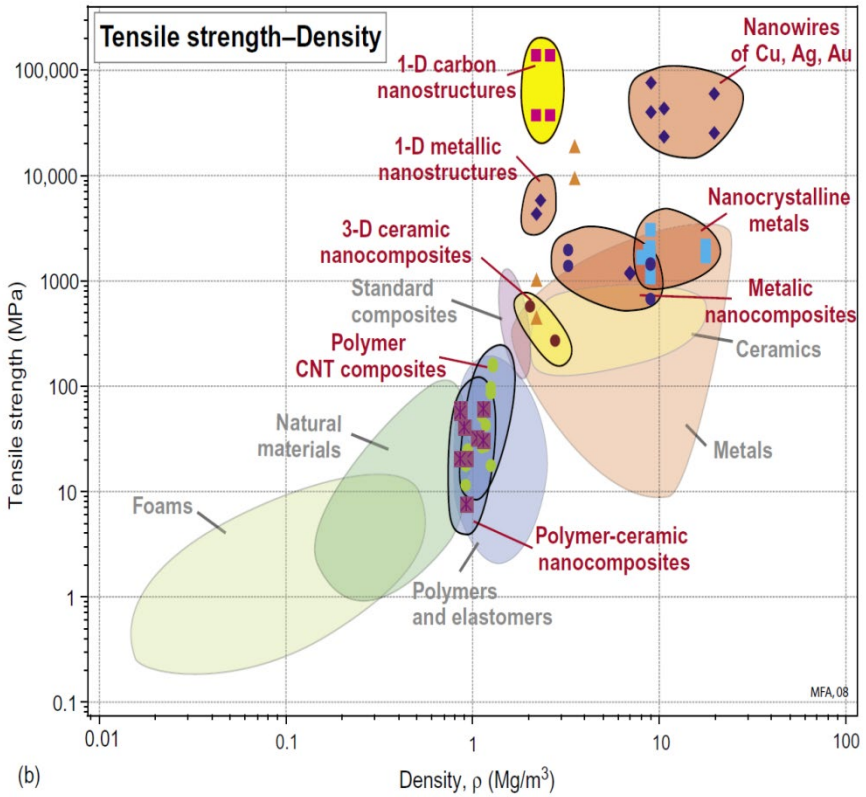

fracture and adhesion of thin films

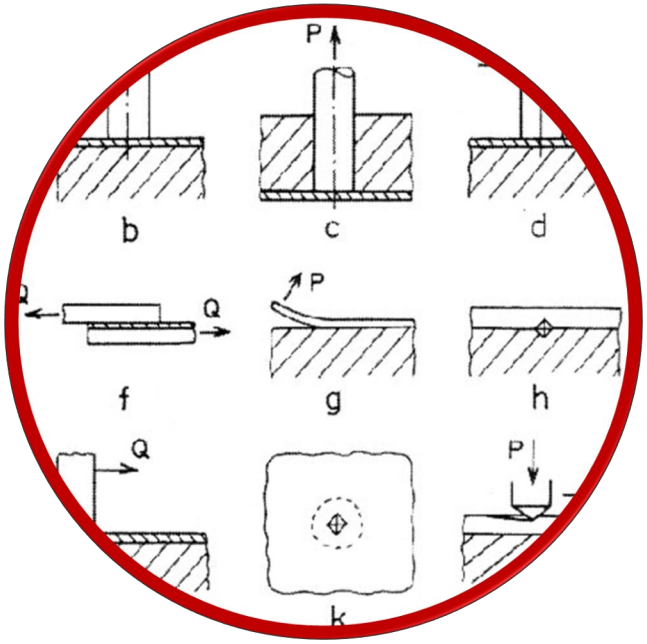

Integral to performance and reliability of materials and materials systems are their resistance to deformation, fracture and delamination!

Content

- Fracture of thin films
- Interfacial fracture mechanics – Adhesion
- Techniques to measure interfacial adhesion

Thin Film Fracture - Basics

Griffith Theory of brittle fracture (1920)

Unstable crack growth (with energy release):

$$\sigma \geq \left(\frac{2\gamma E}{\pi\, a}\right)^{1/2}$$

σ... Stress
γ... Surface energy (≈ 1 J/m^2)
E… Young's modulus
a... Crack length

Orowan extended the approach by taking a **plastic deformation zone** close to the crack. Instead of the surface energy γ becomes the plastic work done to enlarge the crack surface γ_p = 10^2 - 10^3J/m^2, while γ ≈ 1 J/m^2. As γ_p is difficult to measure, the quantity is referred to as the **energy release rate G**.

$$G_c = \frac{\pi a \sigma_{fr}{}^2}{E}$$

For σ < σ_{fr} the material does not break despite the presence of initial crack a. This subcritical loading is described by **stress intensity factor K**.

$$K = \sigma * \sqrt{\pi a} \qquad K = \sqrt{E{*}G}$$

[Pa m$^{1/2}$=Nm$^{-3/2}$]

Quelle: z.B. Mechanical Metallurgy, G.E. Dieter, Mac Graw-Hill, 1988

Influence of component thickness on the stress intensity factor K

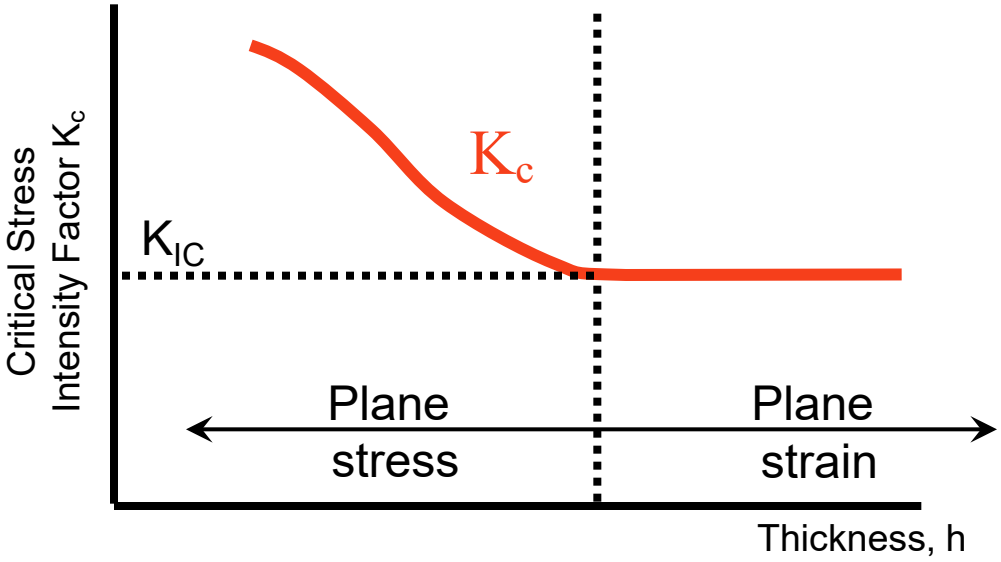

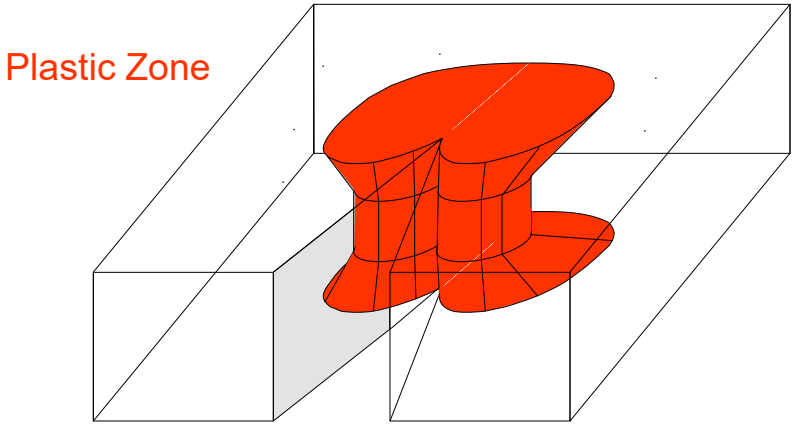

Schematic representation of the stress intensity factor as a function of the structural thickness as well as the plastic zone in front of a crack.

In the vicinity of the **free surfaces**, the plastic zone can spread more, while it is **narrowed** in the **interior**. Correspondingly, a **plane stress state** is present in front of the crack tip in the case of thin specimens, whereas a **plane strain state** occurs in the case of thick specimens.

In the case of a **thin layer on a substrate**, it is assumed that the **plastic zone is constrained by adhesion** to the substrate in such a way that a **plane strain state** forms near the tip of the crack.

Note: plane strain is more dangerous than plane stress due to the smaller K_C values

Quelle: Mechanical Metallurgy, G.E. Dieter, Mac Graw-Hill, 1988

Influence of component thickness on the stress intensity factor K

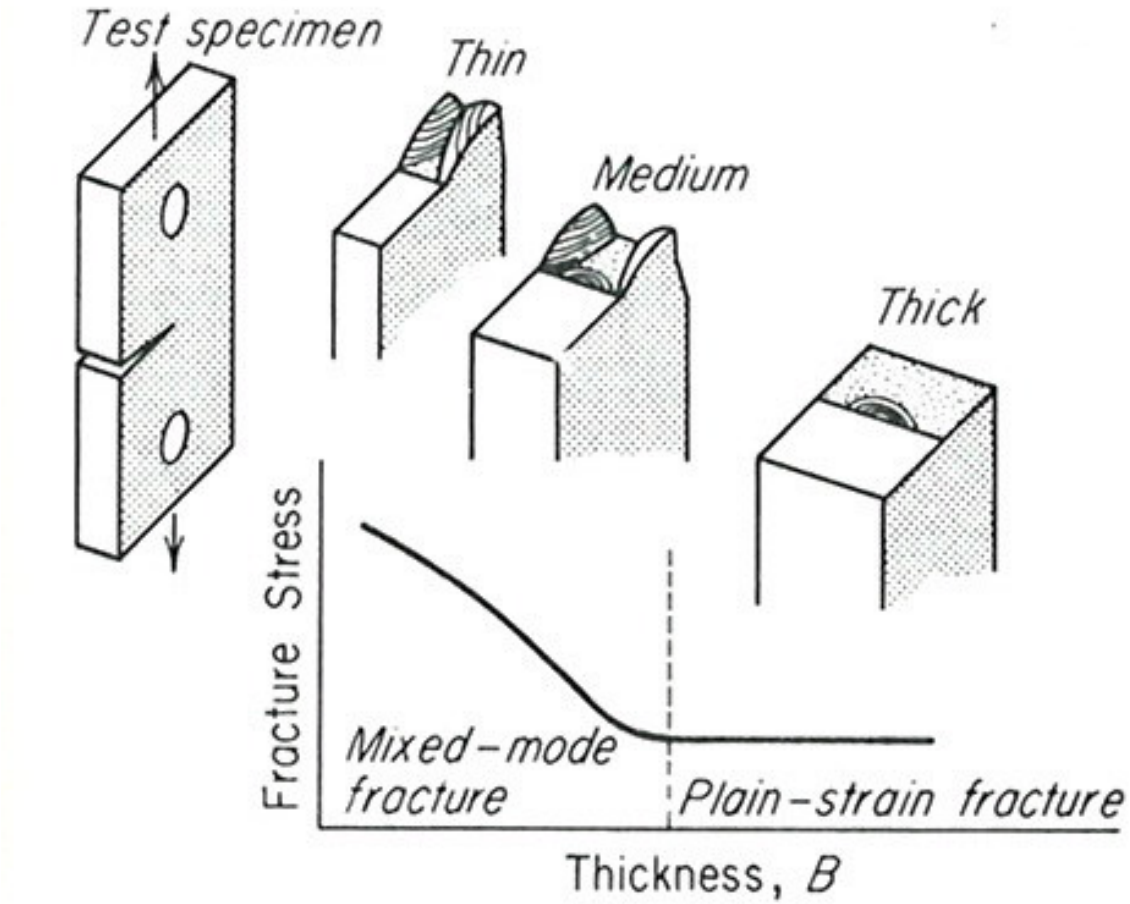

Quelle: Mechanical Metallurgy, G.E. Dieter, Mac Graw-Hill, 1988

Cracking of a plate & thin film on substrate

a... Crack length
h... film thickness

$V_e \sim a^2 h$

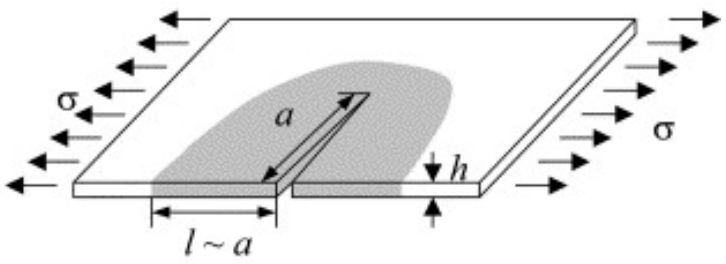

$V_e \sim a h^2$

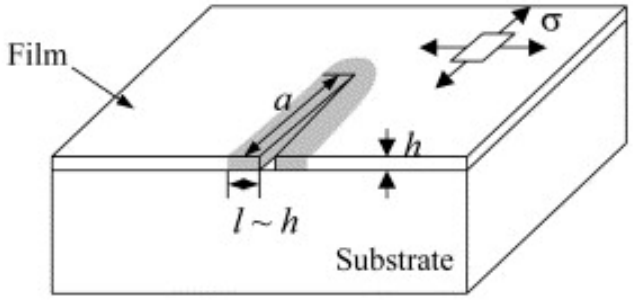

Substrate limits the elastic energy released by the crack propagation

- Energy release rate *G: reduction of* the elastic energy per unit area associated with the advancing crack
- Z… Dimensionless parameters including elastic mismatch between layer / substrate, crack spacing, and crack opening mode

$$\begin{cases} \Delta W_e = -Z\left(\substack{\alpha,\beta,\text{geometry,}\\ \text{loadingpatern}}\right)\dfrac{\sigma^2}{2E}a^2 h \\ G = -\dfrac{\partial W_e}{\partial A} = -\dfrac{1}{h}\dfrac{\Delta W_e}{\Delta a} = Z\dfrac{\sigma^2}{E}a \end{cases}$$

Scales with **crack length *a***

$$\begin{cases} \Delta W_e = -Z\left(\substack{\alpha,\beta,\text{geometry,}\\ \text{loadingpatern}}\right)\dfrac{\sigma^2}{2E}ah^2 \\ G = -\dfrac{\partial W_e}{\partial A} = -\dfrac{1}{h}\dfrac{\Delta W_e}{\Delta a} = Z\dfrac{\sigma^2}{E}h \end{cases}$$

Scales with **film thickness *h***
G is ***independent of a*** for thin films on substrate

$$G = \frac{\partial W_{extForces}}{\partial A} - \frac{\partial W_e}{\partial A} = -\frac{\partial W_e}{\partial A}$$

$$G_c = Z(\alpha,\beta) * \frac{\sigma_{fr}{}^2 * h}{E_f/(1-\nu^2)}$$

R. Huang et al., Acta Materialia 50, 2002

Commonly observed crack patters

Many different cracking patterns in film-substrate systems have been observed.

A crack **nucleates** from a flaw either in the film or at the edge, and propagates both **towards the interface** and **laterally** through the film.

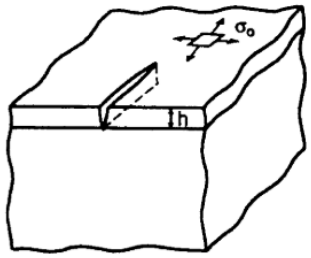

a) Film Cracking

The crack may stop at the interface, penetrate into the substrate, or bifurcate onto the interface depending on the relative values of critical energy release rates for crack propagation of thin film, substrate and interface.

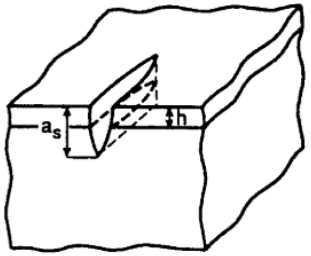

b) Substrate Penetration

These cracks then **channel laterally**. After the channel length exceeds a few times the film thickness h, a steady state is reached, wherein the entire front and the cross-section in the wake maintain their shape as the crack advances.

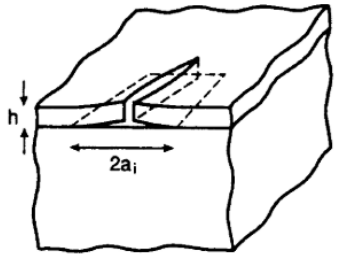

c) Interface Debonding

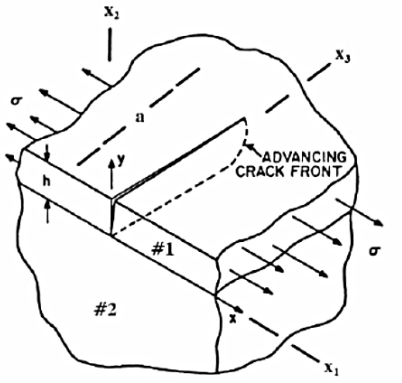

Commonly observed crack patters under tension

Z is given assuming in this case no elastic mismatch between film and substrate and an infinitely thick substrate

Steady state propagation

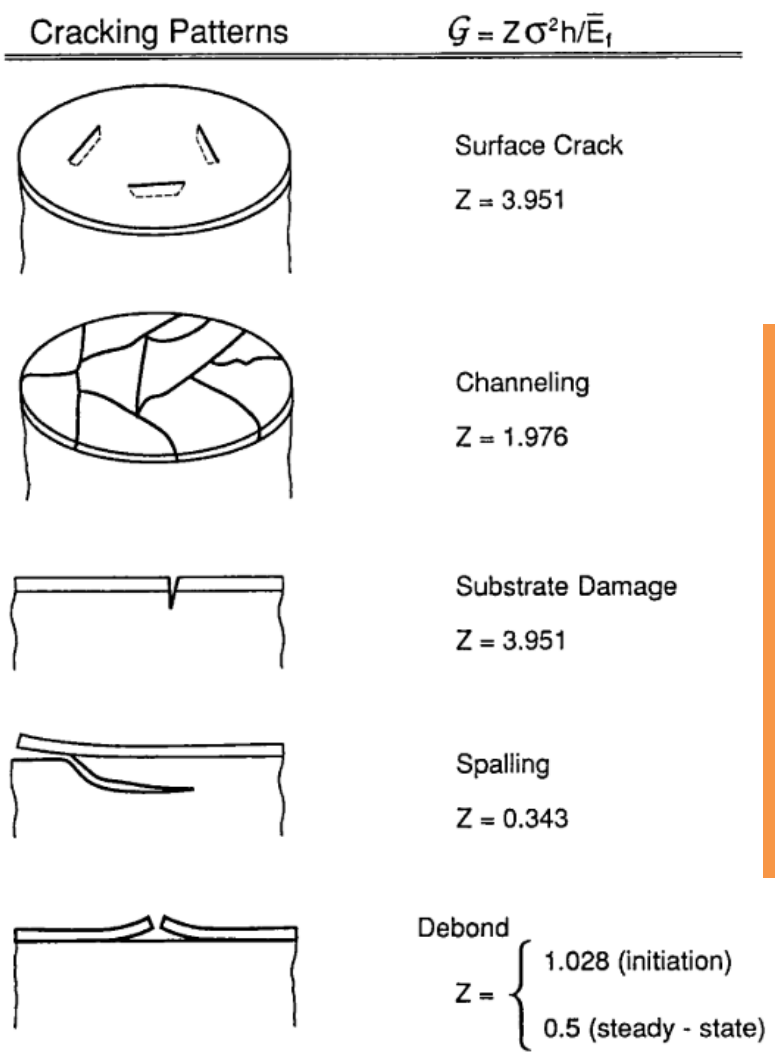

Condition for crack pattern to develop

$$G > G_c = Z(\alpha, \beta) * \frac{{\sigma_{fr}}^2 * h}{E_f/(1-\nu^2)}$$

Note that G_c can stand for the critical energy release rate of the film, the substrate or the interface

Commonly observed crack patters

Many different cracking patterns in film-substrate systems have been observed.

A crack **nucleates** from a flaw either in the film or at the edge, and propagates both **towards the interface** and **laterally** through the film.

Depending on the material, the crack may stop at the interface, penetrate into the substrate, or bifurcate onto the interface.

These cracks then **channel laterally**. After the channel length exceeds a few times the film thickness h, a steady state is reached, wherein the entire front and the cross-section in the wake maintain their shape as the crack advances.

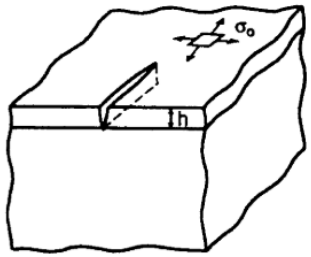

a) Film Cracking

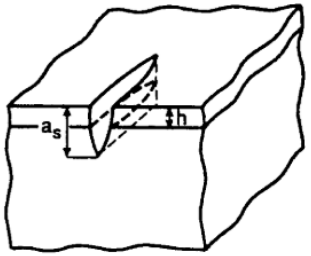

b) Substrate Penetration

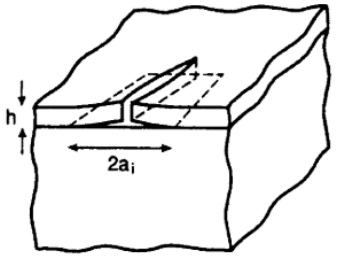

c) Interface Debonding

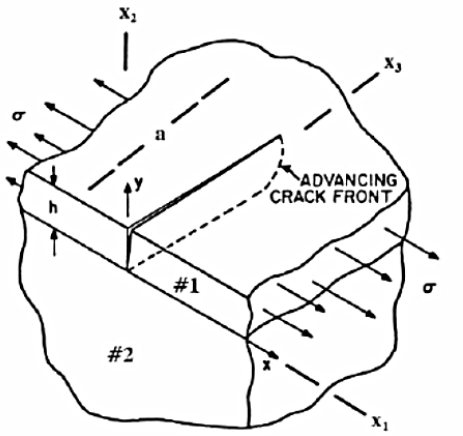

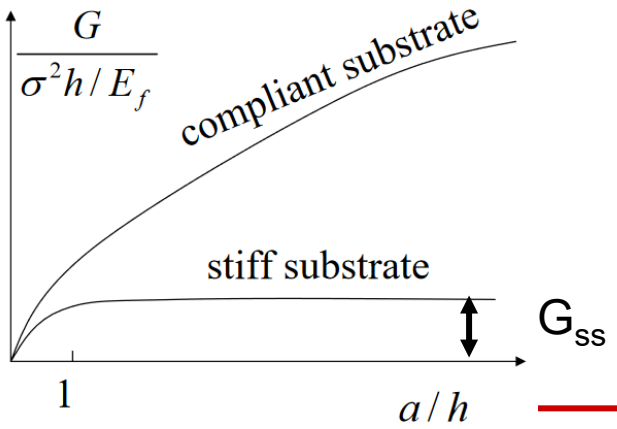

Hutchinson & Suo, Adv. Appl. Mech 1992

Commonly observed crack patters

Equating steady state energy release rate to respective fracture energies yields conditions for:

steady state ***channel cracking without substrate penetration***

$$\overline{G}_{SSchannelcrack} = \frac{1}{2} G_{penetrationcrack} \qquad \Gamma_{csubs} > 2\Gamma_{cfilm}$$

For $\alpha = 0$ and $\beta = 0$
(no elastic mistmatch)

Γ... Fracture energy
G... Energy release rate

steady state ***channel cracking without partial debonding***

$$\overline{G}_{SSchannelcrack} = 2G_{partialdebonding} \qquad \Gamma_{cinterface}(\psi) > \frac{1}{2}\Gamma_{cfilm}$$

SS ***channel cracking with partial debonding***

$$\frac{1}{2} > \frac{\Gamma_{cinterface}(\psi)}{\Gamma_{cfilm}} > \frac{1}{4}$$

SS ***channel cracking with full delamination***

$$\frac{\Gamma_{cinterface}(\psi)}{\Gamma_{cfilm}} < \frac{1}{4}$$

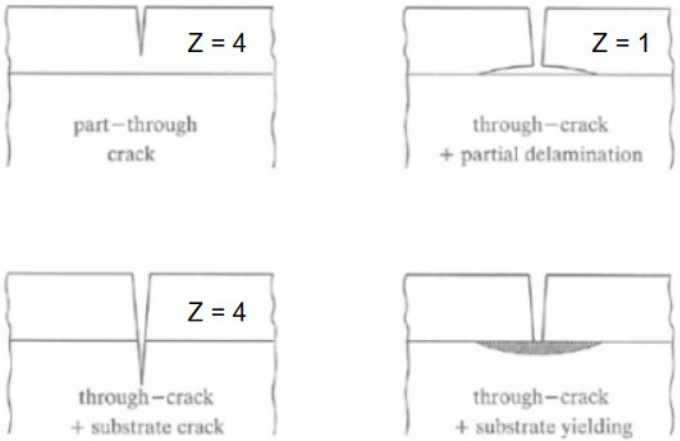

Fail safe design for multiple mechanisms

$$\sqrt{\Omega} = \sqrt{\frac{\sigma^2 h}{E\Gamma_c}}$$

Ω… indicator for risk of failure for supported thin films

Fail safe diagram for brittle failure

$$G = Z\frac{\sigma^2 h}{E}$$

$$\frac{G}{\Gamma_c} = Z\underbrace{\frac{\sigma^2 h}{E\Gamma_c}}_{\Omega}$$

$$\Omega = \frac{\sigma^2 h}{E\Gamma_c}$$

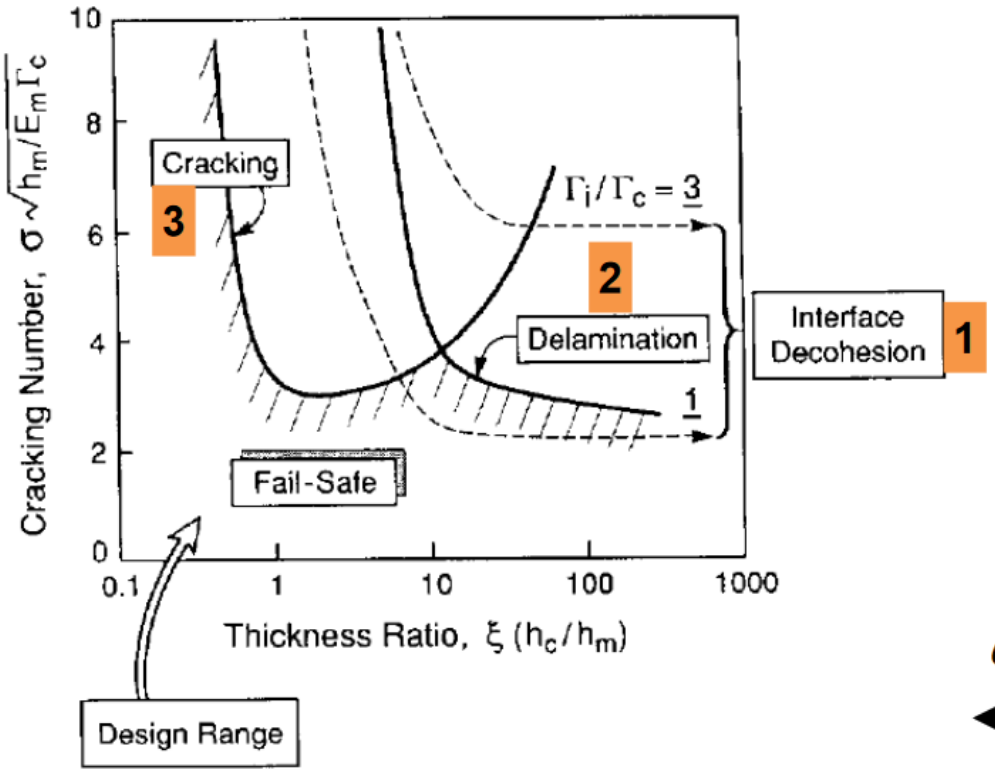

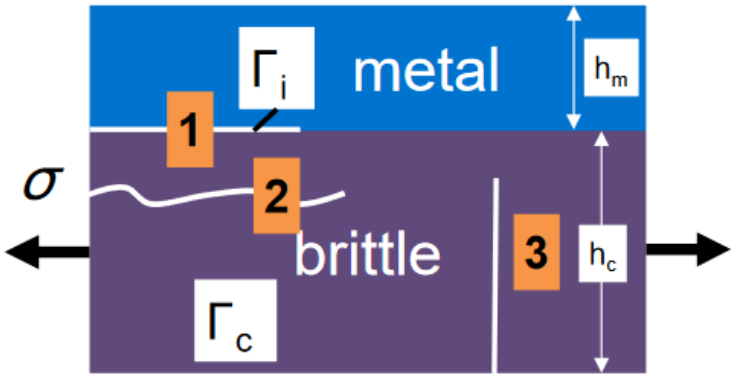

Interfacial Fracture Mechanics

Interfacial fracture energy, G_i (or Γ), typically incorporates several contributions

- W_{ad}-work of adhesion (governed by the composition and structure of the interfaces and the nature of bonding)
- Surface roughness
- Plastic energy dissipation (in one or both materials)

Interface fracture energy is also influenced by **shear (mode II) displacements**. These shear displacements occur in bi-material systems due to the difference in material properties - even when all applied forces are normal to the interface.

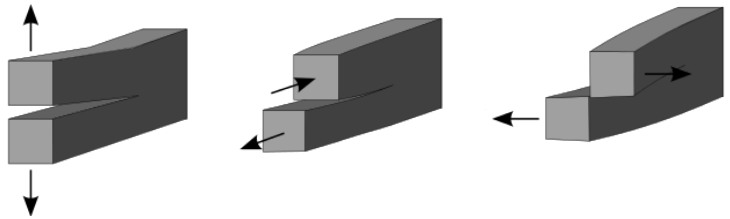

These displacements:

- influence the magnitude of G_i (or Γ)
- determine whether the crack remains at the the interface or propagates into one of the adjoining materials

adhesion

- cracks at interfaces:

  always mixed mode, the four elastic constancts
  (E,ν of coating and substrate)
  can be reduced to two system parameters (Dundurs' parameter)

- Limiting case thin films:

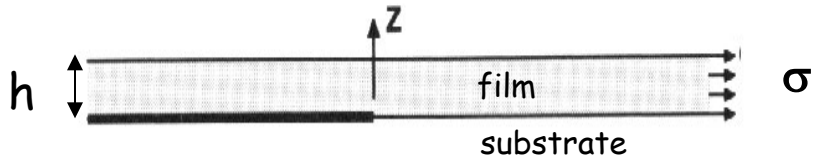

$$k = 0.7\sigma\sqrt{h}$$

$$G = 0.5\frac{1-\nu^2}{E}\sigma^2 h$$

Atomistic view of interface

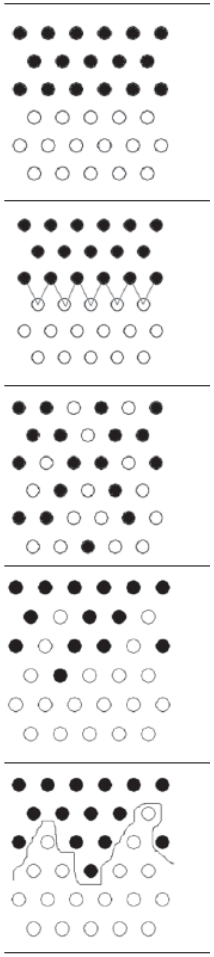

Interface without chemical bonding

Interface with chemical bonding

Transition zone through diffusion (danger of formation of porosity due to Kirkendall effect)

Interface mixing due to ion bombardment

Interface transition zone due to mechanical locking

Interfacial Fracture Mechanics

Fracture energy depends on normal and shear displacements and increases with increasing shear contributions. The parameter that describes this **mix of displacements** is the **phase angle of loading**.

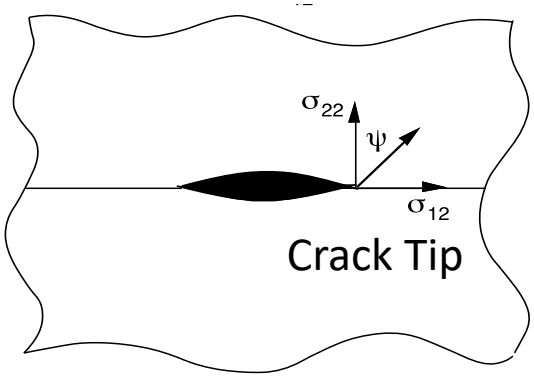

$$\psi = \tan^{-1}\left(\frac{K_{II}}{K_I}\right)$$

Typically G_i increases as Ψ varies from 0 due to the influence of shear on plastic deformation/dissipation processes

Practical work of adhesion measured by interfacial fracture tests

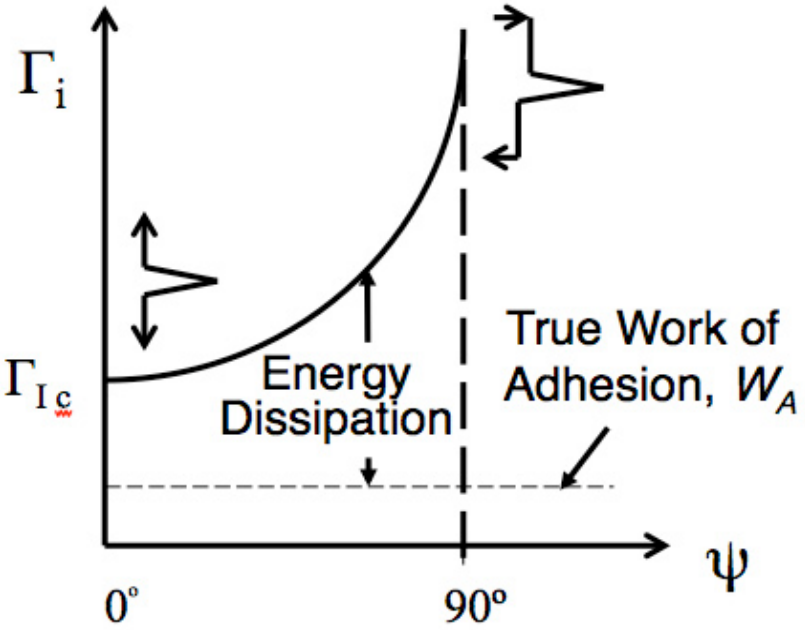

ψ=0 no shear; ψ=± π/2 pure shear

Dundurs Parameters

The elastic behavior of any bi-material system can be described by two combinations of elastic constants.

Dundurs' parameters α and β : combinations of elastic moduli and Poisson's ratios.

Remarkably, the solution holds regardless of how intricate the body shape or mechanical conditions imposed at the interface.

In general form:

$$\alpha = \frac{\mu_1(1-\nu_2)-\mu_2(1-\nu_1)}{[\mu_1(1-\nu_2)+\mu_2(1-\nu_1)]} \qquad \beta = \frac{\mu_1(1-2\nu_2)-\mu_2(1-2\nu_1)}{2[\mu_1(1-\nu_2)+\mu_2(1-\nu_1)]}$$

$$\mu = G = \frac{E}{2(1+\nu)}$$

for plane strain α reduces to the simple equation,

$$\alpha = \frac{\bar{E}_1-\bar{E}_2}{\bar{E}_1+\bar{E}_2} \qquad \text{where,} \qquad \bar{E} = \frac{E}{(1-\nu^2)}$$

Dundurs Parameters

These parameters have also been described **as moduli mismatch parameters-** α and β vanish when there is no material dissimilarity.

α can be interpreted as a measure of dissimilarity in stiffness

- Material 1 is stiffer than Material 2 when $\alpha > 0$
- Material 1 is more compliant than material 2 when $\alpha < 0$

β defines the oscillatory behavior of a crack along an interface.

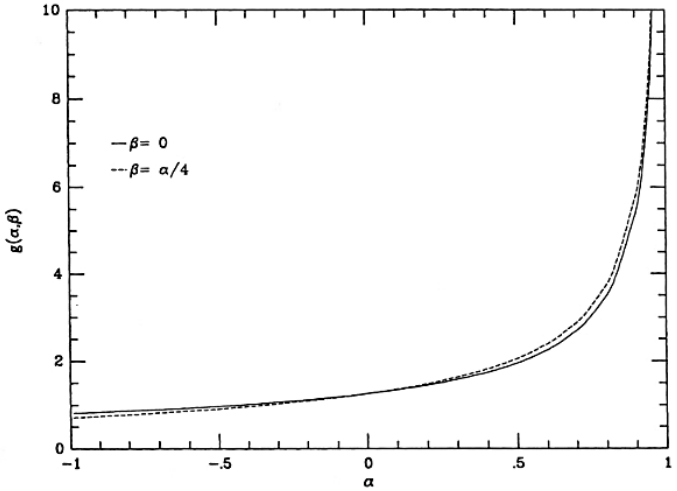

$$G_c = Z(\alpha,\beta) * \frac{{\sigma_{fr}}^2 * h}{E_f/(1-\nu^2)}$$

Interfacial crack path maps

In homogeneous brittle solids (such as glass) cracks tend to propagate under mode I conditions when normal stresses act on the plane of separation – i.e. they follow a trajectory where $K_{II}=0$.

For two brittle materials, $G_1 \sim G_2$, the tendency for a crack to 'kink' out of the interface depends on

- the phase angle
- the ratio between interface and materials fracture energies, G_i/G_s
- the ratio between moduli, α

Crack path maps

The role of fracture energy and moduli mismatch on this tendency is shown in crack path maps / kinking diagram.

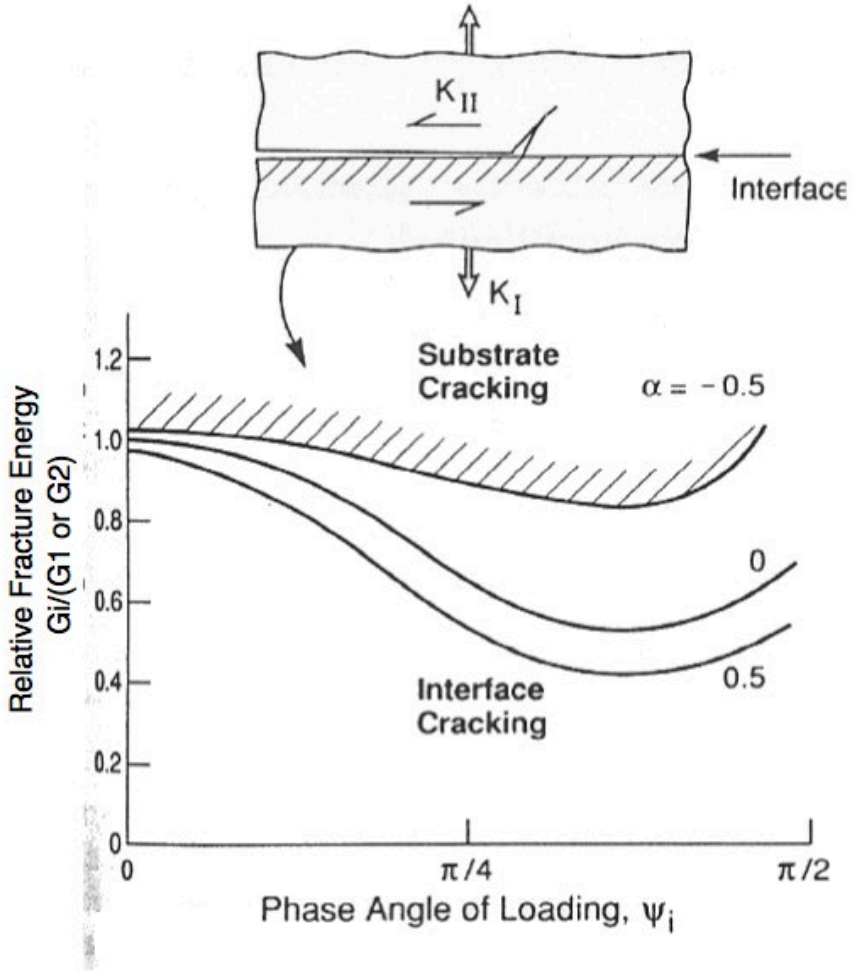

Crack path maps

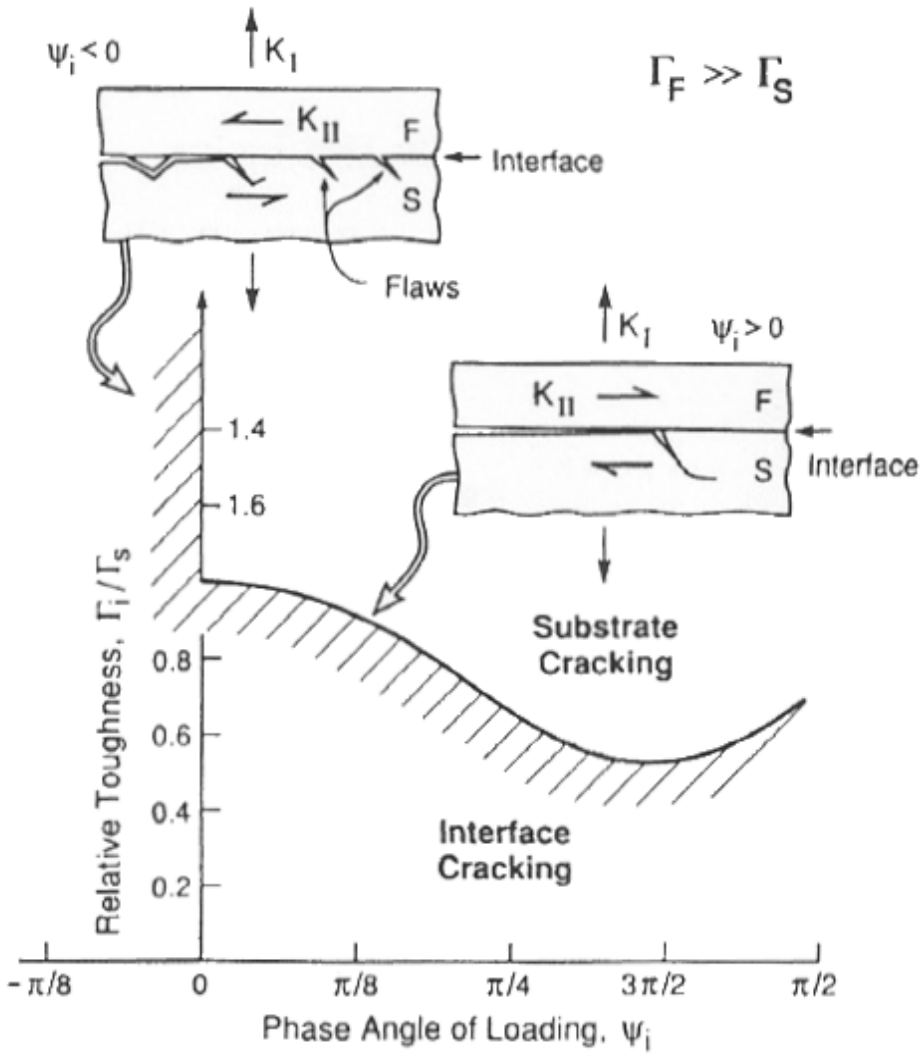

With G_1 and G_2=G(substrate) cracking is most likely when $\psi \geq 70^\circ$, and will extend into the lower modulus material, i.e. material 1 with $\alpha < 0$

Techniques to measure adhesion

The **Work of Adhesion** for interfacial fracture can be expressed in terms of the work for interfacial separation and energy dissipation.

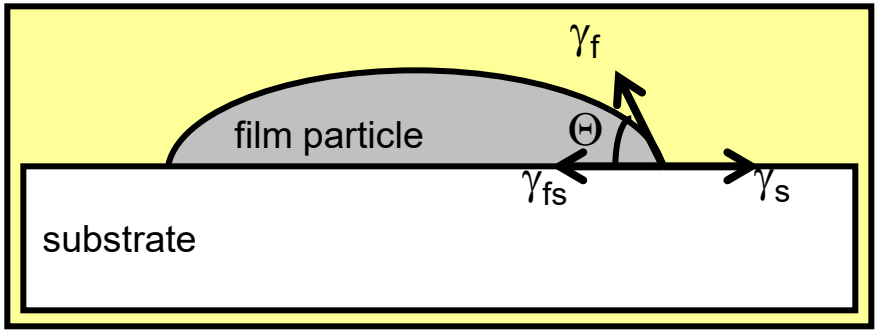

$$\gamma_f \cos\theta = \gamma_s - \gamma_{fs}$$

True work of adhesion

$$G = \gamma_A + \gamma_B - \gamma_{AB} + D_f + D_s$$

Practical work of adhesion

$\gamma_A+\gamma_B-\gamma_{AB}$ = work of interfacial separation (Dupre equation)

D_f = energy dissipation in the film

D_s = energy dissipation in the substrate

Adhesion mechanisms

- Mechanical Interlocking
  - Surface roughness – increase surface area for bonding
- Chemical
  - Chemical bonds are formed between film & substrate
- Electrostatic
  - Charge transfer occurs

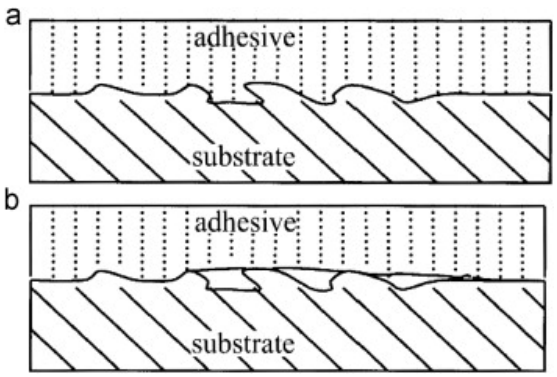

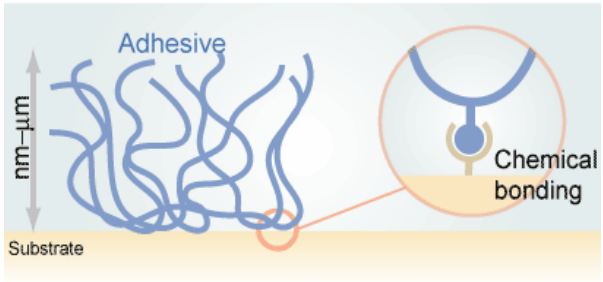

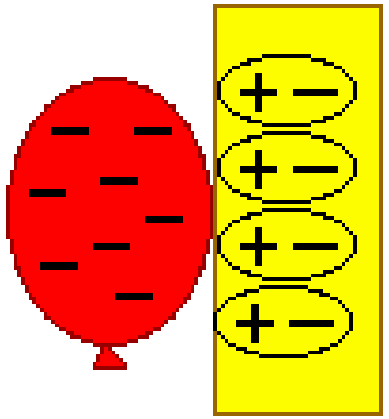

Each mechanism occurs at a different length scale.

Interface fracture toughness

Substrate[a]	Film	Γ (J m^{-2})	Comment
Al_2O_3	Al	1	interface contaminated with C; Al film covered with a Ta superlayer[1]
		>100	tough interface; crack blunting[2, 3]
	Au	2	interface contaminated with C[4]
		10	clean interface; moist air test[5, 6]
		250	tested in dry air[4]
	Ni	5–8	interface contaminated with S[7]
		10–40	tested in moist air[7, 8]
		> 200	dry environment; crack blunting[8]
	Ni(Cr)	> 300	moist air test; crack blunting[9]
	Mo	~ 2	generally brittle interface[10]
	Nb	1–20	tested in moist air[10, 11]
	Cu	120–250	tested in moist air[12]
	Al–Cu	5.6	tested with a Ta superlayer[1]
	Ta_2N	0.5	deposited layer[13]
Si	W	5.5–9.0	substrate covered with thin SiO_2 layer[14]
	Al–Cu	8	tested with W superlayer[15]
SiO_2	Cu	2	tested in moist air[16]
		20	interface coated with Cr[10]
	Cu(Cr)	10	tested in moist air[16]
	TiN	10.4±1.3	tested in moist air[17]
Steel	DLC	> 100	interface coated with Cr[10]
Fused silica	untreated epoxy	2.4	moist air test[18]
Soda-lime glass	untreated epoxy	2.0	moist air test[18]

Strategies against bad film adhesion I – glue layers

Glue Layers

Conventional wisdom, for example, might suggests using very clean substrates to get good adhesion. This may not necessarily work for metal films on glass substrates because optimum adhesion appears to occur only when the metal contacts the substrate through an oxide bond. Thus Al adheres better when there is some Al_2O_3 present between it and the glass substrate. It is not surprising that strong oxide formers adhere well to glass. Intermediate oxide layers can be produced by depositing metals with large heats of oxide formation such as Cr, Ti, Mo, and Ta.

Conversely, noble metals such as Au, Ag, and Cu do not form oxides readily and accordingly, adhere poorly to glass, a fact reflected in low film stresses.

To promote adhesion it is common practice, therefore, to first deposit a few hundred angstroms of an intermediate oxygen-active metal to serve as the "glue" between the film and substrate.

This is the basis of several multilayer-metallization contact systems, including Ti-Au, Ti-Pd-Au and Ti-Pt-Au, Cr-Au, Cr-Pd-Au, Cr-Ag, and Mo-Au. After deposition of the intermediate glue layer, the second film should be deposited without delay, for otherwise the glue metal may oxidize and impede adhesion of the covering metal film. Added layers to improve adhesion are unwelcome because additional deposition steps are costly and often introduce new reliability problems.

Ohring 2003

Strategies against bad film adhesion II – ion beam processing

1. ***Low-energy presputtering.*** Cleaning substrates by a presputtering treatment with ions having energies between 100 eV and a few keV is a good way to enhance subsequent film adhesion. This cleaning procedure removes most contaminants including surface-bonded polymer chains, oil films, and terminal oxide layers.

2. ***Ion-beam-assisted deposition.*** In this case ion beams with several keV energy at fluxes of 5 10^{15} ions/cm^2 accompany film deposition. Therefore, in addition to the benefits of presputtering, the film is densified. The interfacial "pseudodiffusion" layer produced is a type of structurally disordered transition zone, in which the solubility of the involved components exceeds equilibrium limits. All in all, diffusion occurs between materials that do not naturally mix or adhere.

3. ***Reactive ion implantation.*** Whereas the first two processes are carried out at low energies, ion implantation requires an expensive accelerator. However, there are some advantages to reactive ion implantation, including the creation of compositionally graded layers and ballistic mixing at the interface.

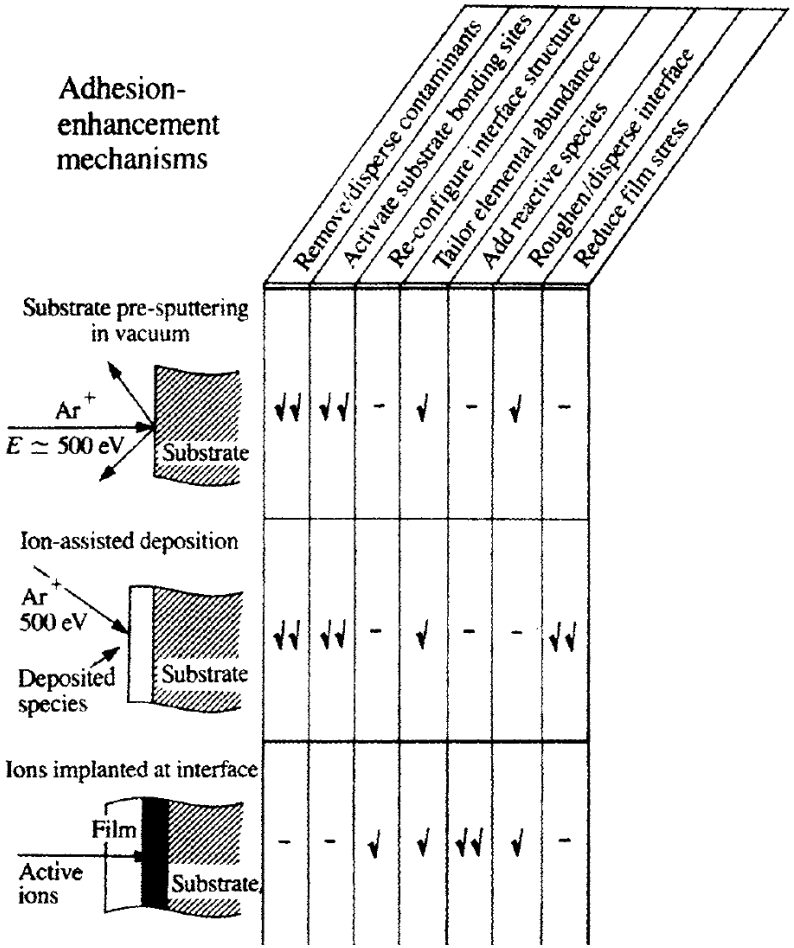

Ohring 2003

Strategies against bad film adhesion III – polymers

There is often a need to deposit thin metal films on polymeric substrates. This often proves a challenge because of great differences in atomic bonding, melting points, and thermal expansion coefficients between the involved materials.

Strategies to improve adhesion broadly attempt to modify polymer surfaces by either physical or chemical means. Alteration of surface topography, mechanical abrasion, and plasma treatment of surfaces are examples of the first approach. Plasmas with their collective assortment of ions, electrons, and photons enhance adhesion by removing contaminants, roughening surfaces, promoting crosslinking, and generally introducing or removing reactive chemical groups.

In particular, the greater chemical reactivity of the surface often enhances nucleation of deposited films. Both oxygen and nitrogen plasmas are often employed to activate polymer surfaces. Oxygen plasmas tend to make the surface more acidic by creating C=O groups. On the other hand, nitrogen or ammonia treatments result in basic surfaces due to the formation of amine and imine groups.

Ohring 2003

residual stress

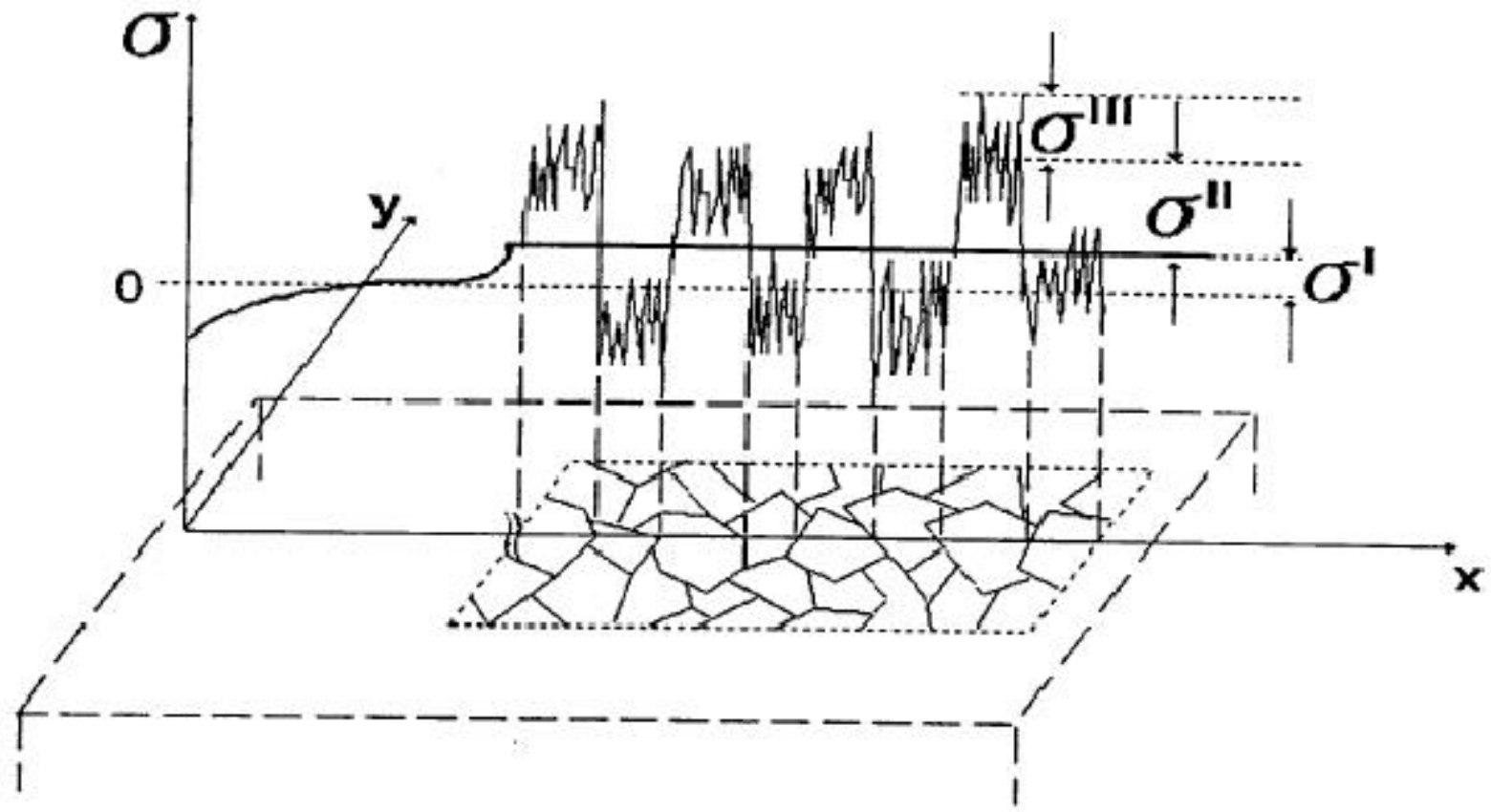

examples for residual stress

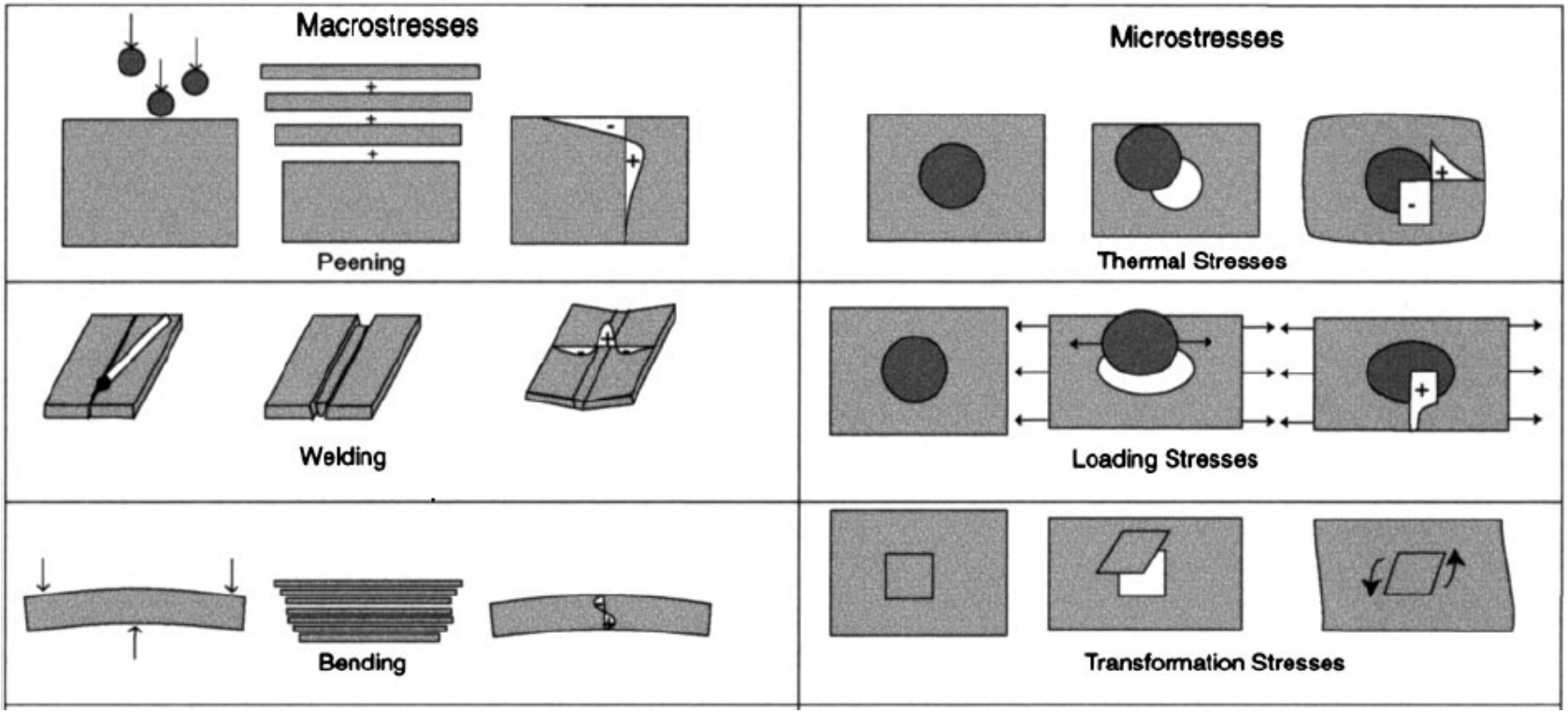

substrate curvature methods

The **most popular technique** for measuring thin film stress is based on **measurements of the curvature** of the substrate on which the film is deposited.

As shown earlier the stress in the film is given by

$$\sigma_f = \left(\frac{E_s}{1-\nu_s}\right)\frac{t_s^2}{6t_f}(\kappa - \kappa_o) = \left(\frac{E}{1-\nu}\right)_s \frac{t_s^2}{6t_f}\Delta\kappa$$

where $\Delta\kappa$ is the curvature change induced by the stress in the film (**Stoney equation**)

In most systems, the curvature (or radius of curvature) is measured by **scanning a laser beam across the wafer (or substrate) and deflecting the position of the reflected beam**.

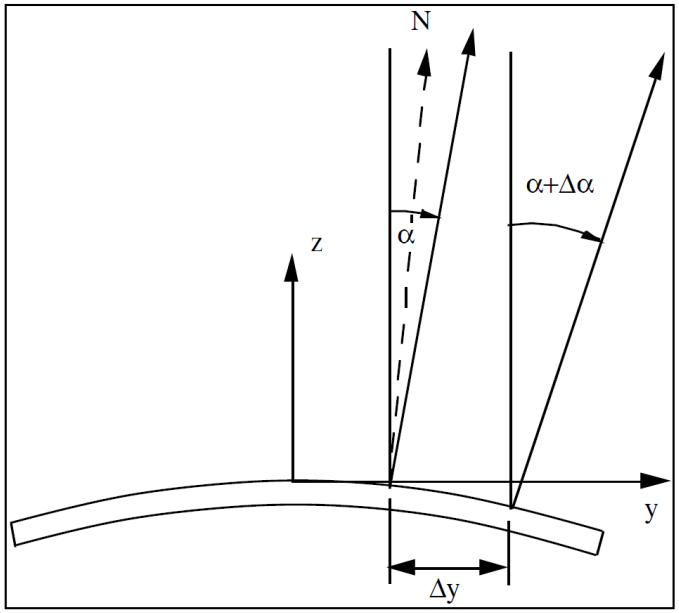

Nix 2014

hole drilling method

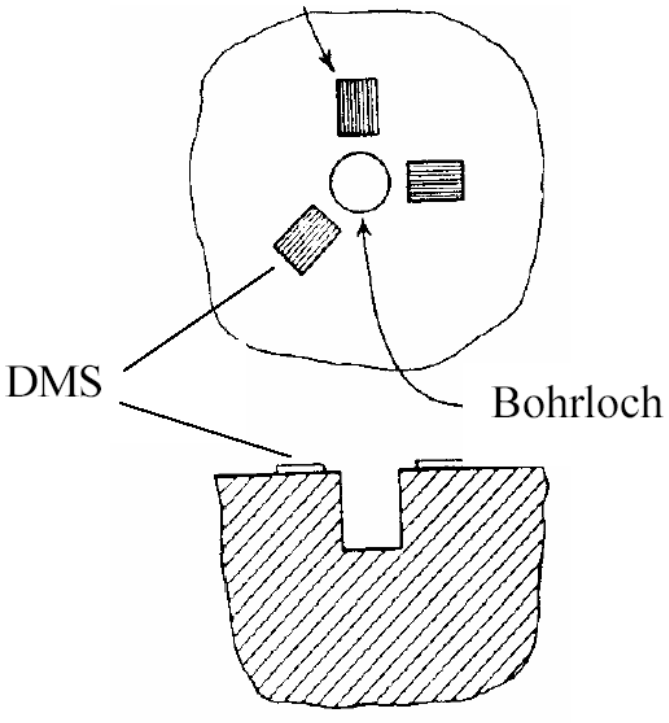

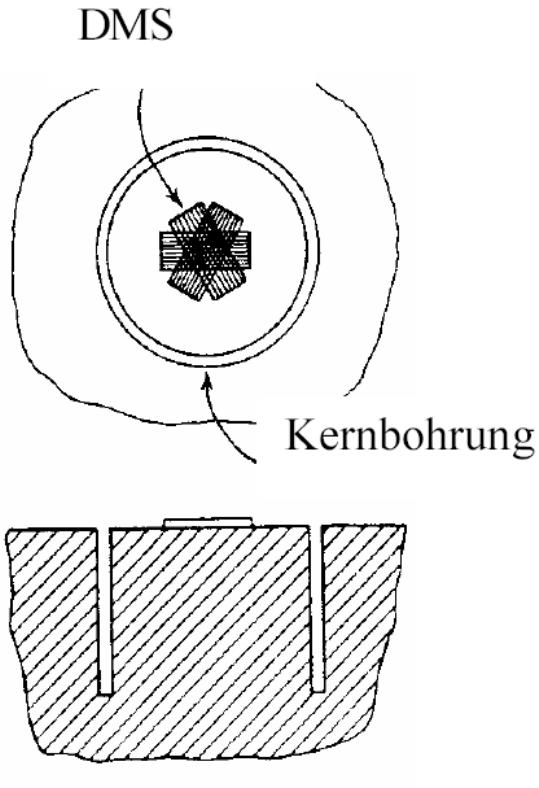

- Scan with AFM before & after milling with FIB
- Digital Image Correlation (DIC) used on both AFM and SEM images to measure stress relaxation wrt marked pattern

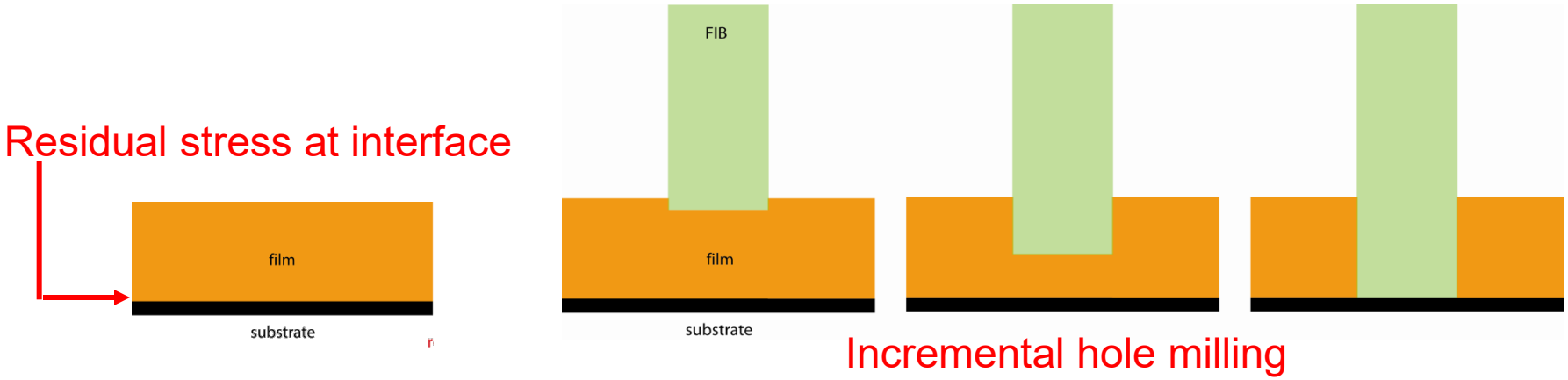

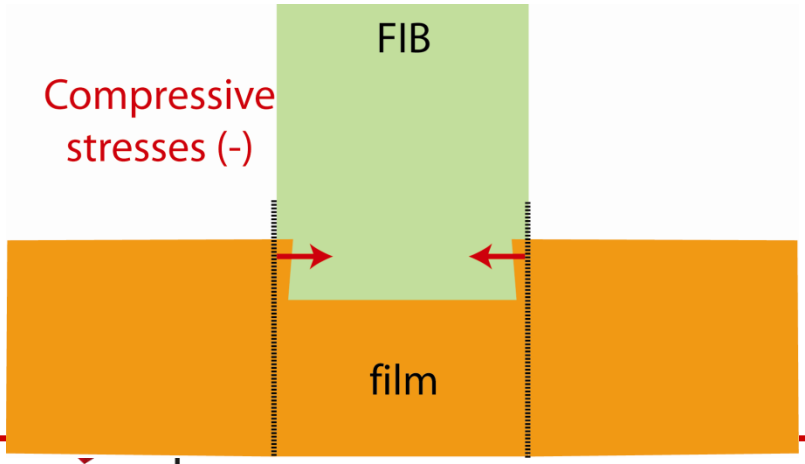

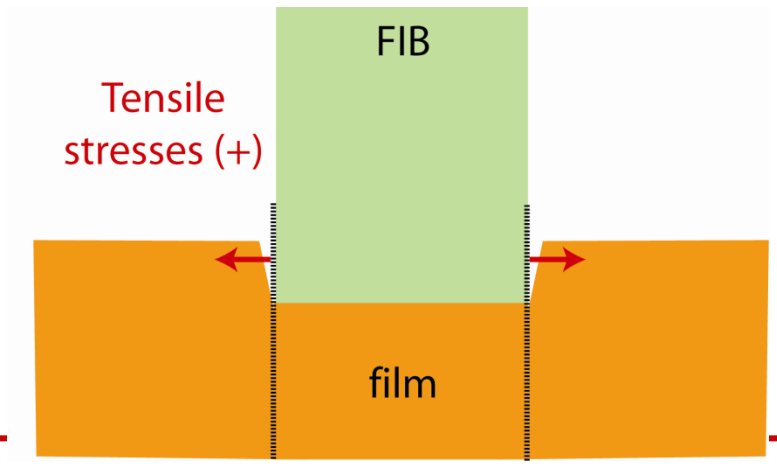

Surface will relax depending on sign of stress

Residual Stress: Milling Geometries

- Incremental slot, hole or annular milling
- Monitor surface relaxation with depth
- Fiducial markers used as reference points during imaging and analysis
- Uniaxial and Biaxial stress distributions of site-specific features measurable

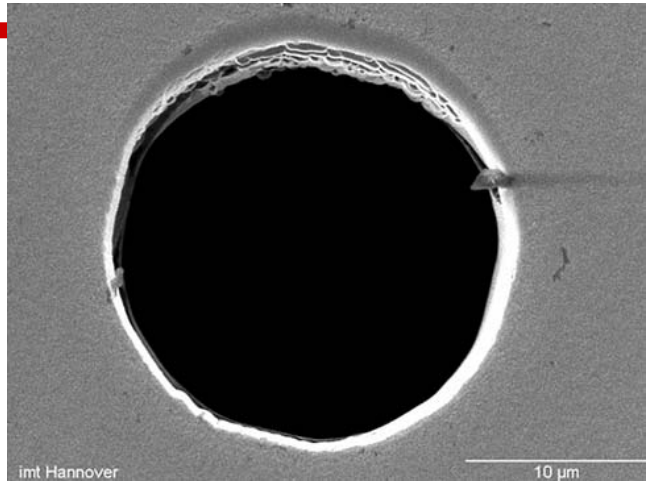

Gerdes & Gatzen, Microsyst. Technol., **15** (2009)

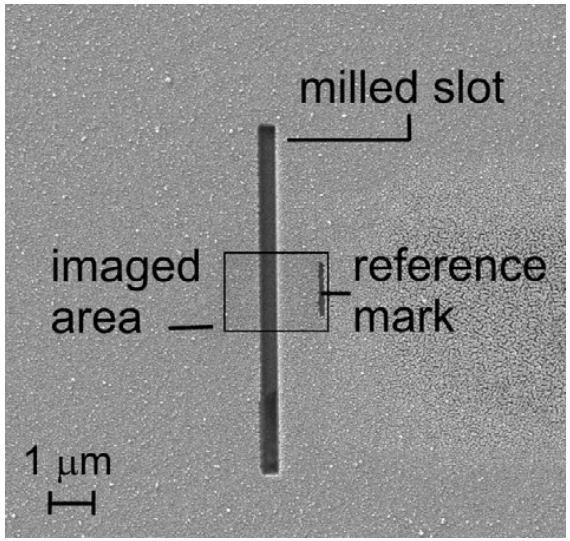

Sabaté, *et al*, Nanotechnology., **17** (2006)

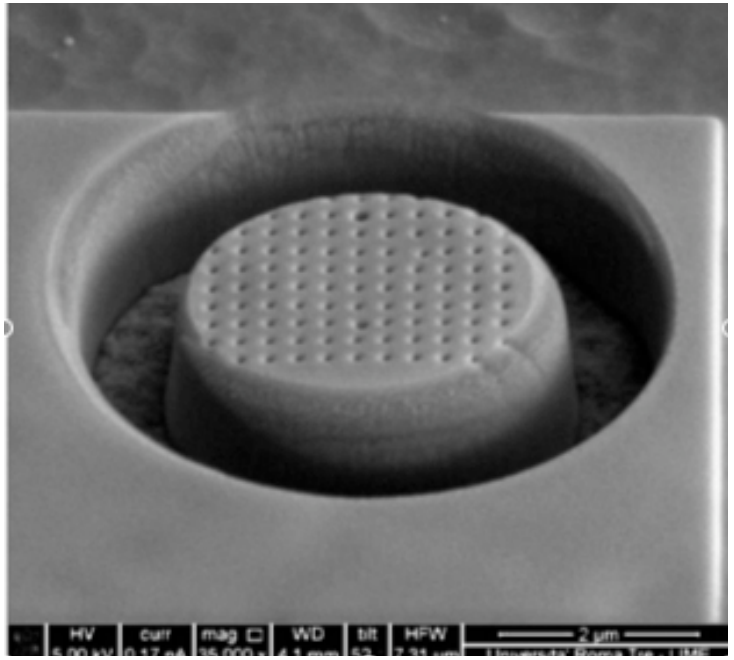

Korsunsky, *et al*, Mater. Lett., **63** (2009)

Cantilever beam methods

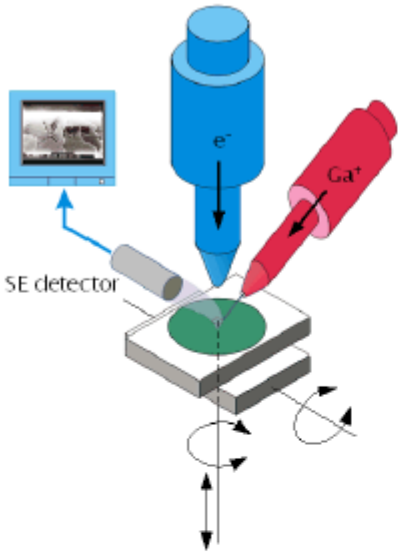

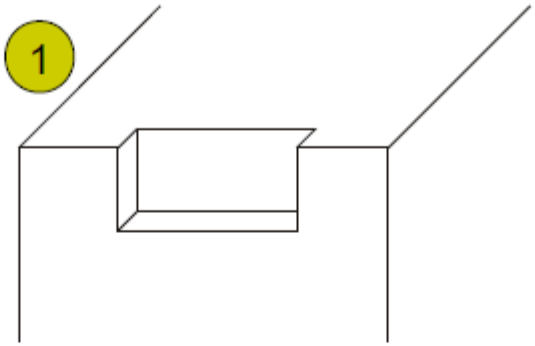

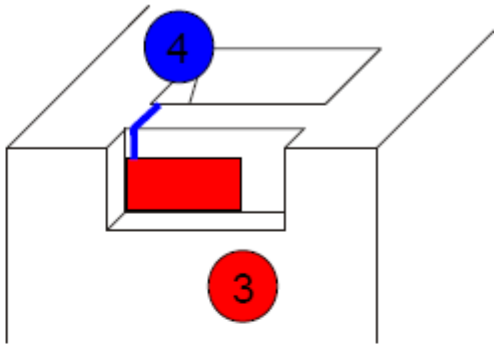

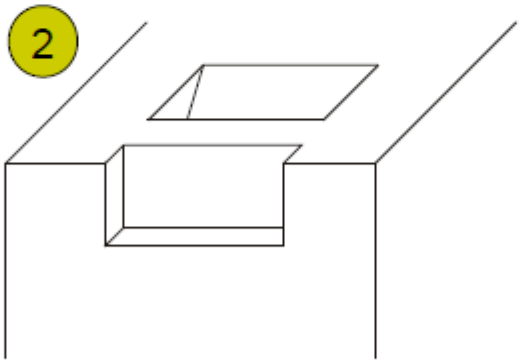

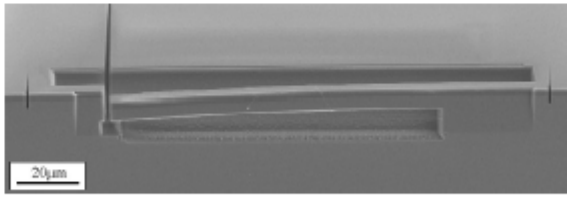

Cantilever beam methods

- fabrication of a micro cantilever by means of a FIB workstation

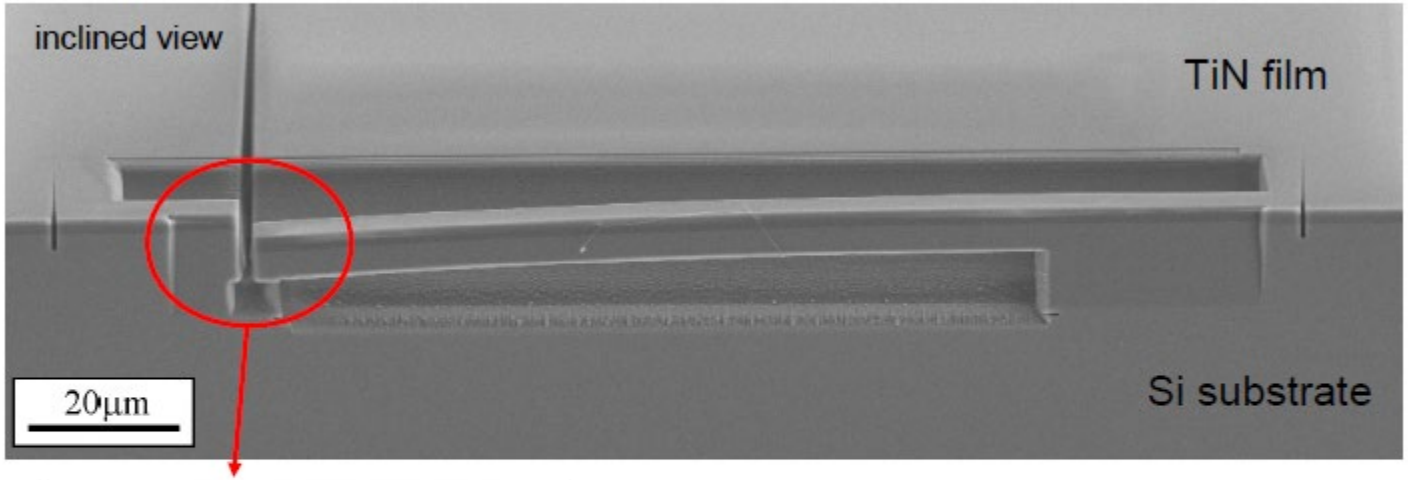

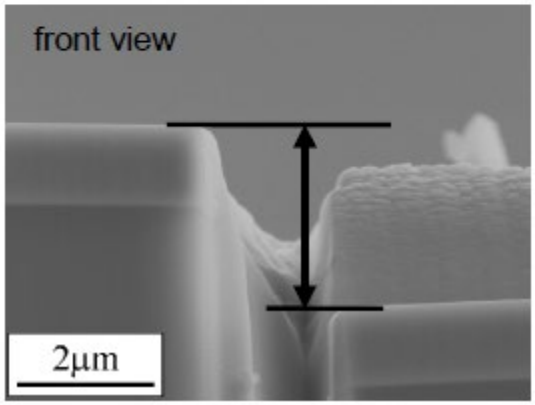

- deflection depends on the residual stresses

X-ray diffraction

Bragg equation

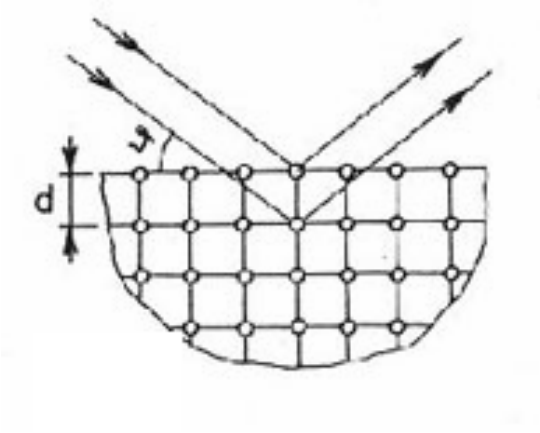

$$2d \sin \vartheta = n\lambda$$

$$\varepsilon_{\varphi\Psi} = \frac{\Delta d}{d}$$

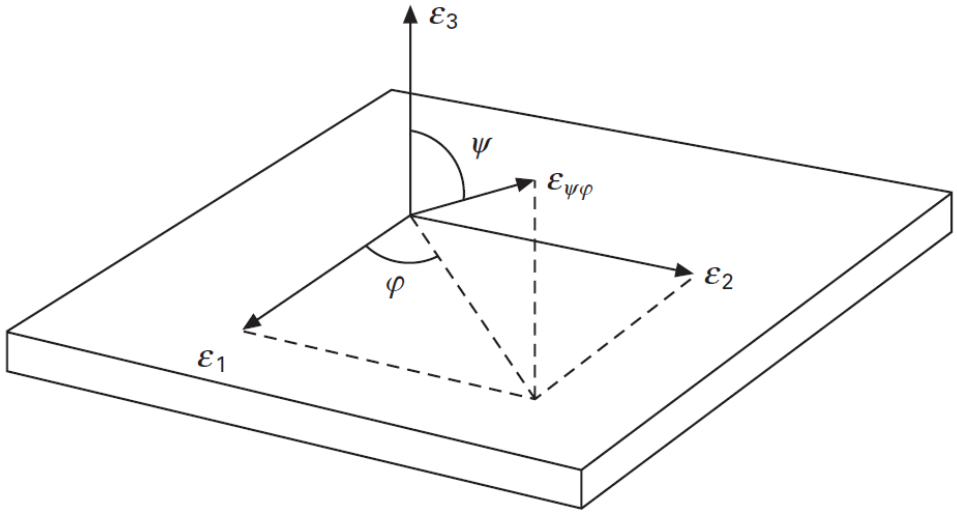

1: Normal to sample
2: Normal to lattice plane (measurement direction)

Any state of strain can be described in terms of the principal strains, the axial strains in the principal coordinate system. In this coordinate system all of the shear stress components are zero. The thin film geometry requires the principal coordinates to lie parallel and perpendicular to the plane of the film. In the coordinate system shown the shear strains ε_{13} and ε_{23} must be zero

Peak shift due to strain

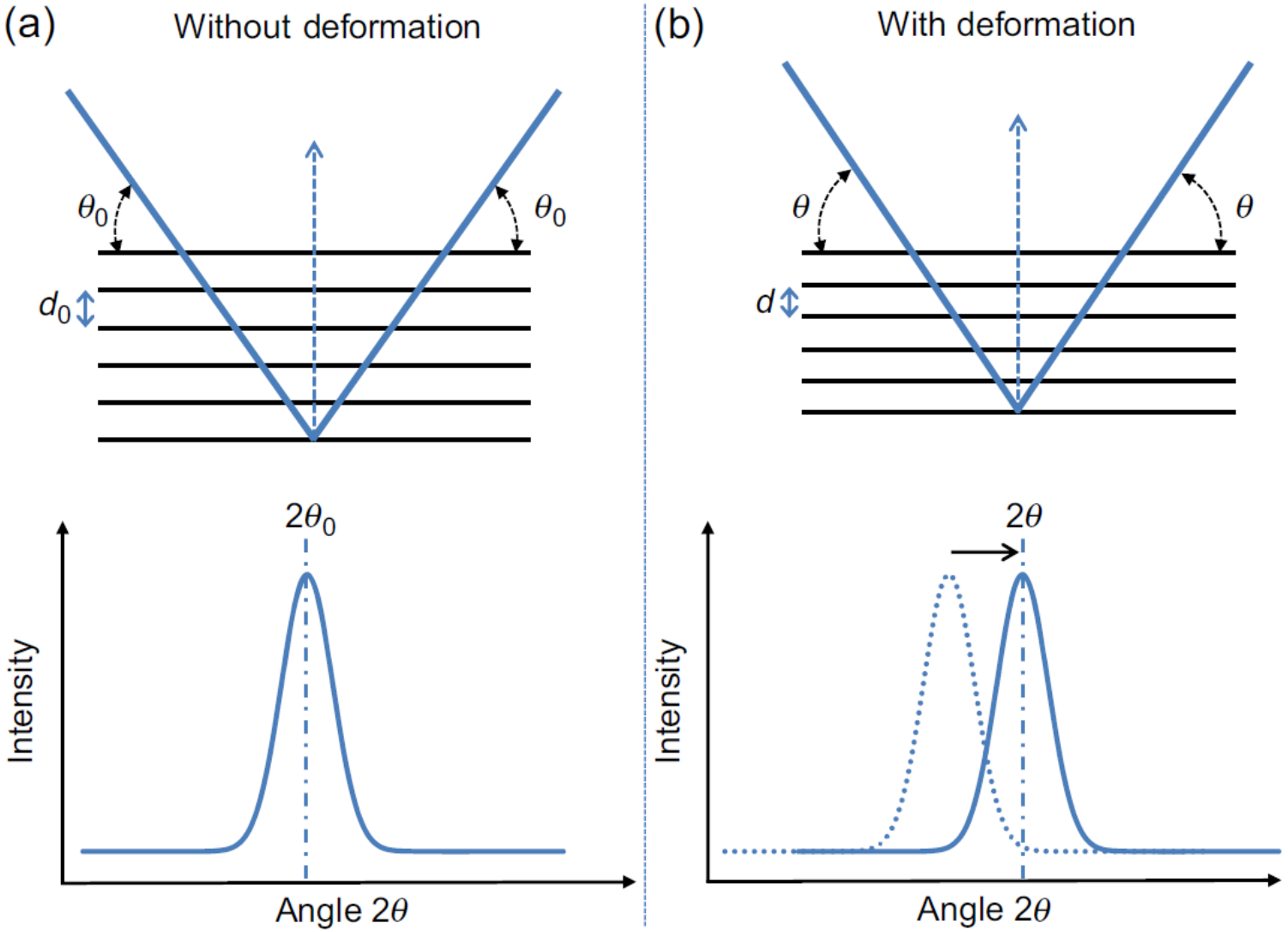

X-ray diffraction

Thus the axial strain, $\varepsilon_{\psi\varphi}$, in any arbitrary direction in the film, $\psi\varphi$ the strain that could be measured by X-ray diffraction, can be related to the principal strains through a coordinate transformation as follows:

$$\varepsilon_{\psi\varphi} = \varepsilon_1 \sin^2\psi \cos^2\varphi + \varepsilon_2 \sin^2\psi \sin^2\varphi + \varepsilon_3 \cos^2\psi$$

We assume the stress state to be biaxial, which reduces to

$$\varepsilon_{\psi} = \varepsilon_1 \sin^2\psi + \varepsilon_3 \cos^2\psi$$

Under these conditions the measured strain depends only on the angle between the film normal and the scattering vector. Using Hook's law

$$\varepsilon_1 = \varepsilon_2 = \frac{1}{E}\left(\sigma_1 - \nu(\sigma_2 + \sigma_3)\right)$$

$$\varepsilon_3 = \frac{1}{E}\left(\sigma_3 - \nu(\sigma_1 + \sigma_2)\right)$$

Leads to $\varepsilon_1 = \varepsilon_2 = \frac{1-\nu}{2\nu}\varepsilon_3$ as $\sigma_1=\sigma_2$ and $\sigma_3=0$

We see from this that the strains and biaxial stress in the film can be determined by measuring the out-of-plane strain, ε_3, by X-ray diffraction.

$$\frac{d_{hkl} - d^o_{hkl}}{d^o_{hkl}} = \varepsilon_{\psi} = \frac{(1+\nu)}{E}\sigma \sin^2\psi - \frac{2\nu}{E}\sigma$$

This relation provides the basis for the so-called '$\sin^2\psi$' method for measuring stresses $\sigma_1=\sigma_2=\sigma$ in thin films. For $\psi=0$ we see

$$\sigma = -\frac{E}{2\nu}\varepsilon_3$$

Thus, measurement of the out of plane strain by X-ray diffraction gives the biaxial stress in the plane

Stress with XRD: $\sin^2 \Psi$ Method

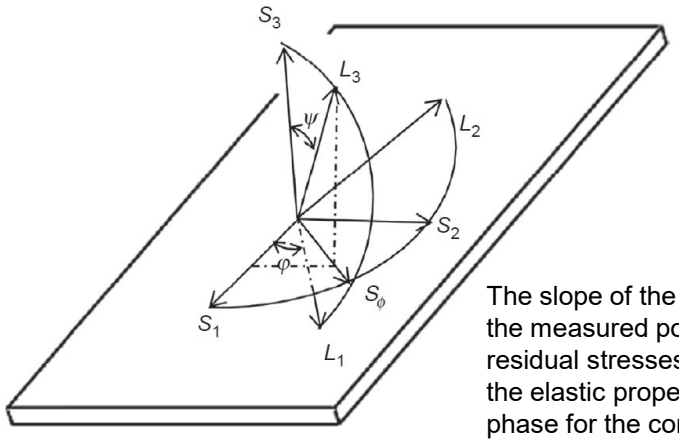

The slope of the regression line between the measured points is proportional to the residual stresses by taking into account the elastic properties of the investigated phase for the considered hkl planes

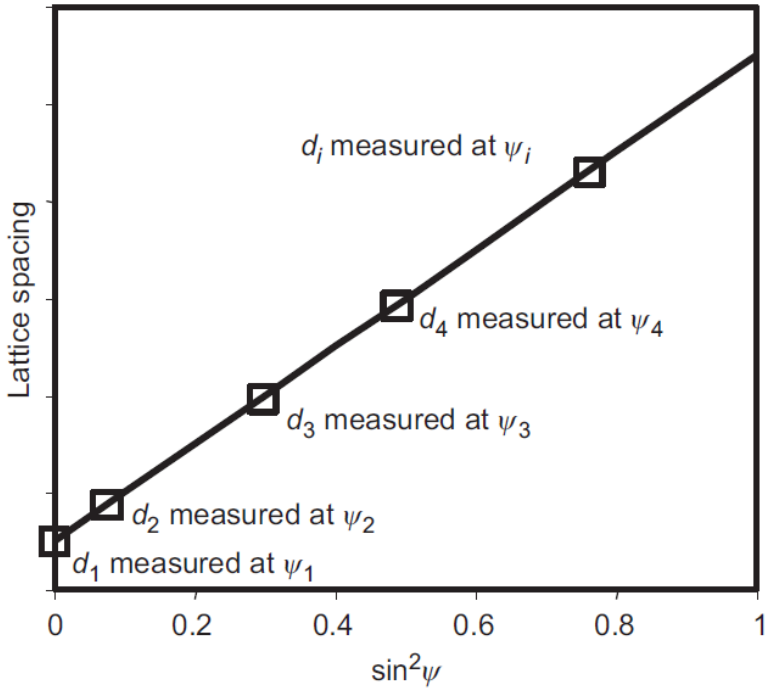

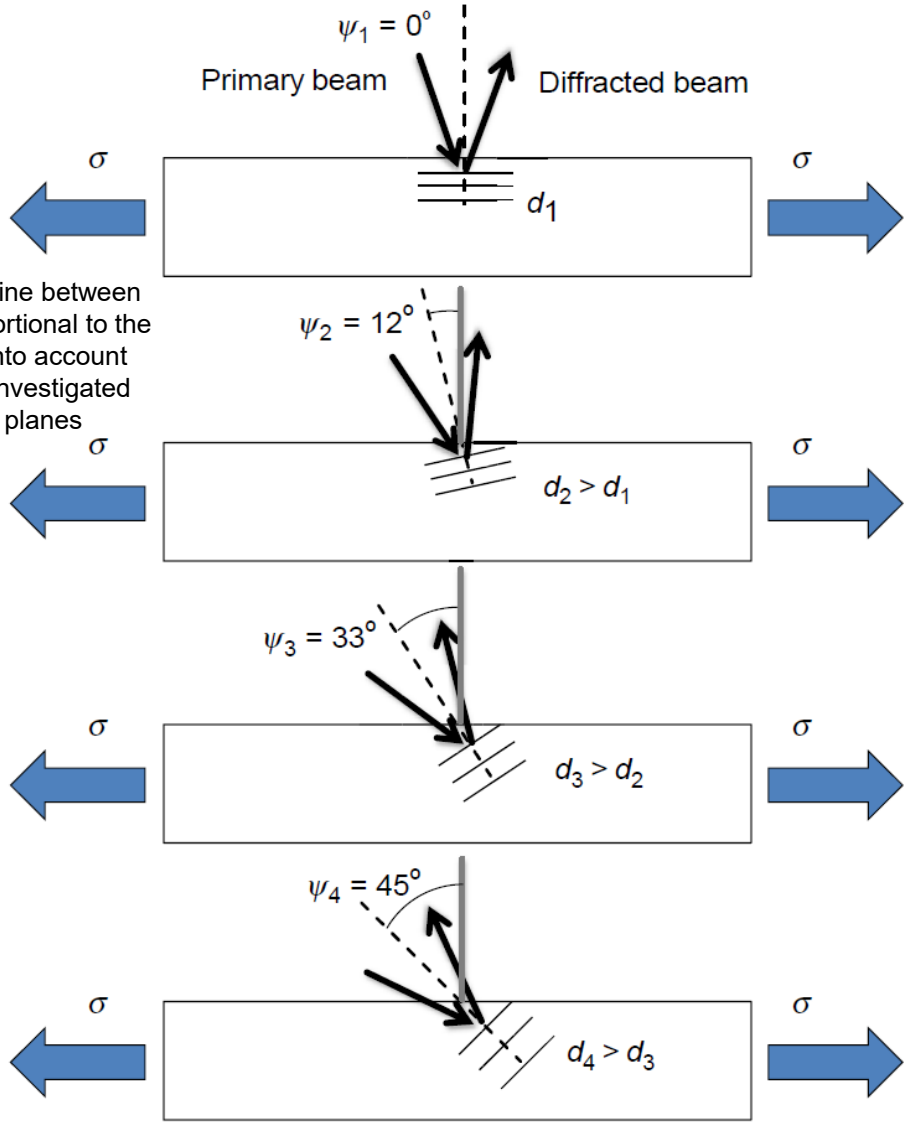

Raman spectroscopy: Light scattering

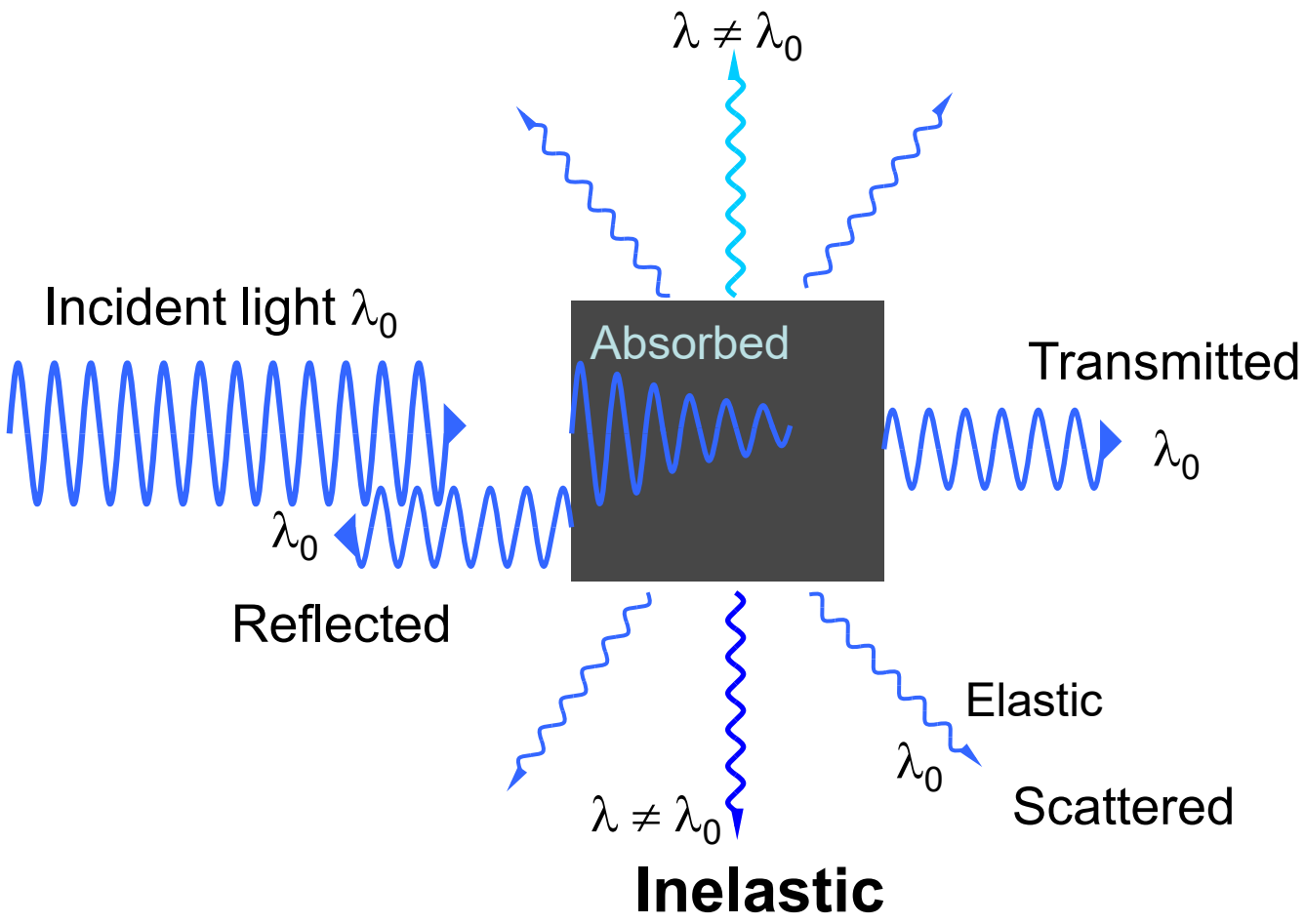

Raman scattering: **Inelastic** light scattering

Residual stresses via Raman spectroscopy

optical phonons

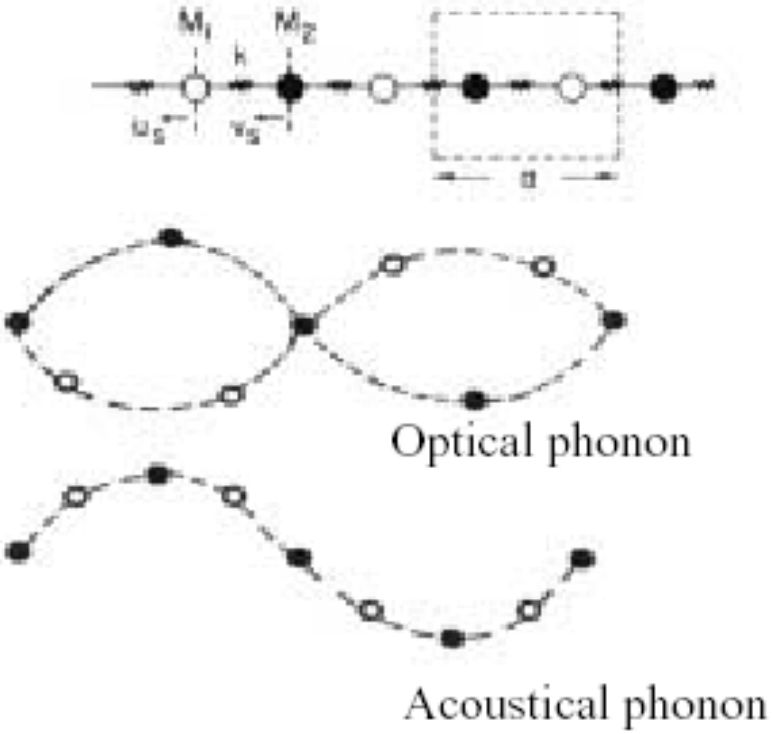

Micro-Raman sprectroscopy

instrument

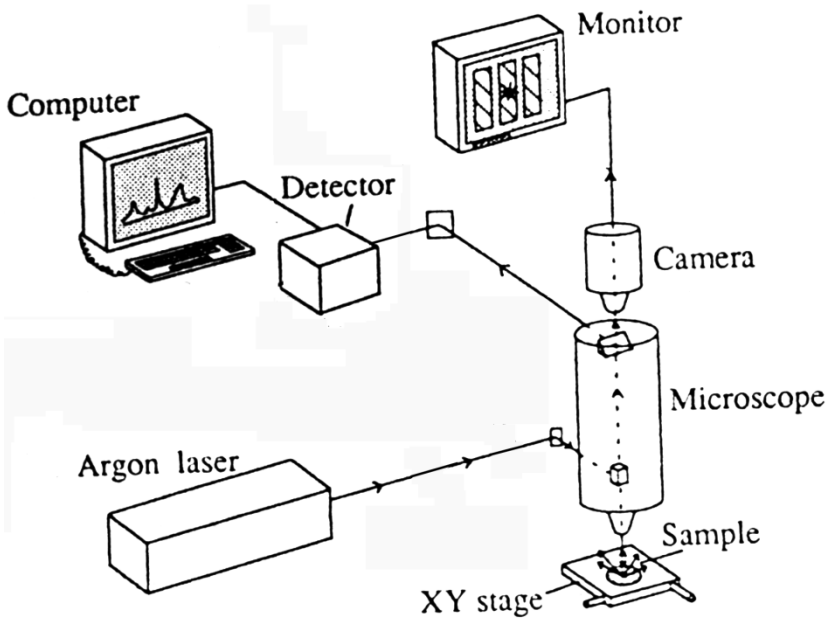

example

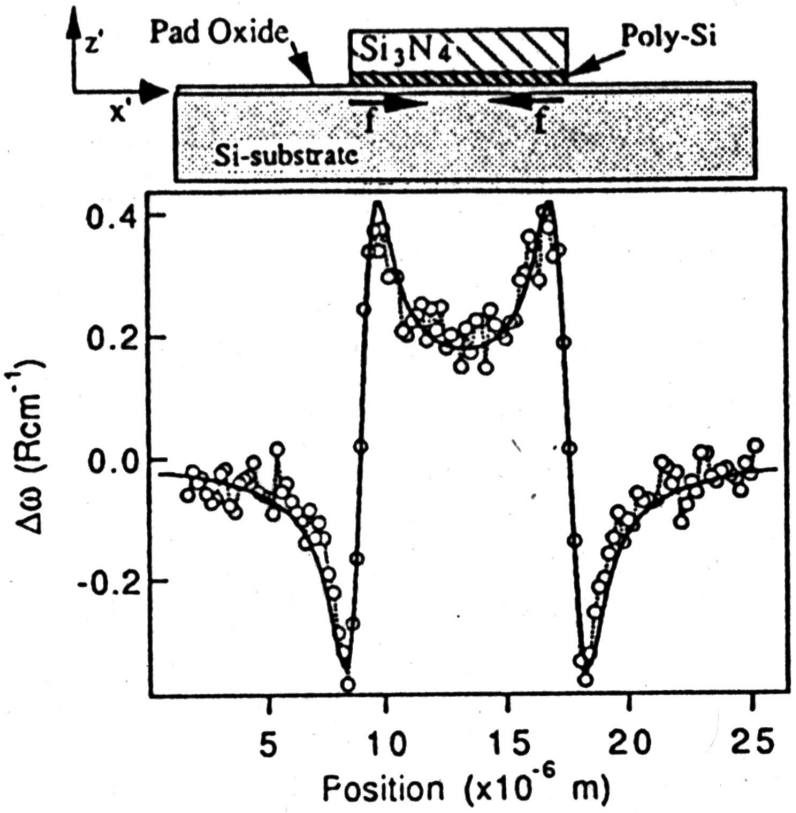

De Wolf 1996, Semicond. Sci Technol. **11**, 139

EBSD: Electron Backscatter Diffraction

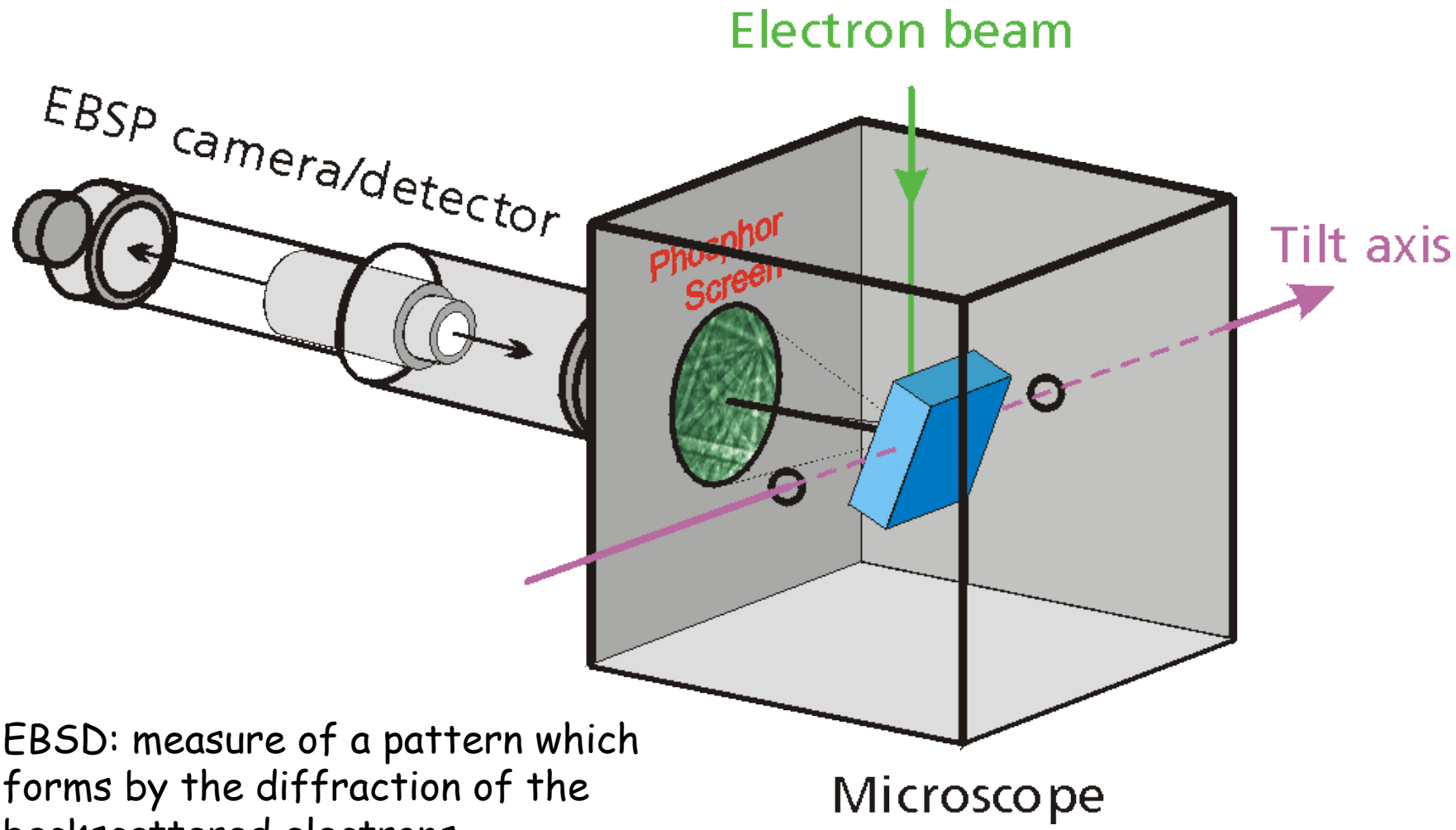

EBSD: measure of a pattern which forms by the diffraction of the backscattered electrons

EBSD Pattern Formation

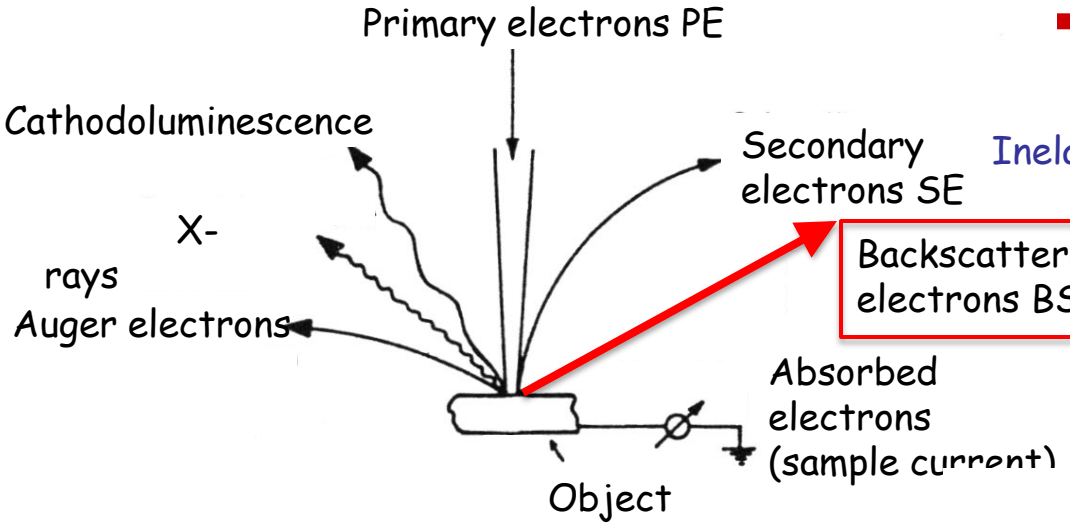

Diffraction on the lattice plane according to the Bragg law

$$\text{Bragg}: 2\, d_{hkl} \sin\theta = n\,\lambda$$

$$20\ \text{keV} \rightarrow \lambda \approx 7\ 10^{-3}\ \text{nm} \rightarrow \theta \approx 0.5°$$

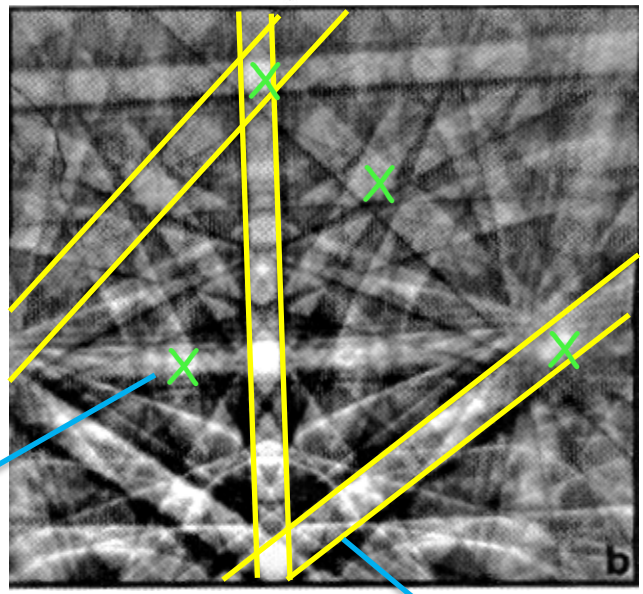

Pole

Lattice plane

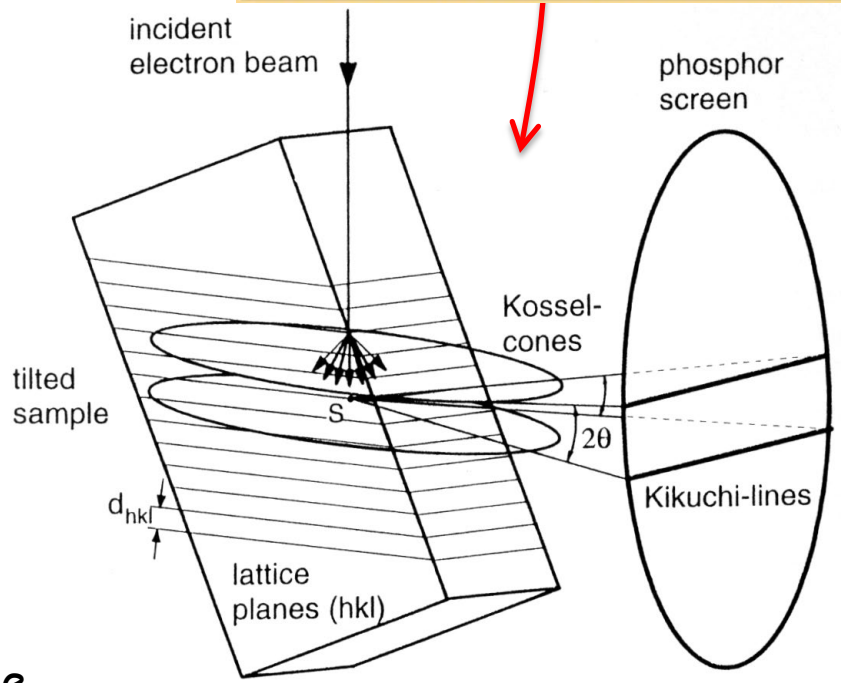

Large scale, multicrystalline thin film silicon

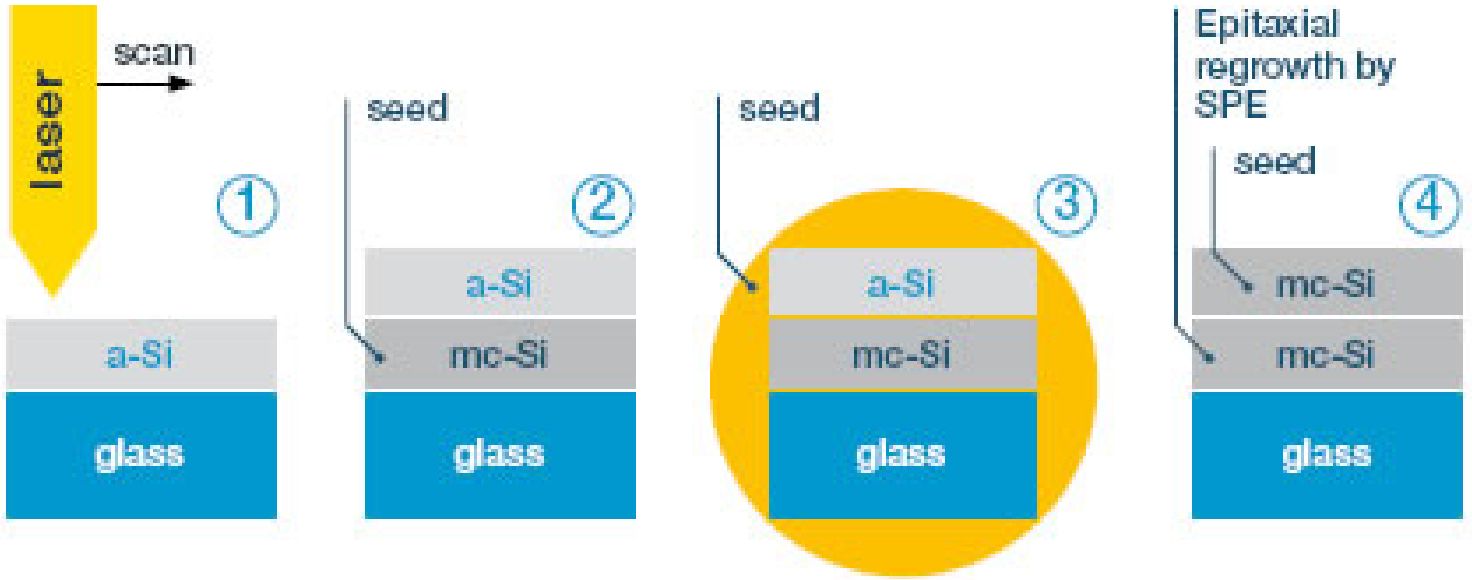

Figure 1:
Schematic of the laser-SPE process which will be established to realize large grained, low defective silicon layers on glass that have the potential for >10% efficiencies.

dislocation distribution: EBIC and OIM

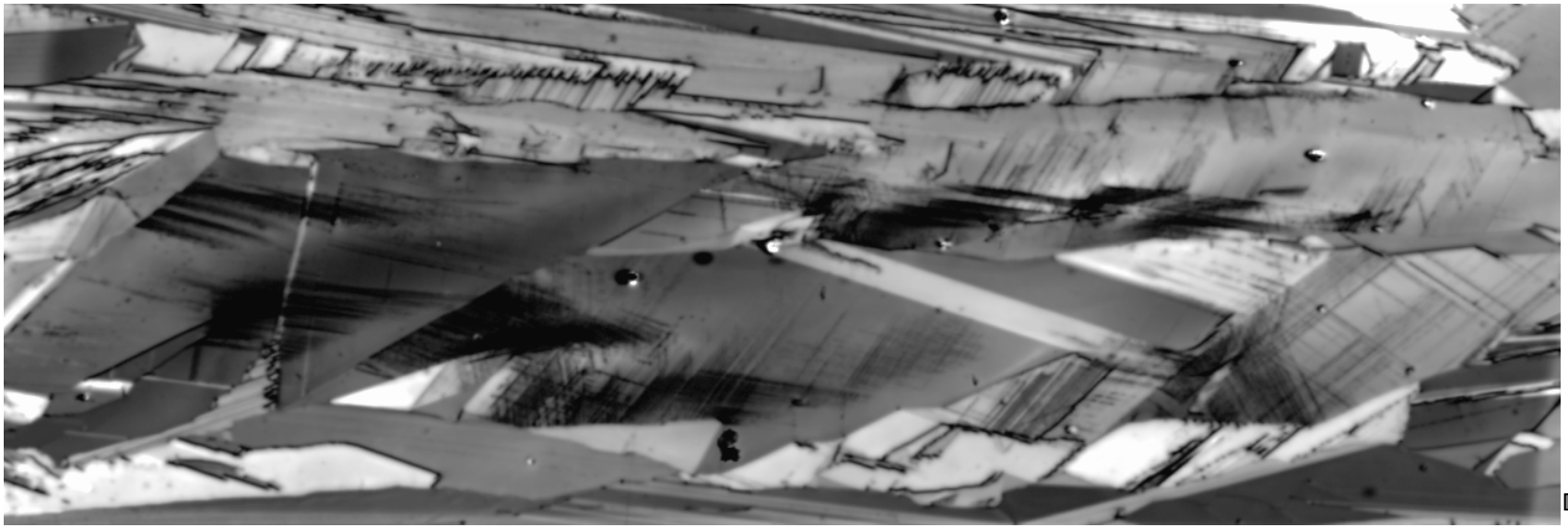

EBIC

100 μm

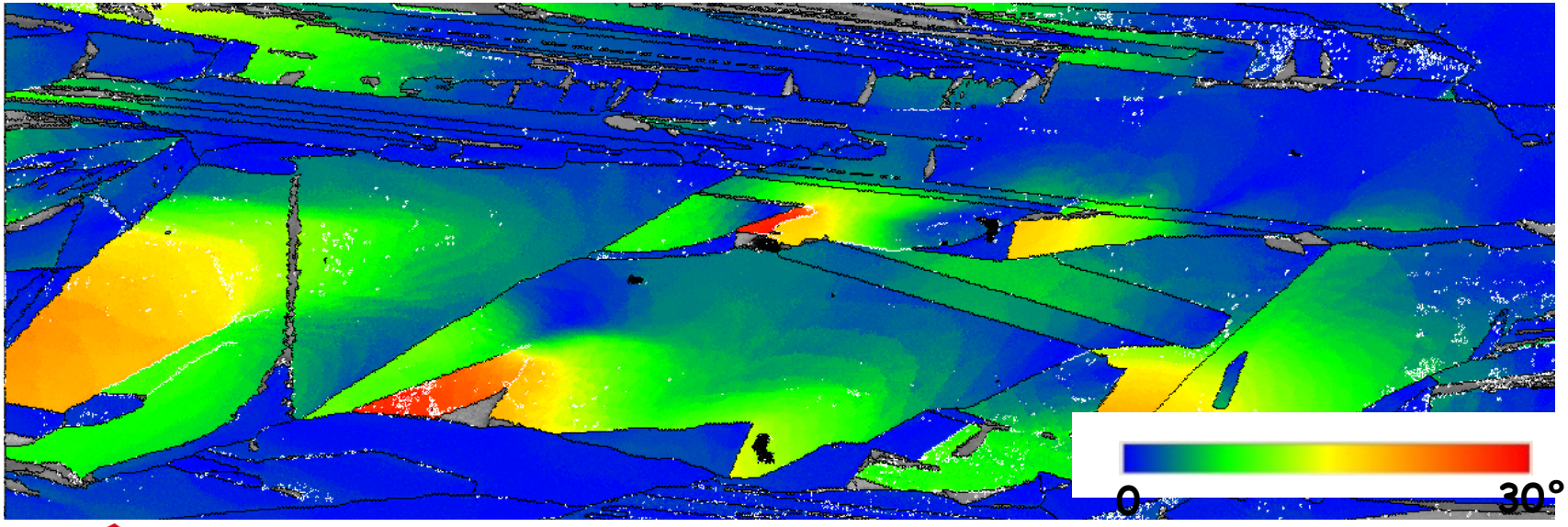

EBSD

stress concentrations: EBSD

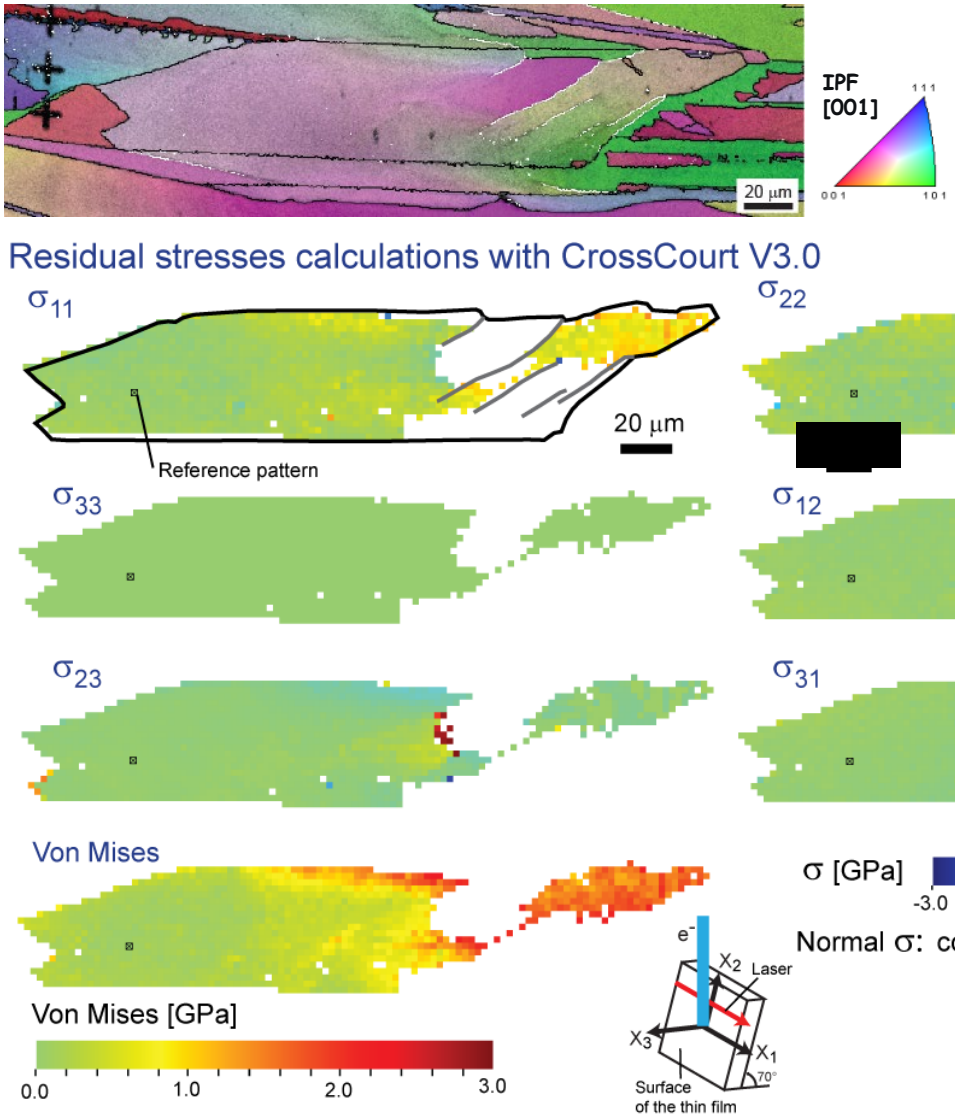

others

- Neutron diffraction
- CBED
- Ultrasonic measurements
- Magnetic methods

comparison

Method	Penetration	Spatial resolution	Accuracy
Hole drilling (distortion caused by stress relaxation)	$\sim 1{\cdot}2 \times$ hole diameter	50 μm depth	± 50 MPa, limited by reduced sensitivity with increasing depth
Curvature (distortion as stresses arise or relax)	0·1–0·5 of thickness	0·05 of thickness; no lateral resolution	Limited by minimum measurable curvature
X-ray diffraction (atomic strain gauge)	<50 μm (Al); <5 μm (Ti); <1 mm (with layer removal)	1 mm laterally; 20 μm depth	± 20 MPa, limited by non-linearities in $\sin^2 \psi$ or surface condition
Hard X-rays (atomic strain gauge)	150–50 mm (Al)	20 μm lateral to incident beam; 1 mm parallel to beam	$\pm 10 \times 10^{-6}$ strain, limited by grain sampling statistics
Neutrons (atomic strain gauge)	200 mm (Al); 25 mm (Fe); 4 mm (Ti)	500 μm	$\pm 50 \times 10^{-6}$ strain, limited by counting statistics and reliability of stress free references
Ultrasonics (stress related changes in elastic wave velocity)	>10 cm	5 mm	10%
Magnetic (variations in magnetic domains with stress)	10 mm	1 mm	10%
Raman	<1 μm	<1 μm approx.	$\Delta\lambda \approx 0{\cdot}1$ cm$^{-1} \equiv 50$ MPa

Measurement of adhesion of thin films

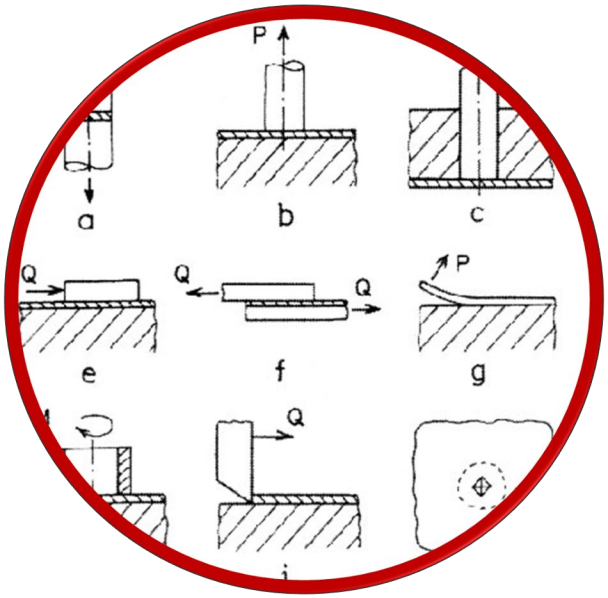

Measurement Techniques

- Qualitative Adhesion: pass/fail
  - Pull-off Test
- Quantitative Adhesion: number (J/m^2)
  - Rockwell test
  - Scratch Test
  - Bulge Test

Coating adhesion testing

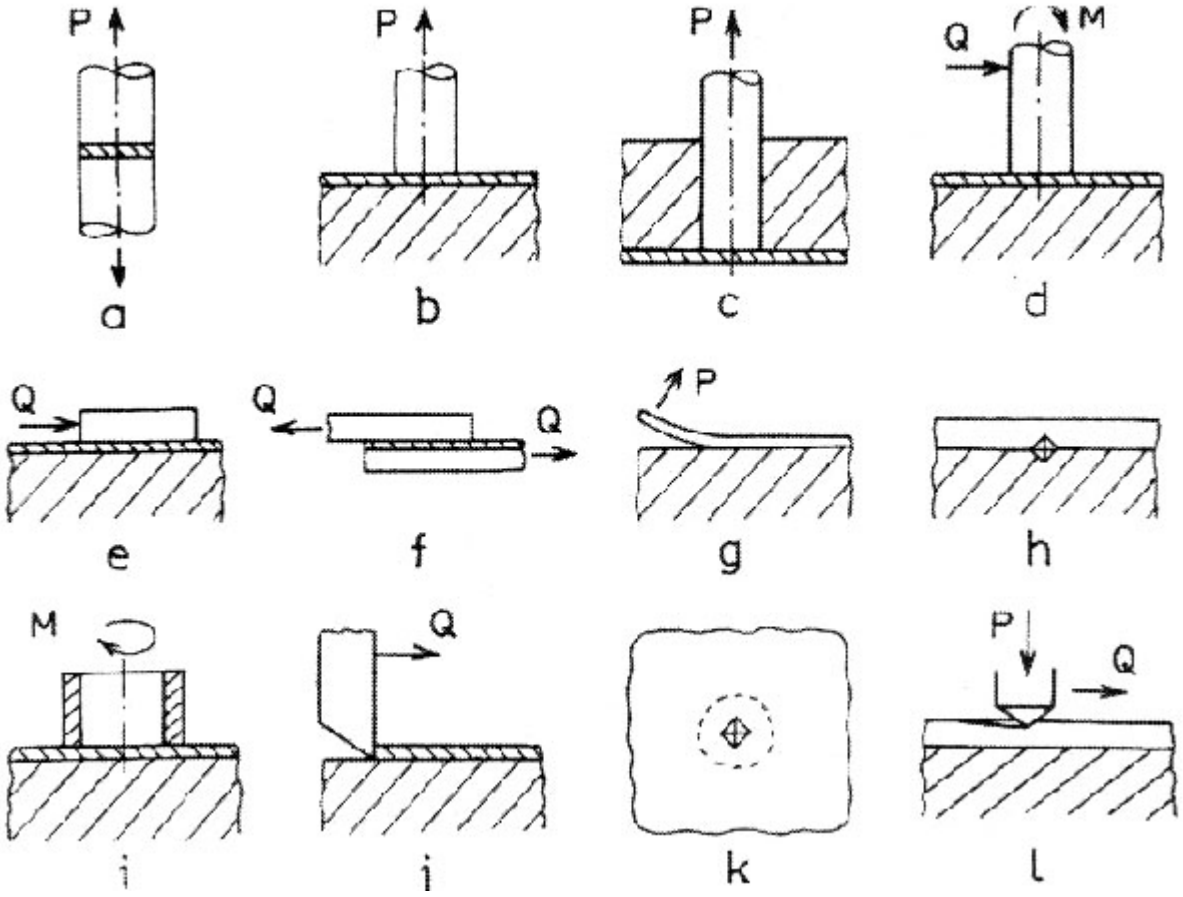

Roughly 300 different methods

Tear-off test

„Tear-off test"

$$\sigma_{max} = \frac{F}{A}$$

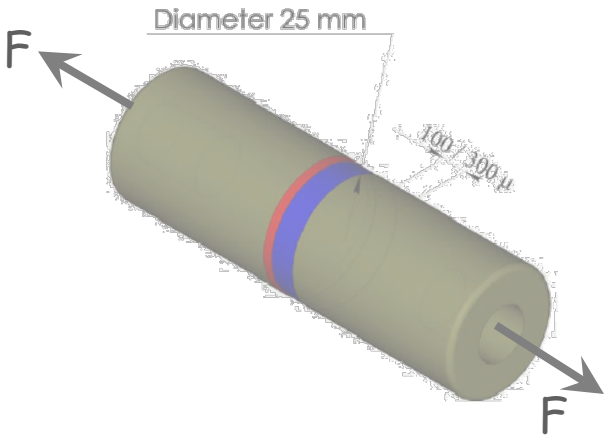

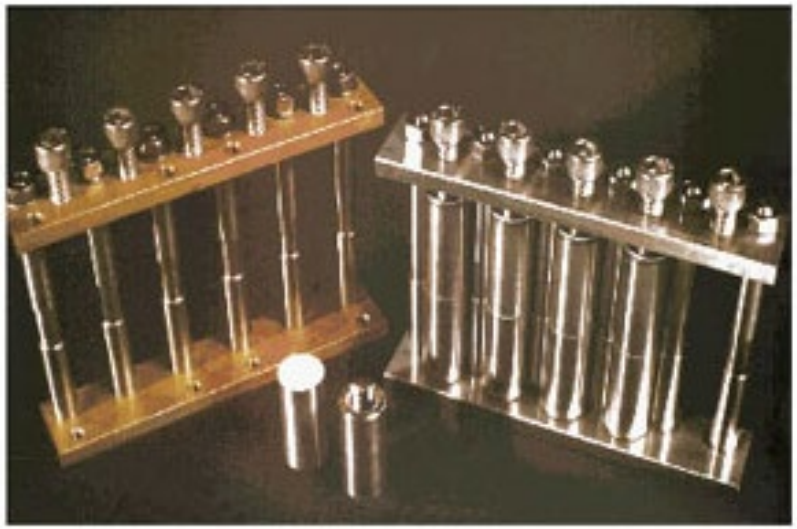

Principle of adhesion measurements by Rockwell indentations

Example:

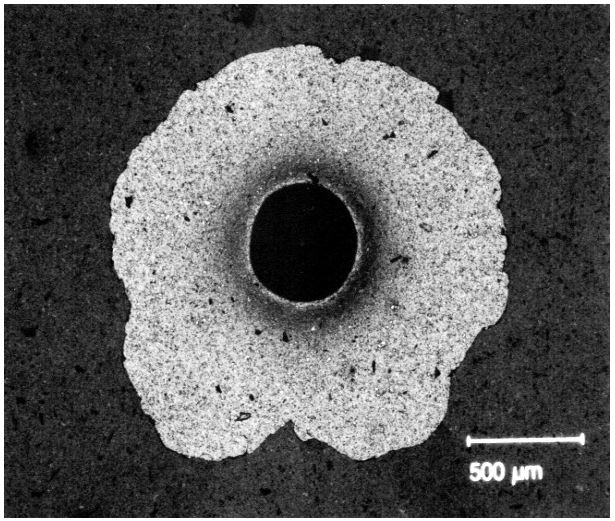

DLC, 1% Si / 500°C

Principle

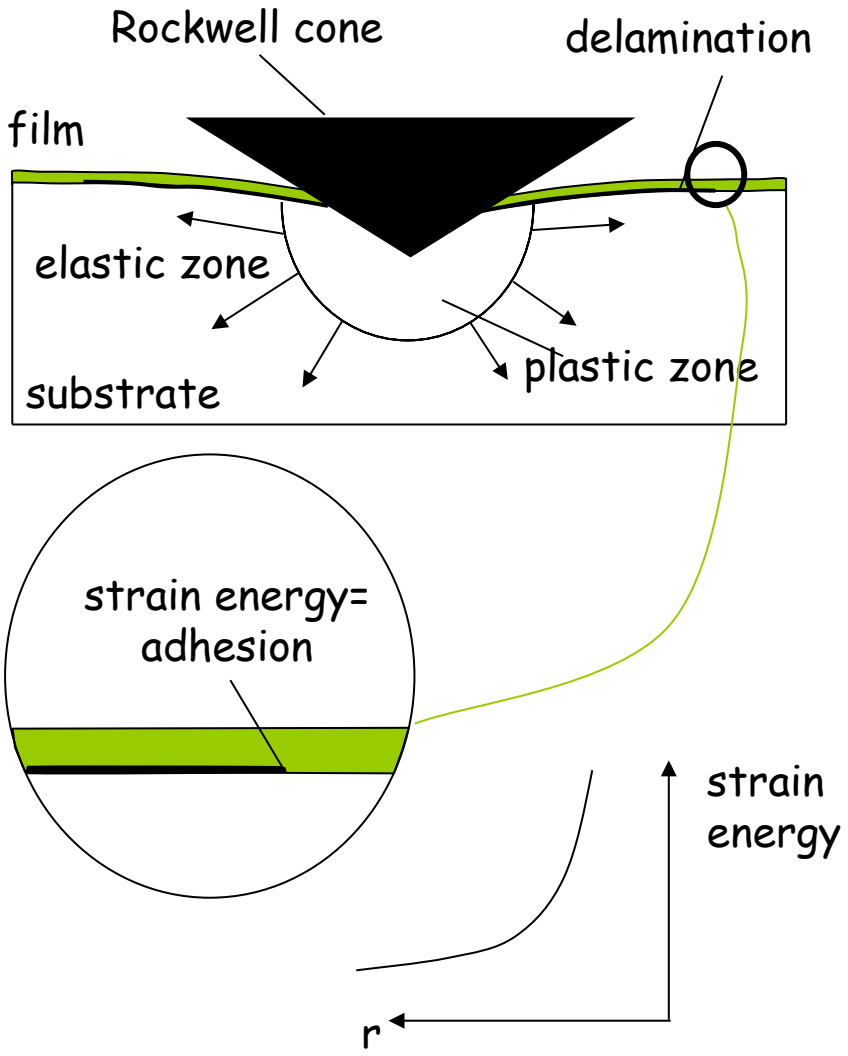

Simulation of surface strain tensor

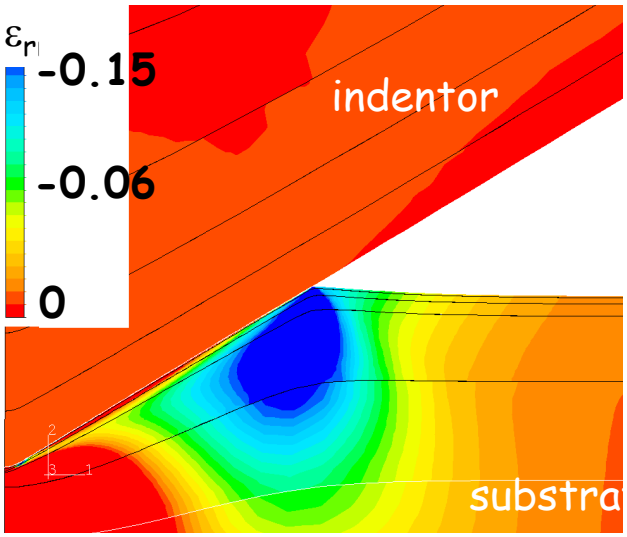

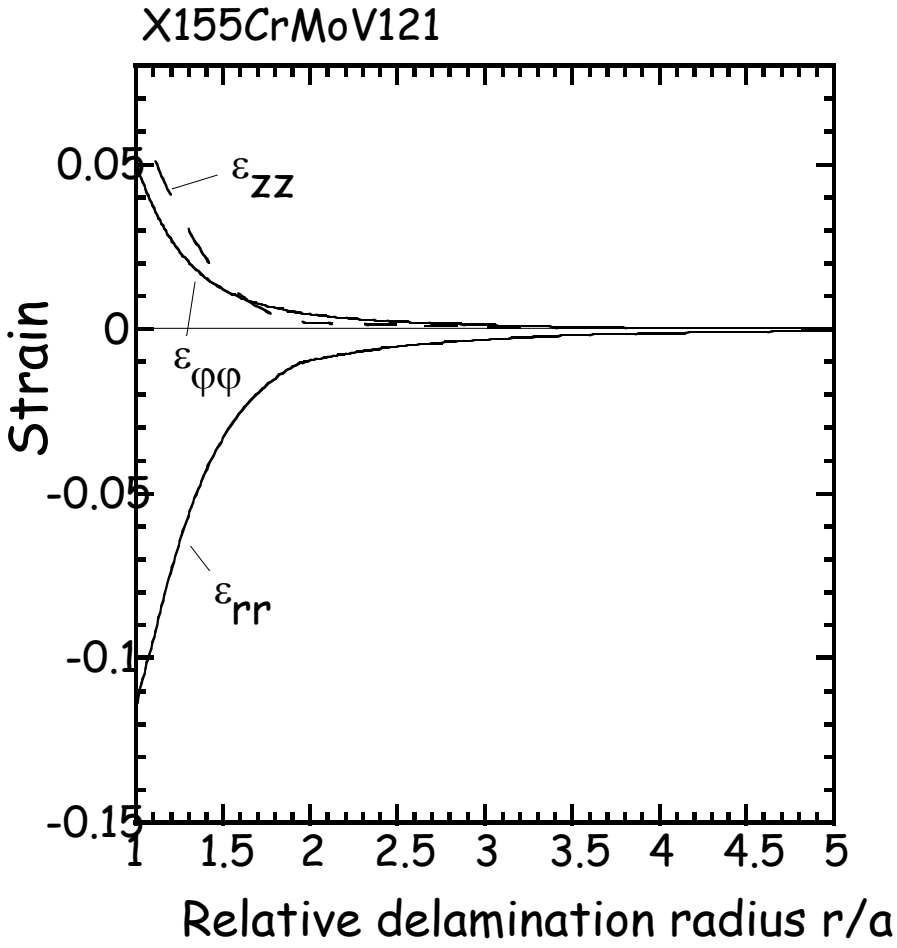

Application of adhesion measurements to DLC films

Rockwell C indentation

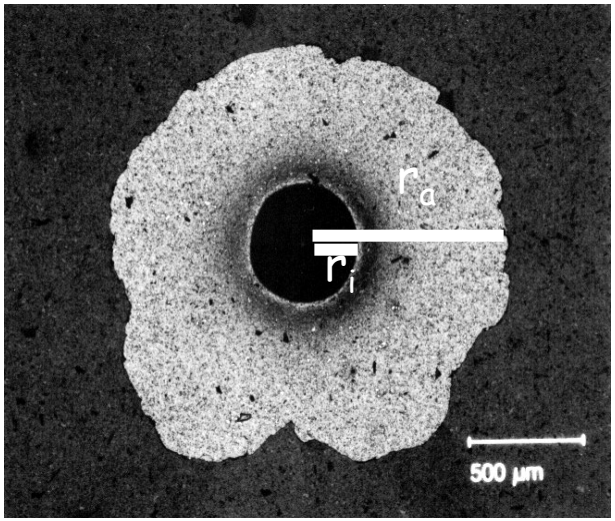

DLC on tool steel

r_a/r_i=3.3
film thickness=3.5µm
E=115GPa
σ_{layer}= -0.9 GPa

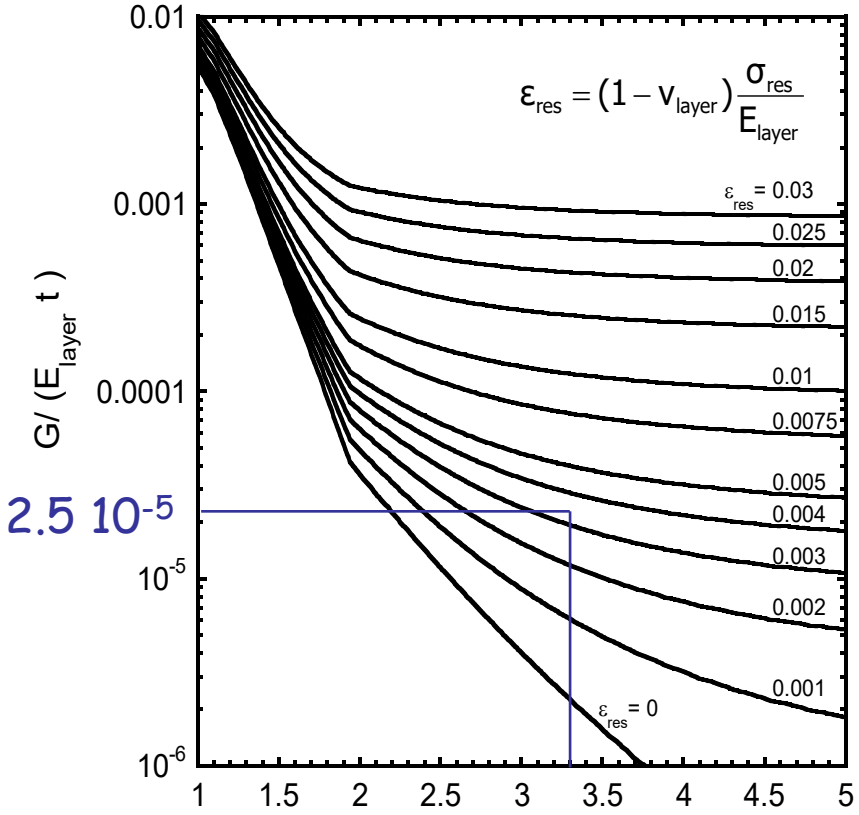

$G \cong$ 2.5 10^{-5} * 115GPa *3.5 10^{-6}

$\cong$ 10 J/m^2 = ADHESION

Michler 1999, Diamond Relat. Mater. **8**, 510-516

Scratch Testing

- Draw diamond tip across surface with increasing normal load until a critcal event occurs
- Film will debond (form buckle) or fracture (form through thickness cracks)
- Results can be difficult to analyze

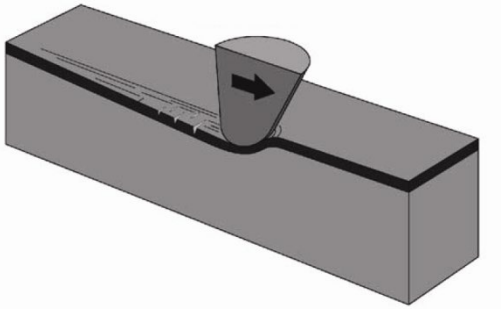

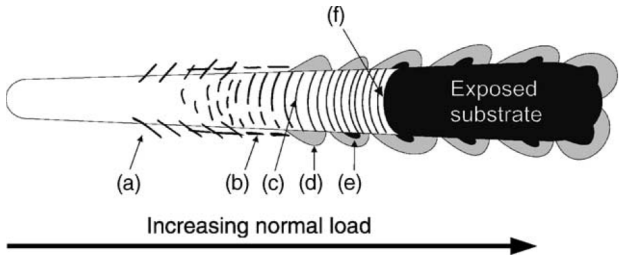

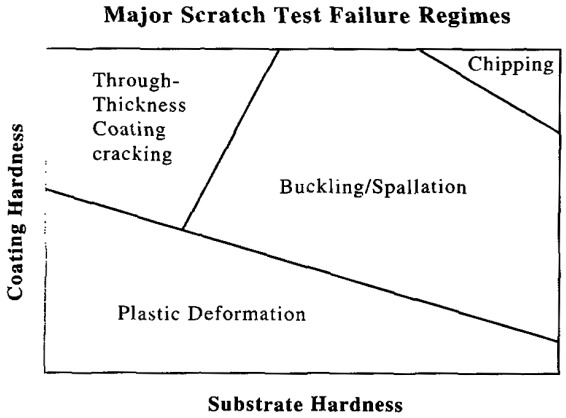

uniform width blisters

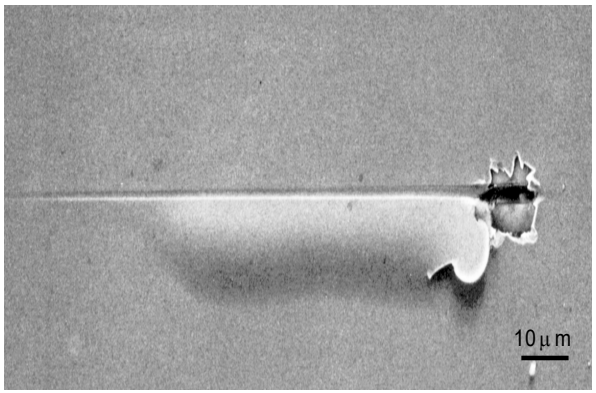

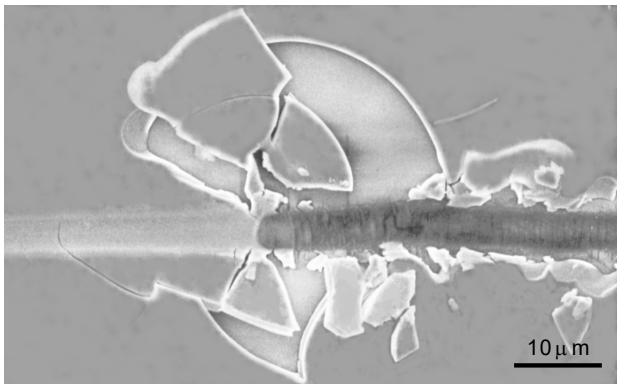

spalled blisters

Holmberg, Laukkanen, et al, *Wear.* 254 (2003) 278.

Hard coatings

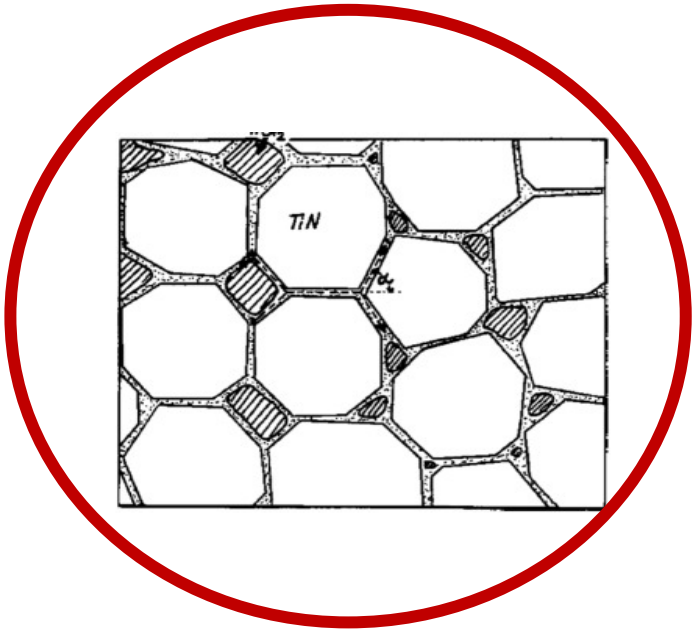

Introduction

Hard Coatings:

Class of **thin films** characterized by extremely **high hardness**, **very high melting points**, and **resistance to chemical attack.**

Deposited on tool substrates to protect engineering components (cutting tools, dies, punches, ball bearings, gas turbines,…) from severe external loading and harsh environments.

Coatings improve desired properties such as **hardness, friction, wear- and corrosion resistance**, without changing the properties of the bulk material.

Hardness: **hard** (20 GPa < H < 40 GPa) and **superhard** (H ≥ 40 GPa)

Typical thickness: 1 to 15 μm, deposited by different PVD and CVD methods

Classification of hard coatings:

I) Intrinsically according to the **nature of their chemical bonds** (covalent, ionic, metallic)
II) Extrinsically according to their **microstructure** (multilayers, nanolaminates, nanocomposites)

Applications

- Cutting tools
- Moulds for plastic processing
- Engine components
- Aircraft components
- Textile machine components
- Cutter blades
- General machine parts
- Household appliances
- Drilling tools for oil/gas industry and wind turbines
- Medical technology
- Decorative applications

DLC – coated piston pin

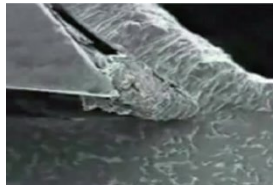

Cutting tools such as TiAlN

DLC-coated thread guide

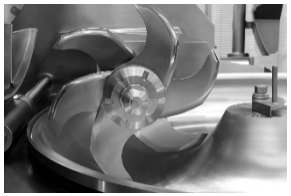

Cutter blades with a CrN coating

TiN or DLC coated Aircraft landing gear

DLC coated roller bearing

LC-coated ceramic washers

TiN-coated medical instruments

rosé gold, Ti or deep black DLC

https://oerlikon-balzers.bibliothek-der-technik.de/

Classification of Hard Coatings

Three groups are distinguished based on chemical bonding.
The nature of bonding relates to specific properties characteristic of each group.

nitrides, carbides and borides of Al, Si, B; diamond

transition metal nitrides, carbides and borides

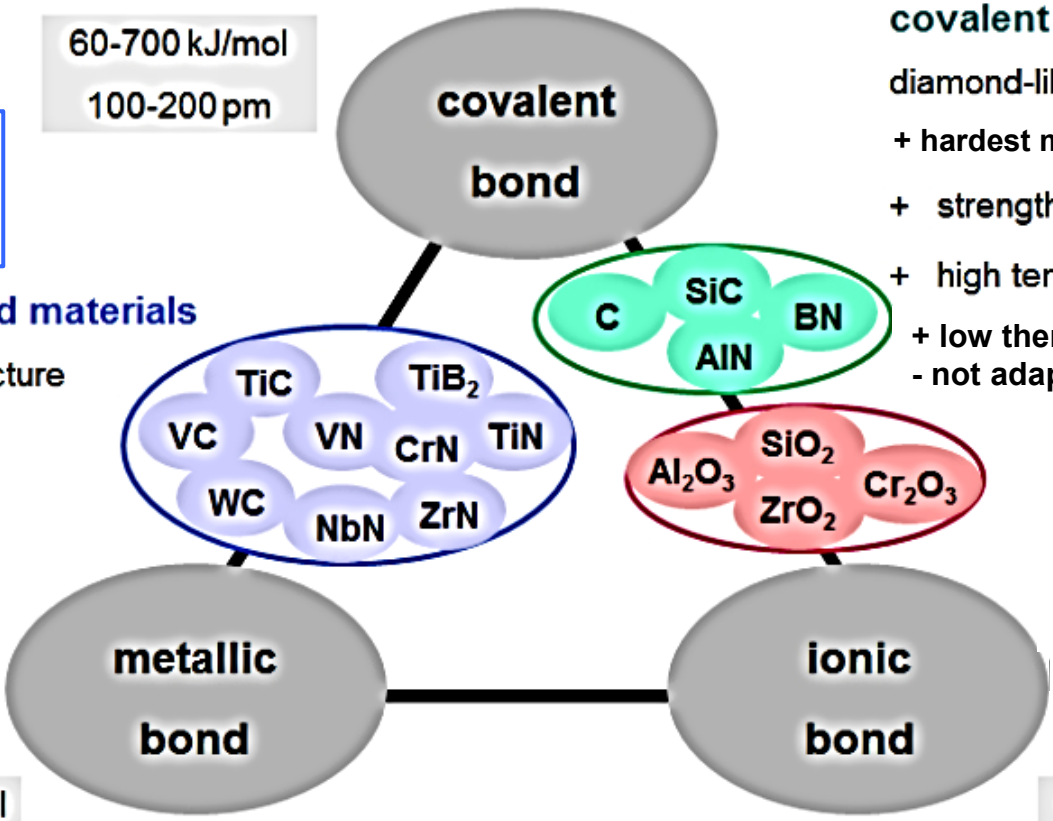

covalent hard materials

diamond-like structure

+ hardest materials (Diamond,c-BN)
+ strength
+ high temperature strength
+ low thermal expansion coefficient
- not adapted to metallic substrate at HT

metallic hard materials

metal-like structure

+ adhesion
+ toughness
+ ductility
+ high elastic modulus

ionic hard materials

ionic structure

+ hardness
+ thermodynamic stability
+ chemical inertness
- very brittle

hard materials: mixed bonds (covalent + metallic + ionic)

Holleck, H. in.Surface Engineering: science and Technology I. 1999.

Introduction

Table 12-1. Mechanical and Thermal Properties of Coating Materials

100 kg mm^{-2} ~ 1 GPa $H = H_0 e^{-aT}$ (Eq. 12-4)

Material	Melting or Decomposition Temperature (°C)	Hardness (kg-mm^{-2})	H_0 (kg-mm^{-2})	a (10^{-4} C^{-1})	Density (g-cm^{-3})	Young's Modulus (kN-mm^{-2})	Thermal Expansion Coefficient (10^{-6} K^{-1})	Thermal Conductivity (Wm^{-1} K^{-1})	Fracture Toughness (MPa-m$^{1/2}$)
Ionic									
Al_2O_3	2047	2100	2300	7.85	3.98	400	6.5	~ 25	3.5
TiO_2	1867	1100	1250	5.99	4.25	200	9.0	9	
ZrO_2	2710	1200			5.76	200	8.0	1.5	4–12
SiO_2	1700	1100			2.27	151	0.55	2	< 1
Covalent									
C (Diamond)	3800	~ 8000			3.52	1050	1	1100	
B_4N	2450	~ 4000			2.52	660	5		
BN	2730	~ 5000			3.48	440			
SiC	2760	2600	2800	0.90	3.22	480	5.3	84	3
Si_3N_4	1900	1700	1900	2.79	3.19	310	2.5	17	4
AlN	2250	1200			3.26	350	5.7		
Metal Compounds									
TiB_2	3225	3000	3500	18.9	4.5	560	7.8	30	
TiC	3067	2800	3300	18.3	4.9	460	8.3	34	0.46
TiN	2950	2100	2100	23.5	5.4	590	9.3	30	
HfN			2000	8.57			6.9	13	
HfC	3928	2700	3000	14.7	12.3	460	6.6		
TaC	3985	1600	1800	6.75	14.5	560	7.1	23	
WC	2776	2300	2350	3.62	15.7	720	4.0	35	
Substrate Materials									
High-Speed Steel	1400	900			7.8	250	14	30	50–170
WC-6%Co		1500				640	5.4	80	11.4
Ti	1667	250			4.5	120	11	13	80
Ni Superalloys	1280				7.9	214	12	62	> 100

Ohring 1992

Introduction

Coating	Material	H (GPa)	Main characteristics
Single layer	TiN, TiC, Al_2O_3	21, 28, 21	CVD at T around 1000°C on cemented carbides
Single layer	TiN, TiC	21, 28	PVD at $T \leq 550$°C on steel substrates
Multilayer	TiC/TiB_2	About 10^3 phase boundaries TiC/TiB_2 [2]	
Single layer	c-BN	50 [3]	High chemical affinity of C to iron
Single layer	diamond	90 [4]	Chemical dissolution of B in iron [5]
Single layer	TiAlN	Oxidation resistance up to 800°C [6]	
Single layer	DLC	65	Amorphous phase [7]
Single layer	CN_x	50–60	Substoichiometric (x=0.2–0.35) turbostratic structure [8], [9]
Superlattices	TiN/VN, TiN/NbN, etc.	~50	Superlattice period 5–10 nm [10], [11]
Single layer	nc-MeN/a-nitride	~50	Superlattice period 5–10 nm [10], [11]
Single layer	nc-MeN/metal	~50	Nanocomposite [13]
Single layer	$Ti_{0.4}Al_{0.6}N$	~32	Nanocomposite, oxidation resistance up to 950°C [14]

Musil 2000

Theoretical concept of hardness

- High **intrinsic hardness** related to:
  - a high binding energy (bond strength)
  - a short interatomic distance (small bond length)
  - a high degree of directional covalent bonding (ionicity and metallicity decrease hardness)
  - a high number of valence electrons per atom
  - a high number of bonds per unit volume

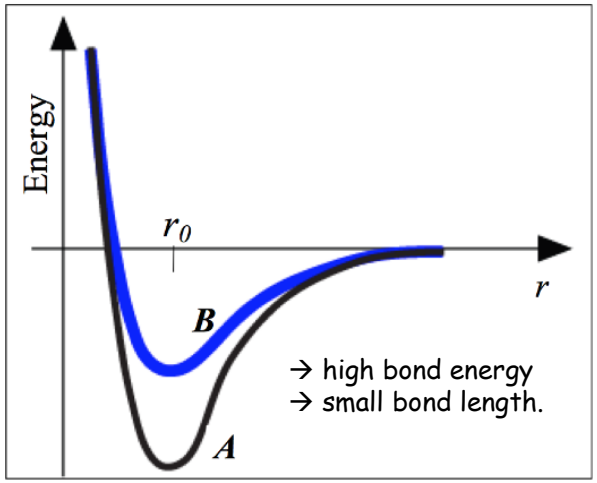

- Information about intrinsic hardness in **interatomic potential**!
- Search for ultra-hard materials supported by density functional theory (DFT) calculations (maximum possible)
- Similar to theoretical strength, crystal defects and microstructure influence actually hardness values.

Design Parameters

Hardness is not the only mechanical property to be considered

Some important parameters to be considered include:

- intrinsic hardness of the selected material (= the resistance to plastic deformation)
- hot hardness (hardness at working temperature of the tool)
- toughness (= the ability to absorb energy up to fracture) !
- adhesion to the substrate
- cohesion between different phases in the case of multi-phase coatings
- the residual stress in the deposited film (e.g. crack retardation by compressive stress)
- interactions with the substrate (inertness against workpiece material, low solubility)
- interaction with the environment in the chosen application (chemical stability, oxidation resistance)
- friction coefficient

- → no material can fulfill all requirements!
- → often the combination of different materials is required!

Design of Hard Coatings

The hard materials can be combined to form nanostructured coatings with e.g. enhanced hardness, toughness and oxidation resistance

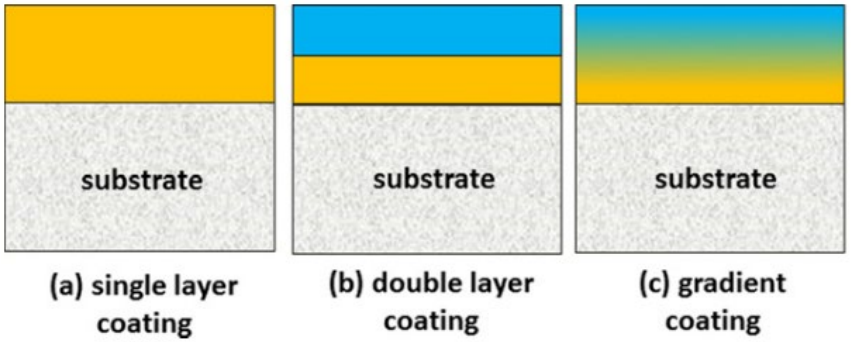

Double layer coating: properties of different materials can be combined.

→ adjust elastic properties and thermal expansion of the top layer to those of the substrate material

e.g. bottom layer: high hardness (high wear resistance)
relatively soft top layer: low friction coefficient & corrosion resistant

Gradient coating: can be used as an alternative to two discrete layers

Example: **TiCN coating**, in which the ratio between carbon and nitrogen atoms changes during deposition process.

Design of Hard Coatings

The hard materials can be combined to form nanostructured coatings with e.g. enhanced hardness, toughness and oxidation resistance

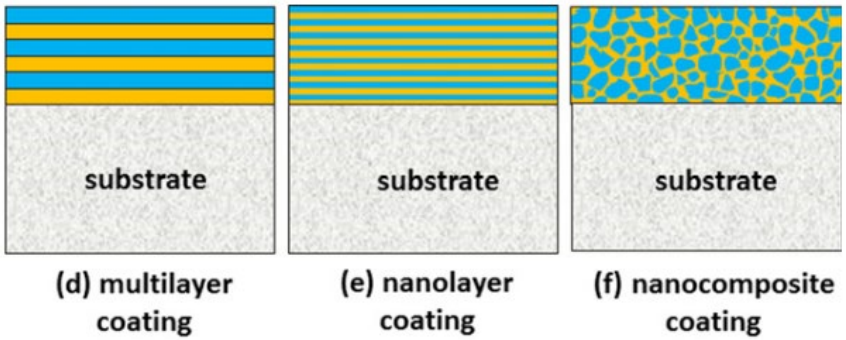

→ Superhard coatings, higher hardness than conventional coatings

Multilayer coating: double layer structure repeated several times. Hardness follows typically rule of mixture.

Nanolayer coating: individual layer thickness < 10 nm , the total number of layers increases to several hundred. Hardness well beyond rule of mixture due to size effects.

Nanocomposite: two-phase structure is formed during deposition. One phase segregates to the grain boundary of the second phase. The size of the grains is in the nanometer range. Hardness beyond rule of mixture.

Example: Nanocrystalline TiN embedded in amorphous SiNx

Nitrides and Carbonitrides I

Coatings based on **transition metal nitrides** like the face-centered **cubic (fcc) TiN**, deposited by CVD (1970) or PVD (1980) have been the **first to be commercially applied** for the reduction of tool wear in machining operations up to 1000°C.

To enhance the abrasion and erosion resistance of **TiN** (which is still often the standard coating used for a huge variety of applications), ***carbon is added at the expense of nitrogen***. This results in the formation of a stable solid solution $\mathbf{TiC_xN_{1-x}}$.

Coefficient of friction and transfer film thickness of TiC_xN_{1-x} versus number of cycles in a sliding test against Al_2O_3, Rebelo de Figueiredo et al., 2010

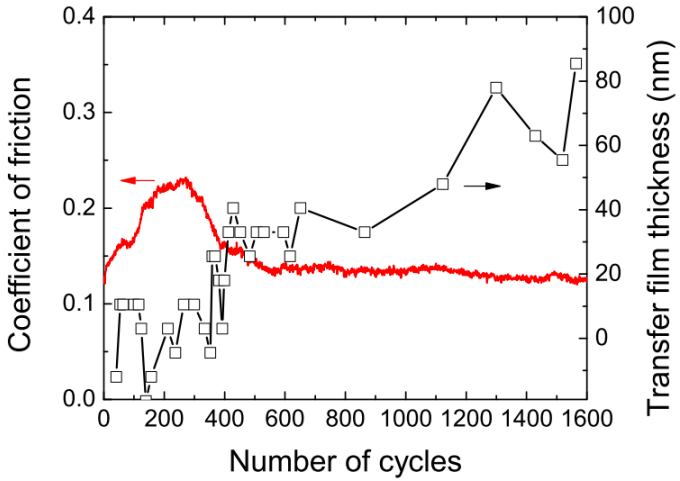

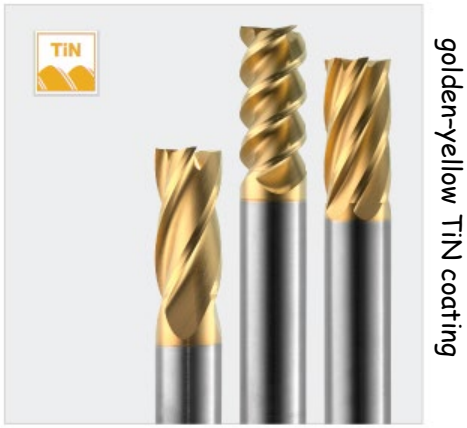

golden-yellow TiN coating

TiC_xN_{1-x} is also has **excellent friction properties.** The friction coefficient against alumina (TiN 0.6–0.8) is reduced to approximately 0.2. This is related to the *in situ* formation of **self-lubricious reaction layers** after a short running-in period in dry sliding contacts. Carbon released from the coating forms an easy shearable, a few nanometer thick reaction layer in humid environment.

Example for a *smart, self-adaptive coating with multifunctional properties*, combining **wear resistance and low friction**.

Nitrides and Carbonitrides II

$Al_xTi_{1-x}N$ introduced (1980). Al replaces Ti in TiN forming a **metastable fcc $Al_xTi_{1-x}N$** solid solution.

Superior **oxidation resistance**: formation of a **dual-layer protective oxide scale**, with a **dense α-Al_2O_3-rich top layer** and a rutile-type **TiO_2-rich layer underneath**. Oxidation onset $T_{ox.}$ could be shifted from ~550 C for TiN (500 for TiC_xN_{1x}) to ~700 C for $Al_xTi_{1x}N$.
$Al_xCr_{1-x}N$: stable and protective α-Al_2O_3-rich and Cr_2O_3-rich layers are formed in oxidative environments ($T_{ox.}$ > 1000°C).

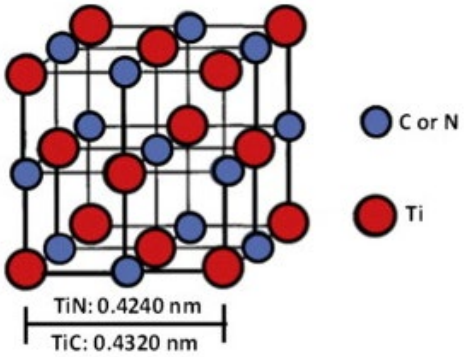

Metastable solid solutions undergo spinodal decomposition and **age hardening** at elevated temperatures. $Al_xTi_{1x}N$ decomposes in fcc TiN and fcc AlN domains between 700 and 900 °C, giving rise to a hardness increase due to coherency strains.

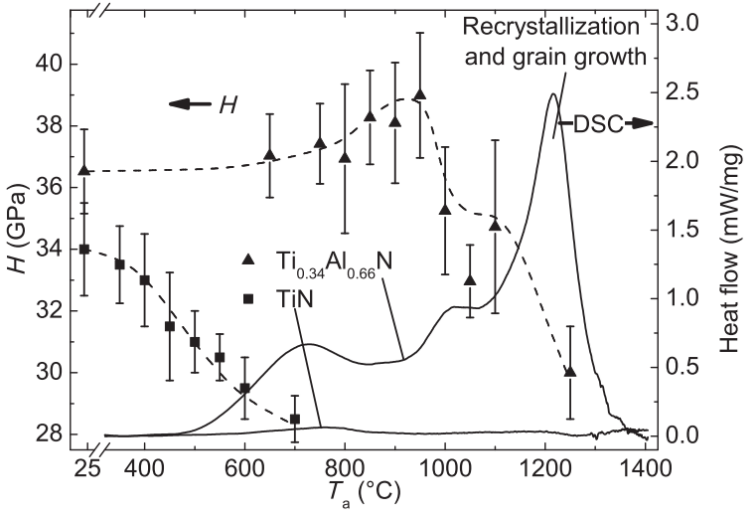

Mayrhofer et al 2003

For higher annealing temperatures, **overaging** with a coarsening of these domains and transformation of the fcc AlN into the stable hexagonal wurtzite-type AlN phase, as evidenced by differential scanning calorimetry (DSC), results in a **loss of hardness**.

Thermal stability: addition of Zr, Hf, Ta to replace Ti atoms
Oxidation resistance: low contents of Si and B → formation of protective oxide scales

Carbides

TiC was the CVD coating dominating the coating market in the early 1970s due to the **higher hardness** compared to TiN, which is a consequence of its **more covalent bonding** characteristics.

Essential **drawback** of CVD TiC coatings: large amount of the carbon needed is also supplied from the cemented carbide substrate. This results in *decarburization* and formation of a ***brittle*** *phase* in *surface-near zones of the* ***substrate***.

TiC coatings have thus been widely substituted by TiC_xN_{1-x}. In particular for carbon to metal ratios exceeding 1, a nanocrystalline dual-phase structure of the respective transition metal carbide plus a carbon modification is formed for both TiC and TiC_xN_{1-x}. The properties of these coatings are essentially dominated by the bonding within the carbon phase and its morphological arrangement, for example, in a **nanocomposite structure**.

"NaCl" structure

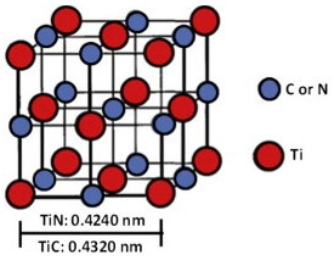

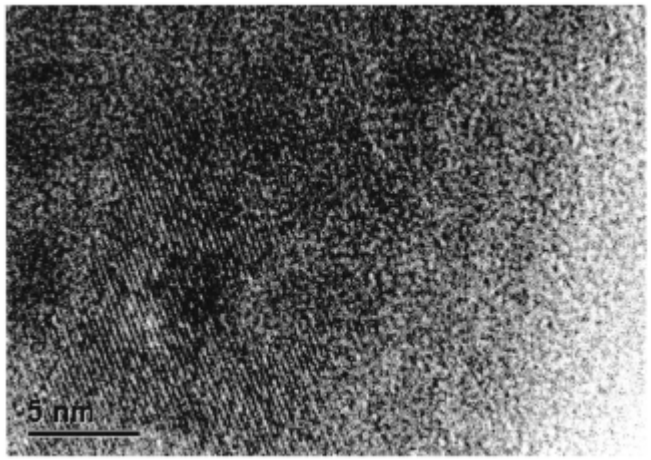

HRTEM of a nanocomposite **nc- TiC/a-C:H** coating.
Phase composition: 84 % TiC, 16% a-C:H,
Zehnder et al (J. Appl. Phys 95, 4327 (2004)

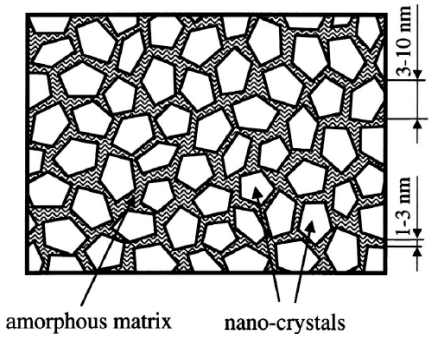

Borides

The structure of **borides** is governed by **covalent B–B bonds**, resulting in a higher bond strength and consequently hardness (> 40 GPa), elastic modulus, and melting temperature (unlike MeN/MeC with their dominating metallic binding character).

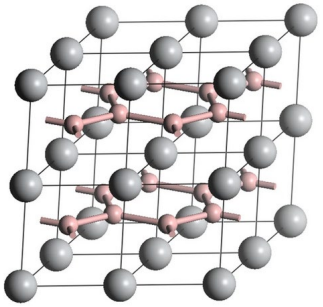

Hardness values are well above those of bulk TiB_2 (approximately 34 GPa) and have been related to a nanocolumnar structure formed by self-organization in sputtered overstoichiometric TiB_{2+x}. Such structures are often found in sputtering from TiB_2 targets due to the different scattering probabilities of Ti and B atoms during the transport from the target to the substrate.

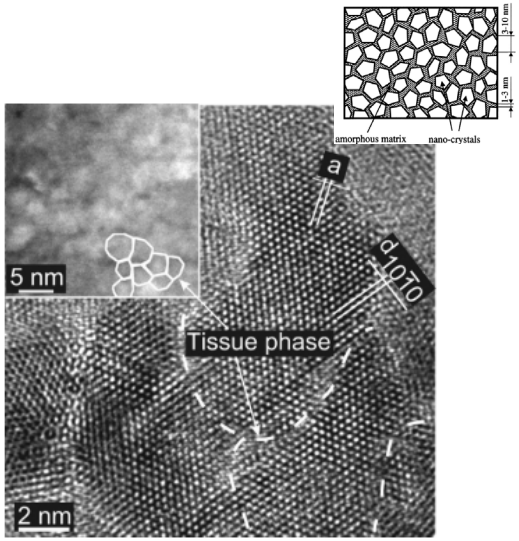

Columns with a (0001) preferred orientation of the hexagonal TiB_2 phase and diameters of ~ 20 nm are encapsulated in the excess B. The columns themselves are composed of bundles of coherent ~ 5 nm diameter TiB_2 subcolumns, separated by a disordered 1–2 monolayers thin B-rich tissue phase. Mayrhofer et al. 2005

TiB_2 coatings are used for machining of aluminum alloys due to high hardness and chemical inertness against Al, which has a pronounced adhesion tendency to nitride coatings in cutting applications, forming build-up edges.

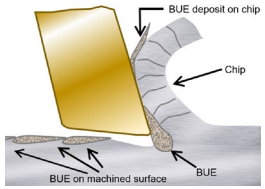

https://www.youtube.com/watch?v=uwh3ouvzSLk

Oxides

Among the oxides, **Al_2O_3** is dominating as a wear-protective coating for cutting tools, due to its unique combination of **chemical inertness, thermal stability, and hot hardness**.

Polymorphism: Beside the **stable hexagonal α-Al_2O_3** (also denoted as corundum, sapphire, or α-alumina), several **metastable polymorphs** (γ, δ, κ, η, θ, χ) and amorphous phases exist. The phase formed is determined by the **deposition process itself and its parameters**, with α- and κ-Al_2O_3 usually being synthesized by CVD and γ-Al_2O_3 by PVD processes.

Essentially, the **substrate temperature** and the application of **seed templates** determine the formation of these polymorphs. Typically, below a deposition temperature of 800 °C in CVD amorphous Al_2O_3 is formed. Most often, a TiC_xN_{1-x} **base layer** is used in CVD, to provide the necessary adhesion of the Al_2O_3 top layer.

Transformation of the orthorhombic κ -Al_2O_3 into the stable α-Al_2O_3 modification occurs at a temperature of approximately 1000 ° and results in **coating cracking and delamination** due to the associated volume change.

The **PVD** of Al_2O_3 coatings is **still a challenge**, mainly due to their **electrically insulating nature**, requiring pulsed d.c. or r.f. plasmas. At low deposition temperatures, coatings are reported to be X-ray amorphous. Between 350 and 550 °C, crystalline cubic γ -Al_2O_3 is grown, the desired α-Al_2O_3 modification requires 700 °C.

To exploit α-Al_2O_3 as a wear-protective coating on high-speed steel cutting tools, deposition **temperatures below 600 °C** are required to avoid **softening of the substrate**. The most efficient **template or stabilizer** for α-Al_2O_3 growth known up to now is Cr_2O_3, which is isostructural with corundum (synonym to α-Al_2O_3).

Nanostructured coatings

→ Different mechanisms can lead to the hardening of a crystalline material, mainly acting by **hindering or the retarding the deformation generated by dislocation movements**.

→ additionally toughness, thermal stability and oxidation resistance are enhanced through microstructural design

Hard nanostructured coatings can be divided into two main classes:

- **Hard multilayers/nanolayers/nanolaminates** (and **superlattices**), with a composition and phase modulation in one direction of space i.e. the growth direction
- **Hard nanocomposites**, the structure of which is modulated in all three direction of space, with a characteristic length at the nanometer scale

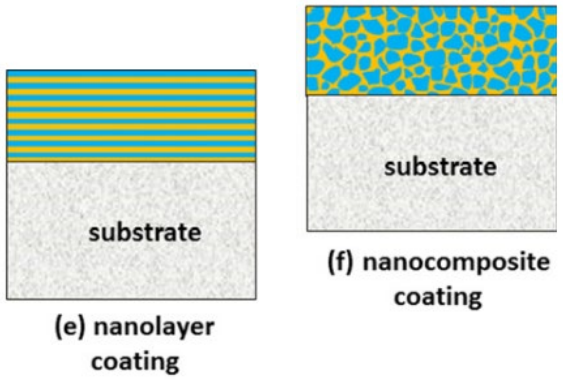

(e) nanolayer coating

(f) nanocomposite coating

Nanostructured Hard Coatings - Multilayers

In multilayered and superlattice films two or more nanometer thick layers of different materials are periodically alternated to produce a total film thickness of several micrometers.

Formation of dislocation and nanocracks and their propagation is strongly prohibited, similar to nanocrystalline materials with strong boundary regions.

Typical toughening mechanisms observed in multilayer films :

- crack deflection at interface between layers,
- ductile interlayer ligament bridging and crack tip blunting
- interface delamination

All cause **extra energy consumption** and dissipation during crack propagation.

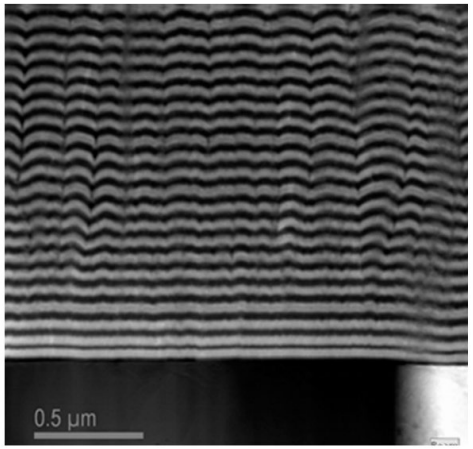

Figure 2 SEM image of CrN/TiAlN layers deposited on a steel substrate.

These effects can be even enhanced if materials with high and low elastic properties are used. Dislocations cannot be transmitted across individual layers since they need to overcome very high repulsive image stresses.

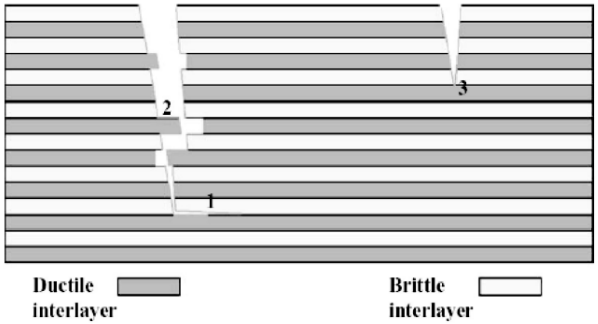

1) Crack deflection
2) Ductile interlayer bridging
3) Crack tip blunting

Superlattices

Heteroepitaxial multilayer structure with an individual layer thickness of nanometer scale.

Source of hardening: high number of interfaces, different shear moduli & coherency strains

Typical maximum hardness and toughness obtained at 5–10 nm bilayer period thickness.

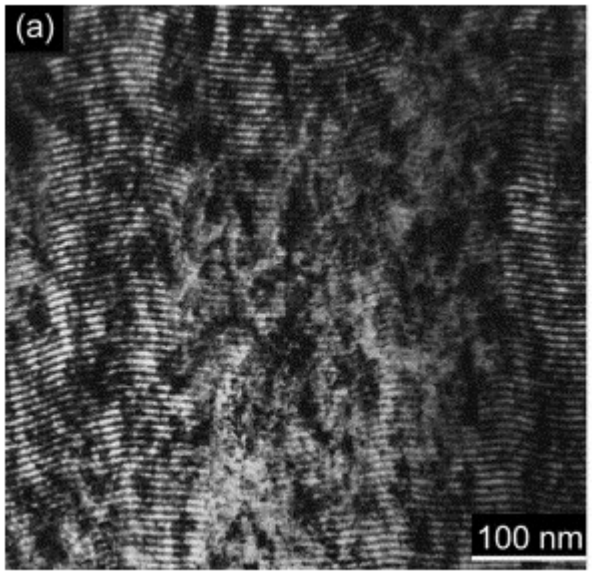

TiN/NbN multilayer
Modulation period 7.2 nm
Mayrhofer et al 2006

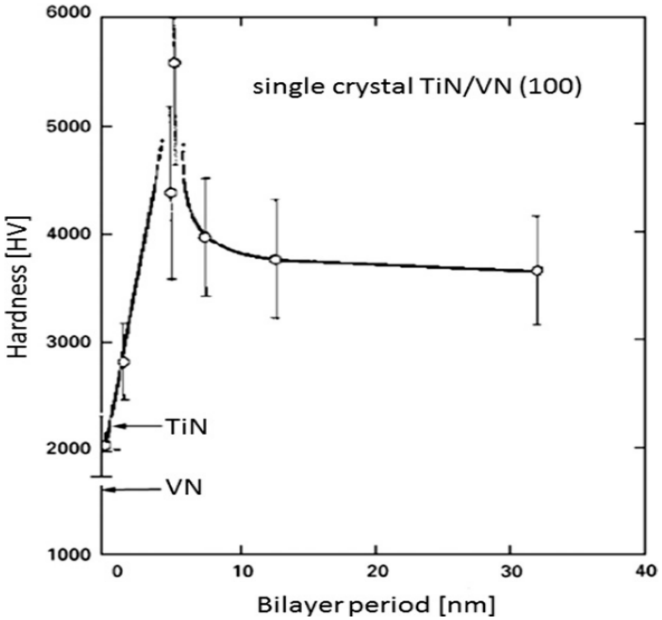

Figure 4 Hardness change of nanolayer TiN/VN coating as a function of bilayer period.[37]

Caliskan et al 2017

More complex Nanolaminates

DF-STEM & EDX

BF-STEM

DF-STEM

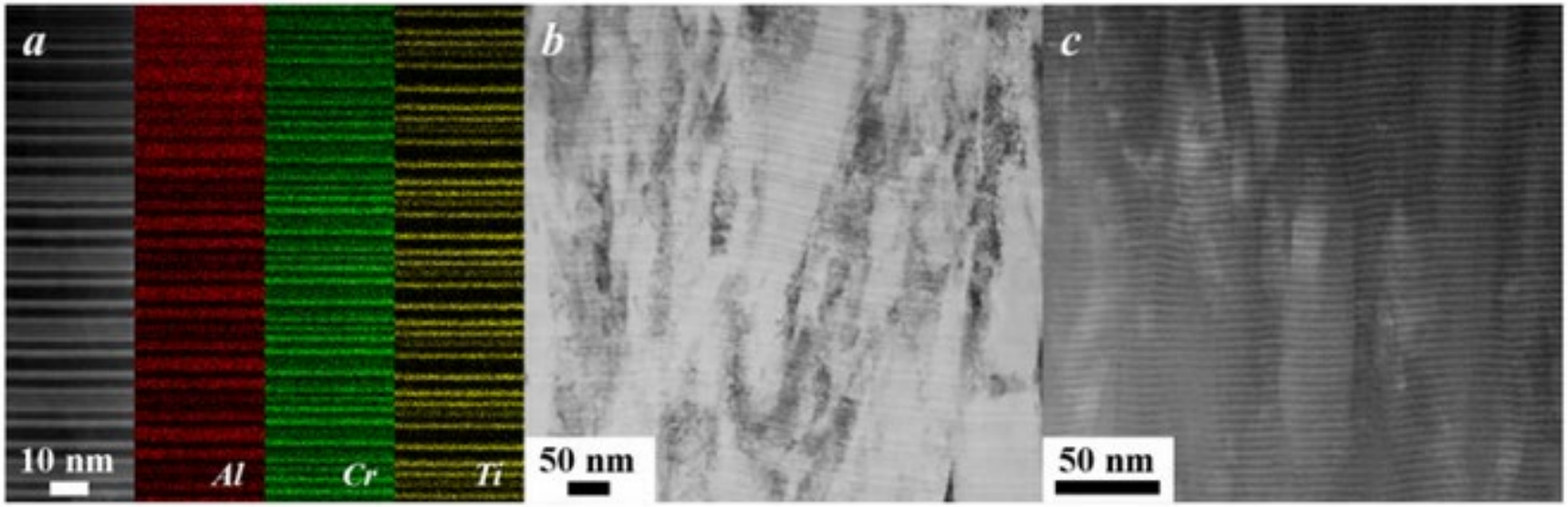

$TiN/AlCr_{30}N/CrN/AlN$ $AlSi_{18}N/CrN/AlCr_{30}N/CrN$ $TiN/AlTi_{33}N/AlTi_{33}N/AlN$

Best et al. 2019

grain growth through the nano-layers.

Nanostructured hard coatings – Nanocomposites I

Nanocomposites composed of at **least two separated phases** with a **nanocrystalline** and/or **amorphous structure**. The formation is principally attributed to a **segregation** of one phase **to the grain boundaries** of the second phase. This effect is hindering grain growth and forms the structure in the nanometer scale.

Hardening mechanism: **Grain refinement** + **Grain boundary hardening**

H_0 ...intrinsic hardness
d... grain size
k... constant for a given material

$$H = H_0 + k d^{-0.5}$$

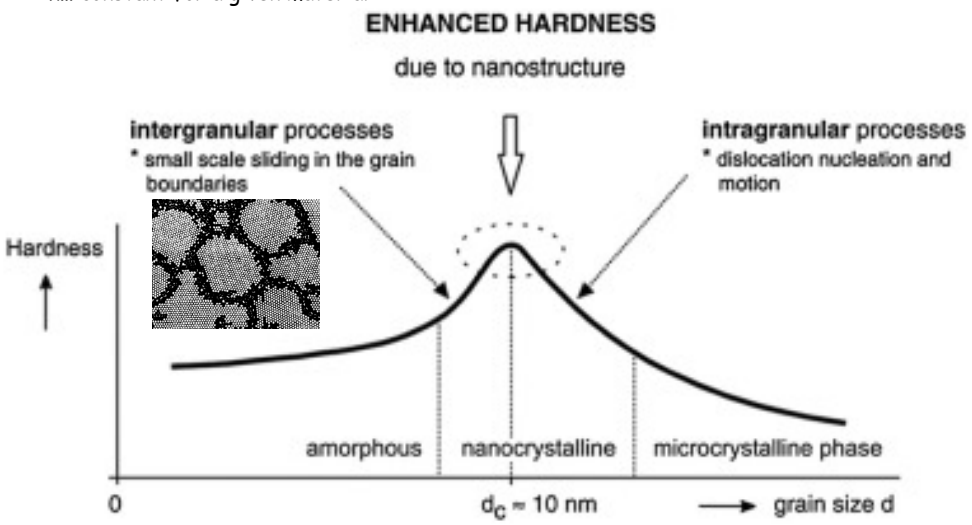

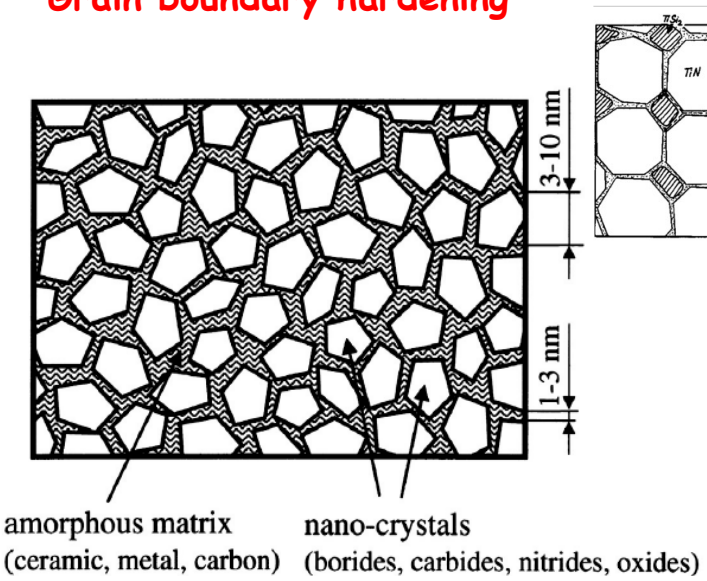

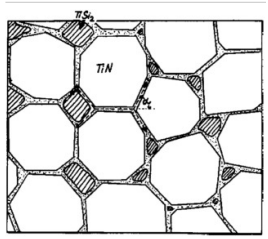

- Hall Patch equation governs coarse-grained materials (d > ca. 30 nm).
- Maximum hardness is achieved when d is close to ca. 10 nm.
- Below grain boundary sliding becomes dominant as a large fraction of atoms is located at interfaces
  → inverse or reverse Hall-Petch effect.

- Further hardening via **grain boundary strengthening**
- **Very small grains (≤ 10 nm)** separated by second, mainly amorphous phase
- Highest hardness > 40 GPa when separating tissue is only a few monolayers (1-3 nm)
- plastic deformation of the tissue phase by grain boundary sliding is limited

Nanocomposites II: TiN/Si_xN_y

Simultaneous evolution of nanohardness and coating microstructure as a function of Si content

A: Hardness increases due to grain refinement induced by the introduction of a-Si_3N_4

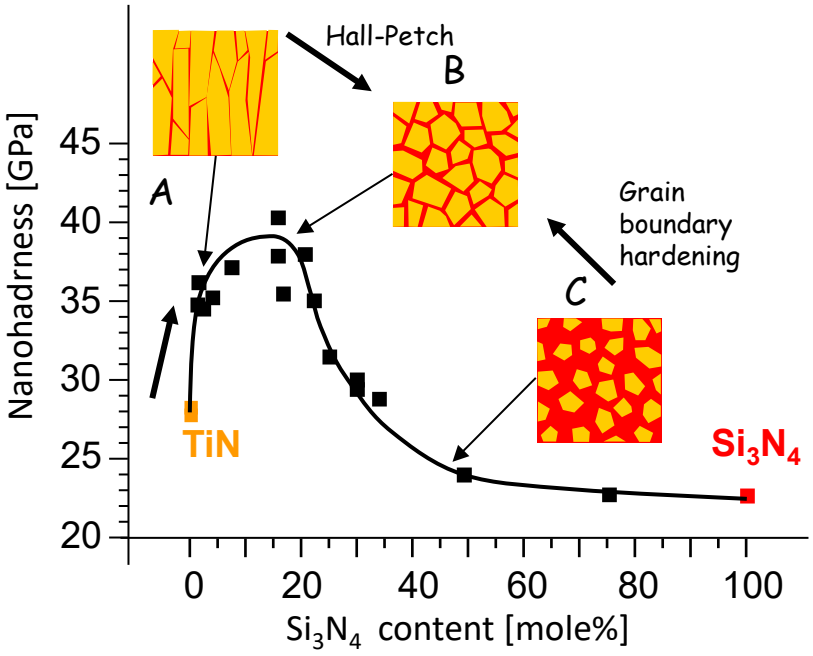

B

Hardness maximum is located in relatively small range of silicon concentration. Dislocation activity is hindered in grains < 10 nm. Thin Si_3N_4 (1-4 monolayers) prevents grain boundary sliding

C

Propagation of nanocracks in a-Si_3N_4 progressively becomes the dominant process. Hardness reaches values of pure Si_3N_4 phase

Two main groups of nanocomposite films:

- **nc-MeN(C,B,O) / hard phase** (e.g. SiN_x) is composed of **two hard phases**
- **nc-MeN(C,B,O) / soft phase** composed of **one hard and one soft** phase (e.g. Cu, Ni, Fe, Mo, Y, Ag, Co etc.)

(Me =Ti, W, V, Zr, Cr,[Ti1−xAlx], [Cr1−xAlx], [Zr1−xAlx], etc.)

Courtesy of J. Patscheider, Empa

TiN/Si_xN_y nanocomposite coatings

The nanostructure is a consequence of composition and process conditions
Principle: small crystalline grains + strong boundaries

Overall properties:

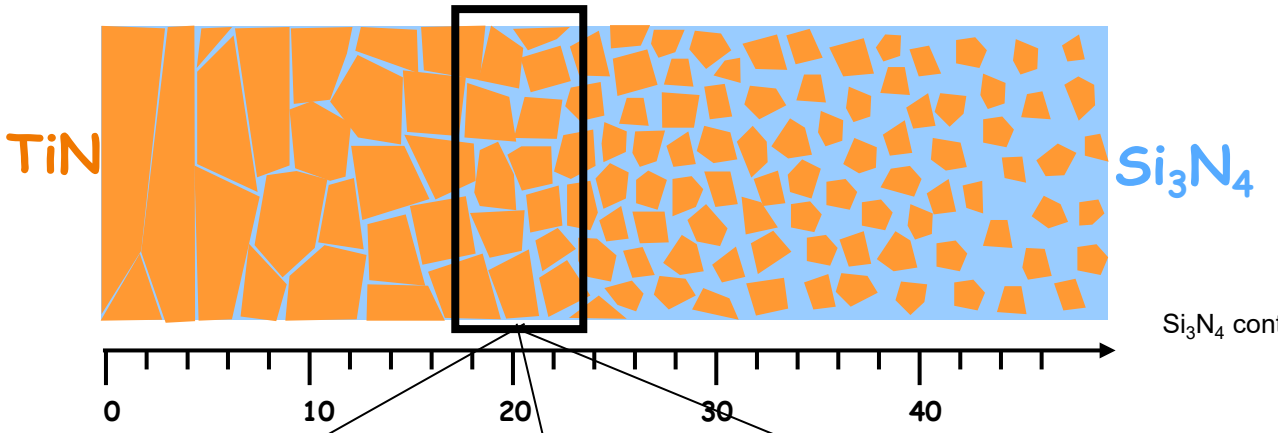

High hardness
above 30 GPa
due to the nanostructure

Oxidation resistant
by encapsulation with Si_4N_3
20 x better than TiN

Nanostructure is **thermally**
stable up to 950°C

Improvement of thermal stability by addition of various phases may result in reduction of hardness or other mechanical properties.

Include elements or phases of high thermal stability that hinder grain growth for a stable film structure

Courtesy of J. Patscheider, Empa

Arc plasma deposition

Arcs are **high-current** (tens to hundreds of amps), **low DC voltage** (tens of volts) gas discharges.

A very luminous small cathode spot (10^{-8} to 10^{-4}m diameter) forms that passes **extremely high current densities (~ 10^8 to 10^{12} A/m^2)**. This causes **erosion of the cathode by melting and vaporization** as well as **ejection of solid and molten particles**.

A schematic of a cathodic-arc deposition system is shown, where microscopic events at a cathode spot are also depicted. Particularly important in these systems is the **arc ignition mechanism**, sometimes a mechanical Striker but more often ignition by means of a break arc, and the means to confine the arc spot to the cathode surface.

To achieve **uniform film deposition the arc is steered magnetically**, which causes material to be eroded from the cathode in a series of flash evaporation events.

The metal ions and neutrals emitted are normally the desired species, whereas **microdroplets that manage to impinge on the substrate are a primary concern**. They arise from ablation of molten or solid cathode particles due to thermal shock

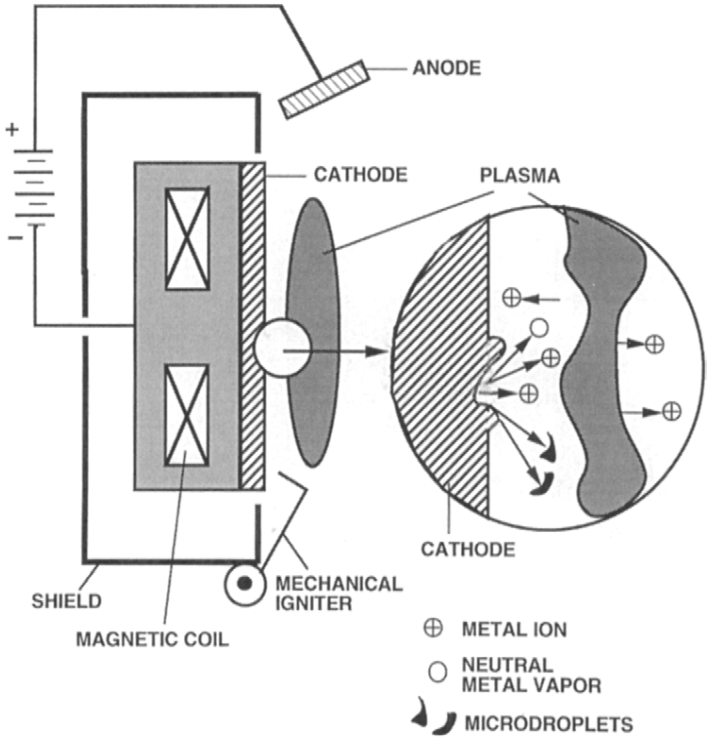

Ohring 2002

Cathodic arc plasma deposition

The medium which is the **primary current conductor is the ionised vapour** from one of the two electrodes.

Local melting spots with diameters in the range between a few tens of µm up to several hundred µm are formed.

These spots typically exist simultaneously at different locations on the surface of the cathode. **Atoms and ions are emitted together with droplets** of metal in a diameter range of a few hundred nm to a few tens of µm.

Due to the high local currents (power densities), **the majority of the vaporised material becomes ionised**, usually with a **degree of ionisation between 20 % up to nearly 100 %.** The ions often exhibit multiple ionisation and are accelerated to velocities between 10^4 m/s and 10^5 m/s during the evaporation process.

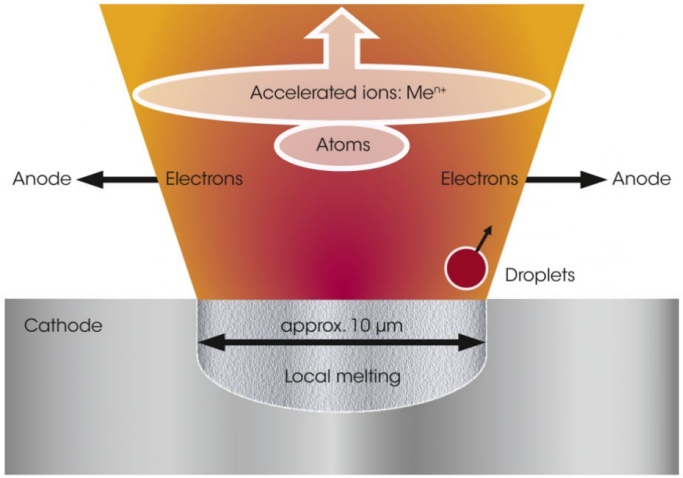

https://oerlikon-balzers.bibliothek-der-technik.de/

Cathodic arc plasma deposition

To cool the cathode, it is typically attached to a water-cooled evaporator body.

The arc is guided to the surface which is to be vaporised by means of suitable magnetic fields (magnetic flux density of typically 1 mT to 10 mT), which are generated using permanent magnets, electromagnets or a combination of these magnet types.

The image shows the arc track in a nitrogen atmosphere. The red glow is caused by the plasma excitation of the nitrogen. The medium which is the **primary current conductor is the ionised vapour** from one of the two electrodes.

The plasma exhibits a high concentration of ionised metal vapor with energies up to 100eV, which leads to dense and well adhering coatings.

For materials with high vapor pressure the ionisation degree is 5% and for those with low vapor pressure up to 100%. This leads to almost **stöchiometric compounds** through reaction with reactive gases.

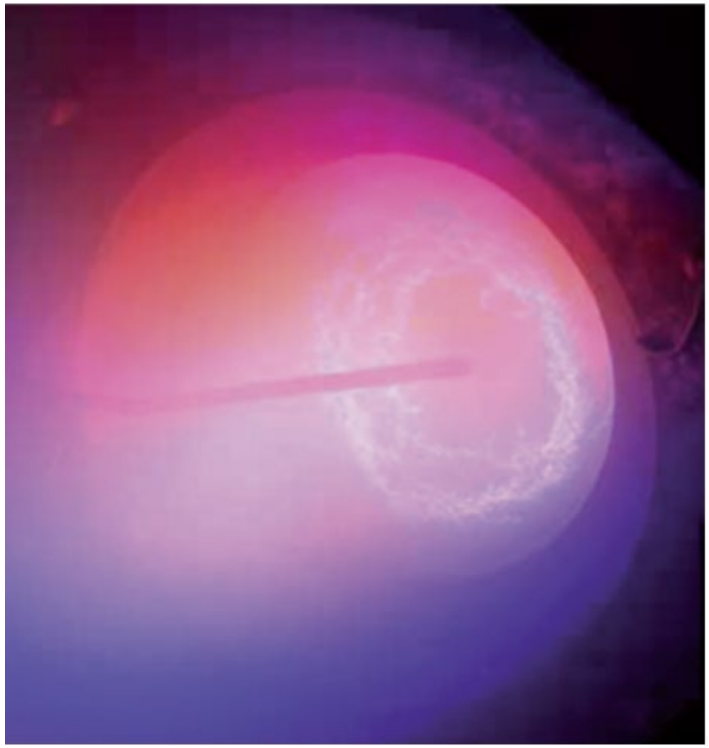

https://oerlikon-balzers.bibliothek-der-technik.de/

Cathodic arc plasma deposition

reactive gases are added at a controlled rate in a pressure range of 0.1 Pa to 10 Pa,

the round evaporators are flanged onto the wall of the chamber. Mechanical triggers generate the break arc for igniting the discharge.

several rows of evaporators allow for deposition of multilayer coating systems.

Using a row of evaporators with TiAl cathodes and an additional row of evaporators with TiSi cathodes, it is possible to create alternating TiAlN/TiSiN nanolaminates on rotating substrates.

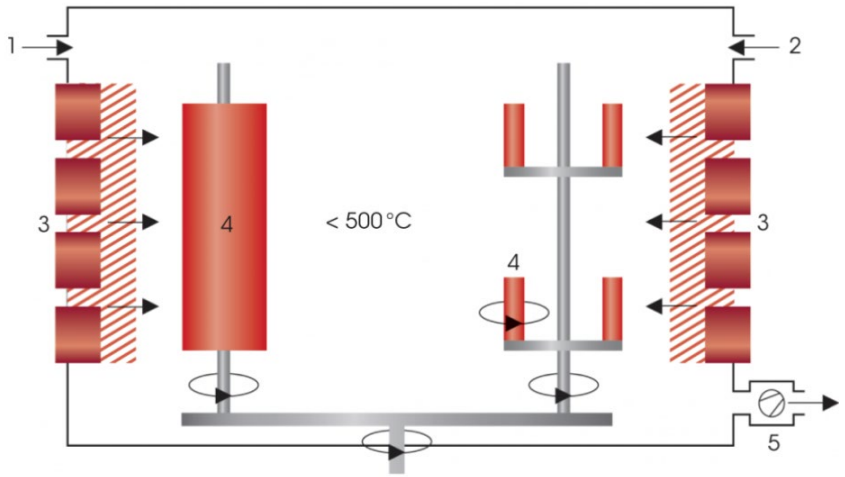

Fig. 11: Schematic layout of a coating chamber for cathodic vacuum arc evaporation
1 Argon
2 Reactive gas
3 Arc evaporator with coating material
4 Components
5 Vacuum pump

https://oerlikon-balzers.bibliothek-der-technik.de/

Cathodic arc plasma deposition – example from Platit AG

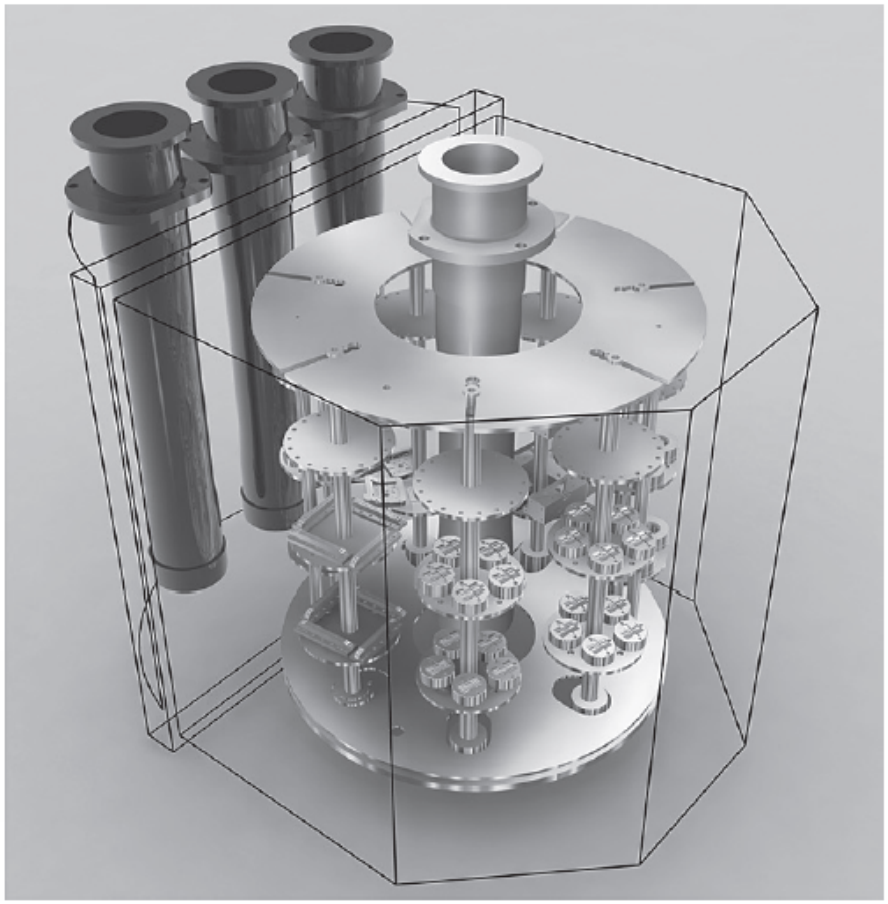

Blasek 2010

Cathodic arc plasma deposition

Cathodic arcs have been widely used in vacuum as well as reactive atmospheres to commercially deposit a large assortment of metal alloy and compound films.

In general **nitrides, carbides, oxides** and **mixtures** of these as well as **hard amorphous carbon coatings (DLC)** and **metal films** can be depositied.

The major application of refractory nitrides, carbonitrides, and carbides has been to wear- and abrasion-resistant **coatings in forming and cutting tools.**

Unlike CVD methods, the coatings are deposited at lower temperatures which **generally yield harder, finer grained deposits; furthermore, tool distortion is minimized**.

Interestingly, advantage is taken of the broad color range of **several binary and ternary nitrides in decorative coatings, e.g., for watch bands and eyeglass frames.**

Additionally, amorphous and diamond-like carbon films have been deposited in cathodic arcs, and optical coatings have been produced using anodic arcs.

Ohring 2002

high-power impulse magnetron sputtering (HiPIMS)

In the **magnetron modes of operation** described thus far, **the ionisation of the plasma lies significantly below that of cathodic vacuum arc evaporation** and the sputtered material in particular evidences a low degree of ionisation. In some cases, this has a negative effect on the coating properties.

In traditional magnetron sputtering processes for hard coatings, the **power density at the target is between 5 W/cm² and 30 W/cm²**. To significantly increase the ionisation of the material, the power density at the target must be **increased by a factor of 10 to 100**. This can be accomplished using **high-power impulse magnetron sputtering** (HiPIMS).

In classic high-power impulse magnetron sputtering, power densities in the range **hundred W/cm² up to several thousand W/cm²** are achieved temporarily.

A process of this nature **cannot be operated continuously** because otherwise the **target would overheat**.

https://oerlikon-balzers.bibliothek-der-technik.de/

high-power impulse magnetron sputtering (HiPIMS)

Consequently, short pulse durations with a high pulse power are employed (even into the MW range).

The pulse duration is usually in the range of 25 µs to 250 µs.

The pauses between two pulses are typically a few milliseconds long.

Often, frequencies of 10 Hz to 100 Hz are pulsed.

Depending on the target material and the pulse shape, the ionisation values of the sputtered material in the plasma can be several 10 % up to nearly 90 % of the values obtained with cathodic vacuum arc evaporation.

This makes the deposition of very dense coatings possible.

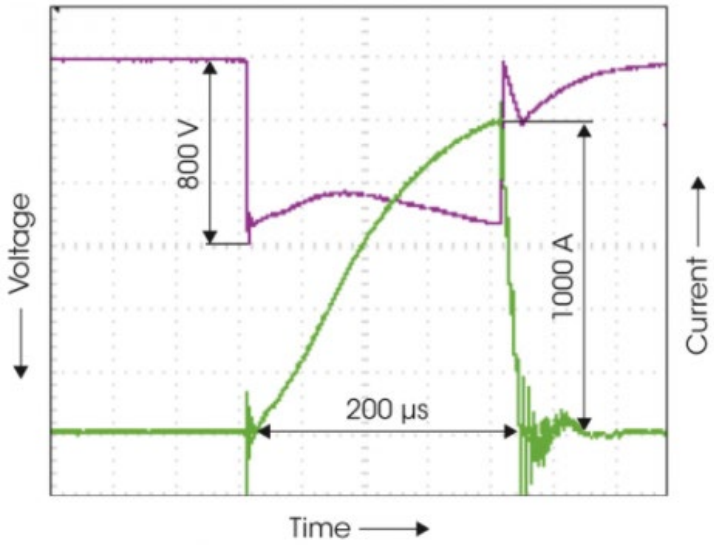

https://oerlikon-balzers.bibliothek-der-technik.de/

a coating centre (Platit AG)

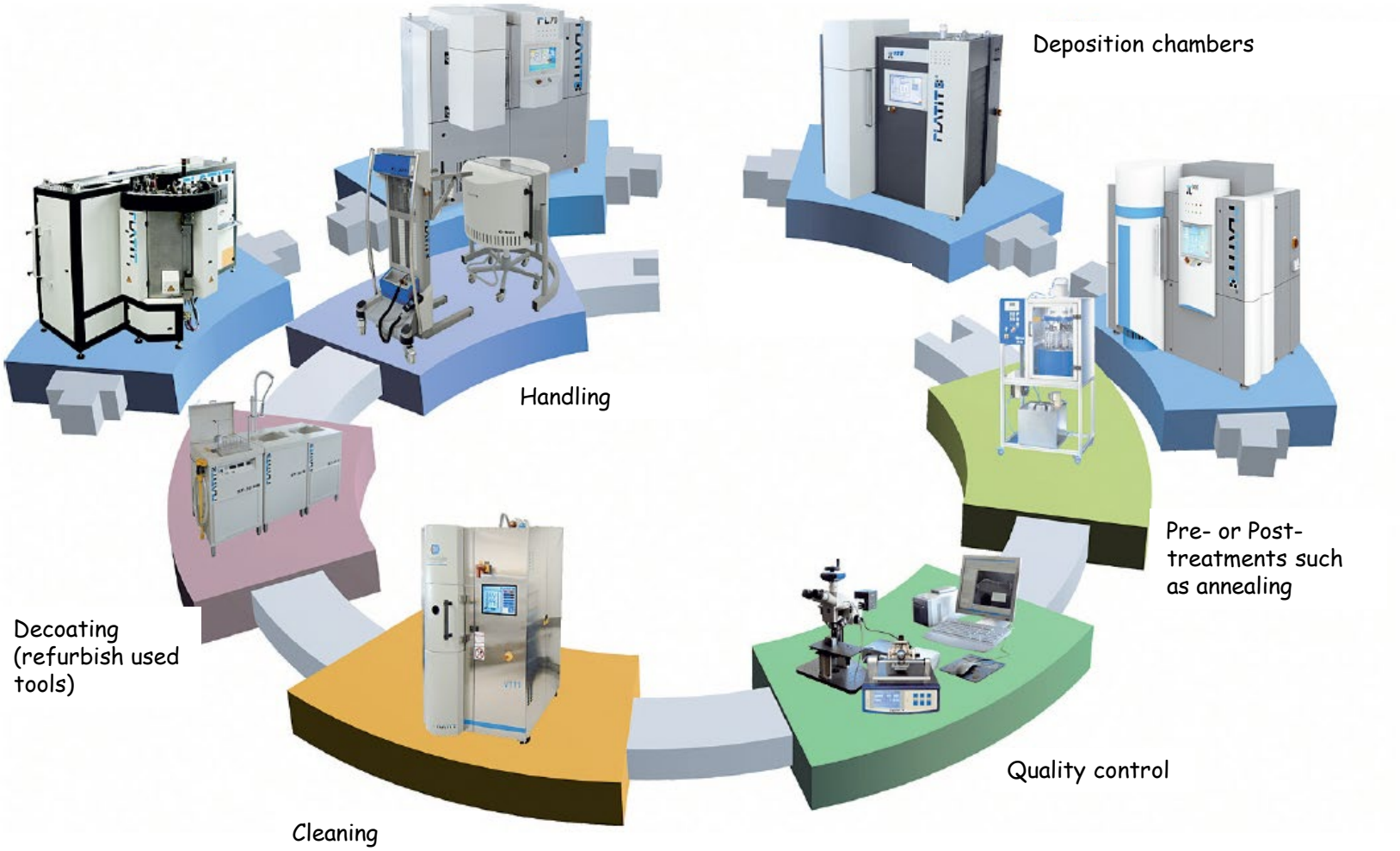

Blasek 2010

summary I

- Interface crit. energy release rate vs residual stress
- Atomistic view: chemical bonding?, Kirkendall effects, interface mixing due to ion bombardment, mechanical locking
- Adhesion mechanisms, improvement: glue layer (oxide role), ion beam processing (energy!), polymers (plasma) activation of surface
- Measurement techniques adhesion: tear-off test (not quantitative), Rockwell adhesion, scratch techniques
- Nanoindentation: hardness under maximum load of 3-sided Berkovich tip. Young's modulus from linear unloading curve
- Thin film indentation: thin ice effect, 1/10 , fracture toughness difficult due to unknown crack path

summary II

- Definition hard coatings: hard 20-40GPa, superhard >40GPa, ~10 μm thick, intrinsically + extrinsically hardness contributions
- Applications: cutting tools, moulds, machine parts, medical & decorative
- Classifications: metallic: transition metal –N/C/B; covalent: c-BN, SiC, Diamond; ionic: Al/Si/Zr/Cr – O
- high intrinsic hardness: high binding energy, short interatomic distance, high degree of covalent bonding, high number of bonds per unit volume, modelling opportunity for search by DFT
- Desired properties: High (hot) H, K_c, $G_{adhesion}$, G_c between phases, low $\sigma_{res,}$ no reaction with substrate & environment, low friction coeff against material in application -> layered/gradient film to catch all properties & nanostructured for high extrinsic hardness
- Nitrides & Carbonitrides: "fcc TiN archetype", TiCN self-lubricating C layer, AlTiN and $Al_xCr_{1-x}N$: oxidation resistant -> oxides of Al & Cr, AlTiSiN forms superhard coating with AlTiN nanocrystals in a-SiN matrix
- Carbides: "fcc TiC archetype" with more covalent bond compared to TiN, TiC_xN_{1-x} better against C outdiffusion, TiCN nanocrystals in a-C:H matrix
- Borides: hexagonal TiB_2 with covalent B-B bonds, TiB2 nanocrystals in excess B-rich matrix, used for cutting of Al as Nitrides don't work
- Oxides: "hex Al_2O_3 archetype" but many polytypes, dominating for cutting tools (oxid resistance & hot hardness)
- Nanolayers: nanolaminates incl. epitaxial superlattices; toughening of nanolayers via crack deflection, ductile interlayers and interface delamination; superlattices with additional toughening with coherency strains, dislocation arrays at interfaces and oscillating Youngs Modulus (compared to single crystals)

summary III

- Nanocomposites: strength due to grain refinement (Hall-Petch) and preventing GB sliding due to amorphous tissue phase at GB. Max hardness with 10nm grain size and 1-3nm tissue phase
- Arc plasma deposition: high I - low DC voltage, magnetically steered μm - sized spot with 10^{10} A/cm^2 leads to melting/evaporation/ejection of particles, ionization degree up to 100% leads to stöchimetric compounds in reactive arc deposition, ion energies up to 100eV leads to dense, well adhering films; samples (cutting tools etc.) on rotating planetary holder allows for nanolaminate deposition, all hard coatings possible but mostly used for forming and cutting tools as smaller grains compared to CVD as lower deposition T
- high-power impulse magnetron sputtering (HiPIMS): power densities on target like arc through 100μs pulses with 10-100Hz with almost 100% ionization degree and high energy ions leading to dense and well adhering coatings, but without particles as in arc deposition
- Coating process line includes handling, decoating, cleaning, QS, pre/post annealing and actual deposition equipment

Summary – stresses in thin films

Stress in thin films

- Film exerts bending moment on substrate plate which leads to curvature=1/R
- Stoney equation is independent of film properties: $\sigma_f = \left(\frac{E_s}{1-\nu_s}\right)\frac{t_s^2}{6t_f}(\kappa - \kappa_o)$
- In textured films biaxial film modulus for <111> and <001> textures used, <110> more complicated
- In plane Young's modulus depends on grain size (10%less for <10nm), texture (up to 2x), porosity (~ porevolume^2)
- Stress of 1st, 2nd, 3rd order
- methods for residual stress
  - Mechanical methods: Substrate curvature via laser deflection, bending of FIB bi-metal beam
  - (Fib-)Hole drilling & edge relaxation,
  - XRD (sin2 Ψ - method measures out of plane strain and converted to in-plane stress, epi-layers and reciprocal space map,
  - Raman spectroscopy stress dependence of opt phonon frequency,
  - EBSD cross.correlation method
  - Cantilver beam methods
  - Method comparison: spatial (lateral & depth), and spectral resolution
- Types of stresses (thermal, instrinsic, epitaxial) $\sigma = \left(\frac{E}{1-\nu}\right)_f \varepsilon = -\left(\frac{E}{1-\nu}\right)_f (\alpha_f - \alpha_s)\Delta T$ $\sigma_1 = \sigma_2 = \left(c_{11} + c_{12} - \frac{2c_{12}^2}{c_{11}}\right)\varepsilon_1 = \left(c_{11} + c_{12} - \frac{2c_{12}^2}{c_{11}}\right)\left(\frac{a_s - a_f}{a_s}\right)$
- Intrinsic: Capillary, Laplace pressure of islands, Zip stress during coalescence
- Stress evolution after coalescence, Impurities, vacancies, ion bombardment
- Evolution during growth: Capillary stress: Laplace-Young equation $p=2\gamma_s/r.$; Zip stress like healing crack, following coalescence either compressive due to epitaxy, relaxed due to adatom mobility or compressive due to incorporation of excess atoms (at GB, or bigger Ar atoms)
- Evolution during or after: vacancy annihilation, densification, crystallization, grain growth
- The stress dilemma: intrinsic stress relaxes at high deposition T, thermal increases

summary – mech properties and hard coatings I

- Interface crit. energy release rate vs residual stress
- Atomistic view: chemical bonding?, Kirkendall effects, interface mixing due to ion bombardment, mechanical locking
- Adhesion mechanisms, improvement: glue layer (oxide role), ion beam processing (energy!), polymers (plasma) activation of surface
- Measurement techniques adhesion: tear-off test (not quantitative), Rockwell adhesion, scratch techniques
- Nanoindentation: hardness under maximum load of 3-sided Berkovich tip. Young's modulus from linear unloading curve
- Thin film indentation: thin ice effect, 1/10 , fracture toughness difficult due to unknown crack path

summary – mech properties and hard coatings II

- Definition hard coatings: hard 20-40GPa, superhard >40GPa, ~10 μm thick, intrinsically + extrinsically hardness contributions
- Applications: cutting tools, moulds, machine parts, medical & decorative
- Classifications: metallic: transition metal –N/C/B; covalent: c-BN, SiC, Diamond; ionic: Al/Si/Zr/Cr – O
- high intrinsic hardness: high binding energy, short interatomic distance, high degree of covalent bonding, high number of bonds per unit volume, modelling opportunity for search by DFT
- Desired properties: High (hot) H, K_c, $G_{adhesion}$, G_c between phases, low $\sigma_{res,}$ no reaction with substrate & environment, low friction coeff against material in application -> layered/gradient film to catch all properties & nanostructured for high extrinsic hardness
- Nitrides & Carbonitrides: "fcc TiN archetype", TiCN self-lubricating C layer, AlTiN and $Al_xCr_{1-x}N$: oxidation resistant -> oxides of Al & Cr, AlTiSiN forms superhard coating with AlTiN nanocrystals in a-SiN matrix
- Carbides: "fcc TiC archetype" with more covalent bond compared to TiN, TiC_xN_{1-x} better against C outdiffusion, TiCN nanocrystals in a-C:H matrix
- Borides: hexagonal TiB_2 with covalent B-B bonds, TiB2 nanocrystals in excess B-rich matrix, used for cutting of Al as Nitrides don't work
- Oxides: "hex Al_2O_3 archetype" but many polytypes, dominating for cutting tools (oxid resistance & hot hardness)
- Nanolayers: nanolaminates incl. epitaxial superlattices; toughening of nanolayers via crack deflection, ductile interlayers and interface delamination; superlattices with additional toughening with coherency strains, dislocation arrays at interfaces and oscillating Youngs Modulus (compared to single crystals)

summary – mech properties and hard coatings III

- Nanocomposites: strength due to grain refinement (Hall-Petch) and preventing GB sliding due to amorphous tissue phase at GB. Max hardness with 10nm grain size and 1-3nm tissue phase
- Arc plasma deposition: high I - low DC voltage, magnetically steered μm - sized spot with 10^{10} A/cm^2 leads to melting/evaporation/ejection of particles, ionization degree up to 100% leads to stöchimetric compounds in reactive arc deposition, ion energies up to 100eV leads to dense, well adhering films; samples (cutting tools etc.) on rotating planetary holder allows for nanolaminate deposition, all hard coatings possible but mostly used for forming and cutting tools as smaller grains compared to CVD as lower deposition T
- high-power impulse magnetron sputtering (HiPIMS): power densities on target like arc through 100μs pulses with 10-100Hz with almost 100% ionization degree and high energy ions leading to dense and well adhering coatings, but without particles as in arc deposition
- Coating process line includes handling, decoating, cleaning, QS, pre/post annealing and actual deposition equipment

Contact mechanics and tribology of thin films

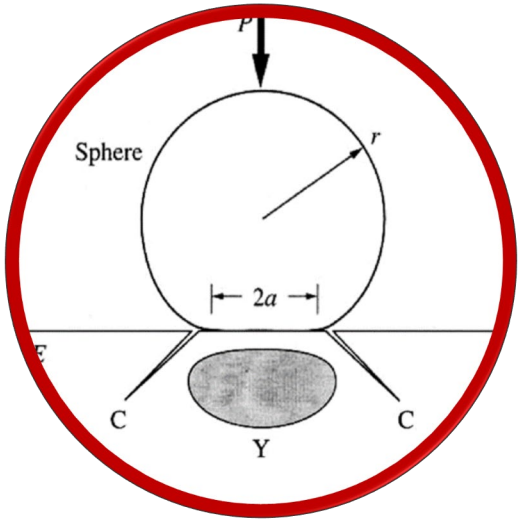

Tribological properties of coatings

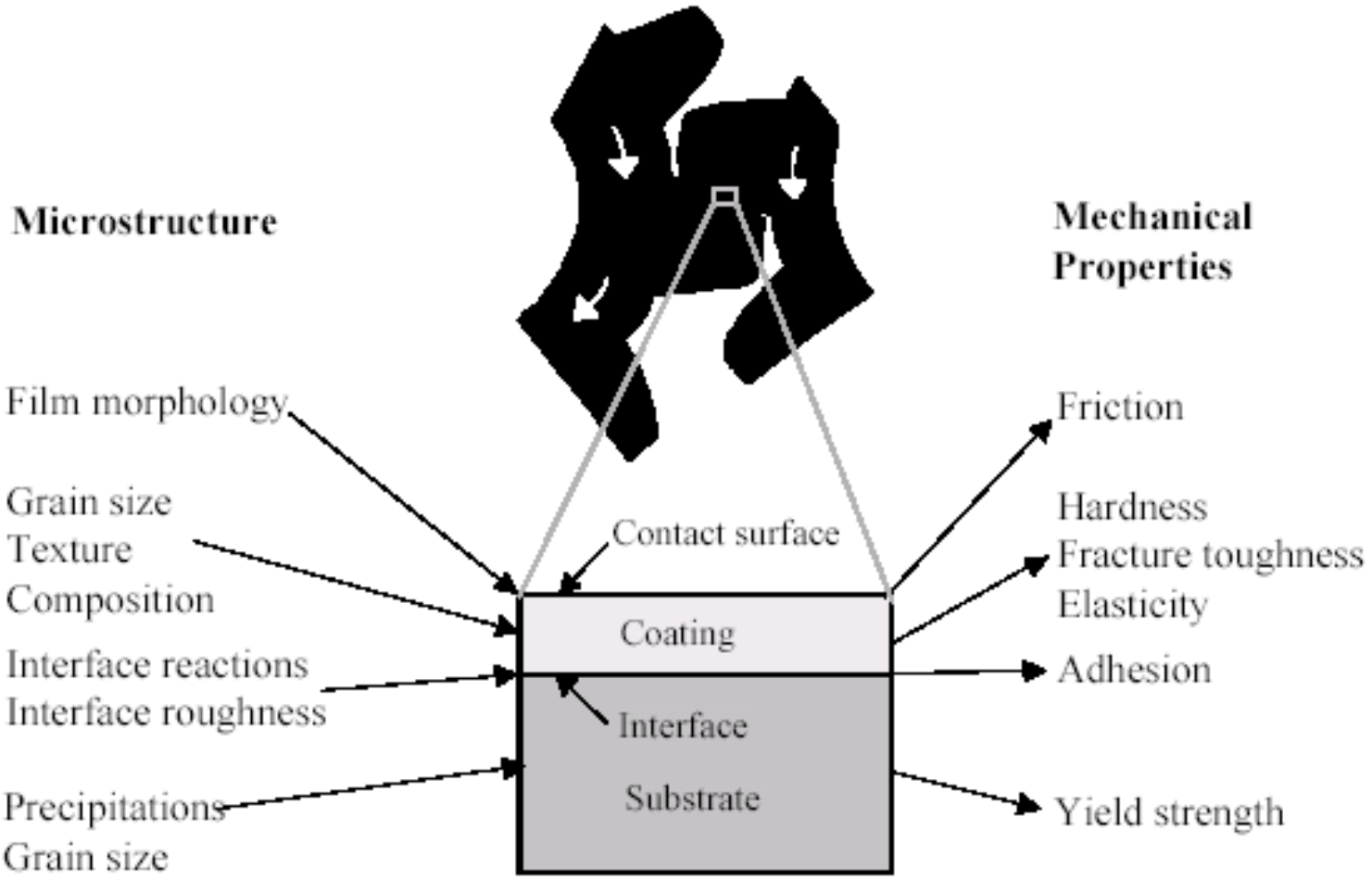

Contact Stress Analysis: Hertz theory

- Hertz Theory provides good approximations for contact problems between spherical or cylindrical elastic bodies with similar moduli

Heinrich Hertz, 1857-1894

- Assumptions:
  - Contact areas are small with respect to the size of the bodies in contact
  - Both surfaces deform
  - The elastic moduli of the contacting components are similar
  - No adhesion or friction between bodies
  - Elliptical pressure distribution between the contacting bodies

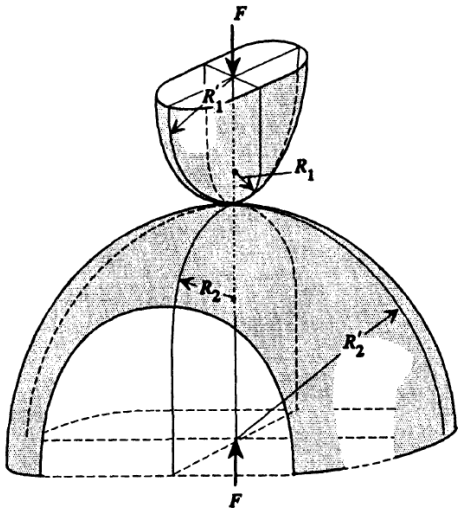

Hertz theory

- Maximum Pressure:

$$p_{max} = \frac{1.5P}{\pi a^2}$$

- Radius of contact area:

$$a = 0.721(PC_G C_M)^{1/3}$$

- Relative displacement:

$$\delta = 1.04\left(\frac{P^2 C_M^2}{C_G}\right)^{1/3}$$

- Where C_M and C_G account for the material properties/geometry

$$C_M = \frac{1-\nu_1^2}{E_1} + \frac{1-\nu_2^2}{E_2}$$

$$C_G = \frac{D_1 D_2}{D_1 + D_2}$$

- Contact load is proportional to relative displacement to the power 1.5

$$P \sim \delta^{1.5}$$

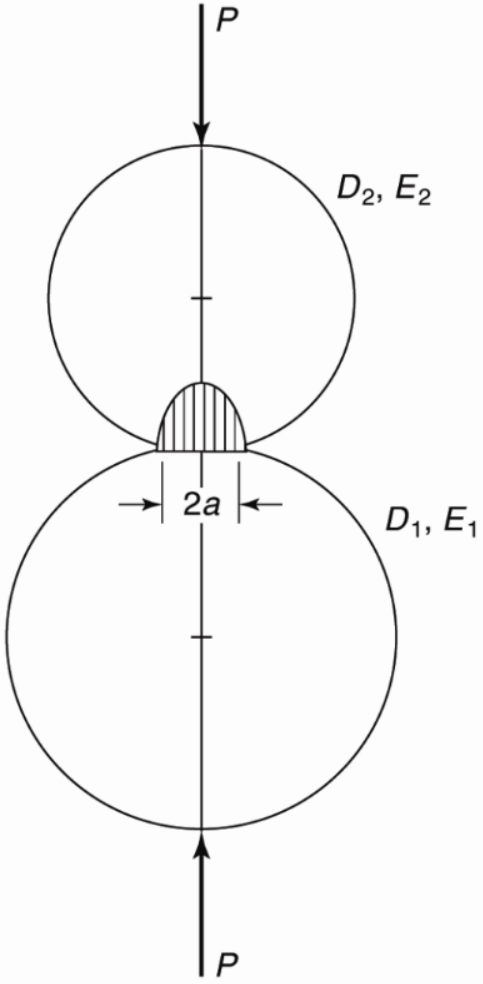

Hertz theory

- Both contact area and maximum contact pressure are functions of load, modulus, and conformity -> inherently nonlinear

- Fundamental characteristics:

  - When the load increases, the contact area and the contact pressure both increase
  - If the diameter of the spheres decreases (contact is less conforming), the contact area decreases and the contact pressure increases
  - If the elastic modulus increases, then the contact area decreases and the maximum pressure increases

Hertz theory

- Contact between spherical components
  - Special case: A sphere on a flat plate $(D_1 \to \infty)$

$$C_G = \lim_{D_1 \to \infty} \frac{D_1 D_2}{D_1 + D_2}$$

$$C_G = \lim_{D_1 \to \infty} \frac{(D_1 D_2)/D_1}{D_1/D_1 + D_2/D_1}$$

$$C_G = \lim_{D_1 \to \infty} \frac{D_2}{1 + D_2/D_1} = D_2$$

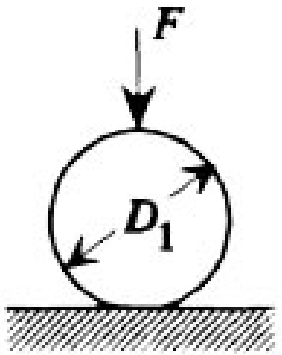

Sphere on Flat Plate

Hertz theory

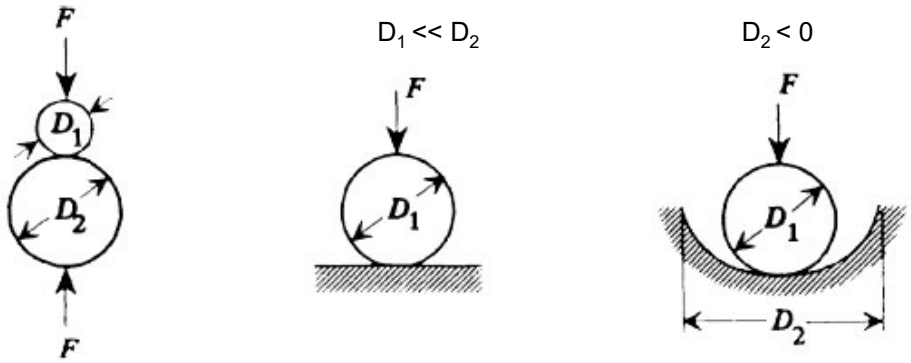

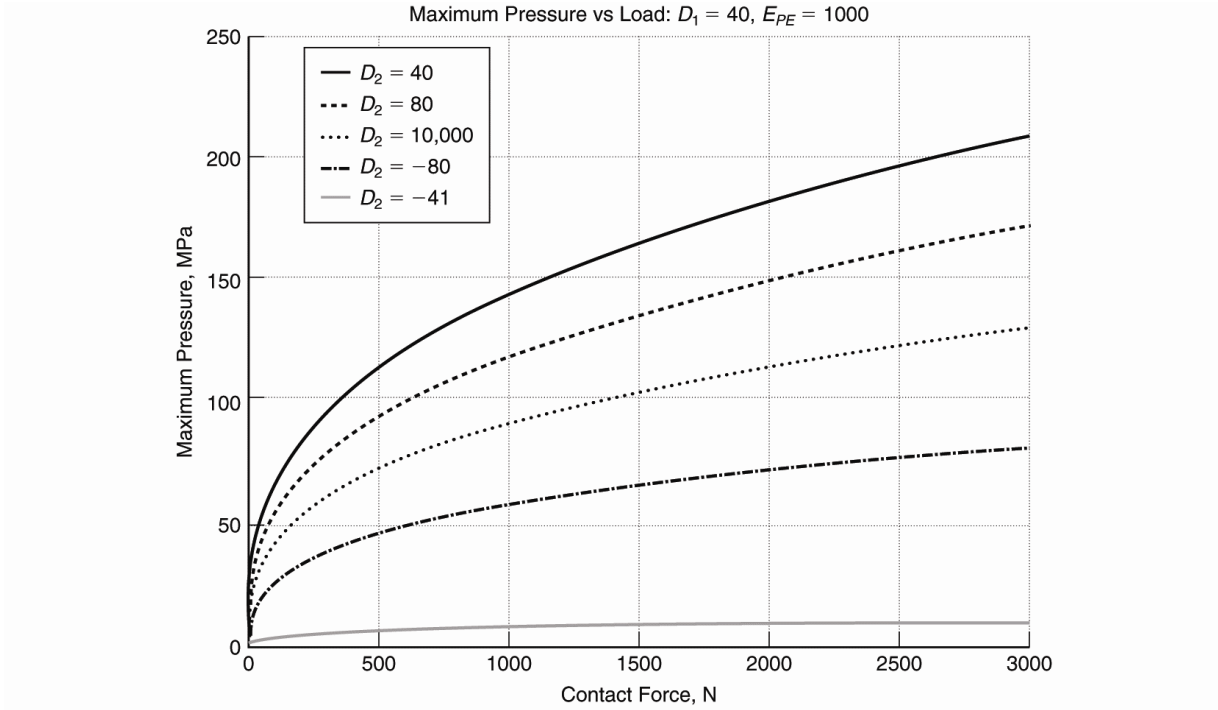

Hertz theory

- Normal stress components at the surface (across the contact area; top)
- Stresses beneath the center of the contact area as a function of depth (bottom)

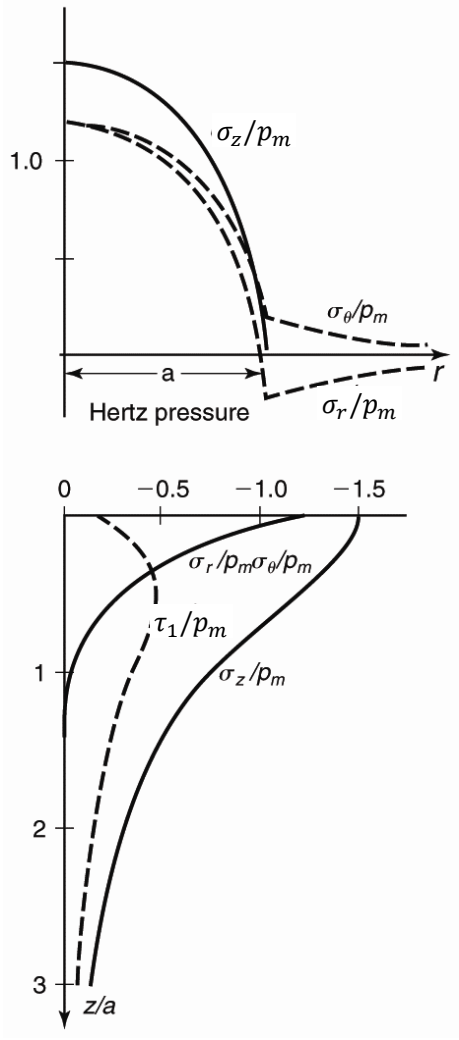

Hertz theory

- Important characteristics
  - Tensile stresses occur in radial direction at the edge of the contact
  - At the center of the contact a nearly hydrostatic stress state occurs
  - The maximum shear stress occurs below the center of the contact area at $z/a = 0.51$ and its magnitude is $\tau_{max} = 0.31 p_{max}$

$$\sigma_{r,\max} = (1 - 2\nu) p_0 / 3$$

$$\tau_{\max} \approx (0.378 - 0.225\,\nu) p_0$$

Near hydrostatic stress

Maximum tensile stress

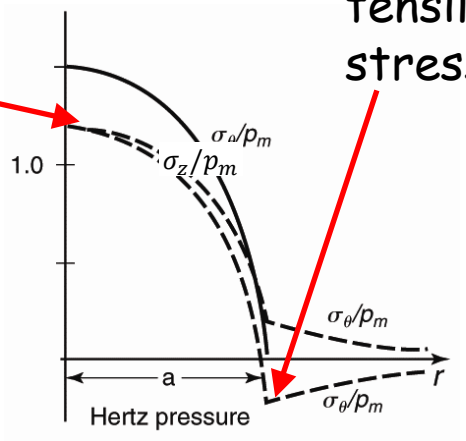

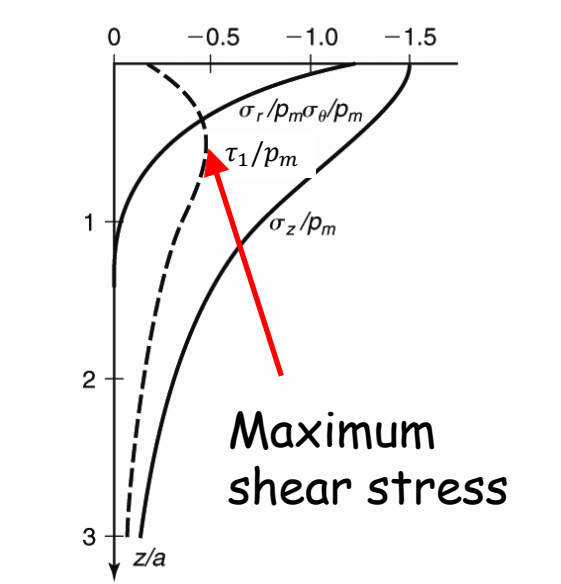

Maximum shear stress

Contact mechanics – tangential loading

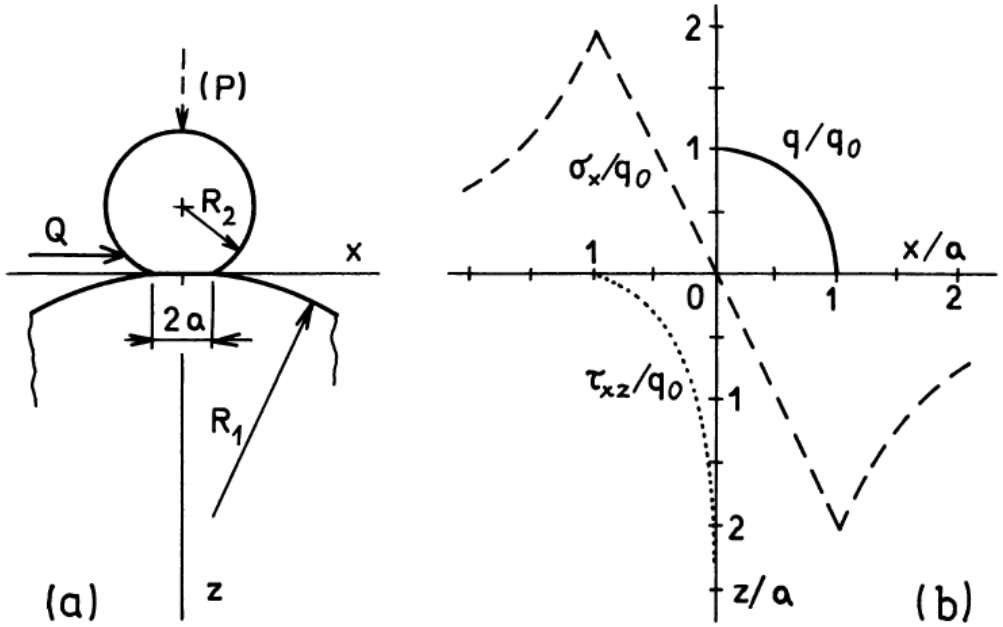

Fig. 35 Contact of two cylinders loaded by tangential force: a - general layout, b - distribution of shear stress (q) and normal stress (σ_x) on the surface and shear stress τ_{xz} along the z-axis. q_0 - maximum shear stress in the middle of the contact surface.

- Assumptions:
  - Normal pressure distribution remains unchanged
  - Shear stresses proportional to the pressure
- Stress σ_x is highest at the edge of the contact!

Contact mechanics – simultaneous normal and shear load

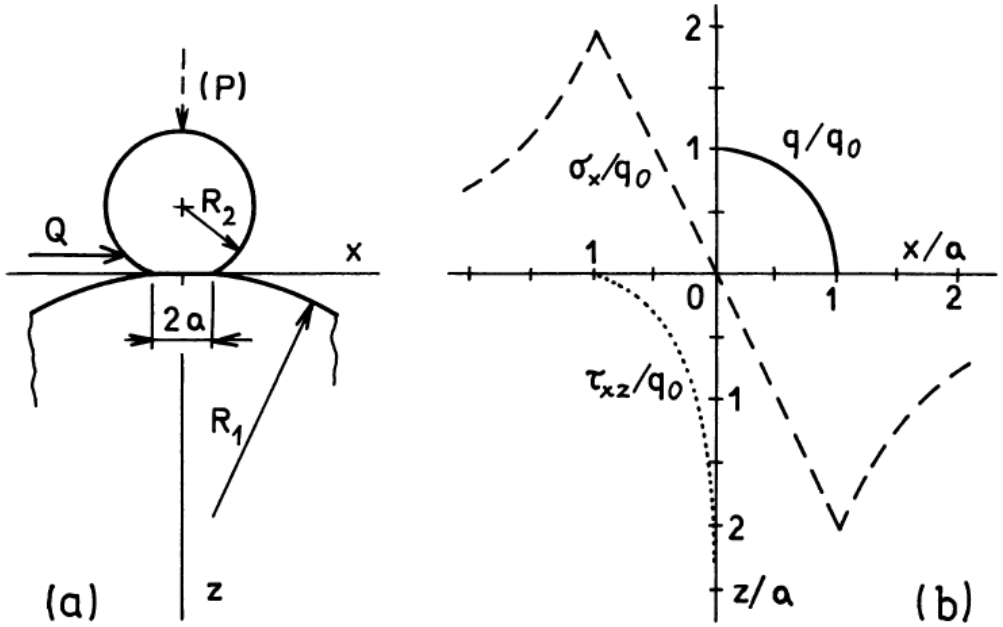

Fig. 35 Contact of two cylinders loaded by tangential force: a - general layout, b - distribution of shear stress (q) and normal stress (σ_x) on the surface and shear stress τ_{xz} along the z-axis. q_0 - maximum shear stress in the middle of the contact surface.

- Compared to normal force only:
  - Higher shear stress (approx. 10%)
  - Position of max. shear stress is shifted towards surface

Contact mechanics – simultaneous normal and shear load

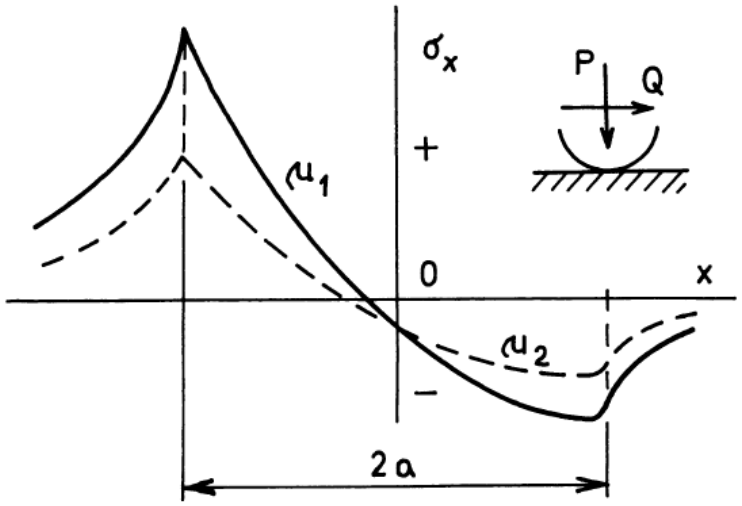

Fig. 36 Distribution of the stress σ_x along the contact surface caused by the simultaneous action of normal force P and tangential force $Q = \mu P$ (after Richerson *et al.*, 1981). The arrangement see Fig. 35. $\mu_1 > \mu_2$, + tension, - compression

- Higher friction coefficient leads to higher σ_x

Example: Scratch Testing

- Draw diamond tip across surface with increasing normal load until a critcal event occurs
- Film can debond (form delamination cracks) and buckle or chip or fracture (form through thickness cracks), substrate can yield

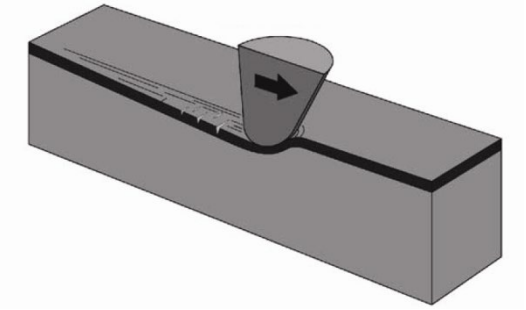

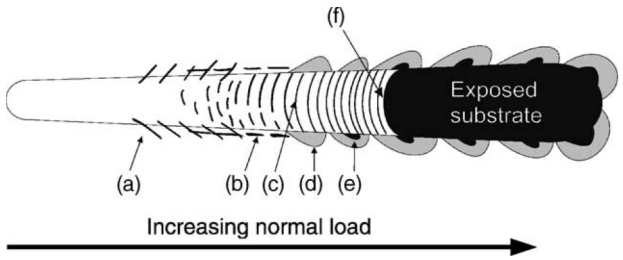

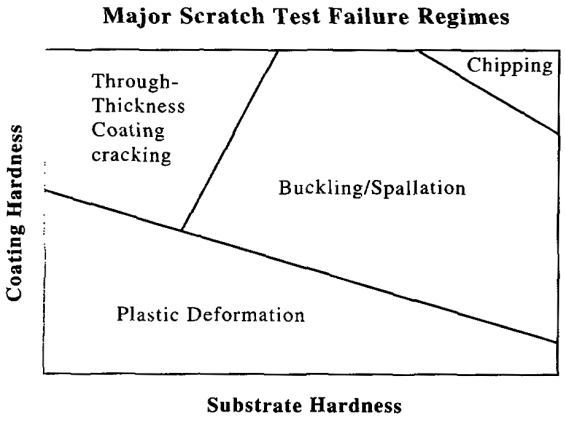

uniform width blisters

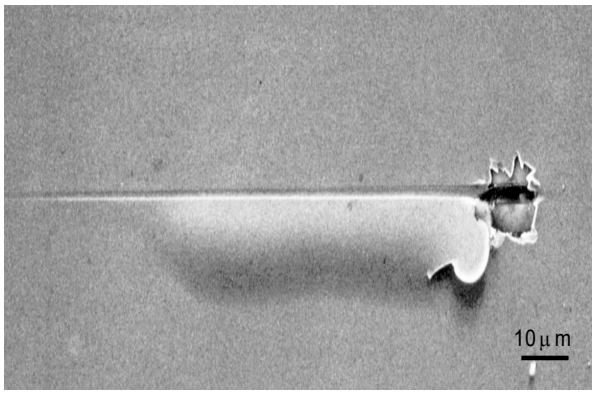

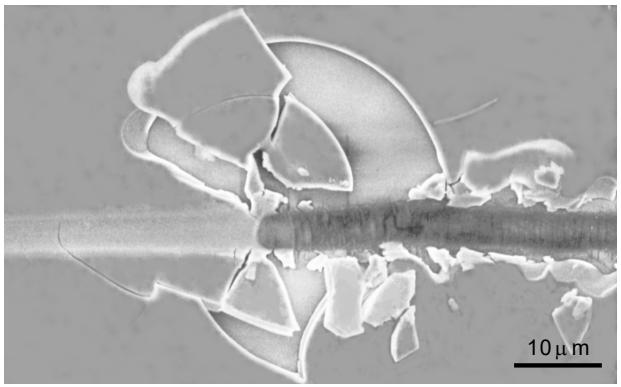

spalled blisters

Holmberg, Laukkanen, et al, *Wear.* 254 (2003) 278.

Rigid cylinder in contact with a coated body

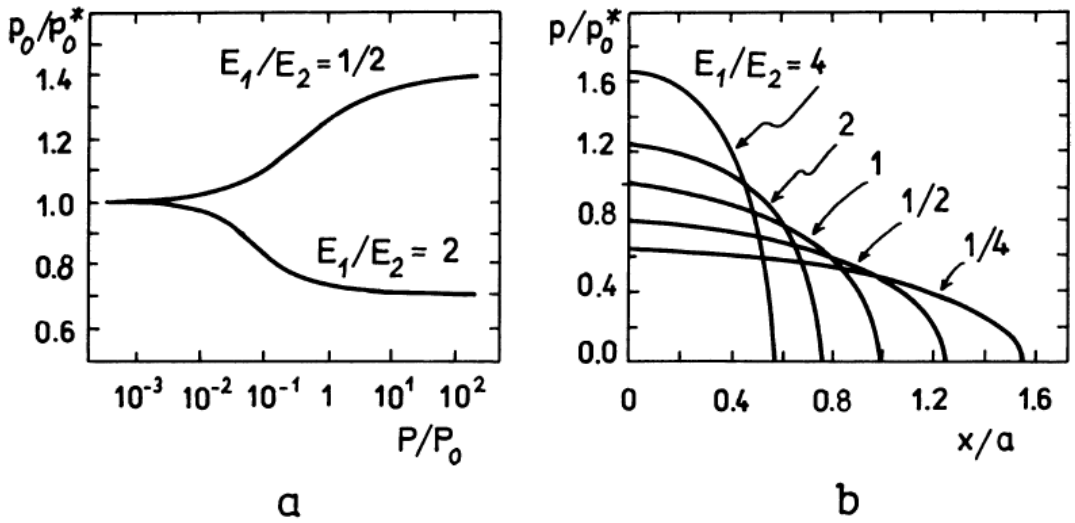

Fig. 38 Contact stresses on pressing a rigid cylinder into a massive elastic body 2 with a surface layer 1: a - pressure in the middle of the contact surface - the influence of the load and ratio of elastic moduli, b - distribution of the pressure on the contact surface (after King & O´Sullivan, 1987). h - thickness of the surface layer, a - half-width of the contact surface, P - load, P_0 - load, for which $a = h$, p - pressure, p_0 - pressure in the middle of the contact surface (p_0^*corresponds to the case $E_1 = E_2$)

- Influence of contact pressure on
  - ratio of elastic moduli E_1/E_2
  - Ratio of coating thickness h vs. contact radius a (or load P)
- Contact pressure distribution depends on E_1/E_2

Sneddon theory

- Boussinesq problem: Solution for the stress and displacement field for an arbitrary pressure distribution on the surface of an elastic halfspace
- Solution for a concentrated force (Boussinesq 1882)

$$u_z(r) = \frac{1}{\pi E^*} \frac{P}{r}$$

- Superposition principle allows generalization to arbitrary pressure distributions

$$u_z(x,y) = \frac{1}{\pi E^*} \iint p(x',y') \frac{dx'dy'}{r}$$

- No friction, no adhesion are considered
- Based on integral transforms of the system of partial differential equations governing the elastic contact problem

Flat punch indenter

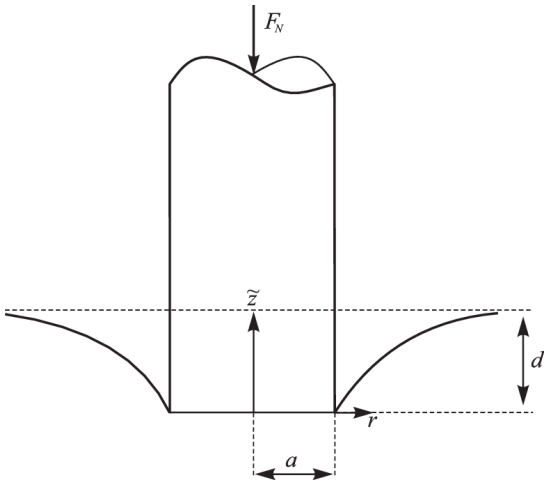

- Load-depth curve:

$$P = \frac{4Gad}{1-\nu}$$

- Pressure distribution at the surface:

$$\sigma_z(r,0) = \frac{2Gd}{\pi(1-\nu)}(a^2-r^2)^{-0.5}$$

- Shape of the deformed surface:

$$u_z(r,0) = \frac{2d}{\pi}sin^{-1}(\frac{a}{r})$$

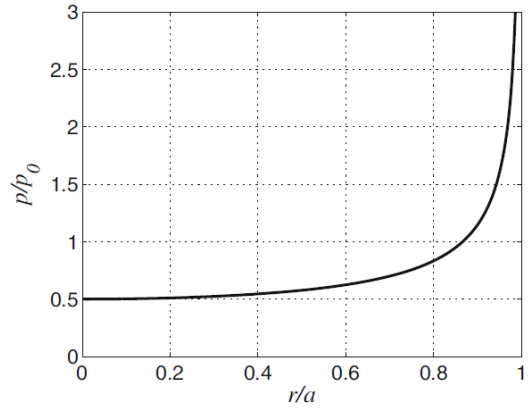

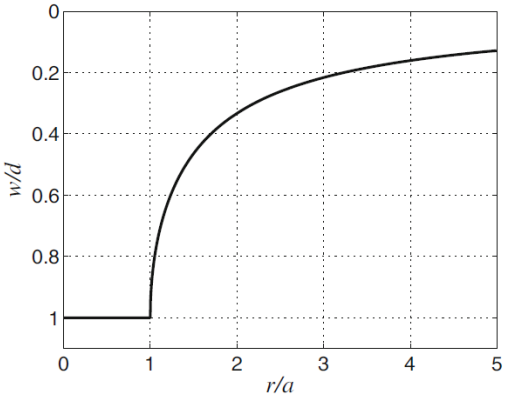

Conical indenter

- Load-depth curve:

$$P = \frac{4G\cot\vartheta}{\pi(1-\nu)}d^2$$

- Pressure distribution at the surface:

$$\sigma_z(r,0) = \frac{2Gd}{a\pi(1-\nu)}\cosh^{-1}\left(\frac{a}{r}\right)$$

- Shape of the deformed surface:

$$u_z(r,0) = \frac{2d}{\pi a}\left(a\sin^{-1}\left(\frac{a}{r}\right) - r + \sqrt{(r^2-a^2)}\right)$$

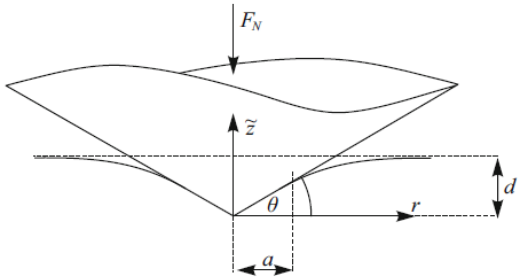

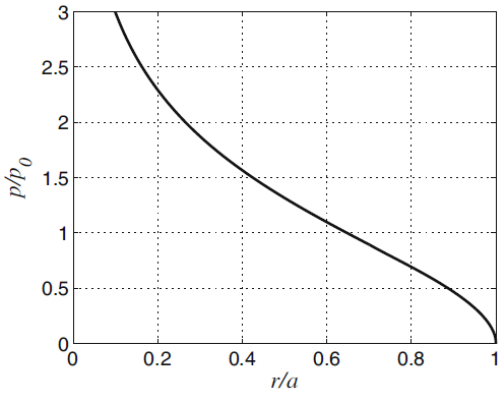

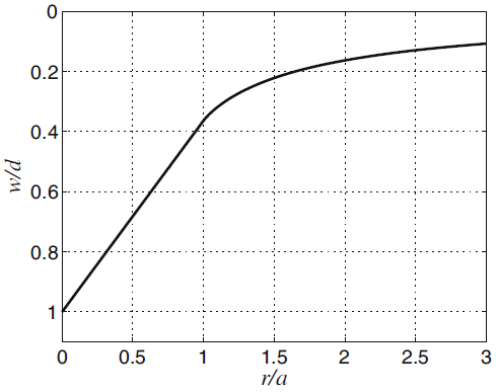

Contact mechanics of thin films

An illustrative example based on DLC on steel

A typical load case: Surface contact of a spherical body

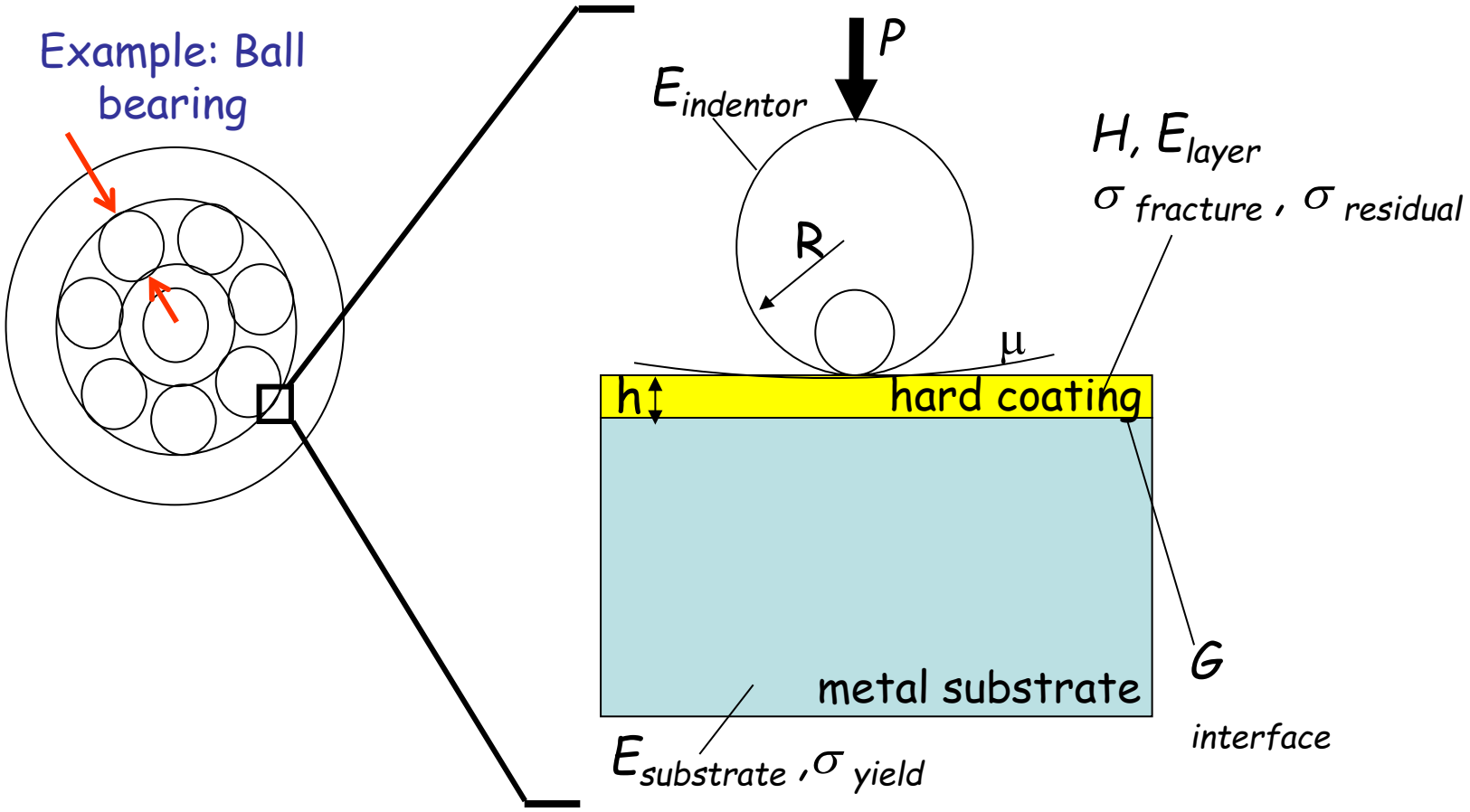

Failure of coated device? **Measurement of materials parameters** → **Analysis of load case**

Application of spherical nanoindentations to DLC films

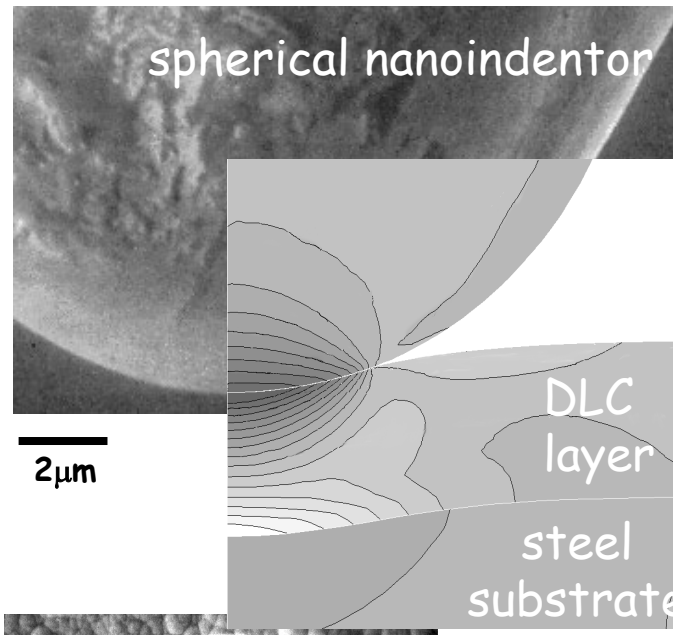

maximal principal stress GPa

-29

0

22

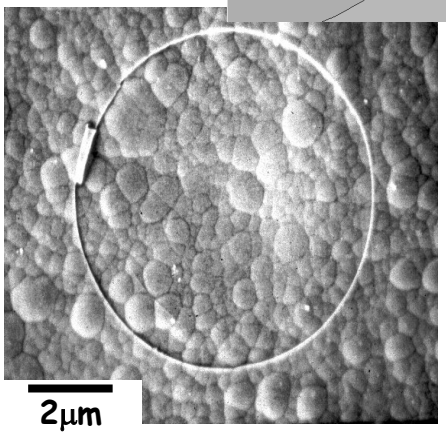

hertzian-type ring crack in DLC

hertzian-type ringcracks
+
finite element simulation of the indentation

↓

fracture strength of the layer

Michler 1999, Diamond Relat. Mater. **8**, 510-516

Fracture strength and fracture morphology of DLC films

Two extreme cases:

1at% Si-DLC/ as deposited: σ_f=8GPa, ringcracks

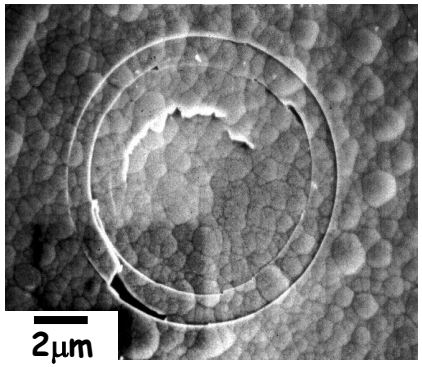

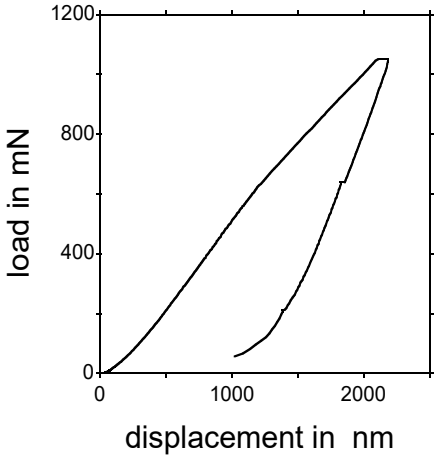

27at% Si-DLC / 500°C: σ_f=4GPa, debris formation

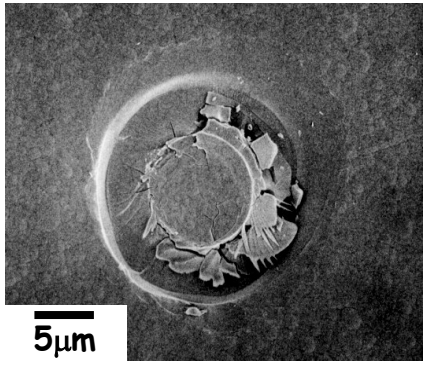

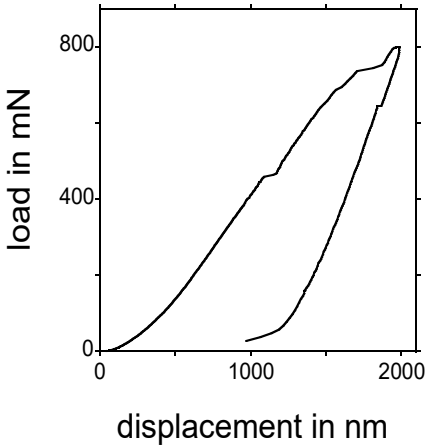

fracture morphology:
embrittlement of layer with increasing silicon content

Michler 1999, Diamond Relat. Mater. **8**, 510-516

Spherical contact: Load bearing capacity and coating failure

Homogeneous solids:
Hertz contact problem

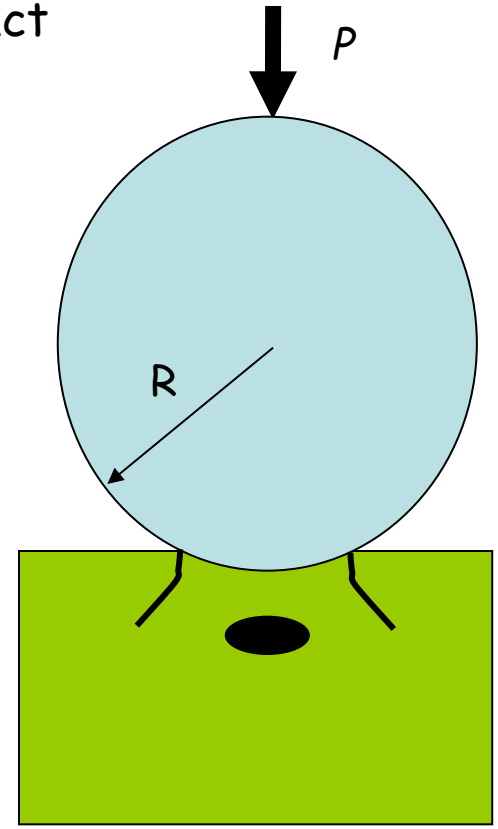

- ring-cracks at surface due to tensile radial stress
- subsurface plastic deformation due to shear stress

Coated solids:
No analytical solution

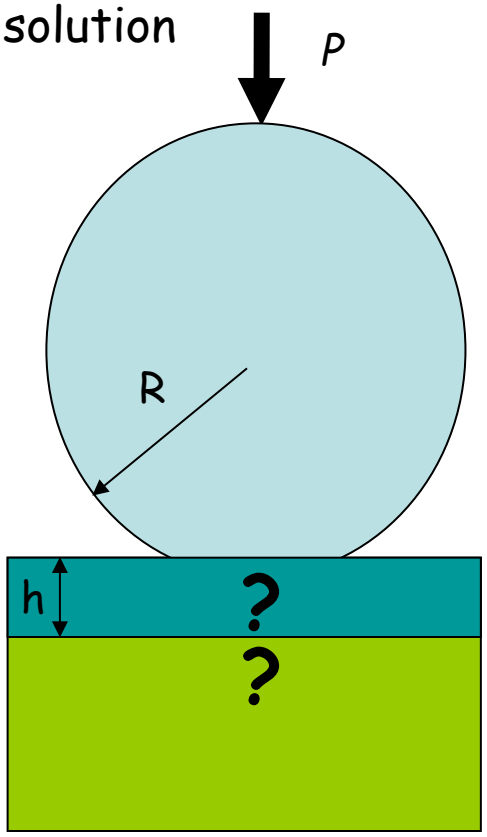

failure mode depends on $h^*=h/R$

Load bearing capacity

thin layers

plastic deformation
below the interface

thick layers

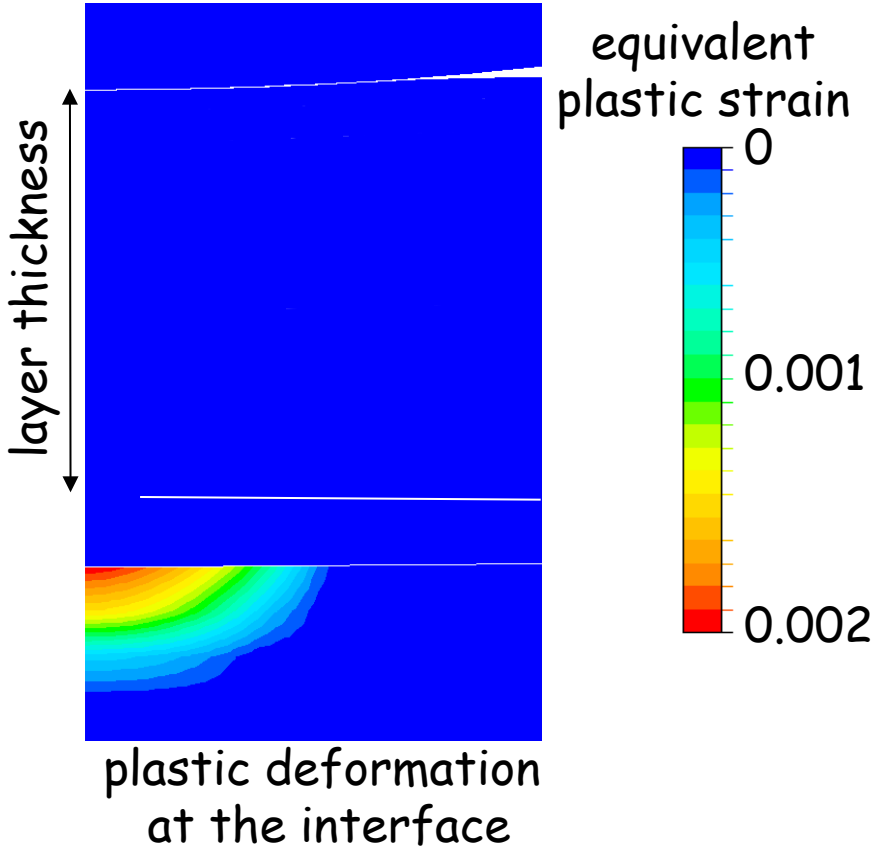

plastic deformation
at the interface

Material models:
Indenter: Diamond, elastic, μ=0
Layer: DLC, elastic, $\sigma_{fracture}$= 20GPa
Substr.: Steel, elastic ideal-plastic
$\sigma_{yield,\ substrate}$ = 2GPa

Blank 1998, Adv. Solid State Phys. **38**, 593-605

Fracture modes in case of spherical contact

thick layers

maximum principal
stress in GPa

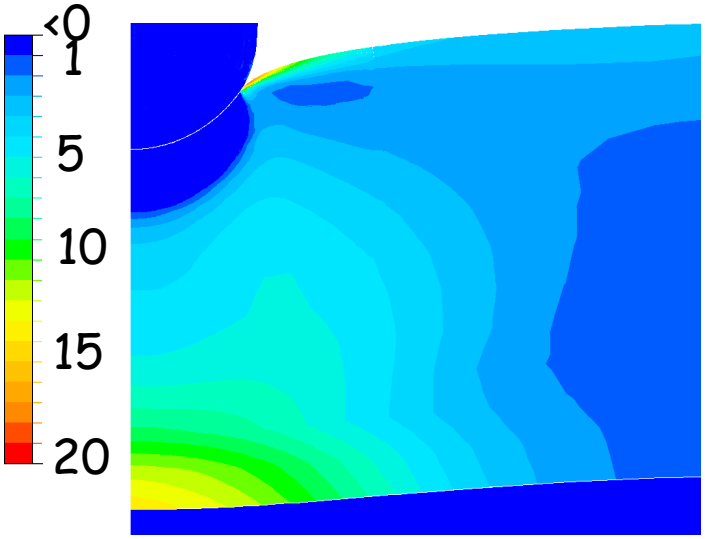

thin layers

maximum principal
stress in GPa

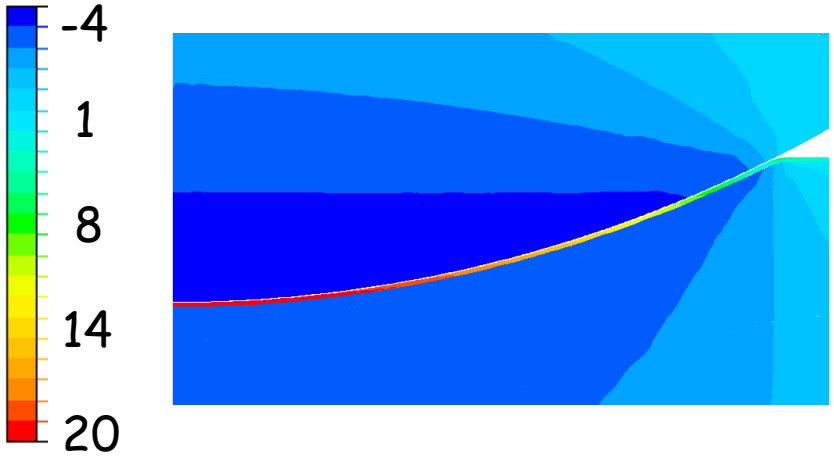

Failure map: load bearing capacity and fracture

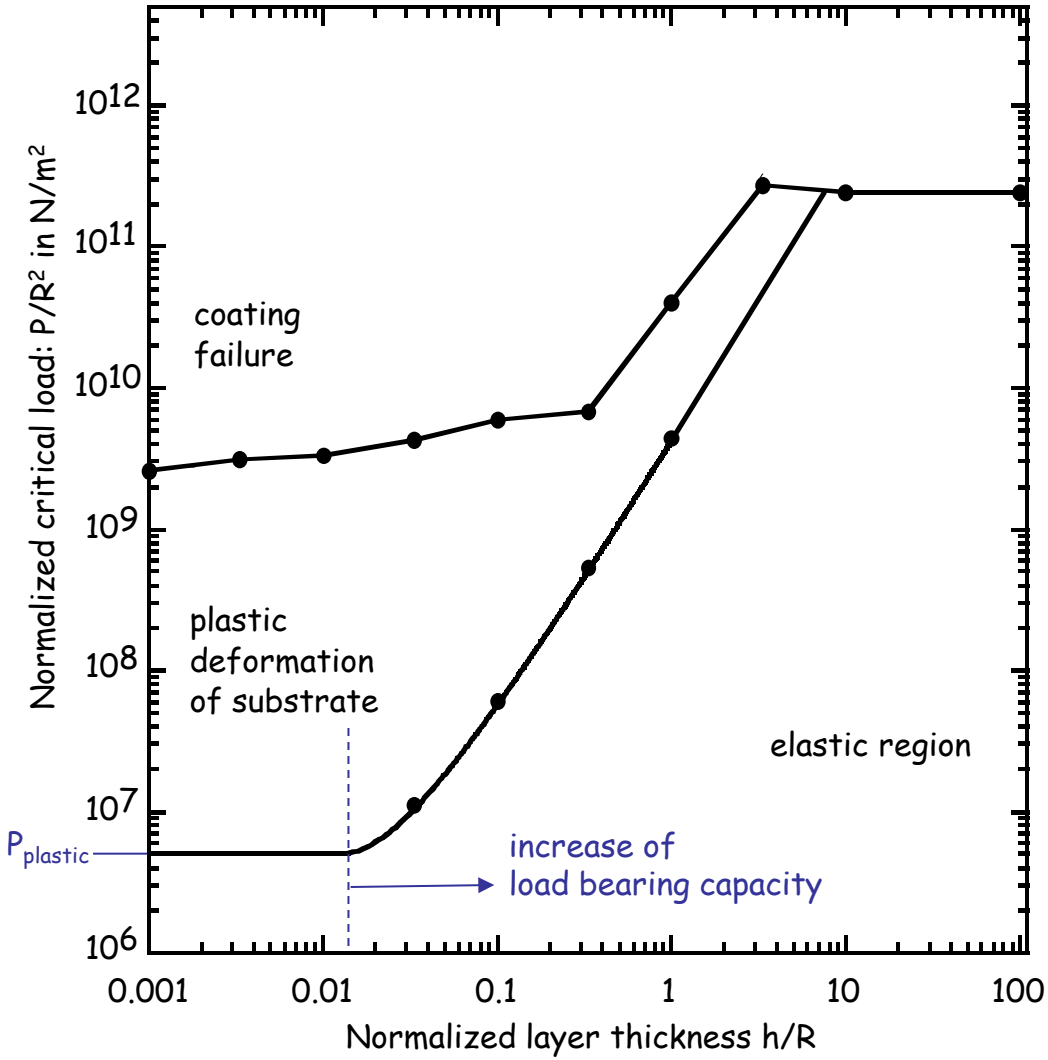

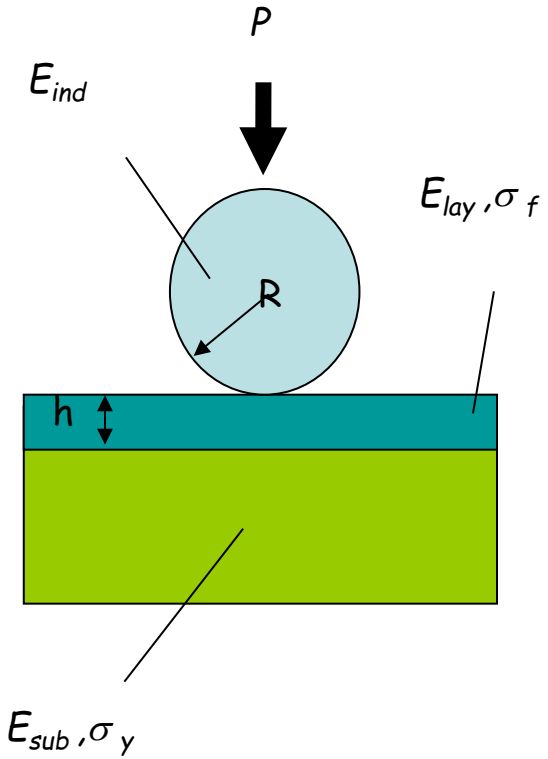

Example: R=0.5mm
- For increased load bearing capacity: h>5μm
-For h<5μm, $P_{plastic}$= 1.25N

Michler & Blank 2001, Thin Solid Films **381**, 119-134

Extension of failure maps by analytical solutions

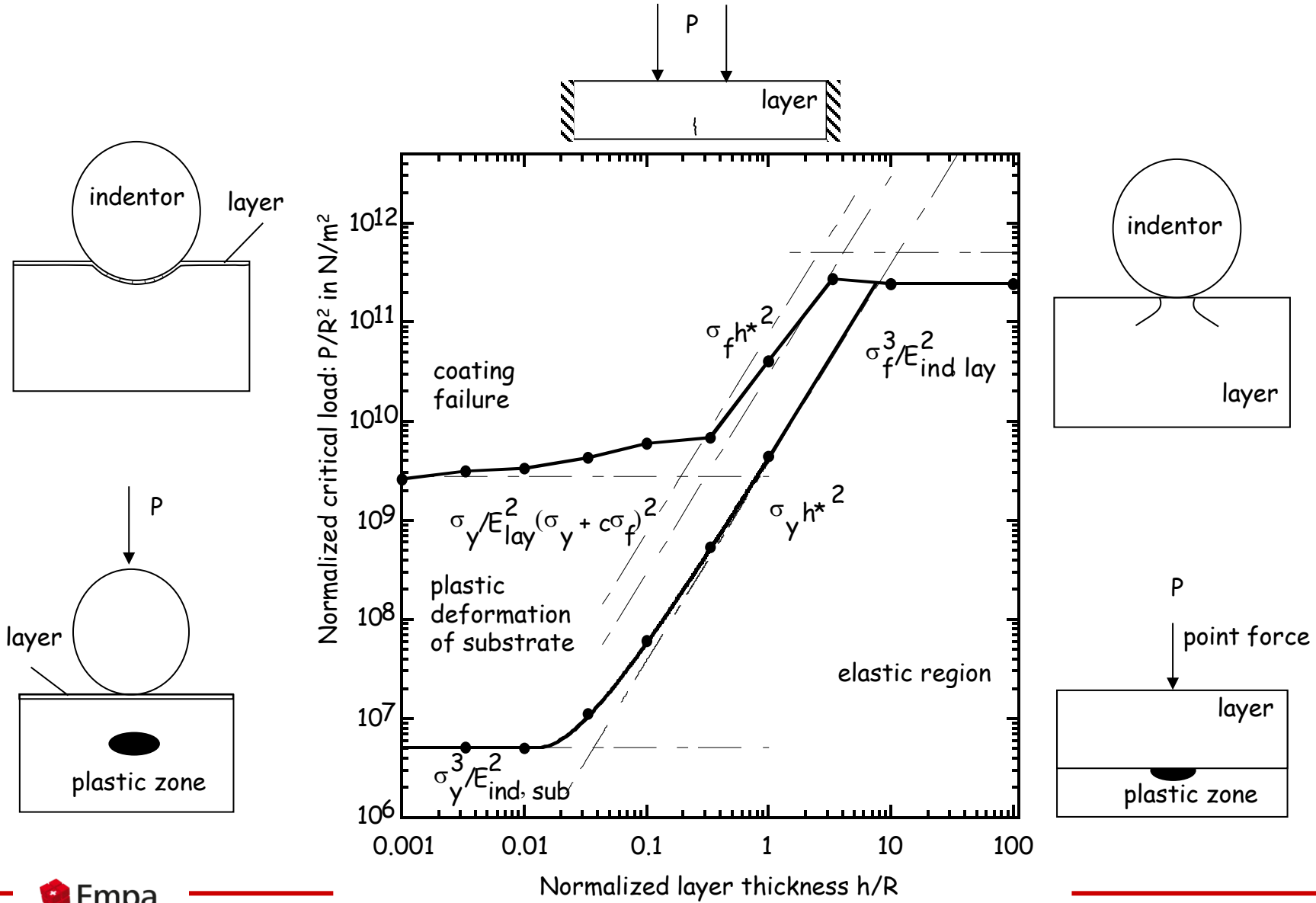

Michler & Blank 2001, Thin Solid Films **381**, 119-134

Mechanical analogues: Fracture h*>33

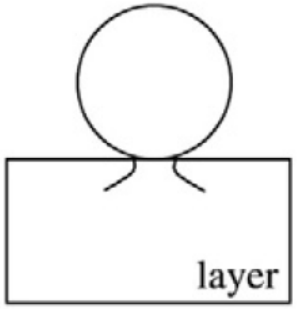

- When the film is thick compared to the indenter radius (h*=h/R>33), the problem may be modeled as a Hertzian contact
- For frictionless contact, the maximum principal stress is at the edge of the contact with the elastic properties of the film E_b,ν_b.

$$\sigma_{max} = \frac{(1-2\nu_b)}{2\pi}\left(\frac{4E_b}{3}\right)^{2/3} P^{1/3}R^{2/3}$$

- Solving for the critical load at a known fracture stress σ_f yields:

$$P^* = \frac{P}{R^2} = \frac{9\pi^3\sigma_f^3}{2E_b(1-2\nu_b)^3}$$

Mechanical analogues: Fracture h*>33

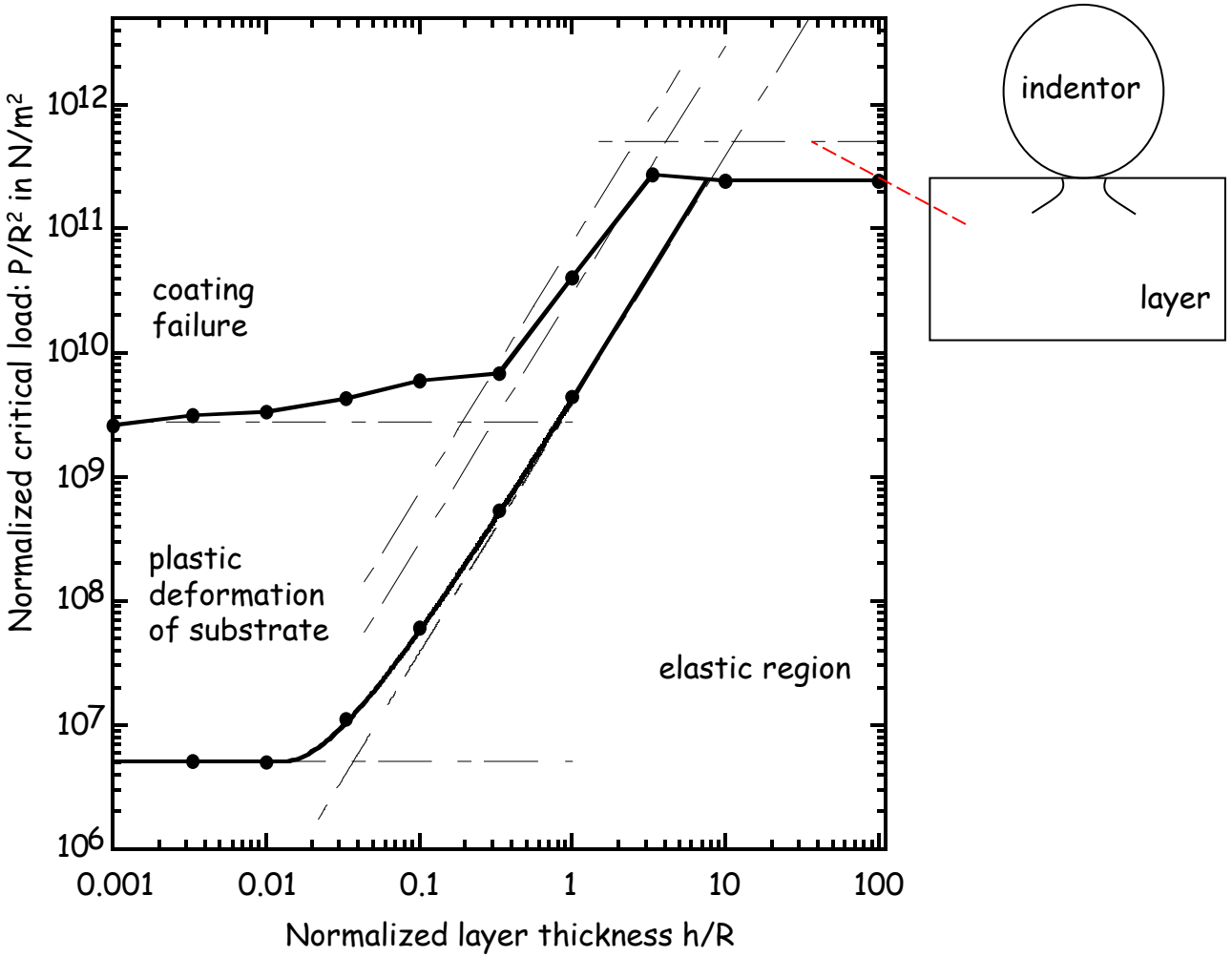

Michler & Blank 2001, Thin Solid Films **381**, 119-134

Mechanical analogues: Fracture h*>0.33

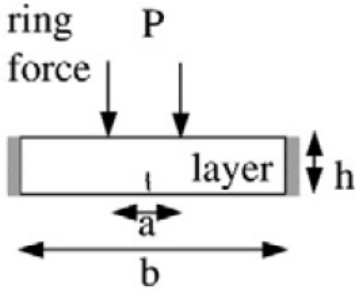

- If the layer thickness is comparable to the indenter radius, film fracture starts at the interface directly under the indenter
- The layer is bent with a constant curvature and can be modeled as a radially clamped plated loaded by a ring force.
- Maximum tensile stress at the bottom of the plate:

$$\sigma_{max} = \frac{3P}{4\pi h^2}(1+\nu_b)\left(\left(\frac{a}{b}\right)^2 - 1 + 2ln\left(\frac{b}{a}\right)\right)$$

- Solving for the critical load at a known fracture stress σ_f yields:

$$P^* = \frac{4\pi(h^*)^2\sigma_f}{2.56(1+\nu_b)}$$

Mechanical analogues: Fracture h*>0.33

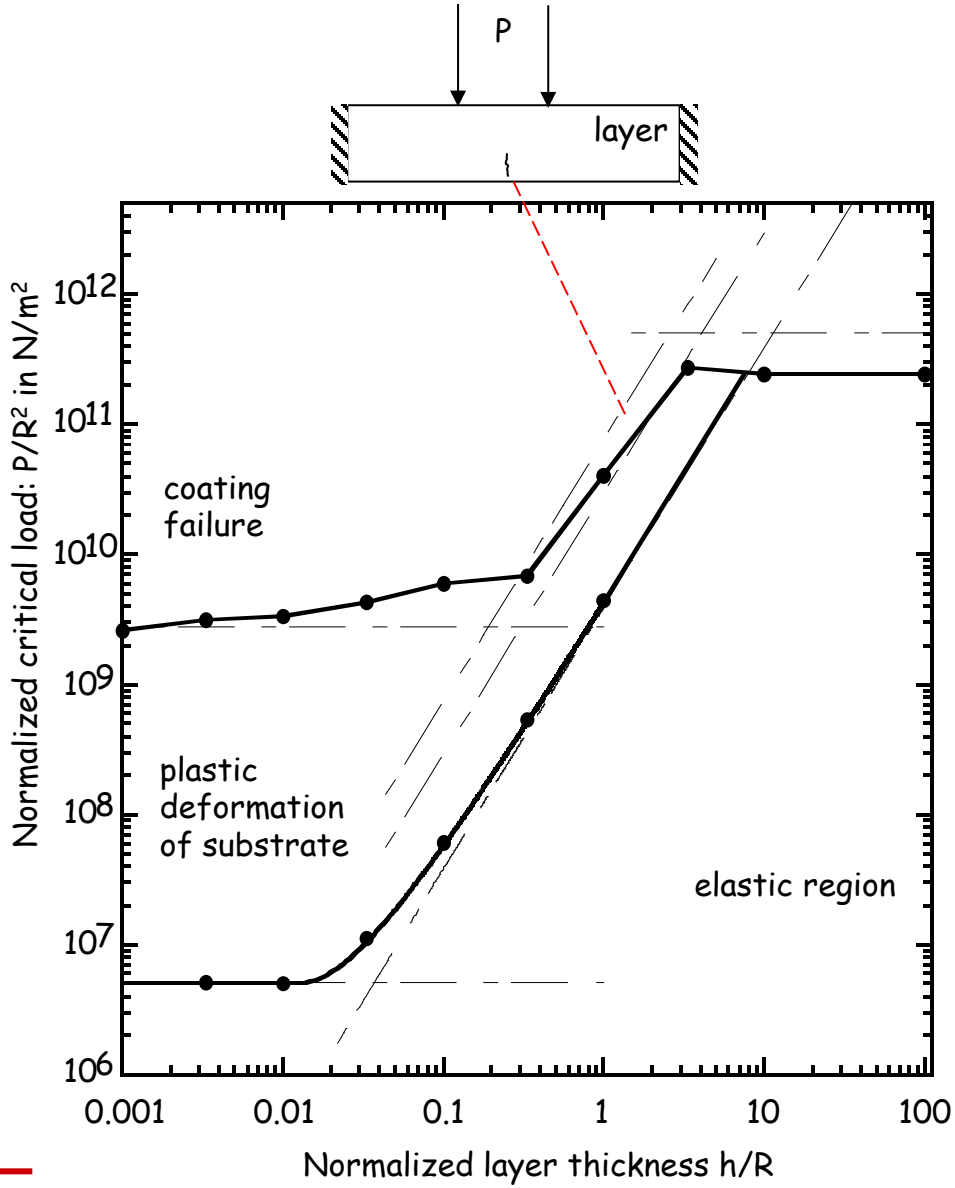

Michler & Blank 2001, Thin Solid Films **381**, 119-134

Mechanical analogues: Fracture h*<0.33

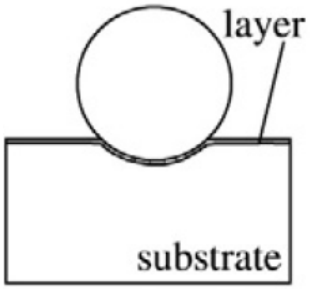

- If the layer thickness is very thin, strains in the layer are dominated by substrate deformation.
- Substrate is deformed plastically, force-depth relationship [Johnson 1985]:

$$\frac{P}{P_y} = 5.5\frac{\delta}{\delta_y}$$

- Force at which yielding occurs [Johnson 1985]:

$$P_y = \frac{R^2\pi^3\left(1.6\sigma_y\right)^3}{6E_s}$$

Mechanical analogues: Fracture h*<0.33

- The corresponding indentation depth at yield is given by

$$\delta_y = \left(\frac{9P_y^2}{16RE_s^2}\right)^{1/3}$$

- The strain in the plastic region can be approximated by a representative strain [Tabor 1951, Johnson 1985]:

$$\varepsilon_{rep} = 0.2\frac{a}{R}$$

- The biaxial strain in the layer is approximated as $\varepsilon_{rr} = \varepsilon_{\vartheta\vartheta} = \varepsilon_{rep}$. The contact pressure is approximated as $p_0 = -3\sigma_y$. Using Hooke's law, the unknown biaxial stresses σ_{rr} and $\sigma_{\vartheta\vartheta}$ are calculated. The critical force for film fracture is given by:

$$P^* = \frac{230\sigma_y}{E_b^2}\left(\sigma_f(1-\nu_b) + 3\nu_b\sigma_y\right)^2$$

Mechanical analogues: Fracture h*<0.33

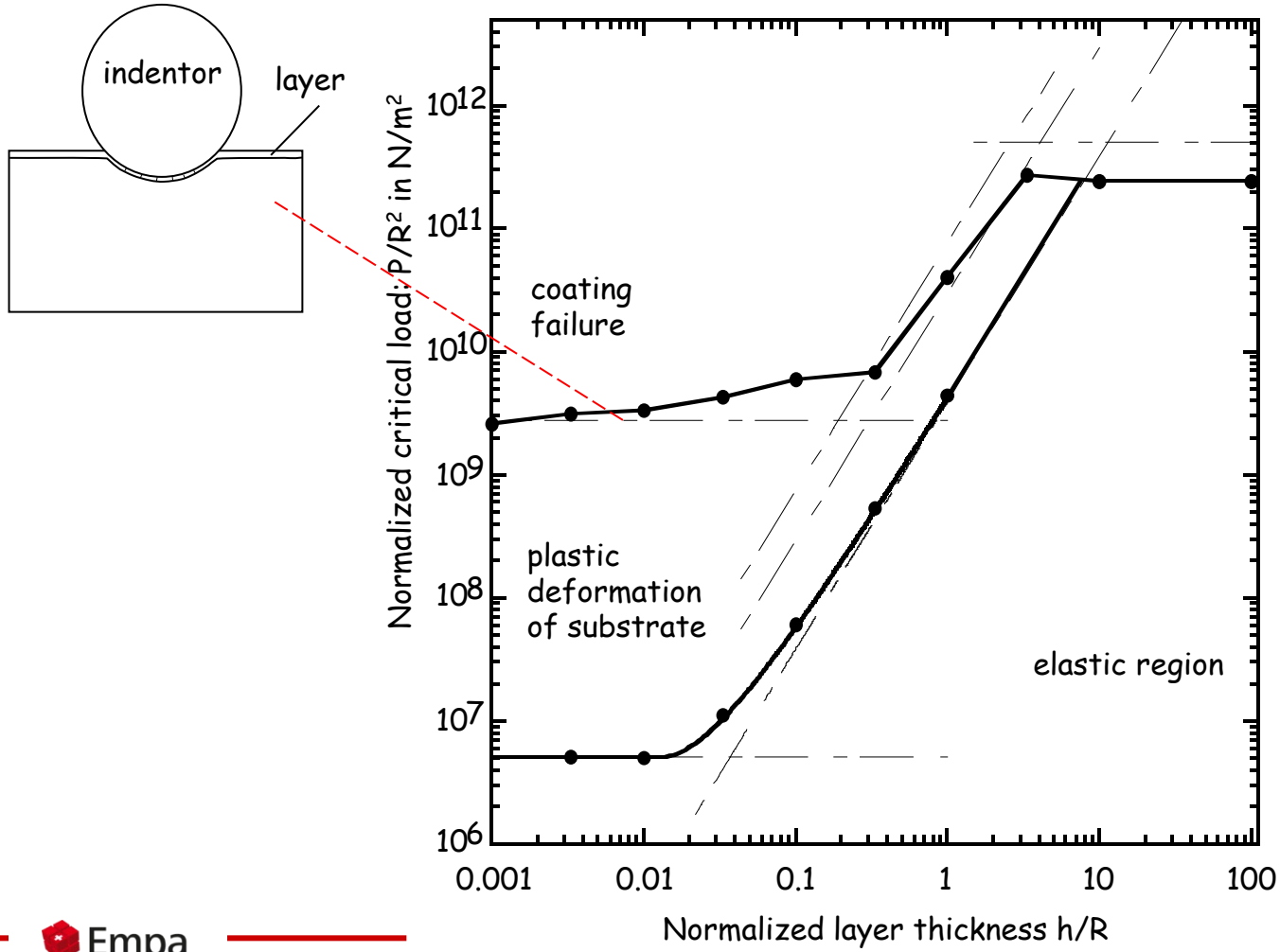

Michler & Blank 2001, Thin Solid Films **381**, 119-134

Mechanical analogues: Yielding h*<0.01

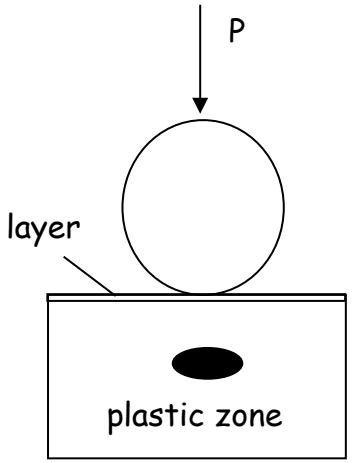

- If the layer thickness is very thin, the stress field in the substrate is approximately Hertzian
- Yielding occurs at the point of highest shear stress: approximately z=0.48 for v=0.3
- If substrate follows von Mises criterion, the critical load is given by:

$$P^* = \frac{\pi^3 \left(1.6\sigma_y\right)^3}{6E_s}$$

Mechanical analogues: Yielding h*<0.01

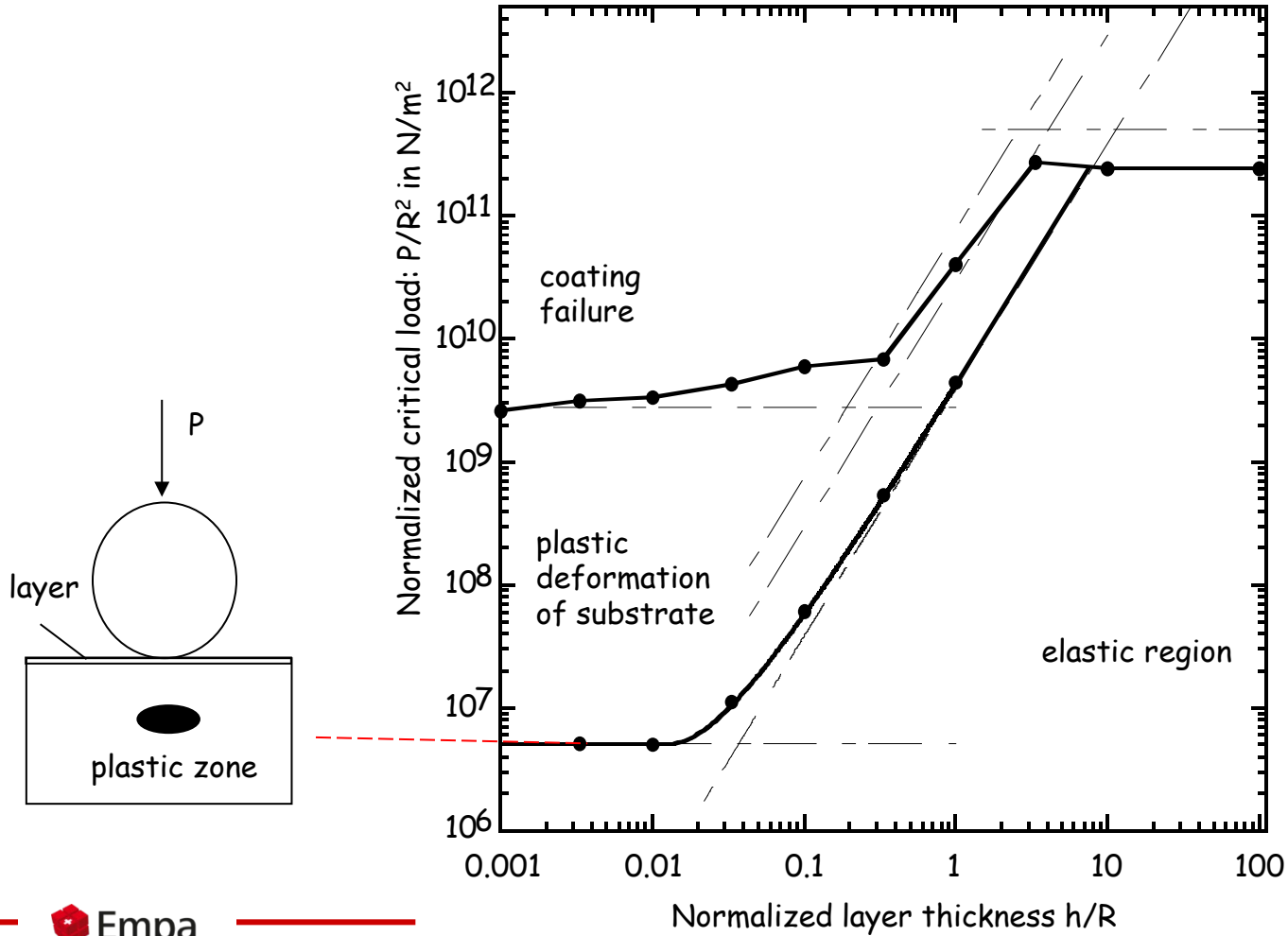

Michler & Blank 2001, Thin Solid Films **381**, 119-134

Mechanical analogues: Yielding h*>>0.01

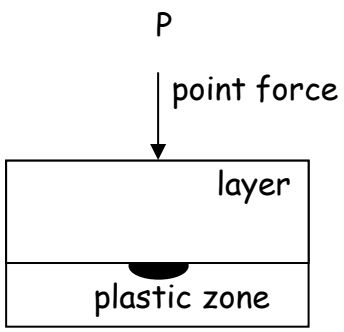

- If the layer thickness is thick compared to the indenter radius and the elastic properties of layer and substrate are similar, the Boussinesq solution can be used
- Highest shear stress occurs in the hard layer
- Yielding occurs at the interface between layer and substrate
- If substrate follows von Mises criterion, the critical load is:

$$P^* = \frac{2\pi h^{*2}\sigma_y}{\sqrt{13 - 10\nu_s + \nu_s^2}}$$

Mechanical analogues: Yielding h*>>0.01

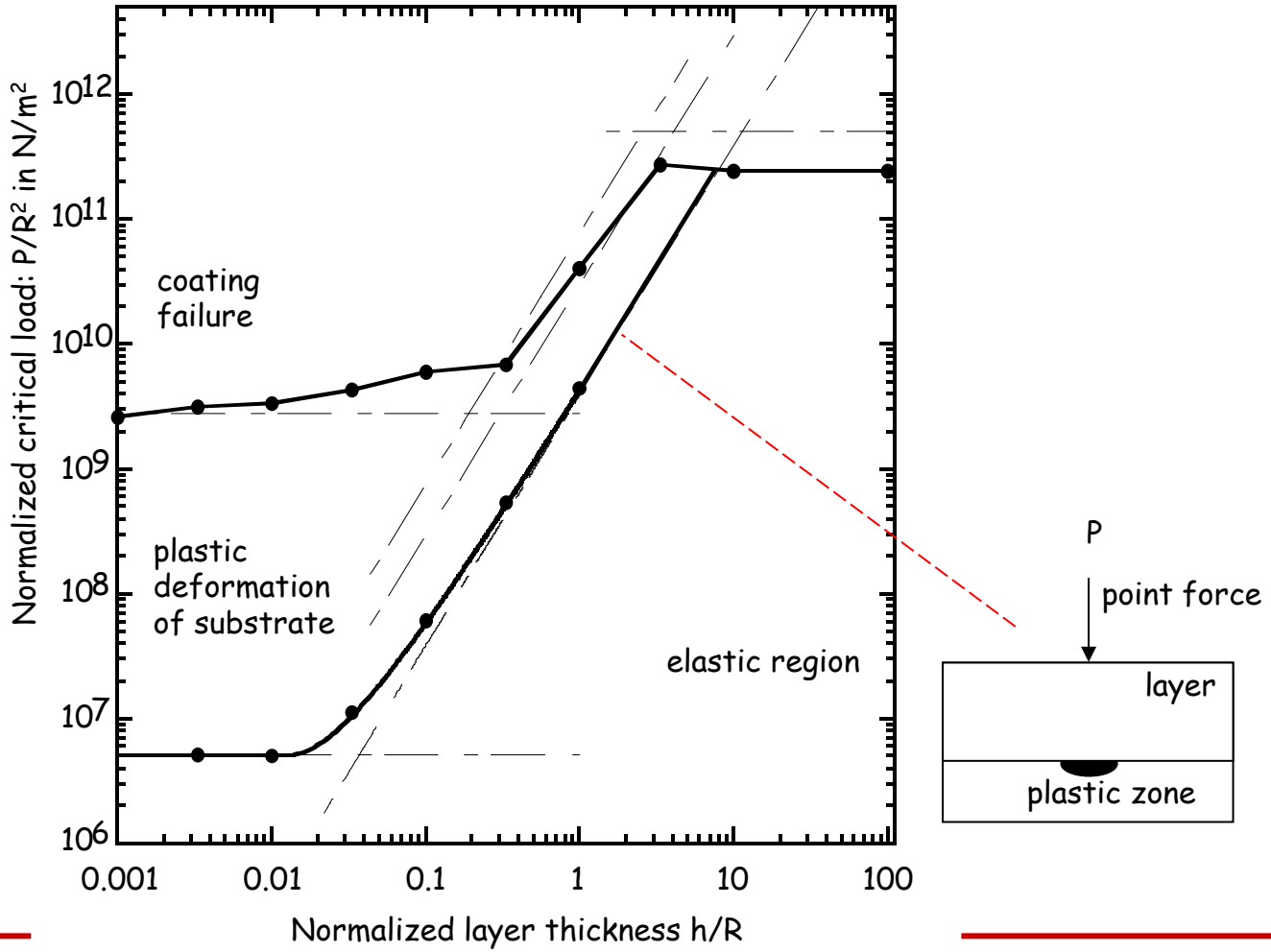

Michler & Blank 2001, Thin Solid Films **381**, 119-134

Failure map DLC on tool steel

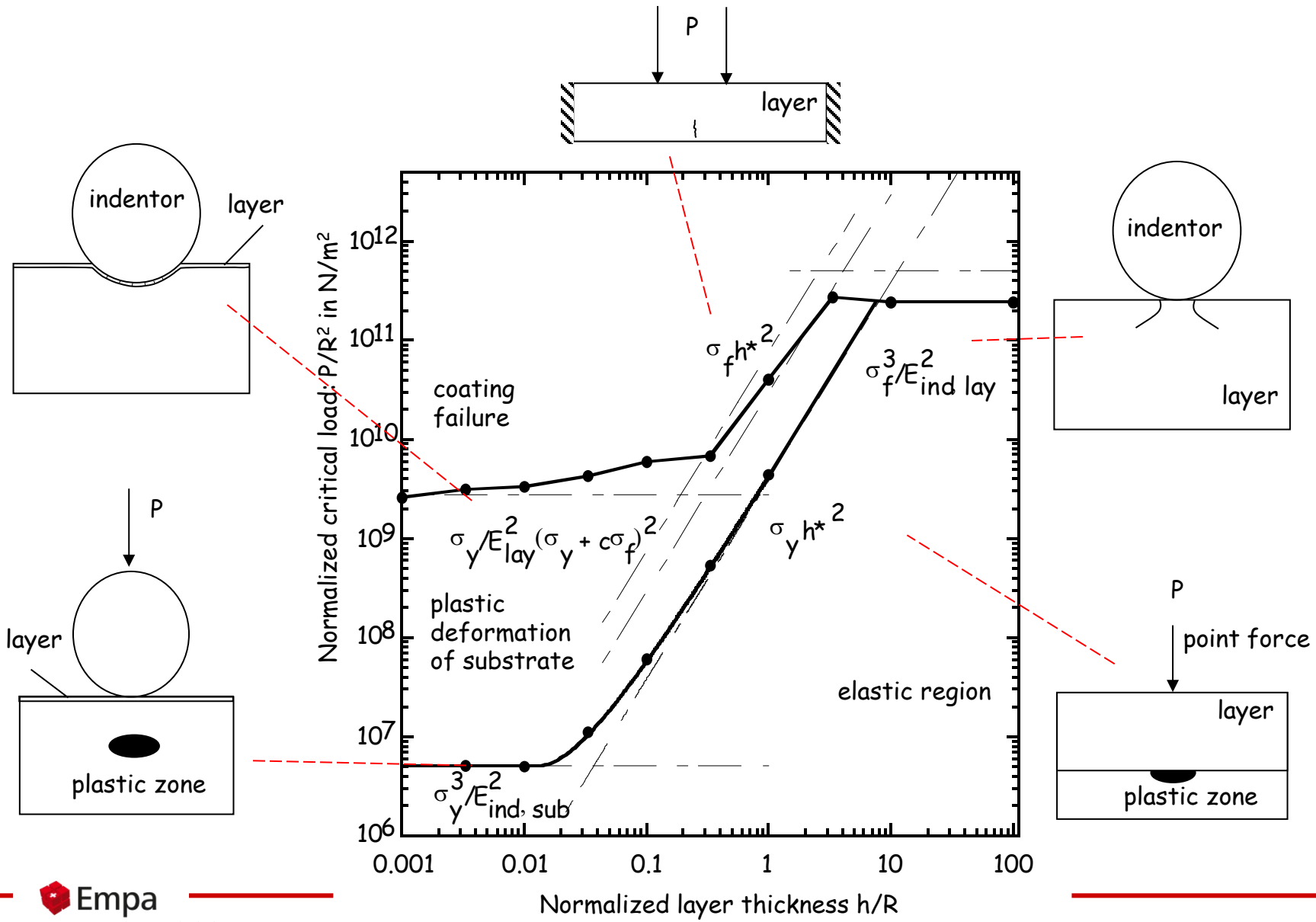

What if E_1 and E_2 differ? Failure map AlCrTiN on N-W300

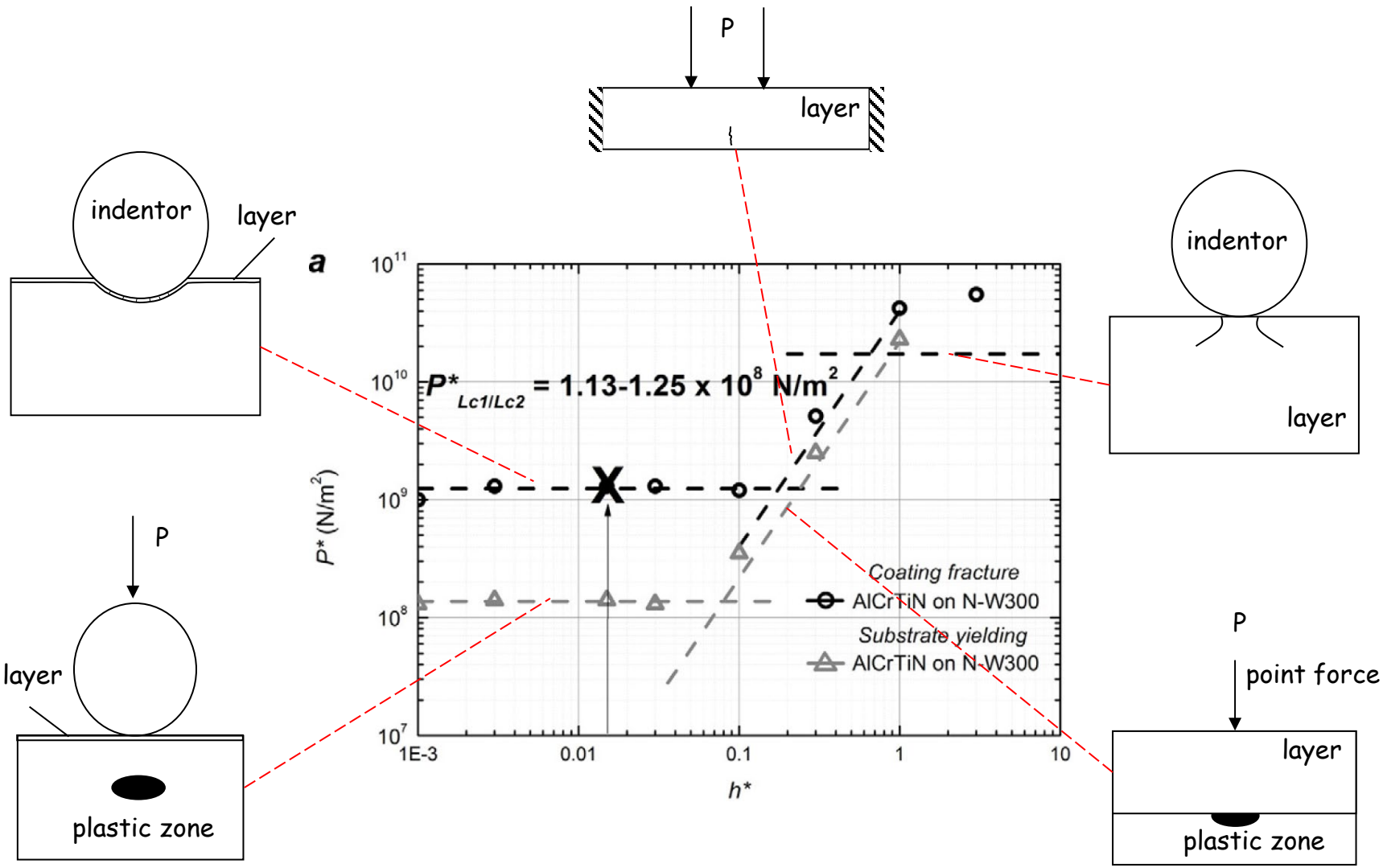

Mechanical analogue: Yielding h*>0.01 – thin plate model

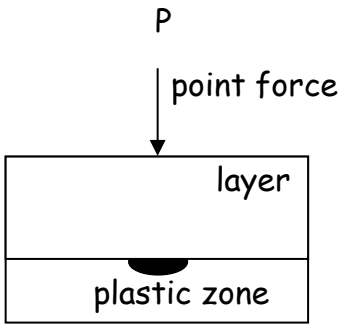

- If the layer thickness is thick compared to the indenter radius but the elastic properties of layer and substrate are dissimilar, a model for a point load on a thin plate bonded to an elastic halfspace is used.
- Hankel transforms are used to find a solution to this problem:
- Plate deflection: $w(r) = \frac{P(1-\nu_s)}{2\pi G_s a}\int_0^\infty \frac{J_0(\xi r/a)}{1+\xi^3}d\xi$, $w(0) = \frac{\sqrt{3}}{9}\frac{P(1-\nu_s)}{G_s a}$
- Pressure distribution: $q(r) = \frac{P}{2\pi a^2}\int_0^\infty \frac{\xi J_0(\xi r/a)}{1+\xi^3}d\xi$, $q(0) = \frac{\sqrt{3}}{9}\frac{P}{a^2}$

Mechanical analogue: Yielding h*>0.01 – thin plate model

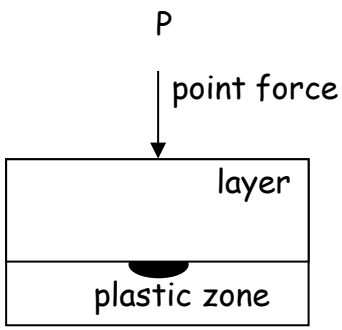

- The deflection and its derivatives may be approximated by a series expansion around r=0 (Holl 1938, Selvadurai 1979), the same can be done for the contact pressure.
- The radial and circumferential strains at the bottom of the plate are given by $\varepsilon_{rr}\left(0,\frac{h}{2}\right)=\frac{h}{2}\frac{d^2w}{dr^2}(0)$ and $\varepsilon_{\vartheta\vartheta}\left(0,\frac{h}{2}\right)=\frac{h}{2}\frac{1}{r}\frac{dw}{dr}(0)$ and are continuous over the perfectly bonded interface.
- The radial and circumferential strains can be calculated using Hooke's law
- The axial stress in the substrate at the interface to the plate is equal to the contact pressure: $\sigma_{zz,s}\left(0,\frac{h}{2}\right)=q(0)=\frac{\sqrt{3}}{9}\frac{P}{a^2}$

Mechanical analogue: Yielding h*>0.01 – thin plate model

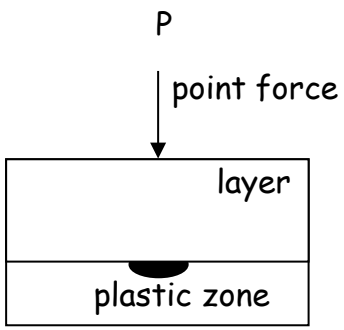

- Due to the thin plate theory and continuity of shear stress at the boundary of the plate and the continuum, the shear stress at the interface vanishes: $\tau_{rz,s}\left(0,\frac{h}{2}\right)=0$
- Yielding occurs in the substrate at the interface and is governed by a von Mises criterion:

$$\sigma_{vM}=\sqrt{\frac{1}{2}\left(\left(\sigma_{rr,s}-\sigma_{\vartheta\vartheta,s}\right)^2+\left(\sigma_{rr,s}-\sigma_{zz,s}\right)^2+\left(\sigma_{\vartheta\vartheta,s}-\sigma_{zz,s}\right)^2\right)+3{\tau_{rz,s}}^2}$$

- Yielding occurs when the von Mises stress reaches the equivalent yield stress of the substrate. This can be solved for P*, if the yield stress of the substrate is known.

Mechanical analogue: Yielding h*>0.01 – thin plate model

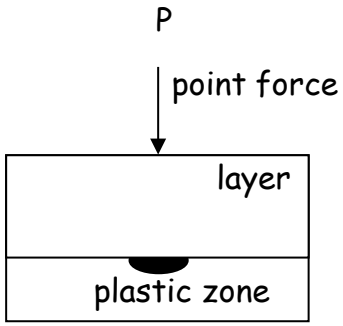

$$
\begin{aligned}
&P^* \\
&= \left(1.4141 \frac{E_b}{E_s} (h^*)^2 \sigma_y (0.5 - \nu_s)(1 - \nu_s^2)^2\right) \\
&\cdot \left(0.265 \left(\left(\nu_b^2 - 1\right)(-2.471\nu_s^3 + 1.853\nu_s - 0.618) \sqrt[3]{\frac{E_b(\nu_s^2 - 1)}{E_s(\nu_b^2 - 1)}} \right.\right. \\
&\left. + \left(\nu_b^2 - 1\right)(\nu_s^4 + 1.428\nu_s^3 - 1.964\nu_s^2 - 1.428\nu_s + 0.964) \right)^2 \\
&+ 0.984 \left(\left(\nu_b^2 - 1\right)(-1.281\nu_s^3 + 0.961\nu_s - 0.320) \sqrt[3]{\frac{E_b(\nu_s^2 - 1)}{E_s(\nu_b^2 - 1)}} \right. \\
&\left. + \left(\nu_b^2 - 1\right)(\nu_s^4 + 0.0186\nu_s^3 - 1.259\nu_s^2 - 0.019\nu_s + 0.259) \right)^2 \\
&\left. + 0.228 \left(\left(\nu_b^2 - 1\right)(\nu_s^4 - 1.5\nu_s^3 - 0.5\nu_s^2 + 1.5\nu_s - 0.5) \right)^2 \right)^{-1/2}
\end{aligned}
$$

Comparison to the Boussinesq model

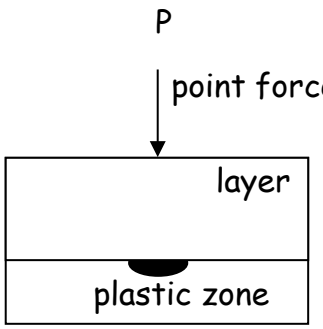

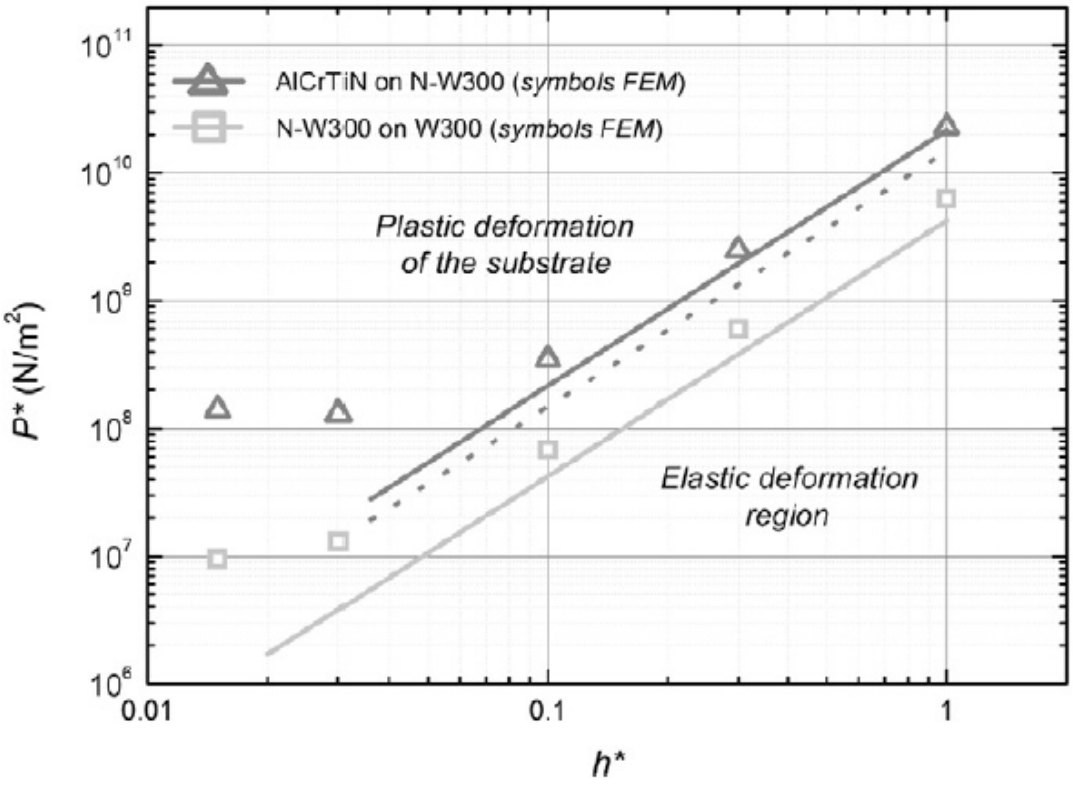

Failure map AlCrTiN on N-W300

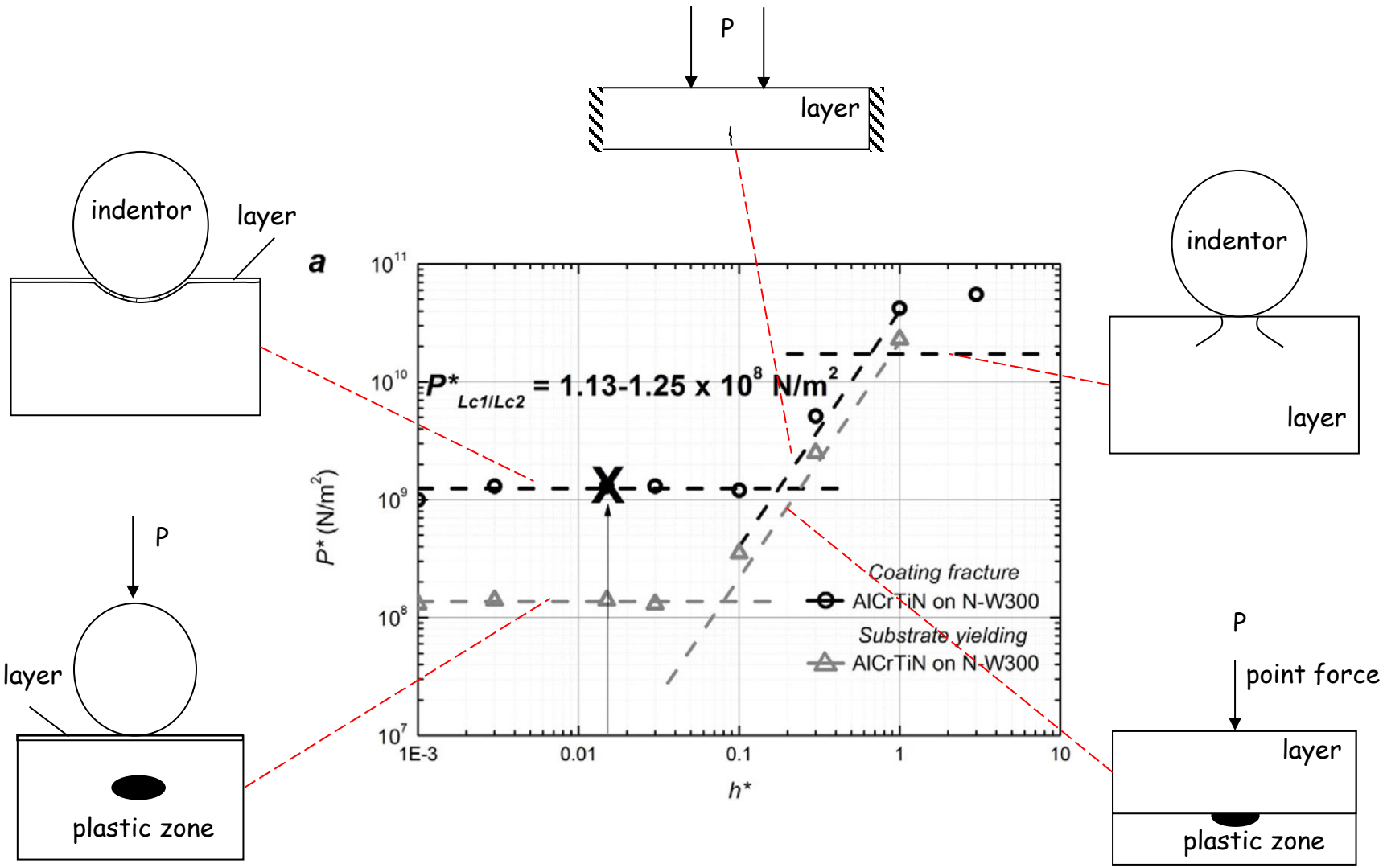

Tribology and wear

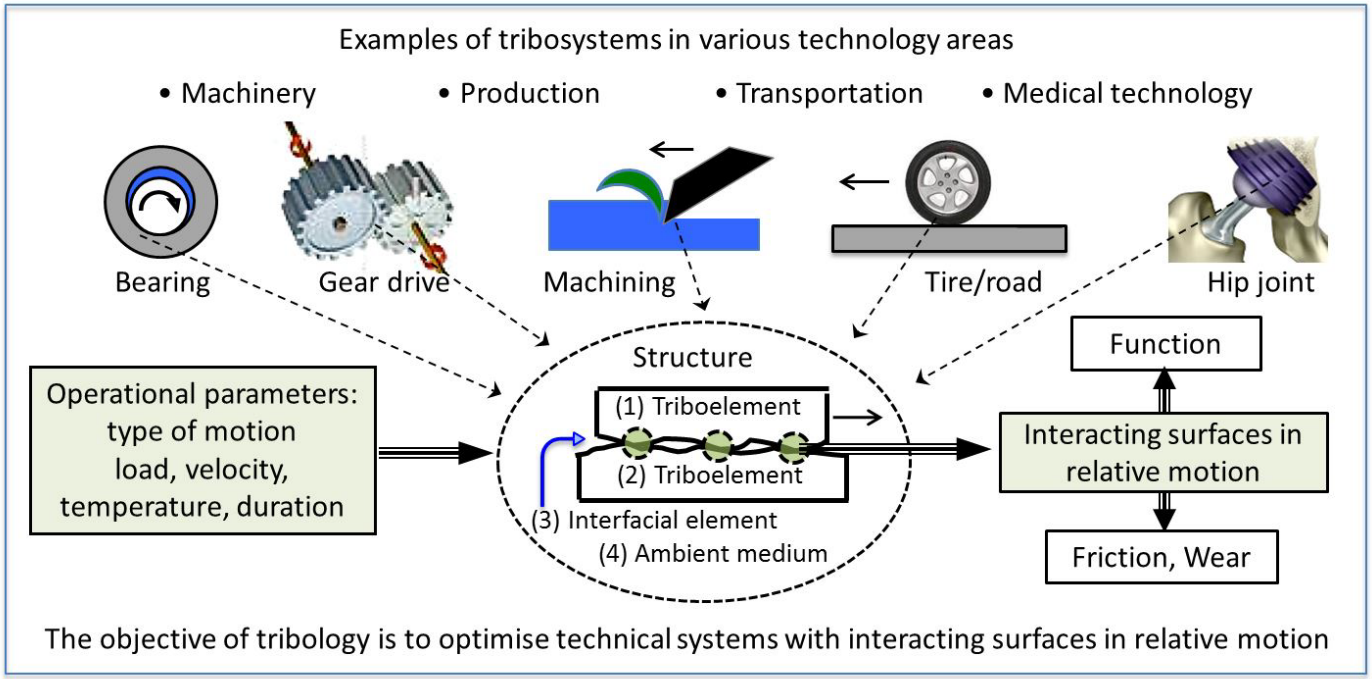

Source: H. Czichos and M. Woydt: Introduction to Tribology and Tribological Parameters. ASM Handbook, Volume 18, Friction, Lubrication, and Wear Technology, 2017

- Tribology is the study of phenomena associated with interacting surfaces in relative motion.
- Adhesion, hardness, friction, wear, erosion, and lubrication are among some of the scientific and technological concerns of this important subject.

The frist tribo-engineer

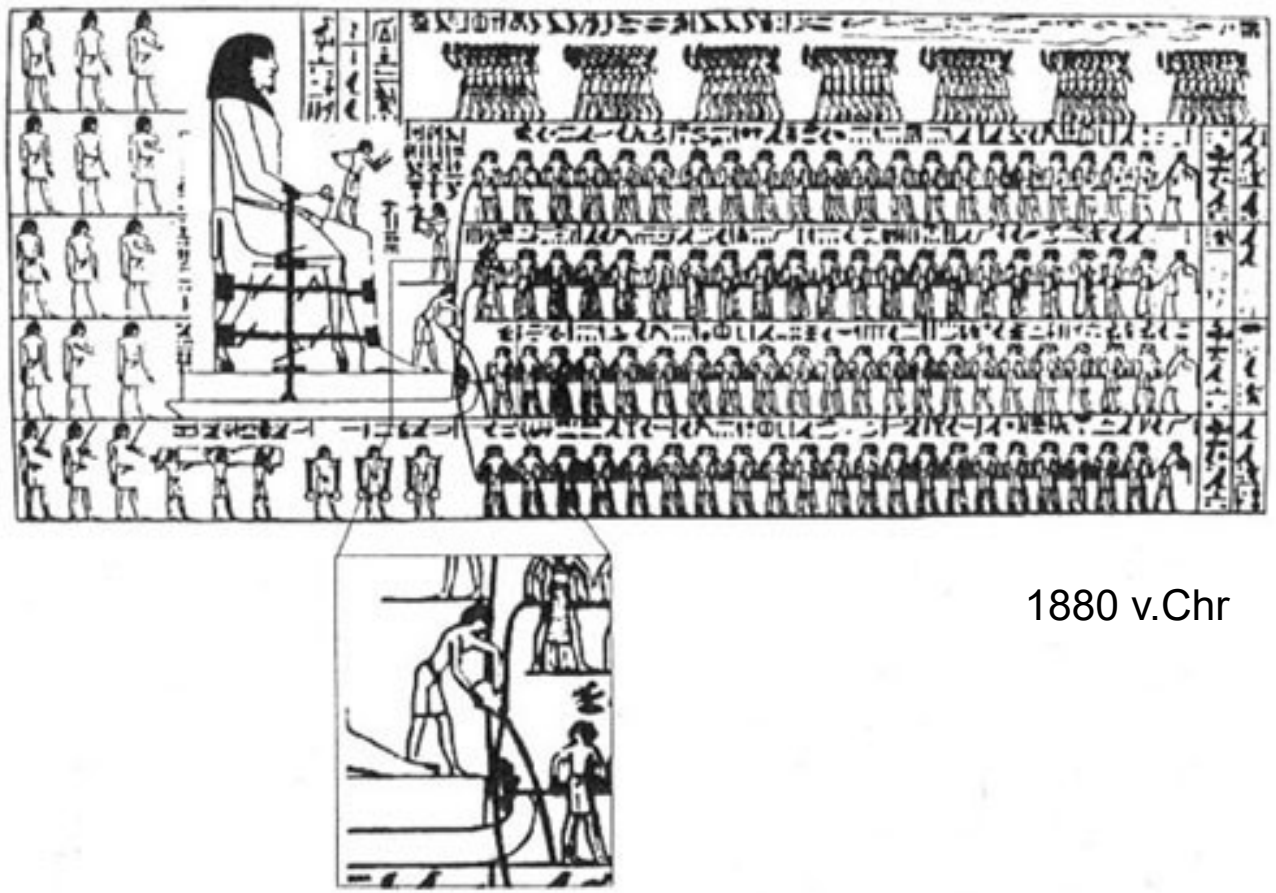

1880 v.Chr

Dry sand/wood:
Friction coefficient 0.5
Wet sand/wood:
Friction coefficient 0.2

->Muscle force of 172 Aegyptions/Weght of statue~0.25

Friction in everyday life

a) Sliding bearing

b) Rolling wheel on road

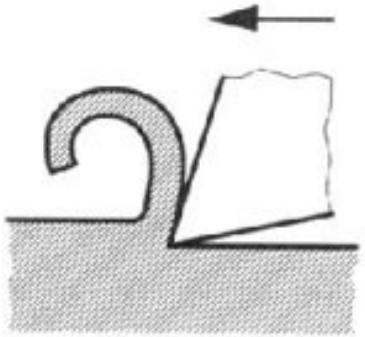

c) Metal cutting

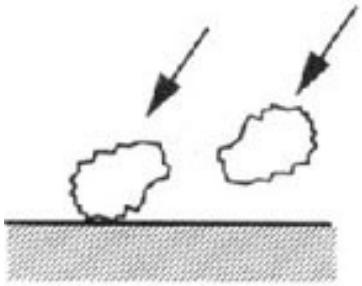

d) Mining

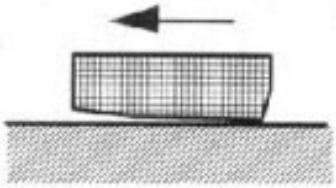

e) Magnetic storage systems

f) Human joint

friction

All **engineering surfaces are rough** and characterized by a density of asperities with some distribution of heights.

The **sum of these local contact areas represents the real area of contact**, which may only be but a fraction of the apparent geometric contact area.

In the majority of contacts **surface films are present with properties different from the underlying bulk material**. Surface films may be gases, fluids (e.g., oil), or deposited solid layers such as graphite, metals, or ceramic coatings.

Sliding friction is linked to the adhesion, ploughing and asperity deformation.

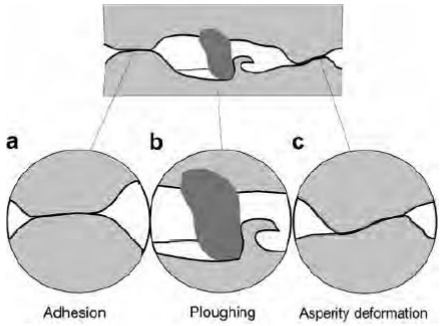

Fig. 3.6. The three components of sliding friction are (a) adhesion, (b) ploughing and (c) asperity deformation.

wear

Wear may be defined as the progressive removal of material from surfaces that are under load in relative motion. Several different mechanisms have been identified to characterize contact wear.

Fatigue Wear: Fatigue wear occurs in situations where there is repeated loading and unloading of surfaces in contact. Failure may initiate at both surface flaws or cracks or at subsurface inhomogeneities.

Abrasive Wear: Abrasive wear is a form of cutting wear where the material is removed by hard wear particles, by hard asperities, or by hard particles entering the interface from the environment.

Adhesive Wear: Adhesive wear occurs when applied tangential forces cause fracture between surfaces bonded at asperities.

Tribocorrosion: such as oxidation wear arises from the continuous rubbing and removal of surface films produced by reaction with the environment.

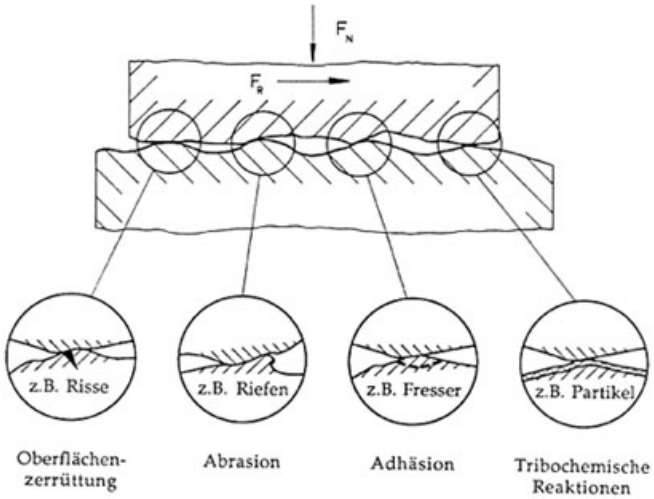

Fatigue ***Abrasion*** ***Adhesion*** ***Tribocorrosion***

Strategies against friction and wear

Tribology is a complex topic and no analytical solution exits. Holmberg stated, however, a number of design rules:

Rule 1 – Contact stresses: Stresses generated by the surface loads should be below the yield strength and the fracture limits of the surface.

Rule 2 – Sliding: Contact temperatures, surface roughness and wear particle generation should be at a level which avoids effects such as accumulated surface melting, asperity and debris interlocking and ploughing. Then the conditions are characterized by stable sliding, typically with generated surface layers having low shear strength and minimum wear.

Rule 3 – Surface fatigue: Coating elasticity and thickness should be of a level to allow deflection and avoid high-stress peaks and simultaneously distribute the stresses. The coating structure should inhibit crack growth. The substrate and coating strength should be above the level needed to avoid fatigue fracture. The surface should have optimized roughness to allow polishing.

Rule 4 – Fretting: The coating should enhance the generation of a low-friction surface layer to accommodate the movement or be elastic to accommodate deflection and reduce high stresses. The coating should increase surface inertness in relation to surface destructive chemical reactions. The coating should hinder crack initiation and crack growth.

Strategies agains friction and wear

Rule 5 – Abrasion: In abrasion the coating should have high hardness to inhibit groove formation and be thick enough to prevent abradant penetration.

Rule 6 – Impact: The coating and substrate should be sufficiently elastic to deflect and absorb impact energy and a flexible well-adhered coating/substrate interface layer is required. In erosion with normal impacts the coating should be sufficiently elastic to avoid high-stress peaks. In inclined erosion the coating should be hard enough to avoid grooving.

Rule 7 - Corrosion condition: The coating should be inert, dense and pore free to prevent chemical attack of it and the substrate or it should have suitable sacrificial properties.

Rule 8 – Lubricated condition: The coating surface should function beneficially with the lubricant. It should either react with the lubricant additives to generate a low shear strength boundary lubricant surface film or it should have the ability to generate a low shear strength surface layer despite the presence of the lubricant.

Summary

Thin films under load: Contact mechanics and tribology

- Materials Selection Indices: distinguish function, constraint, objective, free variable and identify materials index in performance equation and use Ashby chart for selection
- Selection rules for spherical contact: cone cracks emanate from contact edge and plastic deformation under contact maximum at 0.5xcontact radius a
- Selection rules for coated surface: no exact analytical solutions but approximations for different damage cases (plastic, or fracture) depending on ration film thickness/counterbody ratio such as analytical solution of homogeneous plastic deformation for spherical cavity and thin membrane stretching over surface
- Wear mechanisms: fatige wear, abrasive wear, adhesive wear, Tribocorrosion
- Design rules: reflect mostly contact mechanics of coated surface.

Microlattices

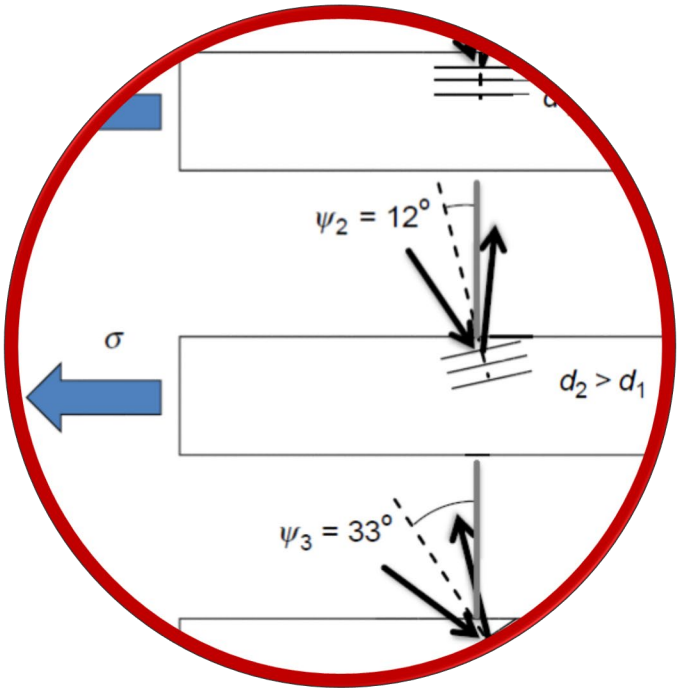

Recommended literature

- Books
  - Gibson, L. J. and Ashby, M. F. *Cellular Solids: Structure and Properties*. 2nd ed. Cambridge University Press. 1997.
  - Gibson, L. J., M. F. Ashby and Harley, B. A. *Cellular Materials in Nature and Medicine*. Cambridge University Press. 2010.

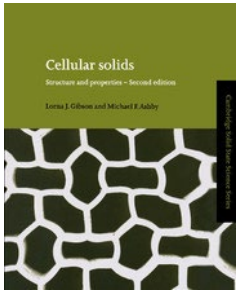

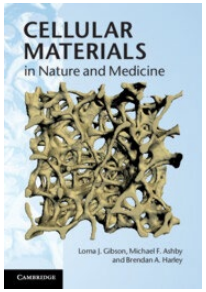

- Overview articles
  - Ashby, M. F. The properties of foams and lattices. *Phil. Trans. R. Soc. A*, 364, 15–30. 2006.
  - Gibson, L. J. The hierarchical structure and mechanics of plant materials. *J. R. Soc. Interface*, 9, 2749–2766, 2012.

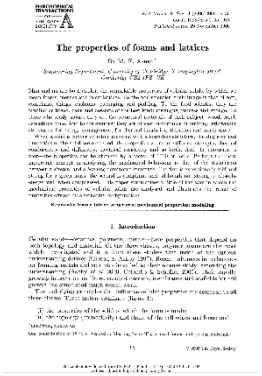

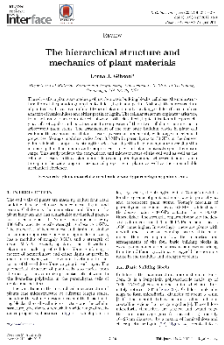

Analysis of design requirements

*Express design requirements as **constraints** and **objectives***

Bike frame

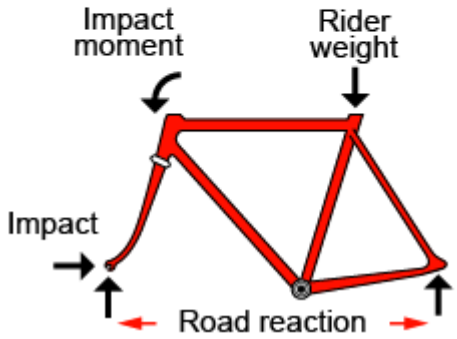

Design requirements

A label

- **Function** — *What does the component do ?*
- **Constraints** — *What essential conditions must be met ?*
- **Objectives** — *What is the criterion of excellence ?*
- **Free variable** — *What can be varied ?*

Must be

- *Stiff enough*
- *Strong enough*
- *Tough enough*
- *Able to be welded*

Minimize

- *Cost*
- *Weight*
- *Volume*
- *Eco-impact*

Choice of material and associated mechanical properties

Source: EduPack, Cambridge Materials Selector, Granta Design

Example 2: stiff, light beam

Function

Beam

Stiff beam of length L and minimum mass

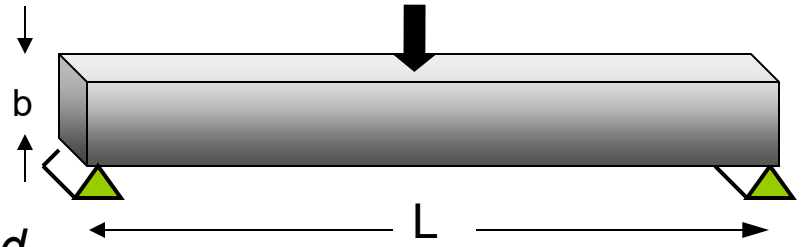

Square section, area $A = b^2$

Constraints

- *Length L is specified*
- *Must have bending stiffness > S**

Equation for constraint on A:

$$S = \frac{CEI}{L^3} = \frac{CEA^2}{12L^3} \quad (1)$$

Objective

Minimize mass m:

$$m = A L \rho \quad (2)$$

m = mass
A = area
L = length
ρ = density
E = Young's modulus
I = second moment of area
($I = b^4/12 = A^2/12$)
C = constant (here, 48)

Free variables

- *Material choice*
- *Section area A.*

Eliminate A in (2) using (1):

Performance metric m

$$m = \left(\frac{12L^5 S^*}{C}\right)^{1/2} \left(\frac{\rho}{E^{1/2}}\right)$$

Chose materials with smallest $\left(\frac{\rho}{E^{1/2}}\right)$

Minimum weight design

Tensile ties

$\left(\frac{\sigma_y}{\rho}\right)$

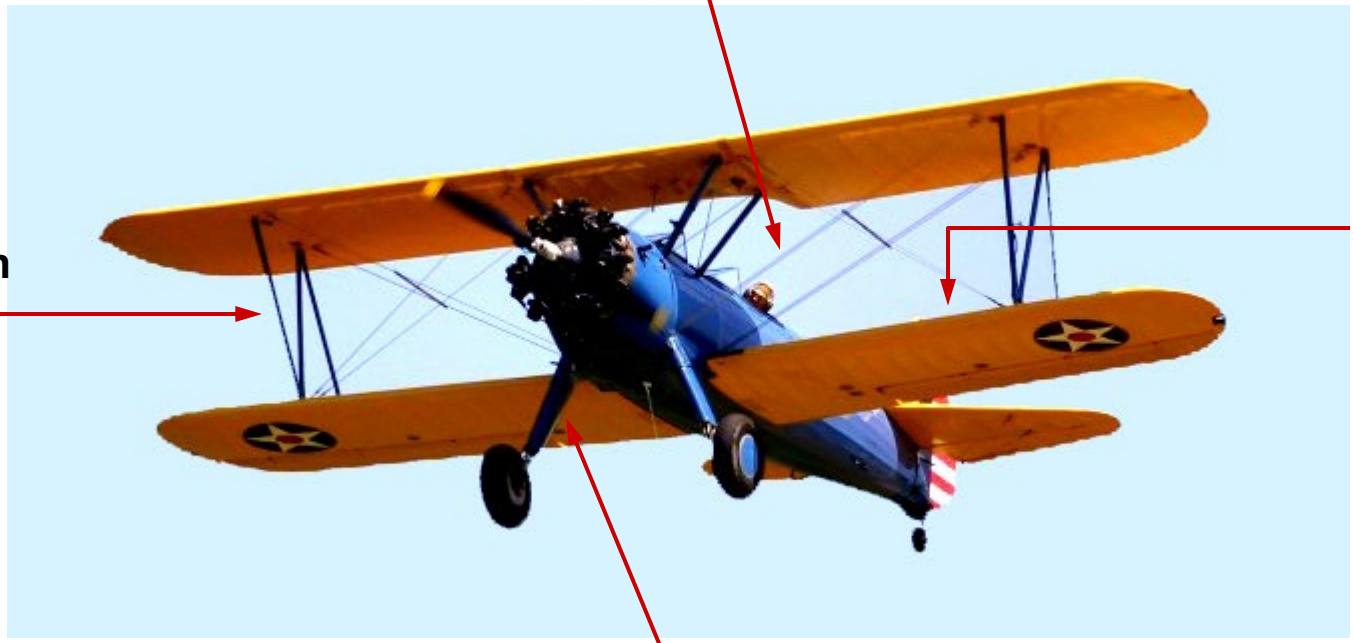

Compression strut

$\left(\frac{E^{1/2}}{\rho}\right)$

Main spar - beam

$\left(\frac{E^{1/2}}{\rho}\right)$

Undercarriage

$\left(\frac{\sigma_y^{2/3}}{\rho}\right)$

E = Young's modulus ρ = Density σ_y = Yield strength

Demystifying material indices

- A **material index** is just the **combination of material properties** that appears in the equation for **performance** (eg minimizing mass or cost).

- Sometimes a single property
- Sometimes a combination

} Either is a **material index**

Example:

Objective -- minimise **mass**

Performance metric = **mass**

Function Strength	Stiffness **Constraints**	
Tension (tie) 	ρ/E	ρ/σ_y
Bending (beam) 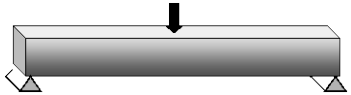	$\rho/E^{1/2}$	$\rho/\sigma_y^{2/3}$
Bending (panel) 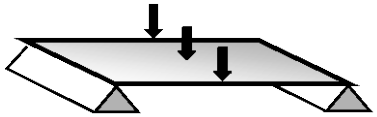	$\rho/E^{1/3}$	$\rho/\sigma_y^{1/2}$

Minimize these!

(Or maximize reciprocals)

Material indices and function

Each combination of { **Function** **Constraint** **Objective** } has a characterizing **material index**

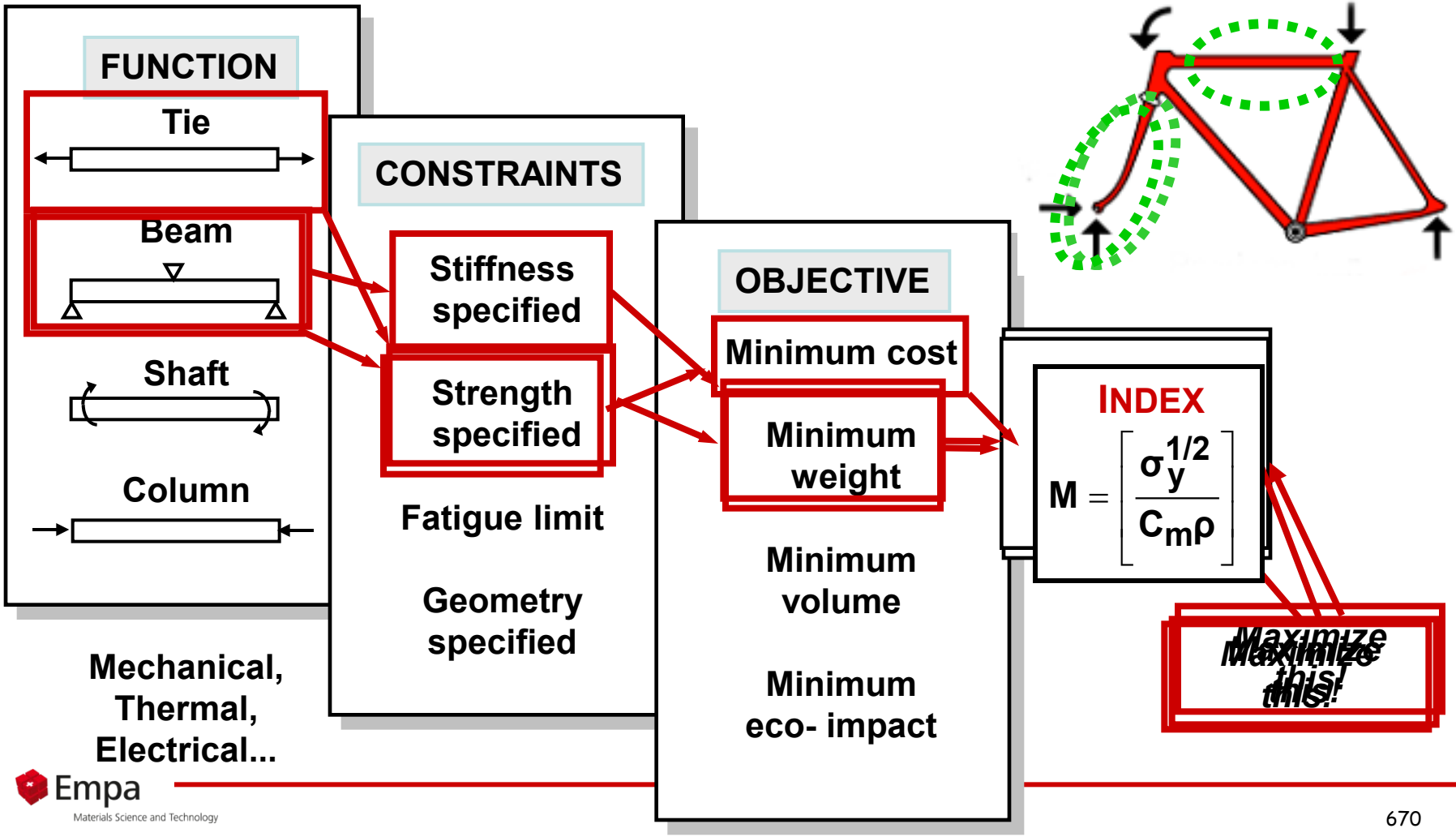

Optimized selection using charts

Light stiff beam:

Index $M = \frac{\rho}{E^{1/2}}$

Rearrange:

$E = \rho^2 / M^2$

Take logs:

Log E = 2 log ρ - 2 log M

Contours of constant M are lines of slope 2 on an E-ρ chart

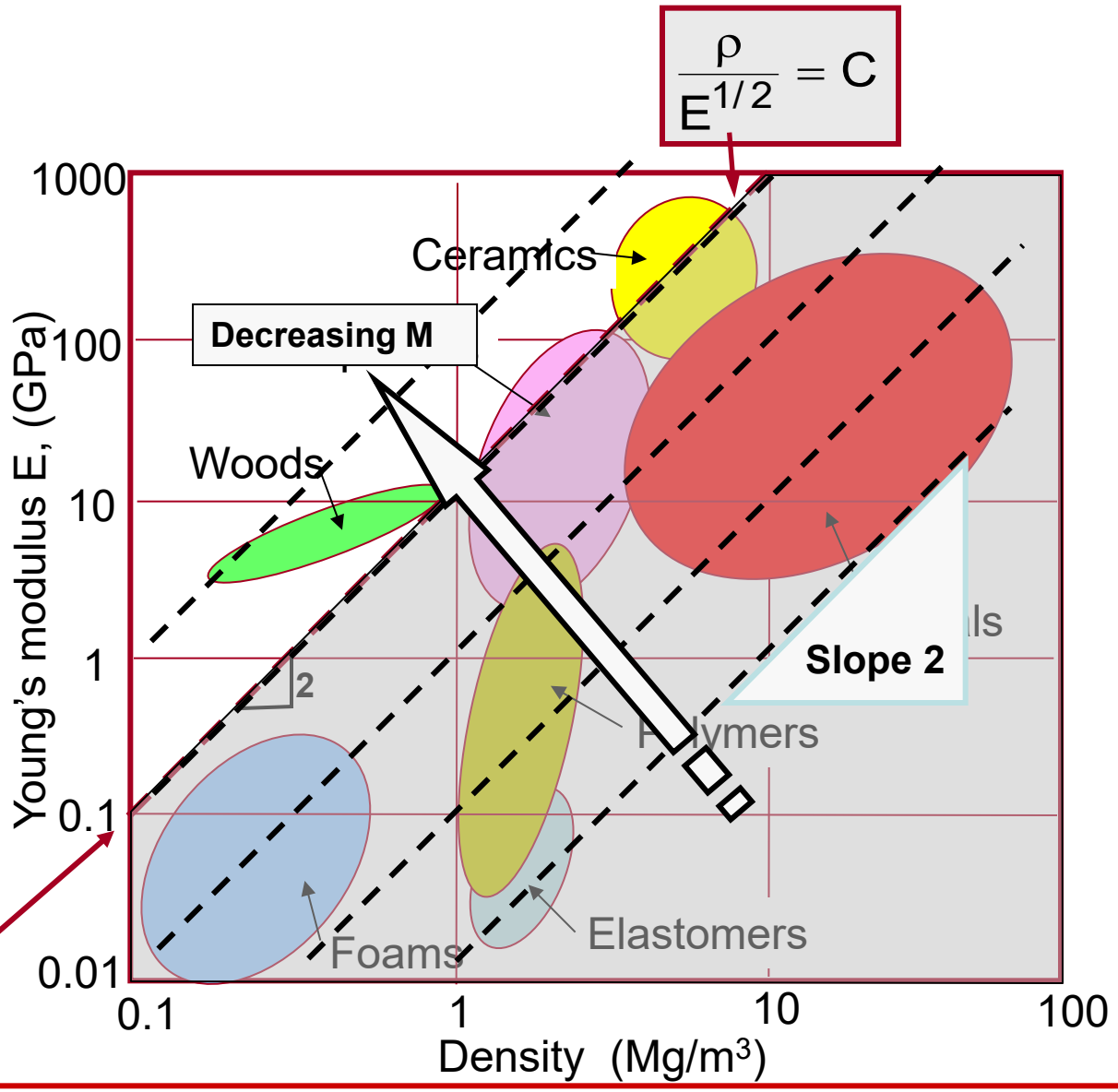

Optimised selection using charts

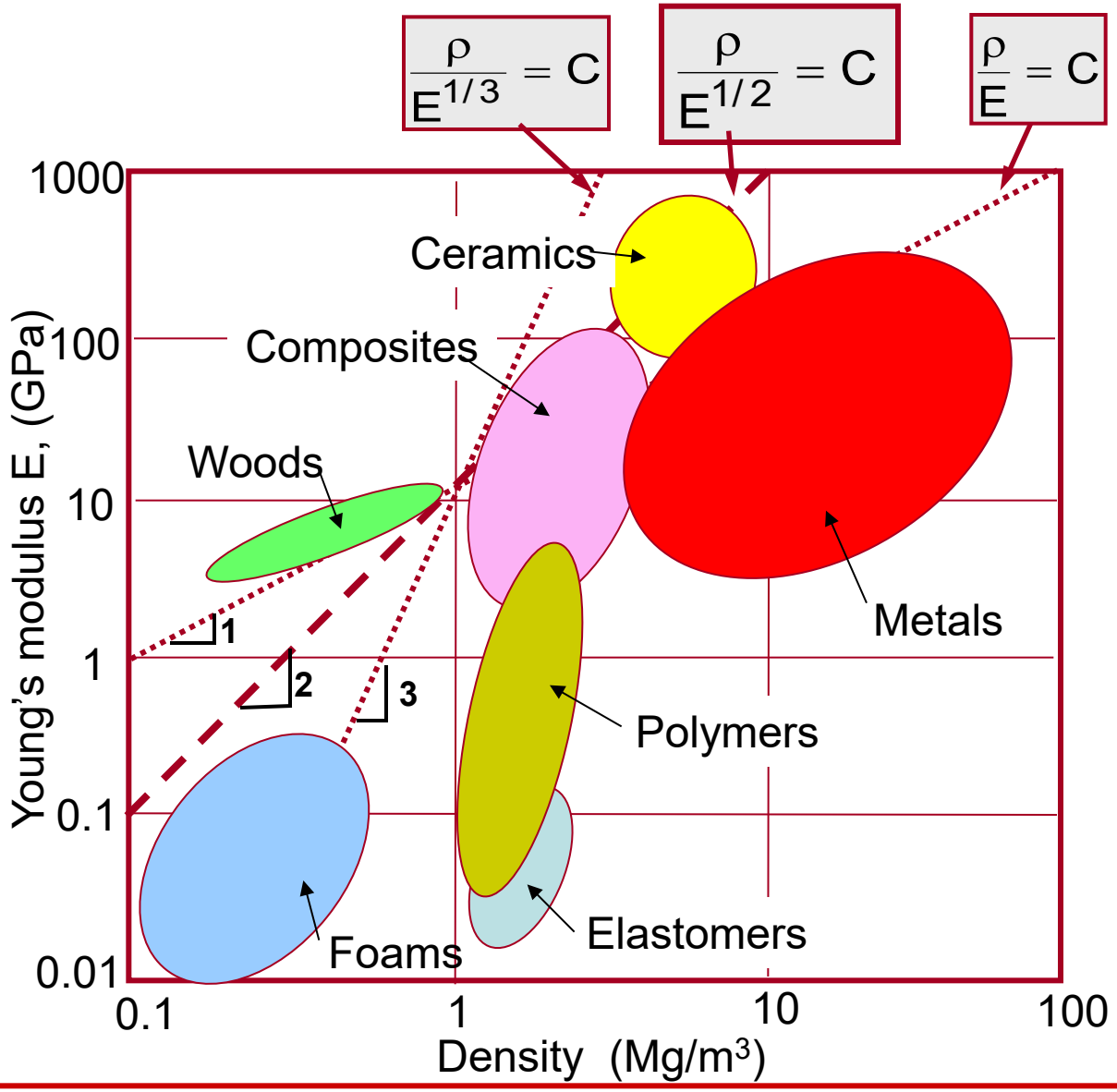

Property control by chemistry and microstructure

Metals: Precipitation hardening

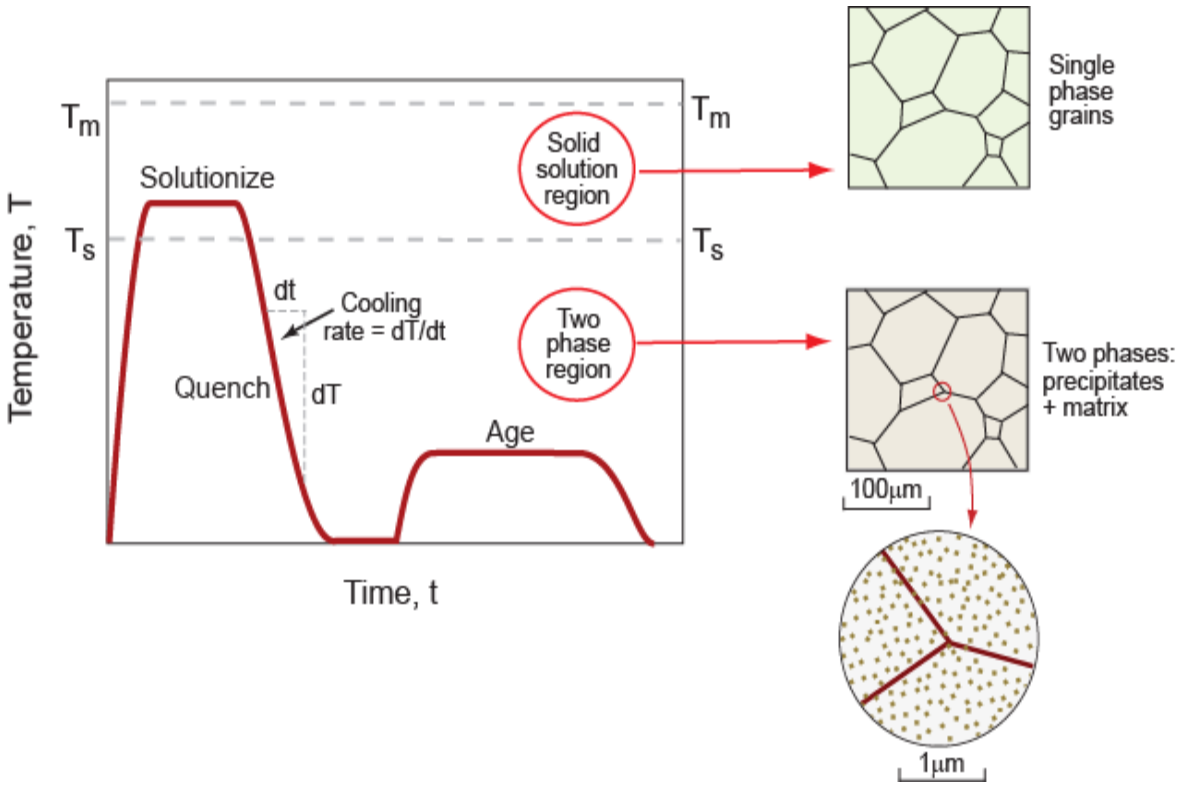

Examples:

Heat-treatable Al alloys
(age hardening)

Carbon & alloy steels
(quench and temper)

Control by chemistry and microstructure

Aluminum alloys: precipitation, solution and work hardening

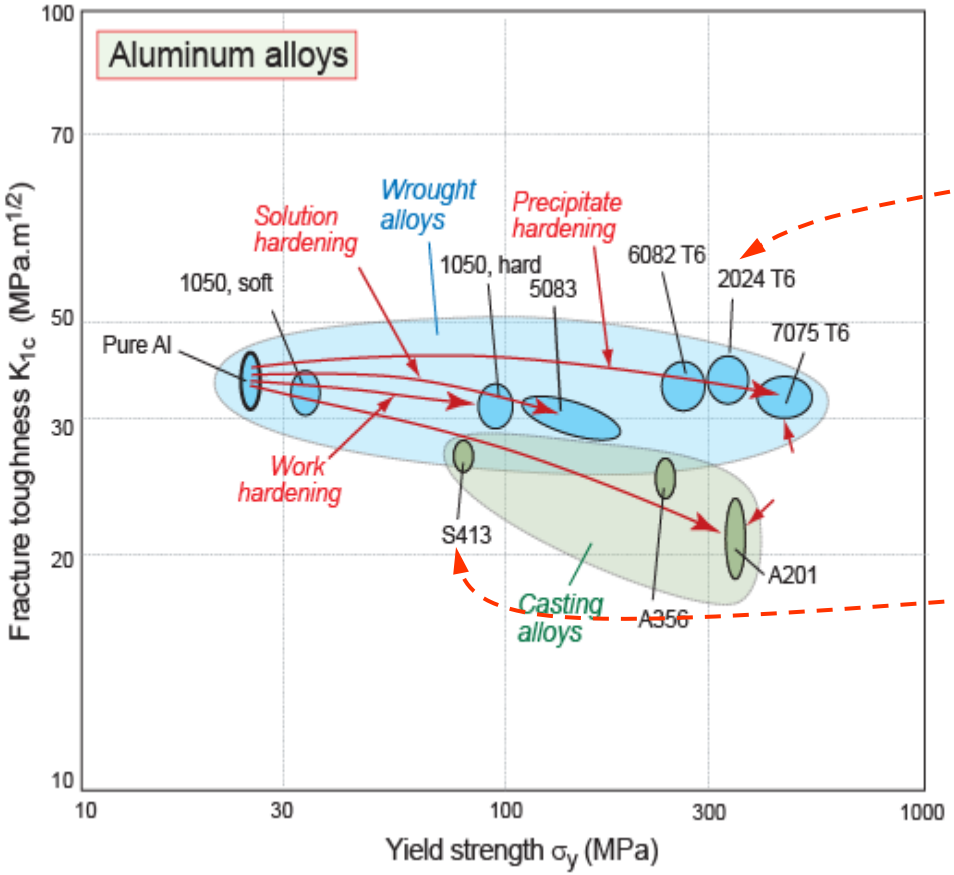

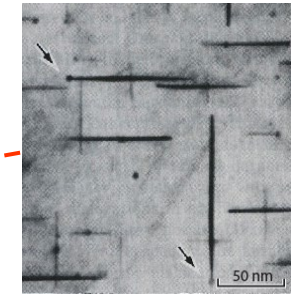

Al -Cu 2024

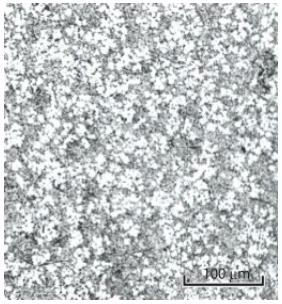

Al -Si S413

Control of modulus by architecture

Foams: "solid – air hybrids"

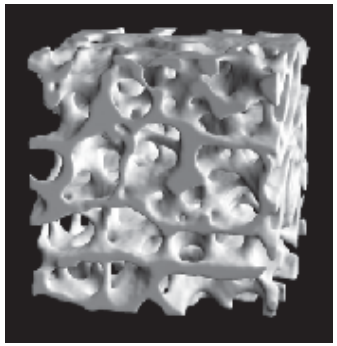

Ceramic foam

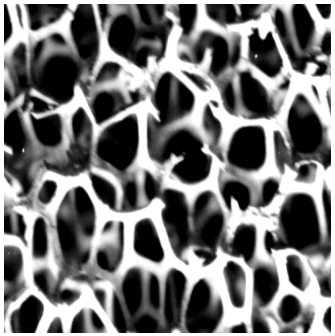

Metal foam

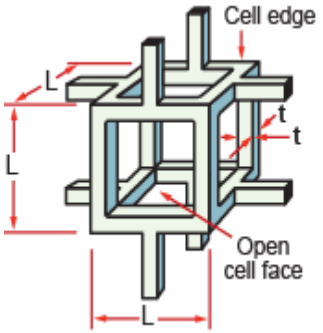

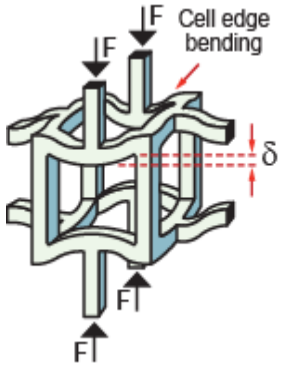

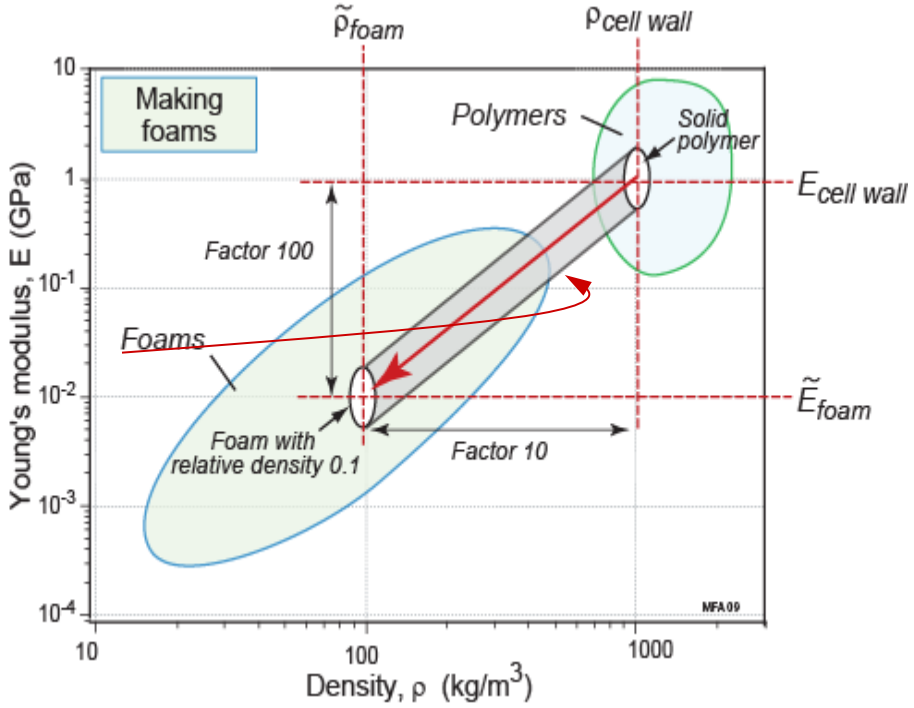

$$\frac{\tilde{E}_{foam}}{E_{solid}} = \left(\frac{\tilde{\rho}_{foam}}{\rho_{solid}}\right)^2$$

Control of modulus by architecture

Composites: "solid – solid hybrids"

CFRP

GFRP

Upper bound:

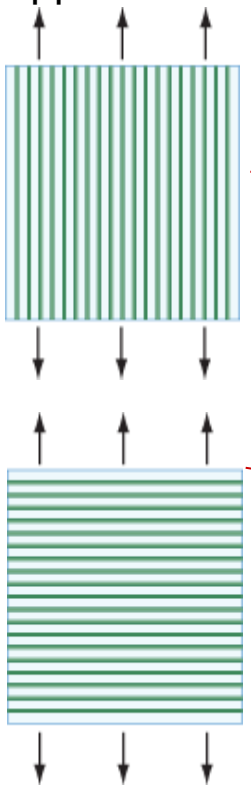

Lower bound: E_l

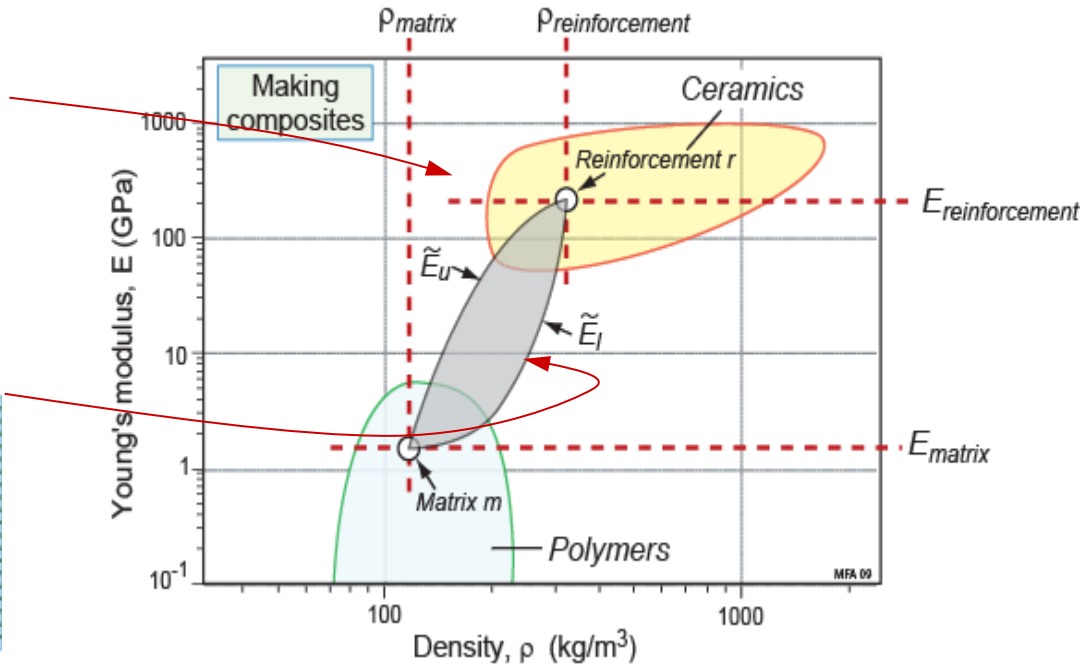

Control by size effects

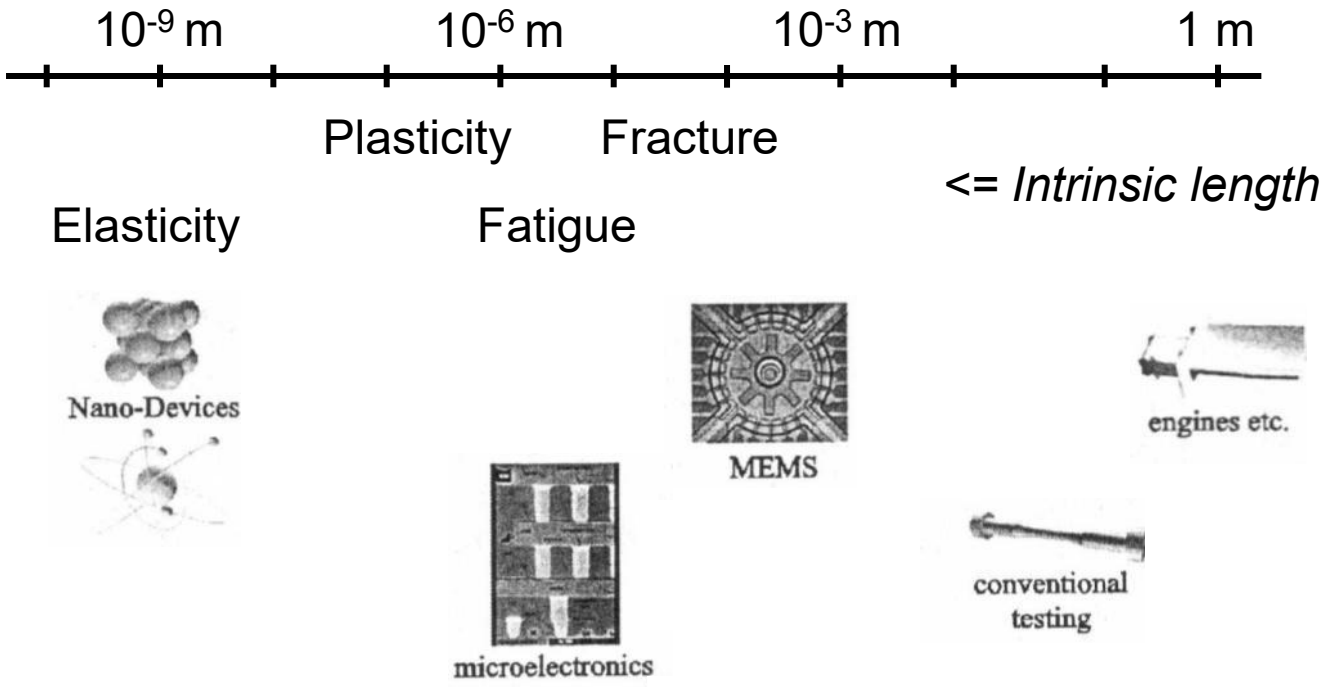

Object dimensions < intrinsic length scale => mechanical properties differ from the macroscale

O. Kraft, C. Volkert (2001) Adv. Eng. Mater. 3, 99

Control by size effects

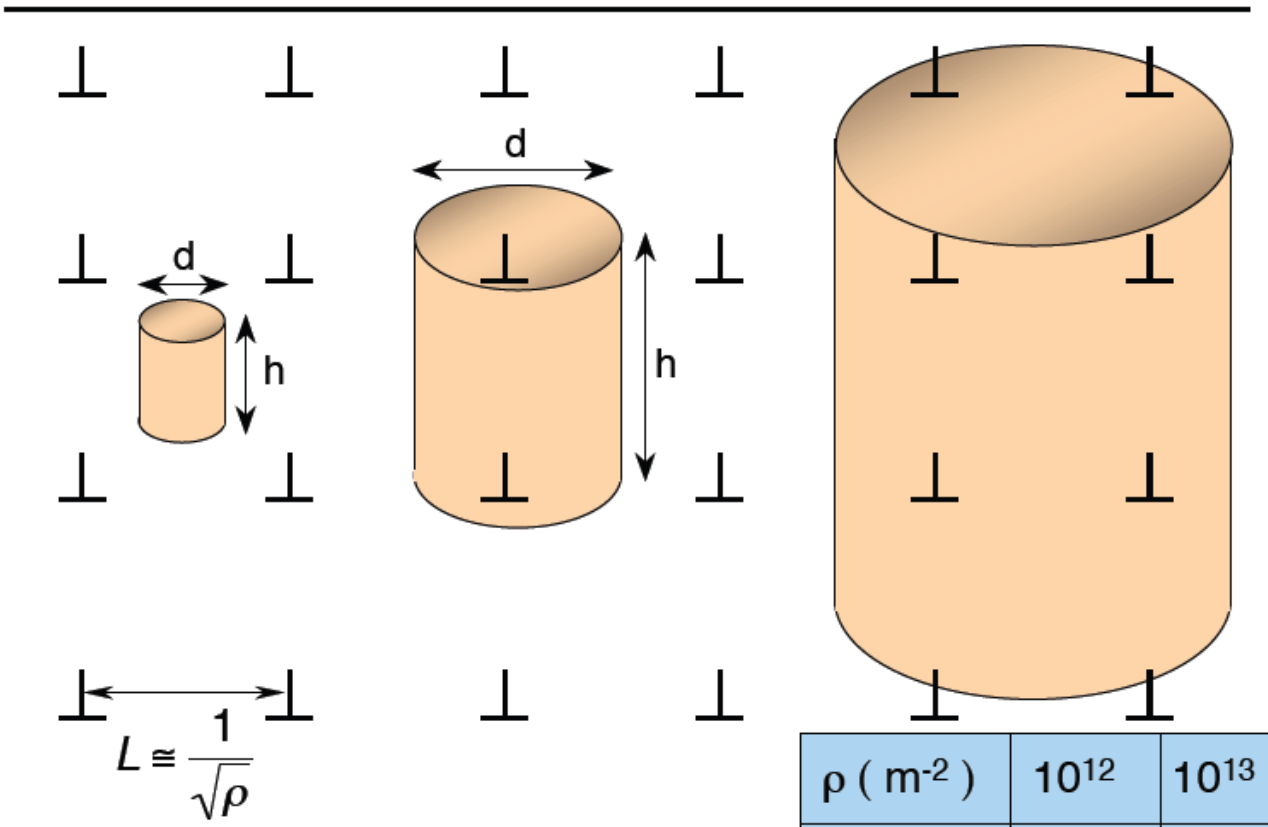

ρ (m^{-2})	10^{12}	10^{13}	10^{14}
L (μm)	1.0	0.3	0.1

Control by size effects

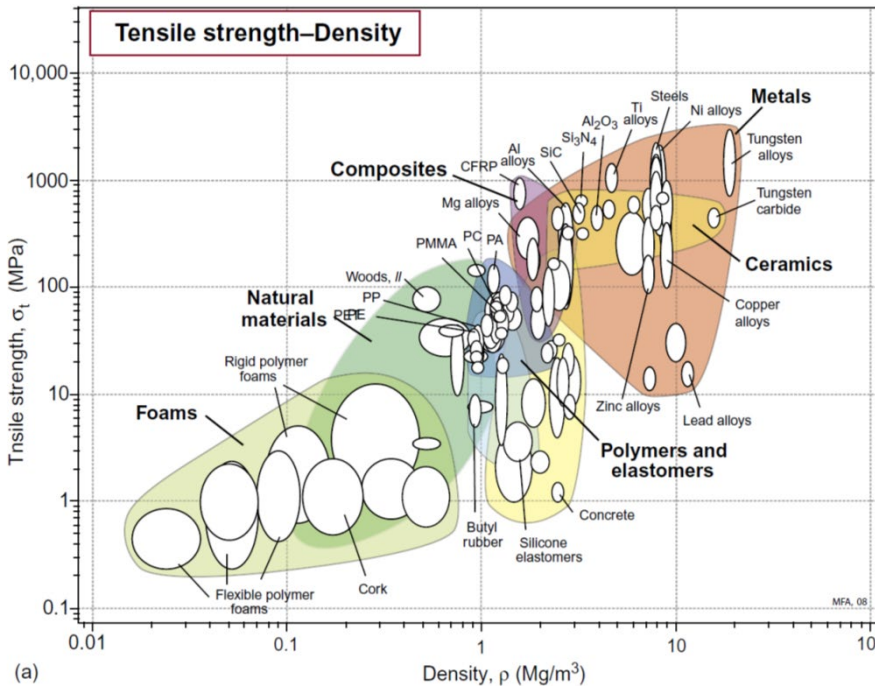

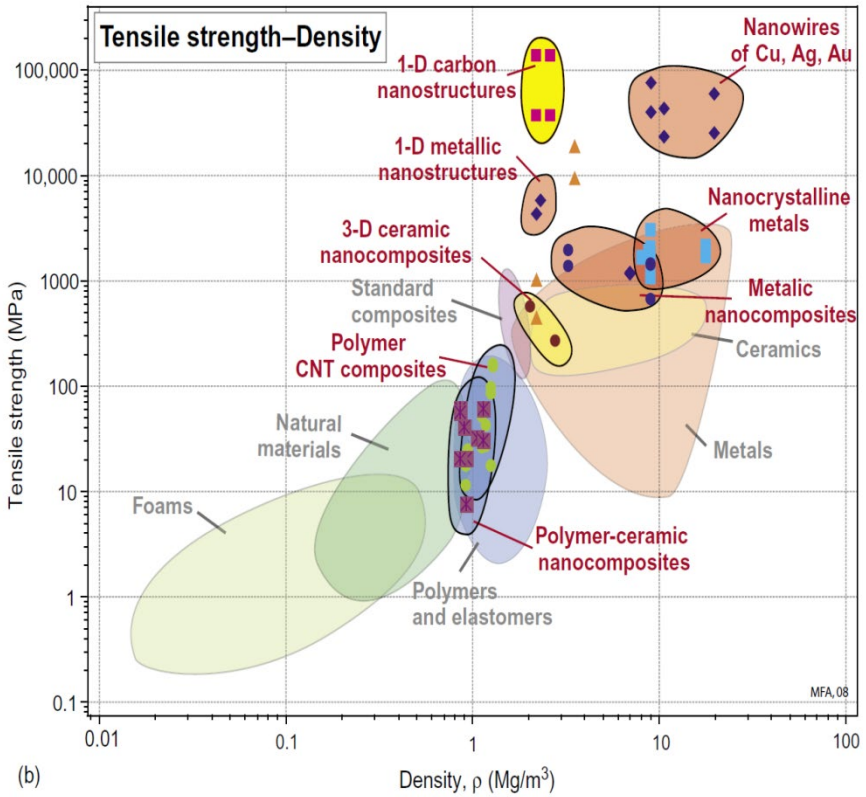

Manipulating properties: modulus – density

Composition, microstructure and architecture

Composites: Architecture – Components, lay-up

Natural materials: Composition, microstructure, architecture

Foams: Architecture – cell structure

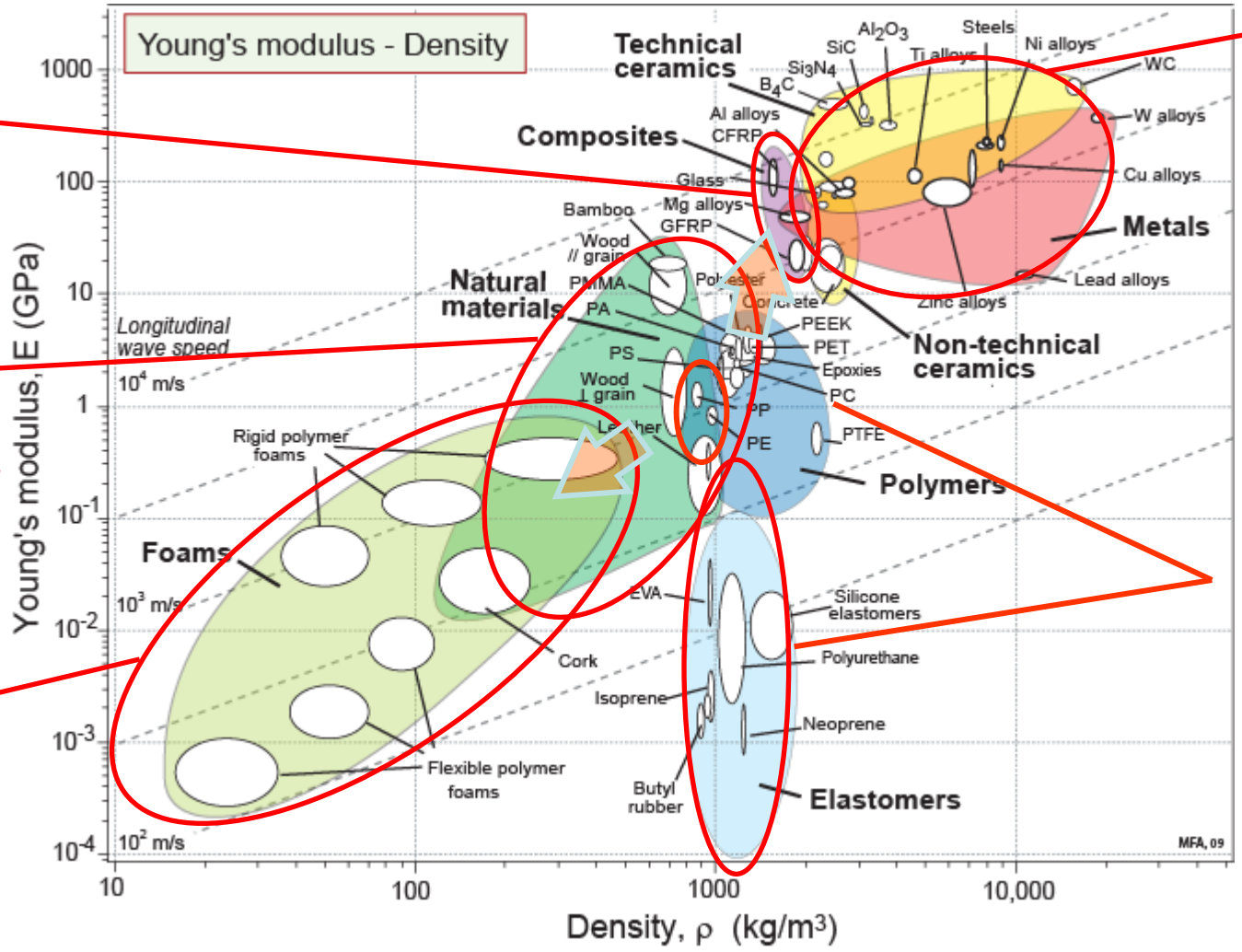

Crystalline materials: Composition metallic bond vs. ionic/covalent bonds.

Polymers & Elastomers: Composition & Microstruct. hydrogen-bonded C-chains; cross-linking and crystallinity.

Discovery of the cellular structure by Robert Hooke

Cell from Latin "*cella*" meaning:
A small compartment

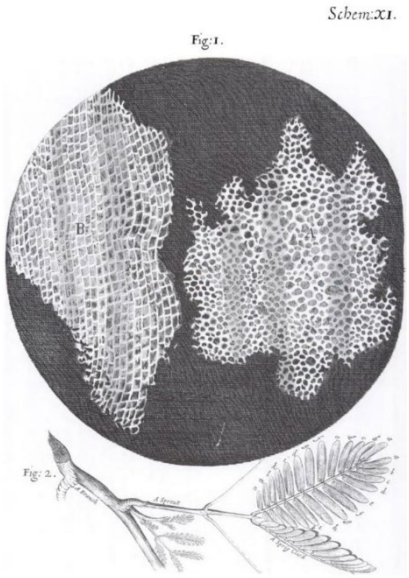

Robert Hooke's observation on cork:
"I could exceedingly plainly perceive it to be all perforated and porous, much like a Honey-comb, but that the pores of it were not regular… these pores, or cells,…were indeed the first microscopical pores I ever saw, and perhaps, that were ever seen, for I had not met with any Writer or Person, that had made any mention of them before this…"

Hooke, Robert (1665). *Micrographia: Or Some Physiological Descriptions of Minute Bodies Made by Magnifying Glasses, with Observations and Inquiries Thereupon.* Courier Dover Publications.

Painting by Rita Greer, digitised by the Department of Engineering Science, Oxford University.

Definitions of cellular or "lattice" materials

Small scale truss structures (mm & µm)

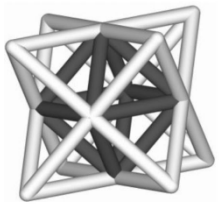

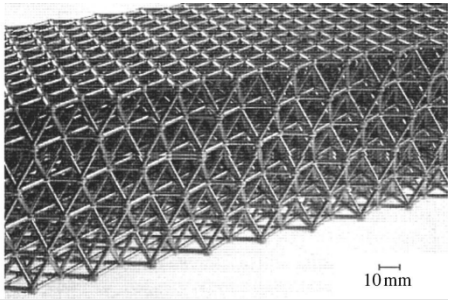

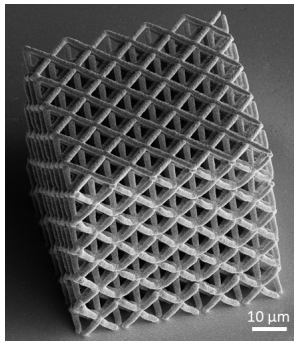

Empa, intern

A lattice is a connected network of struts.

"Cellular or "lattice" materials are made up of a connected array of struts or plates, and like the crystal lattice, they are characterized by a typical cell with certain symmetry elements; some, but not all, have translational symmetry […]"

Structural engineering:
"A lattice truss or space frame means an array of struts, pin-jointed or rigidly bonded at their connections, usually made of one of the conventional materials of construction: wood, steel or aluminium."

Materials and design aspect:
"The purpose of lattices is to create stiff, strong load-bearing structures using as little material as possible, or, where this is useful, to be as light as possible."

Ashby, *Phil. Trans. R. Soc. A,* 364, 15–30. 2006.

Design principles for cellular materials

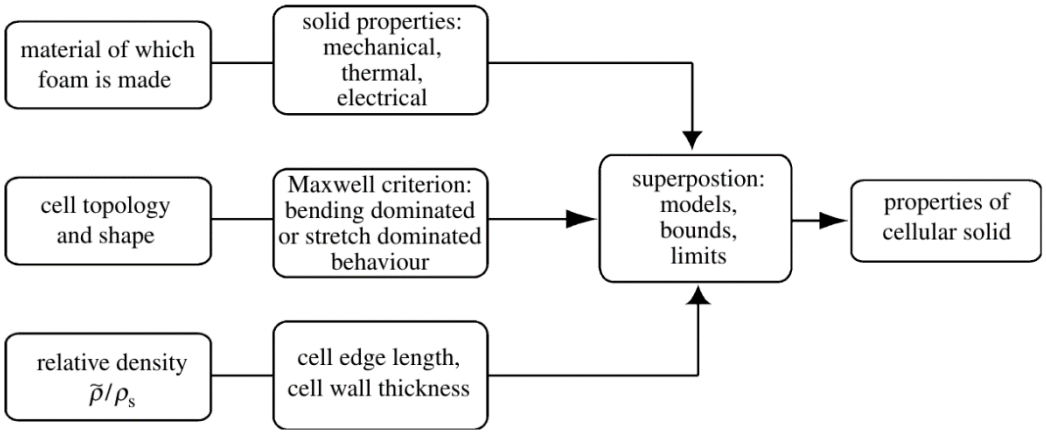

Foams: "solid – air hybrids"

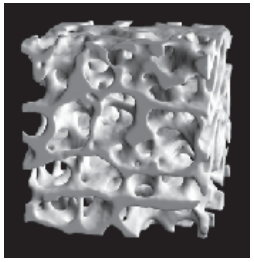

Ceramic foam

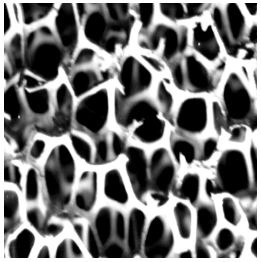

Metal foam

Properties of cellular materials depend on:

- **Material** of the cell wall
- Cell **topology**
- **Relative density** $\tilde{\rho}/\rho_s$

Mechanical behaviour of cellular materials

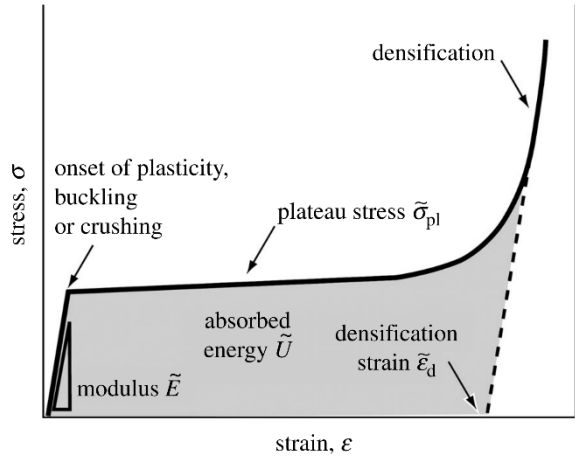

Figure 4. A stress–strain curve of a cellular solid, showing the important parameters.

Work $\tilde{U}$ done in compressing an open-cell foam is absorbed by:

- elastic buckling
- plastic yielding
- brittle crushing of cell walls

Energy absorption per unit volume:

$$\tilde{U} = \int_0^{\varepsilon} \sigma(\varepsilon)\, d\varepsilon$$

Question to ask:

What is the intended function of a material?

Bending- vs. stretch-dominated structures

Kelvin foam

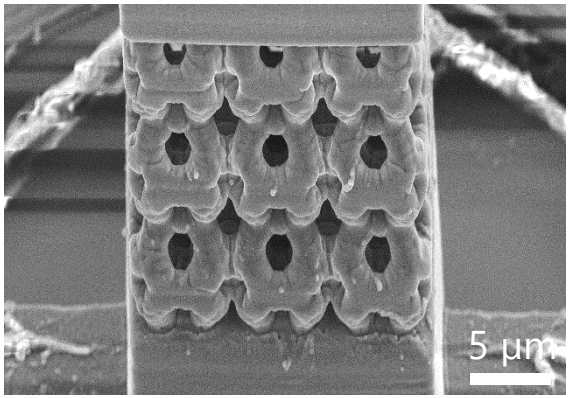

Most foams are bending-dominated

Stretch-dominated structures typified by a fully triangulated lattice

Dimensional methods to approximate scaling laws

Octet truss

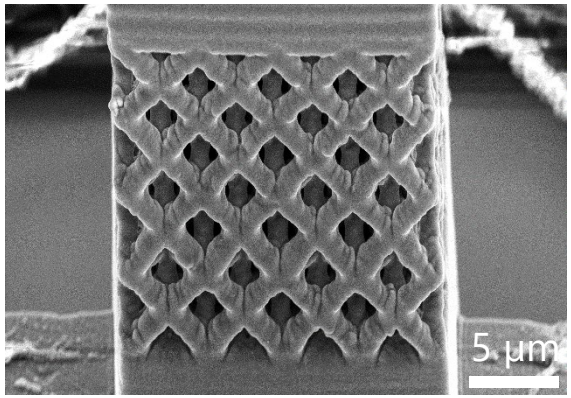

Bending-dominated structures

~10x increase in stiffness at $\tilde{\rho}/\rho_s$ = const.

Stretch-dominated structures

Low structural efficiency

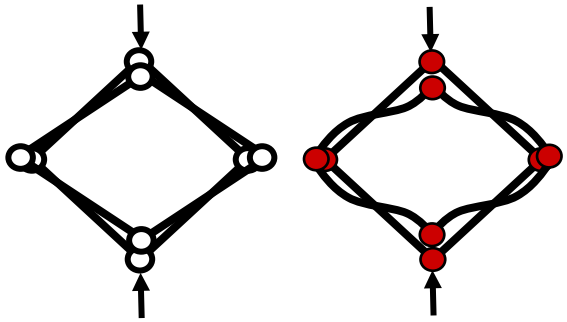

High structural efficiency

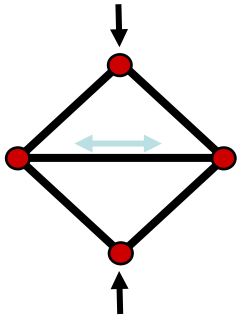

Bending-dominated structures

Idealised undeformed cell

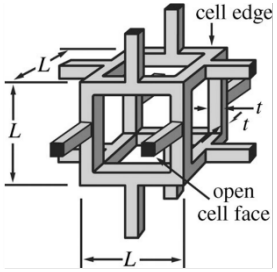

L: Unit cell length
t: Strut width

Relative density: $\frac{\rho}{\rho_s} \propto \left(\frac{t}{L}\right)^2$

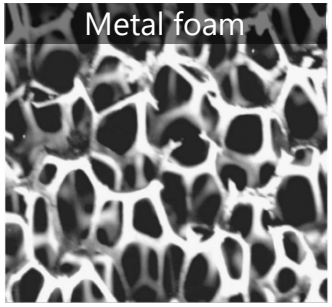

Idealised deformed cell

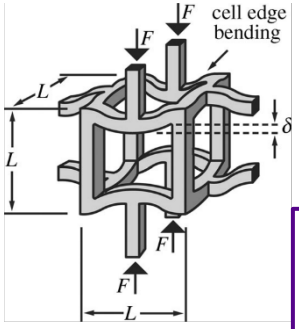

$$F \propto \sigma L^2$$

$$\delta \propto \frac{FL^3}{E_s I}$$

$$\frac{\tilde{E}}{E_s} \propto \left(\frac{\tilde{\rho}}{\rho_s}\right)^2$$

Uniaxial force on cell edges

↓

Deflection of bended beams

$\tilde{E}$: Modulus of foam
E: Modulus of solid

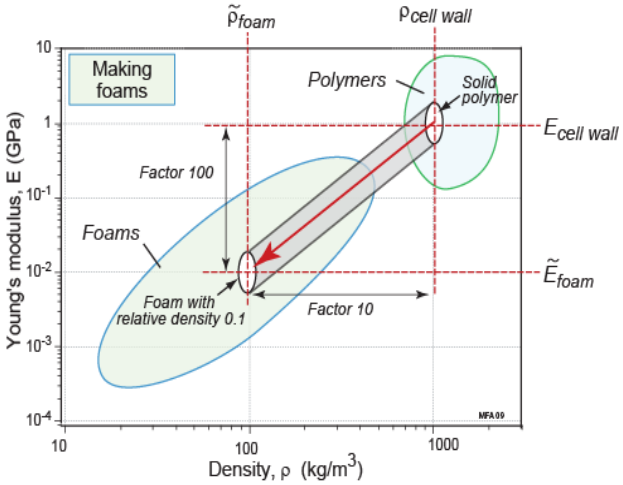

Collapse of bending-dominated structures

Collapse load and plateau stress of ductile materials by plastic bending

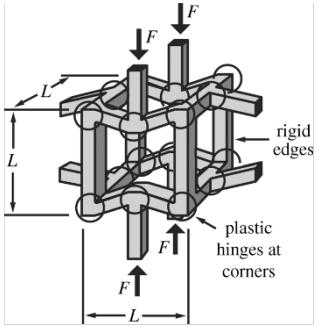

$$M_{\mathrm{f}} = \frac{\sigma_{\mathrm{y,s}} t^3}{4}$$

Cell walls yield when reaching fully plastic moment M_f; yield strength $\sigma_{y,s}$ of solid

$$\frac{\tilde{\sigma}_{\mathrm{pl}}}{\sigma_{\mathrm{y,s}}} \propto \left(\frac{\tilde{\rho}}{\rho_{\mathrm{s}}}\right)^{3/2}$$

Failure strength or plateau stress $\tilde{\sigma}_{pl}$ of solid

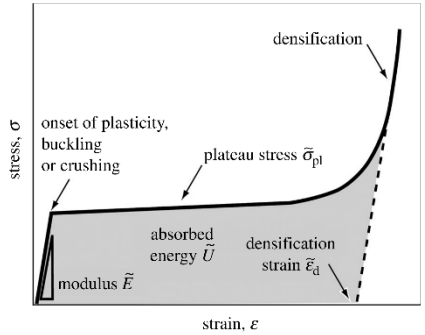

Elastomeric foams collapse by elastic buckling

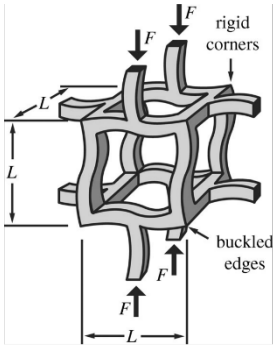

$$F_{\mathrm{b}} \propto \frac{E_{\mathrm{s}} I}{L^2} \propto \frac{E_{\mathrm{s}} t^4}{L^2}$$

Euler buckling load

$$\frac{\tilde{\sigma}_{\mathrm{el}}}{E_{\mathrm{s}}} \propto \left(\frac{\tilde{\rho}}{\rho_{\mathrm{s}}}\right)^2$$

Critical stress for elastic buckling

Brittle foams collapse by cell wall fracture

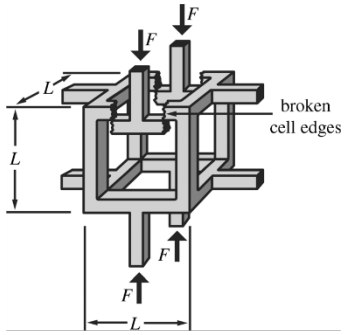

$$\frac{\tilde{\sigma}_{\mathrm{cr}}}{\sigma_{\mathrm{MOR}}} \propto \left(\frac{\tilde{\rho}}{\rho_{\mathrm{s}}}\right)^{3/2}$$

$\tilde{\sigma}_{cr}$: crushing stress
MOR: modulus of rupture

Maxwell's stability criterion – Bending- vs. stretch dominated

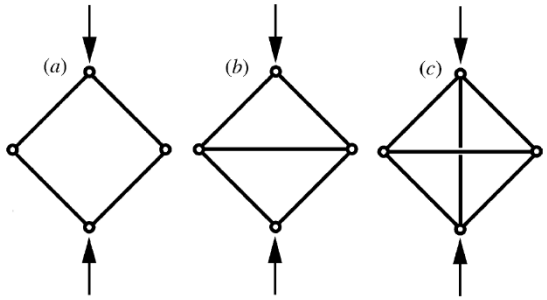

Figure 9. The pin-jointed frame at (*a*) folds up when loaded—it is a mechanism. If its joints are welded together, the struts bend (as in figure 5)—it becomes a *bending-dominated structure*. The triangulated frame at (*b*) is stiff when loaded because the transverse strut carries tension—it is a *stretch-dominated structure*. The frame at (*c*) is over-constrained; if the horizontal bar is shortened the vertical one is put into tension even when no external loads are applied (giving a state of self-stress).

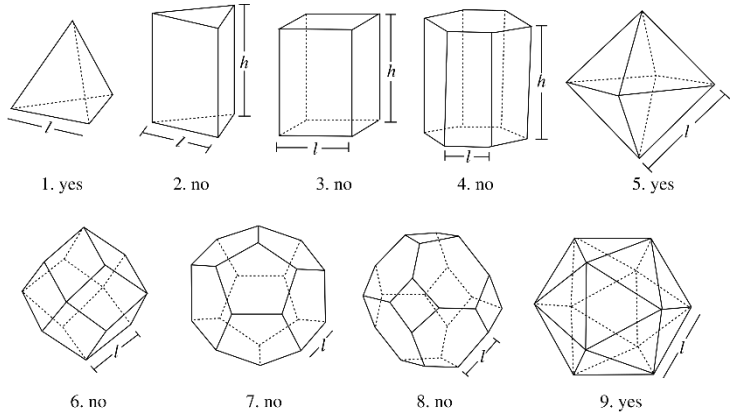

Figure 10. Polyhedral cells. Those that are space filling (numbers 2 4, 6 and 8) all have $M<0$, meaning that they are bending-dominated structures.

Pin-jointed frame with *b* struts and *j* frictionless joints:

$$M = b - 2j + 3 = 0$$ **2D**

$$M = b - 3j + 6 = 0$$ **3D**

$$M = b - 3j + 6 = s - m$$ **3D – generalised** (Calladine 1983)

M<0: Bending-dominated structures (frame is a mechanism; rotation is prevented; members bend)

M≥0: Stretch-dominated structures (at M=0, frame ceases to be a mechanism; members carry tension or compression)

Stretch-dominated structures

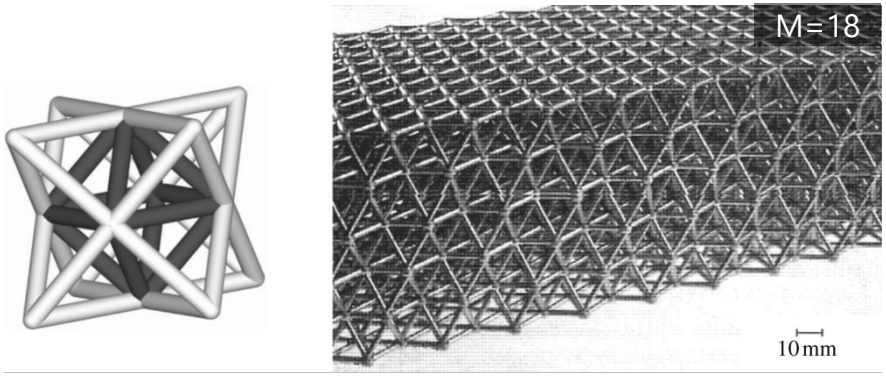

Figure 11. A micro-truss structure with $M>0$, together with its unit cell.

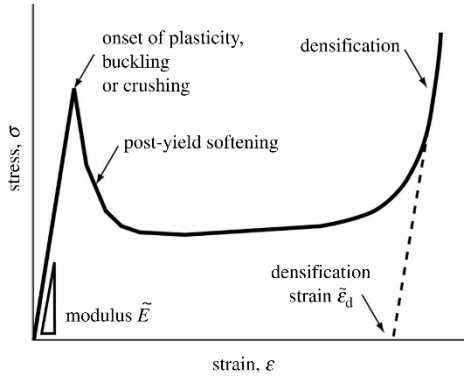

Figure 12. A schematic stress–strain curve for a stretch-dominated structure. It has high stiffness and high initial strength, but can show post-yield softening.

$$\frac{\tilde{E}}{E_s} \approx \frac{1}{3}\left(\frac{\tilde{\rho}}{\rho_s}\right)$$ Stretch-dominated behaviour

$$\frac{\tilde{\sigma}_{el}}{E_s} \propto \left(\frac{\tilde{\rho}}{\rho_s}\right)^2$$ Plastic-stretch-dominated behaviour

$$\frac{\tilde{\sigma}_{cr}}{\sigma_{cr,s}} \propto \left(\frac{\tilde{\rho}}{\rho_s}\right)$$ Buckling-dominated behaviour

$$\frac{\tilde{\sigma}_{pl}}{\sigma_{y,s}} \approx \frac{1}{3}\left(\frac{\tilde{\rho}}{\rho_s}\right)$$ Stretch-fracture-dominated behaviour

Ashby, *Phil. Trans. R. Soc. A*, 364, 15–30. 2006.

Bending- vs. stretch-dominated lattices – Specific properties

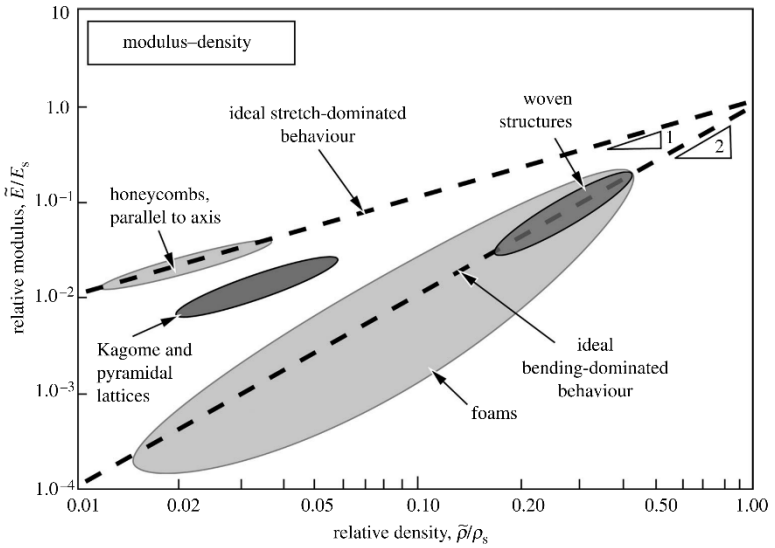

Figure 13. Relative modulus plotted against relative density on logarithmic scales for cellular structures with alternative topologies. Bending-dominated structures lie along a trajectory of slope 2; stretch-dominated structures along a line of slope 1.

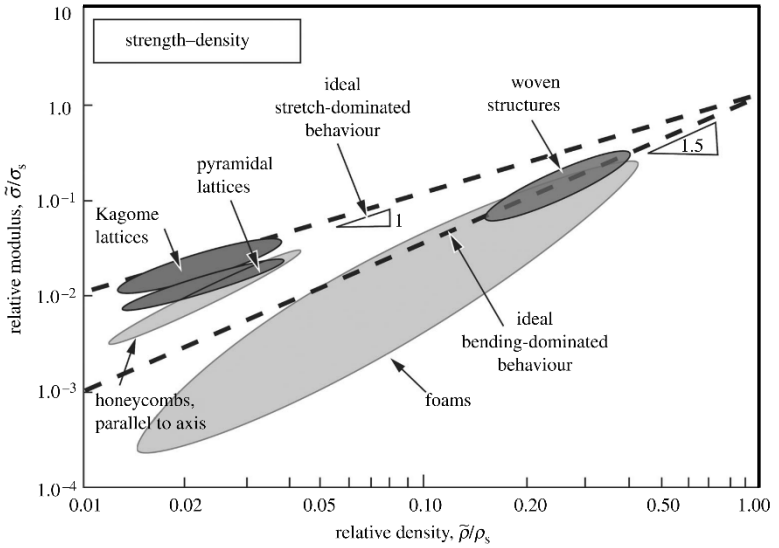

Figure 14. Relative strength plotted against relative density on logarithmic scales for cellular structures with alternative topologies. Bending-dominated structures lie along a trajectory of slope 1.5; stretch-dominated structures along a line of slope 1.

Ashby, *Phil. Trans. R. Soc. A*, 364, 15–30. 2006.

Densification

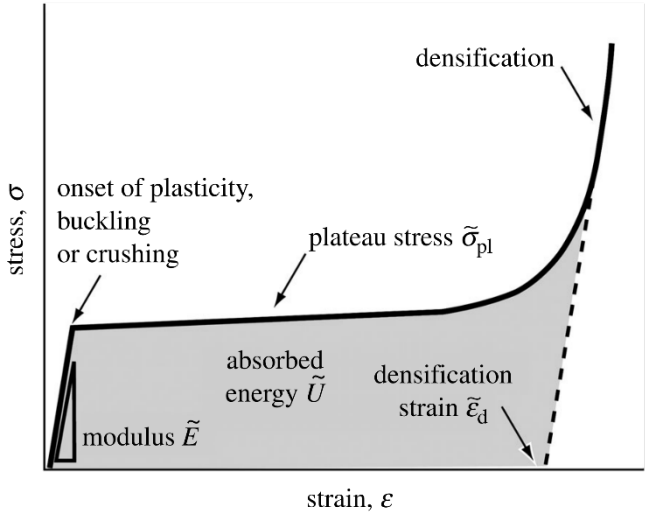

Energy absorption per unit volume: $\tilde{U} = \int_0^{\varepsilon} \sigma(\varepsilon)\, d\varepsilon$

Next: Poll Everywhere

Densification is a purely geometric effect: Opposite sides of the cells are forced into contact and further bending or buckling are not possible.

Strain-induced increase in relative density

$$\tilde{\varepsilon}_d = 1 - \left(\frac{\tilde{\rho}}{\rho_s}\right) \Big/ \left(\frac{\rho_{crit}}{\rho_s}\right)$$ Densification strain

ρ_{crit}/ρ_s Relative density at which the structure locks up

$\rho_{crit}/\rho_s \approx 0.6$ Experimental found value for lock-up density

$\tilde{U} \approx \tilde{\sigma}_{pl}\tilde{\varepsilon}_d$ Useful energy than can be absorbed by foams that protect against impact

Long flat plateau of σ(ε)- curve for cushioning and packaging materials.

Energy-absorption mechanisms

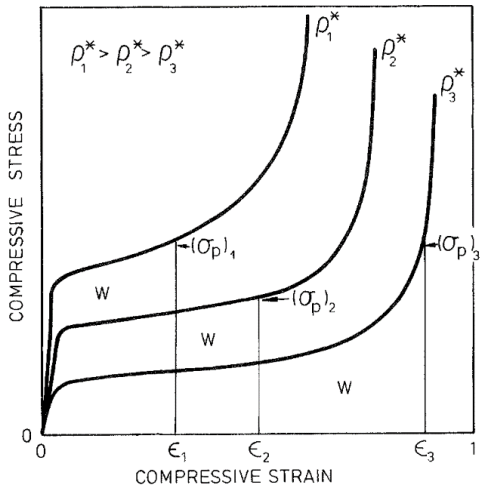

Peak stresses in foams with:

- different densities
- absorbing the same energy

Work W done in compressing an open-cell foam is absorbed by:

- elastic buckling
- plastic yielding
- brittle crushing of the cell walls

Energy absorption per unit volume:

$$W = \int_0^{\varepsilon} \sigma(\varepsilon)\, d\varepsilon$$

Foam with density ρ_2 is the optimum since it absorbs the energy, W, at the lowest peak stress.

Red curve! ✓

Energy absorption diagrams - Optimising the choice of foam

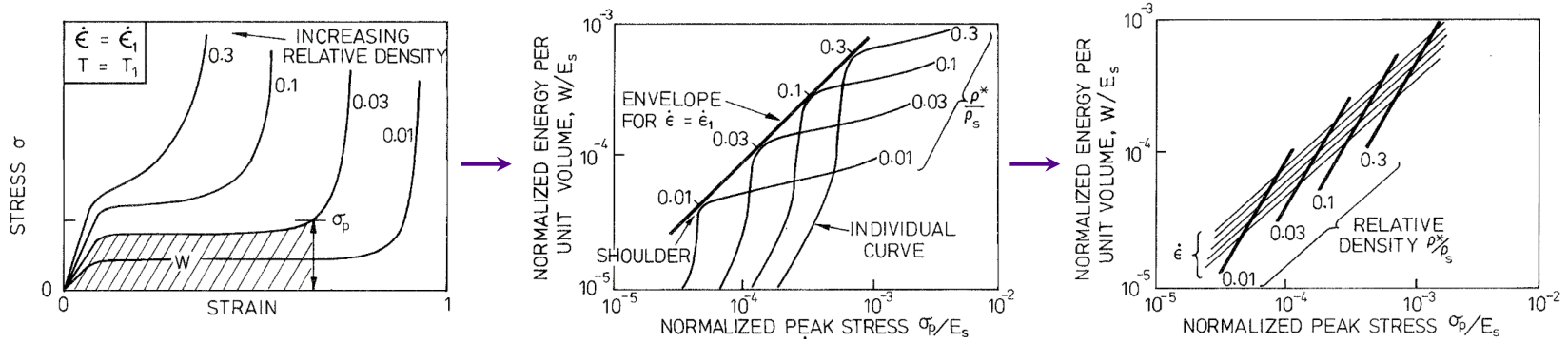

1 Stress-strain curves are measured at a single strain-rate.

2 The envelope which just touches each curve defines the optimum choice of foam at a given strain-rate.

3 The envelope is replotted on the same axes, and marked with density points. A family of created by repeating it for different curves. Then density points are connected.

The maps help in design and in the selection of the optimal foam for a given load-bearing or energy-absorbing application.

Maiti et al., *Acta Metallurgica*, 32(11), 1963-75, 1984; Gibson & Ashby. Cellular Solids: Structure and Properties. 2nd ed., 1997.

Plate based lattices – Towards the theoretical strength limit

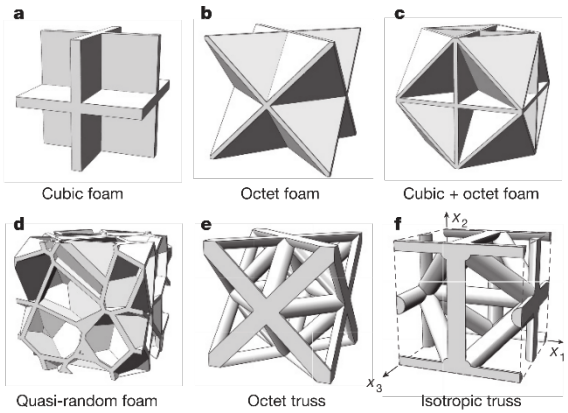

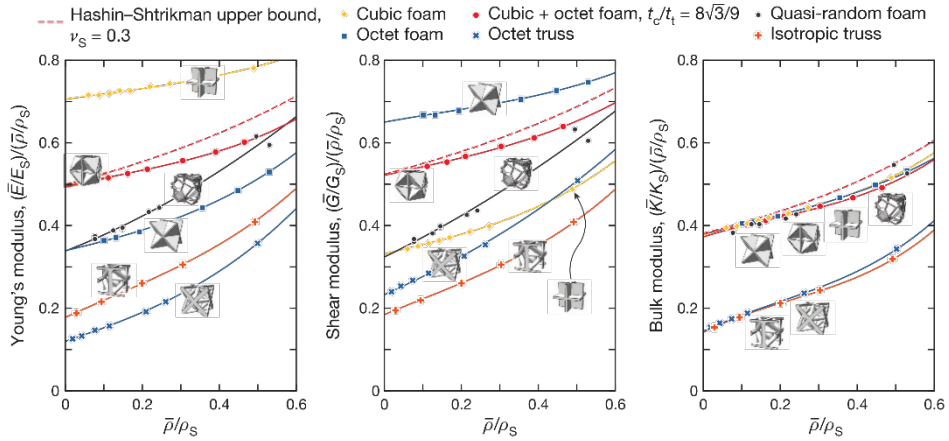

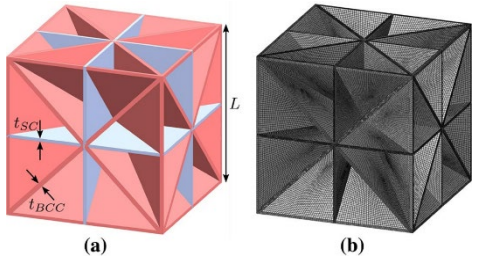

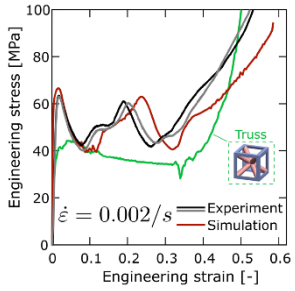

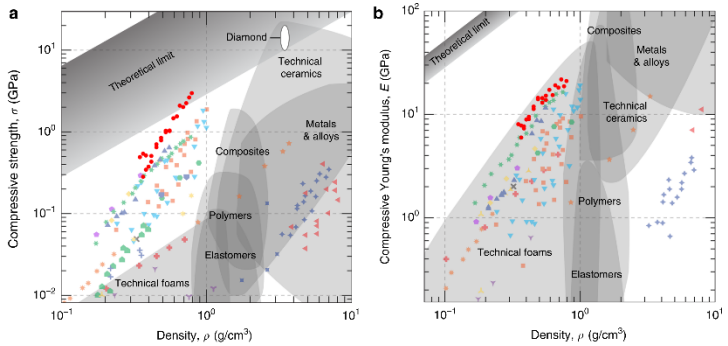

Berger et al., *Nature* (Letter), 534, 2017; Tancogne-Dejean et al., *Journal of Dynamic Behavior of Materials*, 5:361–375, 2019; Crook et al., *Nat Comm*, 11:1579, 2020

Surface based lattices

Strut based cellular structures

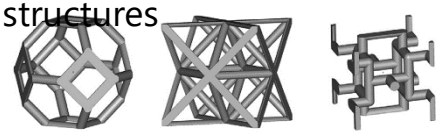

Sheet (surface) based cellular structures

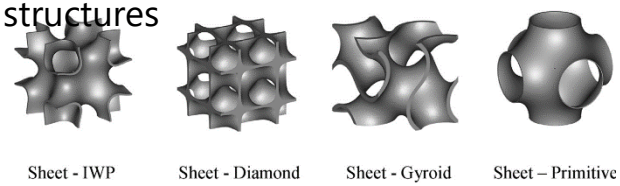

Lattice cell types based on periodic surface equations.

Triply periodic minimal surface (TPMS) structures with high surface-to-volume ratio

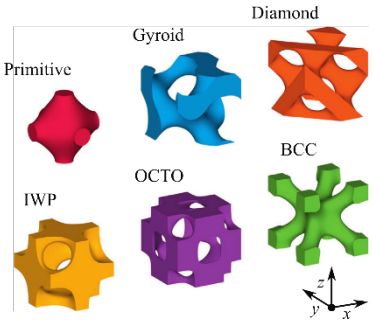

TPMS lattice structures with arbitrary numbers of cells and volume fractions by finding the U = 0 isosurface of the TPMS equations:

$$U_G = \cos(k_x x)\sin(k_y y) + \cos(k_y y)\sin(k_z z) + \cos(k_z z)\sin(k_x x) - t,$$

with periodicities:

$$k_i = 2\pi \frac{n_i}{L_i} \quad (\text{with } i = x, y, z)$$

Parameter t to control the volume fraction of the resulting lattice structure. Relationship is unique for each TPMS cell type.

Maskery et al., *Polymer*, 152, 62-71, 2018; Al-Ketan et al., *Additive Manufacturing*, 19, 167-183, 2018; Maskery et al., *Materials and Design*,155, 220-232, 2018.

Triply periodic minimal surface (TPMS) structures

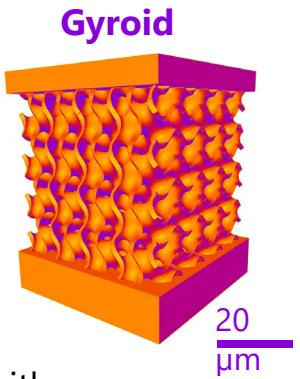

- Periodic surface structures in three principal directions
  - special class of surface with a mean curvature of zero at every point
  - metamaterials with smooth topologies
  - high porosity ⇨ low density and light-weight designs
  - non-self-intersecting ⇨ minimise potential stress concentration points
  - combination of multiple TPMS lattices possible ⇨ interpenetrating structures with unique optical, electrical and mechanical properties
- Complicated and highly symmetrical structures, with optimised physical properties for numerous applications
- Appearance in nature, e.g. *callophrys rubi* ⇨ gyroid biophotonic nanostructures
- Unexplored materials and architectures especially at the microscale
  (3D printing of TPMS Ni micro-lattices including characterisation not done so far)

Schwarz, 1890, *Gesammelte Mathematische Abhandlungen*, Springer, Berlin, Germany; Schoen, 1970, *NASA Technical Report* D-5541, NASA, USA; Corkery & Tyrode, 2017, *Royal Society Interface Focus 7*, 20160154; Khaderi et al., 2017, *Extreme Mechanics Letters* 10,15–23; Han & Che, 2018, *Advanced Materials*, 30, 1705708

Study: 3D 2PP printed polymeric TPMS geometries

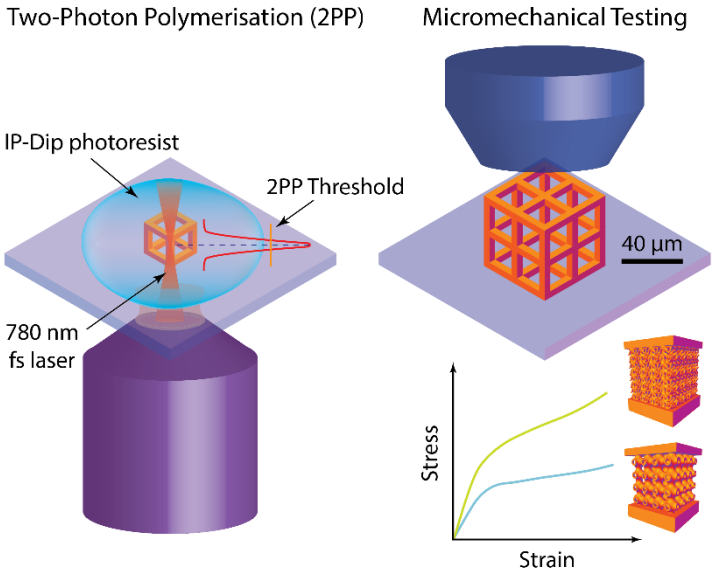

11 different TPMS geometries

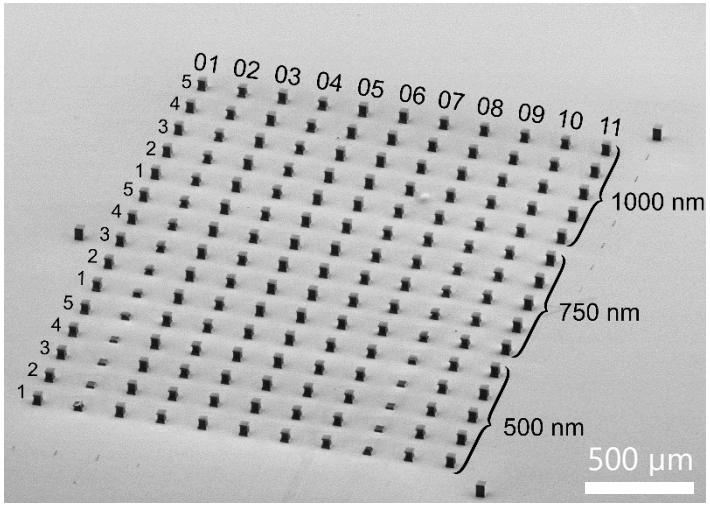

01: scell
02: pcell_vol
03: octoadj_vol
04: neovius
05: n26-2
06: n26-1
07: n14-2
08: n14-1
09: iwp_vol
10: gyroid-cube
11: frdadj_vol

Groetsch et al., 2022, in prep.

Variable TPMS geometries (4x4x4 unit cells, 40x40x40 µm^3) with different strut diameters

3D 2PP printability of structures regarding geometry and strut width (CAD vs. print)

Influence of relative density / porosity on the mechanical properties → **structural changes**

Highest specific strength and optimum energy absorption for a geometry and strut diameter

Polymeric TPMS geometries

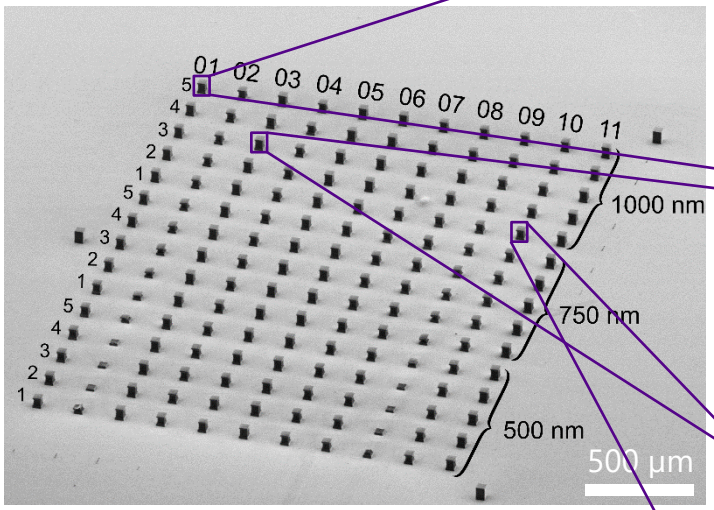

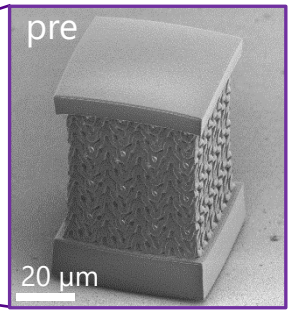

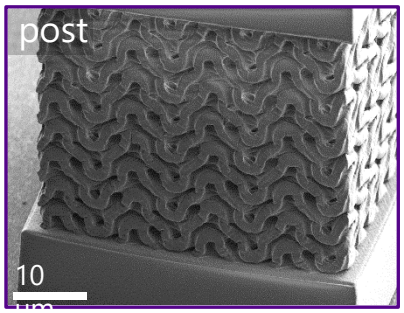

scell

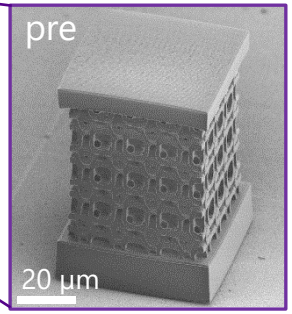

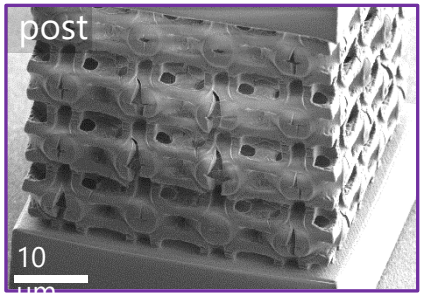

octoadj

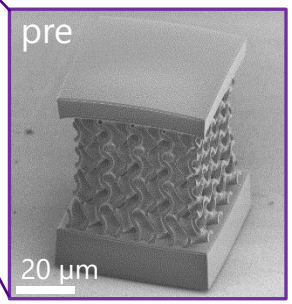

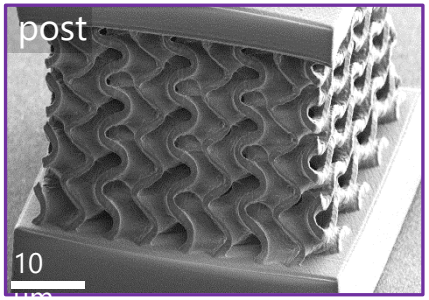

gyroid

Uniaxial compression with unloading segment in elastic region (N=66)

Ambient conditions (*ex situ*)

Strain rate of 10^{-3} s^{-1}

Maximum strain of 55%

CAD vs. 3D printing & stress-strain behaviour

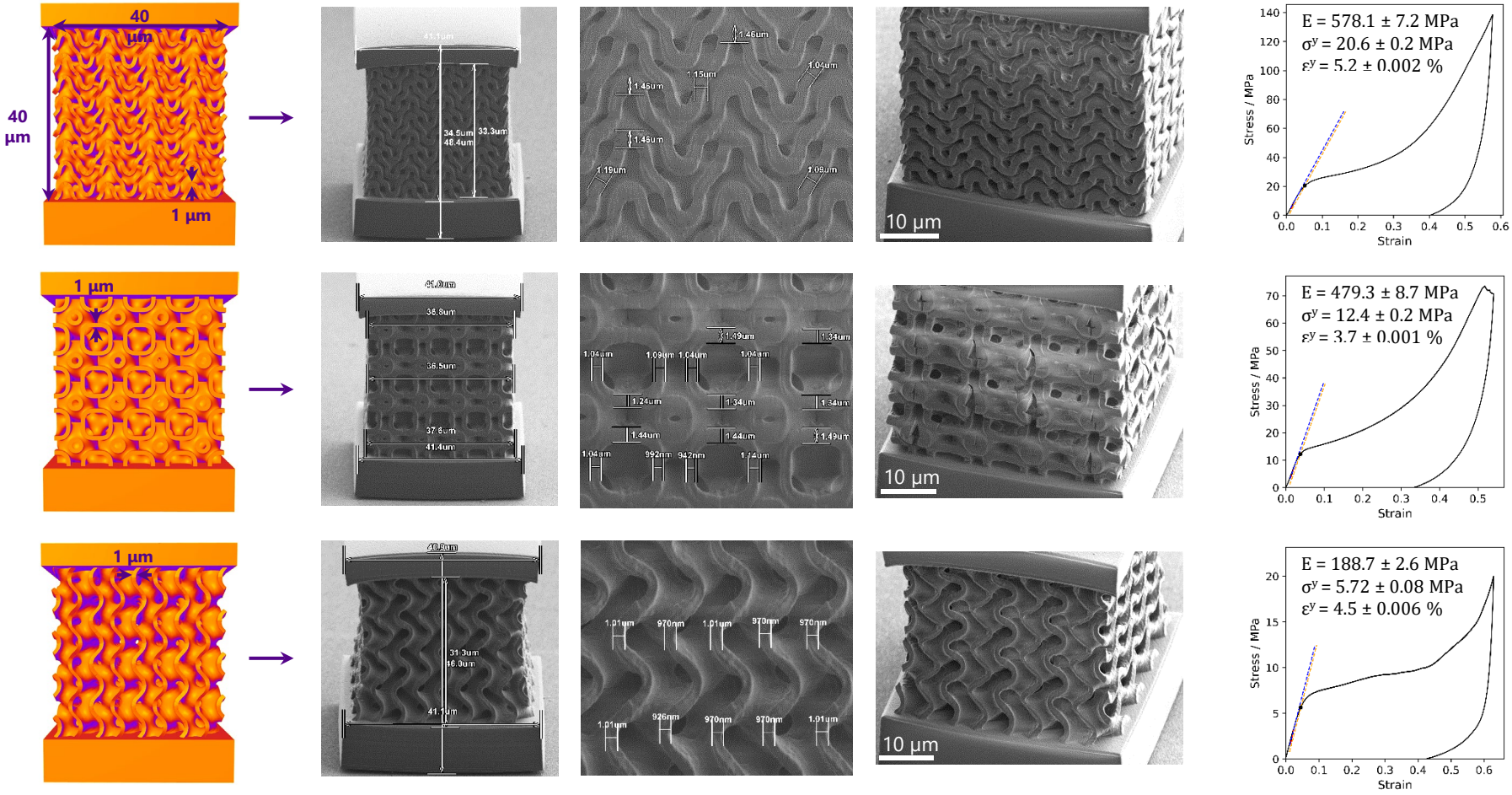

Enhancing strength – CNC reinforced nanocomposites

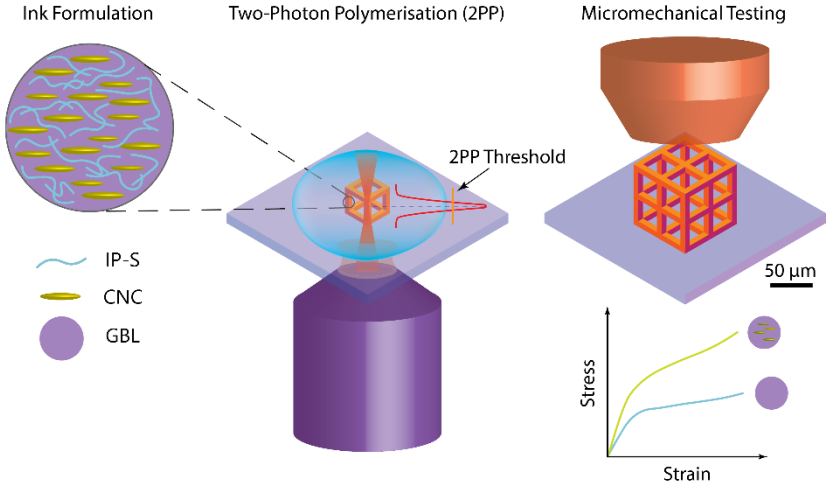

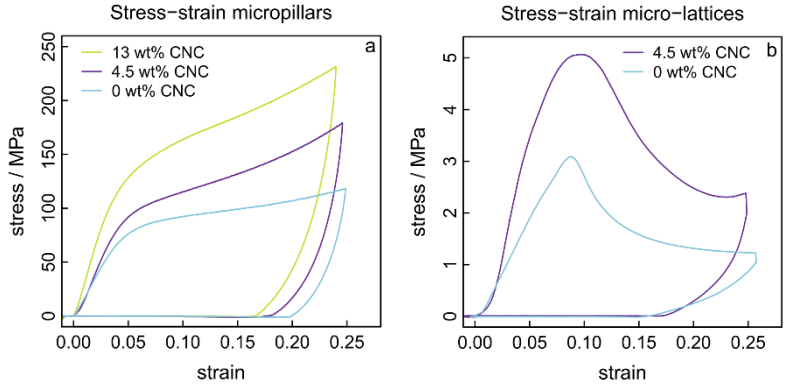

Bio-compatible nanocomposite ink using a sustainable reinforcement material:
Cellulose nanocrystals (CNC) from wood pulp

Up to 100% increase in yield stress and stiffness with 4.5 wt% CNC

First report of 3D printed microscale architectures using 2PP and CNC reinforced ink

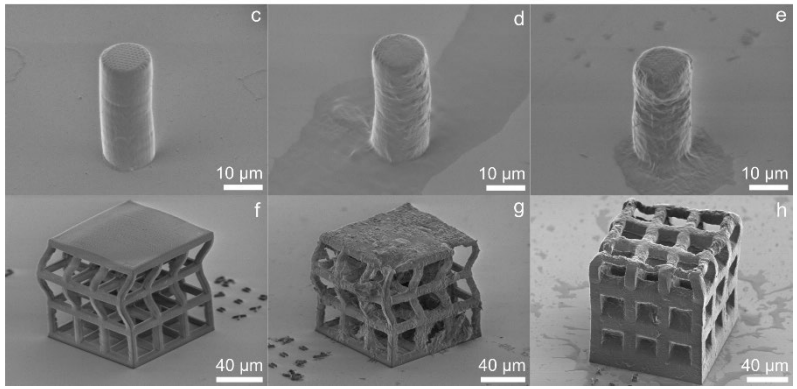

Groetsch et al., 2022, to be submitted

Enhanced strength of architectures – Hybrid systems

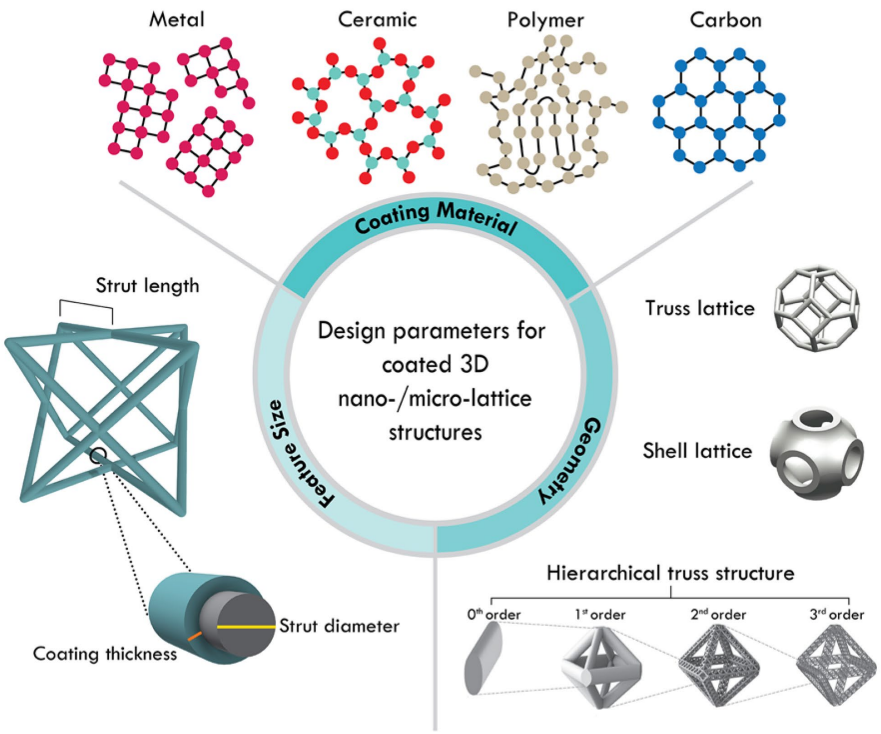

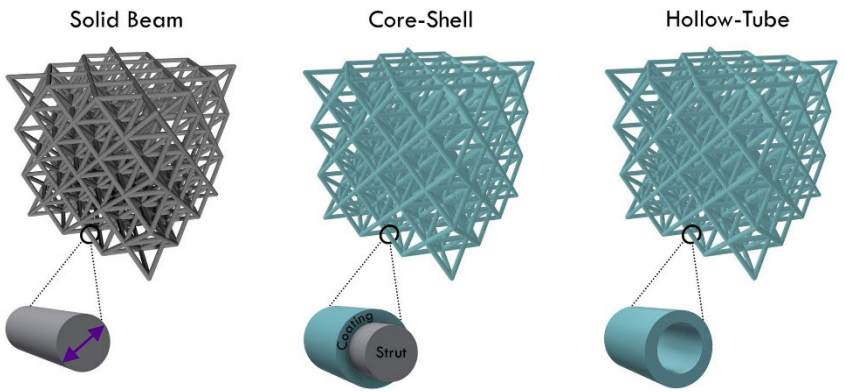

Exploit size effects and coating materials to achieve unique properties!

Adapted from: Garcia-Taormina et al. (2021) *J. Mater Res.*, 36(18), 3607-3627.

Material properties - Control by architecture and size effects

White areas = opportunity to expand the material property space

Cellular metals with tailored:

- Microstructure
- Geometrical constraints
- Design

Superposition of size effects

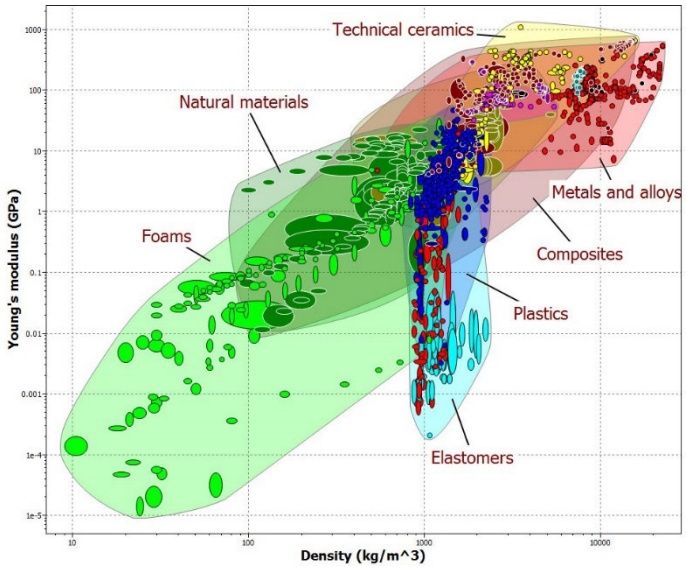

Case study: Control by architecture and size effects

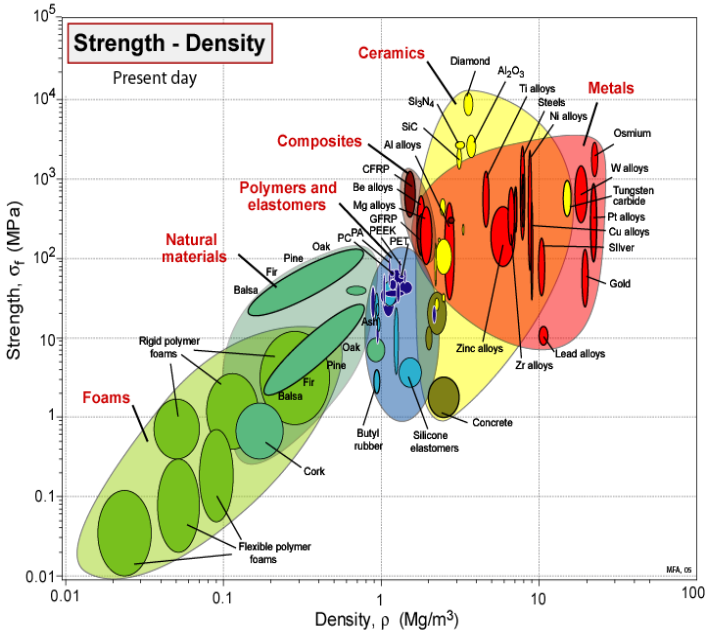

Fabrication of microlattices: architecture

- 3D laser lithography: 2 photon polymerization

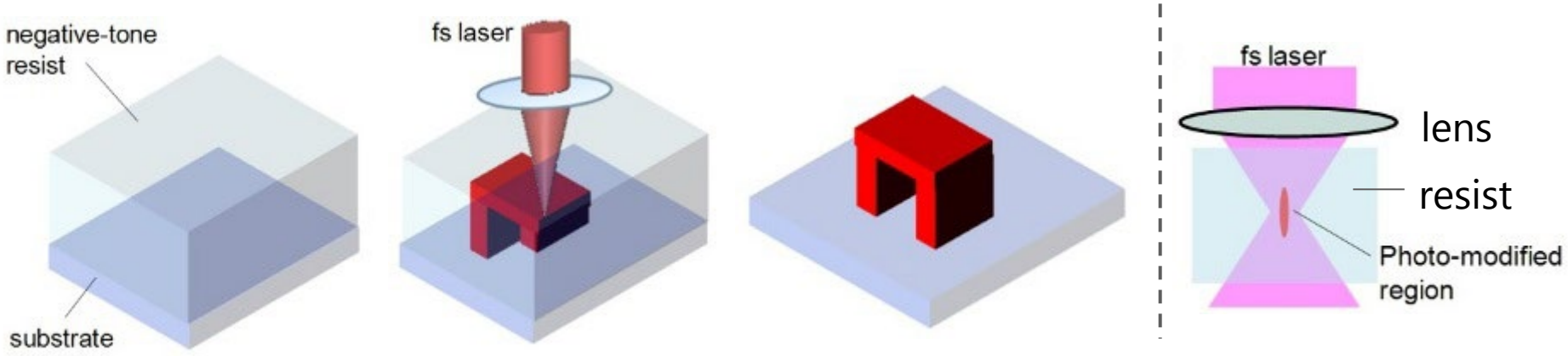

(Adapted from: Nishiyama and Hirata, 2010)

- Micro-architectures

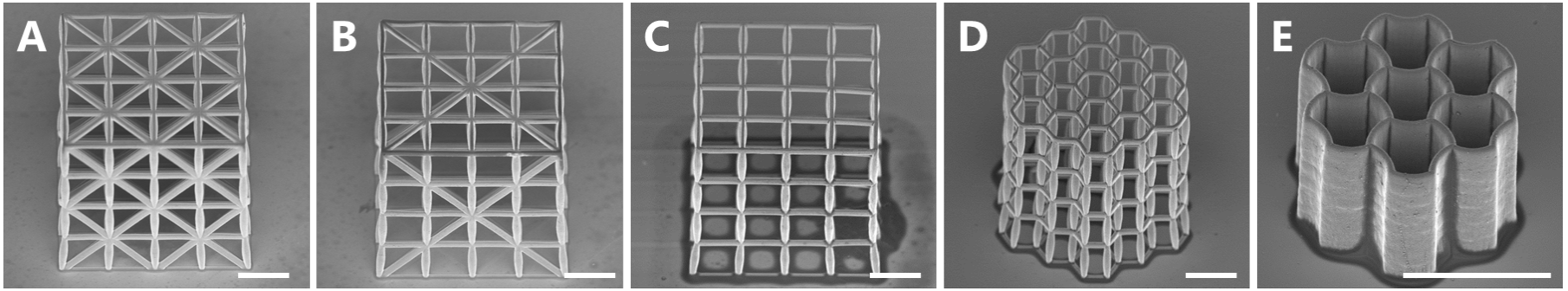

(Scale bars: 10 µm)

Coating of microlattices: size effect

NiB electroless deposition on polymer template

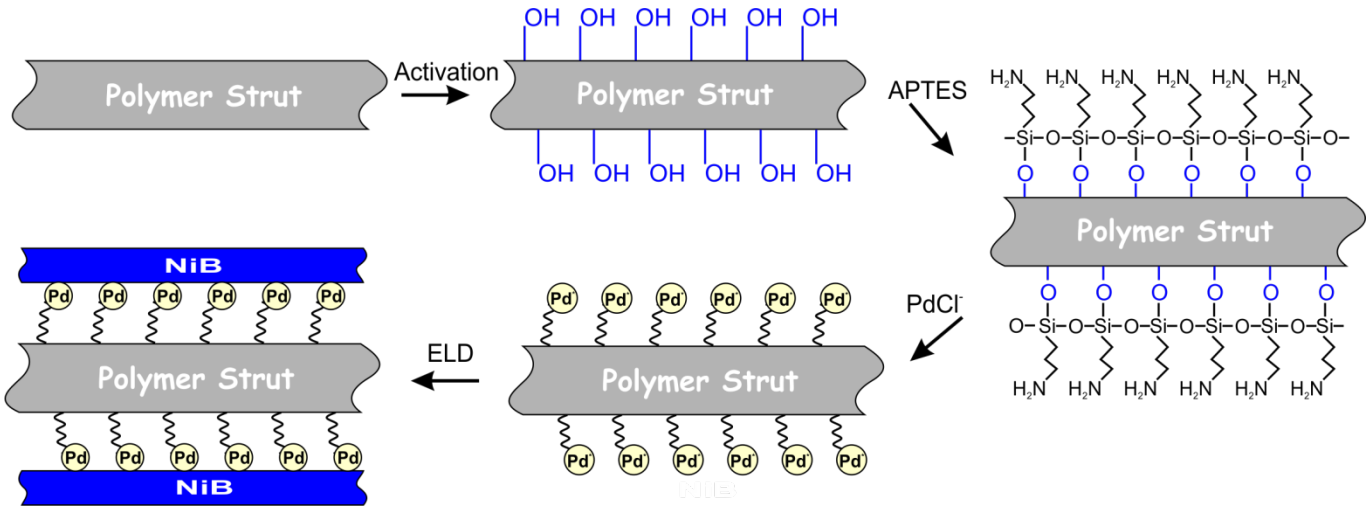

Deposition time controls NiB thickness

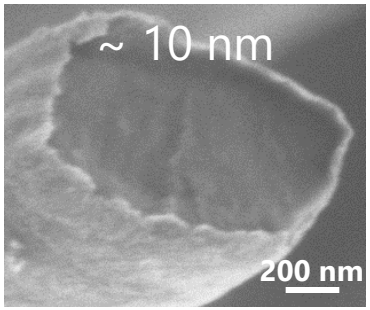

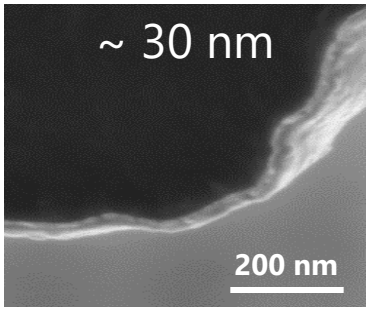

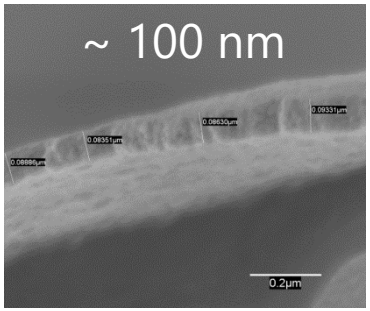

Effect of the NiB thickness

- *In situ* microcompression test

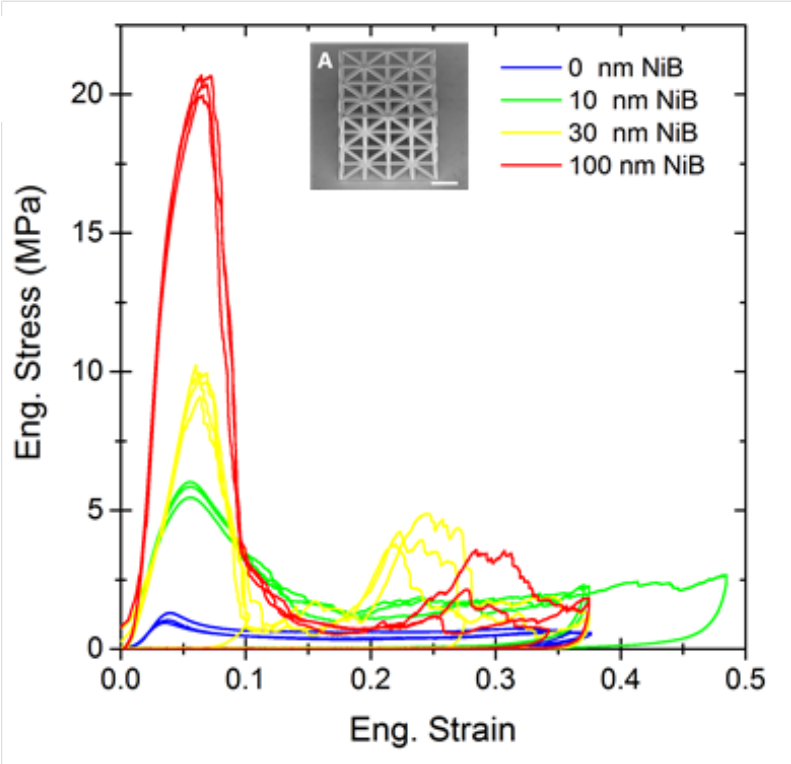

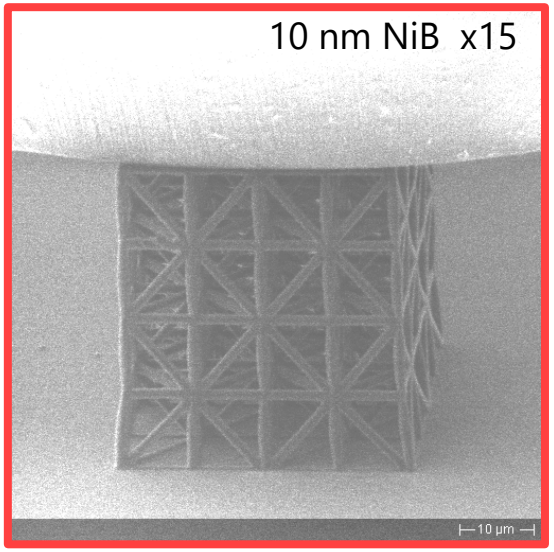

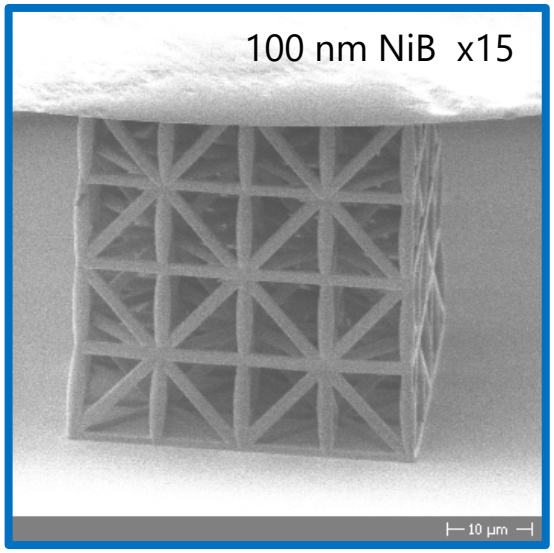

- 10 nm NiB: global failure of the structure via buckling and plastic deformation
- 100 nm NiB: brittle failure mechanism

Size effect and architecture

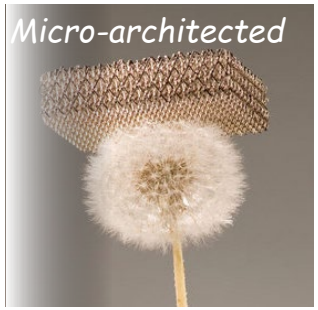

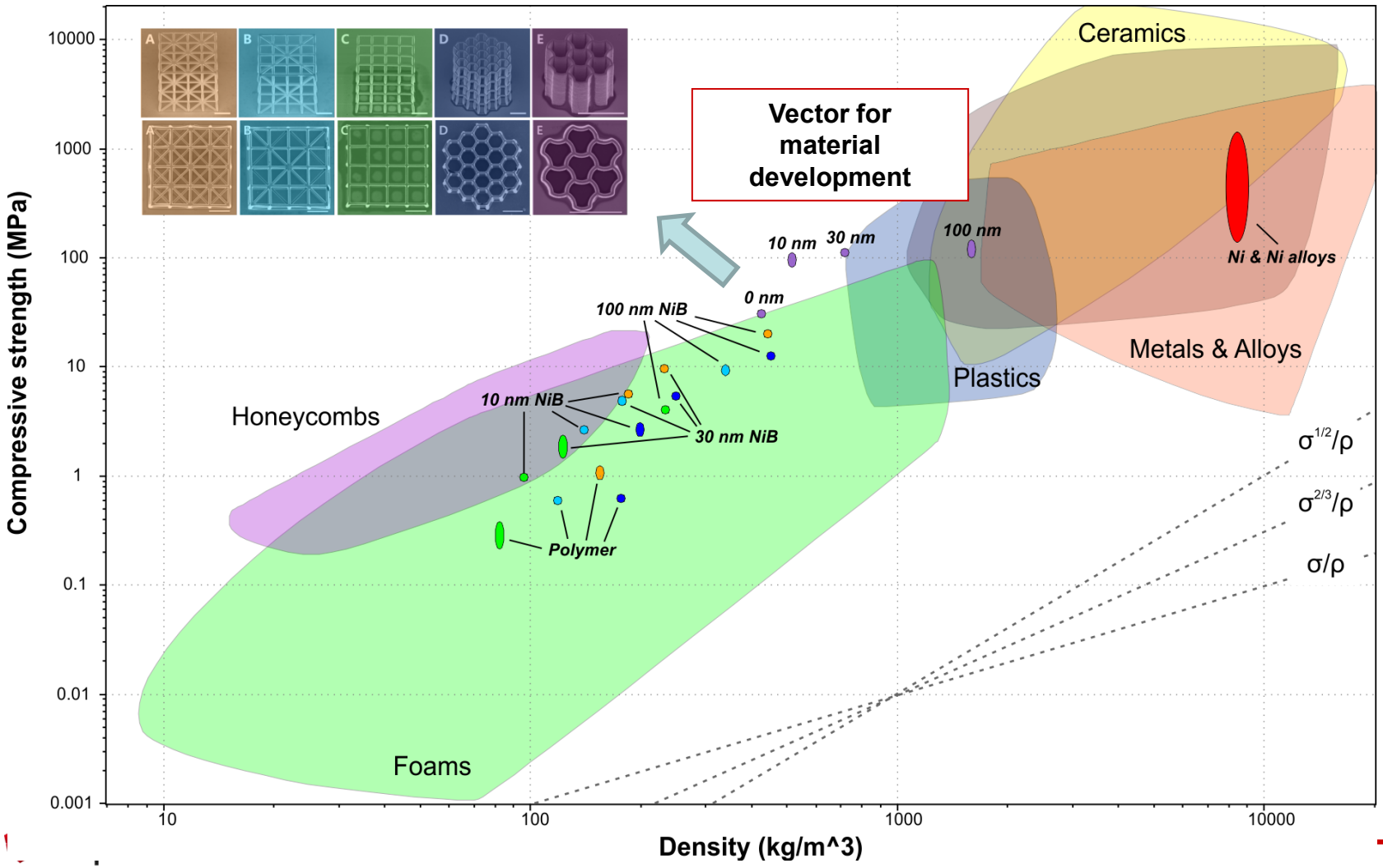

So what?

- **Multi-dimensional material-property space**
  - **Only part-filled** by monolithic materials
  - True of **mechanical, thermal, electrical, magnetic** and **optical** properties
- **Material development strategies**
  - **Classical** (classical alloy development, polymer chemistry….)
  - **"Nano" (sub-micron) scale** (exploiting scale-dependence of properties)
  - **Architecture & hybridisation**
- **The strategy:**
  - Map out the filled areas
  - Explore the ultimate boundaries
  - Explore ways of filling the empty space.
  - Hybrids, exploiting potential of novel configurations, have potential for this

Strain rate and temperature dependence

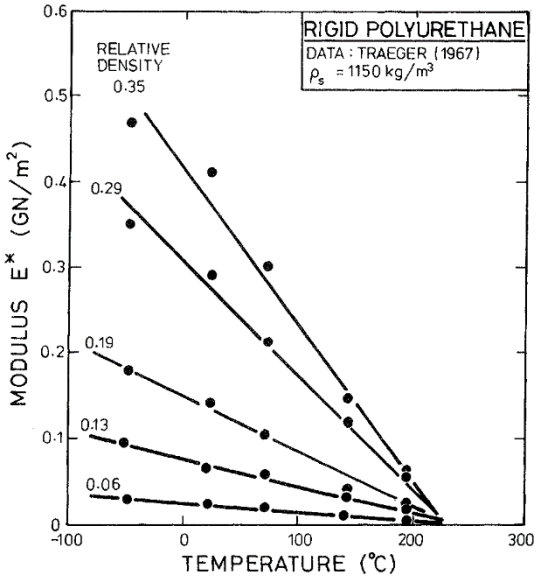

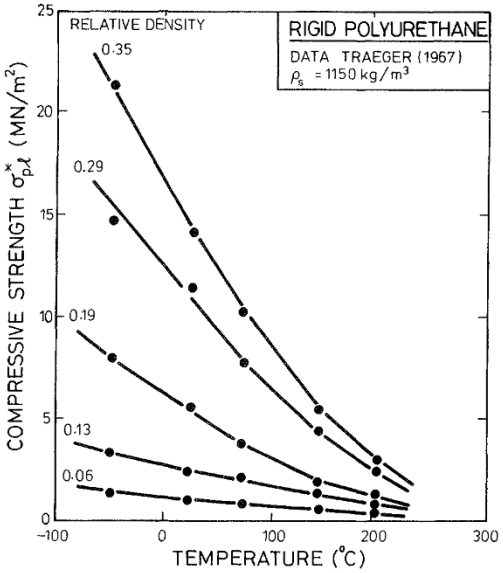

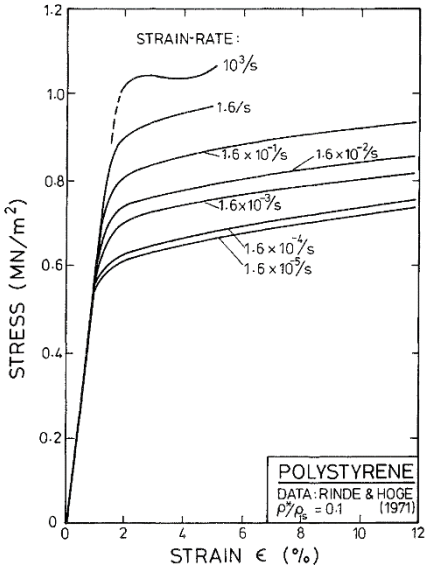

For polymers: $E_s = E_s^0\left(1 - \alpha_m \frac{T}{T_g}\right)$

For metals and ceramics: $E_s = E_s^0\left(1 - \alpha_m \frac{T}{T_m}\right)$

$$\dot{\epsilon} + \frac{E_{s2}}{\eta_s}\epsilon = \frac{1}{C_1(\rho^*/\rho_s)^2}\left(\frac{\dot{\sigma}}{E_{s1}} + \frac{\sigma}{\eta_s}\left(\frac{E_{s1}+E_{s2}}{E_{s1}}\right)\right)$$

Differential equation for viscoelastic deformation of an open-cell foam

Octet truss lattice – Quasi-static vs. high strain rates

Quasi-static strain rate – 0.001/s

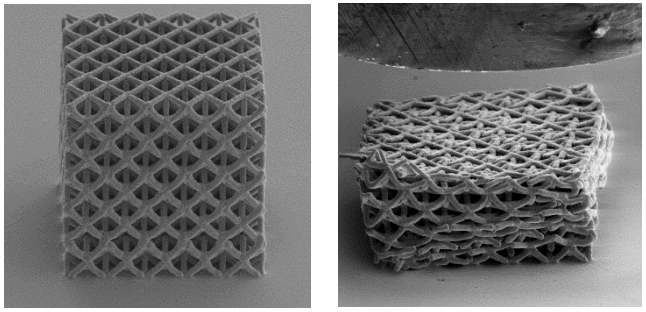

High strain rate – 45/s

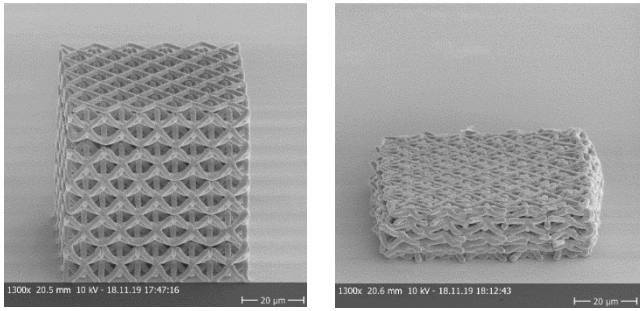

Ramachandramoorthy et al., 2022, in prep

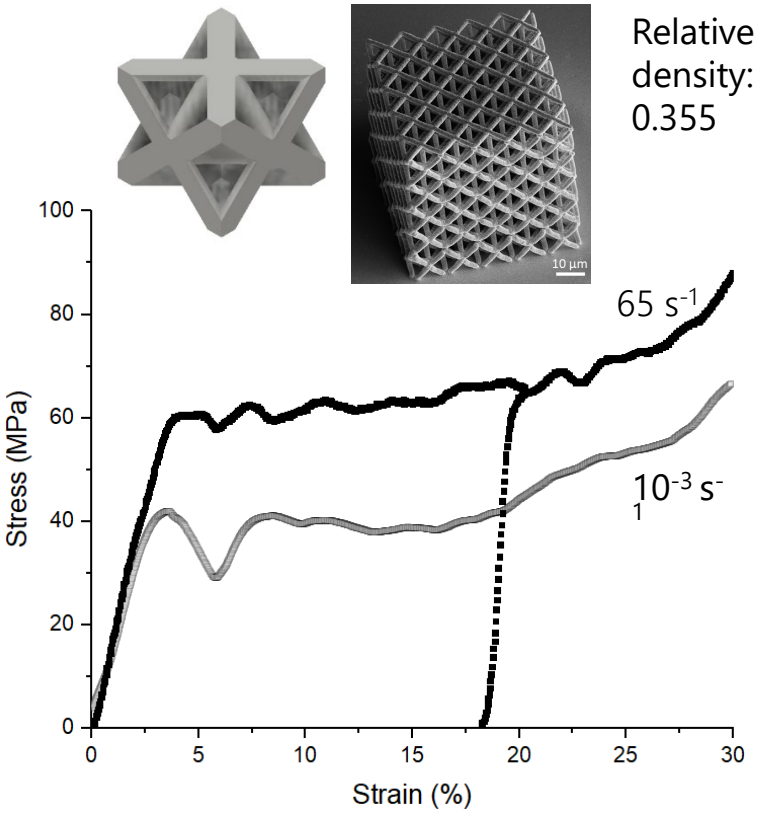

Increase in plateau stress at high strain rates – **20 MPa**

Summary


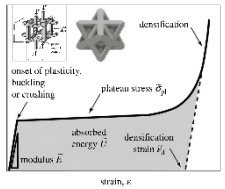

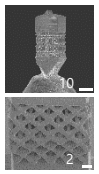
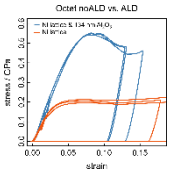

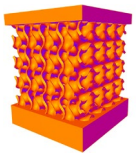

- Mechanical properties of cellular solids can be tailored to explore new realms in the material property space by choosing architecture and design parameters including size
- Design principles: Material of the cell wall, cell topology, relative density $\tilde{\rho}/\rho_s$
- Stretch-dominated lattices show a higher stiffness and structural efficiency than bending-dominated ones; classification via Maxwell's stability criterion
- Cellular solids collapse by plastic bending, elastic buckling or cell wall fracture
- Densification of cellular materials a purely geometric effect with a steep increase in stress
- Strut, plate and surface based lattices show different mechanical characteristics
- Strength of micro-architectures can be increased by material and structural changes
- Energy absorption diagrams can be used to optimise the design of cellular materials
- Strain rate and temperature dependence important to test *in operando* conditions
- Several studies on micro-lattices at Empa including synchrotron science at PSI